

Thesis (partial draft)

J. Divahar

November 10, 2021

Pending actions and discussions

<input type="checkbox"/> [2] TODO. AJR5: Justify these lengths (10^{-2} m, 10^3 m). cite xref	8
<input type="checkbox"/> [3] TODO. AJR5: cite evidence	8
<input type="checkbox"/> [4] TODO. AJR9: a few more cites?	9
<input type="checkbox"/> [5] TODO. Justify why they are small	155
<input type="checkbox"/> [6] TODO/update IC ref to a chap4 sec	263
<input type="checkbox"/> [8] TODO. Move this to the Chapter 1 to arouse some early interest for the reader.	275
<input type="checkbox"/> [10] TODO. Move this to the Chapter 1 to arouse some early interest for the reader.	315

Contents

1	Introduction	6
2	Patch schemes extend staggered grids to multiscale simulations	7
2.1	Introduction	7
2.2	Staggered patches of staggered micro-grid for multiscale simulation of waves	9
2.2.1	Staggered grids are best for full-domain numerical simulation of waves	10
2.2.2	Generalising the staggered grid to patch scheme multiscale simulation	12
2.2.3	Multi-layer edge nodes for higher order spatial derivatives	19
2.3	Patch-coupling connects the scales	21
2.3.1	Global spectral interpolation for patch coupling	22
2.3.2	A family of local polynomial interpolations for patch coupling	23
3	Patch schemes accurately simulate general linear waves	42
3.1	Introduction	42
3.2	Staggered patch schemes are accurate	45
3.2.1	Eigenvalue analysis of the PDEs	47
3.2.2	Eigenvalue analysis of staggered grid full-domain micro-scale system	49
3.2.3	Analytic eigenvalue analysis of staggered patch schemes	51
3.2.4	Computing numerical Jacobian of the staggered grid full-domain micro-scale system	59
3.2.5	Computing numerical Jacobian of the staggered patch schemes	60
3.2.6	Staggered patch schemes are accurate for macro-scale waves	61

3.3	A method of wavenumber-wise scale separation for patch scheme eigenvalues	85
3.4	Staggered patch schemes are not sensitive to numerical round-off errors	89
3.5	Staggered patch schemes are stable	99
3.5.1	Patch scheme stability requires geometric symmetry	100
3.5.2	Spectral staggered patch scheme is stable for different system parameters	102
3.5.3	The five staggered patch schemes are stable for different grid parameters	106
3.6	Staggered patch schemes are consistent	113
3.6.1	Spectral patch scheme is uniformly consistent without any dependence on the macro-grid interval . . .	116
3.6.2	The four polynomial patch schemes are consistent to the order of the polynomial interpolation	120
3.7	Large computational savings in staggered patch scheme time simulation	127
3.7.1	Staggered patch schemes compute only within a small fraction of the space in the full domain	128
3.7.2	Staggered patch schemes compute only for a small number of dynamical state variables	128
3.7.3	Computational complexity of the staggered patch schemes	129
3.7.4	Staggered patch schemes simulate macro-scale waves with small compute time	131
3.7.5	Staggered patch scheme time simulations of general linear waves	138
4	Patch schemes accurately simulate viscous shallow water flows	151
4.1	Introduction	151
4.1.1	Non-dimensionalise viscous shallow water PDEs to keep same domain size	153
4.1.2	Full-domain micro-scale system and staggered patch schemes for viscous shallow water PDEs	158
4.1.3	Selection of relevant parameter regime for patch scheme exploration	166
4.2	Staggered patch schemes are accurate	167
4.2.1	Eigenvalue analysis of the PDEs	170
4.2.2	Eigenvalue analysis of staggered grid full-domain micro-scale system	172
4.2.3	Analytic eigenvalue analysis of staggered patch schemes	175

4.2.4	Computing numerical Jacobian of the staggered grid full-domain micro-scale system	181
4.2.5	Computing numerical Jacobian of the staggered patch schemes	183
4.2.6	Staggered patch schemes are accurate for macro-scale waves	184
4.3	Staggered patch schemes are not sensitive to numerical round-off errors	202
4.4	Staggered patch schemes are not artificially unstable for appropriate patch grids	211
4.4.1	Spectral staggered patch scheme is not artificially unstable for different system parameters	213
4.4.2	Maximum artificial instability is due to micro-scale modes modulated over smallest macro-scale waves .	225
4.4.3	The five staggered patch schemes are not artificially unstable for different grid parameters	235
4.5	Staggered patch schemes are consistent	241
4.5.1	Spectral patch scheme is uniformly consistent without any dependence on the macro-grid interval . . .	243
4.5.2	The four polynomial patch schemes are consistent to the order of the polynomial interpolation	250
4.6	Staggered patch schemes are frame invariant	256
4.7	Large computational savings in patch scheme time simulation	259
4.7.1	Staggered patch schemes compute only for a small number of dynamical state variables over small space	259
4.7.2	Computational complexity of the staggered patch schemes	261
4.7.3	Staggered patch schemes simulate macro-scale waves with small compute time	263
4.7.4	Staggered patch scheme time simulations of viscous shallow water flows	272
4.7.5	Some practical issues in staggered patch scheme simulations of viscous shallow water flows	276
5	Patch schemes accurately simulate turbulent shallow water flows over large space	283
5.1	Introduction	283
5.1.1	Non-dimensionalise turbulent shallow water PDEs to keep same domain size	284
5.1.2	Full-domain micro-scale system and staggered patch schemes for turbulent shallow water PDEs	287

5.1.3	Selection of relevant parameter regime for patch scheme exploration	290
5.2	Staggered patch schemes are accurate	291
5.2.1	Eigenvalue analysis of the PDEs	293
5.2.2	Eigenvalue analysis of staggered grid full-domain micro-scale system	294
5.2.3	Analytic eigenvalue analysis of staggered patch schemes	295
5.2.4	Staggered patch schemes are accurate for macro-scale waves	298
5.3	Staggered patch schemes are not artificially unstable for appropriate patch grids	307
5.4	Staggered patch schemes are consistent	311
5.5	Staggered patch scheme time simulations of turbulent shallow water flows	312
6	Conclusion	317

Chapter 1

Introduction

TODO

Chapter 2

Patch schemes extend staggered grids to multiscale simulations

2.1 Introduction

[TODO/update-ajr-w093]

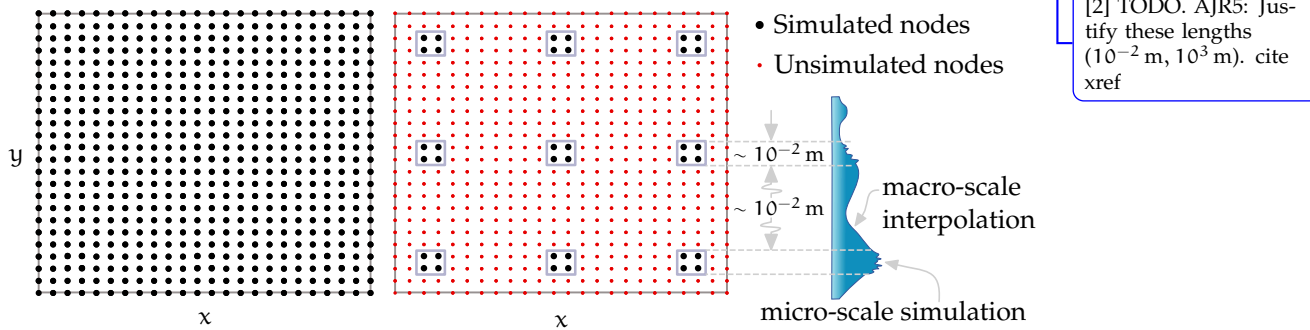
1. Always remember: EVERY paragraph in the Introduction MUST EXPLICITLY refer to the work within the title—often with cross-reference.
2. This Introduction needs: wave discussion; 2D discussion; scope of coupling discussion; results discussion. Include reminders of these, and later fill in details.

[TODO/update-after-body]

- Update after completing the body
- Needs some graphic wave simulation early to excite the reader.
- Somewhere when following terms appear first, typeset them within quotes with additional information in footnote
 - ... “*full-domain simulation*” (the usual detailed computation over whole domain) ...
- Introduce usual patch scheme (non staggered grid)

Many multiscale modelling methods (Welsh et al. 2018; Grooms and Julien 2018; Emereuwa 2020) aim to accurately model macro-scale physics

Figure 2.1.1: Schematic of a typical multiscale modelling by simulating only within small coupled regions in the domain. Smooth waves on the right, over the unsimulated nodes, is interpolated over the large space without detailed simulation.



by simulating only within small coupled regions in the domain as depicted in Fig. 2.1.1. The unsimulated nodes corresponding to the intermediate scales are interpolated from the small number of simulated nodes that are located sparsely over large space achieving large computational savings. Not simulating the physics at intermediate scales is not an issue in many application areas (geophysical fluid dynamics, food drying, energy storage systems, etc.) as generally such unsimulated scales are adequately predicted by interpolating key properties of the simulated nodes.

The patch scheme is an emerging equation-free multiscale framework. The patch schemes perform detailed micro-scale simulations within small “patches” and couples the patches (“patch coupling”) via generic interpolation over the macro-scale space (Kevrekidis, Gear, and Hummer 2004; Kevrekidis and Samaey 2009; Hyman 2005). One can achieve arbitrarily high order of macro-scale consistency for patch schemes via appropriate high order interpolation for patch coupling (Roberts and Kevrekidis 2005; Roberts and Kevrekidis 2007).

- Patch schemes are “equation-free” as connecting the scales is done through generic interpolation instead of explicit equations as done in homogenisation and similar other multiscale methods; that is, there is no derived equation which describes the macro-scale model. The only information we obtain about the macro-scale model is computational data (Kevrekidis and Samaey 2009).
- Patch scheme, as a framework, is generally agnostic of the underlying micro-scale system; one can use as micro-scale mesh based model like finite difference, finite volume, finite element or its recent variant

of particle finite element (Franci et al. 2020), or meshless models like smoothed particle hydrodynamics, lattice–Boltzmann (Kevrekidis, Gear, Hyman, et al. 2003), Monte–Carlo, molecular dynamics, or agent based models.

[4] TODO. AJR9: a few more cites?

- So the patch scheme is a general framework with high flexibility for many different application domains and different kind of problems [TODO/cite].

For grid based discrete models of continuum problems (e.g., numerically solving PDEs over a finite grid of discrete points in space and time), the patches contain interior nodes and the patch coupling interpolates the values of edge nodes from the centre values of neighbouring patches (Fig. 2.2.2 of §2.2.2). Patch schemes have been developed and studied for various dissipative systems... [TODO/continue]

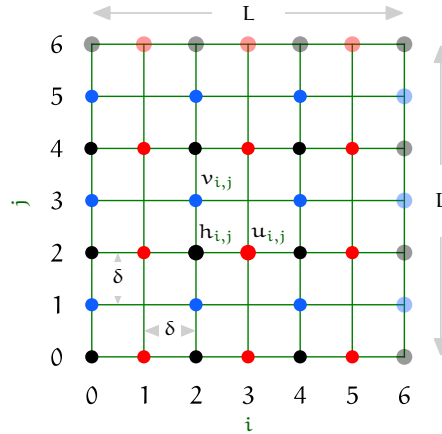
2.2 Staggered patches of staggered micro-grid for multiscale simulation of waves

In general, numerical simulation is challenging for wave-like (near Hamiltonian) systems with little or no dissipation. The numerical schemes for such systems with negligible dissipation are often unstable; numerical dissipation and roundoff errors quickly degrades the accuracy. Hence numerical simulation of wave-like systems often fail to represent the physical characteristics of wave phenomena ([TODO:cite]). §2.2.1 introduces one of the common strategies used in full-domain numerical simulation of wave-like systems known as the staggered grid that is a robust numerical scheme for wave-like systems.

Section 2.2.2 explains how our research extends the full-domain concept of a staggered grid, to multiscale simulation, using staggered patches of a staggered “*micro-grid*” (fine micro-scale grid within the patches). We expect most of the characteristics of this staggered grid generalisation to apply in general for many multiscale wave-like simulations.

[TODO/move elsewhere, such as 2.1]we expect most of the characteristics of this staggered grid generalisation to hold also for any multiscale simulation in general (not necessarily wave-like systems). But the particular focus of this thesis is on staggered patch schemes towards accurate simulation of wave-like systems.

Figure 2.2.1: Schematic of the full-domain micro-scale *staggered grid* where variables are simulated only on staggered/alternating discrete points (*nodes*, e.g., \bullet h , \bullet u and \bullet v nodes). There are $n = 6$ grid intervals in the green grid, both in x and y directions. Transparent filled circles on the boundaries indicate the discrete n -periodic boundary values.



2.2.1 Staggered grids are best for full-domain numerical simulation of waves

Consider a generic 2D wave-like system over the macro-scale periodic spatial domain $[0, L] \times [0, L]$. Such systems in terms of $h(x, y, t)$, $u(x, y, t)$ and $v(x, y, t)$ are modelled as PDEs,

$$\frac{\partial h}{\partial t} = -\frac{\partial u}{\partial x} - \frac{\partial v}{\partial y} + \dots, \quad (2.2.1a)$$

$$\frac{\partial u}{\partial t} = -\frac{\partial h}{\partial x} + \dots, \quad (2.2.1b)$$

$$\frac{\partial v}{\partial t} = -\frac{\partial h}{\partial y} + \dots, \quad (2.2.1c)$$

with the boundary conditions that the three fields h , u and v are L -periodic in both x and y . The “ \dots ” in the PDEs (2.2.1) indicate other linear or non-linear terms that model additional physics in addition to the wave phenomena, such as bed drag, viscous/turbulent diffusion and surface tension. The dependent variables in PDEs (2.2.1) let us interpret the model as a shallow water flow with h as depth and u, v as horizontal velocities, but it is a generic model of many 2D wave phenomena.

With their second order accuracy and ability of preserving much of the wave characteristics, *staggered grids* (Fig. 2.2.1) are simple and robust

for full-domain numerical simulation of waves ([TODO:cite]). [Fig. 2.2.1](#) depicts a staggered grid over the square domain $[0, L] \times [0, L]$, with micro-scale grid interval δ , for illustration shown with a very small number of grid intervals $n = 6$.

Approximating the spatial derivatives in the generic wave PDEs (2.2.1) by central finite differences on the nodes (filled solid circles) in [Fig. 2.2.1](#), gives the *full-domain micro-scale system* corresponding to the generic wave-like system (2.2.1)

$$\bullet \frac{dh_{i,j}}{dt} = -\frac{u_{i+1,j} - u_{i-1,j}}{2\delta} - \frac{v_{i,j+1} - v_{i,j-1}}{2\delta} + \dots \quad (2.2.2a)$$

for $i \in \{0, 2, 4, \dots, n-2\}$, $j \in \{0, 2, 4, \dots, n-2\}$,

$$\bullet \frac{du_{i,j}}{dt} = -\frac{h_{i+1,j} - h_{i-1,j}}{2\delta} + \dots \quad (2.2.2b)$$

for $i \in \{1, 3, 5, \dots, n-1\}$, $j \in \{0, 2, 4, \dots, n-2\}$,

$$\bullet \frac{dv_{i,j}}{dt} = -\frac{h_{i,j+1} - h_{i,j-1}}{2\delta} + \dots \quad (2.2.2c)$$

for $i \in \{0, 2, 4, \dots, n-2\}$, $j \in \{1, 3, 5, \dots, n-1\}$.

Analogous to the periodic boundary conditions of the PDEs (2.2.1), the three fields h, u, v are n -periodic in both i and j , where $n = L/\delta$. The “ \dots ” indicate discrete approximations of other linear or non-linear terms corresponding to the “ \dots ” in the PDEs (2.2.1). The coloured bullets $\bullet, \bullet, \bullet$ in the full-domain micro-scale system (2.2.2) indicate respectively the h, u and v nodes.

The PDEs (2.2.1) inspire the micro-scale computational system (2.2.2). Hence occasionally we aim to compare the characteristics of the staggered patch scheme and full-domain micro-scale system with the characteristics of the PDEs. But, *it is the micro-scale computational system that the staggered patch scheme seeks to predict accurately, not the solutions of the PDEs*. Thus, how well the full-domain micro-scale (2.2.2) system predicts the solutions of the PDEs (2.2.1) is irrelevant in this study.

Arranging the field variables of (2.2.2), which are over the staggered grid in [Fig. 2.2.1](#), into a vector gives the state vector of the full-domain micro-scale system

$$\begin{aligned} \mathbf{x} = (& h_{0,0}, h_{0,2}, h_{0,4}, \dots, h_{2,0}, h_{2,2}, h_{2,4}, \dots, \\ & \dots, u_{1,0}, u_{1,2}, u_{1,4}, \dots, u_{3,0}, u_{3,2}, u_{3,4}, \dots, \\ & \dots, v_{0,1}, v_{0,3}, v_{0,5}, \dots, v_{2,1}, v_{2,3}, v_{2,5}, \dots). \end{aligned} \quad (2.2.3)$$

In terms of the state vector \mathbf{x} , the full-domain micro-scale system (2.2.2) is

represented as a dynamical system by the ODES

$$\frac{dx}{dt} = f(x), \quad (2.2.4)$$

with the micro-scale system f for the generic wave-like system (2.2.1).

A full-domain micro-scale simulation is performed by numerical time-integration of the ODES (2.2.2) on the nodes (filled solid circles in Fig. 2.2.1) of the full-domain micro-scale grid.

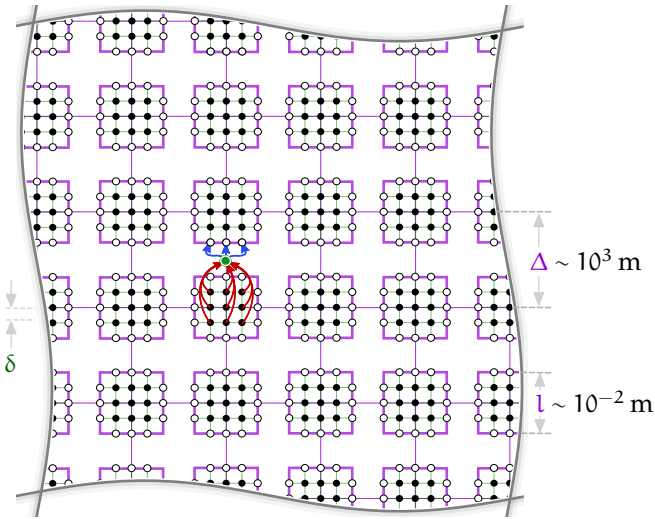
All the time simulations for this thesis (both the full-domain micro-scale system and the staggered patch scheme) are performed using the ODE integrator BS3 provided by DifferentialEquations.jl package (Rackauckas and Nie 2017) in the Julia programming language (Bezanson et al. 2017). BS3 is a non-stiff ODE integrator based on Bogacki–Shampine (2, 3) pair, similar to ode23 of MATLAB (DifferentialEquations.jl 2021; L. F. Shampine and Reichelt 1997). We chose BS3 after a detailed exploration of various ODE solvers based on the accuracy and computation speed. We find that various higher order ODE integrators take significantly longer computational time yet providing only a small improvement in the time solutions. We use relative and absolute error tolerances of respectively $10^{-3}, 10^{-6}$ for all time simulations using the BS3 ODE integrator; higher error tolerances only increase the computational time with only negligible change in the computed solution.

2.2.2 Generalising the staggered grid to patch scheme multiscale simulation

We adapt the usual (collocated) patch scheme to wave-like systems by appropriately incorporating the essential “wave-friendly” features of the staggered grids (§2.2.1). Fig. 2.2.2 shows the usual (collocated) patch grid, a non-staggered grid, with square patches. The following list defines the parameters for both collocated and staggered patch grids containing square patches over a square domain.

- Number of *macro-grid intervals* N is the number of **violet** grid intervals in the periodic domain x - and y -directions.
- *Inter-patch distance* Δ is the smallest distance between the patches (size of the **violet** grid intervals) in x - and y -directions (uniformly spaced patches over a square domain is our focus).
- *Patch size* l is the dimension of the square patch in x - and y -directions.

Figure 2.2.2: Usual (collocated) patch grid, filled circles represent interior nodes and unfilled circles represent edge nodes that are computed by patch coupling ([compute macro-scale patch values](#) + [compute micro-scale edge values](#)). Patches are enlarged here for visual clarity, in practice patch size l is few order of magnitudes smaller than the inter-patch distance Δ ; δ is sub-patch micro-scale grid interval.

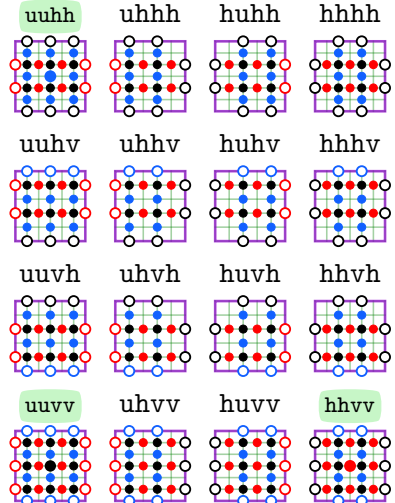


- *Patch scale ratio $r = l/(2\Delta)$* quantifies the unsimulated space in the domain in one direction.
- Number of *sub-patch micro-grid intervals n* is the number of [green](#) grid intervals within a patch in x - and y -directions.
- *Sub-patch micro-grid interval δ* is the smallest distance between the micro-grid nodes (size of the [green](#) grid intervals) in x - and y -directions (uniformly spaced micro-grid nodes over a square patch is our focus).

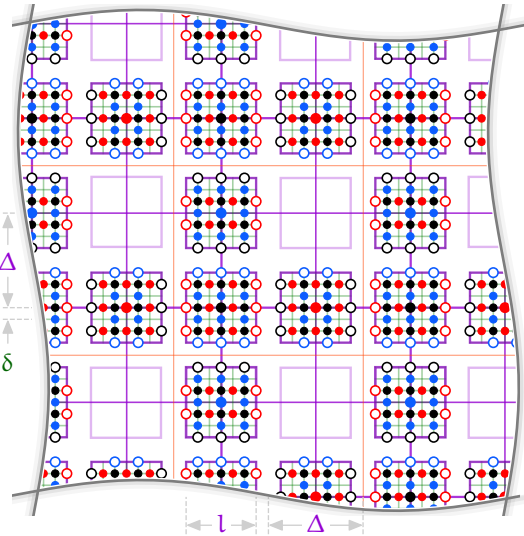
In a patch scheme, at each time step the edge values (by coupling the patches) and the interior node initial values (from previous time step) are known. Given the edge values and the interior values at the current time step, an ODE integrator such as BS3 of `DifferentialEquations.jl` (Rackauckas and Nie 2017), computes the interior values at the next time step by computing time derivatives from the governing ODES (2.2.2). In an usual patch scheme over the collocated patch grid, constructing and using a micro-grid within a patch, is straightforward as there is only one way to arrange patch edge nodes, as depicted in Fig. 2.2.2. But when we use a staggered grid (depicted in Fig. 2.2.1) as the micro-grid within a patch,

Figure 2.2.3: Possible micro-grids and the chosen staggered patch grid (patch size l , inter-patch distance Δ , sub-patch micro-scale grid interval δ).

(a) All 16 possible staggered micro-grids compatible for PDEs of wave-like systems (2.2.2). Name indicates edge node type.



(b) Chosen staggered patch grid uses micro-grids uuvv, hhvv and uuhh, for stable and accurate patch schemes with minimal computational effort.



the heterogeneous nodes lead to different arrangements of the patch edge nodes. To have all the necessary edge nodes for calculating the required spatial derivatives at all the interior nodes for wave-like systems using ODES (2.2.2), a total of 16 different kinds of micro-grid are possible within each patch (Fig. 2.2.3a). We denote each micro-grid by the type of nodes on left, right, bottom and top edges respectively. For example, as illustrated in the left-bottom of Fig. 2.2.3a, uuvv means that the micro-grid has u -edge nodes on left and right edges, and v -edge nodes on bottom and top edge nodes. Among the 16 possible types, only three patch micro-grids uuvv, hhvv and uuhh (green highlighted in Fig. 2.2.3a) have a node at the centre of the patch, these types of patches are called *h-centred*, *u-centred* and *v-centred* patches respectively.

Consider a possible staggered patch grid to be designed, comprising the cells (orange squares in Fig. 2.2.3b) each containing $2 \times 2 = 4$ patches (purple squares in Fig. 2.2.3b). Each of the four patches within a cell could be either empty or contain one of the 16 possible micro-grids of Fig. 2.2.3a. Thus the total number of possible staggered patch grids (in a 2×2 cell configuration) is $(16 + 1)^4 = 83\,521$.

We define a staggered patch grid to be geometrically *compatible* when the

patches have all the necessary edge nodes to calculate spatial derivative of all the interior nodes using the governing ODEs (2.2.2). For example, in the uhvv micro-grid (second in the bottom row of Fig. 2.2.3a) is not compatible when the right edge contains v -nodes instead of h -nodes, as the h -edge nodes are necessary to compute $\partial h / \partial x$ on the right most interior u -nodes.

Whereas all the possible 83 521 staggered patch grids are geometrically compatible discretisations for simulating multiscale wave physics, most of them constitute unstable patch schemes (§3.5.1). As discussed in §3.5.1, patch grids containing any sub-patch micro-grid without a centre node (i.e., micro-grids other than the green highlighted ones in Fig. 2.2.3a), lead to unstable patch schemes. Among the staggered patch grids that have centre node in each of the patches, from the stability analysis we found only two staggered patch grids over which the staggered patch schemes are stable, they are plotted in Figs. 2.2.3b and 3.5.1b. From the two staggered patch grids that constitute stable patch schemes, we find the staggered patch grid depicted in Fig. 2.2.3b to be the best in terms of computational effort and accuracy (§3.5.1 discusses the details). Except §3.5.1, which discusses the choosing of the patch grid in Fig. 2.2.3b, all other discussions in this thesis are based on the staggered patch grid in Fig. 2.2.3b, with one or more layers of edge nodes (§2.2.3).

The chosen staggered patch grid in Fig. 2.2.3b, in addition to having the reflective symmetry, also has *self-similarity* among the micro- and macro-scale scales: just as $h\text{-}u$ and $h\text{-}v$ nodes are staggered (alternating) along the x - and y -directions (horizontal and vertical in Fig. 2.2.3b) within the micro-grid, $h\text{-}u$ and $h\text{-}v$ centred patches are staggered for the macro-scale.

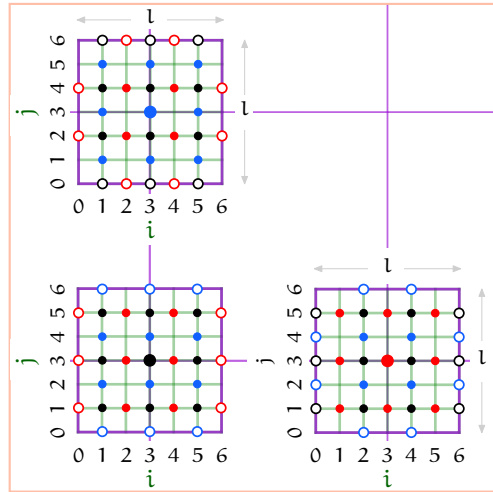
Fig. 2.2.4 illustrates the following three kinds of indices we use to identify the patches and sub-patch micro-grid nodes in Fig. 2.2.3b:

- the pair $I, J \in \{0, 1, \dots, N - 1\}$ is the global (macro-scale) patch index;
- the pair p, q with $p = I \bmod 2$, $q = J \bmod 2$, is the local (macro-scale) sub-cell patch index, that is, $p, q \in \{0, 1\}$ within each macro-cell (**orange** squares in Fig. 2.2.4b);
- (i, j) is the sub-patch micro-grid node index with $i, j \in \{1, \dots, n - 1\}$ for interior nodes (filled circles $\bullet, \bullet, \bullet$ in Figs. 2.2.4a and 2.2.5a) and $i, j \in \{0, n\}$ for patch edge nodes (unfilled circles \circ, \circ, \circ in Figs. 2.2.4a and 2.2.5a).

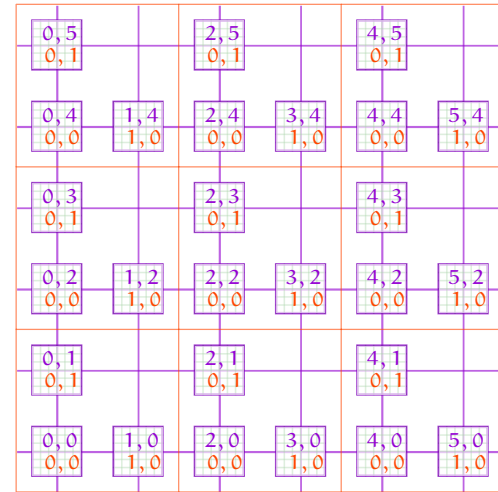
Using the micro-scale system (2.2.2) within the patches in a staggered patch grid (Fig. 2.2.3b) with N macro-grid intervals (i.e., total of $N/2 \times N/2$ macro-cells with each macro-cell containing 3 patches h -centred, u -centred and v -centred), where each patch consists of n sub-patch micro-grid

Figure 2.2.4: Index convention for the staggered patch grid with $N = 6$ macro-grid intervals in the **violet** grid, containing staggered patches of $n = 6$ micro-grid intervals in the **green** grid.

(a) Sub-patch micro-grid node index $i, j \in \{1, 2, \dots, n - 1\}$ for the interior nodes (filled circles $\bullet, \bullet, \bullet$) and $i, j \in \{0, n\}$ for patch edge nodes (unfilled circles \circ, \circ, \circ).



(b) Global (macro-scale) patch index $I, J \in \{0, 1, \dots, N - 1\}$; local sub-cell patch index $p, q \in \{0, 1\}$ within each macro-cell (**orange** squares).



intervals (e.g., Fig. 2.2.3b shows a staggered patch grid with $n = 6$), gives the *staggered patch scheme* for the micro-scale system (2.2.2) of a generic wave-like system as

$$\bullet \frac{d}{dt} h_{i,j}^{I,J}(t) = -\frac{u_{i+1,j}^{I,J} - u_{i-1,j}^{I,J}}{2\delta} - \frac{v_{i,j+1}^{I,J} - v_{i,j-1}^{I,J}}{2\delta} + \dots, \quad (2.2.5a)$$

$i \in \{1, 3, 5, \dots, n-1\}, \quad j \in \{1, 3, 5, \dots, n-1\}$ for $p=0, q=0$,
 $i \in \{1, 3, 5, \dots, n-1\}, \quad j \in \{2, 4, \dots, n-2\}$ for $p=0, q=1$,
 $i \in \{2, 4, \dots, n-2\}, \quad j \in \{1, 3, 5, \dots, n-1\}$ for $p=1, q=0$,

$$\bullet \frac{d}{dt} u_{i,j}^{I,J}(t) = -\frac{h_{i+1,j}^{I,J} - h_{i-1,j}^{I,J}}{2\delta} + \dots, \quad (2.2.5b)$$

$i \in \{2, 4, \dots, n-2\}, \quad j \in \{1, 3, 5, \dots, n-1\}$ for $p=0, q=0$,
 $i \in \{2, 4, \dots, n-2\}, \quad j \in \{2, 4, \dots, n-2\}$ for $p=0, q=1$,
 $i \in \{1, 3, 5, \dots, n-1\}, \quad j \in \{1, 3, 5, \dots, n-1\}$ for $p=1, q=0$,

$$\bullet \frac{d}{dt} v_{i,j}^{I,J}(t) = -\frac{h_{i,j+1}^{I,J} - h_{i,j-1}^{I,J}}{2\delta} + \dots, \quad (2.2.5c)$$

$i \in \{1, 3, 5, \dots, n-1\}, \quad j \in \{2, 4, \dots, n-2\}$ for $p=0, q=0$,
 $i \in \{1, 3, 5, \dots, n-1\}, \quad j \in \{1, 3, 5, \dots, n-1\}$ for $p=0, q=1$,
 $i \in \{2, 4, \dots, n-2\}, \quad j \in \{2, 4, \dots, n-2\}$ for $p=1, q=0$,

and a patch coupling (e.g., Square-p4) to compute the edge values

- $h_{i,j}^{I,J}, u_{i,j}^{I,J}, v_{i,j}^{I,J}$ for
 $i \in \{0, n\}, j \in \{1, 2, \dots, n-1\}$ for left and right edges and
 $i \in \{1, 2, \dots, n-1\}, j \in \{0, n\}$ for bottom and top edges,

(2.2.5d)

$I \in \{0, 2, 4, \dots, N-2\}$ for $h, v, I \in \{1, 3, 5, \dots, N-1\}$ for u ,
 $J \in \{0, 2, 4, \dots, N-2\}$ for $h, u, J \in \{1, 3, 5, \dots, N-1\}$ for v .

Analogous to the periodic boundary conditions for the full-domain micro-scale system (2.2.2), the three fields h, u, v are macro-scale N -periodic in both I and J , where $N = L/\Delta$. A specific patch coupling method computes patch edge nodes ($\circ h_{i,j}^{I,J}, \circ u_{i,j}^{I,J}, \circ v_{i,j}^{I,J}$ in Fig. 2.2.5a) from the interior nodes of the neighbouring patches ($\bullet h_{i,j}^{I,J}, \bullet u_{i,j}^{I,J}, \bullet v_{i,j}^{I,J}$ with $i=j=n/2$ in Fig. 2.2.5a), and provides the mechanism whereby patches influence each other. Section 2.3 discusses details of different patch coupling.

Arranging the patch interior values of (2.2.5), which are over the staggered patch grid in Fig. 2.2.4, into a vector gives the state vector x^I of the staggered patch scheme, which is a dynamic state variable evolving in time. The superscript $(\cdot)^I$ is not an index or exponent, instead a qualifier denoting the patch interior nodes. The general form of a staggered patch

scheme state vector \mathbf{x}^I of size n_I containing all the interior values of all the patches is,

$$\begin{aligned}\mathbf{x}^I = & \left(h_{1,1}^{0,0}, h_{1,3}^{0,0}, \dots, u_{2,1}^{0,0}, u_{2,3}^{0,0}, \dots, v_{1,2}^{0,0}, v_{1,4}^{0,0}, \dots, \right. \\ & h_{1,2}^{0,1}, h_{1,4}^{0,1}, \dots, u_{2,2}^{0,1}, u_{2,4}^{0,1}, \dots, v_{1,1}^{0,1}, v_{1,3}^{0,1}, \dots, \\ & h_{1,1}^{0,2}, h_{1,3}^{0,2}, \dots, u_{2,1}^{0,2}, u_{2,3}^{0,2}, \dots, v_{1,2}^{0,2}, v_{1,4}^{0,2}, \dots, \\ & h_{2,1}^{1,0}, h_{2,3}^{1,0}, \dots, u_{1,1}^{1,0}, u_{1,3}^{1,0}, \dots, v_{2,2}^{1,0}, v_{2,4}^{1,0}, \dots, \\ & h_{2,1}^{1,2}, h_{2,3}^{1,2}, \dots, u_{1,1}^{1,2}, u_{1,3}^{1,2}, \dots, v_{2,2}^{1,2}, v_{2,4}^{1,2}, \dots, \\ & \left. h_{1,1}^{0,2}, h_{1,3}^{0,2}, \dots, u_{2,1}^{0,2}, u_{2,3}^{0,2}, \dots, v_{1,2}^{0,2}, v_{1,4}^{0,2}, \dots \right).\end{aligned}\quad (2.2.6)$$

The total number of patch interior nodes, that is the size of the state vector \mathbf{x}^I ,

$$n_p^I = (N^2/4)(9n^2/4 - 4n + 2), \quad (2.2.7)$$

where N is the number of macro-grid intervals and n is the number of sub-patch micro-grid intervals. For example, for $N = 6, 10, 14, 18, 22, 26$ macro-grid intervals with $n = 6$ sub-patch micro-grid intervals, $n_p^I = 531, 1475, 2891, 4779, 7139, 9971$ respectively.

Arranging the patch edge values of (2.2.5) with $i, j \in \{0, n\}$ (Fig. 2.2.4) into a vector gives the edge vector \mathbf{x}^E of size n_p^E containing all the edge values of all the patches. The edge vector \mathbf{x}^E is computed by the patch coupling $\mathbf{x}^E(\mathbf{x}^I)$ of a particular patch scheme. For the general linear wave with drag and viscous diffusion (i.e., with second order spatial derivatives), a staggered patch grid needs two layers of edge nodes in the normal direction to the edges (§2.2.3) as in Fig. 2.2.5a. For the staggered patch grid in Fig. 2.2.5a, the total number of patch edge nodes, that is the size of the edge vector \mathbf{x}^E ,

$$n_p^E = (N^2/4)(18n - 16), \quad (2.2.8)$$

where N is the number of macro-grid intervals and n is the number of sub-patch micro-grid intervals. For example, for the staggered patch grid in Fig. 2.2.5a with $N = 6, 10, 14, 18, 22, 26$ and $n = 6$, $n_p^E = 828, 2300, 4508, 7452, 11132, 15548$ respectively.

In terms of the state vector \mathbf{x}^I and the edge vector \mathbf{x}^E , the staggered patch scheme (2.2.5) is represented as a dynamical system by the ODEs

$$\frac{d\mathbf{x}^I}{dt} = \mathbf{F}(\mathbf{x}^I; \mathbf{x}^E(\mathbf{x}^I)). \quad (2.2.9)$$

The $\mathbf{F}(\mathbf{x}^I; \mathbf{x}^E(\mathbf{x}^I))$ in the staggered patch scheme dynamical system (2.2.9) corresponds to the $\mathbf{f}(\mathbf{x})$ in the full-domain micro-scale system (2.2.4). The functions \mathbf{F} and \mathbf{f} encode same the micro-scale system for the generic wave-like system (2.2.1), the following difference:

- the only argument of \mathbf{f} is the nodal values \mathbf{x} in the full-domain micro-scale grid;
- the two arguments of \mathbf{F} are the patch interior values \mathbf{x}^I and the patch edge values \mathbf{x}^E in the staggered patch grid.

Patch scheme simulation is performed by numerical time-integration of the ODEs (2.2.5) on the interior nodes of the patch grid (filled solid circles in Fig. 2.2.3b). Evaluating the time derivatives in the staggered patch scheme (2.2.5) is done in two steps:

1. Macro-scale patch coupling (§2.3) to compute the patch edge nodes (unfilled circles in Fig. 2.2.5a);
2. Computing time derivative of the interior nodes (filled circles in Fig. 2.2.5a) for the micro-scale system (2.2.2) using both interior and edge values of the patches, which is expressed in complete detail by the staggered patch scheme equations (2.2.5).

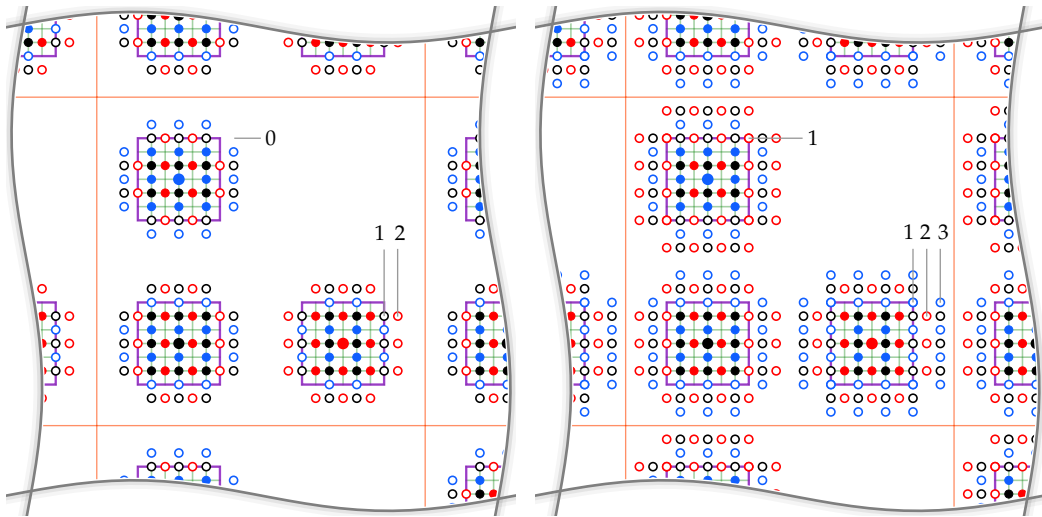
2.2.3 Multi-layer edge nodes for higher order spatial derivatives

The staggered patch grid in Fig. 2.2.3b is used for the staggered patch scheme simulations of an ideal wave (PDEs (2.2.1) with only the terms that are explicitly written, that is, without the additional terms denoted by “...”) and other wave PDEs involving only first order spatial derivatives. Finite difference discrete approximations for higher order spatial derivatives (such as second spatial derivative for viscous diffusion) use more surrounding nodes. More surrounding nodes participating in the calculation of higher order spatial derivatives is not an issue for most of the interior nodes, but the interior nodes closest to the edges of a patch need values of nodes that lie outside the patches shown in Fig. 2.2.3b. We explored the following two cases of handling this situation.

- We first used the staggered patch grid Fig. 2.2.3b also for calculating higher order spatial derivatives (e.g., second order derivative for viscous diffusion), but whenever the finite difference approximation involves nodes outside the patch edges, extrapolated the required

Figure 2.2.5: Staggered patch grids with multi-layer edge nodes, for a given number of sub-patch micro-grid intervals ($n = 6$ here), contain the same number of interior nodes $\bullet h_{i,j}^{I,J}$, $\bullet u_{i,j}^{I,J}$, $\bullet v_{i,j}^{I,J}$ for $i, j \in \{1, \dots, n - 1\}$. But the number of edge values $\circ h_{i,j}^{I,J}$, $\circ u_{i,j}^{I,J}$, and $\circ v_{i,j}^{I,J}$ depend on the number of layers of edge nodes.

- (a) Two layers of edge nodes in normal direction to the edges, no edge nodes in tangential direction to the edges (e.g., no v node on corners of u -centred patch). (b) Three layers of edge nodes in normal direction to the edges, one layer of edge nodes in tangential direction to the edges.



additional nodes using the nearest edge and interior nodes (we tried constant values, linear and quadratic extrapolation). But those extrapolations make the staggered patch schemes unstable (the solutions blow up in time).

- The second alternative is to append an additional layer of edge nodes to the staggered patch grid as in Figs. 2.2.5a and 2.2.5b and calculate their values at each iteration by macro-scale patch coupling interpolation (similar to how the edge nodes in Fig. 2.2.3b are calculated). Because this way of calculating higher order spatial derivatives does not cause any instability for the staggered patch scheme, we use multi-layer edge nodes for the calculation of any higher order spatial derivatives (e.g., computing second spatial derivatives of viscous diffusion).

Fig. 2.2.5 shows two example staggered patch grids with additional layers of edge nodes compared to the Fig. 2.2.3b with one layer of edge

nodes in normal direction and no edge nodes in tangential direction to the edges.

1. Irrespective of the number of layers of the edge nodes, the staggered patch grids contain the same number of interior nodes for a given number of sub-patch micro-grid intervals ($n = 6$ in Fig. 2.2.5). That is, the interior values are $\bullet h_{i,j}^{I,J}$, $\bullet u_{i,j}^{I,J}$, $\bullet v_{i,j}^{I,J}$ for $i, j \in \{1, \dots, n - 1\}$.
2. Total number of edge nodes depends on the number of layers of the edge nodes.

For Fig. 2.2.5a with two layers of edge nodes in normal direction to the edges and no edge nodes in tangential direction to the edges, the left and right edge values are $\circ h_{i,j}^{I,J}$, $\circ u_{i,j}^{I,J}$, $\circ v_{i,j}^{I,J}$, for $i \in \{-1, 0, n, n + 1\}$ and $j \in \{1, 2, \dots, n - 1\}$. Similarly the bottom and top edge value indices are $i \in \{1, 2, \dots, n - 1\}$ and $j \in \{-1, 0, n, n + 1\}$.

For Fig. 2.2.5b with three layers of edge nodes in normal direction to the edges and one layer of edge nodes in tangential direction to the edges, the left and right edge values are $\circ h_{i,j}^{I,J}$, $\circ u_{i,j}^{I,J}$, $\circ v_{i,j}^{I,J}$, for $i \in \{-2, -1, 0, n, n + 1, n + 2\}$ and $j \in \{0, 1, 2, \dots, n - 1, n\}$. Similarly the bottom and top edge value indices are $i \in \{0, 1, 2, \dots, n - 1, n\}$ and $j \in \{-2, -1, 0, n, n + 1, n + 2\}$.

2.3 Patch-coupling connects the scales

As explained in §2.2.2, a patch scheme simulation is done in two steps:

1. Macro-scale patch coupling to compute the patch edge nodes;
2. Computing time derivative of the interior nodes from the micro-scale system using both interior and edge values.

Computing patch edge values via patch coupling consists of two steps:

1. first compute the *macro-scale patch value* (a representative aggregate value, also called amplitude or order parameter), for each patch from their respective interior values within the small patches;
2. next compute the *micro-scale* edge values of each patch by interpolating from the macro-scale values of the neighbouring patches across the relatively large inter-patch distances.

Thus, patch coupling invokes a two-way connection between the micro-scale and macro-scale.

The staggered patch schemes that we design essentially provide a reduced order multiscale model of the given corresponding full-domain micro-scale system, where, the macro-scale (aggregate) values of patches are state variables in a slow manifold of reduced state space dimension [TODO/cite]. The simple approach of, taking the centre node value of a patch as the macro-scale value of that patch, is adopted in this work. Whereas many of the patch micro-grids in Fig. 2.2.3a do not have a node at their centre, all three types of patches in the chosen staggered patch grid in Fig. 2.2.3b each have one centre node— h , u or v node. So the simple approach of taking the centre node value of a patch as the macro-scale value, is particularly suitable for the chosen staggered patch grid (Fig. 2.2.3b). Hence we define the centre values H , U , V as the macro-scale (aggregate) values of respectively the h -, u - and v -centred patches.

We have three macro-scale values H , U - and V per macro-cell, corresponding to the h -, u - and v -centred patches within each macro-cell in the chosen staggered patch grid (orange square Fig. 2.2.3b). Hence with N macro-grid intervals in the domain, we have three $N/2 \times N/2$ arrays of H , U and V macro-scale values of all the patches in the staggered patch grid. Many choices of multivariate interpolations could be used for the patch coupling to compute the micro-scale patch edge values from the three $N/2 \times N/2$ arrays of H , U and V macro-scale values.

We use global spectral interpolation in §2.3.1 and local polynomial interpolations §2.3.2 for a family of staggered patch schemes.

2.3.1 Global spectral interpolation for patch coupling

For a staggered patch grid with N macro-grid intervals (N is even) across the square domain, we have three $N/2 \times N/2$ arrays of H , U and V macro-scale values of all the patches, which are patch centre node values of h -, u - and v -centred patches. The inter-patch distance between patches with same centre nodes is same as the inter-cell distance 2Δ , that is h -centred patches are equally spaced among themselves and similarly the u - and v - centred patches. Hence, the *spectral patch scheme* we describe in this section uses the spectral interpolation to compute the micro-scale patch edge values h , u and v from the equi-spaced patch macro-scale values H , U and V .

This section illustrates spectral interpolation patch coupling for calculating h edge values, the calculations of u and v edge values follow the same procedure. Consider the 2D discrete Fourier transform (DFT) of

an $N/2 \times N/2$ array H containing h -patch aggregate values,

$$\tilde{H}_{k_x, k_y} = DFT(H) = \sum_{i,j=1}^{N/2} H_{i,j} \exp(-i(2\pi k_x x_i/L + 2\pi k_y y_j/L)) \quad (2.3.1)$$

where the wavenumbers $k_x, k_y \in \{-(N/2 - 1)/2, \dots, (N/2 - 1)/2\}$.

The 2D inverse *semi*-discrete Fourier transform of the discrete Fourier transform \tilde{H} ($N/2 \times N/2$ array) gives a continuous function $\hat{H}(x, y)$, which is the macro-scale field at any arbitrary position (x, y) . That is, the macro-scale variation of the micro-scale field h is,

$$\hat{H}(x, y) = ISDFT(\tilde{H}) = \frac{1}{(N/2)^2} \sum_{k_x, k_y} \tilde{H}_{k_x, k_y} \exp(i(2\pi k_x x/L + 2\pi k_y y/L)) \quad (2.3.2)$$

When the size $N/2$ is even (e.g., the number of macro-grid intervals N is a multiple of four), special handling is required due to the presence of Nyquist frequency component—as we consider only even N where $N/2$ is odd, that is, $N \in \{6, 10, 14, 18, \dots\}$, this is not an issue here.

The Fast Fourier transform FFT provides efficient calculation of the transforms (2.3.1) and (2.3.2). Using FFT, one edge value of all the $h/u/v$ -centred patches (e.g., left-bottom h nodes of all u -centred patches in Fig. 2.2.3b), are calculated in one pass (one FFT, Fourier shift and one inverse fast Fourier transform IFFT) as in Algorithm 1. We use the left-bottom $h/u/v$ -centred patches as reference patches in Algorithm 1 for the edge node offsets (Fourier shifts); but any patch with a same type centre node as the edge node being coupled could be used as the reference patch.

By capturing all the global information from wave components, spectral interpolation achieves high accuracy (Bunder et al. 2020); but the spectral interpolation also imposes strict restrictions for its use such as equi-spaced patches and periodic macro-scale boundary conditions. On the other hand, a local polynomial interpolation (§2.3.2) is more widely applicable for non-uniform complex geometries and boundary conditions.

2.3.2 A family of local polynomial interpolations for patch coupling

The requirements of spectral interpolation based patch coupling (namely, equi-spaced patches and periodic macro-scale boundary conditions) poses restrictions for the practical use of patch schemes. Using 2D polynomial interpolation in the patch coupling to compute patch edge values avoids

Algorithm 1 Patch coupling for h -nodes by global spectral interpolation

1: $H \leftarrow \text{GETALLAGGREGATESTATES('}h\text{'})$ “ $N/2 \times N/2$ array”
 “Gets aggregate values of all the h -centred patches.”

2: $\tilde{H} \leftarrow \text{FFT}(H)$

3: **for all** offsets (ξ, η) (w.r.t centre node of left-bottom h -centred patch), of
 all h edge nodes of left-bottom h -centred patch **do**

4: $\tilde{H}_{m,n}^e = \tilde{H} \exp [i(k_{x,m}\xi + k_{y,n}\eta)]$ “ $N/2 \times N/2$ array”
 “Fourier shift of patch centre node values of all h -centred patches,
 by h edge node offset (ξ, η) .”

5: $H^e = \text{IFFT}(\tilde{H}^e)$ “ $N/2 \times N/2$ array”
 “Interpolated (ξ, η) -offset h edge value for all h -centred patches.”

6: Assign H^e to (ξ, η) -offset h edge node of all h -centred patches

7: **end for**

8: **for all** offsets (ξ, η) (w.r.t centre node of left-bottom h -centred patch), of
 all h edge nodes of left-bottom u -centred patch **do**

9: $\tilde{H}_{m,n}^e = \tilde{H} \exp [i(k_{x,m}\xi + k_{y,n}\eta)]$

10: $H^e = \text{IFFT}(\tilde{H}^e)$

11: Assign H^e to (ξ, η) -offset h edge node of all u -centred patches

12: **end for**

13: **for all** offsets (ξ, η) (w.r.t centre node of left-bottom h -centred patch), of
 all h edge nodes of left-bottom v -centred patch **do**

14: $\tilde{H}_{m,n}^e = \tilde{H} \exp [i(k_{x,m}\xi + k_{y,n}\eta)]$

15: $H^e = \text{IFFT}(\tilde{H}^e)$

16: Assign H^e to (ξ, η) -offset h edge node of all v -centred patches

17: **end for**

Table 2.3.1: Meaning of visual elements of interpolation stencil plots. [Figs. 2.3.2](#) to [2.3.5](#), each presents the interpolation stencils for computing the edge values of h -, u -, v -centred patches in one macro-cell illustrated as . For example interpolating v node values on edges of h -, u -, v -centred patches (indicated respectively by , , and ) uses macro-scale values of v -centred patches (indicated by ) in the stencil.

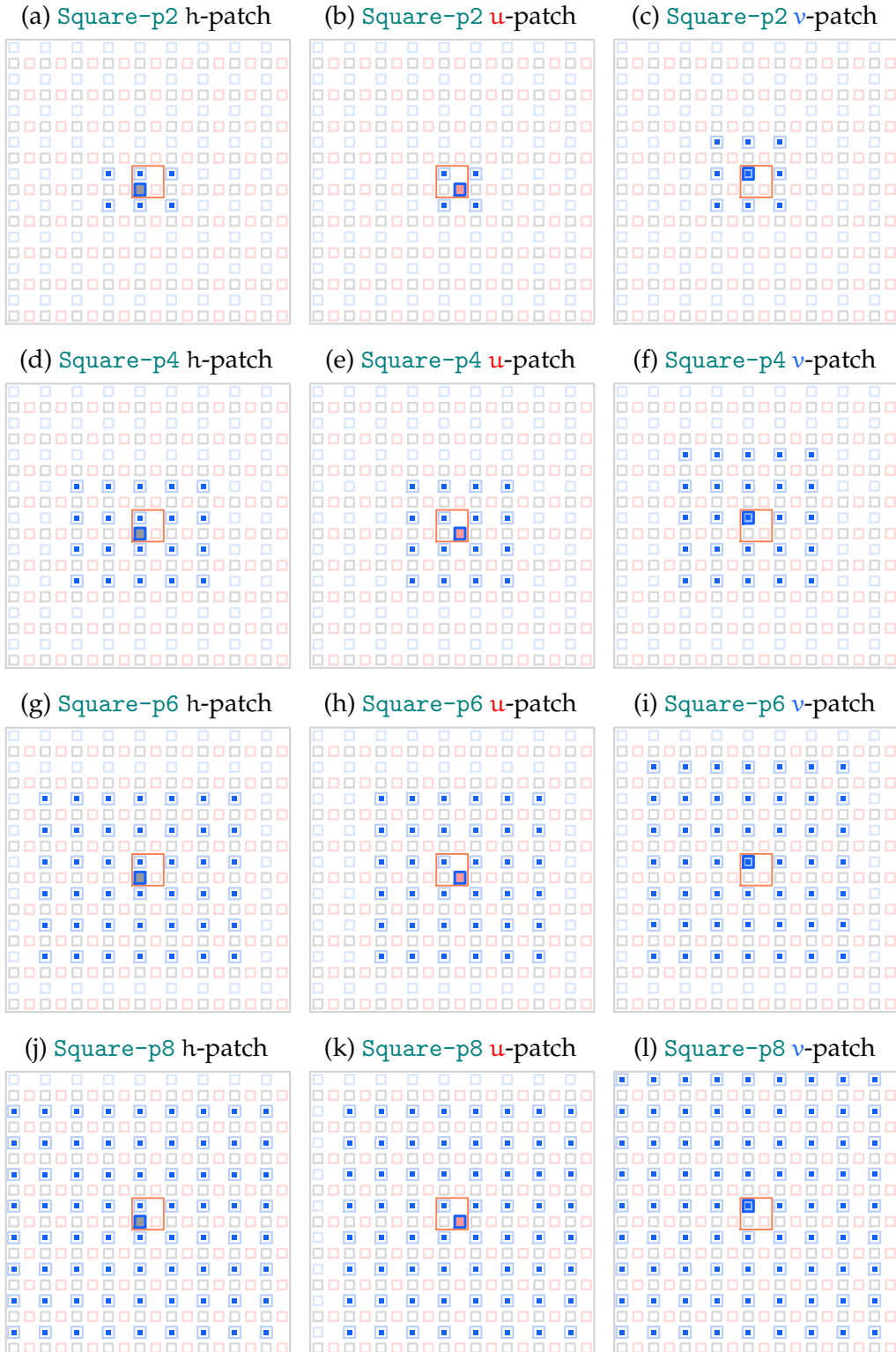
	Edge node being interpolated		
	h edge nodes	u edge nodes	v edge nodes
For h -centred patch			
For u -centred patch			
For v -centred patch			

	Interpolating patches		
	h -centred patch	u -centred patch	v -centred patch
For h edge nodes			
For u edge nodes			
For v edge nodes			

such restrictions. So, we developed four *polynomial staggered patch schemes*, namely Square-p2, Square-p4, Square-p6, and Square-8, whose patch coupling is based on 2D Lagrangian polynomial interpolation over a *roughly* square region where the parameter p in the name is the interpolation polynomial order. As opposed to the global spectral interpolation which uses the macro-scale values of all patches to interpolate the edge values of a patch, local polynomial interpolation computes the edge values of a patch using macro-scale values of only its near neighbouring patches.

The neighbourhood of a patch, characterised by the interpolation stencil, could be of different sizes leading to different order p of the interpolating polynomial. For example, [Fig. 2.3.1](#) shows one individual interpolation stencil for each of the four polynomial staggered patch schemes, for interpolating v edge values of h -, u -, v -centred patches, using macro-scale values of v -centred patches in the square stencil. [Table 2.3.1](#) explains the meaning of the visual elements in the stencil plots. [Figs. 2.3.2](#) to [2.3.5](#) show all the individual interpolation stencils (for coupling $h/u/v$ edge values of $h/u/v$ -centred patches) for each of the four polynomial schemes. Each of [Figs. 2.3.2](#) to [2.3.5](#) show the interpolation stencils for coupling h,u,v edge

Figure 2.3.1: Example interpolation stencils of the four polynomial staggered patch schemes, for interpolating v node values on edges of h -, u -, v -centred patches (indicated respectively by \blacksquare , \square , and \blacksquare), using macro-scale values of v -centred patches (indicated by \blacksquare) in the stencil.



values on left-right and bottom-top edge nodes of h -, u -, v -centred patches in one cell.

- The square shape of the stencil is only in approximate and qualitative sense. But depending upon the type of edge nodes ($h/u/v$) being interpolated and the type of the patch ($h/u/v$ -centred) for which edge nodes are interpolated, some of the individual stencils of a staggered patch scheme take rectangular shape. For example, for all the four polynomial staggered patch schemes in [Fig. 2.3.1](#), all the left most stencils for interpolating the v edge nodes of h -centred patches take rectangular shape.
- All the four polynomial staggered patch schemes have roughly the same square-shaped interpolation stencils, but differ in size and hence have different polynomial interpolation orders $p \in \{2, 4, 6, 8\}$, indicated respectively in their names by p_2, p_4, p_6 and p_8 .

We define the polynomial interpolation order p as the maximum degree of the variables in the 2D Lagrangian basis polynomials of all the interpolation stencils of a staggered patch scheme. For example, for the Square- p_2 staggered patch scheme the maximum degree of ξ, η in [Tables 2.3.2](#) to [2.3.4](#) is two ([Fig. 2.3.2](#) shows all the individual stencils), hence the polynomial interpolation order $p = 2$. But the maximum degree of ξ, η is one in [Table 2.3.3](#) of the Square- p_2 (for interpolating the v edge values of u -centred patch). Thus, not all the individual stencils of a staggered patch scheme has the same interpolation order. The maximum degree of ξ, η of individual stencils of a staggered patch scheme is either p or $p - 1$, hence the number of points in the interpolating stencils in ξ, η directions are either p or $p + 1$ as in [Figs. 2.3.2](#) to [2.3.5](#).

In realistic uses of the patch schemes, the patch size l is much smaller than the inter-patch patch spacing Δ (patch scale ratio $r \ll 1$), hence we expect that the stencil points (centre nodes of the interpolating patches) that lie on the two coordinate lines passing through the current patch (whose edge nodes are interpolated) have the dominant influence on the patch coupling interpolation. In contrast to the square or rectangle stencils, using few different shaped stencil shapes such as a plus and cruciform shape, we also found that patches that lie on a line perpendicular to the patch edge being interpolated have stronger influence on the patch coupling than the patches that lie on a line parallel to the patch edge being interpolated. So interpolation stencils with fewer stencil points such as a plus or cruciform shape compared to the square or rectangle stencils, could be a more efficient alternative and maybe worth investigating in the future.

We perform the standard 2D Lagrangian interpolation ([TODO:cite]) in patch local coordinate (ξ, η) , using following coordinate transformation from global coordinate (x, y) ,

$$\xi = (x - x^I)/\Delta, \quad (2.3.3a)$$

$$\eta = (y - y^J)/\Delta, \quad (2.3.3b)$$

where, Δ is inter-patch spacing and the patch local coordinate system origin (x^I, y^J) is the centre of current patch (the patch whose edge is values are being interpolated). For example, Tables 2.3.2 to 2.3.4 show the local coordinates of interpolation stencils of Square-p2 staggered patch scheme, for coupling v edge nodes respectively for h -, u -, v -centred patches.

Let's assign a *stencil index* $S \in \{0, 1, \dots, n_s - 1\}$ for each of the n_s patches in a polynomial patch coupling interpolation stencil (e.g., Tables 2.3.2 to 2.3.4). Let the stencil coordinate sets

$$\mathbb{X} = \{\xi_s : S = 0, 1, \dots, n_s - 1\}, \quad (2.3.4a)$$

$$\mathbb{Y} = \{\eta_s : S = 0, 1, \dots, n_s - 1\}, \quad (2.3.4b)$$

each contain the patch local coordinates ξ_s and η_s respectively of all the stencil points (i.e., interpolating patch centres shown by in Fig. 2.3.1). All the stencil points $\{(\xi_s, \eta_s) : S = 0, 1, \dots, n_s - 1\} = \mathbb{X} \times \mathbb{Y}$. The expressions we use for the 2D Lagrangian basis polynomials for every stencil index $S \in \{0, 1, \dots, n_s - 1\}$ are

$$\mathcal{B}_S(\xi, \eta) = \left(\prod_{\xi_k \in \mathbb{X} \setminus \{\xi_s\}} \frac{\xi - \xi_k}{\xi_s - \xi_k} \right) \left(\prod_{\eta_k \in \mathbb{Y} \setminus \{\eta_s\}} \frac{\eta - \eta_k}{\eta_s - \eta_k} \right). \quad (2.3.5)$$

Tables 2.3.2 to 2.3.4 illustrate the local coordinates, stencil indices and the corresponding 2D Lagrangian basis polynomials (2.3.5) of the interpolation stencils for Square-p2 staggered patch scheme, for coupling v edge nodes respectively for h -, u -, v -centred patches. The Lagrangian basis polynomials (2.3.5) are the standard 2D Lagrangian basis polynomials ([TODO:cite]) but defined in terms of the stencil index S , for a regular grid of points with a spacing of 2Δ , over the square or rectangular stencil. Section 2.3.2.1 discusses these basis polynomials for the four polynomial staggered patch schemes.

In terms of the basis polynomials (2.3.5) and the known values f_s , the 2D Lagrangian interpolation polynomial, generic for the patch coupling of all the four polynomial staggered patch schemes is

$$\mathcal{L}(\xi, \eta) = \sum_{S=0}^{n_s-1} \mathcal{B}_S(\xi, \eta) f_s. \quad (2.3.6)$$

Algorithm 2 Patch coupling by 2D Lagrangian polynomial interpolation

1: Stencil \leftarrow <stencilName> “for example Stencil \leftarrow ‘Cruciform2-p4’”

2: **for all** patch P in patch grid **do**

3: **for all** node type T in [‘h’, ‘u’, ‘v’] **do** “to interpolate h/u/v edge nodes”

4: **for all** edge side S in [‘left-right’, ‘bottom-top’] **do**

5: Nbrs_{T,S} \leftarrow GETNEIGHBOURPATCHES(P, stencil, T, S)
“For patch P, gets neighbouring T-centred patches within the specified stencil for interpolating S side edge nodes of type T.”

6: Macros_{T,S} \leftarrow GETSTENCILMACROSCALEVALUES(Nbrs_{T,S})
“Gets macro-scale values for all the patches in the set of neighbouring patches Nbrs_{T,S}.”

7: $\mathcal{L}(\xi, \eta) \leftarrow$ MAKEINTERPFUNCTION(Nbrs_{T,S}, Macros_{T,S})
“Constructs 2D Lagrangian interpolating polynomial \mathcal{L} (2.3.6) in terms of the basis polynomials B_S (2.3.5) for centre positions of the stencil patches Nbrs_{T,S} and their macro-scale values Macros_{T,S}.
“ $\mathcal{L}(\xi, \eta)$ interpolates T-node values at any input position ξ, η relative to the centre of patch P.”

8: **for all** edge node E of type T on the S side of patch P **do**

9: Compute position ξ_E, η_E of edge nodes
“Patch local coordinate relative to the centre of patch P, using the coordinate transformation (2.3.3).”

10: Assign edge node E of type T with a value $\mathcal{L}(\xi_E, \eta_E)$

11: **end for**

12: **end for**

13: **end for**

14: **end for**

Algorithm 2 shows the key steps in coupling the patches using 2D Lagrangian interpolation polynomial (2.3.6).

Figure 2.3.2: Stencils of Square-p2 scheme (maximum order of basis polynomials $p = 2$), for interpolating h, u, v values on left-right and bottom-top edge nodes of h, u, v -centred patches in one cell (orange square).

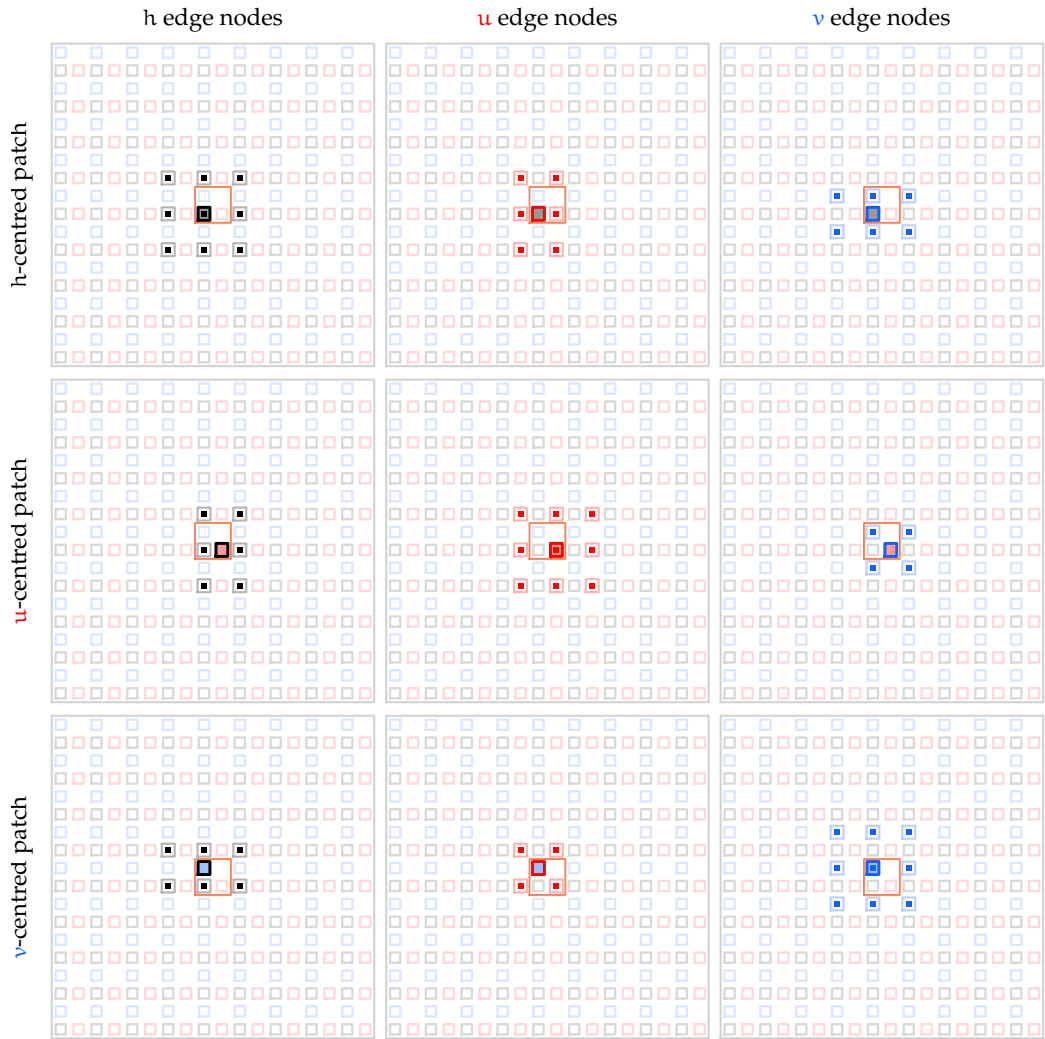


Figure 2.3.3: Stencils of Square-p4 scheme (maximum order of basis polynomials $p = 4$), for interpolating h, u, v values on left-right and bottom-top edge nodes of h, u, v -centred patches in one cell (orange square).

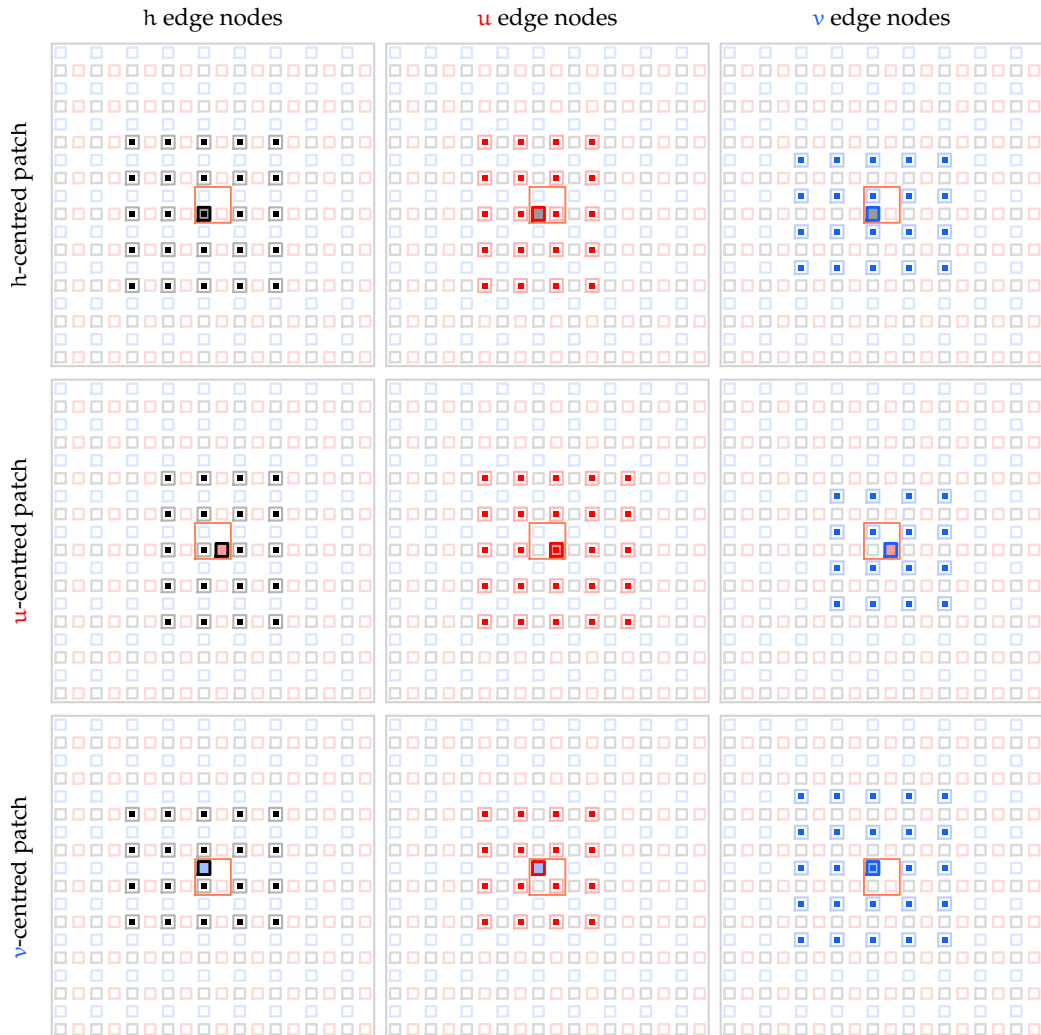


Figure 2.3.4: Stencils of Square-p6 scheme (maximum order of basis polynomials $p = 6$), for interpolating h, u, v values on left-right and bottom-top edge nodes of h, u, v -centred patches in one cell (orange square).

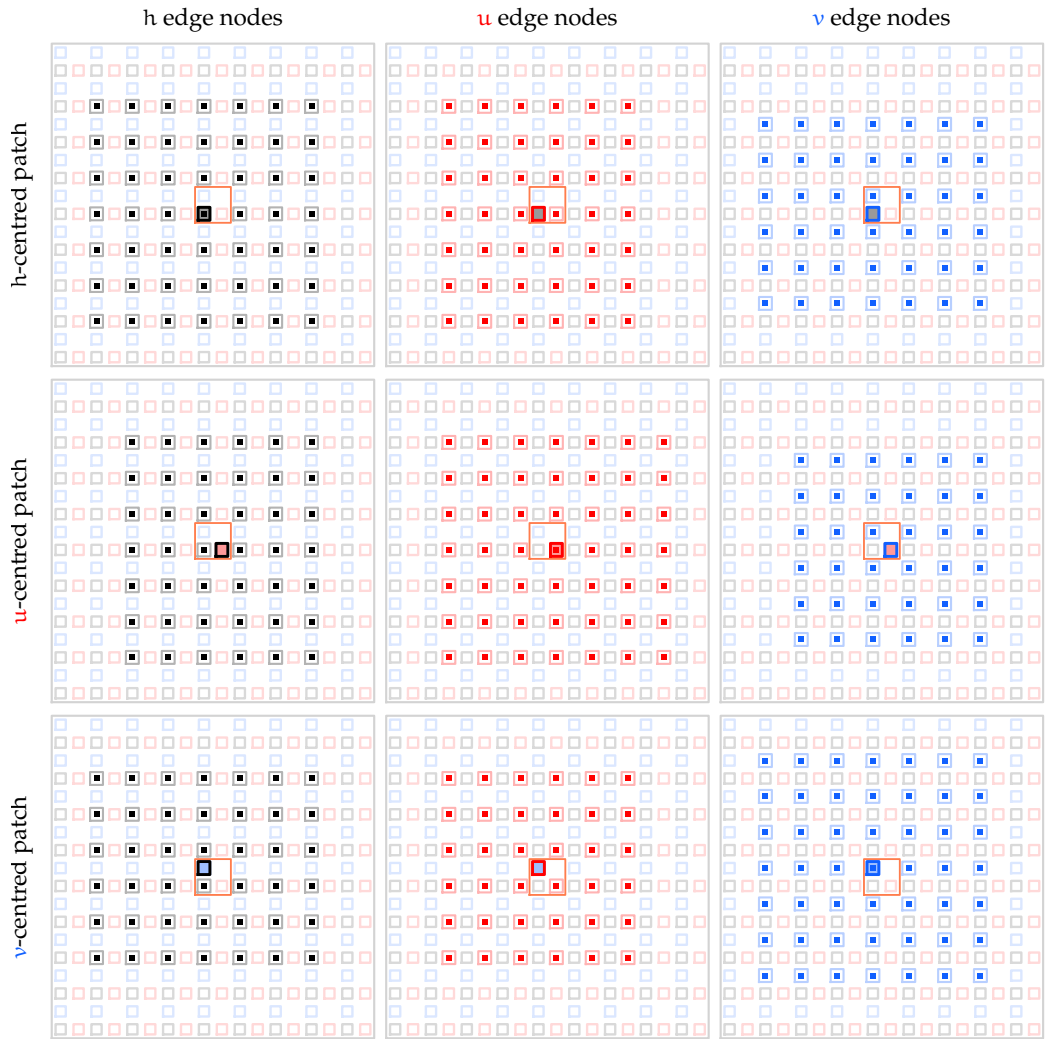


Figure 2.3.5: Stencils of Square-p8 scheme (maximum order of basis polynomials $p = 8$), for interpolating h, u, v values on left-right and bottom-top edge nodes of h, u, v -centred patches in one cell (orange square).

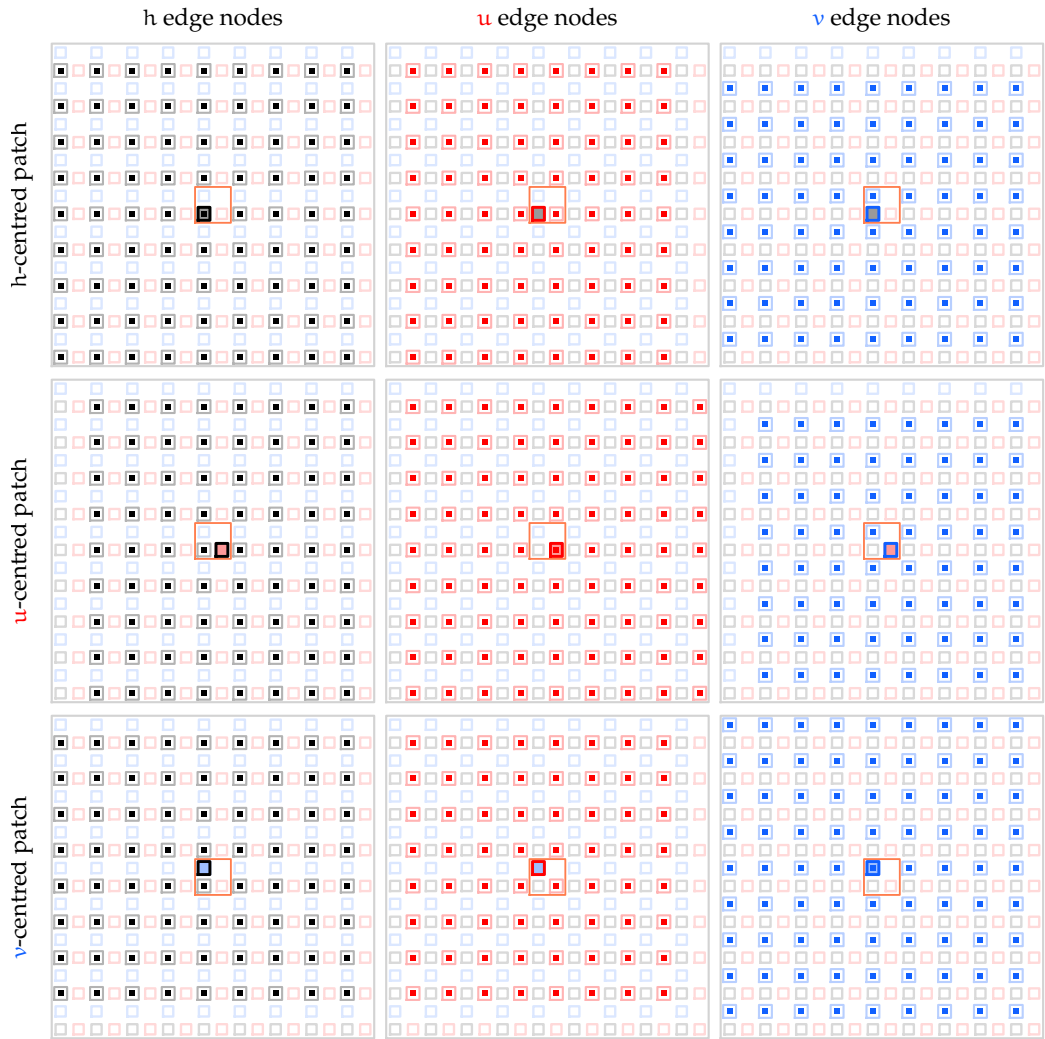
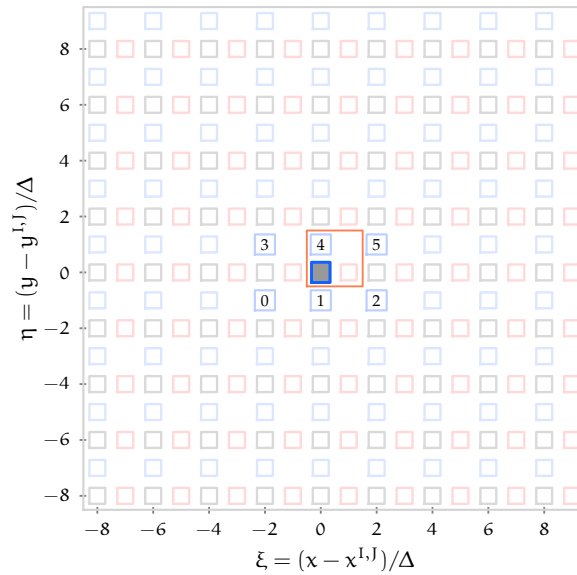
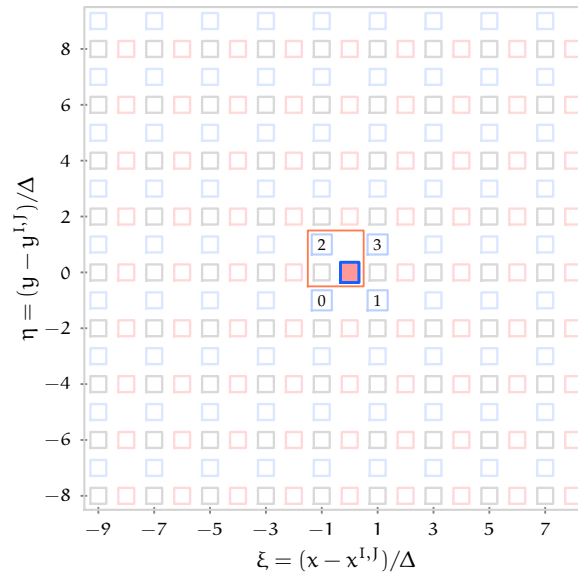


Table 2.3.2: 2D Lagrangian basis polynomials for Square-p2 patch coupling, for interpolating v edge node values of h-centred patch (indicated by \blacksquare). Stencil index $S \in \{0, 1, \dots, n_s - 1 = 5\}$. Global coordinate (x, y) corresponds to patch local coordinate (ξ, η) with origin (x^I, y^I)



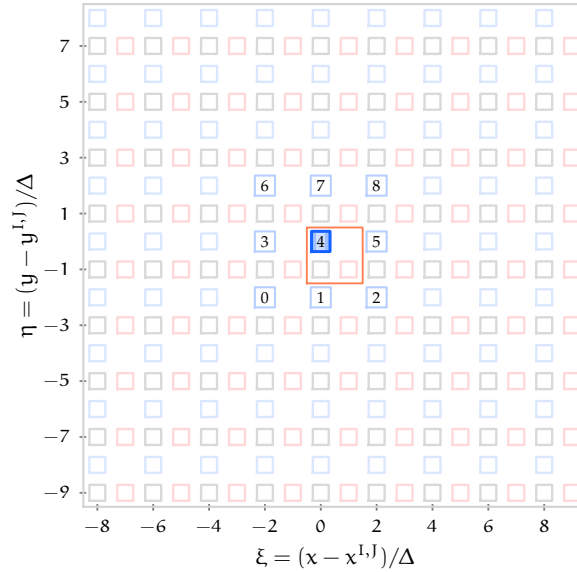
S	Basis polynomials $\mathcal{B}_S(\xi, \eta)$
0	$-\frac{\xi-2}{4} \cdot \frac{\xi}{2} \cdot \frac{\eta-1}{2}$
1	$\frac{\xi-2}{2} \cdot \frac{\xi+2}{2} \cdot \frac{\eta-1}{2}$
2	$-\frac{\xi}{2} \cdot \frac{\xi+2}{4} \cdot \frac{\eta-1}{2}$
3	$\frac{\xi-2}{4} \cdot \frac{\xi}{2} \cdot \frac{\eta+1}{2}$
4	$-\frac{\xi-2}{2} \cdot \frac{\xi+2}{2} \cdot \frac{\eta+1}{2}$
5	$\frac{\xi}{2} \cdot \frac{\xi+2}{4} \cdot \frac{\eta+1}{2}$
Sum: 1	

Table 2.3.3: 2D Lagrangian basis polynomials for Square-p2 patch coupling, for interpolating v edge node values of u -centred patch (indicated by \blacksquare). Stencil index $S \in \{0, 1, \dots, n_s - 1 = 3\}$. Global coordinate (x, y) corresponds to patch local coordinate (ξ, η) with origin (x^I, y^I)



S	Basis polynomials $\mathcal{B}_S(\xi, \eta)$
0	$\frac{\xi-1}{2} \cdot \frac{\eta-1}{2}$
1	$-\frac{\xi+1}{2} \cdot \frac{\eta-1}{2}$
2	$-\frac{\xi-1}{2} \cdot \frac{\eta+1}{2}$
3	$\frac{\xi+1}{2} \cdot \frac{\eta+1}{2}$
Sum: 1	

Table 2.3.4: 2D Lagrangian basis polynomials for Square-p2 patch coupling, for interpolating v edge node values of v -centred patch (indicated by \blacksquare). Stencil index $S \in \{0, 1, \dots, n_s - 1 = 8\}$. Global coordinate (x, y) corresponds to patch local coordinate (ξ, η) with origin (x^I, y^I)



S	Basis polynomials $\mathcal{B}_S(\xi, \eta)$
0	$\frac{\xi-2}{4} \cdot \frac{\xi}{2} \cdot \frac{\eta-2}{4} \cdot \frac{\eta}{2}$
1	$-\frac{\xi-2}{2} \cdot \frac{\xi+2}{2} \cdot \frac{\eta-2}{4} \cdot \frac{\eta}{2}$
2	$\frac{\xi}{2} \cdot \frac{\xi+2}{4} \cdot \frac{\eta-2}{4} \cdot \frac{\eta}{2}$
3	$-\frac{\xi-2}{4} \cdot \frac{\xi}{2} \cdot \frac{\eta-2}{2} \cdot \frac{\eta+2}{2}$
4	$\frac{\xi-2}{2} \cdot \frac{\xi+2}{2} \cdot \frac{\eta-2}{2} \cdot \frac{\eta+2}{2}$
5	$-\frac{\xi}{2} \cdot \frac{\xi+2}{4} \cdot \frac{\eta-2}{2} \cdot \frac{\eta+2}{2}$
6	$\frac{\xi-2}{4} \cdot \frac{\xi}{2} \cdot \frac{\eta}{2} \cdot \frac{\eta+2}{4}$
7	$-\frac{\xi-2}{2} \cdot \frac{\xi+2}{2} \cdot \frac{\eta}{2} \cdot \frac{\eta+2}{4}$
8	$\frac{\xi}{2} \cdot \frac{\xi+2}{4} \cdot \frac{\eta}{2} \cdot \frac{\eta+2}{4}$
Sum: 1	

2.3.2.1 Comparison of patch coupling for the four polynomial staggered patch schemes

[Tables 2.3.5 to 2.3.8](#) list the leading order terms of the interpolation errors $\mathcal{L}(\xi, \eta) - f(\xi, \eta)$ for a set of binomial terms as test function f respectively for the four polynomial staggered patch schemes. As our definition of the interpolation order p allows basis polynomials whose maximum degree is $p - 1$ (e.g., Square-p2 staggered patch scheme has linear basis polynomials in [Table 2.3.3](#)), hence a p th order staggered patch scheme has the interpolation error of $O(\xi^p + \eta^p)$, which is evident in the interpolation errors in [Tables 2.3.5 to 2.3.8](#) for each of the four polynomial staggered patch schemes.

As the basis polynomials [\(2.3.5\)](#) are the standard 2D Lagrangian basis polynomials, the basis polynomials [\(2.3.5\)](#) posses all the properties of the standard Lagrangian basis polynomials ([\[TODO:cite\]](#)). Following are some of the key properties of the Lagrangian basis polynomials [\(2.3.5\)](#) that are common to all the four polynomial staggered patch schemes, namely Square-p2, Square-p4, Square-p6, and Square-8.

1. $B_S(\xi_T, \eta_T) = 1$ at the stencil index $T = S$, as evident from the basis polynomials in [Tables 2.3.2 to 2.3.4](#).
2. $B_S(\xi_T, \eta_T) = 0$ at the stencil index $T \neq S$, also as evident from the basis polynomials in [Tables 2.3.2 to 2.3.4](#).
3. Sum of all the basis polynomials of a stencil $\sum_{S=0}^{n_s-1} B_S(\xi, \eta) = 1$, as listed [Tables 2.3.2 to 2.3.4](#). This property ensures that constant functions are interpolated exactly, holds for all the four polynomial staggered patch schemes, for example the constant function c in [Table 2.3.5](#) for Square-p2 staggered patch scheme.
4. $\sum_{S=0}^{n_s-1} B_S(\xi, \eta) \cdot \xi_S = \xi$ and $\sum_{S=0}^{n_s-1} B_S(\xi, \eta) \cdot \eta_S = \eta$. This property ensures that linear functions are interpolated exactly, holds for all the four polynomial staggered patch schemes, for example the linear functions ξ, η in [Table 2.3.5](#) for Square-p2 staggered patch scheme.

Table 2.3.5: Leading order terms of interpolation errors $\mathcal{L}(\xi, \eta) - f(\xi, \eta)$, of Square-p2 patch scheme, for coupling h/u/v edge nodes (each in two rows respectively for left-right and bottom-top edges) of h/u/v-centred patches. Interpolation errors are $\mathcal{O}(\xi^2 + \eta^2)$.

c	ξ	η	$\eta\xi$	ξ^2	η^2	$\eta^2\xi$	$\eta\xi^2$	ξ^3	η^3	$\eta^2\xi^2$	$\eta^3\xi$	$\eta\xi^3$	ξ^4	η^4			
h-centred patch	h-nodes	0	0	0	0	0	0	4\xi	4\eta	0	4\eta\xi	4\eta\xi	4\xi^2	4\eta^2			
		0	0	0	0	0	0	4\xi	4\eta	0	4\eta\xi	4\eta\xi	4\xi^2	4\eta^2			
	u-nodes	0	0	0	0	1	0	0	-\eta\xi^2 + \eta	\xi	4\eta	-\eta^2\xi^2 + \eta^2	4\eta\xi	\eta\xi	1	4\eta^2	
		0	0	0	0	1	0	0	-\eta\xi^2 + \eta	\xi	4\eta	-\eta^2\xi^2 + \eta^2	4\eta\xi	\eta\xi	1	4\eta^2	
	v-nodes	0	0	0	0	0	1	-\eta^2\xi + \xi	0	4\xi	\eta	-\eta^2\xi^2 + \xi^2	\eta\xi	4\eta\xi	4\xi^2	1	
		0	0	0	0	0	1	-\eta^2\xi + \xi	0	4\xi	\eta	-\eta^2\xi^2 + \xi^2	\eta\xi	4\eta\xi	4\xi^2	1	
	w-centred patch	h-nodes	0	0	0	0	1	0	0	-\eta\xi^2 + \eta	\xi	4\eta	-\eta^2\xi^2 + \eta^2	4\eta\xi	\eta\xi	1	4\eta^2
			0	0	0	0	1	0	0	-\eta\xi^2 + \eta	\xi	4\eta	-\eta^2\xi^2 + \eta^2	4\eta\xi	\eta\xi	1	4\eta^2
		u-nodes	0	0	0	0	0	0	0	0	4\xi	4\eta	0	4\eta\xi	4\eta\xi	4\xi^2	4\eta^2
			0	0	0	0	0	0	0	0	4\xi	4\eta	0	4\eta\xi	4\eta\xi	4\xi^2	4\eta^2
		v-nodes	0	0	0	0	1	1	-\eta^2\xi + \xi	-\eta\xi^2 + \eta	\xi	\eta	1	\eta\xi	\eta\xi	1	1
			0	0	0	0	1	1	-\eta^2\xi + \xi	-\eta\xi^2 + \eta	\xi	\eta	1	\eta\xi	\eta\xi	1	1
		h-nodes	0	0	0	0	0	1	-\eta^2\xi + \xi	0	4\xi	\eta	-\eta^2\xi^2 + \xi^2	\eta\xi	4\eta\xi	4\xi^2	1
			0	0	0	0	0	1	-\eta^2\xi + \xi	0	4\xi	\eta	-\eta^2\xi^2 + \xi^2	\eta\xi	4\eta\xi	4\xi^2	1
		u-nodes	0	0	0	0	1	1	-\eta^2\xi + \xi	-\eta\xi^2 + \eta	\xi	\eta	1	\eta\xi	\eta\xi	1	1
			0	0	0	0	1	1	-\eta^2\xi + \xi	-\eta\xi^2 + \eta	\xi	\eta	1	\eta\xi	\eta\xi	1	1
		v-nodes	0	0	0	0	0	0	0	0	4\xi	4\eta	0	4\eta\xi	4\eta\xi	4\xi^2	4\eta^2
			0	0	0	0	0	0	0	0	4\xi	4\eta	0	4\eta\xi	4\eta\xi	4\xi^2	4\eta^2

Table 2.3.6: Leading order terms of interpolation errors $\mathcal{L}(\xi, \eta) - f(\xi, \eta)$, of Square-p4 patch scheme, for coupling h/ $\textcolor{red}{u}$ / $\textcolor{blue}{v}$ edge nodes (each in two rows respectively for left-right and bottom-top edges) of h/ $\textcolor{red}{u}$ / $\textcolor{blue}{v}$ -centred patches. Interpolation errors are $\mathcal{O}(\xi^4 + \eta^4)$. Functions $f = \xi^a \cdot \eta^b$ with $a + b < 3$ are interpolated exactly.

	ξ^3	$\eta\xi^2$	$\eta^2\xi$	η^3	ξ^4	$\eta\xi^3$	$\eta^2\xi^2$	$\eta^3\xi$	η^4	ξ^5	$\eta\xi^4$	$\eta^2\xi^3$	$\eta^3\xi^2$	$\eta^4\xi$
h-centred patch h-nodes	0	0	0	0	0	0	0	0	0	-64ξ	0	0	0	0
	0	0	0	0	0	0	0	0	0	-64ξ	0	0	0	0
	0	0	0	0	-9	0	0	0	0	-9ξ	$10\eta\xi^2 - 9\eta$	0	0	0
	0	0	0	0	-9	0	0	0	0	-9ξ	$10\eta\xi^2 - 9\eta$	0	0	0
	0	0	0	0	0	0	0	0	-9	-64ξ	0	0	0	$10\eta^2\xi - 9\xi$
	0	0	0	0	0	0	0	0	-9	-64ξ	0	0	0	$10\eta^2\xi - 9\xi$
$\textcolor{red}{u}$ -centred patch $\textcolor{red}{u}$ -nodes	0	0	0	0	-9	0	0	0	0	-9ξ	$10\eta\xi^2 - 9\eta$	0	0	0
	0	0	0	0	-9	0	0	0	0	-9ξ	$10\eta\xi^2 - 9\eta$	0	0	0
	0	0	0	0	0	0	0	0	0	-64ξ	0	0	0	0
	0	0	0	0	0	0	0	0	0	-64ξ	0	0	0	0
	0	0	0	0	-9	0	0	0	-9	-9ξ	$10\eta\xi^2 - 9\eta$	0	0	$10\eta^2\xi - 9\xi$
	0	0	0	0	-9	0	0	0	-9	-9ξ	$10\eta\xi^2 - 9\eta$	0	0	$10\eta^2\xi - 9\xi$
$\textcolor{blue}{v}$ -centred patch $\textcolor{blue}{v}$ -nodes	0	0	0	0	0	0	0	0	-9	-64ξ	0	0	0	$10\eta^2\xi - 9\xi$
	0	0	0	0	0	0	0	0	-9	-64ξ	0	0	0	$10\eta^2\xi - 9\xi$
	0	0	0	0	-9	0	0	0	-9	-9ξ	$10\eta\xi^2 - 9\eta$	0	0	$10\eta^2\xi - 9\xi$
	0	0	0	0	-9	0	0	0	-9	-9ξ	$10\eta\xi^2 - 9\eta$	0	0	$10\eta^2\xi - 9\xi$
	0	0	0	0	0	0	0	0	0	-64ξ	0	0	0	0
	0	0	0	0	0	0	0	0	0	-64ξ	0	0	0	0

Table 2.3.7: Leading order terms of interpolation errors $\mathcal{L}(\xi, \eta) - f(\xi, \eta)$, of Square-p6 patch scheme, for coupling h/u/v edge nodes (each in two rows respectively for left-right and bottom-top edges) of h/u/v-centred patches. Interpolation errors are $\mathcal{O}(\xi^6 + \eta^6)$. Functions $f = \xi^a \cdot \eta^b$ with $a + b < 5$ are interpolated exactly.

	ξ^5	$\eta\xi^4$	$\eta^2\xi^3$	$\eta^3\xi^2$	$\eta^4\xi$	η^5	ξ^6	$\eta\xi^5$	$\eta^2\xi^4$	$\eta^3\xi^3$	$\eta^4\xi^2$	$\eta^5\xi$	η^6	ξ^7
h-centred patch h-nodes	0	0	0	0	0	0	0	0	0	0	0	0	0	2304ξ
	0	0	0	0	0	0	0	0	0	0	0	0	0	2304ξ
	0	0	0	0	0	0	225	0	0	0	0	0	0	225ξ
	0	0	0	0	0	0	225	0	0	0	0	0	0	225ξ
	0	0	0	0	0	0	0	0	0	0	0	0	0	2304ξ
	0	0	0	0	0	0	0	0	0	0	0	0	225	2304ξ
h-centred patch u-nodes	0	0	0	0	0	0	0	0	0	0	0	0	0	225ξ
	0	0	0	0	0	0	225	0	0	0	0	0	0	225ξ
	0	0	0	0	0	0	0	0	0	0	0	0	0	2304ξ
	0	0	0	0	0	0	0	0	0	0	0	0	0	2304ξ
	0	0	0	0	0	0	225	0	0	0	0	0	0	225ξ
	0	0	0	0	0	0	0	0	0	0	0	0	0	225ξ
h-centred patch v-nodes	0	0	0	0	0	0	0	0	0	0	0	0	0	2304ξ
	0	0	0	0	0	0	0	0	0	0	0	0	0	225ξ
	0	0	0	0	0	0	0	0	0	0	0	0	0	2304ξ
	0	0	0	0	0	0	0	0	0	0	0	0	0	2304ξ
	0	0	0	0	0	0	0	0	0	0	0	0	0	225ξ
	0	0	0	0	0	0	0	0	0	0	0	0	0	225ξ
u-centred patch h-nodes	0	0	0	0	0	0	0	0	0	0	0	0	0	2304ξ
	0	0	0	0	0	0	0	0	0	0	0	0	0	225ξ
	0	0	0	0	0	0	0	0	0	0	0	0	0	2304ξ
	0	0	0	0	0	0	0	0	0	0	0	0	0	2304ξ
	0	0	0	0	0	0	0	0	0	0	0	0	0	225ξ
	0	0	0	0	0	0	0	0	0	0	0	0	0	225ξ
u-centred patch u-nodes	0	0	0	0	0	0	0	0	0	0	0	0	0	2304ξ
	0	0	0	0	0	0	0	0	0	0	0	0	0	225ξ
	0	0	0	0	0	0	0	0	0	0	0	0	0	2304ξ
	0	0	0	0	0	0	0	0	0	0	0	0	0	2304ξ
	0	0	0	0	0	0	0	0	0	0	0	0	0	225ξ
	0	0	0	0	0	0	0	0	0	0	0	0	0	225ξ
u-centred patch v-nodes	0	0	0	0	0	0	0	0	0	0	0	0	0	2304ξ
	0	0	0	0	0	0	0	0	0	0	0	0	0	225ξ
	0	0	0	0	0	0	0	0	0	0	0	0	0	2304ξ
	0	0	0	0	0	0	0	0	0	0	0	0	0	2304ξ
	0	0	0	0	0	0	0	0	0	0	0	0	0	225ξ
	0	0	0	0	0	0	0	0	0	0	0	0	0	225ξ
v-centred patch h-nodes	0	0	0	0	0	0	0	0	0	0	0	0	0	2304ξ
	0	0	0	0	0	0	0	0	0	0	0	0	0	2304ξ
	0	0	0	0	0	0	0	0	0	0	0	0	0	225ξ
	0	0	0	0	0	0	0	0	0	0	0	0	0	225ξ
	0	0	0	0	0	0	0	0	0	0	0	0	0	2304ξ
	0	0	0	0	0	0	0	0	0	0	0	0	0	2304ξ

Table 2.3.8: Leading order terms of interpolation errors $\mathcal{L}(\xi, \eta) - f(\xi, \eta)$, of Square-p8 patch scheme, for coupling h/u/v edge nodes (each in two rows respectively for left-right and bottom-top edges) of h/u/v-centred patches. Interpolation errors are $\mathcal{O}(\xi^8 + \eta^8)$. Functions $f = \xi^a \cdot \eta^b$ with $a + b < 7$ are interpolated exactly.

	ξ^7	$\eta \xi^6$	$\eta^2 \xi^5$	$\eta^3 \xi^4$	$\eta^4 \xi^3$	$\eta^5 \xi^2$	$\eta^6 \xi$	η^7	ξ^8	$\eta \xi^7$	$\eta^2 \xi^6$	$\eta^3 \xi^5$	$\eta^4 \xi^4$	$\eta^5 \xi^3$
h-centred patch h-nodes	0	0	0	0	0	0	0	0	0	0	0	0	0	0
	0	0	0	0	0	0	0	0	0	0	0	0	0	0
	0	0	0	0	0	0	0	0	-11025	0	0	0	0	0
	0	0	0	0	0	0	0	0	-11025	0	0	0	0	0
	0	0	0	0	0	0	0	0	0	0	0	0	0	0
	0	0	0	0	0	0	0	0	0	0	0	0	0	0
h-centred patch v-nodes	0	0	0	0	0	0	0	0	-11025	0	0	0	0	0
	0	0	0	0	0	0	0	0	-11025	0	0	0	0	0
	0	0	0	0	0	0	0	0	0	0	0	0	0	0
	0	0	0	0	0	0	0	0	0	0	0	0	0	0
	0	0	0	0	0	0	0	0	-11025	0	0	0	0	0
	0	0	0	0	0	0	0	0	-11025	0	0	0	0	0
v-centred patch h-nodes	0	0	0	0	0	0	0	0	0	0	0	0	0	0
	0	0	0	0	0	0	0	0	-11025	0	0	0	0	0
	0	0	0	0	0	0	0	0	-11025	0	0	0	0	0
	0	0	0	0	0	0	0	0	0	0	0	0	0	0
	0	0	0	0	0	0	0	0	-11025	0	0	0	0	0
	0	0	0	0	0	0	0	0	-11025	0	0	0	0	0
v-centred patch u-nodes	0	0	0	0	0	0	0	0	0	0	0	0	0	0
	0	0	0	0	0	0	0	0	-11025	0	0	0	0	0
	0	0	0	0	0	0	0	0	-11025	0	0	0	0	0
	0	0	0	0	0	0	0	0	0	0	0	0	0	0
	0	0	0	0	0	0	0	0	-11025	0	0	0	0	0
	0	0	0	0	0	0	0	0	-11025	0	0	0	0	0

Chapter 3

Patch schemes accurately simulate general linear waves

3.1 Introduction

This chapter shows that the staggered patch schemes accurately simulate the macro-scale dynamics of a general dissipative linear wave PDE, with linear drag and viscous diffusion respectively characterised by the coefficients c_D, c_V ,

$$\frac{\partial h}{\partial t} = -\frac{\partial u}{\partial x} - \frac{\partial v}{\partial y}, \quad (3.1.1a)$$

$$\frac{\partial u}{\partial t} = -\frac{\partial h}{\partial x} - c_D u + c_V \frac{\partial^2 u}{\partial x^2} + c_V \frac{\partial^2 u}{\partial y^2}, \quad (3.1.1b)$$

$$\frac{\partial v}{\partial t} = -\frac{\partial h}{\partial y} - c_D v + c_V \frac{\partial^2 v}{\partial x^2} + c_V \frac{\partial^2 v}{\partial y^2}, \quad (3.1.1c)$$

with the boundary conditions that the three fields h, u and v are L -periodic in both x and y . The case $c_D = c_V = 0$ corresponds to the *ideal wave*, that is without any dissipation (Dean and Dalrymple 1991, pp. 136–137; Mehaute 1976, pp. 257–258).

[TODO/AJR10: Throughout this introduction, summarise the most important outcome of each of the following sections.]

As in the generic 2D wave-like system (2.2.1) of §2.2.1, the dependent variables in PDEs (3.1.1) let us interpret the model as a shallow water flow with h as depth and u, v as horizontal velocities, but the set of PDEs (3.1.1) is a generic model of many 2D *linear* wave phenomena.

Approximating the spatial derivatives in the general dissipative linear wave PDEs (3.1.1) by central finite differences on the staggered grid nodes

(filled solid circles in Fig. 2.2.1 of §2.2.1), gives the *full-domain micro-scale system* corresponding to the general dissipative linear wave PDEs (3.1.1) as

- $\frac{dh_{i,j}}{dt} = -\frac{u_{i+1,j} - u_{i-1,j}}{2\delta} - \frac{v_{i,j+1} - v_{i,j-1}}{2\delta}$ (3.1.2a)
for $i \in \{0, 2, 4, \dots, n-2\}$, $j \in \{0, 2, 4, \dots, n-2\}$;

- $\frac{du_{i,j}}{dt} = -\frac{h_{i+1,j} - h_{i-1,j}}{2\delta} - c_D u_{i,j}$
 $+ c_V \frac{u_{i-2,j} - 2u_{i,j} + u_{i+2,j}}{4\delta^2} + c_V \frac{u_{i,j-2} - 2u_{i,j} + u_{i,j+2}}{4\delta^2}$ (3.1.2b)
for $i \in \{1, 3, 5, \dots, n-1\}$, $j \in \{0, 2, 4, \dots, n-2\}$;

- $\frac{dv_{i,j}}{dt} = -\frac{h_{i,j+1} - h_{i,j-1}}{2\delta} - c_D v_{i,j}$
 $+ c_V \frac{v_{i-2,j} - 2v_{i,j} + v_{i+2,j}}{4\delta^2} + c_V \frac{v_{i,j-2} - 2v_{i,j} + v_{i,j+2}}{4\delta^2}$ (3.1.2c)
for $i \in \{0, 2, 4, \dots, n-2\}$, $j \in \{1, 3, 5, \dots, n-1\}$,

Analogous to the periodic boundary conditions of the PDEs (3.1.1), the three fields h , u , v are n -periodic in both i and j , where $n = L/\delta$. As a dynamical system, the full-domain micro-scale system (3.1.2) in vector notation, for the general dissipative linear wave (3.1.1) is

$$\frac{dx}{dt} = f(x), \quad (3.1.3)$$

where x is the same state vector (2.2.3) of the full-domain micro-scale system for generic wave-like system in §2.2.1.

A full-domain micro-scale simulation is performed by numerical time-integration of the ODEs (3.1.2) on the nodes of the micro-scale staggered grid (filled solid circles in Fig. 2.2.1), with the discrete macro-scale n -periodic boundary conditions in both i and j .

Now let's consider the patch scheme for the system (3.1.2), over a staggered patch grid with $N \times N$ macro-grid intervals and each patch containing $n \times n$ sub-patch micro-grid intervals.. To use the finite difference equations (3.1.2) as the micro-scale system within the patches, a staggered patch grid with one layer of edge nodes, such as in Fig. 2.2.3b of §2.2.2, is not sufficient. For example, in equation (3.1.2b), to compute the time derivative $du_{i,j}/dt$ for the bottom left u node of the u -centred patch, the second spatial derivative in viscous diffusion term needs the value of $u_{i-2,j}$, which is outside to the left of the u -centred patch and not available in Fig. 2.2.3b. The additional layer of edge nodes in Fig. 2.2.5a of §2.2.3 provides the

$u_{i-2,j}$ for the bottom left u node of the u -centred patch. Hence, a staggered patch scheme with the 2D general dissipative linear wave (3.1.2) as the underlying micro-scale system within the patches, requires a patch grid with two layers of edge nodes as in Fig. 2.2.5a of §2.2.3.

Using the full-domain micro-scale system (3.1.2) within the patches of the a suitable staggered patch grid (e.g., the patch grid of Fig. 2.2.5a with $n = 6$), gives the *staggered patch scheme*

$$\bullet \frac{d}{dt} h_{i,j}^{I,J}(t) = -\frac{u_{i+1,j}^{I,J} - u_{i-1,j}^{I,J}}{2\delta} - \frac{v_{i,j+1}^{I,J} - v_{i,j-1}^{I,J}}{2\delta}, \quad (3.1.4a)$$

$$\bullet \frac{d}{dt} u_{i,j}^{I,J}(t) = -\frac{h_{i+1,j}^{I,J} - h_{i-1,j}^{I,J}}{2\delta} - c_D u_{i,j}^{I,J} + c_V \frac{u_{i-2,j}^{I,J} - 2u_{i,j}^{I,J} + u_{i+2,j}^{I,J}}{4\delta^2} + c_V \frac{u_{i,j-2}^{I,J} - 2u_{i,j}^{I,J} + u_{i,j+2}^{I,J}}{4\delta^2}, \quad (3.1.4b)$$

$$\bullet \frac{d}{dt} v_{i,j}^{I,J}(t) = -\frac{h_{i,j+1}^{I,J} - h_{i,j-1}^{I,J}}{2\delta} - c_D v_{i,j}^{I,J} + c_V \frac{v_{i-2,j}^{I,J} - 2v_{i,j}^{I,J} + v_{i+2,j}^{I,J}}{4\delta^2} + c_V \frac{v_{i,j-2}^{I,J} - 2v_{i,j}^{I,J} + v_{i,j+2}^{I,J}}{4\delta^2}, \quad (3.1.4c)$$

and a patch coupling (e.g., Square-p4) to compute the edge values

◦ $h_{i,j}^{I,J}$, ◦ $u_{i,j}^{I,J}$, ◦ $v_{i,j}^{I,J}$ for

$$\begin{aligned} i &\in \{-1, 0, n, n+1\}, j \in \{1, 2, \dots, n-1\} \text{ for left and right edges and} \\ i &\in \{1, 2, \dots, n-1\}, j \in \{-1, 0, n, n+1\} \text{ for bottom and top edges,} \end{aligned} \quad (3.1.4d)$$

for the same interior indices i, j and patch indices I, J in (2.2.5) of §2.2.1.

Analogous to the periodic boundary conditions for the full-domain micro-scale system (3.1.2), the three fields h, u, v in the patch scheme (3.1.4) are macro-scale N -periodic in both I and J , where $N = L/\Delta$. As a dynamical system, the staggered patch scheme (3.1.4) in vector notation, corresponding to the full-domain micro-scale system (3.1.2) of dissipative linear wave is

$$\frac{dx^I}{dt} = F(x^I; x^E(x^I)). \quad (3.1.5)$$

with the same state vector x^I (2.2.6) and and a similar edge vector x^E as those of the patch scheme in §2.2.2 for generic wave-like system. The $F(x^I; x^E(x^I))$ in the staggered patch scheme dynamical system (3.1.5) corresponds to the $f(x)$ in the full-domain micro-scale system (3.1.3). The

functions \mathbf{F} and \mathbf{f} encode same the micro-scale system for the general dissipative linear wave PDEs (3.1.1); Section 2.2.2 explains this difference for the generic wave-like system.

As in the patch scheme (2.2.5) of §2.2.2, a specific patch coupling (e.g., Square-p2) computes patch edge values ($\circ h_{i,j}^{I,J}$, $\circ u_{i,j}^{I,J}$, $\circ v_{i,j}^{I,J}$ in Fig. 2.2.5a) from the centre values of neighbouring patches ($\bullet h_{i,j}^{I,J}$, $\bullet u_{i,j}^{I,J}$, $\bullet v_{i,j}^{I,J}$ with $i = j = n/2$ in Fig. 2.2.5a). The patch coupling provides a mechanism whereby patches influence each other, §2.3 discusses various details of different patch couplings.

Patch scheme simulation is performed by numerical time-integration of the ODEs (3.1.4) on the interior nodes of the staggered patch grid (filled solid circles in Fig. 2.2.3b), with the discrete macro-scale N -periodic boundary conditions in both I and J . As in §2.2.2, evaluating the time derivatives in the staggered patch scheme (3.1.4) is done in two steps: first, edge values $x^E(x^I)$ are computed via patch coupling; second, using both interior and edge values of each patch in the staggered patch grid, the time derivatives of x^I are computed for the staggered patch scheme (3.1.4) of dissipative linear wave.

3.2 Staggered patch schemes are accurate

This section studies the accuracy of the developed five staggered patch schemes for the general dissipative linear waves. We establish the accuracy of the staggered patch schemes by comparing the eigenvalues of the staggered patch schemes with the eigenvalues of fine- and coarse-grid full-domain micro-scale system, and for completeness also compare with the eigenvalues of the general dissipative linear wave PDEs (3.1.1).

The objective of the staggered patch scheme is to perform reduced order multiscale simulation of the underlying *micro-scale system*. Hence, for assessing the accuracy of the patch schemes, as p. 11 of §2.2.1 explains, the eigenvalues of the full domain *micro-scale system* are the reference eigenvalues, not that of the PDEs. Our eigenvalue analysis for accuracy in this section is done for representative subsets of macro-grid intervals $N \in \{6, 10, 14\}$ and sub-patch micro-grid intervals $n \in \{6, 10\}$; Section 3.6 studies the consistency of the staggered patch schemes over various number of macro-grid intervals. The following paragraphs introduce the approach of studying the accuracy of the staggered patch schemes and discuss the conventions adapted.

Time dependent solutions of linear ODEs are linear combinations of the spatial modes (i.e., eigenvectors) where the initial condition gives the

amplitudes of the modes [TODO/cite]. Due to spatial homogeneity on the macro-scale dynamics in both the original system and the patch scheme, the macro-scale modes in both the systems are the same macro-scale Fourier modes. Hence, there is no error in the macro-scale spatial structures. The only error in the patch scheme is in the eigenvalues. Thus, when a patch scheme eigenvalues agree closely with the corresponding eigenvalues of the full-domain micro-scale system, the patch scheme simulation is accurate *globally for any initial condition*. The eigenvalues of the staggered patch schemes consist of the two scales.

1. *Macro-scale* eigenvalues correspond to the small wavenumber macro-scale modes over the domain.
2. *Micro-scale* eigenvalues correspond to large wavenumber micro-scale sub-patch modes.

We aim to design the multiscale staggered patch schemes to accurately simulate the large scale waves that are characterised by the macro-scale eigenvalues. A staggered patch scheme is accurate when the macro-scale eigenvalues of that patch scheme agree closely with the corresponding macro-scale eigenvalues of the full-domain micro-scale system. Thus, we aim to design the staggered patch schemes with the macro-scale eigenvalues as close as possible to the corresponding macro-scale eigenvalues of the full domain micro-scale system (3.1.2). Hence, the eigenvalue analysis for accuracy in this section, compares in the complex plane the eigenvalues of the staggered patch schemes with the eigenvalues of the full-domain micro-scale system.

Sections 3.2.1 to 3.2.5 describe the methods of analytically deriving and numerically computing the eigenvalues for

1. the 2D general dissipative linear wave PDEs (3.1.1),
2. the full-domain micro-scale system (3.1.2), and
3. the staggered patch scheme (3.1.4).

Following a standard approach of substituting an arbitrary Fourier mode into the PDEs/ODEs, §§3.2.1 and 3.2.2 derive the analytic eigenvalues of general dissipative linear wave PDEs (3.1.1) and the corresponding discrete full-domain micro-scale system (3.1.2). Similarly §3.2.3 derives the analytic eigenvalues of a staggered patch scheme. To numerically compute the eigenvalues of the numerical staggered patch scheme, which includes any instabilities and inaccuracies due to the numerical roundoff errors,

[§§3.2.4](#) and [3.2.5](#) numerically computes the Jacobians of the evolution functions $\mathbf{f}(\mathbf{x})$ in the full-domain system [\(3.1.3\)](#), and $\mathbf{F}(\mathbf{x}^I; \mathbf{x}^E(\mathbf{x}^I))$ in the patch scheme [\(3.1.5\)](#) respectively.

[Section 3.2.6](#) compares and contrasts various eigenvalues (e.g., analytic and numerical eigenvalues of the PDEs, full-domain micro-scale system, and patch schemes). We use the following notational convention to identify the various eigenvalues.

- Eigenvalue *subscripts* in $\lambda_p^{()}, \lambda_{m\delta}^{()}, \lambda_{m\Delta}^{()}, \lambda_{PDE}^{()}$ denote the system.
 - $\lambda_p^{()}$ are for staggered patch schemes (e.g., λ_p^{NE1} of [§3.2.3](#) and λ_p^N of [§3.2.5](#)).
 - $\lambda_{m\delta}^{()}$ are for fine-grid full domain micro-scale system with same grid-spacing as sub-patch micro-grid interval δ (e.g., $\lambda_{m\delta}^A$ of [§3.2.2](#) and $\lambda_{m\delta}^N$ of [§3.2.4](#)).
 - $\lambda_{m\Delta}^{()}$ are for fine-grid full domain micro-scale system with same grid-spacing as the inter-patch distance Δ (e.g., $\lambda_{m\Delta}^A$ of [§3.2.2](#) and $\lambda_{m\Delta}^N$ of [§3.2.4](#)).
 - $\lambda_{PDE}^{()}$ are for the general linear wave PDE (e.g., λ_{PDE}^A of [§3.2.1](#)).
- Eigenvalue *superscripts* in $\lambda_{()}^N, \lambda_{()}^{NE1}, \lambda_{()}^A$ denote the method of computing numerical eigenvalues values.
 - $\lambda_{()}^N$ are computed from the numerical Jacobian of the system (e.g., $\lambda_{m\delta}^N, \lambda_{m\Delta}^N$ of [§3.2.4](#) and λ_p^N of [§3.2.5](#)).
 - $\lambda_{()}^{NE1}$ are computed from numerically evaluated analytic one-cell Jacobian of the system (e.g., λ_p^{NE1} of [§3.2.3](#)).
 - $\lambda_{()}^A$ are computed from the closed-form analytic expressions for the eigenvalues (e.g., λ_{PDE}^A of [§3.2.1](#) and $\lambda_{m\delta}^A, \lambda_{m\Delta}^A$ of [§3.2.2](#)).

3.2.1 Eigenvalue analysis of the PDEs

This subsection derives the eigenvalues of the 2D general dissipative linear wave PDEs [\(3.1.1\)](#) to compare for a sanity check with the eigenvalues of the full-domain micro-scale system [\(5.1.4\)](#) and the various staggered patch schemes.

One of the standard analytic approach to derive the eigenvalues of a linear PDE (e.g., Hinch [2020](#), pp. 138–139; Griffiths and Schiesser [2011](#)) is to substitute an arbitrary Fourier mode into the PDE, derive an eigensystem in

terms of a system matrix that characterises the time evolution, and subsequently compute the eigenvalues of the system matrix which characterises both the stability and accuracy of the system. Following this standard approach, consider an arbitrary Fourier mode of the general dissipative linear wave PDE (3.1.1), with real wavenumber (k_x, k_y) and complex growth rate λ ,

$$h(x, y, t) = He^{i(k_x x + k_y y) + \lambda t}, \quad (3.2.1a)$$

$$u(x, y, t) = Ue^{i(k_x x + k_y y) + \lambda t}, \quad (3.2.1b)$$

$$v(x, y, t) = Ve^{i(k_x x + k_y y) + \lambda t}. \quad (3.2.1c)$$

Substituting the Fourier mode (3.2.1) into the general dissipative linear wave PDEs (3.1.1), algebraic simplifications, and arranging in matrix form give the eigensystem

$$\begin{bmatrix} 0 & -ik_x & -ik_y \\ -ik_x & -c_D - c_V(k_x^2 + k_y^2) & 0 \\ -ik_y & 0 & -c_D - c_V(k_x^2 + k_y^2) \end{bmatrix} \begin{bmatrix} H \\ U \\ V \end{bmatrix} = \lambda \begin{bmatrix} H \\ U \\ V \end{bmatrix}. \quad (3.2.2)$$

The three eigenvalues of the 3×3 Jacobian in eigensystem (3.2.2) are (one real and a complex conjugate pair),

$$\lambda_{\text{PDE}}^A = \begin{cases} -c_D - c_V(k_x^2 + k_y^2), \\ -\frac{c_D}{2} - \frac{c_V}{2}(k_x^2 + k_y^2) \pm \sqrt{\left[\frac{c_D}{2} + \frac{c_V}{2}(k_x^2 + k_y^2)\right]^2 - (k_x^2 + k_y^2)}. \end{cases} \quad (3.2.3)$$

With no dissipation, that is with $c_D = c_V = 0$ in the expression (3.2.3), the three eigenvalues of the ideal wave are $(0, \pm i\omega_0)$, where the nonzero frequency of this ideal (undamped) wave $\omega_0 = \sqrt{k_x^2 + k_y^2}$. Rewriting the eigenvalues (3.2.3) in terms of ω_0 ,

$$\lambda_{\text{PDE}}^A = \begin{cases} -(c_D + c_V\omega_0^2), \\ -(c_D + c_V\omega_0^2)/2 \pm \sqrt{[(c_D + c_V\omega_0^2)/2]^2 - \omega_0^2}. \end{cases} \quad (3.2.4)$$

With dissipation, that is with $c_D, c_V > 0$, the real parts of all three eigenvalues (3.2.4) are negative, meaning that the wave solutions decay over time.

- For high dissipation (large positive values of c_D and/or c_V), the square root in the expression (3.2.4) gives a real value, making all three eigenvalues real, which correspond to an overdamped system where any initial condition or disturbance will quickly decay to zero, which is not our interest.

- For low dissipation (small positive values of c_D and/or c_V), the square root in the expression (3.2.4) gives an imaginary component, that is the damped frequency, so any initial wave will oscillate and decay slowly to zero.

Expressions (3.2.3) and (3.2.4) give eigenvalues of the 2D general dissipative linear wave PDEs (3.1.1) with linear drag c_D and viscous diffusion c_V [TODO/update: viscosity?]. We numerically evaluate eigenvalue expressions (3.2.3) or (3.2.4) for various macro-scale wavenumbers and compare for a sanity check with the eigenvalues of the full-domain micro-scale system (5.1.4) and the various staggered patch schemes while assessing the accuracy of the patch schemes in §3.2.6.

3.2.2 Eigenvalue analysis of staggered grid full-domain micro-scale system

This subsection derives the eigenvalues of the staggered grid full-domain micro-scale system (3.1.2) for the 2D general dissipative linear wave PDEs (3.1.1). Comparing these eigenvalues of the full-domain system with the eigenvalues of the staggered patch schemes, §3.2.6 studies the accuracy of the patch schemes and §3.5 studies stability of the patch schemes.

We follow the same standard analytic approach (e.g., Hinch 2020, pp. 138–139; Griffiths and Schiesser 2011), as done for the 2D general dissipative linear wave PDE in §3.2.1, but over a discrete infinite micro-scale staggered grid (number of grid intervals $n \rightarrow \infty$ in Fig. 2.2.1). Consider an arbitrary Fourier mode of the full-domain micro-scale system (3.1.2), with real wavenumber (k_x, k_y) and complex growth rate λ ,

$$\bullet h_{i,j}(t) = He^{i(k_x i \delta + k_y j \delta) + \lambda t}, \quad (3.2.5a)$$

$$\bullet u_{i,j}(t) = Ue^{i(k_x i \delta + k_y j \delta) + \lambda t}, \quad (3.2.5b)$$

$$\bullet v_{i,j}(t) = Ve^{i(k_x i \delta + k_y j \delta) + \lambda t}. \quad (3.2.5c)$$

Throughout this thesis, i denotes the micro-grid index in x -direction (for both full-domain and sub-patch micro-grids), whereas $i = \sqrt{-1}$ is the imaginary unit. Substituting the Fourier mode (3.2.5) into the full-domain micro-scale system (3.1.2), some algebraic simplifications, and arranging in matrix form give the eigensystem

$$\mathbf{J} \begin{bmatrix} H \\ U \\ V \end{bmatrix} = \lambda \begin{bmatrix} H \\ U \\ V \end{bmatrix}, \quad (3.2.6)$$

where the Jacobian

$$\mathbf{J} = \begin{bmatrix} 0 & -\frac{i \sin(k_x \delta)}{\delta} & -\frac{i \sin(k_y \delta)}{\delta} \\ -\frac{i \sin(k_x \delta)}{\delta} & -c_D - c_V \left(\frac{\sin^2(k_x \delta)}{\delta^2} + \frac{\sin^2(k_y \delta)}{\delta^2} \right) & 0 \\ -\frac{i \sin(k_y \delta)}{\delta} & 0 & -c_D - c_V \left(\frac{\sin^2(k_x \delta)}{\delta^2} + \frac{\sin^2(k_y \delta)}{\delta^2} \right) \end{bmatrix}.$$

The three eigenvalues of the 3×3 Jacobian \mathbf{J} in the eigensystem (3.2.6) are (one real and a complex conjugate pair),

$$\lambda_m^A = \begin{cases} -(c_D + c_V \omega_{m,0}^2), \\ -(c_D + c_V \omega_{m,0}^2)/2 \pm \sqrt{[(c_D + c_V \omega_{m,0}^2)/2]^2 - \omega_{m,0}^2}, \end{cases} \quad (3.2.7)$$

where

$$\omega_{m,0} = \sqrt{\sin^2(k_x \delta)/\delta^2 + \sin^2(k_y \delta)/\delta^2} \quad (3.2.8)$$

is the frequency of the full-domain micro-scale system for ideal wave (i.e., undamped with $c_D = c_V = 0$). When we numerically evaluate these eigenvalues λ_m^A of the full-domain micro-scale system,

- for the same grid-spacing δ as the sub-patch micro-grid interval (also called δ), we call the eigenvalues $\lambda_{m\delta}^A$,
- for the same grid-spacing Δ as the inter-patch distance Δ , we call the eigenvalues $\lambda_{m\Delta}^A$.

Comparing eigenvalue expression (3.2.7) with the eigenvalue expression (3.2.4) of the PDE, the full-domain micro-scale eigenvalues converge to the eigenvalues of the 2D general dissipative linear wave PDEs (3.1.1) when $\omega_{m,0}^2 \rightarrow \omega_0^2 = k_x^2 + k_y^2$. Expanding $\omega_{m,0}^2$ as power series in either (k_x, k_y) or δ we get,

$$\omega_{m,0}^2 = k_x^2 + k_y^2 - \frac{1}{3} (k_x^4 + k_y^4) \delta^2 + \frac{2}{45} (k_x^6 + k_y^6) \delta^4 - \frac{1}{315} (k_x^8 + k_y^8) \delta^6 + \mathcal{O}((k_x^{10} + k_y^{10}) \delta^8). \quad (3.2.9)$$

The series expansion (3.2.9) shows that the eigenvalues of the full-domain micro-scale system converge to the analytic eigenvalues of the PDEs (3.1.1) as we decrease the grid interval δ and/or wavenumber (k_x, k_y) .

We numerically evaluate eigenvalue expression (3.2.3) or (3.2.4) for various macro-scale wavenumbers and compare with the eigenvalues of the general linear wave PDEs and the patch schemes while assessing the accuracy (§3.2.6) and stability (§3.5) of the patch schemes.

3.2.3 Analytic eigenvalue analysis of staggered patch schemes

This subsection discusses a method of deriving analytic eigenvalues of a generic staggered patch scheme (3.1.4) over a staggered patch grid, for the 2D general dissipative linear wave PDEs (3.1.1). This subsection also gives example expressions for a specific patch coupling among the various staggered patch schemes. We use the patch scheme eigenvalues to assess accuracy (§3.2.6), stability (§3.5), and consistency (§3.6) of the staggered patch schemes.

We follow a similar analytic approach as done for analytic eigenvalue analysis of the staggered grid full-domain micro-scale system in §3.2.2, but over an infinite *staggered patch grid* (number of macro-scale grid intervals ($N \rightarrow \infty$ in Fig. 2.2.5a)). Section 3.1 discusses why the staggered patch grid in Fig. 2.2.5a with such edge node arrangement is required for the current consideration of the 2D general dissipative linear wave.

Unlike the analysis of a staggered grid full-domain micro-scale system in §3.2.2, the dynamics of a staggered patch scheme that we aim to analyse via their eigenvalues has an emergent behaviour due to the coupled dynamics at two different length scales. Once length scale is due to the micro-scale interactions within the patches, and another length scale is due to the different macro-scale patch coupling across the patches (Spectral, Square-p2, Square-p4, etc.). Hence, for eigenvalue analysis of a staggered patch scheme, our arbitrary Fourier mode needs to include spatial structures of the two scales: micro-scale within a patch and macro-scale across the patches.

Our aim is to study the macro-scale behaviour of the staggered patch scheme, which is manifested by the micro-scale behaviour within the patches.

1. As we want to characterise the emergent macro-scale behaviour, as opposed to the complex exponential factor $\exp(i[k_x \mathbf{i}\delta + k_y \mathbf{j}\delta])$ in the arbitrary Fourier mode (3.2.5) of the full-domain micro-scale system, we want the complex exponential factor $\exp(i[k_x \mathbf{I}\Delta + k_y \mathbf{J}\Delta])$ in the arbitrary Fourier mode for staggered patch scheme analysis.
2. As the macro-scale behaviour is emergent from the micro-scale behaviour within the patches, to capture the macro-scale behaviour we want the staggered patch scheme Fourier mode to include a micro-scale spatial structure within the patches. Hence, in contrast to the full-domain micro-scale Fourier mode (3.2.5) with constant amplitudes H, U, V one each respectively for h, u, v , the staggered

patch scheme Fourier mode must cater for a micro-scale spatial structure $h_{i,j}^{p,q}$, $u_{i,j}^{p,q}$, $v_{i,j}^{p,q}$ for the interior nodes of all three patches within a macro-cell; here $p, q \in \{0, 1\}$ is the local sub-macro-cell patch index (Fig. 2.2.4b). As we are not interested in studying the micro-scale time evolution (other than taking their influence into account), instead of the explicit rate term λt in the full-domain micro-scale Fourier mode (3.2.5), we absorb the time dependence within the micro-scale structure as $h_{i,j}^{p,q}(t)$, $u_{i,j}^{p,q}(t)$, $v_{i,j}^{p,q}(t)$.

Thus, for the eigenvalue analysis of a staggered patch scheme, let us consider an arbitrary staggered patch scheme Fourier mode with the *macro-scale* real wavenumber (k_x, k_y) , over an infinite staggered patch grid ($N \rightarrow \infty$ in Fig. 2.2.5a of §2.2.3),

$$\bullet h_{i,j}^{I,J}(t) = h_{i,j}^{p,q}(t) e^{i[k_x I \Delta + k_y J \Delta]}, \quad (3.2.10a)$$

$$\bullet u_{i,j}^{I,J}(t) = u_{i,j}^{p,q}(t) e^{i[k_x I \Delta + k_y J \Delta]}, \quad (3.2.10b)$$

$$\bullet v_{i,j}^{I,J}(t) = v_{i,j}^{p,q}(t) e^{i[k_x I \Delta + k_y J \Delta]}, \quad (3.2.10c)$$

where the pair I, J is the global macro-scale patch index. We define the indices $p, q \in \{0, 1\}$ as the local sub-macro-cell patch index with $p = I \bmod 2$ and $q = J \bmod 2$. The sub-patch micro-grid node index $i, j \in \{1, \dots, n-1\}$ for all the patch interior nodes. Fig. 2.2.4 of §2.2.2 illustrates these indices for the case of finite number of macro-grid intervals N where the global macro-scale patch index $I, J \in \{0, 1, \dots, N-1\}$ as illustrated in Fig. 2.2.4 of §2.2.2. But for our present case of $N \rightarrow \infty$ for analytic eigenvalue analysis, we use the global macro-scale patch index $I, J \in \{\dots, -1, 0, 1, \dots\}$.

In the patch scheme Fourier mode (3.2.10), the time-dependent micro-scale structure $h_{i,j}^{p,q}(t)$, $u_{i,j}^{p,q}(t)$, $v_{i,j}^{p,q}(t)$ is *modulated* over the macro-scale by the wave form $\exp(i[k_x I \Delta + k_y J \Delta])$. So, the micro-scale structure $h_{i,j}^{p,q}(t)$, $u_{i,j}^{p,q}(t)$, $v_{i,j}^{p,q}(t)$ depends only on the sub-macro-cell patch index p, q and the sub-patch micro-grid node index i, j , but not on the global patch index I, J due to the 2Δ -translational symmetry in space because of the Fourier shift. For example, substituting $I \rightarrow I + 2$ for the h -component in the arbitrary staggered patch scheme Fourier mode (3.2.10),

$$h_{i,j}^{I+2,J} = h_{i,j}^{p,q}(t) e^{i[k_x(I+2)\Delta + k_y J \Delta]} = (h_{i,j}^{p,q}(t) e^{i[k_x 2 \Delta]}) e^{i[k_x I \Delta + k_y J \Delta]}.$$

That is, the micro-scale structure within the patch $(I \pm 2, J)$ are 2Δ -Fourier shifts of the micro-scale structure within the patch (I, J) ; similarly the micro-scale structure within the patch $(I, J \pm 2)$ are also 2Δ -Fourier shifts of the micro-scale structure within the patch (I, J) .

In §3.2.2 for analytic eigenvalue analysis of the *full-domain micro-scale system*, the constant amplitudes (H, U, V) in the full-domain micro-scale Fourier mode (3.2.5) correspond to the three nodes (h, u, v nodes) of one micro-cell in the full-domain micro-scale grid (large filled circles in Fig. 2.2.1 of §2.2.1). Hence the eigensystem (3.2.6) has a state vector (H, U, V) of size three, leading to the 3×3 one-cell Jacobian of the full-domain micro-scale system. In analytic eigenvalue analysis of a *patch scheme*, the time-dependent micro-scale structure $h_{i,j}^{p,q}(t), u_{i,j}^{p,q}(t), v_{i,j}^{p,q}(t)$ in the staggered patch scheme Fourier mode (3.2.10) correspond to the interior nodes of all three patches (h -, u -, v -centred patches) in any one macro-cell which we name the *centre macro-cell* illustrated by the orange square in Fig. 2.2.5a of §2.2.3. Collecting the interior values of all three patches in the centre macro-cell into a vector gives the *state vector* x^i ; the superscript $(\cdot)^i$ is not an index or exponent, instead a qualifier denoting the patch interior nodes for the *one-cell system* (we use $(\cdot)^I$ to denote the interior nodes of the full system (2.2.9)). The total number of patch interior nodes per macro-cell, that is the size of x^i ,

$$n_p^i = 9n^2/4 - 4n + 2, \quad (3.2.11)$$

where n is the number of sub-patch grid intervals. For example, for the cases of $n = 6, 10, 14$ sub-patch micro-grid intervals, $n_p^i = 59, 187, 387$ respectively.

For example, for the staggered patch grid in Fig. 2.2.5a of §2.2.3, with $n = 6$ sub-patch grid intervals, the state vector containing 59 elements is

$$\begin{aligned} x^i = & (h_{1,1}^{0,0}, h_{1,3}^{0,0}, h_{1,5}^{0,0}, h_{3,1}^{0,0}, h_{3,3}^{0,0}, h_{3,5}^{0,0}, h_{5,1}^{0,0}, h_{5,3}^{0,0}, h_{5,5}^{0,0}, \\ & u_{2,1}^{0,0}, u_{2,3}^{0,0}, u_{2,5}^{0,0}, u_{4,1}^{0,0}, u_{4,3}^{0,0}, u_{4,5}^{0,0}, \\ & v_{1,2}^{0,0}, v_{1,4}^{0,0}, v_{3,2}^{0,0}, v_{3,4}^{0,0}, v_{5,2}^{0,0}, v_{5,4}^{0,0}, \\ & h_{1,2}^{0,1}, h_{1,4}^{0,1}, h_{3,2}^{0,1}, h_{3,4}^{0,1}, h_{5,2}^{0,1}, h_{5,4}^{0,1}, \\ & u_{2,2}^{0,1}, u_{2,4}^{0,1}, u_{4,2}^{0,1}, u_{4,4}^{0,1}, \\ & v_{1,1}^{0,1}, v_{1,3}^{0,1}, v_{1,5}^{0,1}, v_{3,1}^{0,1}, v_{3,3}^{0,1}, v_{3,5}^{0,1}, v_{5,1}^{0,1}, v_{5,3}^{0,1}, v_{5,5}^{0,1}, \\ & h_{2,1}^{1,0}, h_{2,3}^{1,0}, h_{2,5}^{1,0}, h_{4,1}^{1,0}, h_{4,3}^{1,0}, h_{4,5}^{1,0}, \\ & u_{1,1}^{1,0}, u_{1,3}^{1,0}, u_{1,5}^{1,0}, u_{3,1}^{1,0}, u_{3,3}^{1,0}, u_{3,5}^{1,0}, u_{5,1}^{1,0}, u_{5,3}^{1,0}, u_{5,5}^{1,0}, \\ & v_{2,2}^{1,0}, v_{2,4}^{1,0}, v_{4,2}^{1,0}, v_{4,4}^{1,0}). \end{aligned} \quad (3.2.12)$$

Applying a specific patch coupling (Spectral, Square-p2, Square-p4, etc.) gives edge values of all the patches in a macro-cell, in terms of the substituted Fourier mode. That is, patch coupling gives the edge values of each patch in the centre macro-cell from the centre-node values of patches

in other macro-cells, which are Fourier shifted centre-node values (by multiples of 2Δ) of the centre macro-cell. Collecting the edge values of all three patches in the centre macro-cell into a vector gives the *edge vector* \mathbf{x}^e ; the superscript $(\cdot)^e$ is not an index or exponent, instead a qualifier denoting the edge nodes of the one-cell system (we use E to denote the edge nodes of the full system (2.2.9)). The total number of patch edge nodes per macro-cell for the compatible staggered patch grid (Fig. 2.2.5a) for general linear dissipative wave, that is the size of \mathbf{x}^e ,

$$n_p^e = 18n - 16, \quad (3.2.13)$$

where n is the number of sub-patch grid intervals. For example, for the cases of $n = 6, 10, 14$ sub-patch micro-grid intervals, $n_p^e = 92, 164, 236$ respectively.

For example, the simplest staggered patch scheme Square-p2 for $n = 6$, with the patch coupling stencil in Fig. 2.3.2, gives the edge values near the

left-bottom of the h -centred patch near (Fig. 2.2.5a),

$$h_{-1,1}^{0,0} = h_{3,3}^{0,0}(t) \left[\frac{4r^4}{81} - \frac{5r^2}{9} + 1 \right. \\ + \left(-\frac{2r^4}{81} + \frac{r^3}{27} + \frac{2r^2}{9} - \frac{r}{3} \right) e^{2ik_x\Delta} + \left(-\frac{2r^4}{81} - \frac{r^3}{27} + \frac{2r^2}{9} + \frac{r}{3} \right) e^{-2ik_x\Delta} \\ + \left(-\frac{2r^4}{81} + \frac{2r^3}{27} + \frac{r^2}{18} - \frac{r}{6} \right) e^{2ik_y\Delta} + \left(-\frac{2r^4}{81} - \frac{2r^3}{27} + \frac{r^2}{18} + \frac{r}{6} \right) e^{-2ik_y\Delta} \\ + \left(\frac{r^4}{81} - \frac{r^3}{18} + \frac{r^2}{18} \right) e^{2i(k_x\Delta+k_y\Delta)} + \left(\frac{r^4}{81} + \frac{r^3}{18} + \frac{r^2}{18} \right) e^{-2i(k_x\Delta+k_y\Delta)} \\ \left. + \left(\frac{r^4}{81} + \frac{r^3}{54} - \frac{r^2}{18} \right) e^{2i(k_x\Delta-k_y\Delta)} + \left(\frac{r^4}{81} - \frac{r^3}{54} - \frac{r^2}{18} \right) e^{-2i(k_x\Delta-k_y\Delta)} \right] \quad (3.2.14a)$$

$$u_{0,1}^{0,0} = u_{3,3}^{1,0}(t) \left[\frac{r^3}{18} - \frac{r^2}{18} - \frac{r}{2} + \frac{1}{2} + \left(-\frac{r^3}{18} - \frac{r^2}{18} + \frac{r}{2} + \frac{1}{2} \right) e^{-2ik_x\Delta} \right. \\ + \left(-\frac{r^3}{36} + \frac{r^2}{9} - \frac{r}{12} \right) e^{2ik_y\Delta} + \left(-\frac{r^3}{36} - \frac{r^2}{18} + \frac{r}{12} \right) e^{-2ik_y\Delta} \\ \left. + \left(\frac{r^3}{36} - \frac{r^2}{18} - \frac{r}{12} \right) e^{2i(-k_x\Delta+k_y\Delta)} + \left(\frac{r^3}{36} + \frac{r^2}{9} + \frac{r}{12} \right) e^{-2i(k_x\Delta+k_y\Delta)} \right] \quad (3.2.14b)$$

$$v_{1,0}^{0,0} = v_{3,3}^{0,1}(t) \left[\frac{r^3}{18} - \frac{r^2}{18} - \frac{r}{2} + \frac{1}{2} + \left(-\frac{r^3}{18} - \frac{r^2}{18} + \frac{r}{2} + \frac{1}{2} \right) e^{-2ik_y\Delta} \right. \\ + \left(-\frac{r^3}{36} + \frac{r^2}{9} - \frac{r}{12} \right) e^{2ik_x\Delta} + \left(-\frac{r^3}{36} - \frac{r^2}{18} + \frac{r}{12} \right) e^{-2ik_x\Delta} \\ \left. + \left(\frac{r^3}{36} - \frac{r^2}{18} - \frac{r}{12} \right) e^{2i(k_x\Delta-k_y\Delta)} + \left(\frac{r^3}{36} + \frac{r^2}{9} + \frac{r}{12} \right) e^{-2i(k_x\Delta+k_y\Delta)} \right] \quad (3.2.14c)$$

where the sub-cell patch index $(p, q) = (0, 0)$ (Fig. 2.2.4b). For other staggered patch schemes such as Spectral, Square-p4, Square-p6, and Square-p8, the patch coupling expressions (3.2.14) are longer and more complicated.

For one macro-cell, substituting into the staggered patch scheme (3.1.4), the Fourier mode (3.2.10) and the coupled patch edge values (e.g., (3.2.14)) computed by a specific patch coupling, and cancelling the exponential factors on both sides, gives the time evolution of a staggered patch scheme as a dynamical system

$$\frac{dx^i}{dt} = F(x^i; x^e(x^i)), \quad (3.2.15)$$

only for the specific modes of macro-scale wavenumber (k_x, k_y) . The dynamical system (3.2.15) is in the same form as the full-size staggered patch scheme dynamical system (3.1.5) of §3.1. The state vector \mathbf{x}^I of the full-size staggered patch scheme dynamical system (3.1.5) contain interior values of all the patches in a staggered patch grid, but the state vector \mathbf{x}^i of the staggered patch scheme dynamical system (3.2.15) for one macro-scale wavenumber (k_x, k_y) contain interior values of only one macro-cell. Hence, we call the equation (3.2.15) as *one-cell* staggered patch scheme dynamical system.

The one-cell staggered patch scheme dynamical system (3.2.15), written separately for h, u , and v is in the same form as the corresponding full-size staggered patch scheme (3.1.4) of §3.1 with one difference: state variables h, u , and v are only from one macro-cell expressed in sub-macro-cell patch index p, q as opposed to the state variables from all the macro-cells expressed in the global patch index I, J .

For linear waves, the one-cell staggered patch scheme dynamical system (3.2.15) is a linear system with the one-cell Jacobian $\mathbf{J} = \partial \mathbf{F} / \partial \mathbf{x}$. Hence the one-cell staggered patch scheme dynamical system (3.2.15), with the macro-scale modulation $\exp[i(k_x I\Delta + k_y J\Delta)]$ of the Fourier mode (3.2.10), is written equivalently as

$$\frac{d\mathbf{x}^i}{dt} = \mathbf{J}\mathbf{x}^i. \quad (3.2.16)$$

The $n_p^i \times n_p^i$ one-cell Jacobian \mathbf{J} depends only on the system parameters c_D, c_V , discretisation parameters n, δ and the macro-scale wavenumber (k_x, k_y) . The one-cell Jacobian of the staggered patch schemes is useful in giving insights about the staggered patch schemes and for parametric studies, especially to compute eigenvalues corresponding to a small macro-scale wavenumber (k_x, k_y) for a patch grid any size N . Via all macro-scale wavenumbers, the one-cell Jacobian provides a complete solution for all initial conditions of the general linear wave.

For example, for $n = 6$ sub-patch grid intervals, the one-cell Jacobian \mathbf{J} is a 59×59 sparse matrix generally with only 318 of the 3481 elements being nonzero irrespective of the particular path coupling interpolation of the staggered patch schemes (i.e., same for both the spectral patch scheme and all the polynomial patch schemes). For some particular combination of numerical values of the parameters the sparsity could be higher. The 318 nonzero elements of the one-cell Jacobian of a staggered patch scheme (for $n = 6$) contain all the information about the underlying micro-scale system and the patch coupling for the macro-scale waves of wavenumber (k_x, k_y) . A few elements of the one-cell Jacobian of the simplest staggered patch

scheme Square-p2 are,

$$\begin{aligned}\mathbf{J}_{1,1} &= 0, \quad \mathbf{J}_{1,16} = -\frac{1}{2\delta}, \quad \mathbf{J}_{4,10} = \frac{1}{2\delta}, \quad \mathbf{J}_{12,11} = \frac{c_V}{4\delta^2}, \quad \mathbf{J}_{16,16} = -c_D - \frac{c_V}{\delta^2}, \\ \mathbf{J}_{18,36} &= \left(\frac{c_V}{8\delta^2} + \frac{3c_V}{8\Delta\delta} \right) e^{-2\Delta i k_y} + \frac{c_V}{8\delta^2} - \frac{3c_V}{8\Delta\delta}, \\ \mathbf{J}_{46,36} &= \left(-\frac{1}{8\delta} - \frac{1}{2\Delta} - \frac{3\delta}{8\Delta^2} \right) e^{2\Delta i k_x} + \left(-\frac{1}{8\delta} + \frac{1}{2\Delta} - \frac{3\delta}{8\Delta^2} \right) e^{-2\Delta i k_y} \\ &\quad + \left(-\frac{1}{8\delta} + \frac{1}{4\Delta} + \frac{3\delta}{8\Delta^2} \right) e^{2\Delta i k_x - 2\Delta i k_y} - \frac{1}{8\delta} - \frac{1}{4\Delta} + \frac{3\delta}{8\Delta^2} \\ \mathbf{J}_{50,51} &= \left(-\frac{c_V}{4\Delta\delta} + \frac{c_V}{2\Delta^2} \right) e^{2\Delta i k_y} + \left(\frac{c_V}{4\Delta\delta} + \frac{c_V}{2\Delta^2} \right) e^{-2\Delta i k_y} + \frac{c_V}{2\delta^2} - \frac{c_V}{\Delta^2},.\end{aligned}$$

The example expressions for $\mathbf{J}_{1,16}$, $\mathbf{J}_{4,10}$, $\mathbf{J}_{12,11}$ and $\mathbf{J}_{16,16}$ are independent of the macro-scale wavenumber (k_x, k_y) and macro-grid interval Δ and hence characterise the micro-scale flow physics:

- $\mathbf{J}_{1,16}, \mathbf{J}_{4,10}$ characterise the micro-scale flow physics;
- c_V in $\mathbf{J}_{12,11}$ characterise the micro-scale viscous diffusion;
- c_D, c_V in $\mathbf{J}_{16,16}$ characterise the micro-scale drag and viscous diffusion.

All the Jacobian elements containing c_D are precisely the same and occur only as diagonal elements of the Jacobian. That is, all the nonzero diagonal elements

$$\mathbf{J}_{i,i} = -c_D - c_V/\delta^2 \quad (3.2.17)$$

for $i \in \{10, 11, \dots, 21, 28, 29, \dots, 40, 47, 48, \dots, 59\}$.

The drag terms $-c_D u_{i,j}^{I,J}$ and $-c_D v_{i,j}^{I,J}$ in the patch scheme equations (3.1.4b) and (3.1.4c), involve only the drag coefficient and the respective velocities, leading to c_D appearing only in the diagonal of the Jacobian, without depending on macro-grid interval Δ , patch scale ratio r and the patch coupling.

The example expressions for $\mathbf{J}_{18,36}$, $\mathbf{J}_{46,36}$ and $\mathbf{J}_{50,51}$ depend on the macro-scale wavenumber (k_x, k_y) and macro-grid interval Δ and hence characterise the macro-scale flow physics:

- Expressions for $\mathbf{J}_{18,36}$ and $\mathbf{J}_{50,51}$ characterise macro-scale wave with only viscous diffusion;

- $\mathbf{J}_{46,36}$ characterises a macro-scale wave without any dissipation.

The 2Δ in the argument of the exponential factors in $\mathbf{J}_{18,36}$, $\mathbf{J}_{46,36}$, and $\mathbf{J}_{50,51}$ indicate the patch coupling influence by the patches in surrounding macro-cells which are 2Δ away from the centre macro-cell. Compared to the listed example Jacobian elements of the simple patch coupling Square-p2, more surrounding macro-cells influence the Jacobian elements for the cases of patch coupling with higher order interpolations (Square-p4, Square-p6, and Square-p8). Hence the expressions for the one-cell Jacobian elements are much longer than the listed example expressions.

We attempted to derive closed form expressions for the eigenvalues of the one-cell Jacobian \mathbf{J} , through various algebraic simplification strategies, in various Computer Algebra Systems (CAS) such as Sympy, Reduce and Maple. Even for the simplest staggered patch scheme Square-p2, all the CAS packages we tried fail (no results in 48 hours) to compute the analytic eigenvalues of the 59×59 Jacobian ($n = 6$) for the general macro-scale wavenumber (k_x, k_y). For the special case of the ideal wave ($c_D = c_V = 0$) with $k_x = k_y = 0$, Sympy derives the characteristic polynomial of the one-cell Jacobian \mathbf{J} as

$$\begin{aligned} & \lambda^{19} (\lambda^2 + 1/\delta^2)^4 (\lambda^2 + 2/\delta^2)^3 (\lambda^2 + 3/\delta^2)^4 \\ & (\lambda^2 + 4/\delta^2)^6 (\lambda^2 + 6/\delta^2)^3 = 0. \end{aligned} \quad (3.2.18)$$

The zero macro-scale wavenumber ($k_x = k_y = 0$) means that there is no macro-scale waves across the patches corresponding to the characteristic characteristic polynomial (3.2.18). That is, effectively the patches are not coupled. Hence the non-zero eigenvalues λ in (3.2.18) correspond to the pure micro-scale modes contained within the patches, which is evident from the roots of the characteristic polynomial.

- The nineteen zero eigenvalues are due to the micro- and macro-scale vortex modes and a constant (flat, non-wave) macro-scale mode.
- The forty eigenvalues $\lambda \in \{\pm i/\delta, \pm i\sqrt{2}/\delta, \pm i\sqrt{3}/\delta, \pm i\sqrt{4}/\delta, \pm i\sqrt{6}/\delta\}$ are pure imaginary and due to the sub-patch micro-scale mode as the eigenvalue expressions do not depend on any macro-scale variable (e.g., k_x, k_y, Δ).

Our aim is to compute the macro-scale eigenvalues of the staggered patch scheme mainly for the nonzero wavenumbers (k_x, k_y), so we numerically evaluate the one-cell Jacobian for numerical values of $\Delta, \delta, c_D, c_V, k_x, k_y$ and compute the eigenvalues λ_p^{NE1} . We compare with the eigenvalues λ_p^{NE1}

of the numerically evaluated one-cell Jacobian of the patch schemes, with the eigenvalues of the full domain micro-scale system and the eigenvalues of the general linear wave PDEs, while assessing the accuracy ([§3.2.6](#)) and stability ([§3.5](#)) of the patch schemes.

3.2.4 Computing numerical Jacobian of the staggered grid full-domain micro-scale system

The 3×3 analytic Jacobian ([\(3.2.6\)](#)) gives the closed form expression ([\(3.2.7\)](#)) for the eigenvalues λ_m^A of the full-domain micro-scale system, for one particular wavenumber (k_x, k_y) . A full-domain staggered grid (e.g., [Fig. 2.2.1](#)) with $n \times n$ grid intervals, has $n/2 \times n/2 = n^2/4$ cells, each containing three nodes. Hence the total number of nodes is $n_m = 3n^2/4$, which is same the number of dynamical variables, and hence the same as the number of eigenvalues. For example, the full-domain staggered grid in [Fig. 2.2.1](#) with 6×6 grid intervals ($n = 6$), has $3n^2/4 = 27$ eigenvalues. To compute all the $3n^2/4$ eigenvalues λ_m^A of a full-domain grid with $n \times n$ grid intervals, we evaluate the analytic eigenvalue expression for all the $n^2/4$ wavenumbers corresponding to the $n^2/4$ cells (i.e., expression ([\(3.2.7\)](#)) gives three eigenvalues per wavenumber).

In practice, the full-domain micro-scale simulation is done using the *full-size* numerical scheme (not the 3×3 analytic system), which is subject to the practical issues like numerical roundoff errors. The eigenvalues of the numerical full-size Jacobian \mathbf{J} , characterises the accuracy and stability of the numerical staggered grid full-domain micro-scale system, over a particular finite sized domain (i.e., number of grid intervals n is finite as opposed to the case of 3×3 Jacobian for an infinite staggered grid). Hence we also compute the eigenvalues λ_m^N for a $n_m \times n_m$ numerical Jacobian of the full-domain micro-scale system as discussed in this subsection.

Consider the full-domain micro-scale system ([\(3.1.3\)](#)) (i.e., $dx/dt = \mathbf{f}(\mathbf{x})$) where \mathbf{x} is the state vector ([\(2.2.3\)](#)), for the general linear wave, over a full-domain staggered grid (e.g., [Fig. 2.2.1](#)) with $n \times n$ grid intervals. The linear system ([\(3.1.3\)](#)) is equivalent to $dx/dt = \mathbf{J}\mathbf{x}$, where \mathbf{J} is a $n_m \times n_m$ *full-size* Jacobian, in contrast to the 3×3 Jacobian in the eigensystem ([\(3.2.6\)](#)), of the full-domain micro-scale system. The full-size Jacobian \mathbf{J} of the staggered grid full-domain micro-scale system, depends only on the system parameters c_D, c_V and discretisation parameters n, δ , not on the wavenumber. That is the full-size numerical Jacobian \mathbf{J} encodes all the information about the time evolution, for all the wavenumbers.

As the system parameters c_D, c_V and discretisation parameters n, δ are

not varying with time, the system $dx/dt = Jx$ (and the corresponding full-domain dynamical system (3.1.3)) is a *linear time invariant* system. That is the system f in (3.1.3), is completely characterised by the full-size Jacobian J whose columns are responses to unit impulses. Hence, we compute the i th column of the full-size Jacobian J , by evaluating f for a complete set of unit state vectors \hat{x}_i as

$$J = [f(\hat{x}_1), f(\hat{x}_2), \dots, f(\hat{x}_{n_m})] \quad (3.2.19)$$

where the unit state vectors \hat{x}_i are vectors of size n_m whose i th element is one and all other elements are zero.

Section 3.2.6 uses the eigenvalues of the numerical Jacobian of the full-domain micro-scale system, while comparing the eigenvalues with the patch scheme for the general linear wave. For example, Figs. 3.2.1 and 3.2.2 of §3.2.6, plot the eigenvalues $\lambda_{m\delta}^N, \lambda_{m\Delta}^N$ of the numerical Jacobian of the full-domain micro-scale system, with grid interval equal to the sub-patch grid interval δ and the inter-patch distance Δ respectively, of a staggered patch grid.

3.2.5 Computing numerical Jacobian of the staggered patch schemes

The $n_p^i \times n_p^i$ one-cell Jacobian of the staggered patch schemes in §3.2.3, is useful in giving insights about the staggered patch schemes and to compute eigenvalues corresponding to a small macro-scale wavenumber (k_x, k_y) for a patch grid any size N . But, in practice, the staggered patch scheme numerical time simulation is done using the full-size evolution equation (3.1.4), not using the one-cell evolution equations (3.2.15). To confirm that full-size staggered patch scheme (3.1.5) is accurate, stable and not too sensitive to numerical roundoff errors, this subsection discusses a method to compute the numerical eigenvalues λ_p^N of the staggered patch schemes for the full evolution equations (3.1.4).

Consider the full-size staggered patch scheme dynamical system (3.1.5) as a linear system

$$\frac{dx^I}{dt} = Jx^I \quad (3.2.20)$$

for general dissipative linear wave, similar to the one-cell patch scheme system (3.2.16). The $n_p^I \times n_p^I$ Jacobian J is the full-size numerical Jacobian of the staggered patch scheme (3.1.4) and (3.1.5). The number of state variables $n_p^I = (N^2/4)(9n^2/4 - 4n + 2)$ for the full-size patch scheme system,

as in the expression (2.2.7). In contrast to the one-cell Jacobian, the full-size Jacobian \mathbf{J} of the numerical staggered patch scheme depends only on the system parameters c_D, c_V and discretisation parameters N, n, δ , not on a specific wavenumber (k_x, k_y) . The eigenvalues λ_p^N of the numerical staggered patch scheme Jacobian \mathbf{J} characterises the accuracy and stability of the numerical staggered patch schemes over a particular finite sized domain (i.e., N is finite as opposed to infinite staggered patch grid for the on-cell Jacobian).

As the system parameters c_D, c_V and discretisation parameters N, n, δ are not varying with time, the system $dx^I/dt = \mathbf{J}x^I$ (and the corresponding staggered patch scheme dynamical system (3.1.5)) is a *linear time invariant* system. Hence, we compute the i th column of the staggered patch scheme Jacobian \mathbf{J} by evaluating \mathbf{F} for a complete set of unit state vectors \hat{x}_i^I as

$$\mathbf{J} = [\mathbf{F}(\hat{x}_1^I; \mathbf{x}^E(\hat{x}_1^I)), \mathbf{F}(\hat{x}_2^I; \mathbf{x}^E(\hat{x}_2^I)), \dots, \mathbf{F}(\hat{x}_{n_p^I}^I; \mathbf{x}^E(\hat{x}_{n_p^I}^I))] \quad (3.2.21)$$

where the unit state vectors \hat{x}_i^I are vectors of size n_p^I whose i th element is one and all other elements are zero.

The eigenvalues λ_p^N of the numerical staggered patch scheme Jacobian \mathbf{J} characterises the accuracy and stability of the numerical staggered patch schemes over a particular finite sized domain (i.e., N is finite as opposed to infinite staggered patch grid for the on-cell Jacobian). We compare with the eigenvalues λ_p^N of the staggered patch scheme numerical Jacobian, with the eigenvalues of the full domain micro-scale system and the eigenvalues of the general linear wave PDEs, while assessing the accuracy (§3.2.6) and stability (§3.5) of the patch schemes.

3.2.6 Staggered patch schemes are accurate for macro-scale waves

This section explains the qualitative structure of the staggered patch scheme eigenvalues and eigenvectors, and qualitatively demonstrate the accuracy of the staggered patch schemes for the general linear wave for few cases (e.g., $N \in \{6, 10\}$, $n = 6$, $r = 0.1$). Section 3.6 on the consistency of the staggered patch schemes, quantitatively establish the patch scheme accuracy in more detail, over a much broader range of parameters.

This section demonstrates the accuracy of the developed five staggered patch schemes (Spectral, Square-p2, Square-p4, Square-p6, and Square-p8) by comparing the following eigenvalues in complex plane plots.

1. Eigenvalues λ_p^N of the numerical Jacobian of a staggered patch scheme on a finite domain ([§3.2.5](#)).
2. Eigenvalues λ_p^{NE1} of the numerically evaluated one-cell Jacobian in linear system [\(3.2.16\)](#) in [§3.2.3](#), of a staggered patch scheme on an infinite domain.
3. Eigenvalues $\lambda_{m\delta}^A$ from the analytic expression [\(3.2.7\)](#) in [§3.2.2](#), of fine-grid full-domain micro-scale system, with grid interval equal to the sub-patch grid interval δ . That is, $\delta_{m\delta} \equiv L/n_{m\delta} = \delta \equiv l/n \equiv 2Lr/(Nn)$ as $r = l/(2\Delta)$ and $\Delta = L/N$, where $n_{m\delta}$ is the number of full-domain micro-scale grid intervals and n is the number of sub-patch micro-grid intervals. When the context is clear we drop the subscript $m\delta$ in $n_{m\delta}$ and $\delta_{m\delta}$ for the fine-grid full-domain micro-scale system.
4. Eigenvalues $\lambda_{m\Delta}^A$ from the analytic expression [\(3.2.7\)](#) in [§3.2.2](#) of coarse grid version of the full-domain micro-scale system, with $\delta = \Delta$. That is, $\delta_{m\Delta} \equiv L/n_{m\Delta} = \Delta \equiv L/N$, where $n_{m\Delta}$ is the number of full-domain micro-scale grid intervals and n is the number of sub-patch micro-grid intervals. When the context is clear we drop the subscript $m\Delta$ in $n_{m\delta}$ and $\delta_{m\Delta}$ for the coarse-grid full-domain micro-scale system.
5. Eigenvalues λ_{PDE}^A from the analytic expression [\(3.2.3\)](#) of the 2D general dissipative linear wave PDEs [\(3.1.1\)](#) ([§3.2.1](#)). Comparison with the eigenvalues λ_{PDE}^A is only for completeness.

All the analytic eigenvalues ($\lambda_p^{NE1}, \lambda_{m\delta}^A, \lambda_{m\Delta}^A, \lambda_{PDE}^A$) are numerically evaluated for all the $N^2/4$ macro-scale wavenumbers (k_x, k_y) resolved on a corresponding finite staggered patch grid with $N \times N$ macro-grid intervals. To illustrate the complete structure of eigenvalues (i.e, for all wavenumbers) of the full-domain micro-scale system and to cross-verify analytic and numerical computation of the full-domain micro-scale system eigenvalues, we also compute the eigenvalues of the numerical Jacobian of the full-domain micro-scale system for few cases (e.g., [Figs. 3.2.1](#) and [3.2.2](#)).

The sets of eigenvalues (e.g., $\lambda_p^N, \lambda_p^{NE1}, \lambda_{m\delta}^N, \lambda_{m\Delta}^N, \lambda_{PDE}^A$), in all the complex plane plots, are numbered in the legend entries on the left. In all the complex plane plots, system parameters for each of these eigenvalues are listed in groups *below the legend entries* in a style similar to listing author affiliations. For example, the following listing explains the parameters specifically for [Figs. 3.2.1](#) and [3.2.2](#) with $N = 6, n = 6$.

- The group labelled by (3) (in the left, below the legend entries) says that the third listed eigenvalues $\lambda_{m\delta}^N$ correspond to a fine full-domain micro-grid with 180×180 grid intervals ($n = 180$).

Figure 3.2.1: Spectral staggered patch scheme ($N = 6, n = 6$) eigenvalues ($\lambda_p^N, \lambda_p^{NE1}$) on complex plane (*linear scale*) for general linear wave. Due to large range of magnitudes of eigenvalues, details of eigenvalues for macro-scale modes (mid-right clusters 1, 2, 3) are not clear.

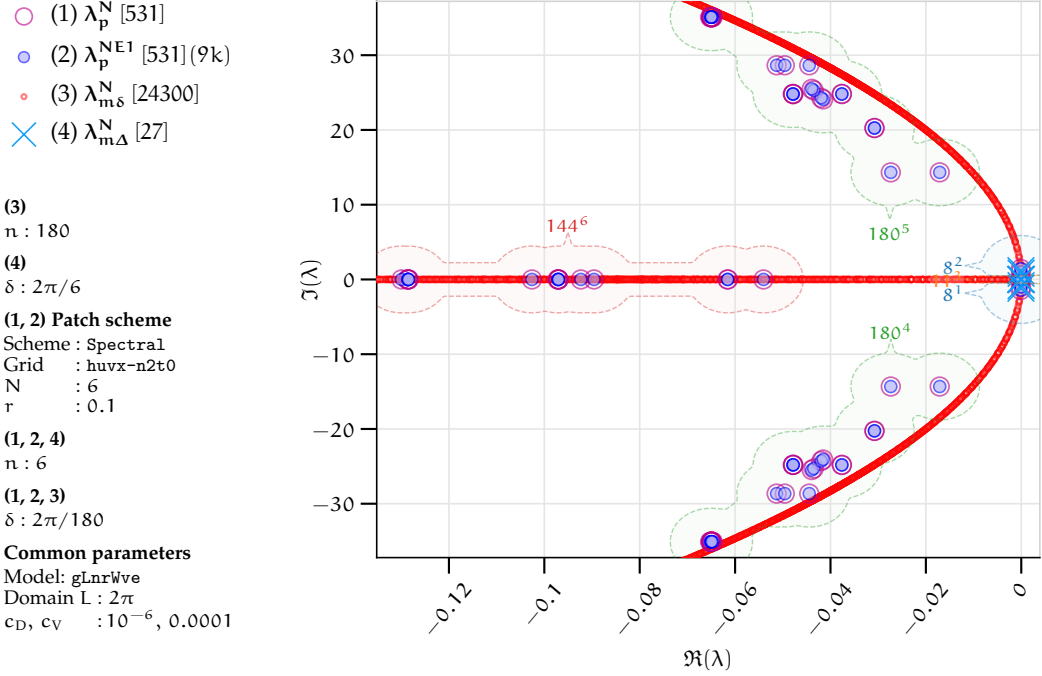
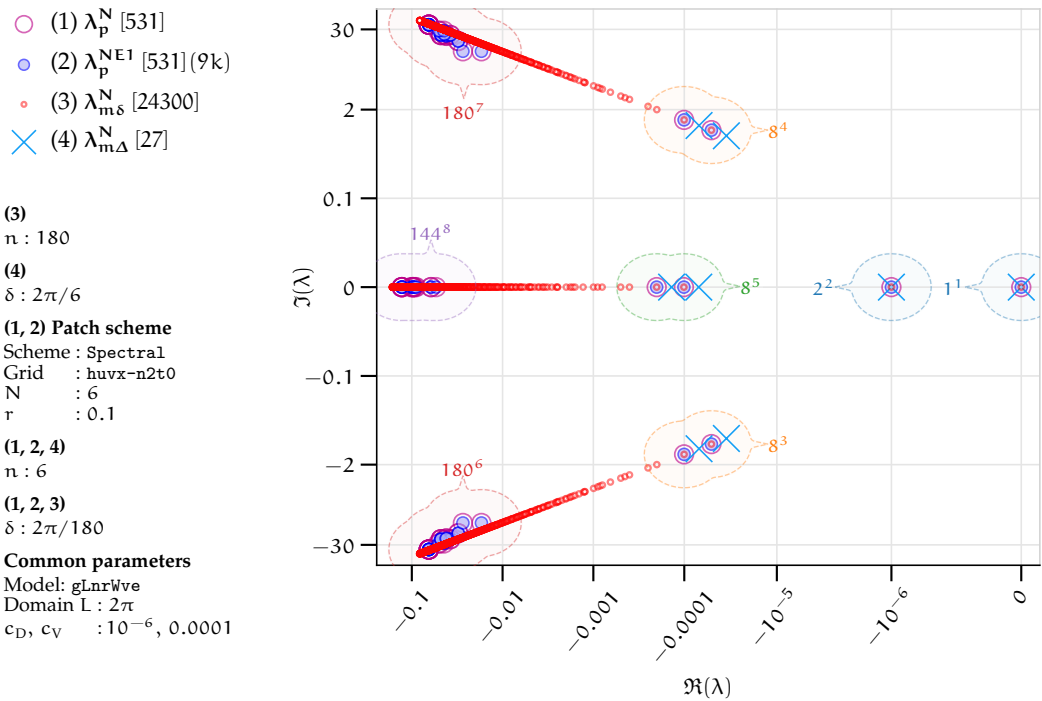


Figure 3.2.2: Spectral staggered patch scheme ($N = 6, n = 6$) eigenvalues ($\lambda_p^N, \lambda_p^{NE1}$) on complex plane (*arcsinh nonlinear scale*) for general linear wave. The arcsinh scaling zooms out the eigenvalues of macro-scale modes (mid-right clusters 1, 2, 3 in Fig. 3.2.1 to clusters 1–5 here).



- The group labelled by (4) says that the fourth listed eigenvalues $\lambda_{m\Delta}^N$ correspond to a full-domain micro-grid with coarse grid interval $\delta = 2\pi/N = 2\pi/6 = \Delta$.
- The group labelled by (1, 2) lists all the parameters common to the first and second listed eigenvalues $\lambda_p^N, \lambda_p^{NE1}$ of the staggered patch scheme.
- The group labelled by (1, 2, 4) says that $n = 6$ for the first, second, and the fourth listed eigenvalues. We use the same symbol n for the number of grid intervals for both the full-domain micro-grid and the sub-patch micro-grid. That is, the eigenvalues $\lambda_p^N, \lambda_p^{NE1}$ correspond to a staggered patch grid where each patch contains 6×6 sub-patch micro-grid intervals ($n = 6$), and the eigenvalues $\lambda_{m\Delta}^N$ correspond to a coarse full-domain micro-grid with 6×6 grid intervals ($n = 6$).
- The group labelled by (1, 2, 3) says that $\delta = 2\pi/180$ for the first, second, and the third listed eigenvalues. We use the same symbol δ for the grid interval for both the full-domain micro-grid and the sub-patch micro-grid. That is, the eigenvalues $\lambda_p^N, \lambda_p^{NE1}$ correspond to a staggered patch grid with sub-patch micro-grid interval $\delta = 2\pi/180$, and the eigenvalues $\lambda_{m\delta}^N$ correspond to a fine full-domain micro-grid interval $\delta = 2\pi/180$.
- The group *Common parameters* lists the parameters common to all the listed eigenvalues.

[Figures 3.2.1](#) and [3.2.2](#) plot the eigenvalues $(\lambda_p^N, \lambda_p^{NE1})$ of the Spectral patch scheme on a staggered patch grid with 6×6 macro-grid intervals ($N = 6$) and each patch containing 6×6 sub-patch micro-grid intervals ($n = 6$). Also plotted are the eigenvalues $\lambda_{m\delta}^N, \lambda_{m\Delta}^N$ of respectively the fine- and coarse-grid versions of the full-domain micro-scale system [\(3.1.2\)](#) and the eigenvalues λ_{PDE}^A of the PDE [\(3.1.1\)](#). Similar to [Figs. 3.2.1](#) and [3.2.2](#), in all the complex plane eigenvalue plots, eigenvalues are grouped within clusters based on eigenvalues λ_p^{NE1} of the staggered patch scheme Jacobian. Each cluster is annotated with the number of eigenvalues λ_p^{NE1} in the cluster and the cluster number in the superscript.

[Figure 3.2.1](#) presents the complex plane plot on a *linear scale*. Hence, due to the large range of magnitude of the eigenvalues, details of the eigenvalues for macro-scale modes (mid-right clusters 1, 2, 3), are not clearly visible. The details of the eigenvalues for macro-scale modes are of primary interest. On the other hand, the arcsinh scaling in [Fig. 3.2.2](#) aptly zooms out

the eigenvalues of macro-scale modes (mid-right clusters 1, 2, 3 in Fig. 3.2.1 to clusters 1–5). That is, the nonlinear arcsinh scaling has a quasi-log nature, which empowers us to see very small (positive and negative) as well as large magnitude of eigenvalues, all together in the same plot. Hence, *most complex plane eigenvalue plots in this thesis are on arcsinh scaling*. Specifically, the complex plane plots on arcsinh scaling, plot an eigenvalue λ as a point on a 2D space with coordinates $(\text{arcsinh}(S_h [\Re \lambda - O_h]) / S_h + O_h, \text{arcsinh}(S_v \Im \lambda) / S_v)$, where S_h, S_v are the horizontal and vertical scale factors and $(O_h, 0)$ is the centre of zoom. In this chapter, most plots on arcsinh scaling use the scale factors $S_h = 5 \cdot 10^6$, $S_v = 100$ and the centre of zoom $(O_h, 0) = (-5 \cdot 10^{-7}, 0)$.

This paragraph explains the general qualitative structure of the patch scheme eigenvalues for the general linear wave, using as reference the complex plane plot of Fig. 3.2.2 for the Spectral staggered patch scheme. Figure 3.2.2 is for a staggered patch grid with 10×10 macro-grid intervals ($N = 10$) and each patch containing 6×6 sub-patch micro-grid intervals ($n = 6$). The following points are based on the Spectral patch scheme eigenvalues in Fig. 3.2.2 and the eigenvectors (the patch scheme modes) in Figs. 3.2.13 to 3.2.18. But these points hold in general for the eigenvalues of, the PDE, full-domain micro-scale system, and all the patch schemes including the polynomial schemes. The number just next to each cluster is the number of eigenvalues in that cluster. The cluster numbers referred to below are indicated on the plots by the *superscript* of the number just next to each cluster.

- Cluster 1 consisting of one zero eigenvalue correspond to the macro-scale mode of stagnant water (zero eigenvalue, hence temporally constant) with uniform height and no flow (i.e., $u = v = 0$) (e.g., eigenvector in Fig. 3.2.13). This mode is due to the conservation of mass/height of water with nonzero mean height (mean height is zero for the other modes).
- Cluster 2 consisting of two real eigenvalues $-c_D$, correspond to the macro-scale mode of *decelerating* (negative real part) *uniform mean flow* (e.g., eigenvector in Fig. 3.2.14) due to drag in x and y directions.
- Clusters 3,4 together consisting of sixteen complex conjugate eigenvalues with small negative real parts, correspond to slowly decaying *macro-scale wave modes* with small wavenumber (e.g., eigenvector in Fig. 3.2.15).
- Cluster 5 consisting of eight small real negative eigenvalues, correspond to slowly decaying *macro-scale vortex modes* (e.g., eigenvector in Fig. 3.2.16).

- Clusters 6, 7 together consisting of 360 complex conjugate eigenvalues with large negative real parts, correspond to fast decaying *sub-patch micro-scale wave modes* with large wavenumber (e.g., eigenvector in Fig. 3.2.17).
- Cluster 8 consisting of 144 large real negative eigenvalues, correspond to fast decaying *sub-patch micro-scale vortex modes* (e.g., eigenvector in Fig. 3.2.18).
- As the clusters 1, 2, 3, 4, and 5 correspond to macro-scale modes, we call their eigenvalues *macro-scale eigenvalues*.
- As the clusters 6, 7, and 8 correspond to macro-scale modes, we call their eigenvalues *micro-scale eigenvalues*.

The previous paragraph shows that the clusters 1–5 (on the right) contain eigenvalues of the macro-scale modes and the clusters 6, 7, 8 (on the left) contain eigenvalues of the micro-scale modes. As Figs. 3.2.1 and 3.2.2 show, a patch scheme contains only the small wavenumber macro-scale modes (on the right) and large wavenumber micro-scale modes (on the left), not the modes of the intermediate scale. On the other hand, the eigenvalues $\lambda_{m\delta}^N$ of the full-domain micro-scale system, span the eigenvalue plot nearly uniformly from left to right, corresponding to all the wavenumbers resolved on the full-domain micro-scale staggered grid. Figures 3.2.1 and 3.2.2 show a *good qualitative agreement of the structure of micro- and macro-scale patch scheme eigenvalues λ_p^N and the complete structure of the eigenvalues $\lambda_{m\delta}^N$ (i.e., for all wavenumbers) of the full-domain micro-scale system*. For the accurate multiscale modelling of the macro-scale waves, the agreement between the macro-scale eigenvalues of the patch scheme and those of the full-domain system is the primary focus. Figure 3.2.2 shows that, within the clusters 1–5, the numerical macro-scale eigenvalues λ_p^N of the patch scheme (large magenta circles) and the numerical macro-scale eigenvalues $\lambda_{m\delta}^N$ (small red circles) visually agree.

As Fig. 3.2.2 shows, for both micro-scale and macro-scale modes, the patch scheme eigenvalues λ_p^{NE1} of the numerically evaluated one-cell analytic Jacobian (§3.2.3) and the patch scheme eigenvalues λ_p^N of the numerical Jacobian (§3.2.5), agree (i.e., the large magenta and blue circles). Hence, *all other complex plane plots in this subsection §3.2.6 use eigenvalues λ_p^{NE1} of the numerically evaluated one-cell analytic Jacobian (§3.2.3), as opposed to the numerical eigenvalues λ_p^N* .

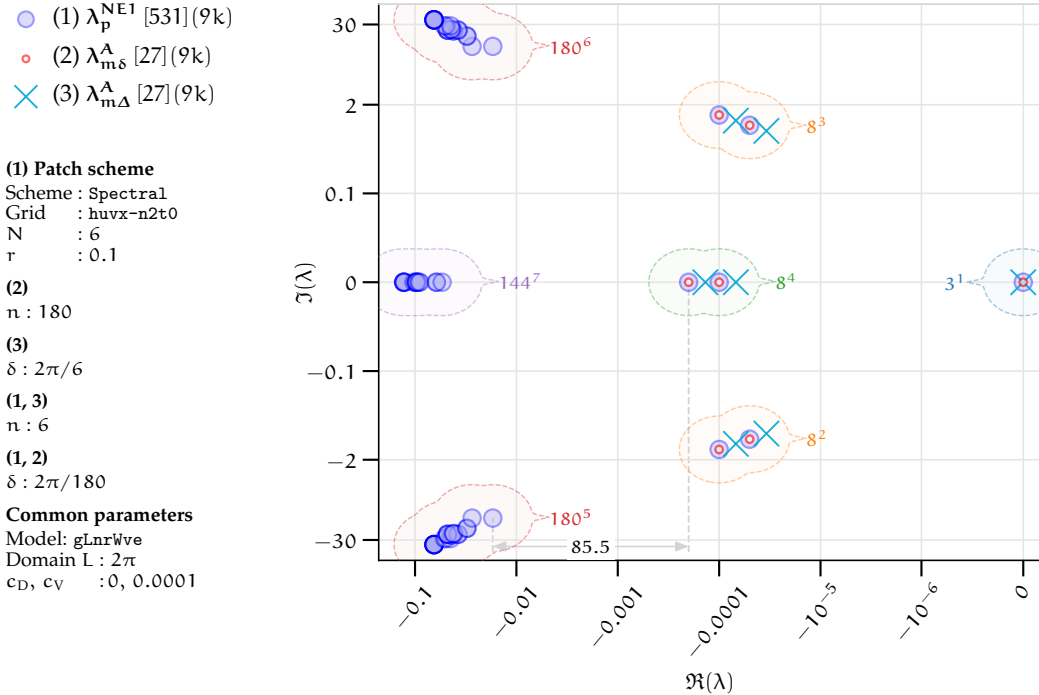
For a staggered patch grid with 6×6 macro-grid intervals ($N = 6$) and each patch containing 6×6 sub-patch micro-grid intervals ($n = 6$), the total

number of nodes and hence the total number of eigenvalues λ_p^N is $n_p^I = 531$. The corresponding number of eigenvalues $\lambda_{m\delta}^N$ of the fine-grid full-domain micro-scale system (with patch scale ratio $r = 0.1$) is $(3/16)(Nn/r)^2 = 24300$, whose full-size numerical Jacobian ([§3.2.4](#)) is of size 24300×24300 containing $5.9 \cdot 10^8$ elements. For patch grids with $N > 6$ and/or $r < 0.1$, the corresponding full-size Jacobians of the fine-grid full-domain micro-scale system, rapidly increase in size, requiring substantially larger computational effort and memory (larger than 64 GB). For the accurate multiscale modelling of the macro-scale waves, the agreement between the macro-scale eigenvalues of the patch scheme and those of the full-domain system is the primary focus, not the eigenvalues corresponding to all the wavenumbers. That is, to assess the patch scheme accuracy, as in [Fig. 3.2.3](#) it suffices to compare only the patch scheme macro-scale eigenvalues with the macro-scale eigenvalues $\lambda_{m\delta}^A$ of the full-domain micro-scale system (by evaluating the analytic expression [\(3.2.7\)](#) only for macro-scale wavenumbers resolved on a staggered patch grid). Hence, to avoid large computational effort and as the primary focus is on the macro-scale eigenvalues, *all other complex plane plots in this subsection §3.2.6 use eigenvalues $\lambda_{m\delta}^A$ from the analytic expression [\(3.2.7\)](#) of the analytic Jacobian ([§3.2.2](#)), as opposed to the numerical eigenvalues $\lambda_{m\delta}^N$.*

The specific location of eigenvalues on the complex plane plot of [Fig. 3.2.2](#), for the Spectral staggered patch scheme, change with the system parameters c_D , and c_V , but the above cluster structure is typical.

- When the drag tends to zero with nonzero viscous diffusion (i.e., $c_D \rightarrow 0, c_V \neq 0$), the two eigenvalues of the decelerating uniform mean flow mode (cluster 2) move to right in the complex plane and merge with cluster 1 of steady uniform mode as in [Fig. 3.2.3](#).
- When the viscous diffusion tends to zero with nonzero drag (i.e., $c_V \rightarrow 0, c_D \neq 0$), two notable structural changes occur:
 1. the eigenvalues of the wave modes (clusters 3,4,7,8 in [Fig. 3.2.2](#)) move to the right to take constant real part value of $-c_D/2$ (clusters 2,3,4,5 in [Fig. 3.2.4](#));
 2. the eigenvalues of the vortex modes (clusters 5,8 in [Fig. 3.2.2](#)) move to the right in the complex plane and merge with cluster 2 of the decelerating uniform mean flow mode, which is cluster 6 in [Fig. 3.2.4](#).
- When both the drag and the viscous diffusion tends to zero, (i.e., $c_D, c_V \rightarrow 0$), two notable structural changes occur:

Figure 3.2.3: Spectral staggered patch scheme ($N = 6, n = 6$) eigenvalues for general linear wave with *no drag and nonzero viscous diffusion* ($c_D = 0, c_V \neq 0$). The macro-scale eigenvalues $\lambda_p^{N=1}$ agree with the macro-scale eigenvalues $\lambda_{m\delta}^A$ of the fine-grid full-domain micro-scale system.



1. the eigenvalues of the wave modes (clusters 3,4,7,8 in Fig. 3.2.2) move to the right to take zero real part (clusters 1,2,4,5 in Fig. 3.2.5);
2. the eigenvalues of the vortex modes (clusters 5,8 in Fig. 3.2.2) and decelerating uniform mean flow modes (cluster 2 in Fig. 3.2.2) move to the right in the complex plane and merge with cluster 3 of the zero eigenvalues in Fig. 3.2.5.

The structure of eigenvalues and its qualitative dependence on the dissipation parameters (c_D, c_V) for the Spectral staggered patch scheme, explained in the preceding paragraph, also hold for all the four polynomial staggered patch schemes of the general linear wave (e.g., the eigenvalues of the polynomial staggered patch schemes in Figs. 3.2.9 to 3.2.12).

The number of wave modes (clusters 3, 4, 6, 7 in Fig. 3.2.2), and the number of vortex modes (clusters 5, 8 in Fig. 3.2.2), depend on N, n of a patch scheme for general linear wave (over a staggered patch grid containing $N \times N$ macro-grid intervals and each patch containing $n \times n$ sub-patch micro-grid intervals). The following listing explains the number of various modes (number of eigenvalues λ_p^N) of a staggered patch scheme for the general linear wave *with nonzero drag and the viscous diffusion*. For example,

Figure 3.2.4: Spectral staggered patch scheme ($N = 6, n = 6$) eigenvalues for general linear wave with *nonzero drag and no viscous diffusion* ($c_D \neq 0, c_V = 0$). The macro-scale eigenvalues λ_p^{NE1} agree with the macro-scale eigenvalues $\lambda_{m\delta}^A$ of the fine-grid full-domain micro-scale system.

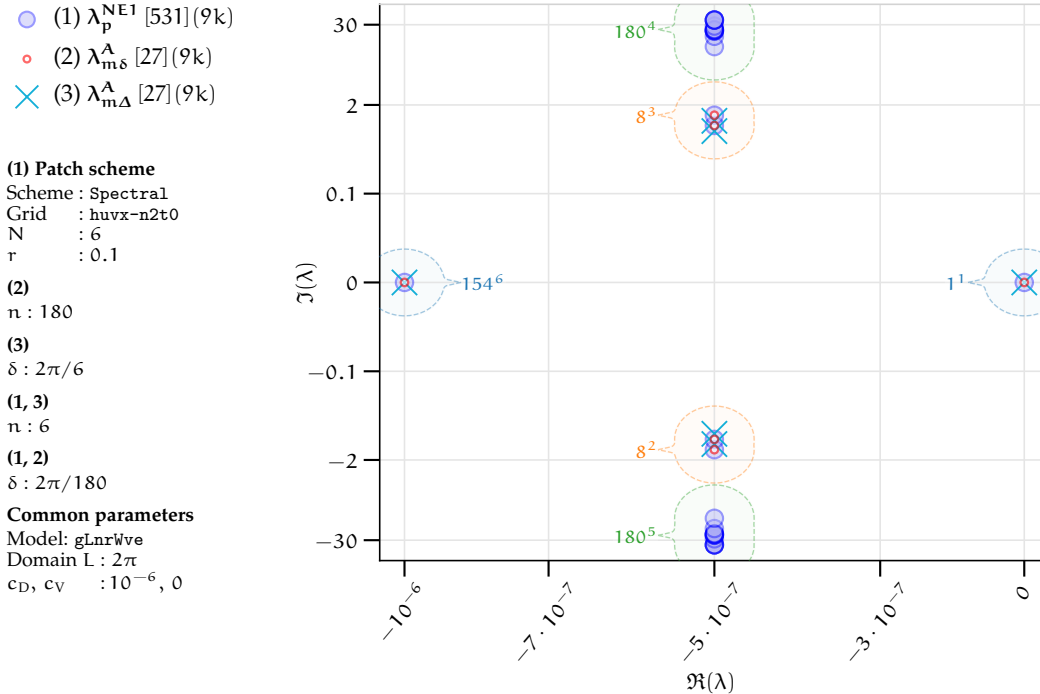


Figure 3.2.5: Spectral staggered patch scheme ($N = 6, n = 6$) eigenvalues for general linear wave with *no drag and no viscous diffusion* (ideal wave, $c_D = c_V = 0$). The macro-scale eigenvalues λ_p^{NE1} agree with the macro-scale eigenvalues $\lambda_{m\delta}^A$ of the fine-grid full-domain micro-scale system.

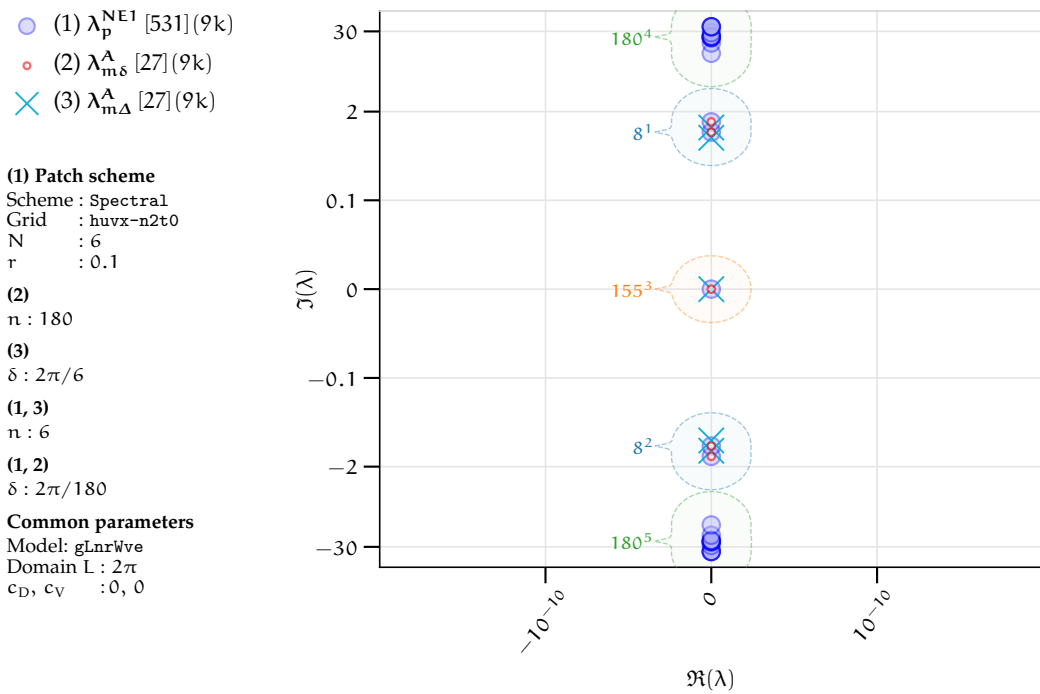


Figure 3.2.6: Spectral staggered patch scheme ($N = 6, n = 10$) eigenvalues for general linear wave with *drag and viscous diffusion*. The macro-scale eigenvalues λ_p^{NE1} agree with the macro-scale eigenvalues $\lambda_{m\delta}^A$ of the fine-grid full-domain micro-scale system.

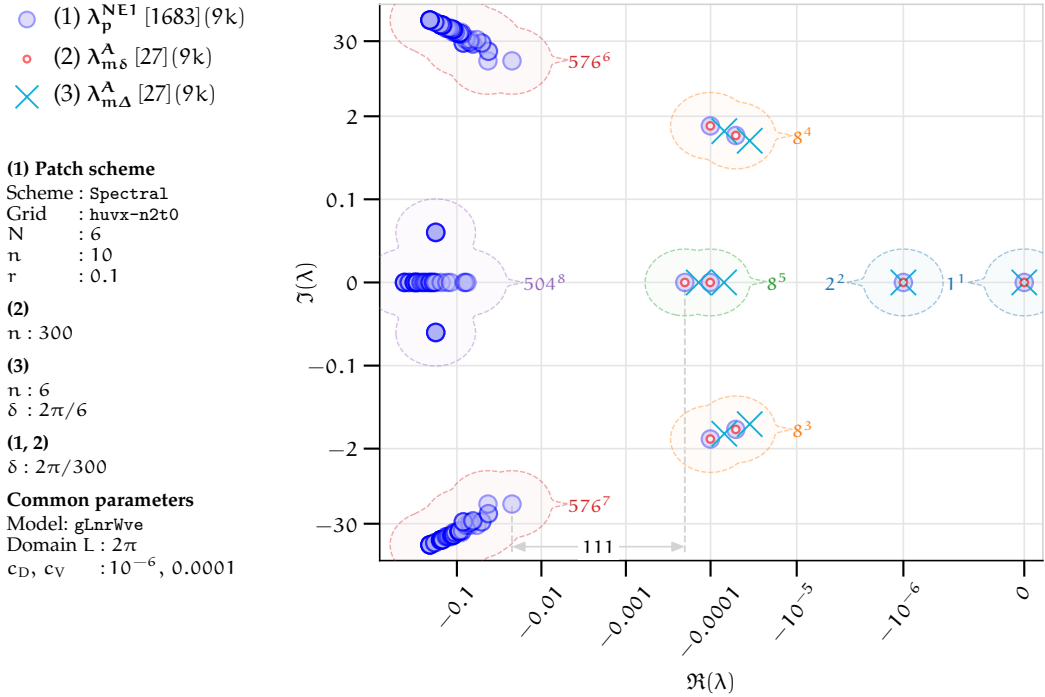
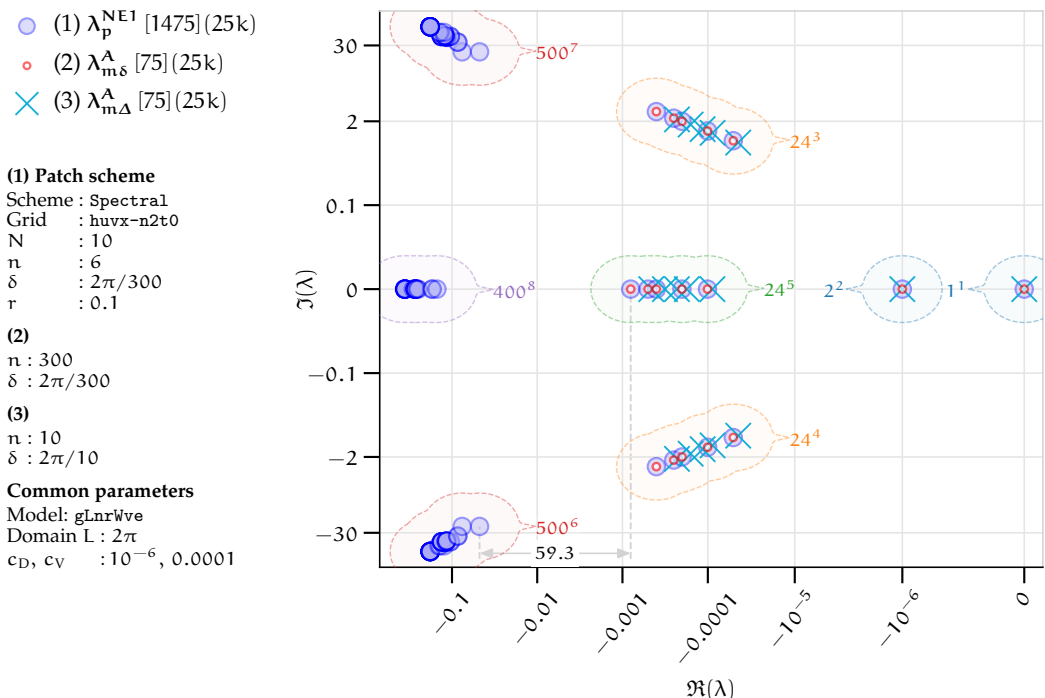


Figure 3.2.7: Spectral staggered patch scheme ($N = 10, n = 6$) eigenvalues for general linear wave with *drag and viscous diffusion*. The macro-scale eigenvalues λ_p^{NE1} agree with the macro-scale eigenvalues $\lambda_{m\delta}^A$ of the fine-grid full-domain micro-scale system.



Figs. 3.2.2, 3.2.6 and 3.2.7 plot eigenvalues of the Spectral staggered patch scheme respectively for $(N, n) = (6, 6), (6, 10), (10, 6)$.

- There is one macro-scale mode for the stagnant water (cluster 1) irrespective of N, n .
- There are two macro-scale modes for the decelerating uniform mean flow (cluster 2) irrespective of N, n .
- The total number of macro-scale wave modes (in clusters 3,4), is $2(N^2/4 - 1)$, which does not depend on the number of sub-patch micro-grid intervals n .
- The number of macro-scale vortex modes (in cluster 5), is $N^2/4 - 1$, which does not depend on n .
- The total number of micro-scale sub-patch wave modes (in clusters 6,7), is $(N^2/2)(3n^2/4 - n - 1)$.
- The number of micro-scale sub-patch vortex modes (in cluster 8), is $(N^2/4)(3n^2/4 - 2n + 1)$.
- The total number of macro-scale modes is $3N^2/4$, which is same as the number of patches in the staggered patch grid with $N \times N$ macro-grid intervals (each of the $(N/2)^2$ macro-cells contains three patches).
- The total number of micro-scale sub-patch modes is $(N^2/4)(9n^2/4 - 4n - 1)$.
- The total number of staggered patch scheme modes (number of eigenvalues λ_p^N) is $n_p^I = (N^2/4)(9n^2/4 - 4n + 2)$, which is same as the number of patch interior nodes (2.2.7) in p. 18 of §2.2.2.

The preceding paragraph explains the number of eigenvalues λ_p^N of the *full-size* numerical Jacobian of the staggered patch scheme (§3.2.5), this paragraph explains the number of eigenvalues λ_p^{NE1} of the *one-cell* analytic Jacobian of the staggered patch scheme (§3.2.3). The total number of eigenvalues λ_p^{NE1} of the numerically evaluated one-cell Jacobian of a staggered patch scheme for one wavenumber (k_x, k_y) , is $n_p^i = (9n^2/4 - 4n + 2)$. The number of eigenvalues n_p^i is same as the total number of state variables, and the number of patch interior nodes (3.2.11) in p. 53 of §3.2.3, for a one-cell analytic description of a staggered patch scheme for one macro-scale wavenumber (k_x, k_y) . For example, as in p. 53 of §3.2.3, for $n = 6, 10, 14$ sub-patch micro-grid intervals, $n_p^i = 59, 187, 387$ respectively.

For how many macro-scale wavenumbers, one must compute the one-cell eigenvalues $\lambda_p^{N\infty}$ towards one-to-one comparison with the full-size numerical eigenvalues λ_p^N ? A staggered patch grid with 6×6 macro-grid intervals $N = 6$ (with each of the $(N/2)^2$ macro-cells containing three patches), resolves a total of $(N/2)^2 = 9$ macro-scale modes with macro-scale wavenumbers $k_x, k_y \in \{-1, 0, 1\}$. To compare the one-cell eigenvalues $\lambda_p^{N\infty}$ with the eigenvalues λ_p^N of the numerical Jacobian for a staggered patch scheme on a patch grid with 6×6 macro-grid intervals, we numerically evaluate the one-cell Jacobian of a staggered patch scheme for all the nine macro-scale wavenumbers. Hence the total number of one-cell eigenvalues $\lambda_p^{N\infty}$ is $59 \times 9 = 531$, matching the total number of numerical eigenvalues λ_p^N . The number of wavenumbers for which the one-cell eigenvalues $\lambda_p^{N\infty}$ are computed, is indicated in the eigenvalue plots next to the legend entry for $\lambda_p^{N\infty}$. For example, the “(9k)” in Fig. 3.2.2 indicates the nine wavenumbers (k_x, k_y) (i.e., $k_x, k_y \in \{-1, 0, 1\}$) and the “(25k)” in Fig. 3.2.7 indicates the 25 wavenumbers (i.e., $k_x, k_y \in \{-2, -1, 0, 1, 2\}$).

Similar to the case of the $\lambda_p^{N\infty}$ in the preceding paragraph, in contrast to plotting all the eigenvalues of the coarse- and fine-grid full-domain micro-scale system, such as the numerical eigenvalues $\lambda_{m\Delta}^N, \lambda_{m\delta}^N$ in Figs. 3.2.1 and 3.2.2, all other eigenvalue plots plot the analytic full-domain eigenvalues $\lambda_{m\delta}^A, \lambda_{m\Delta}^A$ only for the macro-scale wavenumbers. For example, for a patch grid with 6×6 macro-grid intervals, the analytic expression (3.2.7) is evaluated only for the $(N/2)^2 = 9$ macro-scale wavenumbers (i.e., $k_x, k_y \in \{-1, 0, 1\}$). For each wavenumber (k_x, k_y) , the expression (3.2.7) gives three eigenvalues, one real and a pair of complex conjugate eigenvalues. Hence the total number of macro-scale eigenvalues $\lambda_{m\delta}^A$ is $3 \times 9 = 27$, matching the total number of macro-scale staggered patch scheme eigenvalues λ_p^N and $\lambda_p^{N\infty}$ in Fig. 3.2.6 (the “(9k)” next to the legend entry for $\lambda_{m\delta}^A, \lambda_{m\Delta}^A$ indicates the nine wavenumbers).

Comparing the number of eigenvalues in the complex plane plots of the Spectral staggered patch scheme for different sizes of the patch grid (e.g., Figs. 3.2.2, 3.2.6 and 3.2.7 respectively for $(N, n) = (6, 6), (6, 10), (10, 6)$), reveal the following.

1. Increasing the number of macro-grid intervals N of a patch grid increases both the macro-scale modes and the micro-scale modes. For example,
 - a patch grid with 6×6 macro-grid intervals, computes $3N^2/4 = 27$ macro-scale modes and $(N^2/4)(9n^2/4 - 4n - 1) = 504$ micro-scale modes (clusters 1–5 and clusters 6–8 in Fig. 3.2.2), whereas

- a patch grid with 10×10 macro-grid intervals, computes 75 macro-scale modes and 1400 micro-scale modes (clusters 1–5 and clusters 6–8 in Fig. 3.2.7).
2. Increasing the number of sub-patch micro-grid intervals n of a patch grid increases only the micro-scale modes without any change in the number of macro-scale modes. For example,
- a patch grid containing 6×6 sub-patch micro-grid intervals in each patch, computes 504 micro-scale modes (clusters 6–8 in Fig. 3.2.2), whereas
 - a patch grid containing 10×10 sub-patch micro-grid intervals in each patch, computes 1656 micro-scale modes (clusters 6–8 in Fig. 3.2.7), but
 - there are 27 macro-scale modes in both cases.

As the comparison in Fig. 3.2.2 shows, the staggered patch scheme eigenvalues comprises the micro-scale eigenvalues on the left and the macro-scale eigenvalues on the right but not the intermediate scales. To quantify this *spectral gap* in the scales, we define the *spectral gap factor* as the ratio of the maximum real part of the micro-scale eigenvalues (on the left) to the minimum real part of the macro-scale eigenvalues (on the right). All the complex plane eigenvalue plots with arcsinh scaling indicates the spectral gap by a grey arrow annotated with the spectral gap factor. When there is no gap, that is when the micro-scale eigenvalues and macro-scale eigenvalues overlap, to quantify the overlap, we compute the spectral gap as negative of the ratio of the minimum real part of the macro-scale eigenvalues to the maximum real part of the micro-scale eigenvalues.

Increasing the number of macro-grid intervals N resolves more macro-scale modes with progressively higher wavenumbers (e.g., Figs. 3.2.2 and 3.2.7). Hence, *increasing N for the same patch scale ratio r , leads to decreasing spectral gap between the micro-scale and macro-scale eigenvalues*, approaching the full-domain micro-scale system. On the other hand, increasing the number of sub-patch micro-grid intervals n increases the spectral gap (e.g., Figs. 3.2.2 and 3.2.6).

The staggered patch scheme micro-scale modes (e.g, clusters 4, 5, 6 in Fig. 3.2.1 and clusters 6, 7, 8 in Fig. 3.2.2) have large discrepancies (about 10 in magnitude) with the corresponding fine-grid micro-scale eigenvalues $\lambda_{m\delta}^N$. All the five staggered patch schemes have sub-patch micro-scale modes. When the viscous diffusion is nonzero, the large negative real parts of these micro-scale modes means that they decay rapidly and only the

accurate macro-scale modes dominate the long time solution, which are of primary interest for accurate macro-scale modelling. The spectral gap (indicated by a grey arrow) in the eigenvalue plots, quantifies how rapidly the micro-scale modes are dissipated relative to macro-scale dynamics. That is, the *spectral gap quantifies how rapidly the patch scheme macro-scale solution emerge from the underlying micro-scale dynamics*.

Our objective is to design the staggered patch schemes to resolve the macro-scale physics as accurately as possible compared to the corresponding fine-grid full-domain micro-scale system. Hence, we define a staggered patch scheme to be *accurate* when the macro-scale eigenvalues (e.g., $\lambda_p^N, \lambda_p^{NE1}$) of the staggered patch schemes are close to the macro-scale eigenvalues (e.g., $\lambda_{m\delta}^A$) of the corresponding fine-grid full-domain micro-scale system with the same grid interval as the sub-patch micro-grid interval.

[Figures 3.2.2 to 3.2.7](#) present the eigenvalue plots for the Spectral staggered patch schemes, for different dissipation parameters ($c_D \in \{0, 10^{-6}\}$, $c_V \in \{0, 10^{-4}\}$), and for different sizes of the patch grid ($N \in \{6, 10\}$, $n \in \{6, 10\}$) with the patch scale ratio $r = 0.1$. The macro-scale eigenvalues λ_p^{NE1} (large blue circles) of the Spectral staggered patch scheme agree exactly (within numerical roundoff errors) with the corresponding macro-scale eigenvalues $\lambda_{m\delta}^A$ (small red circles) of the fine-grid full-domain micro-scale system. That is, the *Spectral staggered patch scheme accurately resolves the macro-scale modes of the general linear wave*, for these combinations, of the parameters ([§3.6](#) discusses the accuracy for larger range of parameters). Moreover, the Spectral staggered patch scheme resolves the macro-scale physics to the same accuracy

1. for different system parameters $c_D \in \{0, 10^{-6}\}$, $c_V \in \{0, 10^{-4}\}$ ([Figs. 3.2.2 to 3.2.5](#)), and
2. for different sizes of patch grid $N \in \{6, 10\}$, $n \in \{6, 10\}$ ([Figs. 3.2.6, 3.2.7 and 3.2.2](#)).

Similar to the Spectral staggered patch scheme, the accuracy of the four polynomials patch schemes (Square-p2, Square-p4, Square-p6, and Square-p8) do not depend on the system parameters ($c_D \in \{0, 10^{-6}\}$, $c_V \in \{0, 10^{-4}\}$) or the number of sub-patch micro-grid intervals n ; for brevity we omit the corresponding plots. Unlike the Spectral staggered patch scheme, the accuracy of the polynomial staggered patch schemes increases with increasing the macro-grid intervals N . For example, comparing [Figs. 3.2.8 and 3.2.9](#) shows that for $N = 10$ ([Fig. 3.2.9](#)) the macro-scale eigenvalues λ_p^{NE1} (large blue circles), with small real parts, agree more closely with the corresponding macro-scale eigenvalues $\lambda_{m\delta}^A$ (small red circles), compared to the

macro-scale eigenvalues for $N = 6$ (Fig. 3.2.8). Section 3.6 on the consistency of the staggered patch schemes, quantifies how the errors decrease with increasing N .

Each patch is effectively one node in the macro-scale grid. Hence, comparing the macro-scale eigenvalues λ_p^{NE1} of the staggered patch scheme with the macro-scale eigenvalues $\lambda_{m\Delta}^A$ of the coarse-grid full-domain micro-scale system (with same grid interval as the inter-patch spacing Δ) reveals how effective a staggered patch scheme is, as a multiscale scheme coupling across the scales. Figs. 3.2.9 to 3.2.12 plot the eigenvalues for the polynomial staggered patch schemes (§2.3.2) Square-p2, Square-p4, Square-p6, and Square-p8, on a patch grid with 10×10 macro-grid intervals ($N = 10$) and each patch containing 6×6 sub-patch micro-grid intervals ($n = 6$) and patch scale ratio $r = 0.1$. Figs. 3.2.9 to 3.2.12 show that increasing polynomial interpolation orders $p = 2, 4, 6, 8$ increases the accuracy of the polynomial staggered patch schemes due to the increasing interpolation accuracy. That is, the discrepancy, between the macro-scale eigenvalues λ_p^{NE1} (large blue circles) of the patch schemes and the corresponding eigenvalues $\lambda_{m\delta}^A$ (small red circles) of the fine-grid full-domain micro-scale system, decreases with increasing interpolation order p . As the interpolation accuracy increase with increasing p , the macro-scale eigenvalues λ_p^{NE1} of the patch scheme shift from being close to the macro-scale eigenvalues $\lambda_{m\Delta}^A$ (coarse-grid) to being close to the macro-scale eigenvalues $\lambda_{m\delta}^A$ (fine-grid) of the full-domain micro-scale system. Thus, depending upon the accuracy of the patch coupling interpolation, *the accuracy of the staggered patch schemes lies between the accuracy of the coarse- and fine-grid full-domain micro-scale system* (two extremes).

Figs. 3.2.13 to 3.2.18 plot one example eigenvector (mode shape) for each of eigenvalue clusters 1, 2, 3, 5, 6, 8 in Fig. 3.2.12 for the Square-p8 staggered patch scheme (with $N = 10$, $n = 6$, $r = 0.1$). These eigenvectors are computed for the numerical Jacobian (§3.2.5) of the Square-p8 staggered patch scheme. The qualitative shapes of the eigenvectors in Figs. 3.2.13 to 3.2.18 are the same for the Spectral (§2.3.1) and polynomial (§2.3.2) staggered patch schemes Square-p2, Square-p4, Square-p6, and Square-p8.

Figure 3.2.8: Square-p2 staggered patch scheme ($N = 6, n = 6$) eigenvalues for general linear wave with *drag and viscous diffusion*. Low accuracy interpolation leads to poor patch scheme accuracy; that is, large discrepancy between λ_p^{NE1} (large blue circles) and $\lambda_{m\delta}^A$ (small red circles).

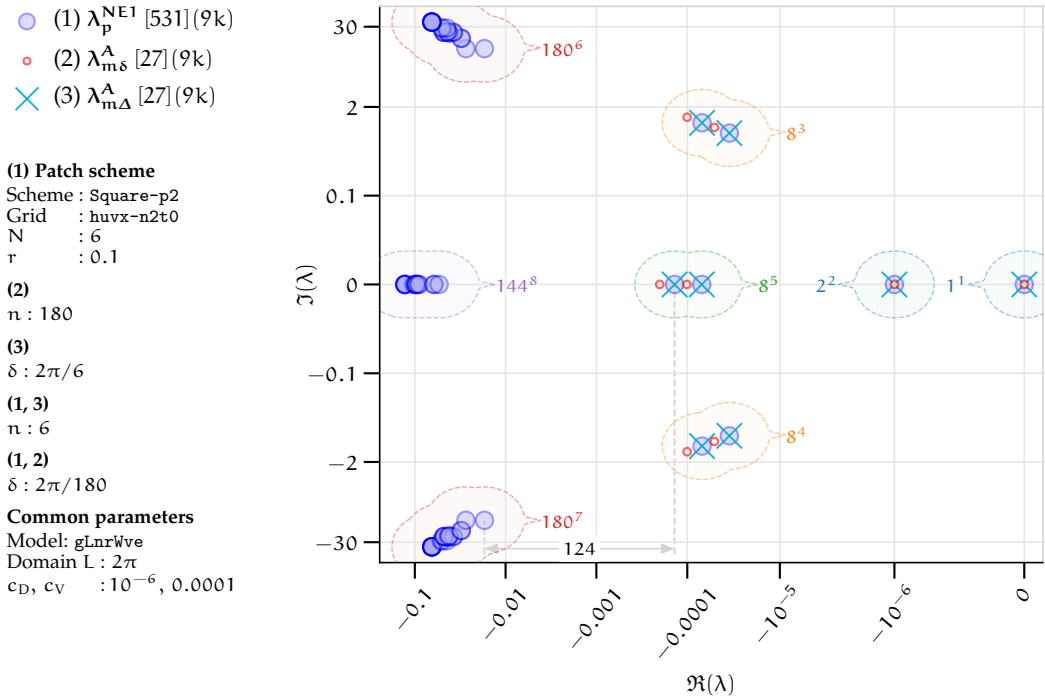


Figure 3.2.9: Square-p2 staggered patch scheme ($N = 10, n = 6$) eigenvalues for general linear wave with *drag and viscous diffusion*. The patch scheme accuracy with $N = 10$ is higher compared to Fig. 3.2.8 for $N = 6$; that is, smaller discrepancy between λ_p^{NE1} and $\lambda_{m\delta}^A$.

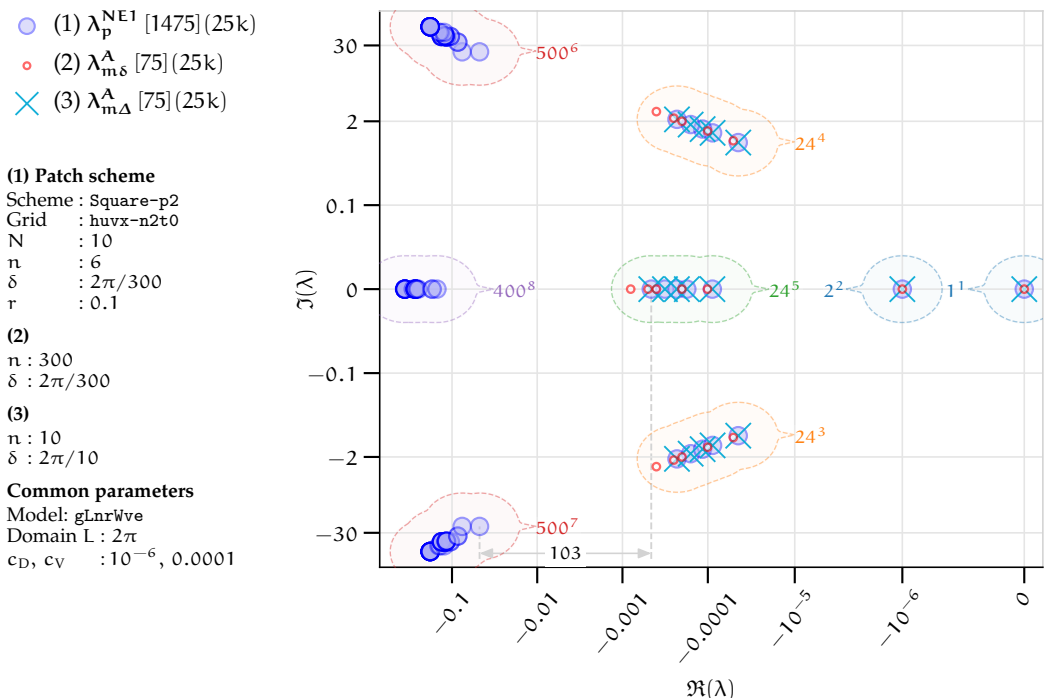


Figure 3.2.10: Square-p4 staggered patch scheme ($N = 10, n = 6$) eigenvalues for general linear wave with *drag and viscous diffusion*. The fourth order polynomial interpolation leads to higher patch scheme accuracy compared to [Fig. 3.2.9](#) for Square-p2, smaller discrepancy between λ_p^{NE1} and $\lambda_{m\delta}^A$.

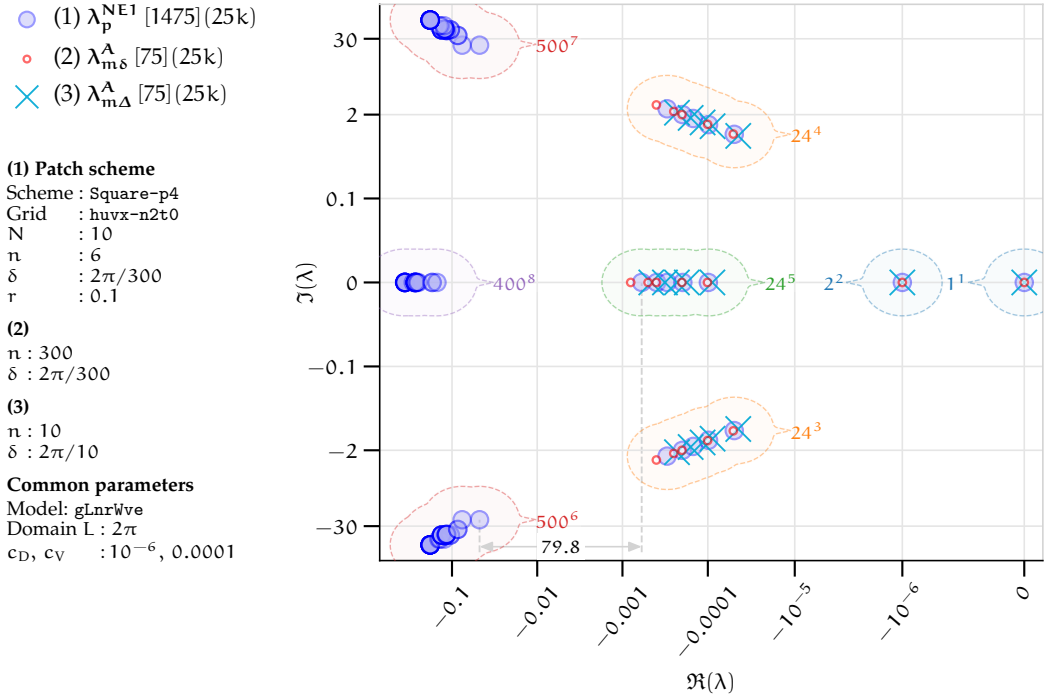


Figure 3.2.11: Square-p6 staggered patch scheme ($N = 10, n = 6$) eigenvalues for general linear wave with *drag and viscous diffusion*. The sixth order polynomial interpolation leads to higher patch scheme accuracy compared to [Fig. 3.2.10](#) for Square-p4, smaller discrepancy between λ_p^{NE1} and $\lambda_{m\delta}^A$.

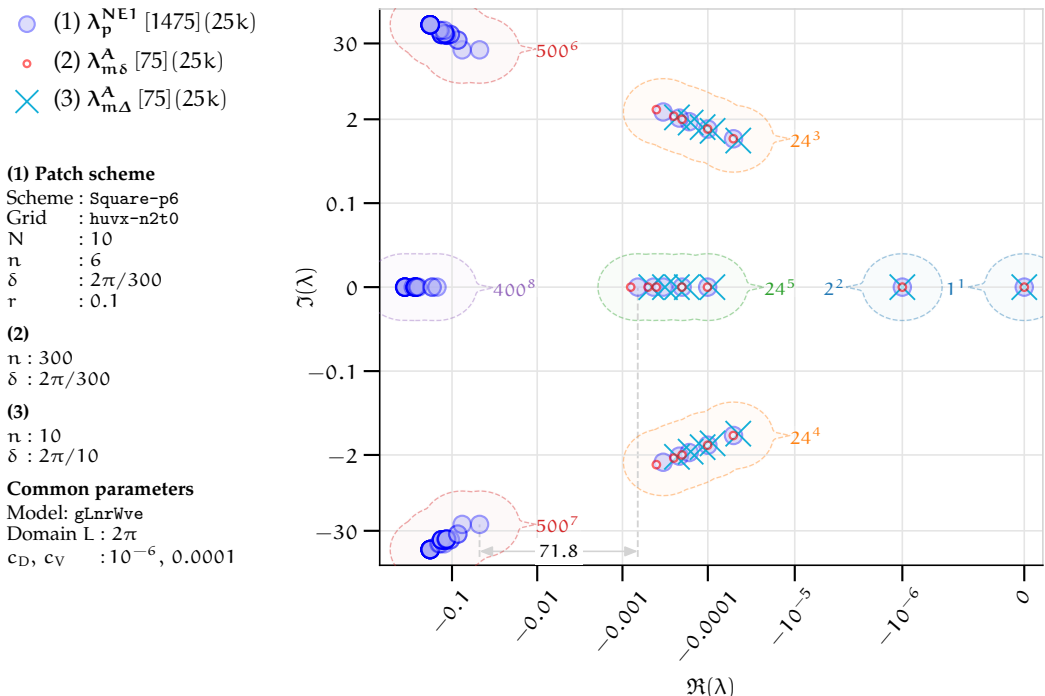


Figure 3.2.12: Square-p8 staggered patch scheme ($N = 10, n = 6$) eigenvalues for general linear wave with *drag and viscous diffusion*. The eighth order polynomial interpolation leads to higher patch scheme accuracy compared to Fig. 3.2.11 for Square-p6, smaller discrepancy between λ_p^{NE1} and $\lambda_{m\delta}^A$.

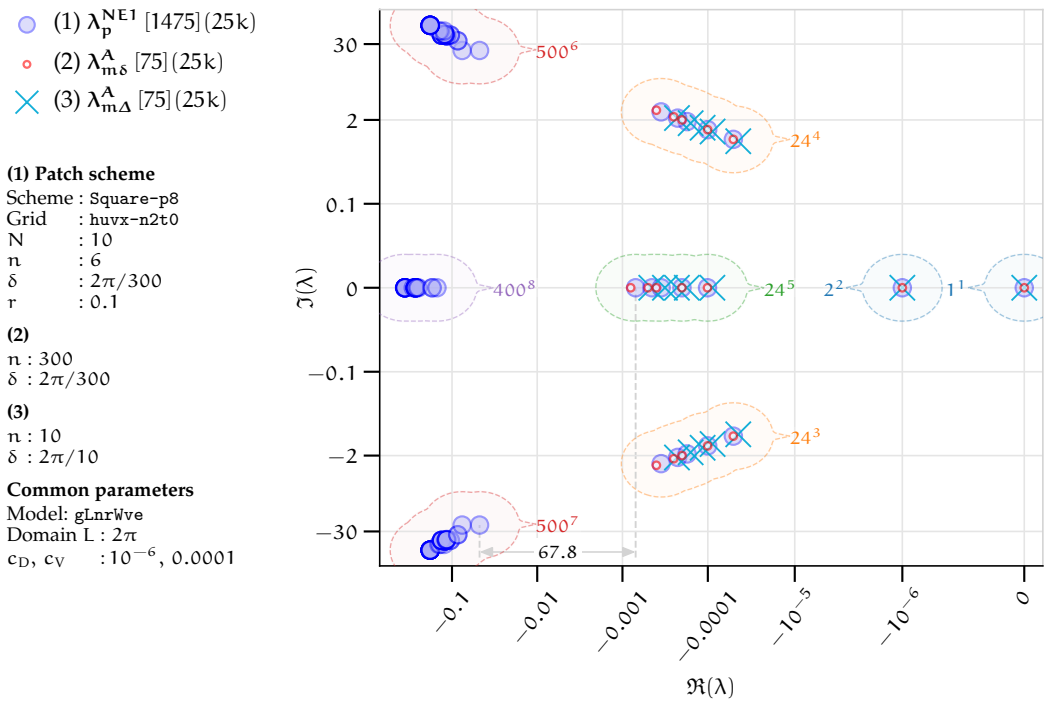


Figure 3.2.13: Eigenvector for eigenvalue $\lambda_p^N = 0 + 0i$ (cluster 1 in Fig. 3.2.12), for Square-p8 staggered patch scheme with $N = 10$, $n = 6$, $r = 0.1$. The macro-scale mode of stagnant water with uniform height h and no flow (i.e., $u = v = 0$) (negligible u, v)

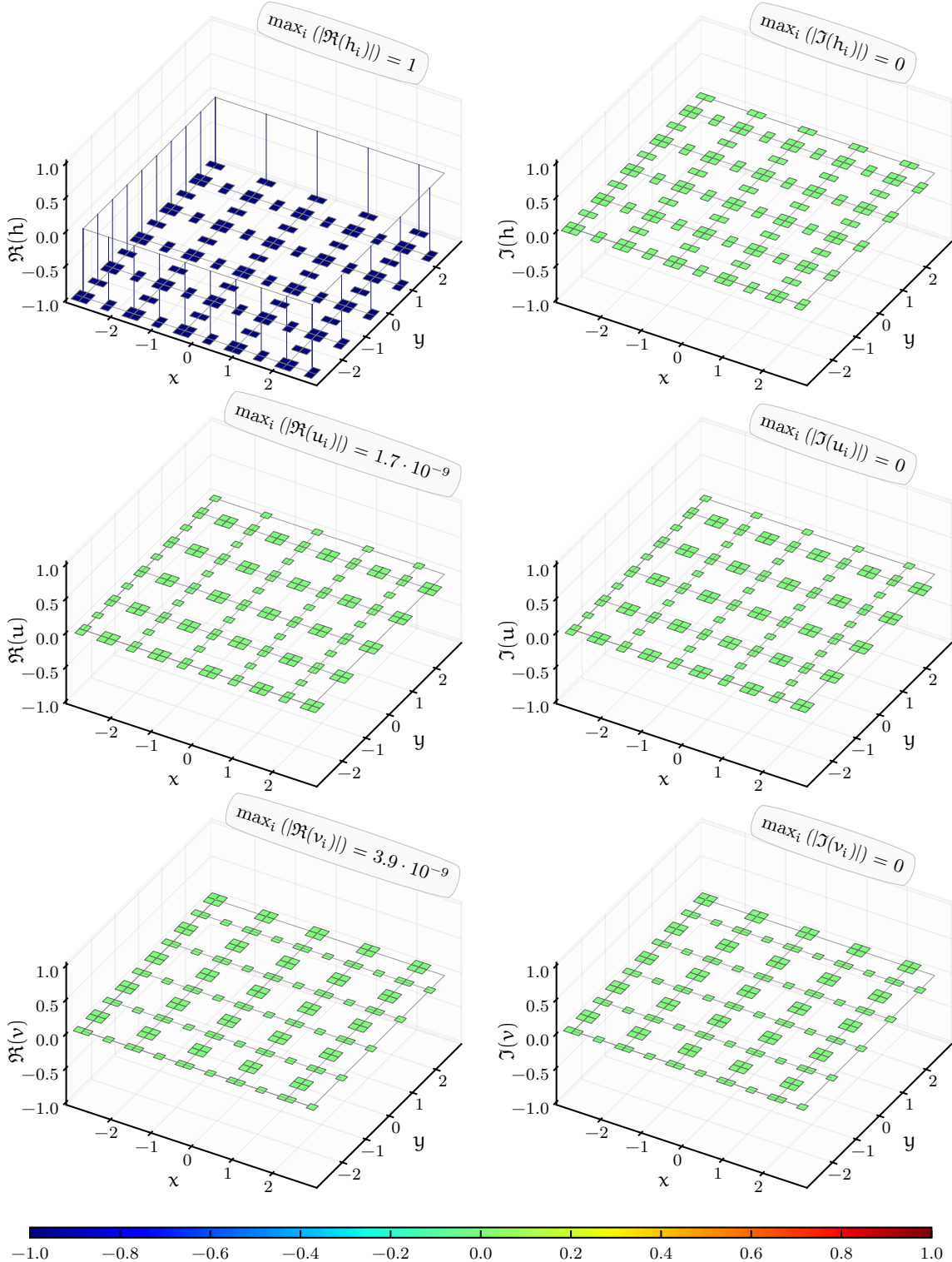


Figure 3.2.14: Eigenvector for eigenvalue $\lambda_p^N = -10^{-6} + 0i$ (cluster 2 in Fig. 3.2.12), for Square-p8 staggered patch scheme with $N = 10$, $n = 6$, $r = 0.1$. One of the two macro-scale modes of decelerating (negative real part λ_p^N) uniform mean flow (spatially constant velocities u and v).

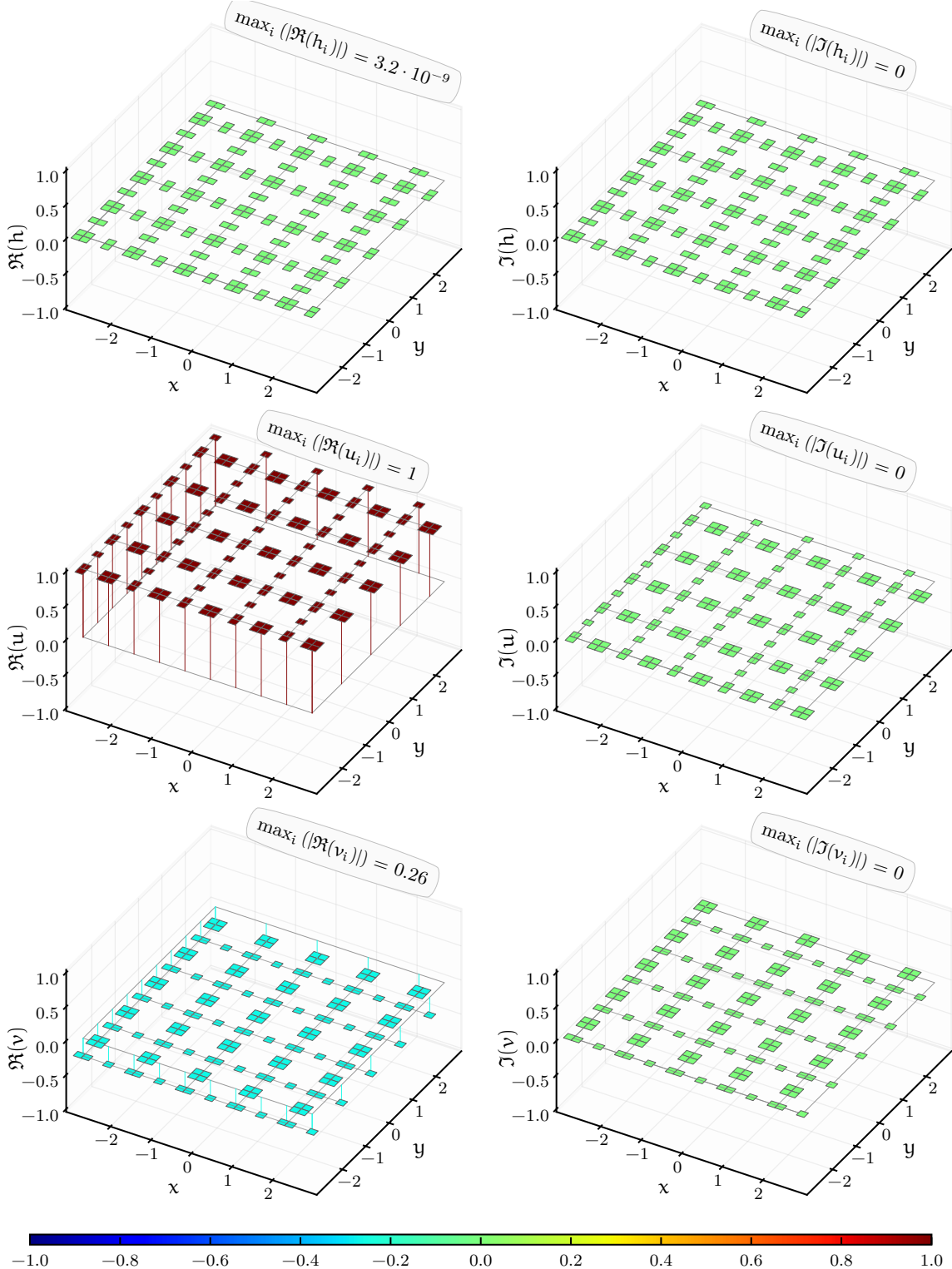


Figure 3.2.15: Eigenvector for eigenvalue $\lambda_p^N = -5 \cdot 10^{-5} + 1i$ (cluster 3 in Fig. 3.2.12), for Square-p8 staggered patch scheme with $N = 10$, $n = 6$, $r = 0.1$. A macro-scale wave mode (only h and u are of significant magnitude) with exchange of potential (h) and kinetic (u) energy.

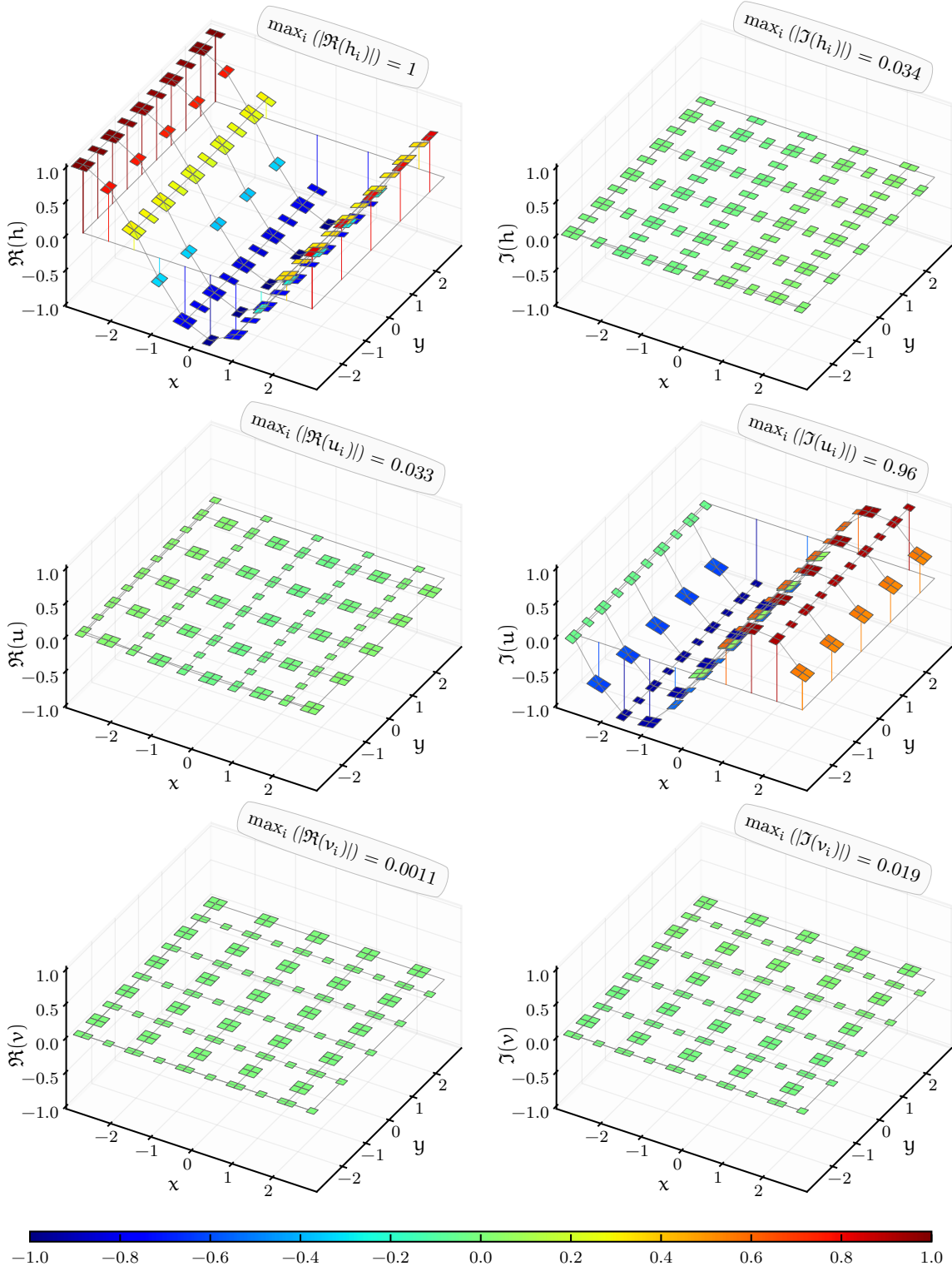


Figure 3.2.16: Eigenvector for eigenvalue $\lambda_p^N = -0.0001 + 0i$ (cluster 5 in Fig. 3.2.12), for Square-p8 staggered patch scheme with $N = 10$, $n = 6$, $r = 0.1$. A macro-scale vortex mode (only u and v are of significant magnitude).

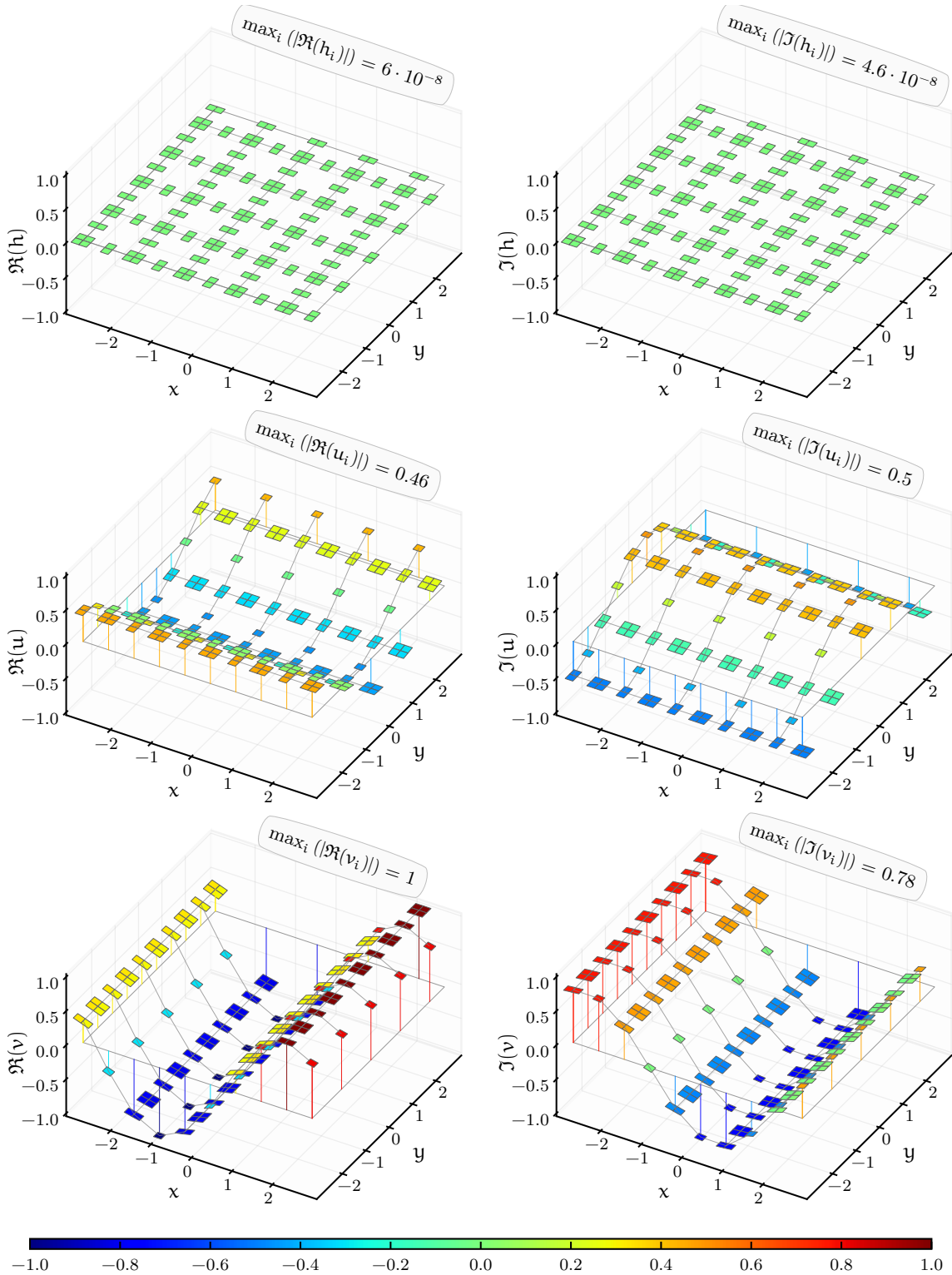


Figure 3.2.17: Eigenvector for eigenvalue $\lambda_p^N = -0.085 + 33.76i$ (cluster 6 in Fig. 3.2.12), for Square-p8 staggered patch scheme with $N = 10$, $n = 6$, $r = 0.1$. A sub-patch micro-scale wave mode (h , u , and v are of significant magnitude) with exchange of potential energy (h) and kinetic energy (u , v).

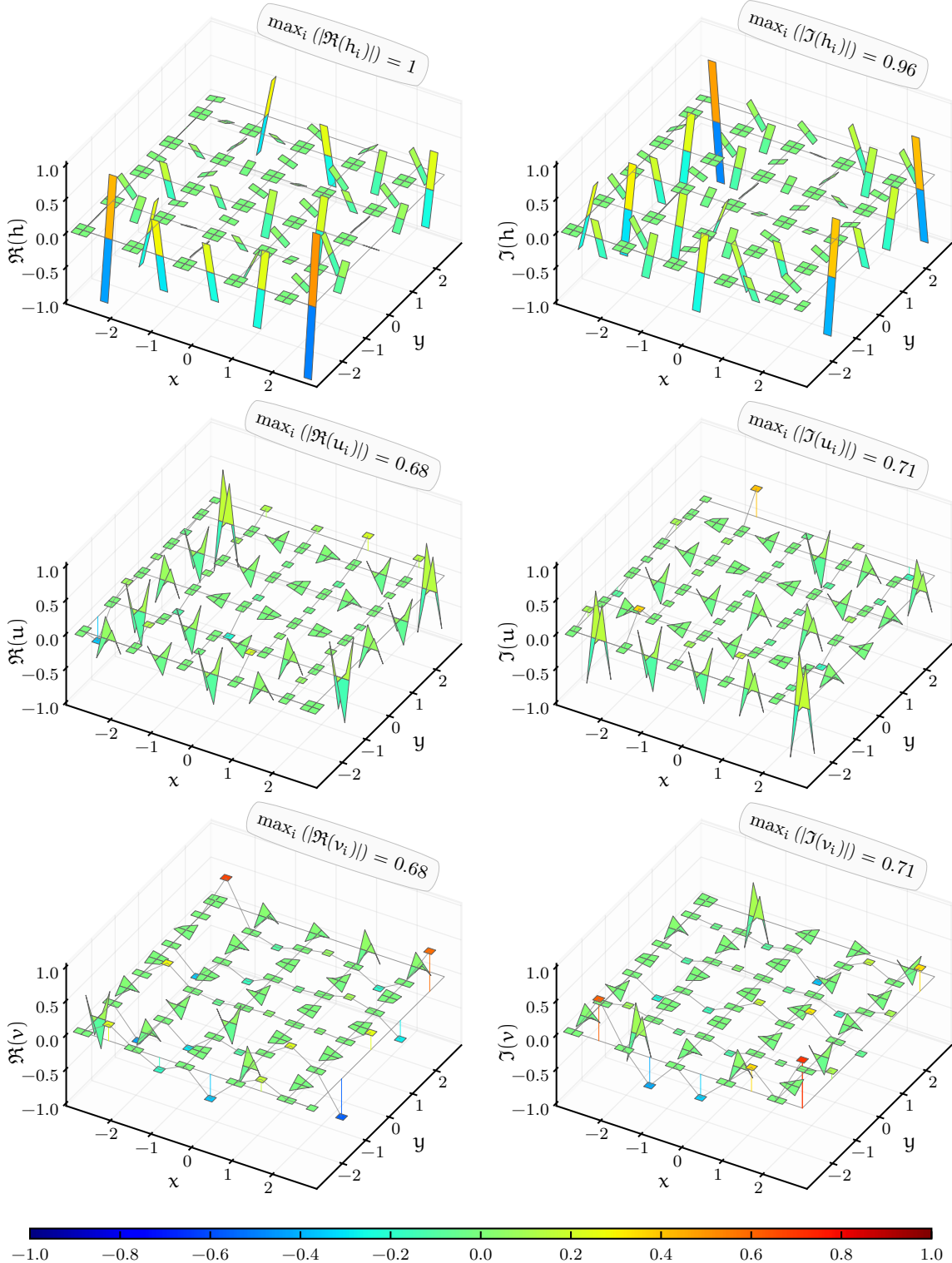
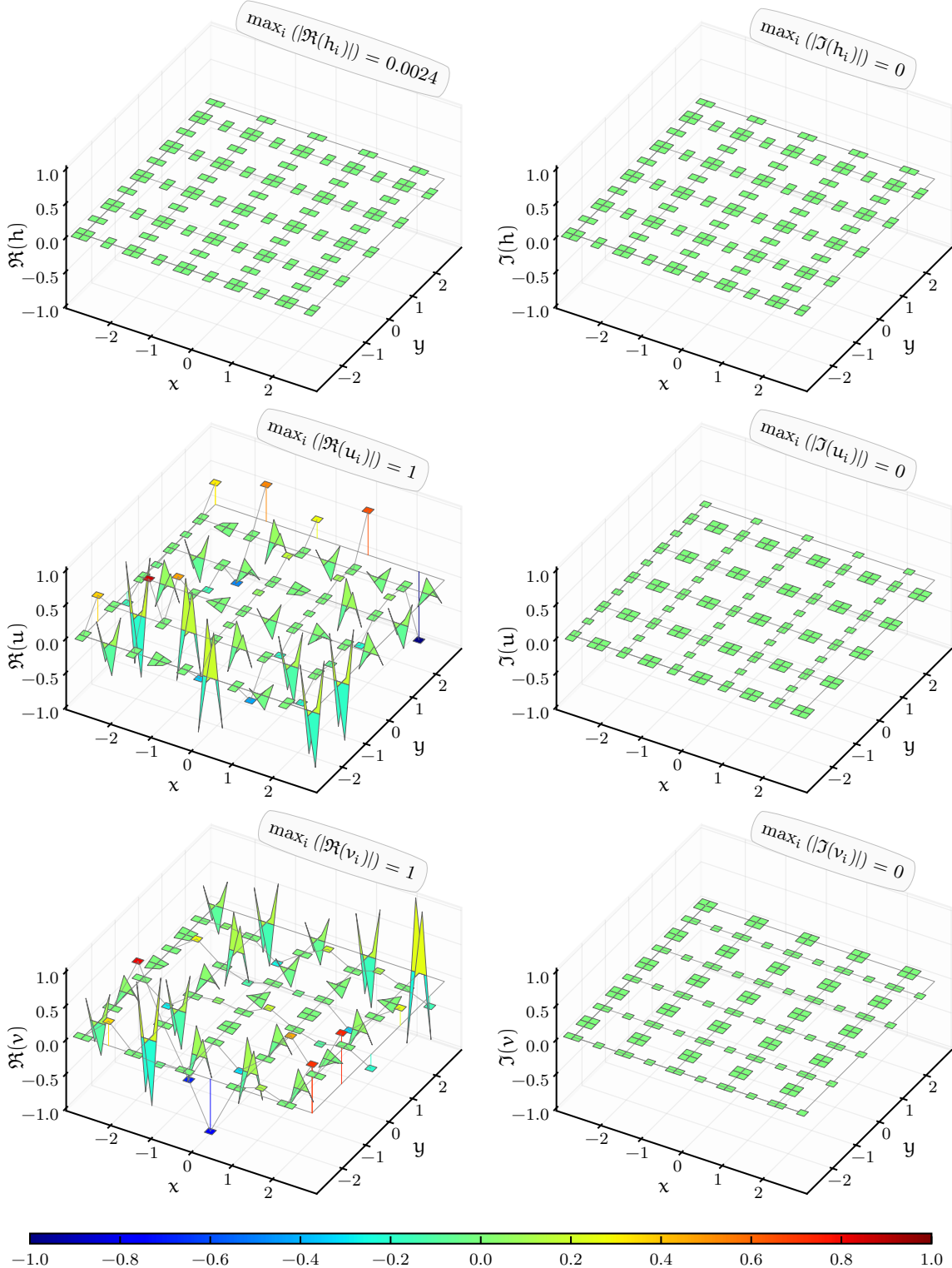


Figure 3.2.18: Eigenvector for eigenvalue $\lambda_p^N = -0.17 + 0i$ (cluster 8 in Fig. 3.2.12), for Square-p8 staggered patch scheme with $N = 10$, $n = 6$, $r = 0.1$. A sub-patch micro-scale vortex mode (only u and v are of significant magnitude).



3.3 A method of wavenumber-wise scale separation for patch scheme eigenvalues

[Section 3.6](#) quantitatively establish the accuracy of the patch schemes by comparing the eigenvalues of the patch schemes and that of the full-domain micro-scale system corresponding to specific macro-scale wave modes (i.e., for macro-scale wavenumbers $(k_x, k_y) \in \{(1, 0), (1, 1), (2, 1)\}$). Similarly, quantitative study of the patch schemes, for the sensitivity to numerical roundoff errors ([§3.4](#)) and the stability ([§3.5](#)) requires separation of micro- and macro-scale patch scheme eigenvalues. This subsection explains a method we name as *method of wavenumber-wise scale separation*, that perform wavenumber-wise classification and separation of micro- and macro-scale patch scheme eigenvalues.

The symbols λ_{pM}^{NE1} and λ_p^N denote the analytic and numerical macro-scale eigenvalues of a patch scheme respectively. Similarly, the symbols $\lambda_{p\mu}^{NE1}$ and $\lambda_{p\mu}^N$ denote the analytic and numerical micro-scale eigenvalues of a patch scheme respectively. The required *method of wavenumber-wise scale separation* has two goals:

1. classify the analytic and numerical eigenvalues $(\lambda_p^{NE1}, \lambda_p^N)$ of a patch scheme for all the $N^2/4$ macro-scale wavenumbers (k_x, k_y) where $k_x, k_y \in \{\dots, -1, 0, 1, \dots\}$ resolved by a patch grid;
2. separate the eigenvalues for each macro-scale wavenumber into *macro-scale eigenvalues* $\lambda_{pM}^{NE1}, \lambda_p^N$ (corresponding to pure macro-scale modes) and *micro-scale eigenvalues* $\lambda_{p\mu}^{NE1}, \lambda_{p\mu}^N$ (corresponding to micro-scale modes modulated over a macro-scale mode).
3. for each wavenumber, associate each of the three macro-scale eigenvalues $\lambda_{m\delta}^A, \lambda_{pM}^{NE1}, \lambda_p^N$ and associate each of the several micro-scale eigenvalues $\lambda_{p\mu}^{NE1}, \lambda_{p\mu}^N$.

The method of wavenumber-wise scale separation identifies the correspondence of the patch scheme eigenvalues $(\lambda_p^{NE1}, \lambda_p^N)$ to each macro-scale wavenumber resolved by a patch grid, and separates the eigenvalues into macro-scale and micro-scale eigenvalues, via the following steps. In all the following 3D arrays, the first two indices correspond to each macro-scale wavenumber resolved by a patch grid.

1. Compute and save the analytic eigenvalues $\lambda_{m\delta}^A$ of full-domain micro-scale system ([§3.2.2](#)) as a 3D $N/2 \times N/2 \times 3$ array for each of the $N^2/4$ macro-scale wavenumbers (k_x, k_y) resolved by a patch grid. That is, three eigenvalues for each wavenumber.

2. Compute and save the analytic eigenvalues λ_p^{NE1} of a patch scheme ([§3.2.3](#)) as a 3D $N/2 \times N/2 \times n_p^i$ array for each of the $N^2/4$ macro-scale wavenumbers (k_x, k_y) resolved by a patch grid. As in the expression [\(3.2.11\)](#) ([p. 53](#) of [§3.2.3](#)), there are $n_p^i = 9n^2/4 - 4n + 2$ eigenvalues λ_p^{NE1} for each wavenumber (e.g., 59 eigenvalues for $N = 10$). For Spectral patch scheme with $N > 14$, as the analytic expressions of the Jacobian elements become too long, we do not compute analytic eigenvalues λ_p^{NE1} ; hence this step does not apply. Among the total n_p^i eigenvalues of the patch scheme per wavenumber, $n_{pM}^i = 3$ eigenvalues (irrespective of N and n) correspond to the pure *macro-scale modes*, and $n_{p\mu}^i = 9n^2/4 - 4n - 1$ eigenvalues correspond to artificial sub-patch *micro-scale modes* modulated over macro-scale modes.
3. Compute and save the numerical eigenvalues λ_p^N of a patch scheme ([§3.2.5](#)) as an 1D array of size n_p^i . As in the expression [\(2.2.7\)](#) ([p. 18](#) of [§2.2.2](#)), there are $n_p^i = (N^2/4)(9n^2/4 - 4n + 2)$ eigenvalues λ_p^N , which include $n_{pM}^i = 3N^2/4$ eigenvalues corresponding to the macro-scale modes and $n_{p\mu}^i = (N^2/4)(9n^2/4 - 4n - 1)$ sub-patch micro-scale modes. Comparing with the number of patch scheme eigenvalues λ_p^{NE1} in step 2, $n_{pM}^i = n_{pM}^i(N^2/4)$, $n_{p\mu}^i = n_{p\mu}^i(N^2/4)$, $n_p^i = n_p^i(N^2/4)$. Thus, the 3D array of λ_p^{NE1} (with size $N/2 \times N/2 \times n_p^i$) in step 2 contain all the eigenvalues corresponding to the 1D array of λ_p^N with size n_p^i .
4. The task of this step is to split the $N/2 \times N/2 \times n_p^i$ array of analytic patch scheme eigenvalues λ_p^{NE1} in step 2 into $N/2 \times N/2 \times 3$ array of macro-scale eigenvalues λ_{pM}^{NE1} (corresponding to the $N/2 \times N/2 \times 3$ array of $\lambda_{m\delta}^A$ in step 1) and $N/2 \times N/2 \times (n_p^i - 3)$ array of micro-scale eigenvalues $\lambda_{p\mu}^{NE1}$. For this task, loop over each of the $N^2/4$ macro-scale wavenumbers (k_x, k_y) with index i, j and do the following sub-steps.
 - (a) To hold the macro- and micro-scale analytic patch scheme eigenvalues $\lambda_{pM}^{NE1}, \lambda_{p\mu}^{NE1}$, create two arrays of size $N/2 \times N/2 \times 3$ and $N/2 \times N/2 \times (n_p^i - 3)$ respectively.
 - (b) Within the $N/2 \times N/2 \times n_p^i$ array of λ_p^{NE1} (in step 2), among the n_p^i eigenvalues with indices i, j and $k = 1, 2, \dots, n_p^i$, find three eigenvalues that are closest to the three eigenvalues $\lambda_{m\delta}^A$ (in step 1). These three among the n_p^i eigenvalues are macro-scale eigenvalues λ_{pM}^{NE1} for this (k_x, k_y) , the remaining $n_p^i - 3$ eigenvalues are micro-scale eigenvalues $\lambda_{p\mu}^{NE1}$ for this (k_x, k_y) .
 - (c) Assign the three macro-scale eigenvalues λ_{pM}^{NE1} to the elements

of $N/2 \times N/2 \times 3$ array of macro-scale analytic patch scheme eigenvalues λ_{pM}^{NE1} (in step 4a) to indices i, j and $k = 1, 2, 3$. Assign the $n_p^i - 3$ micro-scale eigenvalues $\lambda_{p\mu}^{NE1}$ to the elements of $N/2 \times N/2 \times (n_p^i - 3)$ array of micro-scale analytic patch scheme eigenvalues $\lambda_{p\mu}^{NE1}$ (in step 4a) to indices i, j and $k = 1, 2, \dots, n_p^i - 3$.

5. The task of this step is to split the 1D array of numerical patch scheme eigenvalues λ_p^N (in step 3) with size $n_p^I = N/2 \cdot N/2 \cdot n_p^i$ into $N/2 \times N/2 \times 3$ array of macro-scale eigenvalues λ_{pM}^N (corresponding to the $N/2 \times N/2 \times 3$ array of λ_p^{NE1} in step 4) and $N/2 \times N/2 \times (n_p^i - 3)$ array of micro-scale eigenvalues $\lambda_{p\mu}^N$ (corresponding to the $N/2 \times N/2 \times (n_p^i - 3)$ array of λ_p^{NE1} in step 4). For this task, loop over each of the $N^2/4$ macro-scale wavenumbers (k_x, k_y) with index i, j and do the following sub-steps.
 - (a) To hold the macro- and micro-scale numerical patch scheme eigenvalues $\lambda_{pM}^N, \lambda_{p\mu}^N$, create two arrays of size $N/2 \times N/2 \times 3$ and $N/2 \times N/2 \times (n_p^i - 3)$ respectively.
 - (b) Among the 1D array of eigenvalues λ_p^N (in step 3), find three eigenvalues that are closest to the three analytic eigenvalues with indices i, j and $k = 1, 2, 3$ within the $N/2 \times N/2 \times 3$ array of λ_p^{NE1} (in step 4). These three eigenvalues are macro-scale eigenvalues λ_{pM}^N for this (k_x, k_y) . Assign these three eigenvalues λ_{pM}^N to the elements of $N/2 \times N/2 \times 3$ array of macro-scale numerical patch scheme eigenvalues λ_{pM}^N (in step 5a) for indices i, j and $k = 1, 2, 3$. Remove these three eigenvalues from the 1D array of eigenvalues λ_p^N .
 - (c) Among the 1D array of remaining eigenvalues λ_p^N (in step 5b), find $n_p^i - 3$ eigenvalues that are closest to the $n_p^i - 3$ analytic eigenvalues within the $N/2 \times N/2 \times (n_p^i - 3)$ array of λ_p^{NE1} (in step 4) for indices i, j and $k = 1, 2, \dots, n_p^i - 3$. These $n_p^i - 3$ eigenvalues are micro-scale eigenvalues $\lambda_{p\mu}^N$ for this (k_x, k_y) . Assign these $n_p^i - 3$ eigenvalues $\lambda_{p\mu}^N$ to the elements of $N/2 \times N/2 \times (n_p^i - 3)$ array of micro-scale numerical patch scheme eigenvalues $\lambda_{p\mu}^N$ (in step 5a) for indices i, j and $k = 1, 2, \dots, n_p^i - 3$. Remove these $n_p^i - 3$ eigenvalues from the 1D array of eigenvalues λ_p^N .
6. Do this step only when step 5 cannot be done due to unavailability of analytic patch scheme eigenvalues λ_p^{NE1} (in step 2) (e.g., for Spectral patch scheme with $N > 14$). The task of this step is to split the 1D array of numerical patch scheme eigenvalues λ_p^N (in step 3) with

size $n_p^I = N/2 \cdot N/2 \cdot n_p^i$ into $N/2 \times N/2 \times 3$ array of macro-scale eigenvalues λ_{pM}^N (corresponding to the $N/2 \times N/2 \times 3$ array of λ_p^{NE1} in step 4) and a 1D array with size $n_{p\mu}^I = n_{p\mu}^i(N^2/4)$ of micro-scale eigenvalues $\lambda_{p\mu}^N$ (corresponding to the $N/2 \times N/2 \times (n_p^i - 3)$ array of λ_p^{NE1} in step 4). As the analytic patch scheme eigenvalues λ_p^{NE1} are not available, in contrast to step 5, this step cannot compute an $N/2 \times N/2 \times (n_p^i - 3)$ array of micro-scale eigenvalues $\lambda_{p\mu}^N$. This step assumes that the patch scheme is highly accurate and so the macro-scale patch scheme eigenvalues are very close to the eigenvalues $\lambda_{m\delta}^A$ of full-domain micro-scale system. For this task, loop over each of the $N^2/4$ macro-scale wavenumbers (k_x, k_y) with index i, j and do the following sub-steps.

- (a) To hold the macro-scale numerical patch scheme eigenvalues λ_{pM}^N , create an $N/2 \times N/2 \times 3$ array.
- (b) Among the 1D array of eigenvalues λ_p^N (in step 3), find three eigenvalues that are closest to the three eigenvalues with indices i, j and $k = 1, 2, 3$ within the $N/2 \times N/2 \times 3$ array of eigenvalues $\lambda_{m\delta}^A$ of the full-domain micro-scale system (in step 1). These three eigenvalues are the macro-scale eigenvalues λ_{pM}^N for this (k_x, k_y) . Assign these three eigenvalues λ_{pM}^N to the elements of $N/2 \times N/2 \times 3$ array of macro-scale numerical patch scheme eigenvalues λ_{pM}^N (in step 6a) for indices i, j and $k = 1, 2, 3$. Remove these three eigenvalues from the 1D array of eigenvalues λ_p^N .

At the end of the loop over the macro-scale wavenumbers (k_x, k_y) , having removed all the $3N^2/4$ macro-scale eigenvalues λ_{pM}^N , the remaining $n_{p\mu}^I = n_p^I - n_{pM}^I$ eigenvalues are the sub-patch micro-scale eigenvalues.

After the preceding steps 1 to 6, the method of wavenumber-wise scale separation for the patch scheme eigenvalues gives the following arrays.

1. An $N/2 \times N/2 \times 3$ array of analytic eigenvalues $\lambda_{m\delta}^A$ of full-domain micro-scale system .
2. When the analytic patch scheme eigenvalues λ_p^{NE1} are available, both the macro-scale eigenvalues and micro-scale eigenvalues are classified wavenumber-wise.
 - (a) An $N/2 \times N/2 \times 3$ array of macro-scale *analytic* patch scheme eigenvalues λ_{pM}^{NE1} .

- (b) An $N/2 \times N/2 \times 3$ array of macro-scale *numerical* patch scheme eigenvalues λ_{pM}^N .
 - (c) An $N/2 \times N/2 \times (n_p^i - 3)$ array of micro-scale *analytic* patch scheme eigenvalues λ_{pM}^{NE1} .
 - (d) An $N/2 \times N/2 \times (n_p^i - 3)$ array of micro-scale *numerical* patch scheme eigenvalues λ_{pM}^N .
3. When the analytic patch scheme eigenvalues λ_{pM}^{NE1} are not available (e.g., for Spectral patch scheme with $N > 14$), only the macro-scale eigenvalues are classified wavenumber-wise.
- (a) An $N/2 \times N/2 \times 3$ array of macro-scale numerical patch scheme eigenvalues λ_{pM}^N .
 - (b) An 1D array with size $n_{p\mu}^I = n_p^I - n_{pM}^I$ of micro-scale numerical patch scheme eigenvalues λ_{pM}^N , without any association to the wavenumbers.

The association among each of the three macro-scale eigenvalues $\lambda_{m\delta}^A$, λ_{pM}^{NE1} , λ_{pM}^N and association among each of the several micro-scale eigenvalues $\lambda_{p\mu}^{NE1}$, $\lambda_{p\mu}^N$ is established by for each wavenumber through the index order in the third dimension.

3.4 Staggered patch schemes are not sensitive to numerical roundoff errors

Despite the attractive characteristics, if the staggered patch schemes are very sensitive to numerical roundoff errors, they will not be suitable for practical numerical simulations using finite precision floating point representations, for example the common 64 bit format of IEE754 (Goldberg 1991). From both qualitative and quantitative arguments, this section shows that staggered the patch schemes are not sensitive to numerical roundoff errors for the general linear wave.

The staggered patch scheme eigenvalues λ_p^{NE1} (for both the micro-scale and macro-scale modes) of the numerically evaluated one-cell Jacobian ([§3.2.3](#)) and the staggered patch scheme eigenvalues λ_p^N of the numerical Jacobian ([§3.2.5](#)), *visually* agree in the complex plane eigenvalue plots of [§3.2.6](#) (i.e., the large magenta and blue circles in [Fig. 3.2.2](#)). That the numerical and analytic eigenvalues (λ_p^N , λ_p^{NE1}) of a patch scheme visually agree indicates that the patch scheme is not sensitive to numerical roundoff errors. This

Table 3.4.1: [Section 3.4](#) studies the sensitivity of the patch scheme eigenvalues to numerical roundoff errors for all the 1944 combinations (cartesian product) of the listed parameters.

Patch schemes	Spectral, Square-p2, Square-p4, Square-p6, and Square-p8
Drag coefficient	$c_D \in \{0, 10^{-6}, 0.001\}$
Viscous coefficient	$c_V \in \{0, 10^{-4}, 0.01\}$
Macro-grid intervals	$N \in \{6, 10, 14\}$ for Spectral scheme, $N \in \{6, 10, 14, 18, 22, 26\}$ for polynomial schemes.
Sub-patch micro-grid intervals	$n \in \{6, 10\}$
Patch scale ratio	$r \in \{0.0001, 0.001, 0.01, 0.1\}$

subsection first *quantitatively* compares the numerical and analytic eigenvalues of the staggered patch schemes to show that the staggered patch schemes are not sensitive to numerical roundoff errors when sub-patch micro-grid interval is not too small (i.e., $\delta \gtrsim 10^{-5}$). The later part of this subsection argues that even when the sub-patch micro-grid interval δ is too small, the numerical roundoff errors were not due to the patch scheme computations.

For the time simulations, how sensitive are the patch scheme computations to numerical roundoff errors? One approach to answer this question is to study the patch scheme simulations for several specific initial conditions. Instead, this section addresses this question globally for all the possible initial conditions by studying how sensitive the patch scheme eigenvalues are to the numerical roundoff errors. Hence we compare the eigenvalues λ_p^{NE1} of the analytically derived Jacobian ([§3.2.3](#)) with the eigenvalues λ_p^N of the numerically computed Jacobian ([§3.2.5](#)) for a total of 1944 patch scheme cases as [Table 3.4.1](#) lists.

To quantitatively assess the sensitivity of the staggered patch schemes to numerical roundoff errors, we study the discrepancy $|\lambda_{p,i}^N - \lambda_{p,i}^{NE1}|$ separately for the macro-scale and micro-scale eigenvalues. We define the *micro- and macro-scale numerical roundoff errors* for the staggered patch scheme

eigenvalues as

$$\epsilon_{\mu}^{\text{Num}} = \max_i |\lambda_{p\mu,i}^N - \lambda_{p\mu,i}^{NE1}| \quad (3.4.1a)$$

for indices i of the micro-scale eigenvalues,

$$\epsilon_M^{\text{Num}} = \max_i |\lambda_{pM,i}^N - \lambda_{pM,i}^{NE1}| \quad (3.4.1b)$$

for indices i of the macro-scale eigenvalues.

If the errors $\epsilon_{\mu}^{\text{Num}}$ and ϵ_M^{Num} are negligibly small, that is, if the numerical and analytic macro-scale eigenvalues $(\lambda_{pM}^N, \lambda_{pM}^{NE1})$ of a patch scheme agree very closely, the patch scheme is not sensitive to the numerical roundoff errors.

The eigenvalues in the numerical roundoff errors (3.4.1a) and (3.4.1b) require separating the micro- and macro-scale patch scheme eigenvalues and the association between the analytic and numerical eigenvalues. [Section 3.3](#) computes the required eigenvalues as the following 3D arrays (analytic eigenvalues only for $N \leq 14$ for Spectral patch scheme)

1. An $N/2 \times N/2 \times 3$ array of macro-scale *analytic* patch scheme eigenvalues λ_{pM}^{NE1} .
2. An $N/2 \times N/2 \times 3$ array of macro-scale *numerical* patch scheme eigenvalues λ_{pM}^N .
3. An $N/2 \times N/2 \times (n_p^i - 3)$ array of micro-scale *analytic* patch scheme eigenvalues λ_{pM}^{NE1} .
4. An $N/2 \times N/2 \times (n_p^i - 3)$ array of micro-scale *numerical* patch scheme eigenvalues λ_{pM}^N .

The micro- and macro-scale numerical roundoff errors in (3.4.1) are defined for the eigenvalues of a patch scheme with for one specific set of parameters. We define the *peak micro- and macro-scale numerical roundoff errors* as the maximum value of $\max_{c_D, c_V} \epsilon_{\mu}^{\text{Num}}$ and $\max_{c_D, c_V} \epsilon_M^{\text{Num}}$, over the nine combinations of the coefficients $c_D \in \{0, 10^{-6}, 0.001\}$ and $c_V \in \{0, 10^{-4}, 0.01\}$ as [Table 3.4.1](#) lists.

Non-negligible numerical roundoff errors arise only for very small sub-patch micro-grid intervals $\delta \lesssim 10^{-5}$ (i.e., small r and large N, n). [Figures 3.4.1](#) and [3.4.2](#) plot the peak micro- and macro-scale numerical roundoff errors for the five patch schemes, for the 1944 combinations of the parameters [Table 3.4.1](#) lists. [Table 3.4.2](#) presents the peak numerical roundoff errors for different patch scale ratios r (i.e. peak value for each r -slice in [Figs. 3.4.1](#)

Figure 3.4.1: Variation of the peak *micro-scale* numerical roundoff error with the number of macro-grid intervals N , patch scale ratio r and the number of sub-patch micro-grid intervals n . Each point is the peak $\epsilon_{\mu}^{\text{Num}}$ for the nine combinations of the coefficients c_D, c_V in [Table 3.4.1](#), for a patch scheme with particular patch grid parameters (N, r, n) .

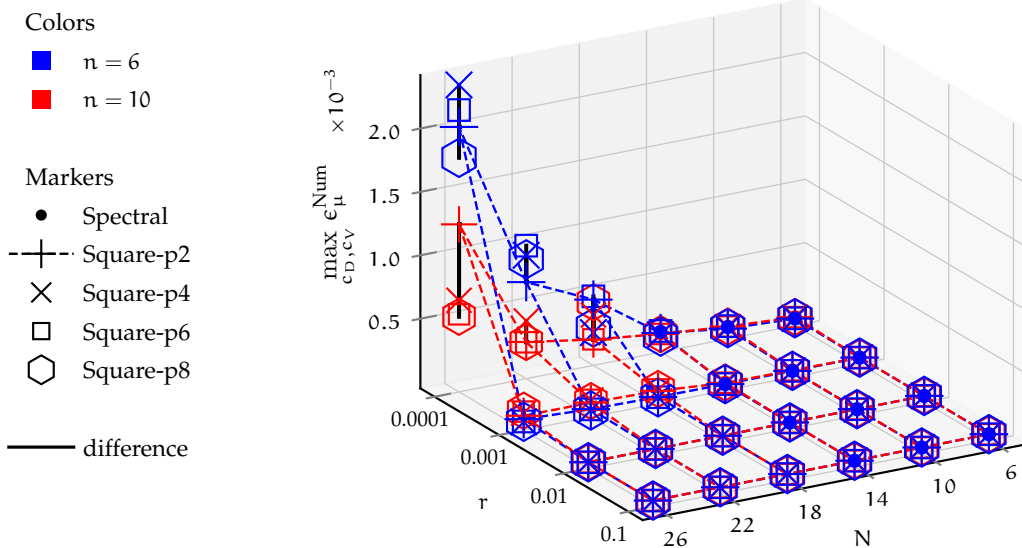


Figure 3.4.2: Variation of the peak *macro-scale* numerical roundoff error with the number of macro-grid intervals N , patch scale ratio r and the number of sub-patch micro-grid intervals n . Each point is the peak ϵ_M^{Num} for the nine combinations of the coefficients c_D, c_V in [Table 3.4.1](#), for a patch scheme with particular patch grid parameters (N, r, n) .

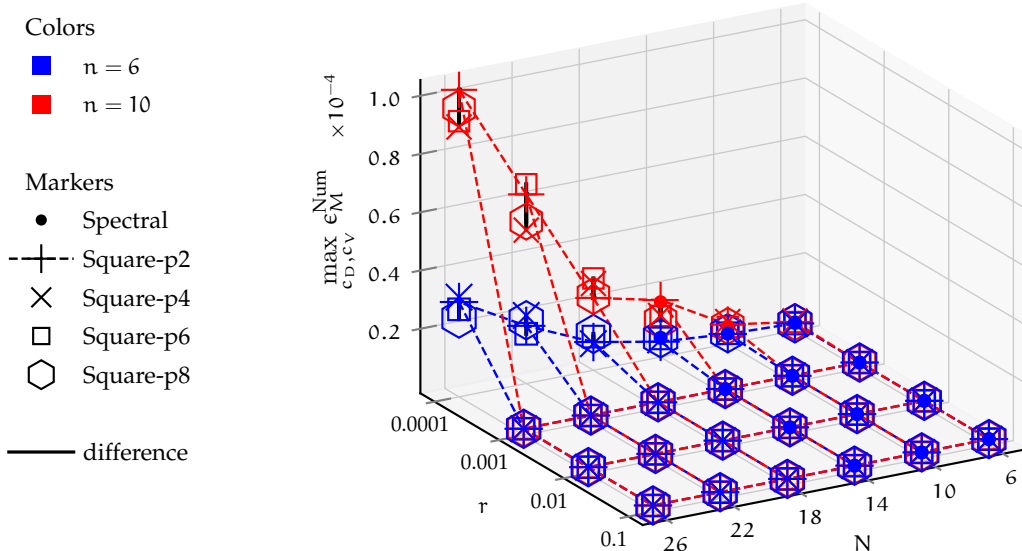


Table 3.4.2: Maximum numerical roundoff errors over all the combinations of the five patch schemes and c_D , c_V , and N in Table 3.4.1 for different patch scale ratio r and n . Red colour highlights largest value in each column (based on full precision when values are same with two significant figures).

		Patch scale ratio r			
		0.0001	0.001	0.01	0.1
$\max \epsilon_{\mu}^{\text{Num}}$	$n = 6$	0.002	$4 \cdot 10^{-5}$	$3 \cdot 10^{-7}$	$6 \cdot 10^{-10}$
	$n = 10$	0.001	0.0001	$3 \cdot 10^{-7}$	$6 \cdot 10^{-9}$
$\max \epsilon_M^{\text{Num}}$	$n = 6$	$3 \cdot 10^{-5}$	$4 \cdot 10^{-8}$	10^{-10}	$2 \cdot 10^{-11}$
	$n = 10$	0.0001	10^{-7}	$5 \cdot 10^{-10}$	$2 \cdot 10^{-11}$

and 3.4.2). The largest micro- and macro-scale numerical roundoff errors among the 1944 cases are 0.0001 and 0.002 respectively, both corresponding to the smallest patch scale ratio $r = 0.0001$. The following are some key observations from Figs. 3.4.1 and 3.4.2 and Table 3.4.2.

1. For a given set of patch grid parameters N , n , r , the peak macro-scale numerical roundoff errors $\max_{c_D, c_V} \epsilon_M^{\text{Num}}$ are about ten to thousand times smaller than the peak micro-scale numerical roundoff errors $\max_{c_D, c_V} \epsilon_{\mu}^{\text{Num}}$. That is, *the macro-scale eigenvalues which are of primary interest are relatively less sensitive to numerical roundoff errors than the micro-scale eigenvalues*.
2. Both the micro-scale and macro-scale peak numerical roundoff errors $\max_{c_D, c_V} \epsilon_{\mu}^{\text{Num}}$, $\max_{c_D, c_V} \epsilon_M^{\text{Num}}$, monotonically increase with increasing number of macro-grid intervals N and decreasing patch scale ratio r . The numerical roundoff errors also increase with increasing number of sub-patch micro-grid intervals n (blue and red colors in Figs. 3.4.1 and 3.4.2), except the off trend for $\max_{c_D, c_V} \epsilon_{\mu}^{\text{Num}}$ in Fig. 3.4.1 for $N \in \{22, 26\}$ and $r = 0.0001$. For a staggered patch grid, increasing N , decreasing r , and increasing n , all these lead to decreasing sub-patch micro-grid interval $\delta = 2Lr/(Nn)$. For example, for $r = 0.001$, $N = 26$, $n = 10$, sub-patch micro-grid interval $\delta \approx 5 \cdot 10^{-5}$. Thus, *non-negligible numerical roundoff errors arise only for very small sub-patch micro-grid intervals $\delta \lesssim 10^{-5}$ (i.e., small r and large N , n)*.
3. In general, except $\epsilon_{\mu}^{\text{Num}}$ for $N \gtrsim 22$, $r = 0.0001$, the numerical roundoff errors of all the five patch schemes are roughly the same. That is, the numerical roundoff errors do not have strong dependence on the specific patch scheme. If the numerical roundoff errors were due to

the patch scheme, the numerical roundoff errors must also depend on the specific patch scheme, showing a clear trend. The lack of such trends, among the patch schemes with different amounts of numerical computations, *indicates that the numerical roundoff errors are not due to the patch scheme computations.*

In [Figs. 3.4.1](#) and [3.4.2](#) and [Table 3.4.2](#), the large peak numerical roundoff errors for small sub-patch micro-grid intervals δ (i.e., small r and large N, n), have the following main sources.

1. The numerical roundoff errors due to the numerical computations in a patch scheme due to the patch coupling.
2. The numerical roundoff errors due to the numerical computations of the underlying micro-scale system (e.g., the finite difference computations).
3. The numerical roundoff errors in numerically computing the eigenvalues of the patch scheme numerical Jacobian.

We take the numerical roundoff errors in numerically computing the Jacobian ([§3.2.5](#)) of a patch scheme, to be small compared to the much higher number of numerical computations in the patch coupling, sub-patch micro-scale system and the eigenvalue computation.

The dependence of the numerical roundoff errors on the system parameters (drag and viscous diffusion) and the lack of dependence of the specific patch schemes show that *the numerical roundoff errors are due to the underlying micro-scale system, not due to the staggered patch scheme*. [Tables 3.4.3](#) and [3.4.4](#) present the micro-scale numerical roundoff errors $\epsilon_{\mu}^{\text{Num}}, \epsilon_M^{\text{Num}}$ for different coefficients of drag c_D and and viscous diffusion c_V . Both the numerical roundoff errors strongly depend on the viscous diffusion; both $\epsilon_{\mu}^{\text{Num}}$ and ϵ_M^{Num} increase with increasing c_V , showing strong increase at small patch scale ratio r . The micro-scale numerical roundoff errors $\epsilon_{\mu}^{\text{Num}}$ in [Table 3.4.3](#) do not have strong dependence on the drag coefficient c_D . But in [Table 3.4.4](#), the maximum ϵ_M^{Num} for $c_D = 10^{-6}$ (for $c_V = 0.01$ and small patch scale ratios $r \in \{0.0001, 0.001\}$), indicates some dependence of the macro-scale numerical roundoff errors on the drag coefficient c_D . In general, the staggered patch schemes are largely agnostic of the underlying micro-scale system. More specifically a discussion in [§3.4](#) of this section, using [Figs. 3.4.1](#) and [3.4.2](#) show that the numerical roundoff errors do not have strong dependence on the specific patch scheme. This lack of dependence on the specific patch schemes despite with different amounts of numerical computations, indicates that the numerical roundoff errors are

Table 3.4.3: Maximum numerical roundoff errors $\epsilon_{\mu}^{\text{Num}}$ in micro-scale eigenvalues over the five patch schemes and all the combinations of N, n in [Table 3.4.1](#), for different patch scale ratio r and coefficients of drag c_D and viscous diffusion c_V . Large $\epsilon_{\mu}^{\text{Num}}$ in each column corresponding to the largest $c_V = 0.01$ are red highlighted.

	Patch scale ratio r			
	0.0001	0.001	0.01	0.1
$c_D = 0, c_V = 0$	$7 \cdot 10^{-5}$	10^{-6}	$3 \cdot 10^{-7}$	$7 \cdot 10^{-10}$
$c_D = 0, c_V = 0.0001$	0.0001	$7 \cdot 10^{-7}$	$7 \cdot 10^{-9}$	$7 \cdot 10^{-10}$
$c_D = 0, c_V = 0.01$	0.002	0.0001	$9 \cdot 10^{-8}$	$6 \cdot 10^{-9}$
$c_D = 10^{-6}, c_V = 0$	$6 \cdot 10^{-5}$	10^{-6}	$3 \cdot 10^{-7}$	$7 \cdot 10^{-10}$
$c_D = 10^{-6}, c_V = 0.0001$	0.0001	$7 \cdot 10^{-7}$	$7 \cdot 10^{-9}$	$7 \cdot 10^{-10}$
$c_D = 10^{-6}, c_V = 0.01$	0.002	0.0001	$9 \cdot 10^{-8}$	$6 \cdot 10^{-9}$
$c_D = 0.001, c_V = 0$	0.0001	10^{-6}	$3 \cdot 10^{-7}$	$7 \cdot 10^{-10}$
$c_D = 0.001, c_V = 0.0001$	0.0001	$7 \cdot 10^{-7}$	$7 \cdot 10^{-9}$	$7 \cdot 10^{-10}$
$c_D = 0.001, c_V = 0.01$	0.002	0.0001	$9 \cdot 10^{-8}$	$6 \cdot 10^{-9}$

Table 3.4.4: Maximum numerical roundoff errors ϵ_M^{Num} in macro-scale eigenvalues over the five patch schemes and all the combinations of N, n in [Table 3.4.1](#), for different patch scale ratio r and coefficients of drag c_D and viscous diffusion c_V . Large ϵ_M^{Num} in each column corresponding to the largest $c_V = 0.01$ are red highlighted.

	Patch scale ratio r			
	0.0001	0.001	0.01	0.1
$c_D = 0, c_V = 0$	$2 \cdot 10^{-9}$	$2 \cdot 10^{-10}$	$3 \cdot 10^{-11}$	$2 \cdot 10^{-11}$
$c_D = 0, c_V = 0.0001$	$4 \cdot 10^{-8}$	$8 \cdot 10^{-10}$	$2 \cdot 10^{-11}$	$2 \cdot 10^{-11}$
$c_D = 0, c_V = 0.01$	$9 \cdot 10^{-5}$	$9 \cdot 10^{-8}$	$5 \cdot 10^{-10}$	$2 \cdot 10^{-11}$
$c_D = 10^{-6}, c_V = 0$	$2 \cdot 10^{-9}$	$2 \cdot 10^{-10}$	$3 \cdot 10^{-11}$	$2 \cdot 10^{-11}$
$c_D = 10^{-6}, c_V = 0.0001$	$4 \cdot 10^{-8}$	$7 \cdot 10^{-10}$	$2 \cdot 10^{-11}$	$2 \cdot 10^{-11}$
$c_D = 10^{-6}, c_V = 0.01$	0.0001	10^{-7}	$5 \cdot 10^{-10}$	$2 \cdot 10^{-11}$
$c_D = 0.001, c_V = 0$	$2 \cdot 10^{-9}$	$2 \cdot 10^{-10}$	$3 \cdot 10^{-11}$	$2 \cdot 10^{-11}$
$c_D = 0.001, c_V = 0.0001$	$4 \cdot 10^{-8}$	$7 \cdot 10^{-10}$	$2 \cdot 10^{-11}$	$2 \cdot 10^{-11}$
$c_D = 0.001, c_V = 0.01$	$9 \cdot 10^{-5}$	$9 \cdot 10^{-8}$	$5 \cdot 10^{-10}$	$2 \cdot 10^{-11}$

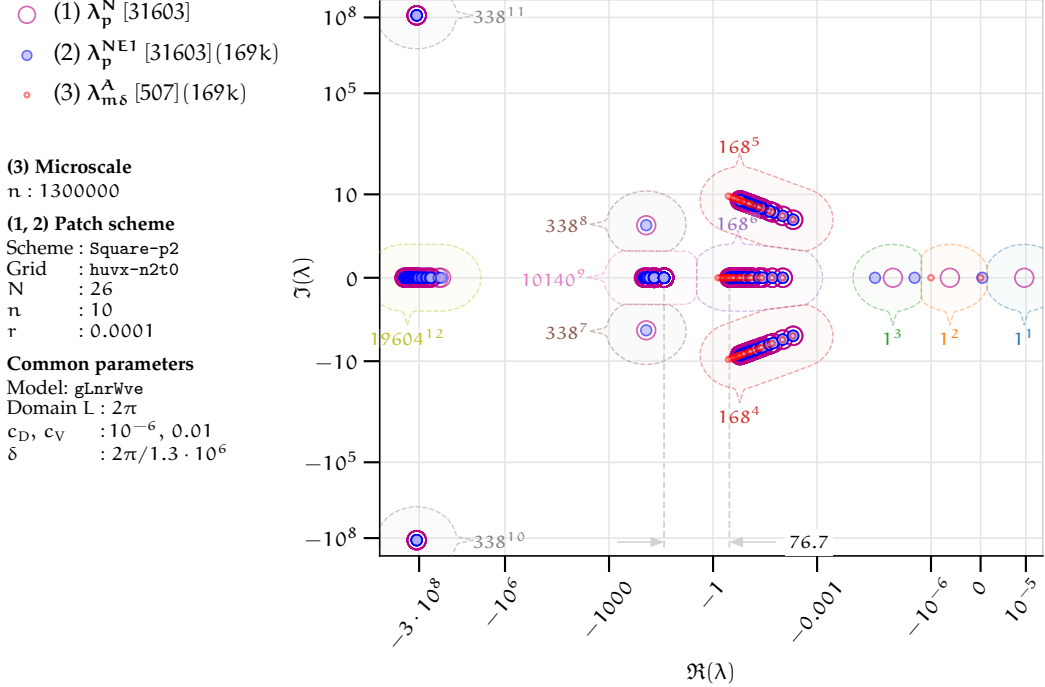
not due to the patch scheme computations. Moreover, if the patch schemes were sensitive to numerical roundoff errors, the errors must have been large irrespective of the system parameters (drag and viscous diffusion). For example, $\epsilon_{\mu}^{\text{Num}}$ and ϵ_M^{Num} must have been large also for small c_V , which is not the case in [Tables 3.4.3](#) and [3.4.4](#). Thus, the dependence of the numerical roundoff errors on the system parameters (c_D and c_V) and the lack of dependence of the specific patch schemes show that *the numerical roundoff errors are due to the underlying micro-scale system, not due to the staggered patch scheme*. Following two paragraphs detail the dependence of the numerical roundoff errors on c_V and c_D respectively.

Scaling arguments on the general linear wave confirm the inherent sensitivity of the micro-scale system to numerical roundoff errors. In the full-domain micro-scale system [\(3.1.2b\)](#) of [§3.1](#), let us compare how the terms scale with the grid-interval δ . The wave term $\sim h/\delta$, the drag term $\sim c_D u$, and the viscous diffusion terms $\sim c_V u/\delta^2$. For example, for small $\delta = 10^{-5}$, the scales of the wave, drag, and viscous diffusion terms are about $10^5 h$, $c_D u$ and $10^{10} c_V u$ respectively. For small height h , when the viscous diffusion is not negligibly small (e.g., $c_V \sim 0.01$), irrespective of c_D , the addition (subtraction) of these small and large values leads to the loss of floating point precision while lining up the decimal points in the finite precision arithmetic (Heister, Rebholz, and Xue [2019](#), p. 8; Goldberg [1991](#), pp. 16, 19). Hence, for non-negligible viscous diffusion ($c_V \gtrsim 0.001$) both the full-domain micro-sale scheme and the sub-patch micro-scale system, are inherently sensitive to numerical roundoff errors, for small grid interval $\delta \lesssim 10^{-5}$. This inherent sensitivity of the micro-scale system to numerical roundoff errors is not severe for the time simulation [**TODO xref to time sim subsection**], but impacts the eigenvalue computation for both the full-domain micro-scale system and the patch scheme. Both the micro- and macro-scale roundoff errors ($\epsilon_{\mu}^{\text{Num}}$ and ϵ_M^{Num}) are large for large c_V in [Tables 3.4.3](#) and [3.4.4](#). Also, both $\epsilon_{\mu}^{\text{Num}}$ and ϵ_M^{Num} monotonically increase with decreasing r (and hence decreasing δ), at an increasing rate with increasing viscous diffusion c_V . Whereas this inherent sensitivity impacts both the micro- and macro-scale eigenvalues, the macro-scale numerical roundoff errors ϵ_M^{Num} are in general ten to thousand times smaller than the peak micro-scale numerical roundoff errors $\epsilon_{\mu}^{\text{Num}}$. We expect that this relatively smaller ϵ_M^{Num} is due to the macro-scale interpolation in the patch coupling, which acts as averaging/smoothing the inherent numerical roundoff errors of the computations within the patches. Thus, for small grid interval $\delta \lesssim 10^{-5}$ and large viscous diffusion ($c_V \gtrsim 0.001$), the non-negligible numerical roundoff errors in both micro- and macro-scale patch scheme eigenvalues are due to the inherent sensitivity of the micro-scale system to numerical roundoff errors.

A part of the numerical roundoff errors are due to numerical computation of near zero eigenvalues. The micro-scale numerical roundoff errors in Table 3.4.3, in general remains independent of the drag coefficient c_D , except the change of about 10^{-5} for $c_D \in \{0, 10^{-6}, 0.0001\}$ with $c_V = 0$ and $r = 0.0001$. But in Table 3.4.4, the maximum ϵ_M^{Num} for $c_D = 10^{-6}$ (for $c_V = 0.01$ and small patch scale ratios $r \in \{0.0001, 0.001\}$), suggest that the macro-scale numerical roundoff errors also depend on the drag coefficient c_D . This paragraph explores the dependence of macro-scale numerical roundoff error ϵ_M^{Num} on the drag coefficient c_D . For nonzero drag and viscous diffusion, patch schemes have one zero eigenvalue (cluster 1 in Fig. 3.2.2) corresponding to the macro-scale mode of stagnant water (Fig. 3.2.13), and two eigenvalues (cluster 2 in Fig. 3.2.2) with $-c_D$ as their real part and zero imaginary part corresponding to the macro-scale mode of decelerating uniform mean flow (Fig. 3.2.14). As $c_D \rightarrow 0$, the two eigenvalues $\lambda = -c_D + 0i$ corresponding to the decelerating uniform mean flow, tends to zero, merging with the zero eigenvalue as in Fig. 3.2.3. Due to these near zero repeated eigenvalues for small drag $c_D \lesssim 10^{-6}$, numerically finding the roots of the characteristic polynomial, for both the patch scheme and the full-domain micro-scale system, becomes sensitive to the numerical roundoff errors. As we compute the analytic eigenvalues λ_p^{NE1} after evaluating the analytic Jacobian, both the analytic and numeric eigenvalues $\lambda_p^{\text{NE1}}, \lambda_p^N$ are sensitive to numerical roundoff errors. Being random, the numerical roundoff errors in the eigenvalues λ_p^{NE1} and λ_p^N , do not cancel in computing the difference in our definition (3.4.1). Thus, for small grid interval $\delta \lesssim 10^{-5}$ and small drag $c_D \lesssim 10^{-6}$, the sensitivity of numerical eigenvalue computation also leads to large numerical roundoff errors in near zero eigenvalues.

Numerical roundoff errors also arise due to near zero repeated eigenvalues for small nonzero drag As discussed in the paragraph before the previous paragraph, the inherent sensitivity of the micro-scale system to numerical roundoff errors is large for large viscous diffusion, leading to increase in both the micro- and macro-scale numerical roundoff errors ($\epsilon_\mu^{\text{Num}}$ and ϵ_M^{Num}). But, as repeated near zero eigenvalues due to small drag corresponds to the macro-scale modes, the sensitivity of eigenvalue computation leads to increase in the macro-scale numerical roundoff errors ϵ_M^{Num} only. Hence, for small grid interval $\delta \lesssim 10^{-5}$, due to both the inherent sensitivity of the micro-scale system (for nonnegligible viscous diffusion $c_V \gtrsim 0.001$) and the sensitivity of eigenvalue computation of near zero repeated eigenvalues (for small drag $c_D \lesssim 10^{-6}$), the macro-scale numerical roundoff errors ϵ_M^{Num} are large. For example, the numerical roundoff errors in Table 3.4.4 for macro-scale eigenvalues has maximum values of $\epsilon_M^{\text{Num}} = 10^{-7}, 0.0001$ for $r = 0.0001, 0.001$ for small nonzero drag $c_D = 10^{-6}$. Figure 3.4.3 shows the

Figure 3.4.3: Eigenvalues of Square-p2 staggered patch scheme ($N = 26$, $n = 10$, $r = 0.0001$) for general linear wave with large viscous diffusion $c_V = 0.01$ and a small drag $c_D = 10^{-6}$. Large numerical roundoff errors are evident from the large discrepancy among the near zero eigenvalues λ_p^N , λ_p^{NE1} , and $\lambda_{m\delta}^A$ (clusters 1, 2, 3).



large numerical roundoff errors in the near zero eigenvalues due to small drag. The numeric eigenvalues λ_p^N in clusters 1, 2, 3 have large numerical roundoff errors, due to the micro-scale system's inherent sensitivity (for large $c_V = 0.01$) and the sensitivity of eigenvalue computation of near zero repeated eigenvalues (for small drag $c_D = 10^{-6}$). The analytic eigenvalues λ_p^{NE1} corresponding to λ_p^N in clusters 1, 2, 3, have relatively smaller numerical roundoff errors, as the computation of the underlying micro-scale system is derived analytically.

Thus, for small grid interval $\delta \lesssim 10^{-5}$, both the inherent sensitivity of the micro-scale system (for nonnegligible viscous diffusion $c_V \gtrsim 0.001$) and the sensitivity of eigenvalue computation of near zero repeated eigenvalues (for small drag $c_D \lesssim 10^{-6}$), are the characteristic of the micro-scale system. Hence, *for small grid interval δ the numerical eigenvalues of the full-domain micro-scale system are also inaccurate*. But this inaccuracy in the eigenvalues of the full-domain micro-scale system is not an issue for us in most cases, as we only evaluate the analytic expression (3.2.7), to compute the eigenvalues $\lambda_{m\delta}^A$ of the full-domain micro-scale system.

The following listing summarises the study of numerical sensitivity in this subsection.

1. For large patch scale ratios $r \gtrsim 0.001$ the patch scheme eigenvalue are not sensitive numerical roundoff errors (columns 2-4 in [Table 3.4.2](#)). Hence for large r the staggered the patch schemes are not sensitive to numerical roundoff errors.
2. For small patch scale ratios $r \lesssim 0.001$ the patch scheme eigenvalues are sensitive numerical roundoff errors (column 1 in [Table 3.4.2](#)). But this sensitivity to numerical roundoff errors for small grid interval $\delta \lesssim 10^{-5}$ is due to both the inherent sensitivity of the micro-scale system (for nonnegligible viscous diffusion $c_V \gtrsim 0.001$) and the sensitivity of eigenvalue computation of near zero repeated eigenvalues (for small drag $c_D \lesssim 10^{-6}$). Hence, even for small patch scale ratios, the computations of staggered the patch schemes are not sensitive numerical roundoff errors.

Except when the patch scale ratio r is too small (i.e., patches are too small compared to the inter-patch distance) and/or the underlying micro-scale model is sensitive to numerical roundoff errors, the staggered patch schemes are not sensitive to numerical roundoff errors. That is, the patch schemes are not any more sensitive to numerical roundoff errors than the underlying micro-scale system. Thus *the new five staggered patch schemes are not sensitive to numerical roundoff errors*.

3.5 Staggered patch schemes are stable

This section demonstrates the stability of the staggered patch schemes and explores the dependence of the patch scheme stability on various aspects like grid symmetry, system parameters (c_d, c_V), and grid parameters such as number of macro-grid intervals N , number of sub-patch micro-grid intervals n and patch scale ratio r .

A dynamical system $dx/dt = f(x)$, where f is the evolution function is *stable* (in the sense of Lyapunov) if the magnitude of the state vector x remains bounded while evolving in time, for trajectories starting from every point in some neighbourhood of an equilibrium state x_0 ([Chicone 2006](#), Dfn. 1.39, p. 21). It follows that a linear dynamical system $dx/dt = Ax$, where A is the system matrix, is stable if all the eigenvalues of the matrix A are non-positive ([Hairer, Wanner, and Nørsett 1993](#), Thm. 13.1, p. 81, §I.13) and A is diagonalisable [[TODO/cite](#)]. We aim to design staggered patch schemes as stable dynamical systems, when the underlying full-domain micro-scale system is stable. Hence we aim to ensure that all the patch scheme eigenvalues, both macro-scale and micro-scale eigenvalues, are

non-positive whenever the corresponding eigenvalues of the full-domain micro-scale eigenvalues non-positive.

For nonnegative dissipation coefficients c_D and c_V , the real parts of all three eigenvalues (3.2.7) in of the full-domain micro-scale system are nonpositive (§3.2.2). That is, the wave solutions either decay over time when $\Re(\lambda_m^\Delta) < 0$ or retain the same amplitude when $\Re(\lambda_m^\Delta) = 0$ as time $t \rightarrow \infty$. Hence as the solutions remain bounded as time $t \rightarrow \infty$, the staggered full-domain micro-scale system is stable. Similarly we aim to establish that the designed staggered patch schemes are stable by showing that the real parts of their eigenvalues are nonpositive. Hence, to assess the stability, we study the maximum real parts of the eigenvalues of the staggered patch schemes.

Section 3.5.1 discusses the requirements of geometric symmetry for a staggered patch scheme to be stable and the constraints the symmetry imposes on the arrangement of sub-patch nodes, number of sub-patch intervals, and the patch coupling.

Section 3.5.2 explores the trends of the maximum real parts of the Spectral patch scheme over a wide range of the coefficients of drag c_D and viscous diffusion c_V for different patch scale ratios r , for a fixed number of macro-grid intervals N and sub-patch micro-grid intervals n .

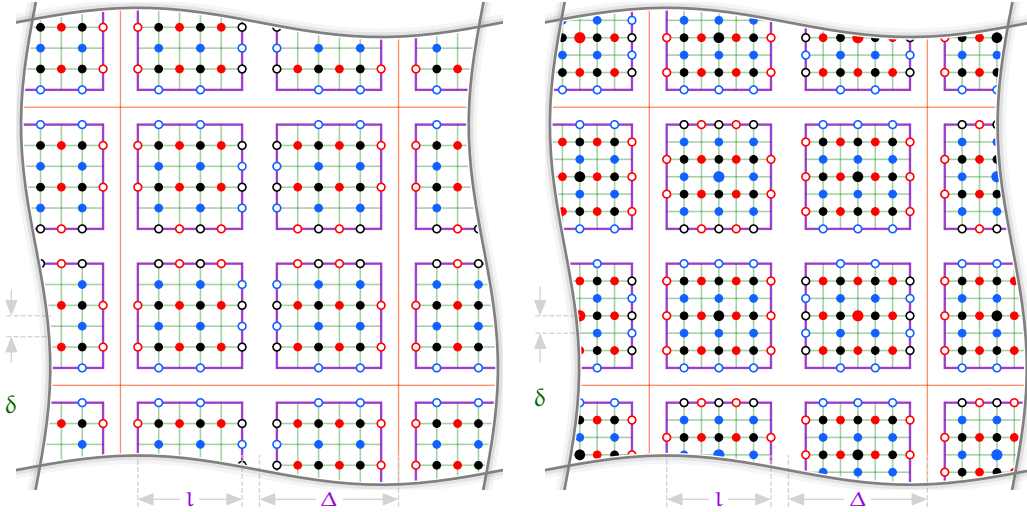
Section 3.5.3 explores the parametric dependence of the maximum real parts on the number of macro-grid intervals N , patch scale ratio r , and the sub-patch micro-grid intervals n for all the five staggered patch schemes for nine combinations of the coefficients c_D, c_V .

3.5.1 Patch scheme stability requires geometric symmetry

Section 2.2.2 discusses the compatible staggered patch grids for wave like systems. Our implementation generates all the possible 83 521 compatible staggered patch grids for the multiscale simulation of wave like systems. From explorations of about fifty grid patterns that are representative of sub-families of the grid patterns among the 83 521 compatible staggered patch grids, it appears that *no patch grid without a centre node can constitute a stable staggered patch scheme*. That is, staggered patch grids containing micro-grids other than uuvv, hhvv and uuhh (green highlighted in Fig. 2.2.3a) even in any one of the patches, lead to unstable staggered patch schemes. For example the patch grid in Fig. 3.5.1a does not contain a centre node in any of its sub-patch micro-grid. In our explorations, even when one patch in a macro-cell (orange squares in Fig. 3.5.1a) does not contain a centre node, the eigenvalues of the staggered patch schemes have large positive real

Figure 3.5.1: Two staggered patch grids with and without a centre node in each of the sub-patch micro-grids.

- (a) A compatible but *unstable* staggered patch grid using micro-grids without a centre node (uhvh, huvh, uhhv, huhv in Fig. 2.2.3a) within each macro-cell.
- (b) A *stable* staggered patch grid with three of the patches same as in Fig. 2.2.3b, and an additional h-centred patch in place of the empty patch.



parts. For patches without a centre node we compute the macro-scale patch value by averaging over the $h/u/v$ values of the nodes closest to the patch centre.

From a further systematic computational explorations, we find that the higher the symmetry in the staggered patch grid, the better the accuracy and stability of the staggered patch schemes. Thus, the dominant role of a centre node in the patch scheme stability, comes from the requirement of geometric symmetry in the patch grids for stability. Among those staggered patch grids that have a centre node in each of their patches, from the stability analysis we found only two staggered patch grids depicted in Figs. 2.2.3b and 3.5.1b over which stable patch schemes are possible.

The sub-patch micro-grids in Fig. 3.5.1a do not have reflective symmetry about x and y axes (horizontal and vertical in Fig. 3.5.1a); for example the edge nodes on left and right edges are not the same for any of the sub-patch micro-grids. Based on our eigenvalue analysis for about fifty patch grids representative of sub-families of the grid patterns, the *lack of such sub-patch micro-grid reflective symmetry leads to unstable patch schemes*.

The sub-patch micro-grids each with a centre node in Fig. 3.5.1b have reflective symmetry about x and y axes; flipping any of the patches about x or y axes does not change the sub-patch nodes. The h -, u - and v -centred

sub-patch micro-grids in Fig. 2.2.3b also have reflective symmetry about x and y axes. Stable patch schemes are possible on both the staggered patch grids in Figs. 3.5.1b and 2.2.3b. The patch grid Fig. 3.5.1b has three of the patches same as in Fig. 2.2.3b, along with an additional h-centred patch in place of the empty patch. The additional h-patch in Fig. 3.5.1b appears to provide slightly higher accuracy compared to the staggered patch grid with only three patches (Fig. 2.2.3b). But the staggered patch grid with only three patches (Fig. 2.2.3b) gives similar accuracy with roughly 25% reduction in computational cost by avoiding the one additional h-patch in Fig. 3.5.1b. From the two staggered patch grids (Figs. 3.5.1b and 2.2.3b) that constitute stable patch schemes, we find the staggered patch grid depicted in Fig. 2.2.3b to be the best in terms of computational effort and accuracy. From here on, all the discussions in this thesis are based on the staggered patch grid in Fig. 2.2.3b, with one or more layers of edge nodes (§2.2.3). The chosen staggered patch grid in Fig. 2.2.3b, in addition to having the reflective symmetry, also has the *self-similarity* among the micro- and macro-scale scales, as discussed in p. 15 of §2.2.2.

The requirement of grid symmetry for the stability of staggered patch schemes, also constrain the number of sub-patch micro-grid intervals n (the number of green grid intervals within a patch in x- and y-directions in Fig. 3.5.1b), such that $n/2$ is an odd number greater than one (i.e., $n \in \{6, 10, 14, 18, \dots\}$).

On the chosen staggered patch grid shown in Fig. 2.2.3b, the macro-scale coupling between the patches could be done in various possible ways. Similar to the geometric asymmetry in patch grids causing the patch scheme instability, asymmetry in the patch coupling also cause patch scheme instability. The five staggered patch schemes we study in this thesis are based on a global spectral interpolation based patch coupling and four local polynomial interpolation based patch coupling (each with different order of interpolation) on a square stencil. The spectral patch scheme and the polynomial patch schemes (on square stencils) couple the patches symmetrically. Hence, the five staggered patch schemes have good stability characteristics as discussed in §§3.5.2 and 3.5.3.

3.5.2 Spectral staggered patch scheme is stable for different system parameters

This subsection shows that the Spectral staggered patch scheme is stable for different system parameters, namely dissipation coefficients c_D , c_V , for a fixed number of macro-grid intervals N and sub-patch micro-grid

Table 3.5.1: [Section 3.5.2](#) studies the stability of the Spectral staggered patch scheme using the eigenvalues for all the 1764 combinations (cartesian product) of the listed parameters.

Drag coefficient	$c_D \in \{0\} \cup \{10^{-j} : j = 6, 5.8, 5.6, \dots, 2.2, 2\}$
Viscous coefficient	$c_V \in \{0\} \cup \{10^{-j} : j = 5, 4.8, 4.6, \dots, 1.2, 1\}$
Macro-grid intervals	$N = 10$
Sub-patch micro-grid intervals	$n = 6$
Patch scale ratio	$r \in \{0.0001, 0.001, 0.01, 0.1\}$

intervals n . We establish the patch scheme stability by showing that the maximum real part of the patch scheme eigenvalues are nonpositive, same as those of full-domain micro-scale system.

[Figure 3.5.2](#) plots the maximum real parts of versus (c_D, c_V) , for the following eigenvalues, for each of the 2646 combinations of the parameters listed in [Table 3.5.1](#) (each subfigure is for one patch scale ratio r).

1. Eigenvalues λ_p^N of the Spectral patch scheme on a staggered patch grid with 10×10 macro-grid intervals ($N = 10$) and each patch containing 6×6 sub-patch micro-grid intervals ($n = 6$).
2. Eigenvalues $\lambda_{m\delta}^A$ of full-domain micro-scale system with same value of micro-scale grid interval $\delta_{m\delta}$ as the sub-patch micro-grid interval δ . That is, $\delta_{m\delta} \equiv L/n_{m\delta} = \delta \equiv l/n \equiv 2Lr/(Nn)$ as $r = l/(2\Delta)$ and $\Delta = L/N$, where $n_{m\delta}$ is the number of full-domain micro-scale grid intervals and n is the number of sub-patch micro-grid intervals. When the context is clear we drop the subscript $m\delta$ in $n_{m\delta}$ and $\delta_{m\delta}$ for the fine-grid full-domain micro-scale system.

[TODO/comment] about the similar plots for smaller $r = 0.0001, 0.001, 0.01$.

[Figures 3.5.2b](#) and [3.5.2a](#) show that, for moderate values of the patch scale ratios $r \in \{0.1, 0.01\}$, the Spectral patch scheme eigenvalues have the maximum real part $\max \Re \lambda_p^N \lesssim 10^{-11}$. The $\max \Re(\lambda)$ is increasing for increasing viscous diffusion c_V for all values of drag c_D in [Figs. 3.5.2b](#) and [3.5.2a](#). The detailed discussion in [p. 96](#) of [§3.4](#), shows that for small grid-interval δ the computations in the micro-scale system are inherently sensitive to numerical roundoff errors for large c_V , leading to inaccurate micro- and macro-scale eigenvalues. Hence, the increase in $\max \Re(\lambda)$ for increasing c_V in [Figs. 3.5.2b](#) and [3.5.2a](#), is due to the inaccurate eigenvalue computation caused by the inherent sensitivity of the micro-scale system to

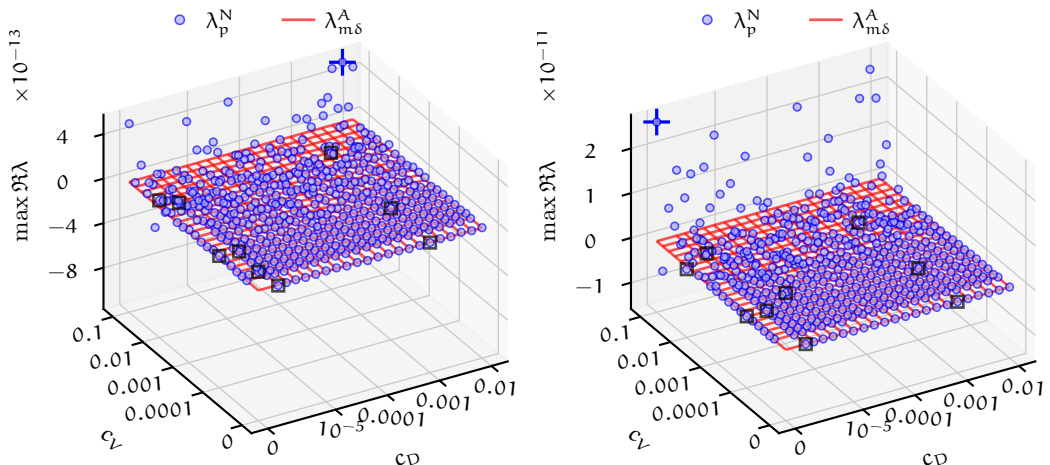
numerical roundoff errors. But such increase in $\max \Re(\lambda)$ for increasing c_V is not severe Figs. 3.5.2b and 3.5.2a because of the moderately large patch scale ratios $r \in \{0.1, 0.01\}$. Thus, Figs. 3.5.2b and 3.5.2a show that, for moderate patch scale ratios $r \gtrsim 0.01$, the maximum real parts of the Spectral patch scheme eigenvalues $\max \Re \lambda_p^N \lesssim 10^{-11}$. That is, *for moderate patch scale ratios $r \gtrsim 0.01$, the Spectral patch scheme is stable for many combinations of the coefficients of drag c_D and viscous diffusion c_V* as listed in Table 3.5.1.

In this paragraph, we argue that the nonnegligible positive maximum real parts (e.g., $\max \Re \lambda_p^N \sim 10^{-5}$ in Fig. 3.5.2d) are not due the Spectral patch scheme instability. Figure 3.5.2d with nonnegligible positive maximum real parts correspond to small patch scale ratio $r = 0.0001$. When the patch scale ratio is small $r \sim 0.0001$ the sub-patch micro-grid interval $\delta = 2Lr/(Nn) \approx 0.0002Lr/(Nn)$. For example, for the domain size $L = 2\pi$, a patch grid with $N = 10$ macro-grid intervals, and $n = 6$ sub-patch micro-grid intervals, has $\delta \approx 0.0004\pi/60 \approx 2 \cdot 10^{-5}$. Figures 3.5.2d and 3.5.2c also show that the peak values of the maximum real parts (blue plusses) correspond to small c_D and large c_V . The discussion in p. 97 of §3.4, shows that, for small grid interval $\delta \lesssim 10^{-5}$, the combination of inherent sensitivity of the micro-scale system (for nonnegligible viscous diffusion $c_V \gtrsim 0.0001$) and the sensitivity of eigenvalue computation of near zero repeated eigenvalues (for small $c_D \lesssim 10^{-6}$), leads to inaccurate near zero macro-scale eigenvalues. For example, Fig. 3.4.3 shows how the numerical roundoff errors in computing near zero eigenvalues falsely give positive real parts. Thus the *large maximum real parts in Figs. 3.5.2d and 3.5.2c are not a reflection of the patch scheme instability*.

As discussed in §3.4, for small grid intervals, the numerical eigenvalues of the full-domain micro-scale system are also sensitive to numerical round-off errors. Hence, for the full-domain micro-scale system with the same small grid interval δ same as the sub-patch grid interval, we expect that the numerical eigenvalues $\lambda_{m\delta}^N$ will also have such nonzero maximum real parts. The computation of the numerical eigenvalues $\lambda_{m\delta}^N$ of the full-size numerical Jacobian (§3.2.4) for a full-domain micro-scale system requires huge computer memory. For example, on a $2\pi \times 2\pi$ domain, a patch grid, with 6×6 macro-grid intervals ($N = 6$) and each patch containing 6×6 sub-patch micro-grid intervals ($n = 6$) and patch scale ratio $r = 0.1$, has the sub-patch micro-grid interval $\delta = 2Lr/(Nn) = 2\pi/180$. The corresponding full-domain micro-scale system with the same grid interval has 180×180 grid intervals (like the 6×6 staggred grid in Fig. 2.2.1), leading to the 24300×24300 full-size numerical Jacobian (e.g., Fig. 3.2.1). For large N and small patch scale ratio r , the corresponding full-domain micro-scale system has a very large $(3/16)(Nn/r)^2 \times (3/16)(Nn/r)^2$ full-size numerical Jacobian.

Figure 3.5.2: Maximum real parts of the eigenvalues for different coefficients of drag c_D and viscous diffusion c_V . The eigenvalues λ_p^N (blue circles) are for the Spectral patch scheme with $N = 10, n = 6$ for patch scale ratios $r \in \{0.0001, 0.001, 0.01, 0.1\}$ in each subfigure. The eigenvalues $\lambda_{m\delta}^A$ (red mesh, *all zeros*) are for the corresponding full-domain micro-scale system. Blue plusses mark the peak value for each subfigure. Black squares show the chosen nine combinations of $c_D \in \{0, 10^{-6}, 0.0001\}$, $c_V \in \{0, 10^{-4}, 0.001\}$ for studying stability for different grid parameters in §3.5.3.

- (a) For $r = 0.1$, the peak value of $\max \Re \lambda_p^N \approx 5 \cdot 10^{-13}$ at $c_D \approx 0.0063$, $c_V = 0.1$.
- (b) For $r = 0.01$, the peak value of $\max \Re \lambda_p^N \approx 2 \cdot 10^{-11}$ at $c_D = 0, c_V = 0.1$.



- (c) For $r = 0.001$, the peak value of $\max \Re \lambda_p^N \approx 10^{-8}$ at $c_D = 0, c_V = 0.1$.
- (d) For $r = 0.0001$, the peak value of $\max \Re \lambda_p^N \approx 5 \cdot 10^{-5}$ (marked by blue plus) at $c_D \approx 4 \cdot 10^{-6}, c_V = 0.1$.

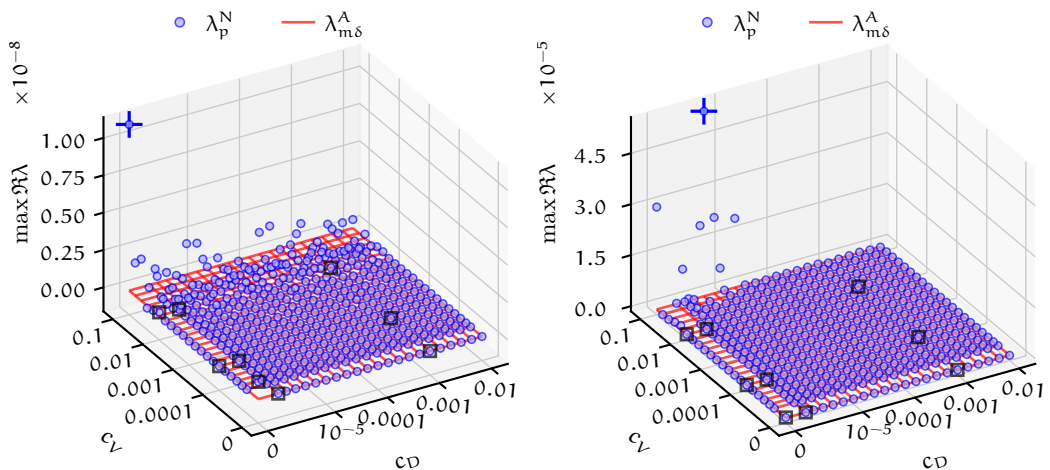


Table 3.5.2: [Section 3.5.3](#) studies the stability of the staggered patch schemes using the eigenvalues for all the 4 374 combinations (cartesian product) of the listed parameters.

Patch schemes	Spectral, Square-p2, Square-p4, Square-p6, and Square-p8
Drag coefficient	$c_D \in \{0, 10^{-6}, 0.001\}$
Viscous coefficient	$c_V \in \{0, 10^{-4}, 0.01\}$
Macro-grid intervals	$N \in \{6, 10, 14\}$ for Spectral scheme, $N \in \{6, 10, 14, 18, 22, 26\}$ for polynomial schemes.
Sub-patch micro-grid intervals	$n \in \{6, 10\}$
Patch scale ratio	$r \in \{0.0001, 0.001, 0.01, 0.1\}$

So we do compute numerical eigenvalues $\lambda_{m,\delta}^N$ corresponding to the same sub-patch micro-grid interval δ for the cases of large N and small r . We only evaluate the analytic expression [\(3.2.7\)](#) to compute the eigenvalues $\lambda_{m,\delta}^A$ of the full-domain micro-scale system. As the analytic eigenvalues [\(3.2.7\)](#) are not sensitive to numerical roundoff errors, they do not have this nonzero maximum real parts (the red mesh in [Fig. 3.5.2](#)).

The nonnegligible positive maximum real parts in [Figs. 3.5.2d](#) and [3.5.2c](#) appear nearly random without any trend with the c_D, c_V . There are also maximum real parts as small as 10^{-10} around the regions of c_D, c_V of the peak value of $\max \Re(\lambda)$ (blue plusses), which suggests that when the numerical roundoff errors are small, the maximum real parts of the Spectral patch scheme are as small as 10^{-10} . Hence we take that the eigenvalues of the Spectral patch scheme has small maximum positive real parts $\sim 10^{-10}$, also for the combination of large viscous diffusion, small drag, and small patch scale ratio. Thus, *the Spectral patch scheme is stable for a wide range of system parameters (c_D, c_V) and for different patch scale ratios*, that is for all the combinations, of the parameters in [Table 3.5.1](#).

3.5.3 The five staggered patch schemes are stable for different grid parameters

[Section 3.5.2](#) showed that the Spectral patch scheme is stable for a wide range of system parameters and the patch scale ratio for a staggered patch grid with $N = 10$ macro-grid intervals, and $n = 6$ sub-patch micro-grid intervals. This subsection characterise the stability of all *the five staggered patch*

Table 3.5.3: Overall maximum real parts of the micro- and macro-scale eigenvalues ($\lambda_{p\mu}^N, \lambda_{pM}^N$) over the five patch schemes and all the combinations of c_D, c_V and N in [Table 3.5.2](#), for different number of sub-patch intervals n and patch scale ratios r . Red colour highlights the largest value in each column separately for micro- and macro-scale eigenvalues (based on full precision when the values are same with one significant figure).

		Patch scale ratio r			
		0.0001	0.001	0.01	0.1
Overall max $\Re \lambda_{p\mu}^N$	$n = 6$	$2 \cdot 10^{-6}$	$2 \cdot 10^{-8}$	$2 \cdot 10^{-10}$	$2 \cdot 10^{-12}$
	$n = 10$	$5 \cdot 10^{-6}$	$7 \cdot 10^{-8}$	$6 \cdot 10^{-10}$	$7 \cdot 10^{-12}$
Overall max $\Re \lambda_{pM}^N$	$n = 6$	$7 \cdot 10^{-6}$	$8 \cdot 10^{-9}$	$3 \cdot 10^{-11}$	$5 \cdot 10^{-13}$
	$n = 10$	$3 \cdot 10^{-5}$	$2 \cdot 10^{-8}$	$2 \cdot 10^{-10}$	$2 \cdot 10^{-12}$

schemes (Spectral, Square-p2, Square-p4, Square-p6, and Square-p8), for different number of macro-grid intervals N and sub-patch micro-grid intervals n .

We find the patch schemes on many asymmetric patch grids to be unstable ([§3.5.1](#)), with large maximum positive real parts in the order of tens and hundreds. In some cases, such instabilities come from the eigenvalues of the macro-scale modes, in some other cases the instabilities come from the eigenvalues of the micro-scale modes. So, we study the maximum real parts of the numerical eigenvalues of the five staggered patch schemes, separately for the micro- and macro-scale modes ($\max \Re \lambda_{p\mu}^N$ and $\max \Re \lambda_{pM}^N$), for the 4374 combinations of the parameters listed in [Table 3.5.2](#). For the stability study in this subsection, we choose the nine combinations of $c_D \in \{0, 10^{-6}, 0.0001\}$, $c_V \in \{0, 10^{-4}, 0.001\}$ in [Table 3.5.2](#), to be a reasonable representative of the wide range of c_D and c_V from [§3.5.2](#) for the Spectral patch scheme (black squares in [Fig. 3.5.2](#)).

[Table 3.5.3](#) presents the peak maximum real parts of the patch scheme eigenvalues over all the combinations of c_D, c_V and N in [Table 3.5.2](#), for different number of sub-patch intervals n and patch scale ratios r . [Table 3.5.3](#) shows that, for moderate values of the patch scale ratios $r \in \{0.1, 0.01\}$, both the micro- and macro-scale eigenvalues of all the five patch schemes have the maximum real parts less than about $6 \cdot 10^{-10}$. Thus, *for moderate patch scale ratios $r \gtrsim 0.01$, all the five patch schemes are stable* for all the combinations of the drag c_D , viscous diffusion c_V , the number of macro-grid intervals N and the number of sub-patch micro-grid intervals n listed in [Table 3.5.2](#).

For small patch scale ratios $r \in \{0.01, 0.0001\}$, some of the patch schemes

Table 3.5.4: Overall maximum real parts of the micro-scale eigenvalues $\lambda_{p\mu}^N$ over the five patch schemes and all the combinations of N and n in [Table 3.5.2](#), for different patch scale ratios r . Red colour highlights the largest value in each column (based on full precision when the values are same with one significant figure).

	Patch scale ratio r			
	0.0001	0.001	0.01	0.1
$c_D = 0, c_V = 0$	$5 \cdot 10^{-6}$	$7 \cdot 10^{-8}$	$6 \cdot 10^{-10}$	$7 \cdot 10^{-12}$
$c_D = 0, c_V = 0.0001$	-3000	-200	-2	-0.02
$c_D = 0, c_V = 0.01$	-3	-3	-3	-2
$c_D = 10^{-6}, c_V = 0$	$4 \cdot 10^{-6}$	$-4 \cdot 10^{-7}$	$-5 \cdot 10^{-7}$	$-5 \cdot 10^{-7}$
$c_D = 10^{-6}, c_V = 0.0001$	-3000	-200	-2	-0.02
$c_D = 10^{-6}, c_V = 0.01$	-3	-3	-3	-2
$c_D = 0.001, c_V = 0$	-0.0005	-0.0005	-0.0005	-0.0005
$c_D = 0.001, c_V = 0.0001$	-3000	-200	-2	-0.02
$c_D = 0.001, c_V = 0.01$	-3	-3	-3	-2

have large maximum real parts of the order of 10^{-5} for some combination of the system parameters (c_D, c_V) and grid parameters N, n , which is investigated in following paragraphs in this subsection.

[Figure 3.5.3](#) plots the maximum real parts of the micro- and macro-scale eigenvalues ($\max \Re \lambda_{p\mu}^N$ and $\max \Re \lambda_{pM}^N$) for the combinations of the parameters in [Table 3.5.2](#), with $c_D = 0$. A similar figure for $c_D = 10^{-6}$ is visually very similar to [Fig. 3.5.3](#), hence we omit including it here. [Figure 3.5.4](#) plots the $\max \Re \lambda_{p\mu}^N$ and $\max \Re \lambda_{pM}^N$ for the combinations of the parameters in [Table 3.5.2](#), with $c_D = 0.001$. [Tables 3.5.4](#) and [3.5.5](#) separately present the overall maximum real parts of the micro- and macro-scale eigenvalues over the five patch schemes and all the combinations of N and n in [Table 3.5.2](#), for different patch scale ratios r .

Subfigures on the left of [Figs. 3.5.3](#) and [3.5.4](#) and [Table 3.5.4](#) show that only for the case of $c_D = c_V = 0$ (ideal wave), the maximum real part of the micro-scale eigenvalues are positive (all red highlighted values in [Table 3.5.4](#)). These maximum positive real parts increase with increasing number of macro-grid intervals N and/or decreasing patch scale ratio r (i.e., decreasing sub-patch micro-grid interval δ). As in [Fig. 3.2.5](#), the eigenvalue spectrum for ideal wave has a total of $N^2(3n^2/16 - n/2 + 1/2) + 2$ zero eigenvalues. For $N = 6, 10, 14, 18, 22, 26$ with $n = 6$, the number of

Figure 3.5.3: The maximum real part of the micro- and macro-scale eigenvalues ($\max \Re \lambda_{p\mu}^N$ on left, $\max \Re \lambda_{pM}^N$ on right) for the coefficients $c_D = 0$ and $c_V = 0, 0.0001, 0.01$ (each row). Markers indicate different patch schemes (Spectral, Square-p2, Square-p4, Square-p6, and Square-p8). Colours indicate the different number of sub-patch intervals n .

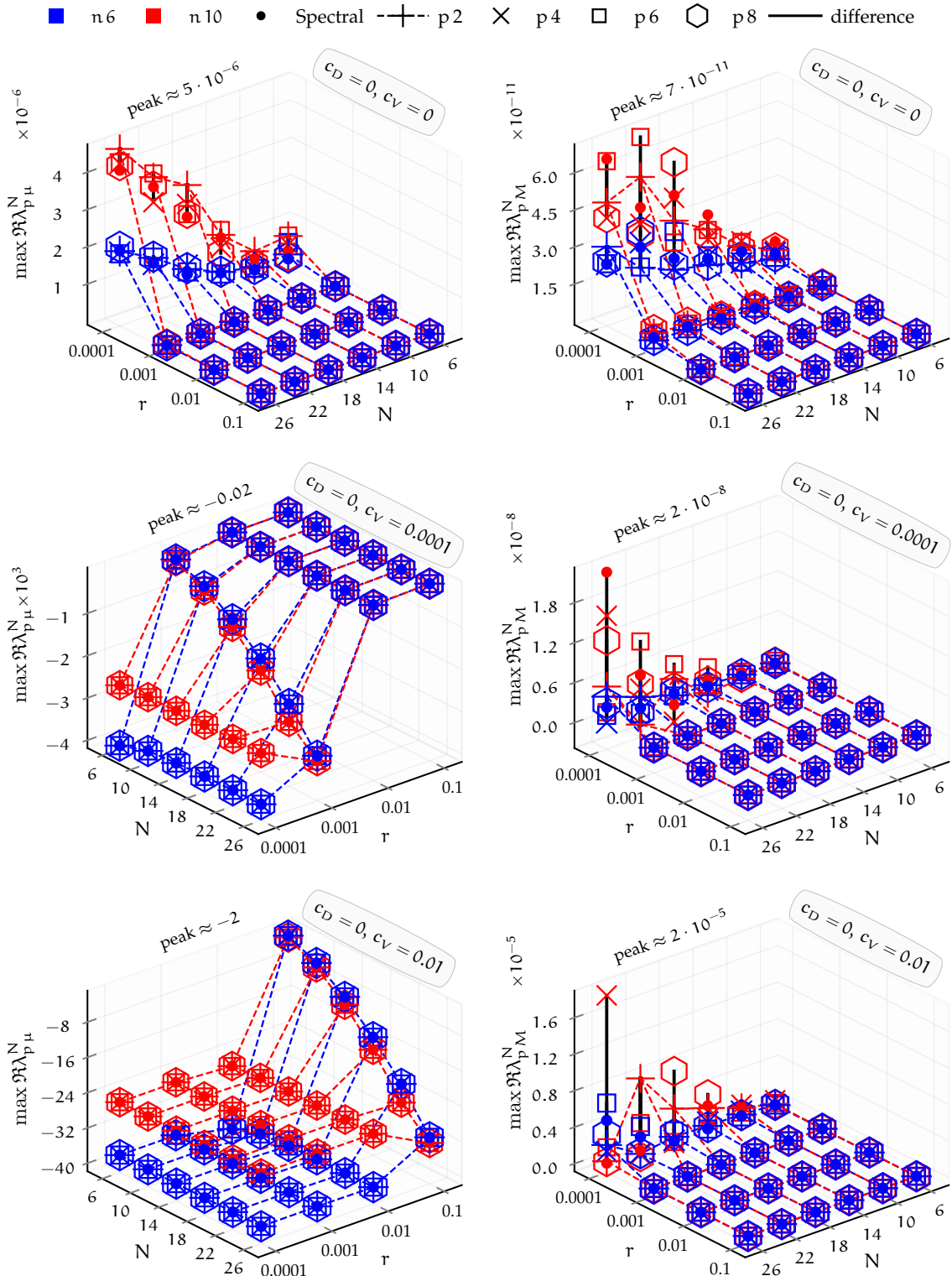
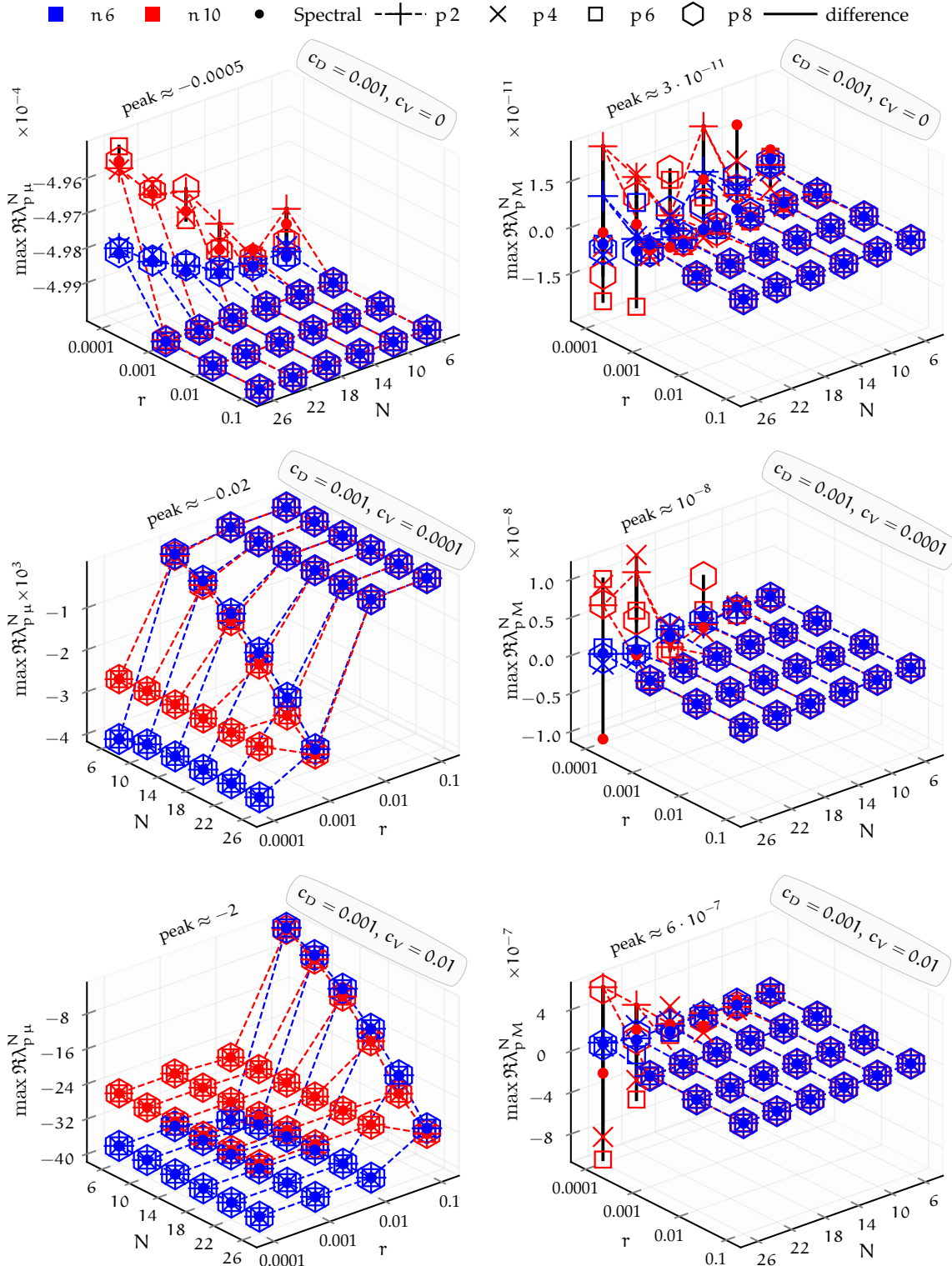


Figure 3.5.4: The maximum real part of the micro- and macro-scale eigenvalues ($\max \Re \lambda_{p\mu}^N$ on left, $\max \Re \lambda_{pM}^N$ on right) for the coefficients $c_D = 0.001$ and $c_V = 0, 0.0001, 0.01$ (each row). Markers indicate different patch schemes (Spectral, Square-p2, Square-p4, Square-p6, and Square-p8). Colours indicate the different number of sub-patch intervals n .



zero eigenvalues are 155, 427, 835, 1379, 2059, 2875 respectively. The detailed discussions in p. 97 of §3.4, shows that, for small grid interval $\delta \lesssim 10^{-5}$, the sensitivity of eigenvalue computation for near zero repeated eigenvalues (for small $c_D \lesssim 10^{-6}$), leads to inaccurate eigenvalues. Hence, for ideal waves, the computation of very many repeated zero eigenvalues of the patch schemes, for small patch scale ratio is inaccurate leading to large maximum real parts. So, we take that, the large maximum real parts of $5 \cdot 10^{-6}, 4 \cdot 10^{-6}$ and $7 \cdot 10^{-8}$ in Table 3.5.4, are due to the inaccurate eigenvalue computation of near zero repeated eigenvalues for small drag $c_D \lesssim 10^{-6}$ and zero viscous diffusion. Thus, *the micro-scale modes of the five staggered patch schemes are stable* for all the combinations of the drag c_D , viscous diffusion c_V , number of macro-grid intervals N , number of sub-patch micro-grid intervals n and the patch scale ratios r listed in Table 3.5.2.

Following are the key additional points from the subfigures on the left of Figs. 3.5.3 and 3.5.4 and Table 3.5.4 for the micro-scale eigenvalues.

- Maximum positive real parts of the micro-scale eigenvalues $\lambda_{p\mu}^N$ of all five patch schemes are approximately the same (all within the same order of magnitude). For $c_D = c_V = 0$, the maximum of, the standard deviation of the maximum positive real parts of $\lambda_{p\mu}^N$ over the five patch schemes, for $n = 6, 10$ are $2 \cdot 10^{-7}, 3 \cdot 10^{-7}$ respectively (both correspond to $r = 0.0001$). As discussed in §3.4 these discrepancies are due to inaccurate eigenvalue computation due to numerical roundoff errors.
- For the same c_D , increasing the viscous diffusion c_V pushes real parts of the micro-scale eigenvalues to larger negative values, increasing the spectral gap. The increasingly large negative values of $\max \Re \lambda_{p\mu}^N$ with increasing c_V is also evident in the eigenvalue spectrum. For example the micro-scale eigenvalues in the clusters 4, 5 in the spectrum of Fig. 3.2.4 for $c_D = 10^{-6}, c_V = 0$ move to the left and become the clusters 6, 7 in Fig. 3.2.2 for $c_D = 10^{-6}, c_V = 0.0001$.
- Decreasing the patch scale ratio also leads to large negative values of $\max \Re \lambda_{p\mu}^N$, leading to large spectral gap.

Subfigures on the right of Figs. 3.5.3 and 3.5.4 and Table 3.5.5 show that the maximum positive real parts of the macro-scale eigenvalues are large, $\max \Re \lambda_{p\mu}^N \gtrsim 10^{-8}$, only for the combinations of $c_V \gtrsim 0.0001$, the small patch scale ratio $r \lesssim 0.001$ and large number of macro-scale intervals N (i.e., for small sub-patch micro-grid interval δ). For the same c_D , increasing the viscous diffusion c_V increases the maximum positive real parts of the

Table 3.5.5: Overall maximum real parts of the macro-scale eigenvalues λ_{pM}^N over the five patch schemes and all the combinations of N and n in Table 3.5.2, for different patch scale ratios r . Red colour highlights the largest value in each column (based on full precision when the values are same with one significant figure).

	Patch scale ratio r			
	0.0001	0.001	0.01	0.1
$c_D = 0, c_V = 0$	$7 \cdot 10^{-11}$	$7 \cdot 10^{-12}$	$7 \cdot 10^{-13}$	$7 \cdot 10^{-14}$
$c_D = 0, c_V = 0.0001$	$2 \cdot 10^{-8}$	$2 \cdot 10^{-10}$	$3 \cdot 10^{-12}$	$3 \cdot 10^{-13}$
$c_D = 0, c_V = 0.01$	$2 \cdot 10^{-5}$	$2 \cdot 10^{-8}$	10^{-10}	$2 \cdot 10^{-12}$
$c_D = 10^{-6}, c_V = 0$	$3 \cdot 10^{-11}$	$2 \cdot 10^{-12}$	10^{-13}	$4 \cdot 10^{-14}$
$c_D = 10^{-6}, c_V = 0.0001$	10^{-8}	$2 \cdot 10^{-10}$	$2 \cdot 10^{-12}$	$4 \cdot 10^{-13}$
$c_D = 10^{-6}, c_V = 0.01$	$3 \cdot 10^{-5}$	$4 \cdot 10^{-9}$	$6 \cdot 10^{-11}$	$2 \cdot 10^{-12}$
$c_D = 0.001, c_V = 0$	$3 \cdot 10^{-11}$	$2 \cdot 10^{-12}$	$3 \cdot 10^{-13}$	$4 \cdot 10^{-14}$
$c_D = 0.001, c_V = 0.0001$	10^{-8}	10^{-10}	$2 \cdot 10^{-12}$	$7 \cdot 10^{-13}$
$c_D = 0.001, c_V = 0.01$	$6 \cdot 10^{-7}$	$6 \cdot 10^{-9}$	$2 \cdot 10^{-10}$	10^{-12}

macro-scale eigenvalues. The discussion in p. 97 of §3.4, shows that, for small grid interval $\delta \lesssim 10^{-5}$, the combination of inherent sensitivity of the micro-scale system (for nonnegligible viscous diffusion $c_V \gtrsim 0.0001$) and the sensitivity of eigenvalue computation of near zero repeated eigenvalues (for small $c_D \lesssim 10^{-6}$), leads to inaccurate near zero macro-scale eigenvalues. For example, Fig. 3.4.3 shows how the numerical roundoff errors in computing near zero eigenvalues falsely give positive real parts. So, we take that, the large maximum real parts of $5 \cdot 10^{-6}$, $4 \cdot 10^{-6}$ and $7 \cdot 10^{-8}$ in Table 3.5.5 for small patch scale ratios $r \in \{0.0001, 0.001\}$, are due to the inaccurate eigenvalue computation due to the inherent sensitivity of the micro-scale system (for nonnegligible viscous diffusion $c_V \gtrsim 0.0001$) and the sensitivity of eigenvalue computation of near zero repeated eigenvalues (for small $c_D \lesssim 10^{-6}$). Thus, *the macro-scale modes of the five staggered patch schemes are stable* for all the combinations of the drag c_D , viscous diffusion c_V , number of macro-grid intervals N , number of sub-patch macro-grid intervals n and the patch scale ratios r listed in Table 3.5.2.

Following are the key additional points from the subfigures on the right of Figs. 3.5.3 and 3.5.4 and Table 3.5.5 for the micro-scale eigenvalues.

- Maximum positive real parts of the macro-scale eigenvalues λ_{pM}^N of all five patch schemes are approximately the same (all within the same

order of magnitude). For all the nine combinations of the c_D , c_V , the maximum of, the standard deviation of the maximum positive real parts of $\lambda_{p\mu}^N$ over the five patch schemes, for $n = 6, 10$ are $10^{-6}, 7 \cdot 10^{-6}$ respectively (both correspond to $N = 26, r = 0.0001$). As discussed in §3.4 these discrepancies are due to inaccurate eigenvalue computation due to numerical roundoff errors.

- For the same c_D , increasing the viscous diffusion c_V leads to large maximum real parts of the macro-scale eigenvalues. Decreasing the patch scale ratio also leads to increasing maximum real parts. As discussed in p. 96 of §3.4 these increasing maximum real parts are due to inherent sensitivity of the micro-scale system to numerical roundoff errors, for nonnegligible viscous diffusion $c_V \gtrsim 0.0001$ and for small grid-interval δ .

The previous paragraphs established the stability of the five staggered patch schemes separately for the micro-scale and macro-scale eigenvalues. The previous detailed arguments show that the observed maximum real parts of the eigenvalues are due to the inaccurate eigenvalue computations; that is, due to either the inherent sensitivity of the micro-scale system, or the sensitivity of eigenvalue computation for near zero repeated eigenvalues, or both. Despite doing different amount of patch coupling computations, all the patch schemes agree within the same order of magnitude. This agreement among the patch schemes also shows that the maximum positive real parts do not reflect any patch scheme instability due to numerical roundoff errors. The insensitivity of the patch schemes to numerical roundoff errors is also shown separately in §3.4. In addition, the patch schemes are stable in our time simulations even for large number macro-grid intervals N and small patch scale ratios r (TODO:xref to the time simulation) Thus, *all the five staggered patch schemes are stable*.

3.6 Staggered patch schemes are consistent

This section shows that the staggered patch schemes are consistent with the given micro-scale system (within the patches). Subsections of this section establish the consistency of the patch schemes by comparing the macro-scale eigenvalues of the patch scheme with the corresponding eigenvalues of the full-domain micro-scale system for increasingly finer patch grids. Section 3.6.1 shows that the Spectral patch scheme is uniformly consistent without any strong dependence on the macro-grid interval Δ . Section 3.6.2

shows that the polynomial patch schemes are consistent to the order of the polynomial interpolation with decreasing macro-grid interval Δ .

The full-domain micro-scale system (3.1.2) is consistent, when the discretized equations (3.1.2) approach to the corresponding PDEs (3.1.1), as the grid interval $\delta \rightarrow 0$ (on the full-domain grid Fig. 2.2.1). Such standard definition of consistency (e.g., Ferziger, Peric, and Street 2020, p. 34) is useful for analysing the full-domain discrete systems whose goal is to accurately represent the corresponding PDEs. But the goal of our multiscale staggered patch scheme (3.1.4) is to accurately represent the *macro-scale* waves of the corresponding *discrete* full-domain micro-scale system (§3.2.2). Hence we define a staggered patch scheme to be consistent, when the macro-scale characteristics of the patch scheme equations (e.g., (3.1.4)) approach to the corresponding macro-scale characteristics of the full-domain micro-scale system (e.g., (3.1.2)), when the macro-grid interval $\Delta \rightarrow 0$ (on the patch grid grid Fig. 2.2.3b).

We show the consistency of the staggered patch schemes by demonstrating that the macro-scale eigenvalues $\underline{\lambda}_{pM}^N$ of the patch schemes *converge* to the macro-scale eigenvalues of the corresponding full-domain micro-scale system as $\Delta \rightarrow 0$. The eigenvalue spectra in Figs. 3.2.2 to 3.2.7, show that the staggered patch scheme macro-scale eigenvalues $\underline{\lambda}_{pM}^{NE1}$ (e.g., clusters 1, 2, 3, 4, 5 in Fig. 3.2.9) are qualitatively similar, and visually close, to the corresponding macro-scale eigenvalues $\underline{\lambda}_{m\delta}^A$ of the fine-grid full-domain micro-scale system (by varying degrees depending upon the specific staggered patch scheme, N , n , and r). To numerically quantify the discrepancy between the macro-scale eigenvalues $\underline{\lambda}_{pM}^N$ of staggered patch scheme and the corresponding macro-scale eigenvalues $\underline{\lambda}_{m\delta}^A$ of fine grid full domain micro-scale system, we define the *eigenvalue error* for the *macro-scale* wavenumber (k_x, k_y) as

$$\epsilon^{k_x, k_y} = \|\underline{\lambda}_{pM}^N(k_x, k_y) - \underline{\lambda}_{m\delta}^A(k_x, k_y)\| / \|\underline{\lambda}_{m\delta}^A(k_x, k_y)\|, \quad (3.6.1)$$

where $\|\cdot\|$ is the Euclidean norm of the three element complex vectors of eigenvalues $\underline{\lambda}_{pM}^N$ and $\underline{\lambda}_{m\delta}^A$ (three macro-scale eigenvalues for each macro-scale wavenumber).

To assess the patch scheme consistency in this section (i.e., eigenvalue convergence), we compute the three eigenvalue errors $\epsilon^{1,0}$, $\epsilon^{1,1}$ and $\epsilon^{2,1}$, for the patch schemes on different staggered patch grids, corresponding to the three macro-scale (angular) wavenumbers $(k_x, k_y) \in \{(1, 0), (1, 1), (2, 1)\}$ over the $2\pi \times 2\pi$ domain. The smallest wavenumber $(1, 0)$ corresponds to the largest wavelength ($2\pi/L, 0$) for an $L \times L$ domain. Specifically, to show the consistency of the staggered patch schemes, this section computes the three

Table 3.6.1: [Section 3.6](#) studies the consistency of the patch schemes using eigenvalues for all the 2160 combinations (cartesian product) of the listed parameters.

Patch schemes	Spectral, Square-p2, Square-p4, Square-p6, and Square-p8
Drag coefficient	$c_D \in \{0, 10^{-6}, 0.001\}$
Viscous coefficient	$c_V \in \{0, 10^{-4}, 0.01\}$
Macro-grid intervals	$N \in \{6, 10, 14, 18, 22, 26\}$
Sub-patch micro-grid intervals	$n \in \{6, 10\}$
Patch scale ratio	$r \in \{0.0001, 0.001, 0.01, 0.1\}$

macro-scale eigenvalue errors $\epsilon^{1,0}$, $\epsilon^{1,1}$ and $\epsilon^{2,1}$ for the 2160 combinations of the parameters listed in [Table 3.6.1](#).

Computing the three element vector of eigenvalues $\underline{\lambda}_{m\delta}^A(k_x, k_y)$ in the eigenvalue error [\(3.6.1\)](#), is straightforward, we evaluate the analytic expression [\(3.2.7\)](#) to get three eigenvalues for each macro-scale wavenumber $(k_x, k_y) \in \{(1, 0), (1, 1), (2, 1)\}$. Among the numerical eigenvalues λ_p^N , finding which three eigenvalues correspond to the three eigenvalues in $\underline{\lambda}_{m\delta}^A(k_x, k_y)$ (for the same macro-scale wavenumber), is not straightforward. A method we name as the *method of wavenumber-wise scale separation* in [§3.3](#), perform wavenumber-wise classification and separation of micro- and macro-scale patch scheme eigenvalues. The method of wavenumber-wise scale separation in [§3.3](#) gives the required eigenvalues as the following 3D arrays (analytic eigenvalues only for $N \leq 14$ for Spectral patch scheme)

1. An $N/2 \times N/2 \times 3$ array of *analytic* eigenvalues $\lambda_{m\delta}^A$ of the full-domain micro-scale system.
2. An $N/2 \times N/2 \times 3$ array of macro-scale *analytic* patch scheme eigenvalues λ_{pM}^{NE1} .
3. An $N/2 \times N/2 \times 3$ array of macro-scale *numerical* patch scheme eigenvalues λ_{pM}^N .

The third dimension of the arrays in the preceding listing with establish the wavenumber-wise correspondence among the three eigenvalues $\lambda_{m\delta}^A$, λ_{pM}^{NE1} and λ_{pM}^N . For any macro-scale wavenumber (k_x, k_y) resolved on a patch grid, each of the three elements along the third dimension of the eigenvalues $\lambda_{m\delta}^A$ and λ_{pM}^N gives required the three element vectors $\underline{\lambda}_{m\delta}^A$ and $\underline{\lambda}_{pM}^N$ in the patch scheme eigenvalue error [\(3.6.1\)](#).

A staggered patch grid with $N \times N$ macro-gid intervals, irrespective of which patch scheme, resolves $3N^2/4$ macro-scale modes (p. 68 of §3.2.6). That is, with increasing macro-grid intervals N , all the patch schemes resolve increasing number of macro-scale modes of increasing wavenumbers. A patch grid with $N = 6$ macro-grid intervals resolves nine macro-scale wavenumbers such that $k_x, k_y \in \{-1, 0, 1\}$. For $N = 6$, since there are no macro-scale eigenvalues with wavenumber $(k_x, k_y) = (2, 1)$, the eigenvalue error $\epsilon^{2,1}$ is computed only for $N > 6$.

3.6.1 Spectral patch scheme is uniformly consistent without any dependence on the macro-grid interval

With the highly accurate global spectral interpolation (§2.3.1), we expect the Spectral patch scheme to resolve the macro-scale modes exactly (within numerical roundoff errors), irrespective of the number of macro-grid intervals N (e.g., the spectrum in Figs. 3.2.6 and 3.2.7). That is, the Spectral patch scheme is uniformly consistent without any dependence on the macro-grid interval Δ . To confirm this uniform consistency of the Spectral patch scheme for the general linear wave, this subsection shows that the accuracy of the macro-scale modes indeed do not deteriorate with decreasing macro-grid interval Δ (increasing N). Specifically, this subsection studies the eigenvalue errors $\epsilon^{1,0}$, $\epsilon^{1,1}$ and $\epsilon^{2,1}$ of the Spectral patch scheme for all the 432 combinations of the parameters c_D , c_V , N , n , r listed in Table 3.6.1.

Tables 3.6.2 to 3.6.4 present the maximum logarithmic eigenvalue errors $\min_N \log_{10}(\epsilon^{1,0})$, $\min_N \log_{10}(\epsilon^{1,1})$ and $\min_N \log_{10}(\epsilon^{2,1})$ respectively, over six different number of macro-grid intervals N in Table 3.6.1. For the cases of the largest eigenvalue error in each table, Figures 3.6.1 to 3.6.3 plot the variation of the eigenvalue errors $\epsilon^{1,0}$, $\epsilon^{1,1}$ and $\epsilon^{2,1}$ respectively, with the number of macro-grid intervals N . Tables 3.6.2 to 3.6.4 show that, except the red highlighted values for the combination of the small patch scale ratio $r \sim 0.0001$, and large viscous diffusion $c_V = 0.01$, all the three eigenvalue errors are about 10^{-8} or smaller. Figures 3.6.1 to 3.6.3 show that the eigenvalue errors of about 10^{-8} corresponding to the small patch scale ratios $r \lesssim 0.01$ increase with increasing number of macro-grid intervals N . Thus, Tables 3.6.2 to 3.6.4 and Figures 3.6.1 to 3.6.3 show that the eigenvalues errors of the Spectral patch scheme are small (about 10^{-8} or smaller), except for the combination of the small patch scale ratio r , large number of macro-grid intervals N and large viscous diffusion c_V . Both the small patch scale ratio r and the large number of macro-grid intervals N lead to small sub-patch micro-grid interval δ . Hence, these eigenvalue errors

Table 3.6.2: Maximum logarithmic eigenvalue error $\min_N \log_{10}(\epsilon^{1,0})$ for the Spectral staggered patch scheme over six different number of macro-grid intervals N in Table 3.6.1. Red colour highlights $\epsilon^{1,0} > 10^{-8}$. Overall maximum $\epsilon^{1,0} = 10^{-5.1}$.

		Patch scale ratio r							
		0.0001		0.001		0.01		0.1	
c_D, c_V		$n = 6$	$n = 10$	$n = 6$	$n = 10$	$n = 6$	$n = 10$	$n = 6$	$n = 10$
0, 0		-10	-9.3	-12	-11	-12	-12	-12	-12
0, 0.0001		-9.4	-8.4	-11	-10	-12	-12	-12	-12
0, 0.01		-5.7	-5.3	-8.5	-8	-11	-10	-12	-12
$10^{-6}, 0$		-9.9	-9.1	-11	-10	-12	-12	-12	-12
$10^{-6}, 0.0001$		-9	-8.3	-11	-10	-12	-12	-12	-12
$10^{-6}, 0.01$		-5.9	-5.2	-8.7	-8.2	-11	-10	-12	-12
0.001, 0		-10	-9.2	-11	-11	-12	-11	-12	-12
0.001, 0.0001		-9	-8.2	-11	-10	-12	-12	-12	-12
0.001, 0.01		-5.7	-5.1	-8.4	-8	-11	-10	-12	-12

Figure 3.6.1: Worst case eigenvalue errors $\epsilon^{1,0}$ (log scale) of the Spectral staggered patch scheme ($\max \log_{10}(\epsilon^{1,0}) \approx -5.1$ in Table 3.6.2), for $c_D = 0.001, c_V = 0.01, n = 10$, for different macro-grid intervals Δ and patch scale ratio r .

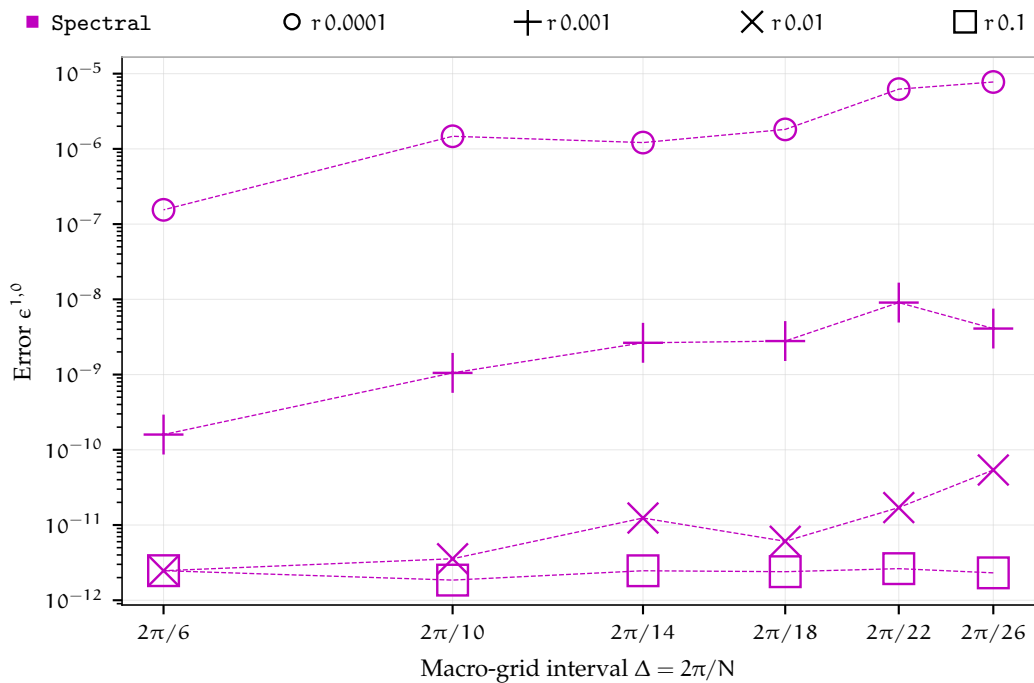


Table 3.6.3: Maximum logarithmic eigenvalue error $\min_N \log_{10}(\epsilon^{1,1})$ for the Spectral staggered patch scheme over six different number of macro-grid intervals N in Table 3.6.1. Red colour highlights $\epsilon^{1,1} > 10^{-8}$. Overall maximum $\epsilon^{1,1} = 10^{-4.9}$.

		Patch scale ratio r							
		0.0001		0.001		0.01		0.1	
c_D, c_V	n	$n=6$	$n=10$	$n=6$	$n=10$	$n=6$	$n=10$	$n=6$	$n=10$
0, 0		-10	-9.6	-12	-11	-12	-12	-12	-12
0, 0.0001		-9.4	-8.2	-11	-10	-12	-11	-12	-12
0, 0.01		-5.6	-5.5	-8.7	-8.5	-11	-10	-12	-12
$10^{-6}, 0$		-11	-9.7	-12	-11	-12	-12	-12	-12
$10^{-6}, 0.0001$		-9.2	-8.5	-11	-10	-12	-12	-12	-12
$10^{-6}, 0.01$		-5.5	-5.1	-8.6	-7.9	-11	-10	-12	-12
0.001, 0		-10	-9.6	-12	-11	-12	-12	-12	-12
0.001, 0.0001		-9.2	-8.2	-11	-11	-12	-12	-12	-12
0.001, 0.01		-5.8	-4.9	-8.6	-8.2	-11	-11	-12	-12

Figure 3.6.2: Worst case eigenvalue errors $\epsilon^{1,1}$ (log scale) of the Spectral staggered patch scheme ($\max \log_{10}(\epsilon^{1,1}) \approx -4.9$ in Table 3.6.3), for $c_D = 0.001, c_V = 0.01, n = 10$, for different macro-grid intervals Δ and patch scale ratio r .

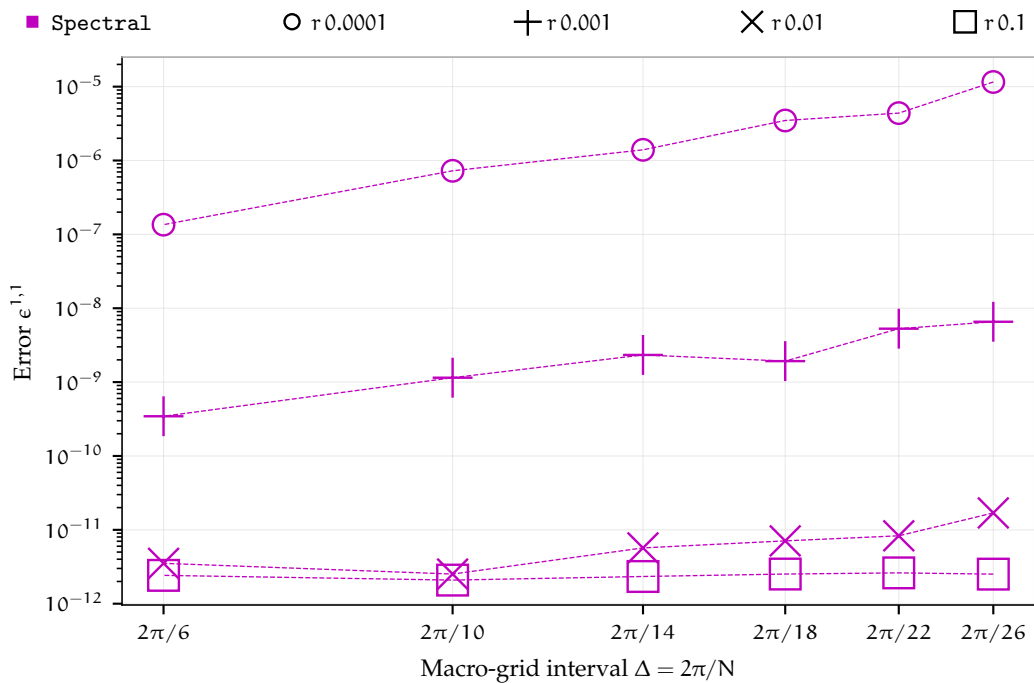
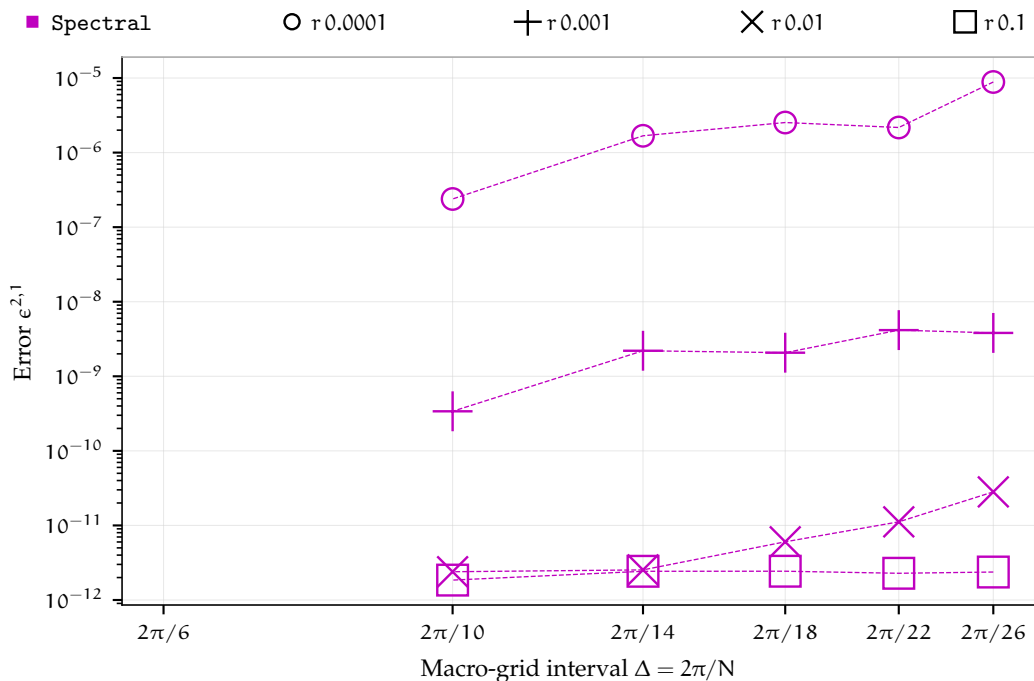


Table 3.6.4: Maximum logarithmic eigenvalue error $\min_N \log_{10}(\epsilon^{2,1})$ for the Spectral staggered patch scheme over six different number of macro-grid intervals N in Table 3.6.1. Red colour highlights $\epsilon^{2,1} > 10^{-8}$. Overall maximum $\epsilon^{2,1} = 10^{-5.1}$.

		Patch scale ratio r							
		0.0001		0.001		0.01		0.1	
c_D, c_V	n	$n=6$	$n=10$	$n=6$	$n=10$	$n=6$	$n=10$	$n=6$	$n=10$
0, 0		-11	-11	-12	-12	-12	-12	-12	-12
0, 0.0001		-9.2	-8.9	-11	-11	-12	-12	-12	-12
0, 0.01		-5.8	-5.3	-8.8	-8.3	-11	-11	-12	-12
$10^{-6}, 0$		-11	-10	-12	-12	-12	-12	-12	-12
$10^{-6}, 0.0001$		-9.6	-9	-11	-11	-12	-12	-12	-12
$10^{-6}, 0.01$		-5.9	-5.1	-9	-8.4	-11	-11	-12	-12
0.001, 0		-11	-11	-12	-12	-12	-12	-12	-12
0.001, 0.0001		-9.4	-8.8	-11	-10	-12	-12	-12	-12
0.001, 0.01		-6	-5.3	-8.9	-8.4	-11	-11	-12	-12

Figure 3.6.3: Worst case eigenvalue errors $\epsilon^{2,1}$ (log scale) of the Spectral staggered patch scheme ($\max \log_{10}(\epsilon^{2,1}) \approx -5.1$ in Table 3.6.4), for $c_D = 10^{-6}$, $c_V = 0.01$, $n = 10$, for different macro-grid intervals Δ and patch scale ratio r . No eigenvalue errors $\epsilon^{2,1}$ for $N = 6$ (p. 115 of §3.6).



(about 10^{-8} or larger) are due to numerical roundoff errors inherent to the micro-scale system, for nonnegligible viscous diffusion $c_V \gtrsim 0.0001$ and for small grid-interval δ ([p. 96](#) of [§3.4](#) discuss this sensitivity in more detail). So we take that the high accuracy of the Spectral patch scheme eigenvalues do not deteriorate with decreasing macro-grid interval Δ (increasing N). That is, *the Spectral patch scheme itself is uniformly consistent without any dependence on the macro-grid interval.*

3.6.2 The four polynomial patch schemes are consistent to the order of the polynomial interpolation

[Figures 3.2.8](#) and [3.2.9](#) of [§3.2.6](#) present the eigenvalue spectra for the Square-p2 patch scheme with $N = 6, 10$ respectively, keeping all other parameters n, r, c_D, c_V the same. Comparing the [Figs. 3.2.8](#) and [3.2.9](#) suggest that increasing the number of macro-grid intervals N (decreasing the macro-grid interval Δ) makes the macro-scale eigenvalues $\lambda_p^{N\rightarrow 1}$ of the patch scheme become increasingly close to the corresponding macro-scale eigenvalues $\lambda_{m\delta}^A$ of the full-domain micro-scale system. For the four polynomial patch schemes (Square-p2, Square-p4, Square-p4, Square-p6, and Square-p8), to verify that the accuracy of the macro-scale modes indeed increases with decreasing macro-grid interval Δ (increasing N), we study the eigenvalue errors $\epsilon^{1,0}, \epsilon^{1,1}$ and $\epsilon^{2,1}$ of the polynomial patch schemes for all the 1728 combinations of the parameters listed in [Table 3.6.1](#).

As [§2.3.2](#) describes, using interpolating polynomials of order $p = 2, 4, 6, 8$ for the patch coupling gives the four polynomial staggered patch schemes Square-p2, Square-p4, Square-p4, Square-p6, and Square-p8 respectively. In our implementation, the patch coupling for these four patch schemes are based on 2D Lagrangian polynomial interpolation over a *roughly* square region (i.e., square stencil), hence the names of polynomial patch schemes contain “Square” in them. [Figures 3.6.4](#) and [3.6.5](#) show the best and the worst “convergence plots” for the eigenvalue error $\epsilon^{1,0}$. Except for a few specific cases, in general, the eigenvalues errors $\epsilon^{1,0}$ of all the four polynomial patch schemes, converge to zero, closely following the power law curve fit $\tilde{\epsilon}^{1,0} = 0.3333 \cdot (0.7 \cdot \Delta)^p$ (solid lines). To quantify the convergence of the polynomial patch schemes, we define the *maximum relative deviation*

from the power law curve fit for as

$$\max_{\Delta} \left[|\epsilon^{k_x, k_y}(\Delta, p) - \tilde{\epsilon}^{k_x, k_y}(\Delta, p)| / \tilde{\epsilon}^{k_x, k_y}(\Delta, p) \right] \quad (3.6.2)$$

for

macro-grid interval $\Delta \in \{2\pi/N : N = 6, 10, 14, 18, 22, 26\}$,
wavenumbers $(k_x, k_y) \in \{(1, 0), (1, 1), (2, 1)\}$,
polynomial order of the patch scheme $p \in \{2, 4, 6, 8\}$.

For example, the maximum relative deviation of the order of 0.5 indicates good eigenvalue convergence (e.g., Fig. 3.6.4) and maximum relative deviations larger than one indicates some deterioration in the eigenvalue convergence (e.g., Fig. 3.6.5). Table 3.6.5 presents the maximum relative deviation of the eigenvalue error $\epsilon^{1,0}$ from the power law curve fit $\tilde{\epsilon}^{1,0} = 0.3333 \cdot (0.7 \cdot \Delta)^p$ over the five staggered patch schemes and six different number of macro-grid intervals N . Table 3.6.5 and Figs. 3.6.4 and 3.6.5 show that the maximum relative deviation of the eigenvalue error $\epsilon^{1,0}$ are about 0.5 or smaller, except the red highlighted values that correspond to the combination of the small patch scale ratio $r = 0.0001$, large interpolation order $p = 8$, large number of macro-grid intervals $N > 14$ and large viscous diffusion $c_V = 0.01$. That is except for the combination of the small r and large N, p, c_V , the macro-scale eigenvalues corresponding to the wavenumber $(k_x, k_y) = (1, 0)$ exponentially converge to the corresponding macro-scale eigenvalues of the full-domain micro-scale system, for all the four polynomial patch schemes, similar to the convergence plot in Fig. 3.6.4.

The eigenvalue errors $\epsilon^{1,1}$ converge to zero following the same power law curve fit for the eigenvalue errors $\epsilon^{1,0}$, $\tilde{\epsilon}^{1,1} = \tilde{\epsilon}^{1,0} = 0.3333 \cdot (0.7 \cdot \Delta)^p$ (solid lines in Figs. 3.6.6 and 3.6.7). The best case convergence plot for the eigenvalue errors $\epsilon^{1,1}$ are visually identical to the Fig. 3.6.4. So, Figs. 3.6.6 and 3.6.7 show the moderately worse and the worst convergence plots for the eigenvalue error $\epsilon^{1,1}$. Table 3.6.6 presents the maximum relative deviation of the eigenvalue error $\epsilon^{1,1}$ from the power law curve fit $\tilde{\epsilon}^{1,1} = 0.3333 \cdot (0.7 \cdot \Delta)^p$ over the five staggered patch schemes and six different number of macro-grid intervals N . Similar to the case of the wave number $(k_x, k_y) = (1, 0)$, except for the combination of the small r and large N, p, c_V , the macro-scale eigenvalues corresponding to the wavenumber $(k_x, k_y) = (1, 1)$ exponentially converge to the corresponding macro-scale eigenvalues of the full-domain micro-scale system, for all the four polynomial patch schemes, similar to the convergence plot in Fig. 3.6.4.

Figures 3.6.8 and 3.6.9 show the best and the worst convergence plots for the eigenvalue error $\epsilon^{2,1}$. As discussed in p. 115 of §3.6, a patch grid

with $N = 6$ macro-grid intervals do not resolve the macro-scale mode with wavenumber $(k_x, k_y) = (2, 1)$. Hence the convergence plots of the eigenvalue error $\epsilon^{2,1}$ do not have a data point corresponding to $N = 6$. The eigenvalue errors $\epsilon^{2,1}$ converge to zero following the power law curve fit $\tilde{\epsilon}^{2,1} = 0.3333 \cdot (1.333 \cdot \Delta)^p$ (solid lines in Figs. 3.6.8 and 3.6.9). Figures 3.6.8 and 3.6.9 of the best and worst convergence plots for the eigenvalue error $\epsilon^{2,1}$, are nearly the same except for the largest polynomial order $p = 8$ with $N = 22$, $r = 0.0001$. Table 3.6.7 presents the maximum relative deviation of the eigenvalue error $\epsilon^{2,1}$ from the power law curve fit $\tilde{\epsilon}^{2,1} = 0.3333 \cdot (1.333 \cdot \Delta)^p$ over the five staggered patch schemes and six different number of macro-grid intervals N . Unlike the case of the eigenvalue errors $\epsilon^{1,0}$ and $\epsilon^{1,1}$, the macro-scale eigenvalues corresponding to the wavenumber $(k_x, k_y) = (2, 1)$ exponentially converge to the corresponding macro-scale eigenvalues of the full-domain micro-scale system, without any exception for r, N, p, c_V .

All the large maximum relative deviation of the eigenvalue errors $\epsilon^{1,0}$ and $\epsilon^{1,1}$ (red highlighted values in Tables 3.6.5 and 3.6.6) correspond to the combination of the small r and large N, p, c_V . Both the small patch scale ratio r and the large number of macro-grid intervals N lead to small subpatch micro-grid interval δ . Hence, as discussed in p. 96 of §3.4 the large maximum relative deviation of the eigenvalue errors are due to inherent sensitivity of the micro-scale system to numerical roundoff errors, for nonnegligible viscous diffusion $c_V \gtrsim 0.0001$ and for small grid-interval δ . So we take that the exponential eigenvalue convergence for the macro-scale wavenumbers do not deteriorate with decreasing macro-grid interval Δ (increasing N), due to any deficiency of the four polynomial patch schemes. That is, *all four Square polynomial patch schemes are exponentially consistent.*

Figure 3.6.4: Best case convergence of $\epsilon^{1,0}$ (log scale) with macro-grid interval Δ , for $c_D = 10^{-6}$, $c_V = 10^{-4}$, $n = 6$, for the four polynomial patch schemes with interpolation orders $p \in \{2, 4, 6, 8\}$ and patch scale ratio r . Solid lines are the power law curve fit $\tilde{\epsilon}^{1,0} = 0.3333 \cdot (0.7 \cdot \Delta)^p$ with maximum relative deviation 0.51 in Table 3.6.5.

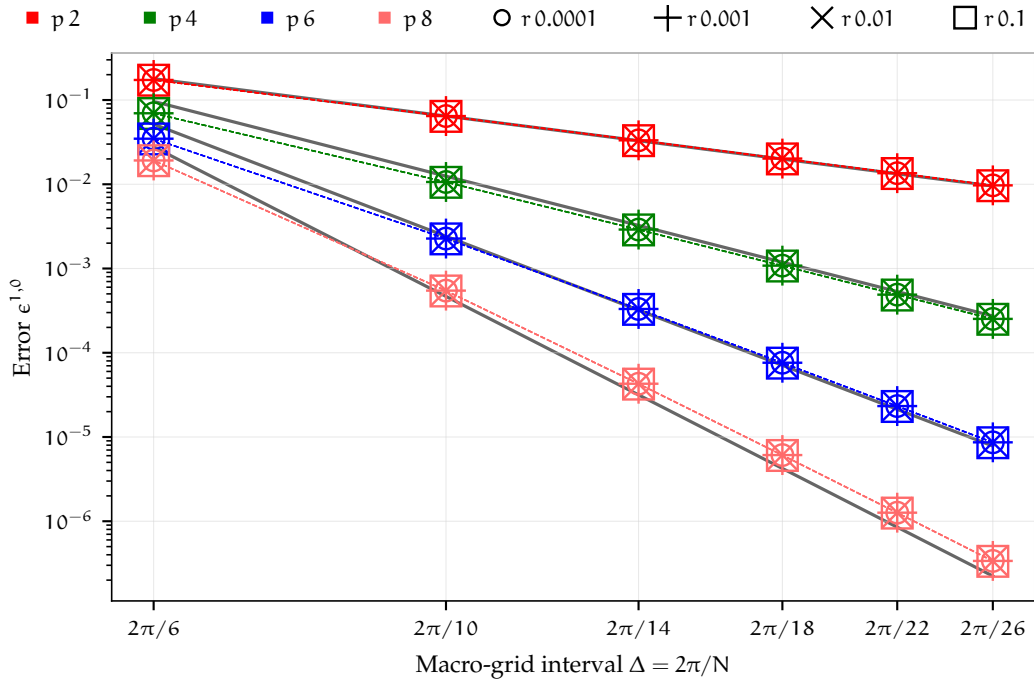


Figure 3.6.5: Worst case convergence of $\epsilon^{1,0}$ (log scale) with macro-grid interval Δ , for $c_D = 0.001$, $c_V = 0.01$, $n = 10$, for the four polynomial patch schemes with interpolation orders $p \in \{2, 4, 6, 8\}$ and patch scale ratio r . Solid lines are the power law curve fit $\tilde{\epsilon}^{1,0} = 0.3333 \cdot (0.7 \cdot \Delta)^p$ with maximum relative deviation 75 in Table 3.6.5.

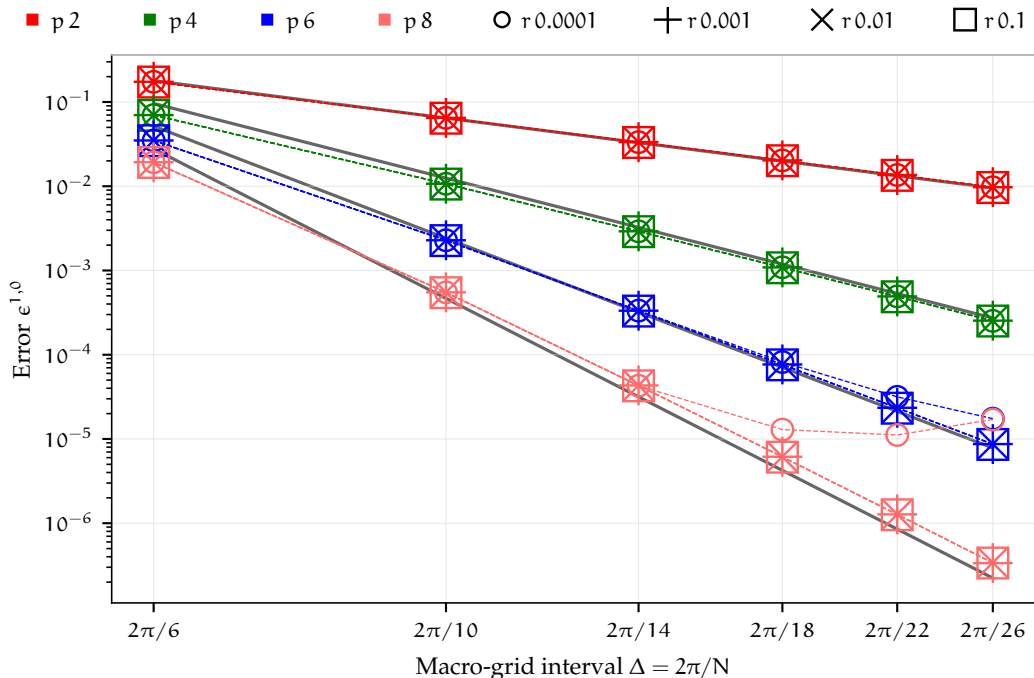


Table 3.6.5: Maximum relative deviation of the eigenvalue error $\epsilon^{1,0}$ from the power law curve fit $\tilde{\epsilon}^{1,0} = 0.3333 \cdot (0.7 \cdot \Delta)^p$ over the five staggered patch schemes and six different number of macro-grid intervals N in [Table 3.6.1](#). Red colour highlights the large deviations $\epsilon^{1,0} > 1$ from the power law.

c_D, c_V	Patch scale ratio r							
	0.0001		0.001		0.01		0.1	
	$n = 6$	$n = 10$	$n = 6$	$n = 10$	$n = 6$	$n = 10$	$n = 6$	$n = 10$
0, 0	0.51	0.51	0.51	0.51	0.51	0.51	0.49	0.49
0, 0.0001	0.51	0.51	0.51	0.51	0.51	0.51	0.49	0.5
0, 0.01	15	63	0.53	0.53	0.52	0.52	0.51	0.51
$10^{-6}, 0$	0.51	0.51	0.51	0.51	0.51	0.51	0.49	0.49
$10^{-6}, 0.0001$	0.51	0.52	0.51	0.51	0.51	0.51	0.49	0.5
$10^{-6}, 0.01$	17	26	0.53	0.53	0.52	0.52	0.51	0.51
0.001, 0	0.51	0.51	0.51	0.51	0.51	0.51	0.49	0.49
0.001, 0.0001	0.51	0.53	0.51	0.51	0.51	0.51	0.49	0.49
0.001, 0.01	6.8	75	0.51	0.5	0.52	0.52	0.51	0.51

Table 3.6.6: Maximum relative deviation of the eigenvalue error $\epsilon^{1,1}$ from the power law curve fit $\tilde{\epsilon}^{1,1} = 0.3333 \cdot (0.7 \cdot \Delta)^p$ over the five staggered patch schemes and six different number of macro-grid intervals N in [Table 3.6.1](#). Red colour highlights the maximum deviations larger than one.

c_D, c_V	Patch scale ratio r							
	0.0001		0.001		0.01		0.1	
	$n = 6$	$n = 10$	$n = 6$	$n = 10$	$n = 6$	$n = 10$	$n = 6$	$n = 10$
0, 0	0.51	0.51	0.51	0.51	0.51	0.51	0.49	0.49
0, 0.0001	0.52	0.51	0.51	0.51	0.51	0.51	0.49	0.5
0, 0.01	14	34	0.52	0.51	0.53	0.53	0.51	0.52
$10^{-6}, 0$	0.51	0.51	0.51	0.51	0.51	0.51	0.49	0.49
$10^{-6}, 0.0001$	0.51	0.52	0.51	0.51	0.51	0.51	0.49	0.5
$10^{-6}, 0.01$	13	50	0.54	0.57	0.53	0.53	0.51	0.52
0.001, 0	0.51	0.51	0.51	0.51	0.51	0.51	0.49	0.49
0.001, 0.0001	0.51	0.52	0.51	0.51	0.51	0.51	0.49	0.49
0.001, 0.01	9.7	62	0.52	0.53	0.53	0.53	0.51	0.52

Figure 3.6.6: Moderately worse case convergence of $\epsilon^{1,1}$ (log scale) with macro-grid interval Δ , or $c_D = 0.001$, $c_V = 0.01$, $n = 10$, for the four polynomial patch schemes with interpolation orders $p \in \{2, 4, 6, 8\}$ and patch scale ratio r . Solid lines are the power law curve fit $\tilde{\epsilon}^{1,1} = 0.3333 \cdot (0.7 \cdot \Delta)^p$ with maximum relative deviation 9.7 in [Table 3.6.6](#).

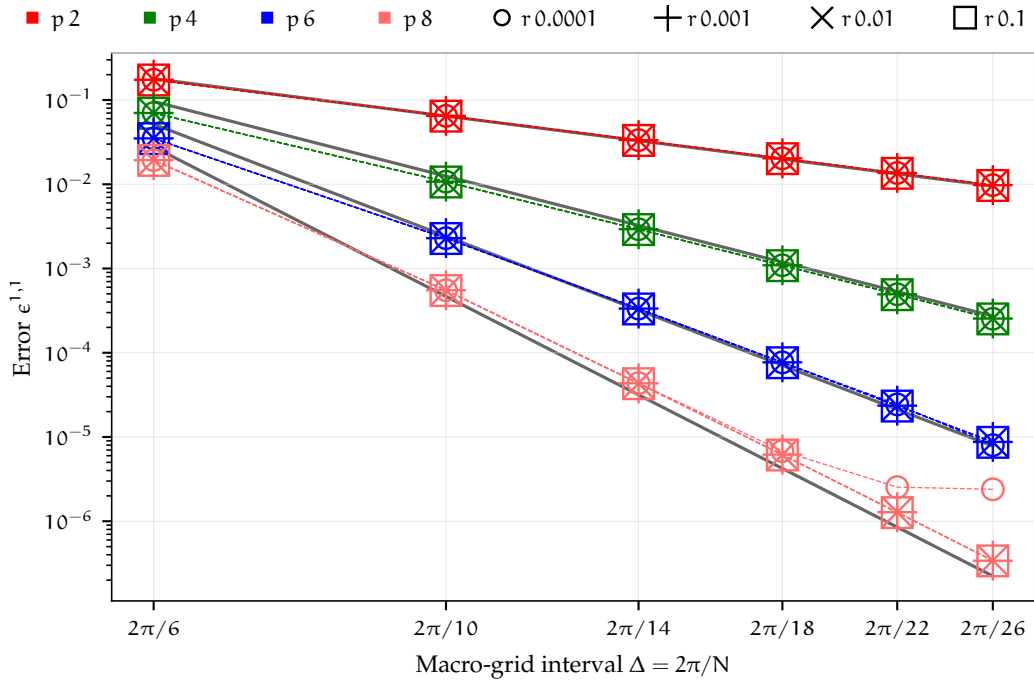


Figure 3.6.7: Worst case convergence of $\epsilon^{1,1}$ (log scale) with macro-grid interval Δ , for $c_D = 0.001$, $c_V = 0.01$, $n = 10$, for the four polynomial patch schemes with interpolation orders $p \in \{2, 4, 6, 8\}$ and patch scale ratio r . Solid lines are the power law curve fit $\tilde{\epsilon}^{1,1} = 0.3333 \cdot (0.7 \cdot \Delta)^p$ with maximum relative deviation 62 in [Table 3.6.6](#).

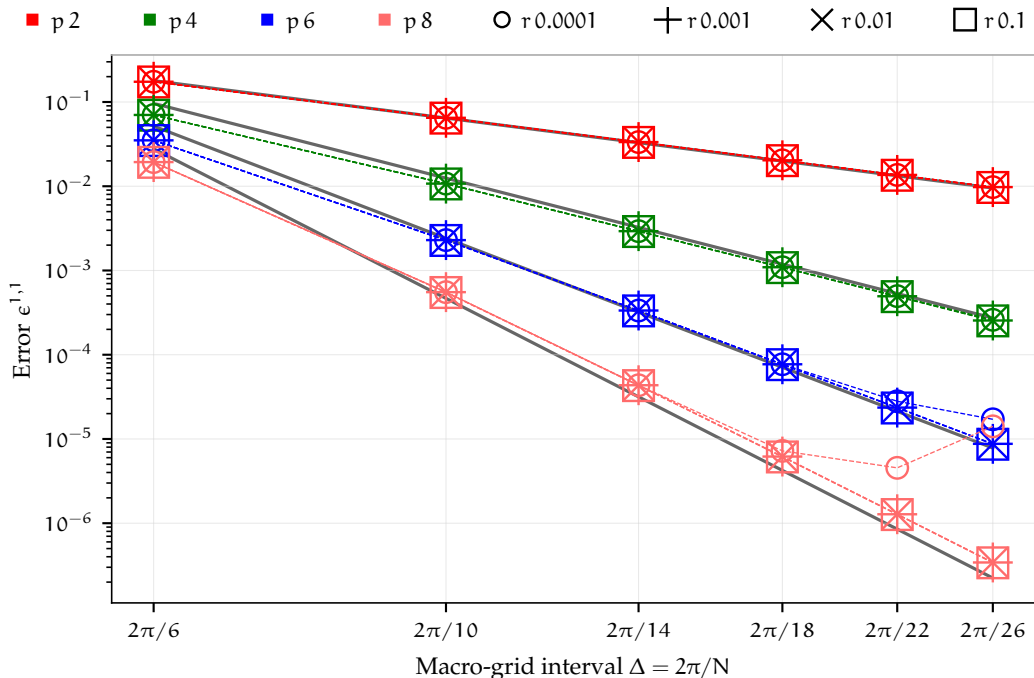


Figure 3.6.8: Best case convergence of $\epsilon^{2,1}$ (log scale) with macro-grid interval Δ , for $c_D = 10^{-6}$, $c_V = 10^{-4}$, $n = 10$, for the four polynomial patch schemes with interpolation orders $p \in \{2, 4, 6, 8\}$ and patch scale ratio r . Solid lines are the power law curve fit $\tilde{\epsilon}^{2,1} = 0.3333 \cdot (1.333 \cdot \Delta)^p$ with maximum relative deviation 0.57 in Table 3.6.7.

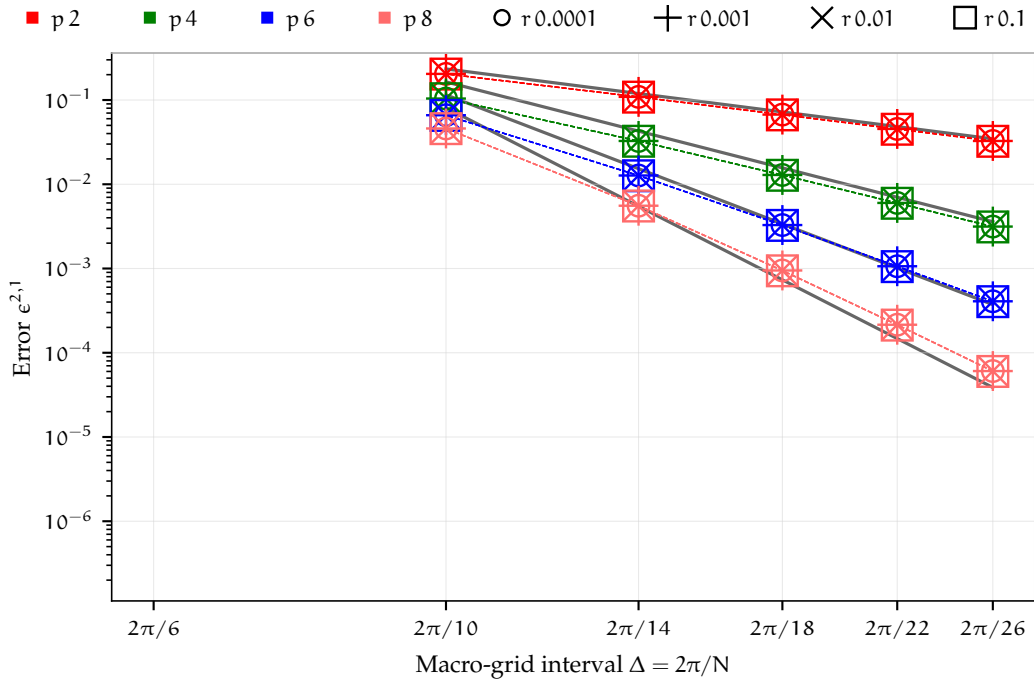


Figure 3.6.9: Worst case convergence of $\epsilon^{2,1}$ (log scale) with macro-grid interval Δ , for $c_D = 0.001$, $c_V = 0.01$, $n = 10$, for the four polynomial patch schemes with interpolation orders $p \in \{2, 4, 6, 8\}$ and patch scale ratio r . Solid lines are the power law curve fit $\tilde{\epsilon}^{2,1} = 0.3333 \cdot (1.333 \cdot \Delta)^p$ with maximum relative deviation 0.75 in Table 3.6.7.

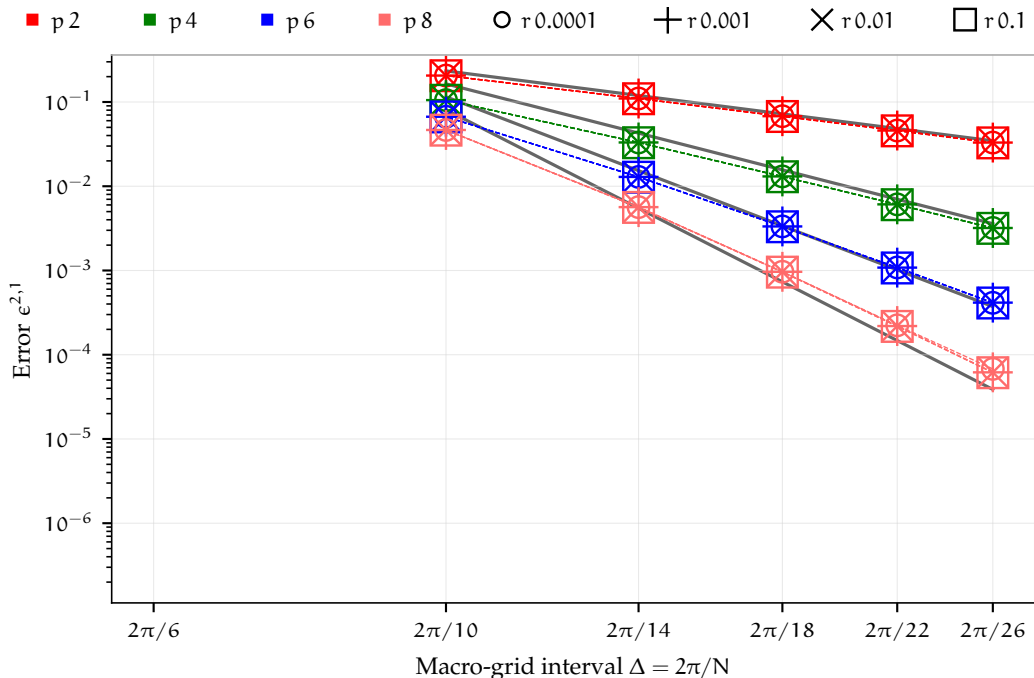


Table 3.6.7: Maximum relative deviation of the eigenvalue error $\epsilon^{2,1}$ from the power law curve fit $\tilde{\epsilon}^{2,1} = 0.3333 \cdot (1.333 \cdot \Delta)^p$ over the five staggered patch schemes and six different number of macro-grid intervals N in [Table 3.6.1](#). The maximum deviations are all less than one (negligible deviation from the fit).

c_D, c_V	Patch scale ratio r							
	0.0001		0.001		0.01		0.1	
	$n = 6$	$n = 10$	$n = 6$	$n = 10$	$n = 6$	$n = 10$	$n = 6$	$n = 10$
0, 0	0.57	0.57	0.57	0.57	0.57	0.57	0.55	0.55
0, 0.0001	0.57	0.57	0.57	0.57	0.57	0.57	0.55	0.55
0, 0.01	0.64	0.71	0.59	0.6	0.59	0.6	0.58	0.58
$10^{-6}, 0$	0.57	0.57	0.57	0.57	0.57	0.57	0.55	0.55
$10^{-6}, 0.0001$	0.57	0.57	0.57	0.57	0.57	0.57	0.55	0.55
$10^{-6}, 0.01$	0.6	0.6	0.59	0.6	0.59	0.6	0.58	0.58
0.001, 0	0.57	0.57	0.57	0.57	0.57	0.57	0.55	0.55
0.001, 0.0001	0.57	0.57	0.57	0.57	0.57	0.57	0.55	0.55
0.001, 0.01	0.62	0.75	0.59	0.6	0.59	0.6	0.58	0.58

3.7 Large computational savings in staggered patch scheme time simulation

This section quantifies and demonstrates the large computational savings of the staggered patch schemes for the general linear wave. [Section 3.7.1](#) shows the computational savings of the 2D staggered patch schemes theoretically in terms of the ratio of the space over which the patch schemes and the full-domain system computes. [Section 3.7.2](#) shows the computational savings of the patch schemes in terms of the ratio of the number of state variables for which the patch schemes and the full-domain system computes. [Section 3.7.4](#) demonstrates the computational savings of the 2D staggered patch schemes by measuring the actual time taken to compute the time derivative of the state vector (one time iteration) using a specific implementation.

3.7.1 Staggered patch schemes compute only within a small fraction of the space in the full domain

For large scale problems, the primary interest is only the large scale waves, not the smallest details. For such large scale problems, to simulate the large scale waves accurately, a fine-grid full-domain micro-scale system (e.g., (3.1.2) for the general linear wave) computes on the whole $L \times L$ domain. But the staggered patch schemes compute only within small patches sparsely located within the domain, occupying a much smaller fraction of the space in the full domain. For example, Fig. 2.2.3b of §2.2.2 shows a staggered patch grid, where the patches are enlarged for visual clarity.

Consider the staggered patch grid in Fig. 2.2.3b with macro-grid interval Δ and patch size l . In terms of the patch scale ratio $r = l/(2\Delta)$, the area of one patch is $l^2 = 4r^2\Delta^2$. When a macro-cell contains three patches in a patch grid (as in the chosen patch grid Fig. 2.2.3b), with $N \times N$ macro-grid intervals, there are a total of $3N^2/4$ patches. Hence the total area occupied by the patches is $3N^2l^2/4 = 3r^2N^2\Delta^2 = 3r^2L^2$ as the macro-grid interval $\Delta = L/N$. That is, the total area of the simulated space in a patch scheme is $3r^2L^2$ whereas the corresponding total area of the simulated space in a fine-grid full-domain micro-scale system is L^2 . For a small patch scale ratio r , the 2D staggered patch schemes compute only within a small fraction $3r^2$ of the area in the full domain. For example, for $r = 0.1, 0.01, 0.001, 0.0001$, the staggered patch schemes compute over the fraction of area $0.03, 3 \cdot 10^{-4}, 3 \cdot 10^{-6}, 3 \cdot 10^{-8}$ respectively. Similar 3D staggered patch schemes compute only within a small fraction $3r^3$ of the volume in the full domain, where the computational saving is much more. Thus, the staggered patch schemes compute only within a small fraction of the space in the full domain.

3.7.2 Staggered patch schemes compute only for a small number of dynamical state variables

Section 3.7.1 shows that 2D staggered patch schemes compute only within a small fraction $3r^2$ of the space in the full domain, which is a rough indication of the computational savings of the staggered patch schemes. This section discusses the computational savings of the staggered patch schemes, more concretely in terms of the number of the dynamical state variables of the 2D staggered patch schemes and that of the corresponding fine-grid full-domain micro-scale system.

For a staggered patch grid in Fig. 2.2.5a with $N \times N$ macro-grid intervals and each patch containing $n \times n$ sub-patch micro-grid intervals, the total

number of patch interior nodes is $n_p^I = (N^2/4)(9n^2/4 - 4n + 2)$, which is same as the number of state variables (p. 18 of §2.2.2). For a staggered grid in Fig. 2.2.1 corresponding to a fine-grid full-domain system, with the same grid interval as the sub-patch micro-grid interval δ , the total number of interior nodes is $n_{m\delta}^I = 3N^2n^2/(16r^2)$. The ratio of the number of state variables of the staggered patch scheme to that of the fine-grid full-domain micro-scale system,

$$n_p^I/n_{m\delta}^I = 3r^2 \left(1 - \frac{16}{9n} + \frac{8}{9n^2} \right). \quad (3.7.1)$$

With increasing n , the ratio $n_p^I/n_{m\delta}^I$ tends to $3r^2$, which is the same fraction of the space derived in §3.7.1 over which the patch schemes compute. For example, for $n = 6, 10, 14$ sub-patch micro-grid intervals with a fixed patch scale ratio $r = 0.1$, the ratio $n_p^I/n_{m\delta}^I = 0.022, 0.025, 0.026$ respectively. For $r = 0.1, 0.01, 0.001, 0.0001$ with a fixed $n = 6$, the ratio of number of nodes $n_p^I/n_{m\delta}^I = 0.022, 2.2 \cdot 10^{-4}, 2.2 \cdot 10^{-6}, 2.2 \cdot 10^{-8}$ respectively. Thus, the *staggered patch schemes compute only for a small number of dynamical state variables* compared to the corresponding fine-grid full-domain micro-scale system with the same grid interval as the sub-patch micro-grid interval δ .

3.7.3 Computational complexity of the staggered patch schemes

This subsection compares the compute times of the staggered patch schemes and that of the full-domain micro-scale system. To simplify and keep the smaller uncertainties aside, for the patch schemes and the full-domain micro-scale system this subsection assumes a similar level of vectorisation, and a similar pattern of cache and memory access.

Let the average compute time for computing the time derivative of one state variable is T_M for the fine-grid full-domain micro-scale system. We call T_M , the *model compute time* per interior node. There are $n_{m\delta}^I = 3N^2n^2/(16r^2)$ state variables in the fine-grid full-domain micro-scale system. Hence, the total compute time for computing the time derivative of the state vector (i.e., the compute time for one iteration in time simulation),

$$T_{m\delta} = n_{m\delta}^I T_M = 3N^2n^2 T_M / (16r^2). \quad (3.7.2)$$

The compute time T_p for computing the time derivative of the state vector dx^I/dt in the patch system (2.2.9) has two components: time for computing the patch coupling; and time for computing the node values using the micro-scale system.

- Let the average compute time for computing one patch edge node from the patch coupling is T_C . We call T_C , the *coupling compute time* per edge node. There are $n_p^E = (N^2/4)(18n - 16)$ edge nodes (expression (2.2.8) in p. 18 of §2.2.2) in the staggered patch grid of Fig. 2.2.5a for the general linear wave with drag and viscous diffusion. Hence, the total compute time for computing the patch edge vector x^E in the patch system (2.2.9) (i.e., the patch coupling compute time for one iteration in time simulation) is $n_p^E T_C = (N^2/4)(18n - 16) T_C$.
- Using the same micro-scale system within the patches as that of the full-domain micro-scale system costs the same average compute time T_M for computing the time derivative of one state variable of patch scheme. There are $n_p^I = (N^2/4)(9n^2/4 - 4n + 2)$ state variables in the staggered patch scheme (p. 18 of §2.2.2). Hence, using the known values of the patch edge nodes x^E and the patch interior nodes x^I , the compute time for computing the time derivative of the state vector dx^I/dt in the patch system (2.2.9) is $n_p^I T_M = (N^2/4)(9n^2/4 - 4n + 2) T_M$.

Thus, the total compute time for computing the time derivative of the state vector dx^I/dt in the patch system (2.2.9),

$$T_p = n_p^E T_C + n_p^I T_M = (N^2/4)(18n - 16) T_C + (N^2/4)(9n^2/4 - 4n + 2) T_M. \quad (3.7.3)$$

The ratio of the compute time for computing the time derivative of the state vector of a patch scheme (3.7.3) to that of the fine-grid ful-domain micro-scale system (3.7.2),

$$T_p/T_{m\delta} = (n_p^E T_C + n_p^I T_M)/(n_{m\delta}^I T_M) = (n_p^E/n_{m\delta}^I) (T_C/T_M) + n_p^I/n_{m\delta}^I. \quad (3.7.4)$$

From the expressions for the number of state variables in a fine-grid full-domain micro-scale system $n_{m\delta}^I = 3N^2n^2/(16r^2)$ and the number of patch edge nodes $n_p^E = (N^2/4)(18n - 16)$, the ratio

$$n_p^E/n_{m\delta}^I = 24r^2/n - 64r^2/(3n^2). \quad (3.7.5)$$

Using the expressions (3.7.1) and (3.7.5), the ratio of compute time for computing the time derivative of the state vector of a patch scheme to that of the fine-grid ful-domain micro-scale system (i.e., the compute time ratio for one iteration in time simulation) is

$$T_p/T_{m\delta} = (T_C/T_M) \left(\frac{24r^2}{n} - \frac{64r^2}{3n^2} \right) + 3r^2 \left(1 - \frac{16}{9n} + \frac{8}{9n^2} \right). \quad (3.7.6)$$

The compute time ratio (3.7.6) for one iteration in time simulation, describes the computational cost savings of the staggered patch schemes. The ratio T_C/T_M of coupling compute time to model compute time, in the compute time ratio (3.7.6), encapsulates the following:

1. the details of the specific patch scheme (Spectral or polynomial patch scheme, interpolation order p of the polynomial patch scheme, etc.);
2. the details of the specific implementation (specific algorithmic choices, data structures, serial or parallel computations, etc.).

In general, for modelling any reasonably complex physical process (e.g., non-hydrostatic nonlinear waves, sediment transport, etc), the model compute time per interior node T_M is greater than the coupling compute time per edge node T_C , with $T_C/T_M \lesssim 1$. Hence, substituting $T_C/T_M = 1$ into the compute time ratio (3.7.6) gives a rough indication of the possible computational cost savings of the staggered patch schemes as

$$T_p/T_{m\delta} \lesssim 3r^2 + \frac{56r^2}{3n} - \frac{56r^2}{3n^2}. \quad (3.7.7)$$

3.7.4 Staggered patch schemes simulate macro-scale waves with small compute time

Sections 3.7.1 and 3.7.2 show the computational savings of the 2D staggered patch schemes theoretically in terms of the ratio of the space and the ratio of the number of state variables respectively. This section shows the computational savings of the 2D staggered patch schemes by measuring the actual time taken to compute the time derivative of the state vector (one time iteration) using a specific implementation in Julia programming language.

This subsection measures the compute time ratio $T_p/T_{m\delta}$ for a specific implementation and compares with the expression (3.7.6) by empirically estimating the model compute time per interior node T_M and the coupling compute time per edge node T_C . The compute times in this subsection are measured on a custom assembled liquid-cooled workstation with Intel i7-6900k processor and 64GB DDR4 RAM. Both the full-domain micro-scale system and the patch schemes are implemented as serial programs.

Figure 3.7.1 plots the measured compute time $T_{m\delta}$ of the fine-grid full-domain micro-scale system (3.1.2) (p. 43 of §3.1), for computing the time derivative of the state vector (i.e., the compute time for one iteration in time simulation) for the initial condition (3.7.8) of the simple progressive

Figure 3.7.1: Measured compute times $T_{m\delta}$ of the fine-grid full-domain system (general linear wave) with the same grid-interval as the sub-patch micro-grid interval δ of a staggered patch grid with different N , n , and patch scale ratio r . Solid lines represent expression (3.7.2) using the estimated model compute time $T_M = 0.062 \mu\text{s}$.

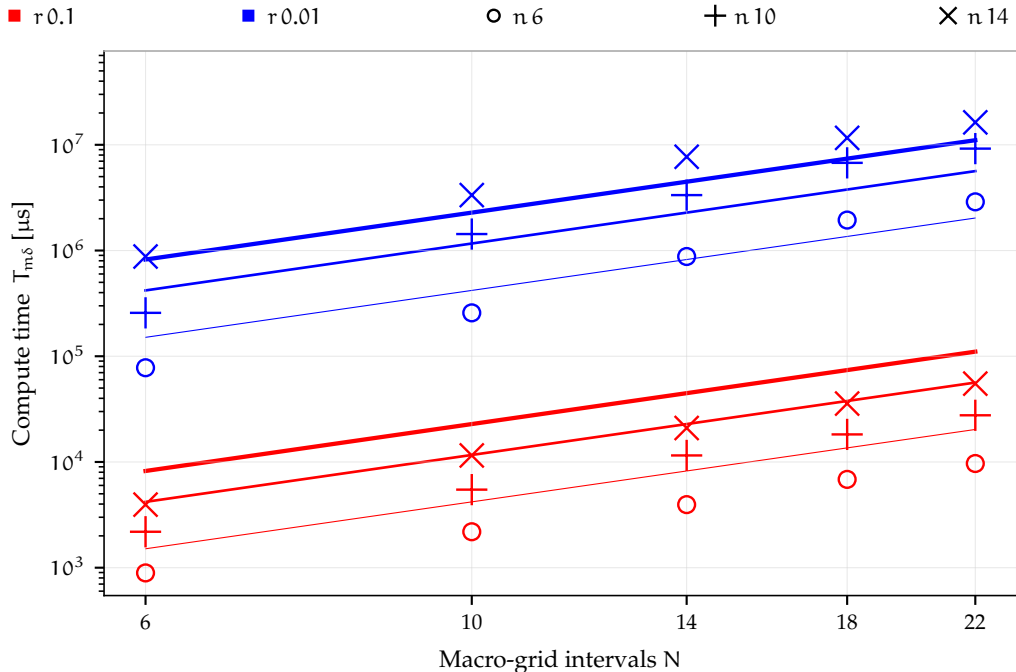
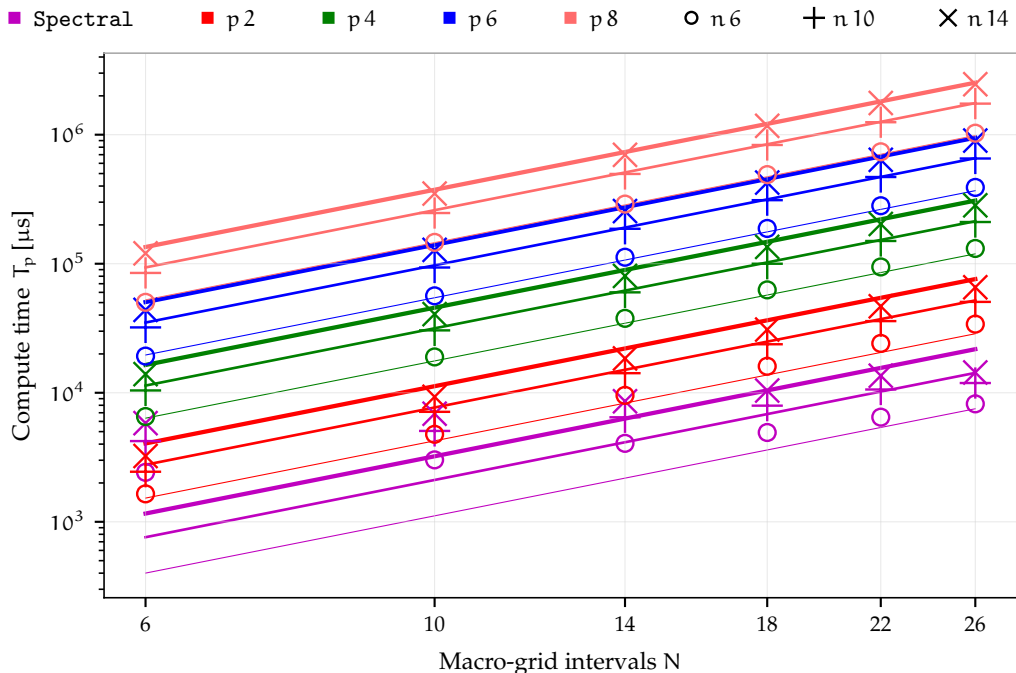


Figure 3.7.2: Measured compute times T_p of the five staggered patch schemes (general linear wave) with different N and n . Solid lines represent expression (3.7.3) using the estimated model compute time $T_M = 0.062 \mu\text{s}$ and the respective estimated coupling compute times T_C for the five patch schemes.



wave (p. 141 of §3.7.5). Figure 3.7.1 plots the compute time $T_{m\delta}$ of the fine-grid full-domain system with the same grid-interval as the sub-patch micro-grid interval δ of a staggered patch grid with different number of macro-grid intervals N , sub-patch micro-grid intervals n , and patch scale ratio r . We measured hundred samples of compute times $T_{m\delta}$ for each of the nine combinations of $c_D \in \{0, 10^{-6}, 0.0001\}$, $c_V \in \{0, 10^{-4}, 0.001\}$. Each point in Fig. 3.7.1 is the mean over the nine combinations of c_D , c_V . For the measured compute times $T_{m\delta}$, fitting one common power law curve (solid lines in Fig. 3.7.1) using the expression (3.7.2), we estimate the model compute time per interior node $T_M = 0.062 \mu s$ (same value for all n, r). The measured compute times $T_{m\delta}$ reasonably closely follow the trend of the expression (3.7.2) (solid lines).

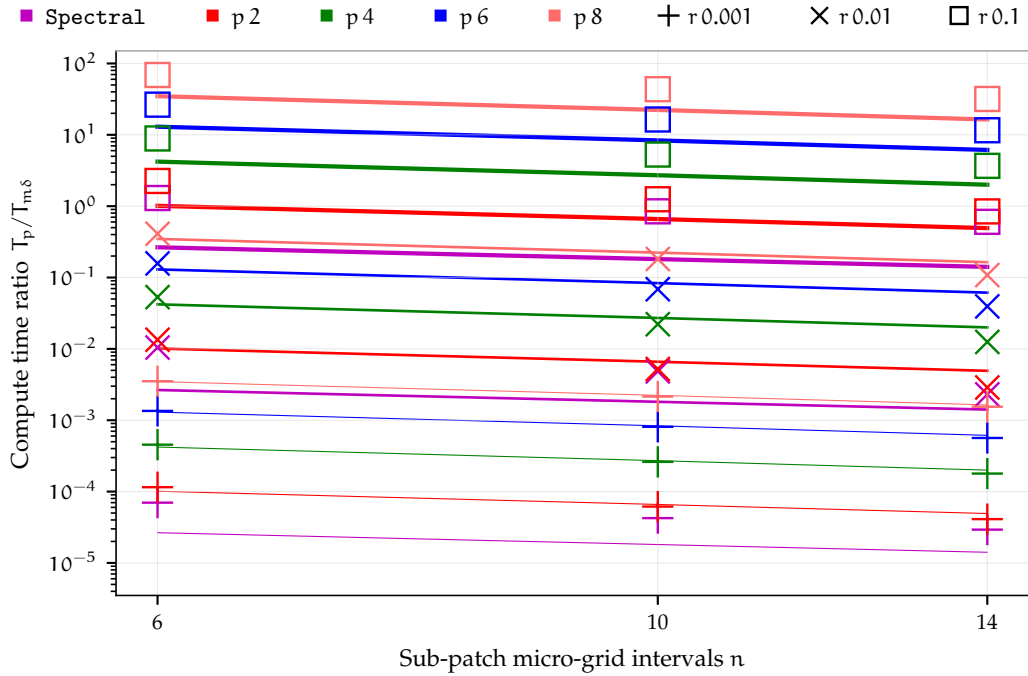
Figure 3.7.2 plots the measured compute time T_p of the five staggered patch schemes for computing the time derivative of the state vector (i.e., the compute time for one iteration in time simulation), for different macro-grid intervals N and sub-patch micro-grid intervals n . We measured hundred samples of compute times T_p for each of the nine combinations of $c_D \in \{0, 10^{-6}, 0.0001\}$, $c_V \in \{0, 10^{-4}, 0.001\}$. Each point in Fig. 3.7.2 is the mean over the nine combinations of c_D , c_V . For the measured compute times T_p , fitting a power law curve for each patch scheme (solid lines in Fig. 3.7.2) using the model compute time $T_M = 0.062 \mu s$ in the expression (3.7.3), we estimate the approximate coupling compute times per edge node $T_C = 0.44, 1.8, 7.6, 24, 63 \mu s$ for the five staggered patch schemes Spectral, Square-p2, Square-p4, Square-p6, and Square-p8 respectively.

The measured compute times T_p of all the five staggered patch schemes reasonably closely follow the trend of the expression (3.7.3) (solid lines).

The smallest coupling compute time $T_C = 0.44 \mu s$ for the spectral patch scheme is because Algorithm 1 efficiently calculates the edge values for all the h/u/v-centred patches in one shot using the fast Fourier transform via the Fourier shift property. But for the polynomial patch schemes, Algorithm 2 calculates looping over each of the h/u/v-centred patches patches individually. For the polynomial patch schemes, the coupling compute time per edge node T_C increases monotonically from $1.8 \mu s$ to $63 \mu s$ with increase in the order p of interpolation from two to eight. This increasing T_C with increasing p is expected as there are more computations involved in higher order interpolation.

The relatively simple micro-scale system of the general linear wave with drag and viscous diffusion has small model compute time per interior node $T_M = 0.062 \mu s$ from Fig. 3.7.1. The focus of the current patch scheme implementation is on the flexibility to explore a large number of possible designs of the patch grid and a large number of possible patch schemes.

Figure 3.7.3: Ratio $T_p/T_{m\delta}$ of the measured compute time of the staggered patch schemes (general linear wave) to that of the fine-grid full-domain system, for different n , r . Solid lines represent expression (3.7.6) for $T_p/T_{m\delta}$ using the estimated model compute time $T_M = 0.062 \mu s$ and the respective estimated coupling compute times T_C for each patch scheme.



So, the current patch scheme implementation, being not computationally efficient, leads to large coupling compute times per edge node T_C from Fig. 3.7.2. Hence, the ratios of the coupling compute times to the model compute times are $T_C/T_M = 7, 29, 123, 381, 1020$, for the five staggered patch schemes Spectral, Square-p2, Square-p4, Square-p6, and Square-p8 respectively.

Figure 3.7.3 plots the ratio $T_p/T_{m\delta}$ of the measured compute time of the fine-grid full-domain system to that of the staggered patch schemes, for different number of sub-patch micro-grid intervals n and patch scale ratio r . Solid lines represent expression (3.7.6) for $T_p/T_{m\delta}$ using the estimated model compute time $T_M = 0.062 \mu s$ and the respective estimated coupling compute times T_C for each patch scheme. A fine-grid for full-domain system (with the same grid interval δ as the sub-patch micro-grid interval), has very large number of interior nodes $n_{m\delta}^I = 3N^2n^2/(16r^2)$ corresponding to a small patch scale ratio, requiring memory larger than 64 GB. Hence, for $r = 0.001$ we compute $T_p/T_{m\delta}$ (plusses in Fig. 3.7.3) using the measured T_p of the

patch schemes and the estimated $T_{m\delta}$ of the full-domain system using the expression (3.7.6). The measured compute time ratio $T_p/T_{m\delta}$ reasonably closely follow the trend of the expression (3.7.6) (solid lines) for the five staggered patch schemes (with the respective T_C).

Figure 3.7.3 show that despite the estimated large T_C/T_M (between 13 and 1031 for the five patch schemes), for sufficiently small patch scale ratio $r = 0.01, 0.001$ the compute time ratios $T_p/T_{m\delta}$ are about $10^{-2}, 10^{-4}$. That is, despite the large T_C/T_M , for small patch scale ratios, *the compute times of the multi-scale patch schemes are about 100 to 10 000 times smaller than the corresponding fine-grid full-domain micro-scale system*. A reduction of 10 000 times is equivalent to reducing the computation time from one week to one minute.

For patch scheme simulations with fixed grid geometry, the patch coupling coefficients can be precomputed as a sparse matrix, which gives the patch edge values when multiplied by the patch centre values at each instant in time. Such patch coupling via sparse matrix multiplication instead of direct patch coupling reduces the coupling compute time T_C , leading to smaller T_C/T_M in (3.7.6), and hence larger computational savings of the staggered patch schemes via smaller $T_p/T_{m\delta}$. Using the sparse matrix multiplication for the patch coupling of the five staggered patch schemes, Fig. 3.7.4 plots the measured compute time T_p for computing the time derivative of the state vector (i.e., the compute time for one iteration in time simulation), for different N and n . We measured 10 000 samples of compute times T_p for each of the nine combinations of $c_D \in \{0, 10^{-6}, 0.0001\}$, $c_V \in \{0, 10^{-4}, 0.001\}$. Each point in Fig. 3.7.4 is the mean over the nine combinations of c_D, c_V .

For the measured compute times T_p in Fig. 3.7.4, fitting a power law curve (solid lines in Fig. 3.7.4) using the model compute time $T_M = 0.062 \mu s$ in the expression (3.7.3), we estimate the approximate coupling compute times per edge node $T_C = 0.51, 0.27, 0.29, 0.32, 0.37 \mu s$ for the five staggered patch schemes Spectral, Square-p2, Square-p4, Square-p6, and Square-p8 respectively. The patch coupling via sparse matrix multiplication reduces the coupling compute time T_C by as large as 170 times compared to the direct coupling compute times ($T_C = 0.44, 1.8, 7.6, 24, 63 \mu s$ computed from Fig. 3.7.2). In contrast to the direct patch coupling, via sparse matrix multiplication the coupling compute time $T_C = 0.51 \mu s$ for the Spectral patch scheme is not the smallest among the five patch schemes. The large $T_C = 0.51 \mu s$ for the Spectral patch scheme, compared to $T_C = 0.27 \mu s$ for the Square-p2 patch scheme, comes from the smaller sparsity of the coupling matrix due to the global spectral interpolation, compared to the larger sparsity of the quadratic interpolation of

Figure 3.7.4: Measured compute times T_p , with *patch coupling via sparse matrix multiplication*, for the five staggered patch schemes with different N and n . Solid lines represent expression (3.7.3) using the estimated model compute time $T_M = 0.062 \mu\text{s}$ and the respective estimated coupling compute times T_C for the five patch schemes.

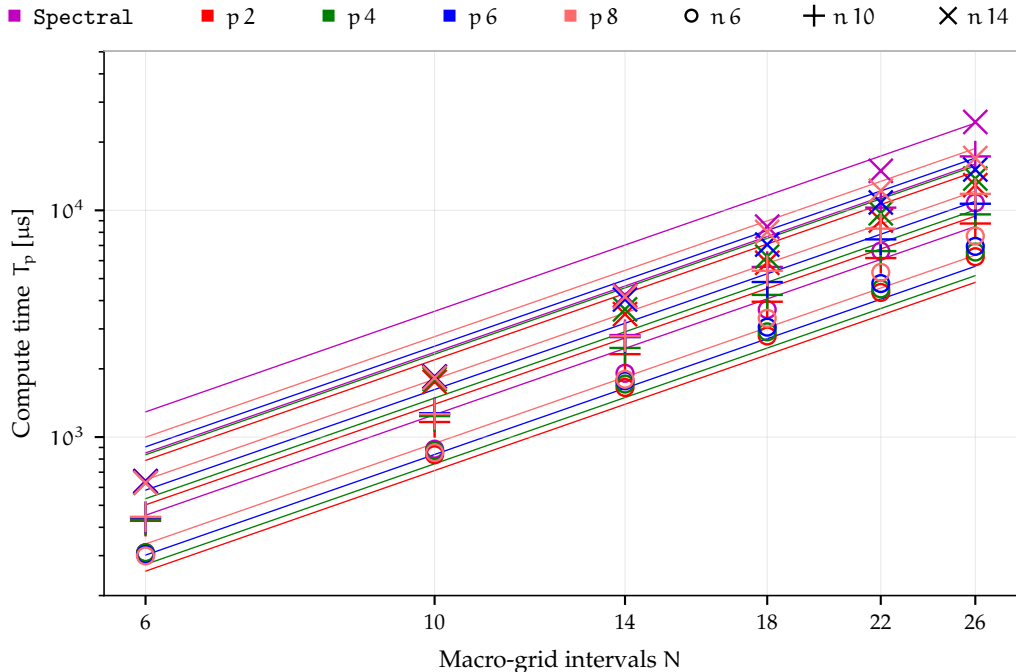
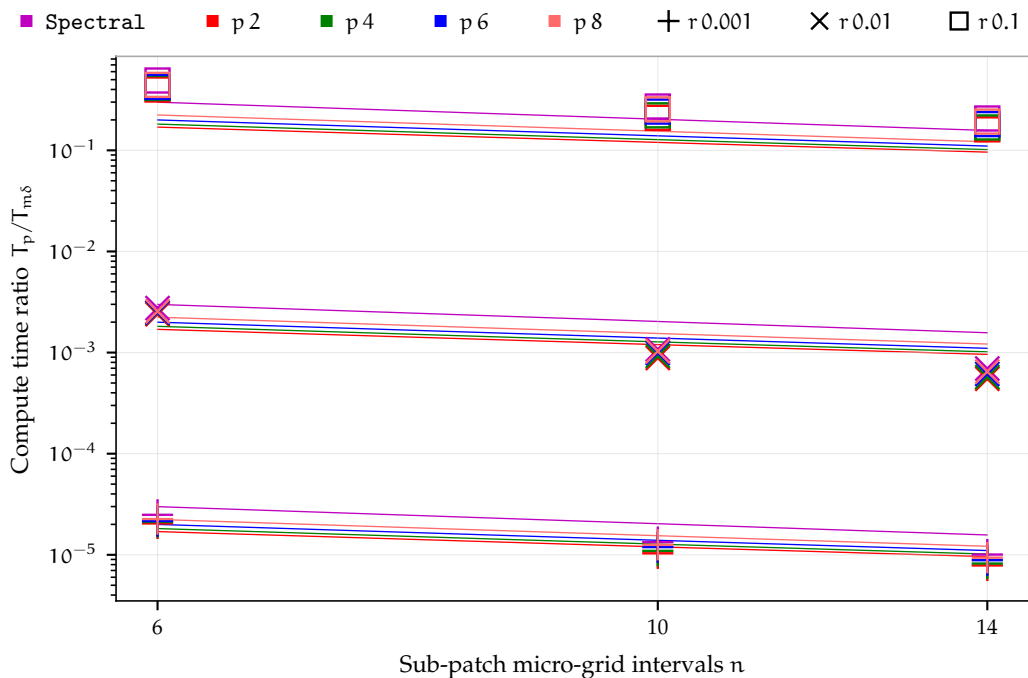


Figure 3.7.5: Ratio $T_p/T_{m\delta}$ of the measured compute time of the staggered patch schemes with *patch coupling via sparse matrix multiplication* to that of the fine-grid full-domain system, for different n , r . Solid lines represent expression (3.7.6) for $T_p/T_{m\delta}$ using the estimated $T_M = 0.062 \mu\text{s}$ and the respective estimated coupling compute times T_C for each patch scheme.



Square-p2 patch scheme. Compared to the patch scheme compute times T_p in Fig. 3.7.2 via direct coupling, the patch scheme compute times T_p in Fig. 3.7.4 with patch coupling via sparse matrix multiplication, do not have strong dependence on the specific patch schemes nor the number of sub-patch intervals n .

Compared to the direct patch coupling, the smaller coupling compute time T_C for the patch coupling via sparse matrix multiplication leads to smaller ratio of the coupling compute time to the model compute time. Using $T_M = 0.062 \mu\text{s}$, the ratio $T_C/T_M = 8.1, 4.3, 4.7, 5.2, 5.9$ for the patch coupling via sparse matrix multiplication, is much smaller compared to the ratio $T_C/T_M = 7, 29, 123, 381, 1020$ of the direct coupling, for the five staggered patch schemes Spectral1, Square-p2, Square-p4, Square-p6, and Square-p8 respectively. As per the expression (3.7.6), this smaller T_C/T_M also results in smaller ratio $T_p/T_{m\delta}$ of the measured compute time of the staggered patch schemes to that of the fine-grid full-domain system.

Figure 3.7.5 plots the ratio $T_p/T_{m\delta}$ of the measured compute time of the staggered patch schemes with *patch coupling via sparse matrix multiplication* to that of the fine-grid full-domain system, for different number of sub-patch micro-grid intervals n and patch scale ratio r . Solid lines represent expression (3.7.6) for $T_p/T_{m\delta}$ using the estimated $T_M = 0.062 \mu\text{s}$ and the respective estimated coupling compute times T_C for each patch scheme. As discussed in the paragraph before (for direct coupling), the computation for fine-grid full-domain system corresponding to a patch grid with small patch scale ratio, requires large memory. Hence, for $r = 0.001$ we compute $T_p/T_{m\delta}$ (plusses in Fig. 3.7.5) using the measured T_p of the patch schemes and the estimated $T_{m\delta}$ of the full-domain system using the expression (3.7.6). The measured compute time ratio $T_p/T_{m\delta}$ reasonably closely follow the trend of the expression (3.7.6) (solid lines) for the five staggered patch schemes (through the respective T_C). Compared to the compute time ratios $T_p/T_{m\delta}$ in Fig. 3.7.3 via direct coupling, the compute time ratios $T_p/T_{m\delta}$ in Fig. 3.7.5 with patch coupling via sparse matrix multiplication, do not have strong dependence on the specific patch schemes nor the patch scale ratio r . Compared to the compute time ratios $T_p/T_{m\delta}$ in Fig. 3.7.3 via direct coupling, the *patch coupling via sparse matrix multiplication (for fixed grid)* reduces the compute time ratios $T_p/T_{m\delta}$ by about ten times as in Fig. 3.7.5, especially for higher order patch schemes.

Figure 3.7.5 shows that despite $T_C/T_M > 1$ (between five and eight), for sufficiently small patch scale ratio $r = 0.01, 0.001$ the compute time ratios $T_p/T_{m\delta}$ are about $10^{-3}, 10^{-5}$. That is, for small patch scale ratios, the compute times of the multi-scale patch schemes are about 1000 to 10^5 times smaller than the corresponding fine-grid full-domain micro-scale system. A reduction of

10^5 times is equivalent to reducing the computation time from one week to six seconds.

The demonstrated large computational savings of the patch schemes via compute time ratio $T_p/T_{m\delta}$ in Figs. 3.7.3 and 3.7.5 are for the case of large ratio of coupling compute time to model compute time, $T_C/T_M > 1$. Even larger computational savings of the patch schemes are possible with smaller ratio T_C/T_M in (3.7.6) in the following cases.

1. Compared to the current simple general linear wave, modelling more complex physical process (non-hydrostatic nonlinear waves, sediment transport, etc) with a larger model compute time T_M , leads to smaller T_C/T_M in (3.7.6), and hence smaller $T_p/T_{m\delta}$, that is larger computational savings of the staggered patch schemes.
2. Compared to the current computationally not efficient implementation (with a focus on exploratory studies), a more efficient implementation (via code specialisation, code optimisation, parallelisation, etc) with a smaller coupling compute time T_C , leads to smaller T_C/T_M in (3.7.6), and larger computational savings of the staggered patch schemes. As discussed in the article by Bunder et al. (2020, p. 962), in a parallel implementation, patch schemes require lesser communication across the compute nodes compared to the fine-grid grid full-domain system, due shorter messages across the patches in different compute nodes. This lesser communication across the compute nodes, leads to additional computational savings of the parallel implementation of the staggered patch schemes compared to the current serial implementation.

3.7.5 Staggered patch scheme time simulations of general linear waves

This subsection demonstrates the effectiveness of the patch schemes via time simulation of the general linear waves for two example cases. This subsection, first compares the time simulation of a patch scheme with that of the fine-grid full-domain system for a simple progressive wave, second demonstrates the patch scheme time simulation for a moving Gaussian hump. Via random perturbation to the initial condition, this section also demonstrates the robustness of the patch schemes.

For the patch scheme time simulations, first we need to choose a suitable ODE integrator and an appropriate error tolerance. We use the package

Figure 3.7.6: Maximum of the mean of Spectral the patch scheme simulation errors ϵ_t^h , ϵ_t^u , ϵ_t^v (discrepancy between the solutions of the patch scheme and the full-domain system at patch centres, defined in (3.7.9)) over the time $t \in (2\pi, 14\pi)$ for a simple progressive wave (3.7.8).

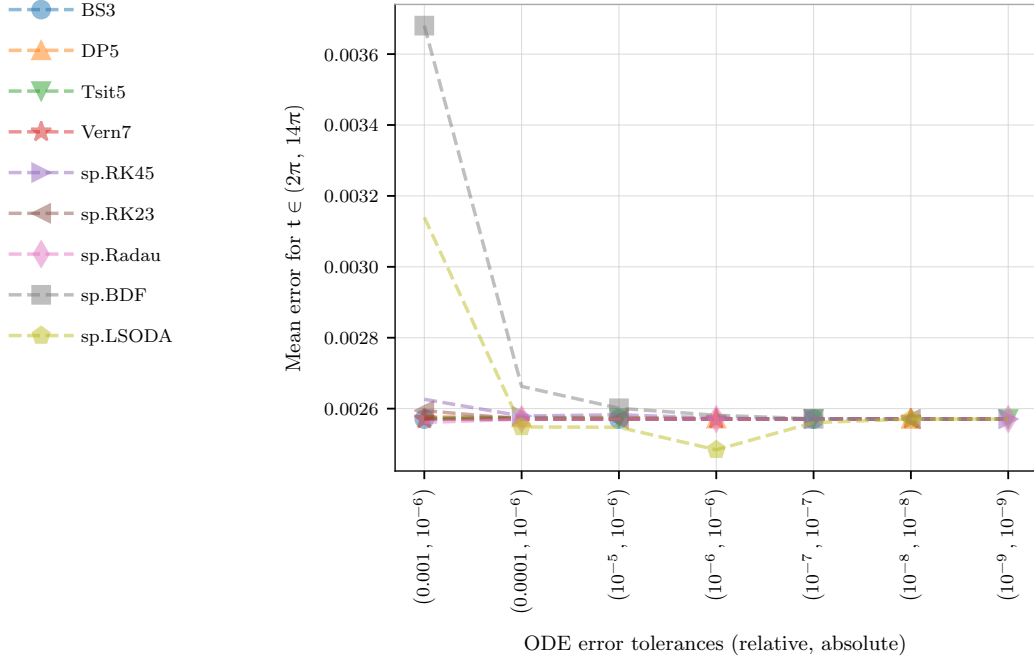


Figure 3.7.7: Computation time of the Spectral the patch scheme simulation for time $t = 0$ to 14π for a simple progressive wave (3.7.8), for the nine ODE integrators and for different relative and absolute error tolerances.

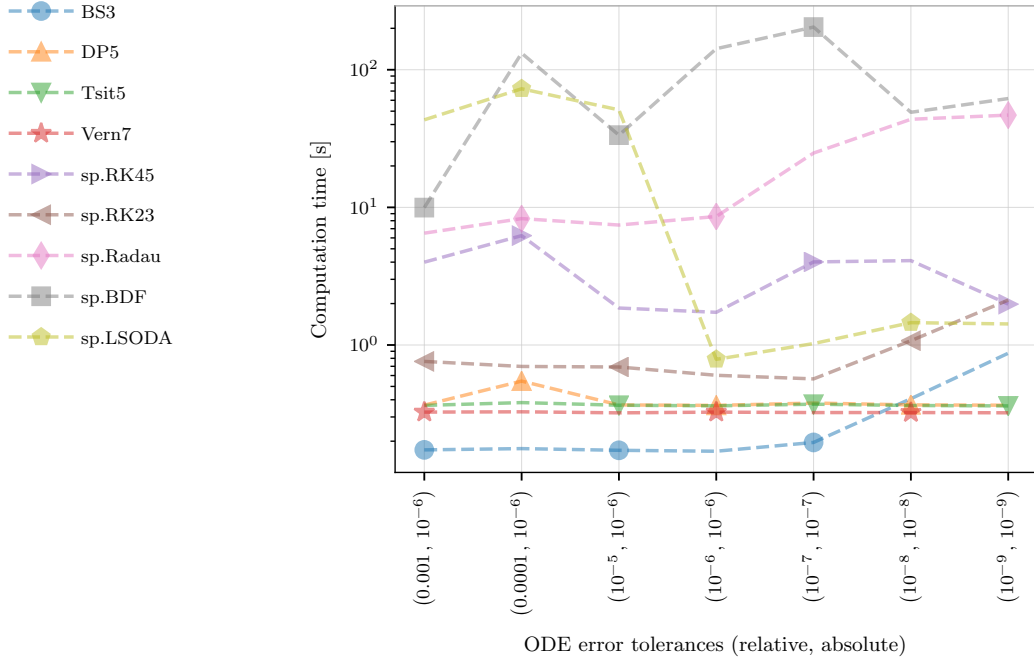
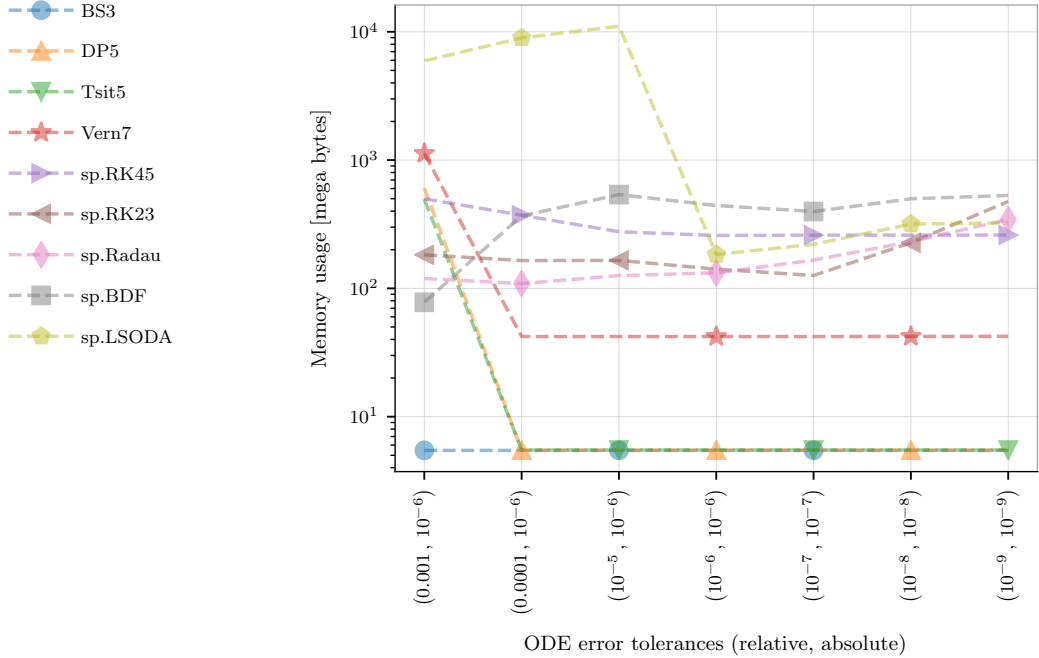


Figure 3.7.8: Memory usage of the Spectral the patch scheme simulation for time $t = 0$ to 14π for a simple progressive wave (3.7.8), for the nine ODE integrators and for different relative and absolute error tolerances.



DifferentialEquations.jl by Rackauckas and Nie (2017), a suite of various ODE integrators in Julia programming language, to study various ODE integrators suitable for the staggered patch scheme. Specifically, we study nine ODE integrators for the suitability for the patch schemes, namely BS3, DP5, Tsit5, Vern7, sp.RK45, sp.RK23, sp.Radau, sp.BDF and sp.LSODA as detailed in DifferentialEquations.jl (2021). Equations (3.7.9) define the relative simulation errors $\epsilon_t^h, \epsilon_t^u, \epsilon_t^v$ to quantify the discrepancy between the solutions of the patch scheme and the full-domain system at patch centres. We compute the maximum of the mean of Spectral the patch scheme simulation errors $\epsilon_t^h, \epsilon_t^u, \epsilon_t^v$ over the time $t \in (2\pi, 14\pi)$ for a simple progressive wave (3.7.8) using the nine ODE integrators. Figures 3.7.6 to 3.7.8 plot the maximum of the mean simulation error, compute time for the ODE integration for $t = 0$ to 14π , and the memory used in the ODE integration, respectively, for the nine ODE integrators and for different relative and absolute error tolerances. The compute times in this subsection are measured on a custom assembled liquid-cooled workstation with Intel i7-6900k processor and 64GB DDR4 RAM. Considering the simulation error, compute time and the memory usage in Figs. 3.7.6 to 3.7.8, we choose

the BS3 ODE integrator and the relative and absolute error tolerances of 10^{-3} and 10^{-6} respectively, for all the time simulations in this thesis. The BS3 is a lower oder Bogacki–Shampine 3/2 method (Bogacki and L. Shampine 1989; L. F. Shampine and Reichelt 1997), similar to the ode23 of MATLAB (DifferentialEquations.jl 2021).

Figures 3.7.9 to 3.7.11 compare the time evolution of the general linear progressive wave with the coefficients $c_D = 10^{-6}$ and $c_V = 10^{-4}$, using the Square-p4 staggered patch scheme (3.1.4) (colour-coded ribbons) with that using the fine-grid full-domain system (3.7.2) (grey mesh), for height h , velocities u, v respectively. The time simulation of both the patch scheme and the fine-grid full-domain system are for the initial condition (plotted in top left of Figs. 3.7.9 to 3.7.11) of the simple progressive wave

$$h_0(x, y) = 0.2 + 0.1 \sin(x + y), \quad (3.7.8a)$$

$$u_0(x, y) = 0.3 + (0.1/\sqrt{2}) \sin(x + y), \quad (3.7.8b)$$

$$v_0(x, y) = 0. \quad (3.7.8c)$$

The Square-p4 patch scheme (fourth order polynomial interpolation patch coupling) in Figs. 3.7.9 to 3.7.11 use $N = 14$ macro-grid intervals, $n = 6$ sub-patch micro-grid intervals, and the patch scale ratio $r = 0.01$. The fine-grid full-domain micro-scale system (3.7.2) (grey mesh) uses same grid interval as the sub-patch micro-grid interval $\delta = 2Lr/(Nn) = 2\pi/4200 \approx 0.0015$. But the grey mesh of full-domain system plots only 29 of the 4201 grid lines, skipping many lines for visual clarity. The colour-coded ribbons of the patch scheme in Fig. 3.7.9 consist of all the lines (along the coordinate axes x and y) passing through all the h nodes within all the patches; similarly Figs. 3.7.10 and 3.7.11 for u, v nodes within all the patches respectively. The color ribbons in y direction for u in Fig. 3.7.10 are narrower due to the smaller number of u nodes in x direction in the h - and v -centred patches (e.g., Fig. 2.2.5a). Similarly the color ribbons in x direction for v in Fig. 3.7.11 are narrower due to the smaller number of v nodes in y direction in the h - and u -centred patches (e.g., Fig. 2.2.5a). Whereas the true patch scale ratio is $r = 0.01$, the patches are enlarged for visual clarity so that the ribbons appear wider.

Figures 3.7.9 to 3.7.11, plot time evolution of h, u, v from $t = 0$ to 10π (five full cycles). In Figs. 3.7.9 to 3.7.11, the solutions $h/u/v$ of fine-grid full-domain micro-scale system are linearly interpolated using nearest four values to the centres of the respective $h/u/v$ -centred patches, illustrated by small black circles. The large circles are the patch scheme solution $h/u/v$. Figures 3.7.9 to 3.7.11 visually show that the discrepancy between the patch scheme and fine-grid full-domain system is small, non concentric black

Figure 3.7.9: Progressive wave time evolution (height h) with initial condition (3.7.8), using Square-p4 patch scheme (3.1.4) (colour-coded ribbons, with $N = 14$, $n = 6$, and $r = 0.01$) agrees closely with that of the fine-grid full-domain system (3.7.2) (grey mesh). Black circles on h -centred patches show small discrepancy. The patch scheme compute time is 1300 times smaller.

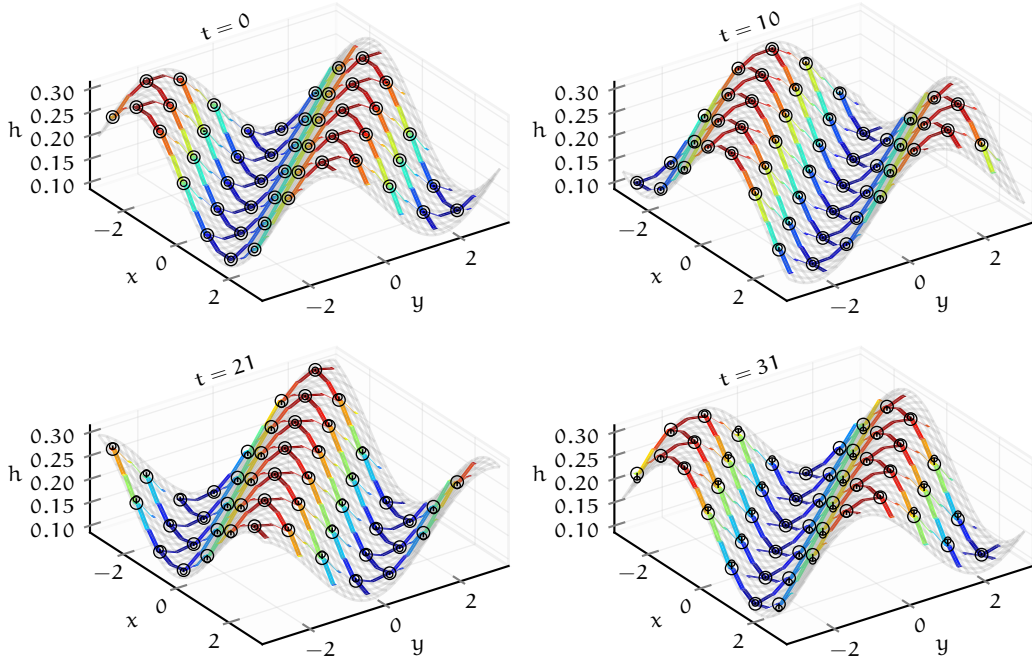


Figure 3.7.10: Progressive wave time evolution (velocity u) for the patch scheme simulation detailed in Fig. 3.7.9. Black circles on u -centred patches show that the discrepancy is small.

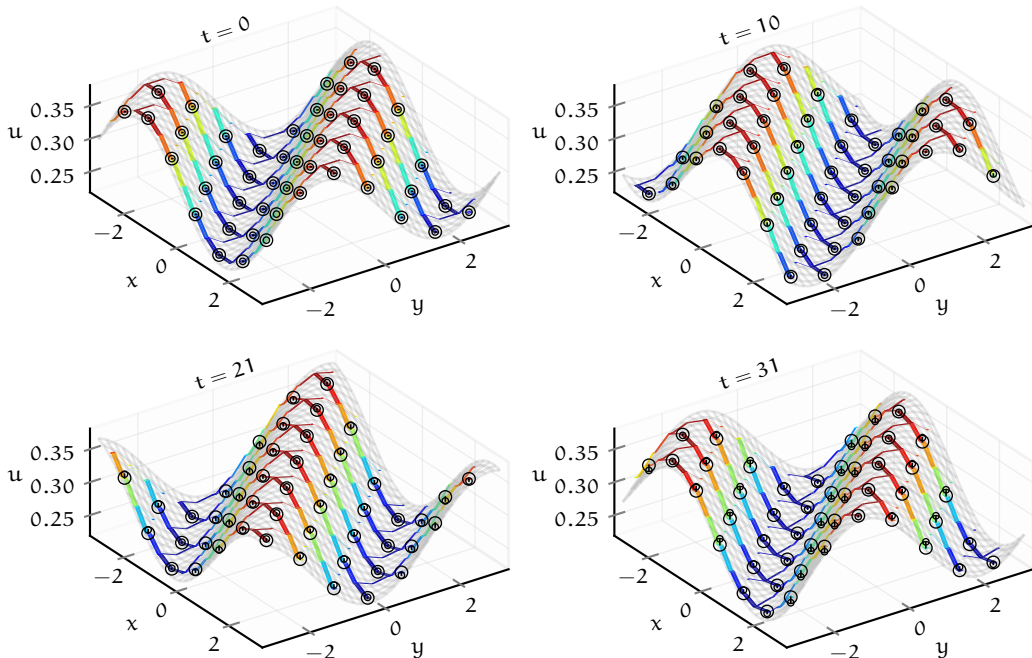
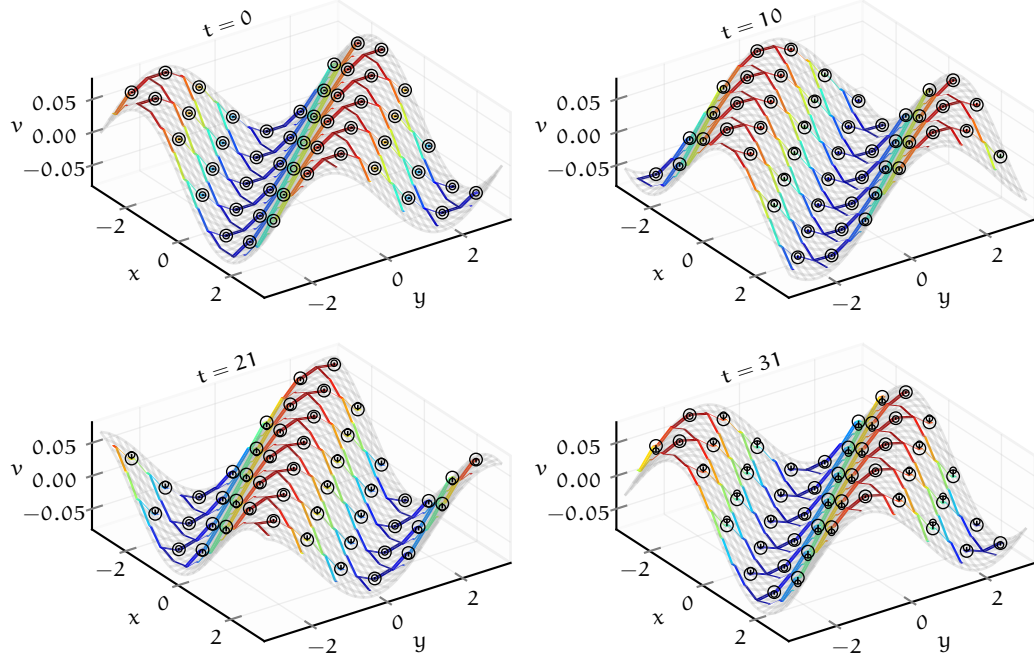


Figure 3.7.11: Progressive wave time evolution (velocity v) for the patch scheme simulation detailed in Fig. 3.7.9. Black circles on v -centred patches show that the discrepancy is small.



circles are offset only slightly. Despite being small, the increasing error (distance between centres of non concentric black circles) with increasing time is due to the accumulation of the ODE integrator error.

Figures 3.7.9 to 3.7.11 qualitatively show that the progressive wave time simulation using Square-p4 patch scheme (3.1.4) (colour-coded ribbons) with $N = 14$, $n = 6$, and $r = 0.01$, agrees closely with that of the fine-grid full-domain system (3.7.2) (grey mesh). Next, we aim to numerically assess how well the time simulations of the full-domain system compare with that of the other patch schemes, and that of the patch schemes with different number of macro-grid grid intervals N and patch scale ratio r . To numerically quantify the discrepancy, we compute the solutions $h_{m\delta}^c, u_{m\delta}^c, v_{m\delta}^c$ of the fine-grid full-domain micro-scale system, at the positions of the respective $h/u/v$ -centred patches, by a bilinear interpolation using the four nearest full-domain node values. For example, Figs. 3.7.9 to 3.7.11 indicate the full-domain solutions at the respective patch centres as small black circles. In terms of the full-domain solutions $h_{m\delta}^c, u_{m\delta}^c, v_{m\delta}^c$ and the patch centre values h_p^c, u_p^c, v_p^c of a patch scheme (large black circles Figs. 3.7.9

Figure 3.7.12: Convergence of patch scheme time solution h in terms of simulation error $\epsilon_{2\pi}^h$ of (3.7.9a) for progressive wave time evolution with initial condition (3.7.8). Solid lines are the power law curve fit $\tilde{\epsilon}_{2\pi}^h = 0.83 \cdot (0.71 \cdot \Delta)^p$.

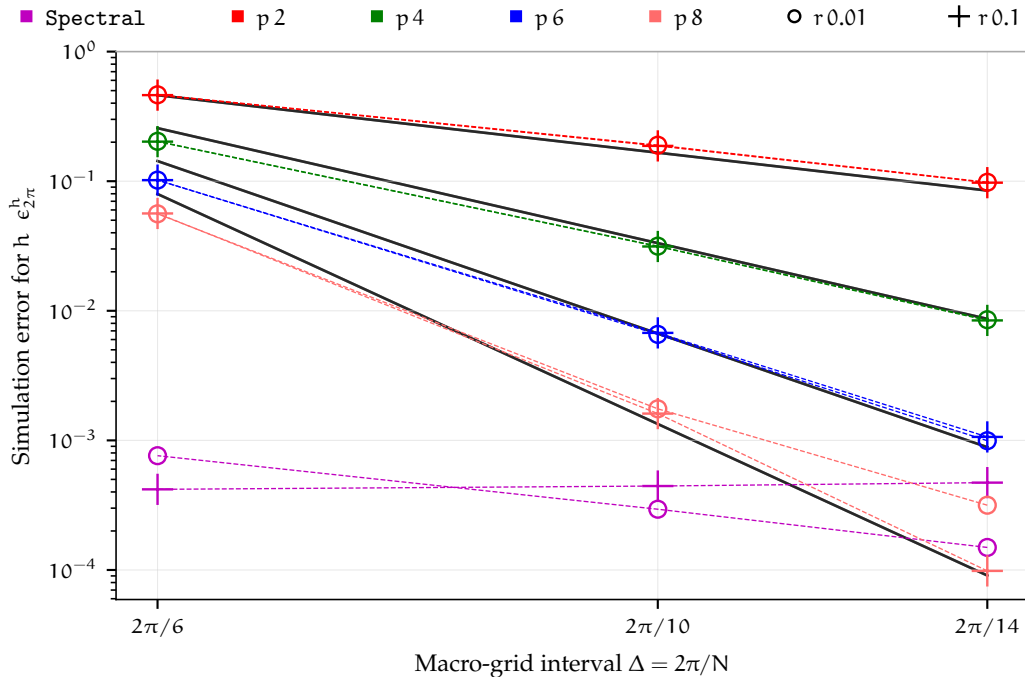


Figure 3.7.13: Convergence of patch scheme time solution u in terms of simulation error $\epsilon_{2\pi}^u$ of (3.7.9b) for progressive wave time evolution with initial condition (3.7.8). Solid lines are the power law curve fit $\tilde{\epsilon}_{2\pi}^u = 0.65 \cdot (0.65 \cdot \Delta)^p$.

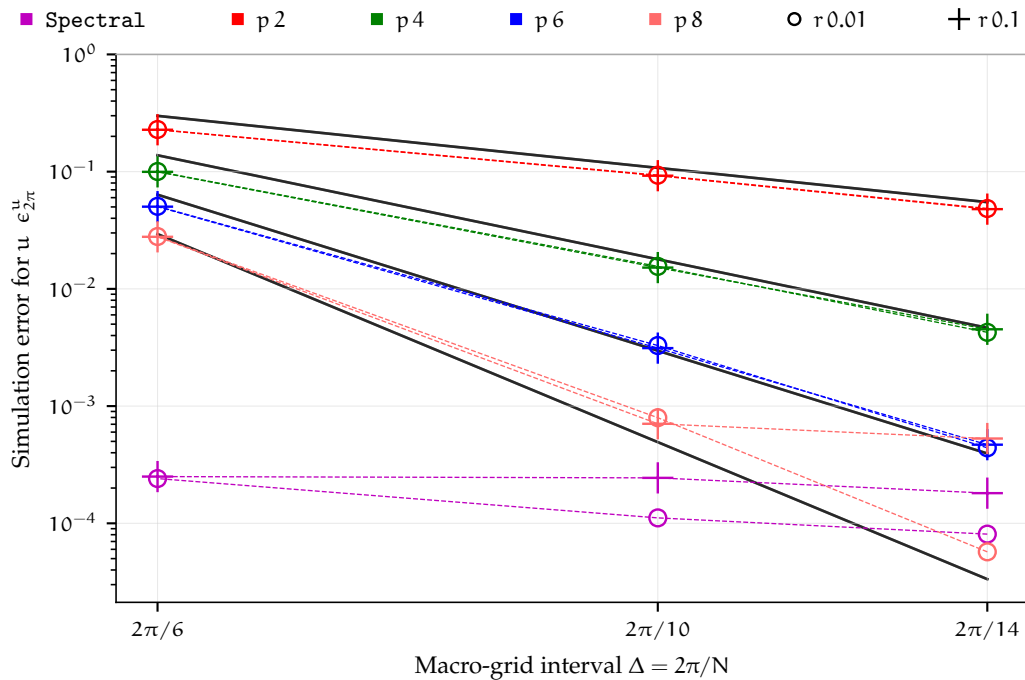
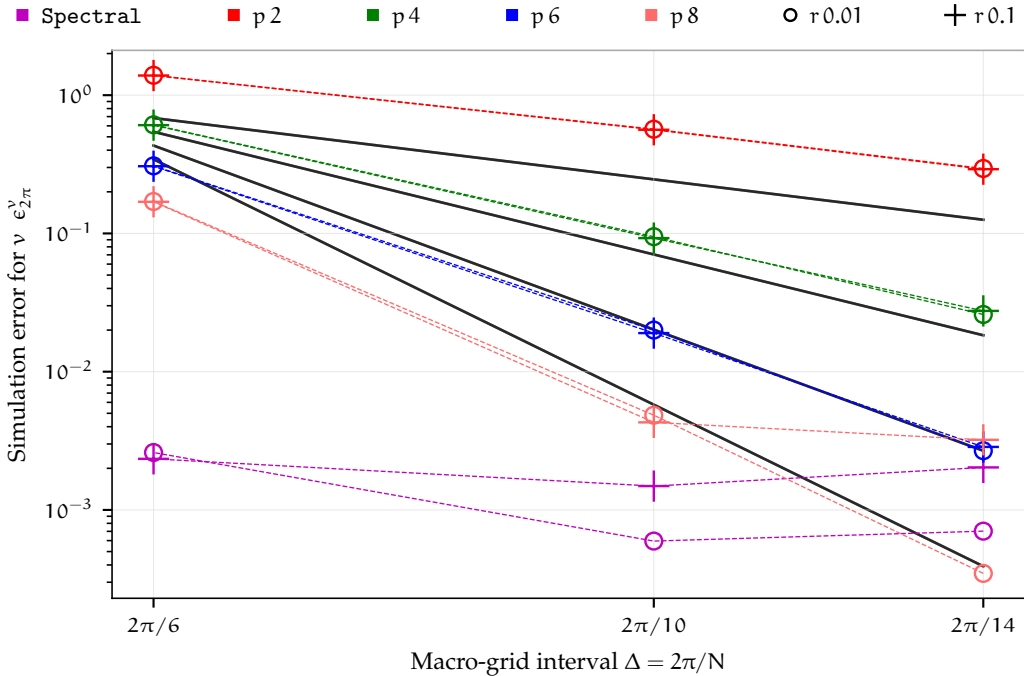


Figure 3.7.14: Convergence of patch scheme time solution v in terms of simulation error $\epsilon_{2\pi}^v$ of (3.7.9c) for progressive wave time evolution with initial condition (3.7.8). Solid lines are the power law curve fit $\tilde{\epsilon}_{2\pi}^v = 0.86 \cdot (0.85 \cdot \Delta)^p$.



to 3.7.11), we define the relative *simulation errors* at time t as

$$\epsilon_t^h = \|h_{m\delta}^c - h_p^c\| / \|h_{m\delta}^c\|, \quad (3.7.9a)$$

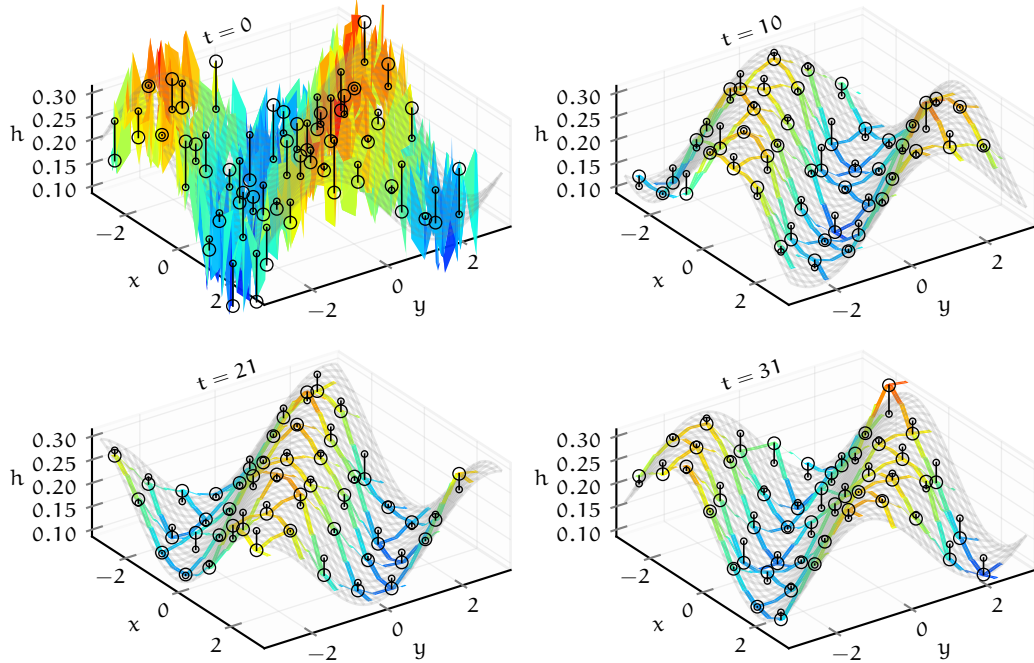
$$\epsilon_t^u = \|u_{m\delta}^c - u_p^c\| / \|u_{m\delta}^c\|, \quad (3.7.9b)$$

$$\epsilon_t^v = \|v_{m\delta}^c - v_p^c\| / \|v_{m\delta}^c\|. \quad (3.7.9c)$$

The norm in the simulation errors (3.7.9) is the Euclidean norm over all solutions at all the patch centres of the same node type. For example, for a patch grid with 14×14 macro-grid intervals ($N = 14$), there are $7 \times 7 = 49$ macro-cells with each cell containing three patches namely h -, u - and v -centred patches. Thus, for $N = 14$, there are 49 values of the full-domain solutions $h_{m\delta}^c$, $u_{m\delta}^c$, $v_{m\delta}^c$ and the patch centre values h_p^c , u_p^c , v_p^c ; hence the norm in (3.7.9) is the Euclidean norm of the 49-element vectors.

Figures 3.7.12 to 3.7.14, the *solution convergence plots*, plot the simulation errors $\epsilon_{2\pi}^h$, $\epsilon_{2\pi}^u$, $\epsilon_{2\pi}^v$ at $t = 2\pi$ for progressive wave time evolution with initial condition (3.7.8), for the general linear wave with the coefficients $c_D = 10^{-6}$ and $c_V = 10^{-4}$. Figures 3.7.12 to 3.7.14 show that the simulation errors are small, about 10^{-3} for the Spectral patch scheme, without any dependence

Figure 3.7.15: Square-p4 patch scheme simulation of height h (colour-coded ribbons, with $N = 14$, $n = 6$, and $r = 0.01$) of the progressive wave with initial uniform random perturbation (3.7.10) (compare with Fig. 3.7.9 without the perturbation). Patch scheme robustly simulate the emergent the macro-scale solution by rapidly dissipating the random perturbation.



on the macro-grid interval Δ . That is, the Spectral patch scheme macro-scale solutions agree closely with the macro-scale solutions of the fine-grid full-domain system, without any dependence on the macro-grid interval Δ , just as the eigenvalue convergence in §3.6.1. The solution convergence plots Figs. 3.7.12 to 3.7.14 also show that the simulation errors converge to zero for the polynomial patch schemes (Square-p2, Square-p4, Square-p6, Square-p8) with decreasing macro-grid interval Δ (increasing N). That is, the polynomial patch scheme macro-scale solutions converge to the macro-scale solutions of the fine-grid full-domain system with decreasing macro-grid intervals Δ (increasing N), just as the eigenvalue convergence in §3.6.2. Thus, the staggered patch schemes accurately simulate the macro-scale general linear waves.

Figure 3.7.15 plots the Square-p4 patch scheme simulation of height h (colour-coded ribbons, with $N = 14$, $n = 6$, and $r = 0.01$) of the progressive

wave for the initial condition with uniform random perturbation

$$h_0(x, y) = 0.2 + 0.1 [\sin(x + y) + 1.2 \text{rand}(-1, 1)], \quad (3.7.10a)$$

$$u_0(x, y) = 0.3 + (0.1/\sqrt{2})[\sin(x + y) + 1.2 \text{rand}(-1, 1)], \quad (3.7.10b)$$

$$v_0(x, y) = 0, \quad (3.7.10c)$$

where $\text{rand}(-1, 1)$ generates a pseudo random number within $[-1, 1]$ via Mersenne Twister algorithm. The initial condition (3.7.10) is same as the initial condition (3.7.8) except the added uniform random perturbation for h_0 and u_0 . Figure 3.7.9 plots the corresponding patch scheme simulation without the random perturbation. Figure 3.7.15 shows that the *patch scheme robustly simulates the emergent macro-scale solution* where the viscous diffusion rapidly dissipates the random perturbation (micro-scale waves). That is, the slow manifold of the patch scheme solution space is exponentially attracting.

For the time simulation in Figs. 3.7.9 to 3.7.11 from $t = 0$ to 10π , Table 3.7.1 lists the total compute times of the fine-grid full-domain system and that of the five staggered patch schemes. The compute times in this subsection are measured on a custom assembled liquid-cooled workstation with Intel i7-6900k processor and 64GB DDR4 RAM. The total function calls by the BS3 ODE integrator to evaluate the derivative of the state vector for the fine-grid full-domain system and that of the patch schemes are similar (i.e., within 10%). But the ratio of the total compute time of the full-domain system to that of a patch schemes, *compute time gain*, in Table 3.7.1 show that on average the *patch scheme compute time is 1300 times smaller*. This computational savings by three orders of magnitude based on the total compute time also agree with the computational savings in terms of the compute time per iteration for $r = 0.01$ in Fig. 3.7.5 (crosses).

As another example we demonstrate a higher order polynomial patch scheme simulation on a finer patch grid for a moving Gaussian hump in x direction with the initial condition

$$h_0(x, y) = 0.2 + 0.4 \exp[-(x + 1.5)^2/(2 \cdot 0.5)^2 - y^2/(2 \cdot 1.1)^2], \quad (3.7.11a)$$

$$u_0(x, y) = 0.3 + 0.5 \exp[-(x + 1.5)^2/(2 \cdot 0.5)^2 - y^2/(2 \cdot 1.1)^2], \quad (3.7.11b)$$

$$v_0(x, y) = 0. \quad (3.7.11c)$$

For the general linear wave with coefficients $c_D = 10^{-6}$ and $c_V = 10^{-4}$, Figs. 3.7.16 to 3.7.18 show the time simulation of a moving Gaussian hump in x direction with the initial condition (3.7.11), using Square-p8 patch scheme with $N = 22$, $n = 6$, and $r = 0.001$. For the patch scheme simulation in Figs. 3.7.16 to 3.7.18 from $t = 0$ to 10π , the total compute time is 85 m. For

Figure 3.7.16: Time simulation (height h) of a moving Gaussian hump in x direction with initial condition (3.7.11), using Square-p8 patch scheme with $N = 22$, $n = 6$, and $r = 0.001$. Patch scheme compute time is 85 m; for the full-domain simulation with the same grid resolution the estimated compute time is about 16 years (i.e., 10^5 times larger, from Fig. 3.7.5).

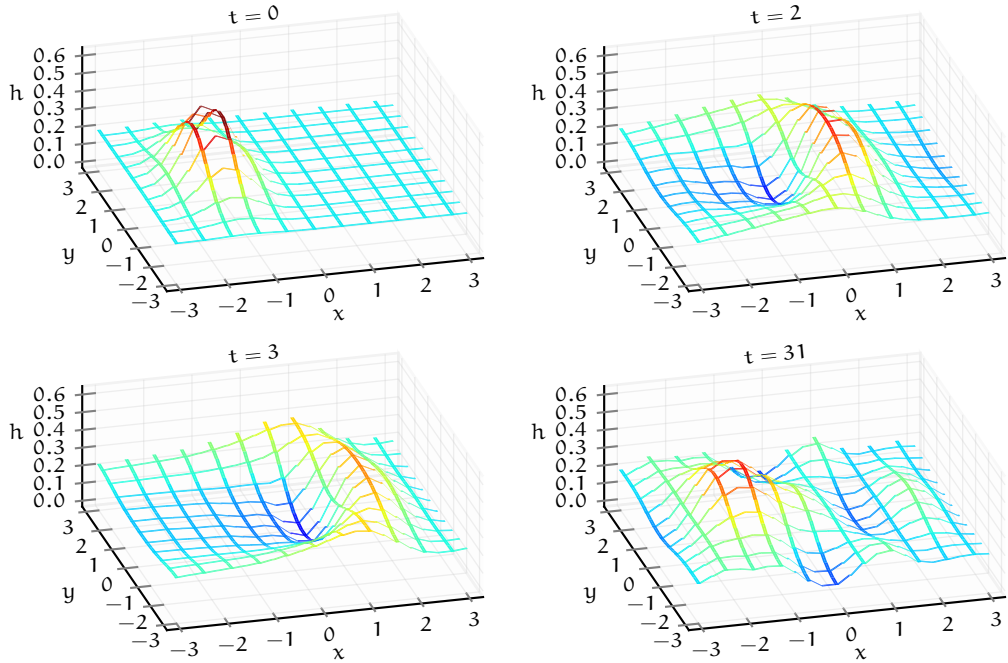


Figure 3.7.17: Time simulation (velocity u) of a moving Gaussian hump for the patch scheme simulation detailed in Fig. 3.7.16.

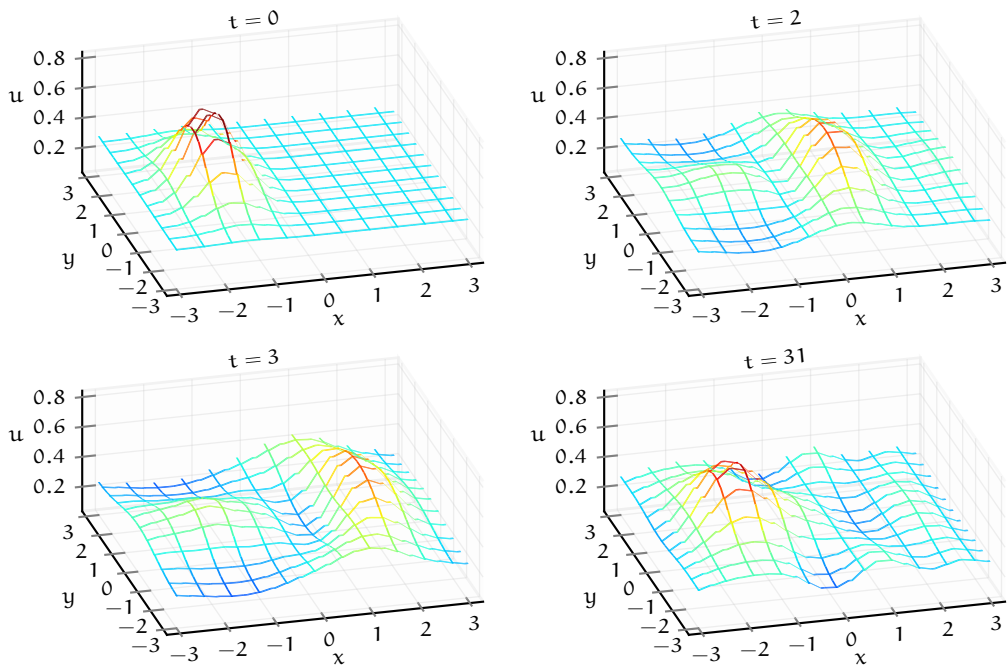


Figure 3.7.18: Time simulation (velocity v) of a moving Gaussian hump for the patch scheme simulation detailed in Fig. 3.7.16.

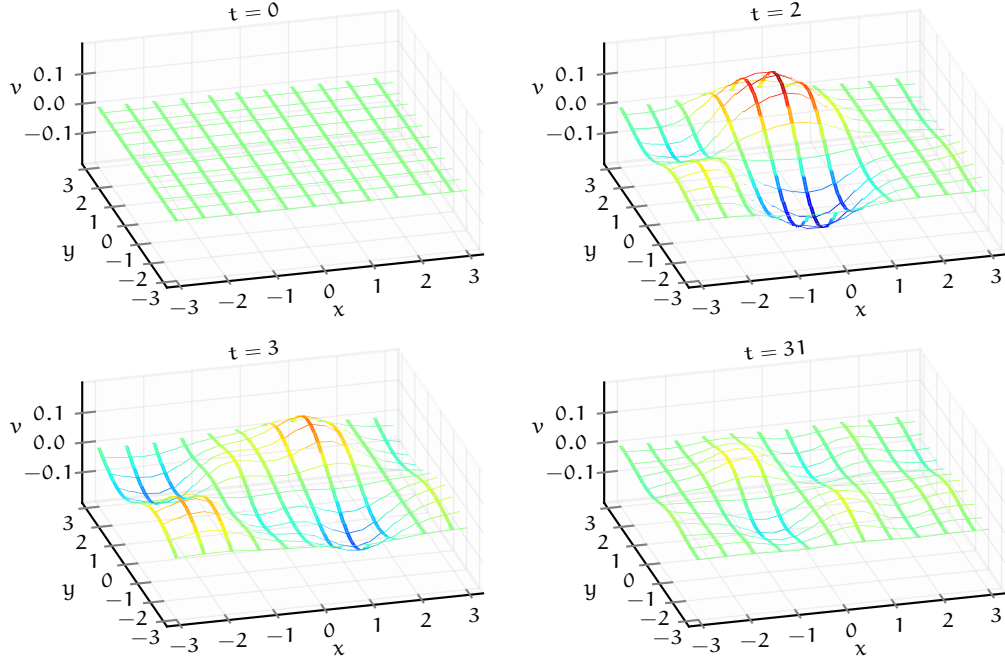


Figure 3.7.19: Time simulation (height h) of a moving Gaussian hump in x direction with initial random perturbation (3.7.12), using Square-p8 patch scheme with $N = 22$, $n = 6$, and $r = 0.001$ (compare with Fig. 3.7.16 without the perturbation). Patch scheme robustly simulates the emergent macro-scale solution.

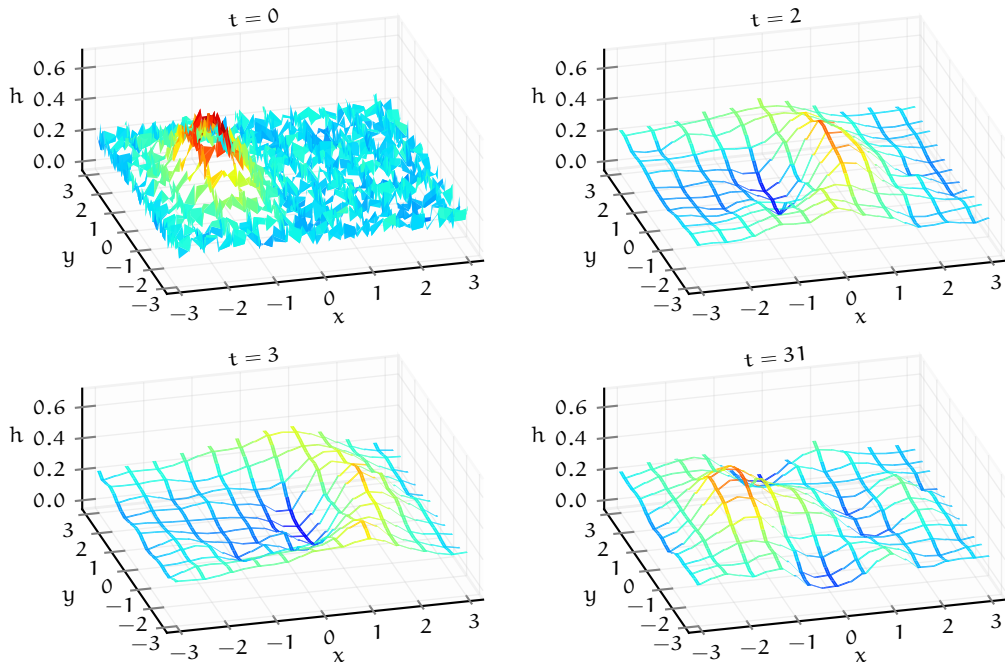


Table 3.7.1: Total compute times in minutes for the progressive wave time simulation from $t = 0$ to 10π (e.g., Figs. 3.7.9 to 3.7.11) with initial condition (3.7.8). Patch schemes use $N = 14$, $n = 6$, and $r = 0.01$. The fine-grid full-domain system has the same grid interval as the sub-patch micro-grid interval δ . Ratio of the total compute time of the full-domain system to that of a patch schemes, *compute time gain*, is on average about 1300.

	Full-domain	Spectral	p2	p4	p6	p8
Total compute time [m]	2925 (48.75 h)	2.10	1.82	2.22	2.18	2.24
Total function calls	45261	39432	40599	40503	40482	40437
Compute time gain (full-domain / patch)	–	1390	1610	1316	1343	1305

the corresponding fine-grid full-domain system (i.e., with the same grid interval as the sub-patch micro-grid interval δ) the compute time is about 10^5 times larger than the patch scheme (the plus marker in Fig. 3.7.5 for $n = 6$ and $r = 0.001$). That is, for the similar grid resolution and accuracy as in Figs. 3.7.16 to 3.7.18, the estimated compute time of a full-domain simulation is about 16 years, but the measured patch scheme compute time is only 85 m.

Figure 3.7.19 plots the Square-p8 patch scheme simulation of height h (with $N = 14$, $n = 6$, and $r = 0.01$) of a moving Gaussian hump in x direction with uniform random perturbation

$$h_0(x, y) = 0.2 + 0.4 \exp[-(x + 1.5)^2/(2 \cdot 0.5)^2 - y^2/(2 \cdot 1.1)^2] + 0.08 \text{rand}(-1, 1), \quad (3.7.12a)$$

$$u_0(x, y) = 0.3 + 0.5 \exp[-(x + 1.5)^2/(2 \cdot 0.5)^2 - y^2/(2 \cdot 1.1)^2] + 0.1 \text{rand}(-1, 1), \quad (3.7.12b)$$

$$v_0(x, y) = 0. \quad (3.7.12c)$$

where $\text{rand}(-1, 1)$ generates a pseudo random number within $[-1, 1]$ via Mersenne Twister algorithm. The initial condition (3.7.12) is same as the initial condition (3.7.11) except the added uniform random perturbation for h_0 and u_0 . Figure 3.7.16 plots the corresponding patch scheme simulation without the random perturbation. Figure 3.7.19 shows that the patch scheme robustly simulate the emergent the macro-scale solution for a moving Gaussian hump.

Thus, the staggered patch schemes accurately simulate the macro-scale general linear waves, with large computational savings such as 10^5 times smaller compute times compared to the fine-grid full-domain system.

Chapter 4

Patch schemes accurately simulate viscous shallow water flows

4.1 Introduction

This chapter shows that the staggered patch schemes accurately simulate the macro-scale dynamics of the viscous shallow water flow, using the PDEs derived by Roberts and Li (2006) as the micro-scale system within the patches. Roberts and Li (2006) derive the comprehensive viscous shallow water PDEs in terms of the depth-averaged variables, but without actually depth averaging the PDEs. Instead, from the full incompressible 3D Navier–Stokes equation, they derive the 2D shallow water flow using the centre manifold theory, only in terms of the depth-averaged variables. Roberts and Li (2006) demonstrate the utility of the viscous shallow water flow by simulating various thin-fluid flows such as drop formation on cylindrical fibres, wave transitions, three-dimensional instabilities, Faraday waves, viscous hydraulic jumps, flow vortices in a compound channel and flow down and up a step.

Section 4.1.1 non-dimensionalises the viscous shallow water PDEs and the boundary conditions derived by Roberts and Li (2006) using a reference length in terms of domain size as opposed to the characteristic height used by Roberts and Li (2006). Section 4.1.2 derives a discrete full-domain micro-scale system corresponding to the viscous shallow water PDEs of §4.1.1. Throughout this chapter, we use this full-domain micro-scale system as reference to assess various characteristics (accuracy, stability, consistency, etc.) of the multiscale staggered patch schemes we develop. Section 4.1.3 chooses a set of values for the non-dimensional parameters towards exploration of patch schemes for viscous shallow water PDEs.

[Section 4.2](#) shows that the developed five staggered patch schemes are accurate for the viscous shallow water flows. [Section 4.2](#) establishes the accuracy of the staggered patch schemes globally (as opposed one initial condition) by comparing the eigenvalues of the staggered patch schemes with the eigenvalues of fine- and coarse-grid full-domain micro-scale system. The eigenvalue analysis for accuracy in [§4.2](#) is done for a representative subset of the system parameters and grid parameters. [Section 4.5](#) on the consistency of the patch schemes establish the accuracy over a wider range of parameters. [Section 4.2](#) derives the eigenvalues of the viscous shallow water PDEs, full-domain micro-scale system, and that of the staggered patch schemes. [Section 4.2](#) also illustrates the structure of the eigenvalues in complex plane and explains the corresponding dynamical modes via eigenvector illustrations.

Despite the attractive characteristics, if the staggered patch schemes are very sensitive to numerical roundoff errors, they will not be suitable for practical numerical simulations using finite precision floating point representations. From both qualitative arguments and quantitative evidence, [§4.3](#) shows that staggered the patch schemes are not sensitive to numerical roundoff errors for the viscous shallow water flow. The quantitative evidence in [§4.3](#) come from comparing the eigenvalues of analytical Jacobian and numerical Jacobians of a patch scheme.

In contrast to the general linear wave in [Chapter 3](#), the viscous shallow water flow has inherent physical instability. Hence, a good patch scheme must be stable as well as unstable in correspondence to the the physical system depending upon the system parameters (Reynolds number Re , mean flow height h_M, u_M, v_M), but *without any additional/artificial instability*. So, [§4.4](#) shows that with appropriate patch grid the staggered patch schemes are not artificially unstable for a wide range of system parameters by comparing the eigenvalues of the patch schemes with those of the full-domain micro-scale system and the PDEs.

[Section 4.5](#) shows that the staggered patch schemes are consistent with the given micro-scale system (within the patches). [Section 4.5](#) establish the consistency of the patch schemes for the viscous shallow water flow by comparing the macro-scale eigenvalues of the patch scheme with the corresponding eigenvalues of the full-domain micro-scale system for increasingly finer patch grids. [Section 4.5.1](#) shows that the Spectral patch scheme is uniformly consistent without any strong dependence on the macro-grid interval Δ . [Section 4.5.2](#) shows that the polynomial patch schemes are consistent to the order of the polynomial interpolation with decreasing macro-grid interval Δ .

Almost all the key studies in this chapter are performed for a range of

parameters but keeping the horizontal mean velocity $v_M = 0$. That is, most results in this chapter correspond to flow angle $\alpha = \arctan(v_M/u_M) = 0$ for the resultant mean velocity $q = \sqrt{u_M^2 + v_M^2}$ of the macro-scale waves, where the velocities are $u_M = q \cos(\alpha)$ and $v_M = q \sin(\alpha)$. [Section 4.6](#) validates that assumption, by showing that the variation of the patch scheme eigenvalue errors (discrepancy between the patch scheme and full-domain system) are negligible with varying flow angles α , or equivalently for varying coordinate frame orientation. That is, [§4.6](#) shows that staggered patch schemes are frame invariant.

[Section 4.7](#) quantifies and demonstrates the large computational savings of the staggered patch schemes for the viscous shallow water flow. [Section 4.7.1](#) shows the computational savings of the 2D staggered patch schemes theoretically in terms of the ratio of the space over which the patch schemes and the full-domain system computes. [Section 4.7.1](#) shows the computational savings of the patch schemes in terms of the ratio of the number of state variables for which the patch schemes and the full-domain system computes. [Section 4.7.2](#) demonstrates the computational savings of the 2D staggered patch schemes by measuring the actual time taken to compute the time derivative of the state vector (one time iteration) using a specific implementation. [Section 4.7.4](#) demonstrates the accuracy and the effectiveness of the staggered patch schemes by numerically simulating a localised nearly discontinuous macro-scale viscous roll waves (e.g., Balmforth and Mandre [2004](#)) emerging from the initial condition of a simple progressive wave within the small sparsely located patches. [Section 4.7.5](#) establishes the accuracy of the staggered patch scheme simulations more quantitatively and explain some subtle details of the practical issues in the patch scheme simulations.

4.1.1 Non-dimensionalise viscous shallow water PDEs to keep same domain size

In deriving the viscous shallow water PDEs which we use as the micro-scale system for patch scheme, Roberts and Li ([2006](#)) non-dimensionalise the space (lengths) by characteristic water height H , which leads to different non-dimensional domain sizes for different characteristic water heights. For example, with their non-dimensionalisation $x' = x/H$, the dimensional domain $x \in [0, L]$ with different characteristic heights $H \in \{H_1, H_2, H_3\}$ correspond to different non-dimensional domains $[0, L/H_1]$, $[0, L/H_2]$, $[0, L/H_3]$. We want to explore patch schemes for the same dimensional domain size with different characteristic water height H , and in doing so *we also want*

to keep the non-dimensional domain size the same, to reuse some of the patch scheme computations. Hence, this §4.1.1 non-dimensionalises the 2D space by a reference length $L/(2\pi)$; that is, $x' = 2\pi x/L$, $y' = 2\pi y/L$ so that the dimensional square domain $[0, L] \times [0, L]$ correspond to the non-dimensional square domain $[0, L'] \times [0, L']$ where $L' = 2\pi$ irrespective of the height H .

The non-dimensional comprehensive viscous shallow water PDEs (64)–(66) in the article by Roberts and Li (2006, pp.56–57) are, omitting the over bar for dependent variables and using primes for the non-dimensional dependent and independent variables $h^\dagger, u^\dagger, v^\dagger, x^\dagger, y^\dagger, t^\dagger$,

$$\frac{\partial h^\dagger}{\partial t^\dagger} \approx -\frac{\partial h^\dagger u^\dagger}{\partial x^\dagger} - \frac{\partial h^\dagger v^\dagger}{\partial y^\dagger}, \quad (4.1.1a)$$

$$\begin{aligned} \text{Re} \frac{\partial u^\dagger}{\partial t^\dagger} &\approx -\frac{\pi^2}{4} \frac{u^\dagger}{h^\dagger} + \frac{\pi^2}{12} \left[\text{Gr} \left(g_x + g_n \frac{\partial h^\dagger}{\partial x^\dagger} \right) + \text{We} \left(\frac{\partial^3 h^\dagger}{\partial x^\dagger} + \frac{\partial^3 h^\dagger}{\partial x^\dagger \partial y^\dagger} \right) \right] \\ &\quad - \text{Re} \left[1.5041 u^\dagger \frac{\partial u^\dagger}{\partial x^\dagger} + 1.3464 v^\dagger \frac{\partial u^\dagger}{\partial y^\dagger} + 0.1577 u^\dagger \frac{\partial v^\dagger}{\partial y^\dagger} + 0.1483 \frac{u^\dagger}{h^\dagger} \left(u^\dagger \frac{\partial h^\dagger}{\partial x^\dagger} + v^\dagger \frac{\partial h^\dagger}{\partial y^\dagger} \right) \right] \\ &\quad + 4.0930 \frac{\partial^2 u^\dagger}{\partial x^\dagger} + \frac{\partial^2 u^\dagger}{\partial y^\dagger} + 3.0930 \frac{\partial^2 v^\dagger}{\partial x^\dagger \partial y^\dagger} + 4.8333 \frac{1}{h^\dagger} \frac{\partial h^\dagger}{\partial x^\dagger} \frac{\partial u^\dagger}{\partial x^\dagger} + \frac{1}{h^\dagger} \frac{\partial h^\dagger}{\partial y^\dagger} \frac{\partial u^\dagger}{\partial y^\dagger} \\ &\quad + 1.9167 \frac{1}{h^\dagger} \frac{\partial h^\dagger}{\partial x^\dagger} \frac{\partial v^\dagger}{\partial y^\dagger} + 1.9167 \frac{1}{h^\dagger} \frac{\partial h^\dagger}{\partial y^\dagger} \frac{\partial v^\dagger}{\partial x^\dagger} \\ &\quad - \left[0.5033 \frac{1}{h^\dagger} \left(\frac{\partial h^\dagger}{\partial y^\dagger} \right)^2 + \frac{1}{2h^\dagger} \frac{\partial^2 h^\dagger}{\partial y^\dagger} - 0.1061 \frac{1}{h^\dagger} \left(\frac{\partial h^\dagger}{\partial x^\dagger} \right)^2 + 0.5834 \frac{1}{h^\dagger} \frac{\partial^2 h^\dagger}{\partial x^\dagger} \right] u^\dagger \\ &\quad + \left[0.6094 \frac{1}{h^\dagger} \frac{\partial h^\dagger}{\partial x^\dagger} \frac{\partial h^\dagger}{\partial y^\dagger} - 0.0833 \frac{1}{h^\dagger} \frac{\partial^2 h^\dagger}{\partial x^\dagger \partial y^\dagger} \right] v^\dagger, \end{aligned} \quad (4.1.1b)$$

$$\begin{aligned} \text{Re} \frac{\partial v^\dagger}{\partial t^\dagger} &\approx -\frac{\pi^2}{4} \frac{v^\dagger}{h^\dagger} + \frac{\pi^2}{12} \left[\text{Gr} \left(g_y + g_n \frac{\partial h^\dagger}{\partial y^\dagger} \right) + \text{We} \left(\frac{\partial^3 h^\dagger}{\partial y^\dagger} + \frac{\partial^3 h^\dagger}{\partial y^\dagger \partial x^\dagger} \right) \right] \\ &\quad - \text{Re} \left[1.5041 v^\dagger \frac{\partial v^\dagger}{\partial y^\dagger} + 1.3464 u^\dagger \frac{\partial v^\dagger}{\partial x^\dagger} + 0.1577 v^\dagger \frac{\partial u^\dagger}{\partial x^\dagger} + 0.1483 \frac{v^\dagger}{h^\dagger} \left(u^\dagger \frac{\partial h^\dagger}{\partial x^\dagger} + v^\dagger \frac{\partial h^\dagger}{\partial y^\dagger} \right) \right] \\ &\quad + 4.0930 \frac{\partial^2 v^\dagger}{\partial y^\dagger} + \frac{\partial^2 v^\dagger}{\partial x^\dagger} + 3.0930 \frac{\partial^2 u^\dagger}{\partial x^\dagger \partial y^\dagger} + 4.8333 \frac{1}{h^\dagger} \frac{\partial h^\dagger}{\partial y^\dagger} \frac{\partial v^\dagger}{\partial y^\dagger} + \frac{1}{h^\dagger} \frac{\partial h^\dagger}{\partial x^\dagger} \frac{\partial v^\dagger}{\partial x^\dagger} \\ &\quad + 1.9167 \frac{1}{h^\dagger} \frac{\partial h^\dagger}{\partial x^\dagger} \frac{\partial u^\dagger}{\partial y^\dagger} + 1.9167 \frac{1}{h^\dagger} \frac{\partial h^\dagger}{\partial y^\dagger} \frac{\partial u^\dagger}{\partial x^\dagger} \\ &\quad - \left[0.5033 \frac{1}{h^\dagger} \left(\frac{\partial h^\dagger}{\partial x^\dagger} \right)^2 + \frac{1}{2h^\dagger} \frac{\partial^2 h^\dagger}{\partial x^\dagger} - 0.1061 \frac{1}{h^\dagger} \left(\frac{\partial h^\dagger}{\partial y^\dagger} \right)^2 + 0.5834 \frac{1}{h^\dagger} \frac{\partial^2 h^\dagger}{\partial y^\dagger} \right] v^\dagger \\ &\quad + \left[0.6094 \frac{1}{h^\dagger} \frac{\partial h^\dagger}{\partial x^\dagger} \frac{\partial h^\dagger}{\partial y^\dagger} - 0.0833 \frac{1}{h^\dagger} \frac{\partial^2 h^\dagger}{\partial x^\dagger \partial y^\dagger} \right] u^\dagger. \end{aligned} \quad (4.1.1c)$$

In the *comprehensive* viscous shallow water PDEs (4.1.1), the non-dimensional parameters *Reynolds number* $Re = \rho U H / \mu$, *Gravity number* $Gr = g \rho H^2 / (\mu U)$ and *Weber number* $We = \sigma / (\mu U)$ are in terms of the following dimensional quantities: gravitational acceleration g ; density of water ρ ; characteristic mean velocity U ; characteristic mean height H kinematic viscosity ν ; surface tension σ . The grey coloured terms in (4.1.1) that are less significant compared to the other terms.

The viscous shallow water PDEs (4.1.1) are written in the bed-attached local coordinate system with the bed in x , y -plane and height h perpendicular to the bed. The constants $g_x = \sin(\theta)$, $g_n = -\cos(\theta)$ are components of the unit vector of gravitational acceleration, where θ is the bed inclination angle relative to the local horizontal plane of earth. That is, theta is the angle of rotation of the bed about the y axis (positive for downward slopping bed along x axis). Throughout this thesis, we assume $g_y = 0$, that is there is no lateral inclination of the bed (no rotation about x axis). For example, for the horizontal flat bed, $\theta = 0$, hence $g_x = 0$ and $g_n = -1$.

[5] TODO. Justify why they are small

The only difference between the non-dimensionalisation of Roberts and Li (2006) in the non-dimensional comprehensive viscous shallow water PDEs (4.1.1) and the non-dimensionalisation we aim to, is that their non-dimensionalisation of lengths are

$$x = x^\dagger H, \quad y = y^\dagger H, \quad h = h^\dagger H, \quad (4.1.2a)$$

$$\Rightarrow \frac{\partial^n}{\partial x^n} = (1/H)^n \frac{\partial^n}{\partial x^\dagger^n}, \quad \frac{\partial^n}{\partial y^n} = (1/H)^n \frac{\partial^n}{\partial y^\dagger^n}, \quad (4.1.2b)$$

which is different from our non-dimensionalisation of lengths, using primes for non-dimensional parameters

$$x = x' L / (2\pi), \quad y = y' L / (2\pi), \quad h = h' L / (2\pi), \quad (4.1.3a)$$

$$\Rightarrow \frac{\partial^n}{\partial x^n} = (2\pi/L)^n \frac{\partial^n}{\partial x'^n}, \quad \frac{\partial^n}{\partial y^n} = (2\pi/L)^n \frac{\partial^n}{\partial y'^n}. \quad (4.1.3b)$$

So, for converting the non-dimensional comprehensive viscous shallow water PDEs (4.1.1) to use our non-dimensionalisation, we do the following substitutions to the PDEs (4.1.1), which we get by equating the dimensional quantities in the two different non-dimensionalisations (4.1.2) and (4.1.3)

$$\begin{aligned} x^\dagger &= x' L / (2\pi H), & y^\dagger &= y' L / (2\pi H), & h^\dagger &= h' L / (2\pi H), \\ \Rightarrow \frac{\partial^n}{\partial x^\dagger^n} &= (2\pi H/L)^n \frac{\partial^n}{\partial x'^n}, & \frac{\partial^n}{\partial y^\dagger^n} &= (2\pi H/L)^n \frac{\partial^n}{\partial y'^n}. \end{aligned}$$

Using the definition of the characteristic mean non-dimensional height

$h_M = 2\pi H/L$, the substitutions become

$$x^\dagger = x'/h_M, \quad y^\dagger = y'/h_M, \quad h^\dagger = h'/h_M, \quad (4.1.4a)$$

$$\Rightarrow \frac{\partial^n}{\partial x^{\dagger n}} = h_M^n \frac{\partial^n}{\partial x'^n}, \quad \frac{\partial^n}{\partial y^{\dagger n}} = h_M^n \frac{\partial^n}{\partial y'^n}. \quad (4.1.4b)$$

After substituting (4.1.4) into the non-dimensional comprehensive viscous shallow water PDEs (4.1.1), we get the non-dimensional *comprehensive viscous shallow water* PDEs with our non-dimensionalisation of space by the reference length $L/(2\pi)$ as

$$\frac{1}{h_M} \frac{\partial h'}{\partial t'} \approx - \frac{\partial h' u'}{\partial x'} - \frac{\partial h' v'}{\partial y'}, \quad (4.1.5a)$$

$$\begin{aligned} \text{Re} \frac{\partial u'}{\partial t'} &\approx -\frac{\pi^2 h_M^2}{4} \frac{u'}{h'^2} + \frac{\pi^2}{12} \left[\text{Gr} \left(g_x + g_n \frac{\partial h'}{\partial x'} \right) + \text{We} h_M^2 \left(\frac{\partial^3 h'}{\partial x'^3} + \frac{\partial^3 h'}{\partial x' \partial y'^2} \right) \right] \\ &\quad - \text{Re} h_M \left[1.5041 u' \frac{\partial u'}{\partial x'} + 1.3464 v' \frac{\partial u'}{\partial y'} + 0.1577 u' \frac{\partial v'}{\partial y'} + 0.1483 \frac{u'}{h'} \left(u' \frac{\partial h'}{\partial x'} + v' \frac{\partial h'}{\partial y'} \right) \right] \\ &\quad + h_M^2 \left[4.0930 \frac{\partial^2 u'}{\partial x'^2} + \frac{\partial^2 u'}{\partial y'^2} + 3.0930 \frac{\partial^2 v'}{\partial x' \partial y'} + 4.8333 \frac{1}{h'} \frac{\partial h'}{\partial x'} \frac{\partial u'}{\partial x'} + \frac{1}{h'} \frac{\partial h'}{\partial y'} \frac{\partial u'}{\partial y'} \right] \\ &\quad + h_M^2 \left[1.9167 \frac{1}{h'} \frac{\partial h'}{\partial x'} \frac{\partial v'}{\partial y'} + 1.9167 \frac{1}{h'} \frac{\partial h'}{\partial y'} \frac{\partial v'}{\partial x'} \right] \\ &\quad - h_M^2 \left[0.5033 \frac{1}{h'^2} \left(\frac{\partial h'}{\partial y'} \right)^2 + \frac{1}{2h'} \frac{\partial^2 h'}{\partial y'^2} - 0.1061 \frac{1}{h'^2} \left(\frac{\partial h'}{\partial x'} \right)^2 + 0.5834 \frac{1}{h'} \frac{\partial^2 h'}{\partial x'^2} \right] u' \\ &\quad + h_M^2 \left[0.6094 \frac{1}{h'^2} \frac{\partial h'}{\partial x'} \frac{\partial h'}{\partial y'} - 0.0833 \frac{1}{h'} \frac{\partial^2 h'}{\partial x' \partial y'} \right] v', \end{aligned} \quad (4.1.5b)$$

$$\begin{aligned} \text{Re} \frac{\partial v'}{\partial t'} &\approx -\frac{\pi^2 h_M^2}{4} \frac{v'}{h'^2} + \frac{\pi^2}{12} \left[\text{Gr} \left(g_y + g_n \frac{\partial h'}{\partial y'} \right) + \text{We} h_M^2 \left(\frac{\partial^3 h'}{\partial y'^3} + \frac{\partial^3 h'}{\partial y' \partial x'^2} \right) \right] \\ &\quad - \text{Re} h_M \left[1.5041 v' \frac{\partial v'}{\partial y'} + 1.3464 u' \frac{\partial v'}{\partial x'} + 0.1577 v' \frac{\partial u'}{\partial x'} + 0.1483 \frac{v'}{h'} \left(u' \frac{\partial h'}{\partial x'} + v' \frac{\partial h'}{\partial y'} \right) \right] \\ &\quad + h_M^2 \left[4.0930 \frac{\partial^2 v'}{\partial y'^2} + \frac{\partial^2 v'}{\partial x'^2} + 3.0930 \frac{\partial^2 u'}{\partial x' \partial y'} + 4.8333 \frac{1}{h'} \frac{\partial h'}{\partial y'} \frac{\partial v'}{\partial y'} + \frac{1}{h'} \frac{\partial h'}{\partial x'} \frac{\partial v'}{\partial x'} \right] \\ &\quad + h_M^2 \left[1.9167 \frac{1}{h'} \frac{\partial h'}{\partial x'} \frac{\partial u'}{\partial y'} + 1.9167 \frac{1}{h'} \frac{\partial h'}{\partial y'} \frac{\partial u'}{\partial x'} \right] \\ &\quad - h_M^2 \left[0.5033 \frac{1}{h'^2} \left(\frac{\partial h'}{\partial x'} \right)^2 + \frac{1}{2h'} \frac{\partial^2 h'}{\partial x'^2} - 0.1061 \frac{1}{h'^2} \left(\frac{\partial h'}{\partial y'} \right)^2 + 0.5834 \frac{1}{h'} \frac{\partial^2 h'}{\partial y'^2} \right] v' \\ &\quad + h_M^2 \left[0.6094 \frac{1}{h'^2} \frac{\partial h'}{\partial x'} \frac{\partial h'}{\partial y'} - 0.0833 \frac{1}{h'} \frac{\partial^2 h'}{\partial x' \partial y'} \right] u', \end{aligned} \quad (4.1.5c)$$

where neglecting the grey coloured terms that are less significant compared to the other terms, gives the *simplified* viscous shallow water PDEs.

Dropping grey coloured terms and the primes, using “=” instead of “ \approx ”, in the PDEs (4.1.5) and dividing both sides of the momentum equations (4.1.5b) and (4.1.5c) by h_M^2 , we get the non-dimensional *simplified viscous shallow water* PDEs, with our non-dimensionalisation of space by the reference length $L/(2\pi)$ as

$$\frac{1}{h_M} \frac{\partial h}{\partial t} = -\frac{\partial hu}{\partial x} - \frac{\partial hv}{\partial y}, \quad (4.1.6a)$$

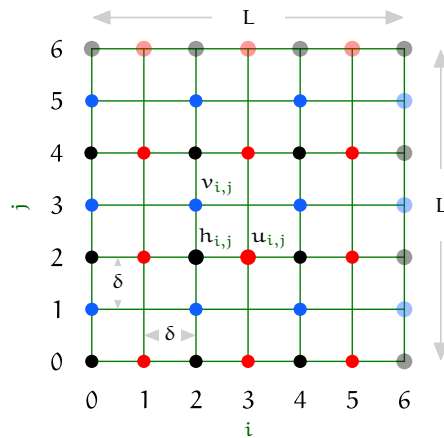
$$\begin{aligned} \frac{Re}{h_M^2} \frac{\partial u}{\partial t} &= -\frac{\pi^2}{4} \frac{u}{h^2} + \frac{\pi^2 Re}{12 h_M^2} \left[g_x + g_n \frac{\partial h}{\partial x} \right] \\ &\quad - \frac{Re}{h_M} \left[1.5041u \frac{\partial u}{\partial x} + 1.3464v \frac{\partial u}{\partial y} + 0.1577u \frac{\partial v}{\partial y} \right] \\ &\quad + 4.0930 \frac{\partial^2 u}{\partial x^2} + \frac{\partial^2 u}{\partial y^2} + 3.0930 \frac{\partial^2 v}{\partial x \partial y}, \end{aligned} \quad (4.1.6b)$$

$$\begin{aligned} \frac{Re}{h_M^2} \frac{\partial v}{\partial t} &= -\frac{\pi^2}{4} \frac{v}{h^2} + \frac{\pi^2 Re}{12 h_M^2} \left[g_y + g_n \frac{\partial h}{\partial y} \right] \\ &\quad - \frac{Re}{h_M} \left[1.5041v \frac{\partial v}{\partial y} + 1.3464u \frac{\partial v}{\partial x} + 0.1577v \frac{\partial u}{\partial x} \right] \\ &\quad + 4.0930 \frac{\partial^2 v}{\partial y^2} + \frac{\partial^2 v}{\partial x^2} + 3.0930 \frac{\partial^2 u}{\partial x \partial y}, \end{aligned} \quad (4.1.6c)$$

where dividing the dimensional velocities by the characteristic inviscid wave velocity $U = \sqrt{gH}$ gives the non-dimensional velocities u, v , and dividing the dimensional spatial variables by reference length $L/(2\pi)$ gives the non-dimensional spatial variables x, y, h . The PDE (4.1.6a) represents the mass conservation, and the PDEs (4.1.6b) and (4.1.6c) represent the momentum equations in the x and y directions respectively.

We use the simplified viscous shallow water PDEs (4.1.6) as the micro-scale system within the patches in our study of the staggered patch schemes. In all our further use “viscous shallow water PDEs” means these *simplified* viscous shallow water PDEs (4.1.6). For the viscous shallow water PDEs (4.1.6), throughout this chapter, we consider the boundary conditions that the three fields h, u and v are L -periodic in both x and y .

Figure 4.1.1: Same as Fig. 2.2.1 for general linear wave. Schematic of the full-domain micro-scale *staggered grid* where variables are simulated only on staggered/alternating discrete points (*nodes*, e.g., \bullet h , \bullet u and \bullet v nodes). There are $n = 6$ grid intervals in the green grid, both in x and y directions. Transparent filled circles on the boundaries indicate the discrete n -periodic boundary conditions in both i and j .



4.1.2 Full-domain micro-scale system and staggered patch schemes for viscous shallow water PDEs

This subsection derives a discrete full-domain micro-scale system corresponding to the viscous shallow water PDEs (4.1.6). Throughout this chapter, we use this full-domain micro-scale system as reference to assess various characteristics (accuracy, stability, consistency, etc.) of the multiscale staggered patch schemes we develop.

Approximating the spatial derivatives in the viscous shallow water PDEs (4.1.6) by central finite differences on the nodes of the full-domain staggered grid (filled solid circles in Fig. 4.1.1), gives the *full-domain micro-scale system* (4.1.11) corresponding to the viscous shallow water PDEs (4.1.6). To compute the “missing” values on the staggered grid (e.g., $h_{3,1}$, $v_{3,1}$, and $v_{3,3}$ are missing in Fig. 4.1.1), the full-domain micro-scale system (4.1.11) uses averaging the nearest values. The following listing gives some examples.

- For computing $[dh/dt]_{i,j}$ at the locations of $h_{i,j}$, the discretisation in

conservative form in (4.1.11a),

$$\begin{aligned} [\partial(hu)/\partial x]_{i,j} &\approx [h_{i+1,j}u_{i+1,j} - h_{i-1,j}u_{i-1,j}] / (2\delta) \\ &= [(h_{i,j} + h_{i+2,j})u_{i+1,j} - (h_{i-2,j} + h_{i,j})u_{i-1,j}] / (4\delta), \end{aligned} \quad (4.1.7)$$

computes the missing h values at the locations of the u nodes on the staggered grid (e.g., missing $h_{3,2}, h_{1,2}$ in Fig. 4.1.1), by averaging over the two neighbouring values $h_{i+1,j} = (h_{i,j} + h_{i+2,j})/2$, and $h_{i-1,j} = (h_{i-2,j} + h_{i,j})/2$.

- For computing $[du/dt]_{i,j}$ at the locations of $u_{i,j}$, the discretisation in (4.1.11b),

$$\begin{aligned} [1.3464v\partial u/\partial y]_{i,j} &\approx 1.3464v_{i,j} \frac{u_{i,j+2} - u_{i,j-2}}{4\delta} \\ &= 1.3464 \frac{(v_{i-1,j-1} + v_{i+1,j-1} + v_{i-1,j+1} + v_{i+1,j+1})}{4} \frac{u_{i,j+2} - u_{i,j-2}}{4\delta}, \end{aligned} \quad (4.1.8)$$

computes the missing v values at the locations of the u nodes on the staggered grid (e.g., missing $v_{3,2}$ in Fig. 4.1.1) by averaging over the four neighbouring v values.

- For computing $[du/dt]_{i,j}$ at the locations of $u_{i,j}$, the discretisation in (4.1.11b),

$$\begin{aligned} 0.1577u\partial v/\partial y &\approx 0.1577u_{i,j}(v_{i,j+1} - v_{i,j-1})/(2\delta) \\ &= 0.1577u_{i,j} \frac{(v_{i-1,j+1} + v_{i+1,j+1})/2 - (v_{i-1,j-1} + v_{i+1,j-1})/2}{2\delta}. \end{aligned} \quad (4.1.9)$$

computes the missing v values at the locations of the empty node on the staggered grid (e.g., missing $v_{3,3}, v_{3,1}$ in Fig. 4.1.1) by averaging.

- For computing $[dv/dt]_{i,j}$ at the locations of $v_{i,j}$, the discretisation in (4.1.11c),

$$\begin{aligned} \left[3.0930 \frac{\partial^2 u}{\partial x \partial y} \right]_{i,j} &\approx 3.093 \frac{(\partial u/\partial x)_{i,j+1} - (\partial u/\partial x)_{i,j-1}}{2\delta} \\ &= 3.093 \frac{(u_{i+1,j+1} - u_{i-1,j+1})/(2\delta) - (u_{i+1,j-1} - u_{i-1,j-1})/(2\delta)}{2\delta}. \end{aligned} \quad (4.1.10)$$

computes the missing u values at the locations of h nodes on the staggered grid (e.g., missing $u_{2,4}, u_{2,2}$ in Fig. 4.1.1).

Corresponding to the viscous shallow water PDEs (4.1.6), the full-domain micro-scale system is

$$\bullet \frac{1}{h_M} \frac{dh_{i,j}}{dt} = -\frac{(h_{i,j} + h_{i+2,j}) u_{i+1,j} - (h_{i-2,j} + h_{i,j}) u_{i-1,j}}{4\delta} - \frac{(h_{i,j} + h_{i,j+2}) v_{i,j+1} - (h_{i,j-2} + h_{i,j}) v_{i,j-1}}{4\delta} \quad (4.1.11a)$$

for $i \in \{0, 2, 4, \dots, n-2\}$, $j \in \{0, 2, 4, \dots, n-2\}$;

$$\bullet \frac{\text{Re}}{h_M^2} \frac{du_{i,j}}{dt} = -\frac{\pi^2}{4} \frac{u_{i,j}}{[(h_{i-1,j} + h_{i+1,j})/2]^2} + \frac{\pi^2 \text{Re}}{12 h_M^2} \left[g_x + g_n \frac{h_{i+1,j} - h_{i-1,j}}{2\delta} \right] - \frac{\text{Re}}{h_M} \left[1.5041 u_{i,j} \frac{u_{i+2,j} - u_{i-2,j}}{4\delta} + 1.3464 \frac{(v_{i-1,j-1} + v_{i+1,j-1} + v_{i-1,j+1} + v_{i+1,j+1})}{4} \frac{u_{i,j+2} - u_{i,j-2}}{4\delta} + 0.1577 u_{i,j} \frac{(v_{i-1,j+1} + v_{i+1,j+1})/2 - (v_{i-1,j-1} + v_{i+1,j-1})/2}{2\delta} \right] + 4.093 \frac{u_{i-2,j} - 2u_{i,j} + u_{i+2,j}}{4\delta^2} + \frac{u_{i,j-2} - 2u_{i,j} + u_{i,j+2}}{4\delta^2} + 3.093 \frac{(v_{i+1,j+1} - v_{i+1,j-1})/(2\delta) - (v_{i-1,j+1} - v_{i-1,j-1})/(2\delta)}{2\delta} \quad (4.1.11b)$$

for $i \in \{1, 3, 5, \dots, n-1\}$, $j \in \{0, 2, 4, \dots, n-2\}$;

$$\bullet \frac{\text{Re}}{h_M^2} \frac{dv_{i,j}}{dt} = -\frac{\pi^2}{4} \frac{v_{i,j}}{[(h_{i,j-1} + h_{i,j+1})/2]^2} + \frac{\pi^2 \text{Re}}{12 h_M^2} \left[g_y + g_n \frac{h_{i,j+1} - h_{i,j-1}}{2\delta} \right] - \frac{\text{Re}}{h_M} \left[1.5041 v_{i,j} \frac{v_{i,j+2} - v_{i,j-2}}{4\delta} + 1.3464 \frac{(u_{i-1,j-1} + u_{i+1,j-1} + u_{i-1,j+1} + u_{i+1,j+1})}{4} \frac{v_{i+2,j} - v_{i-2,j}}{4\delta} + 0.1577 v_{i,j} \frac{(u_{i+1,j-1} + u_{i+1,j+1})/2 - (u_{i-1,j-1} + u_{i-1,j+1})/2}{2\delta} \right] + 4.093 \frac{v_{i,j-2} - 2v_{i,j} + v_{i,j+2}}{4\delta^2} + \frac{v_{i-2,j} - 2v_{i,j} + v_{i+2,j}}{4\delta^2} + 3.093 \frac{(u_{i+1,j+1} - u_{i-1,j+1})/(2\delta) - (u_{i+1,j-1} - u_{i-1,j-1})/(2\delta)}{2\delta} \quad (4.1.11c)$$

for $i \in \{0, 2, 4, \dots, n-2\}$, $j \in \{1, 3, 5, \dots, n-1\}$.

Analogous to the periodic boundary conditions of the PDEs (4.1.6), the three fields h, u, v are n -periodic in both i and j , where $n = L/\delta$.

Substituting the solution of a steady uniform flow $h = h_M, u = u_M, v = v_M$ with mean height h_M and horizontal mean velocity u_M, v_M into the full-domain micro-scale system (4.1.11) and setting the time derivatives to zero gives the fixed points or the *equilibrium solution*

$$h = h_M, \quad u = \text{Re } g_x/3, \quad v = \text{Re } g_y/3, \quad (4.1.12)$$

for the full-domain micro-scale system (4.1.11) for the viscous shallow water flow. The equilibrium solution (4.1.12) is also the equilibrium solution for the viscous shallow water PDEs (4.1.6). For a bed with a positive slope (downward inclination along x), the viscous shallow water flow reaches the equilibrium velocity of the fixed point (4.1.12) when the bed drag and gravitational force are in balance. That is, larger the downward inclination, larger the components g_x, g_y and hence larger the equilibrium velocity is; for a horizontal bed, the only fixed point is stagnant water with $u = 0, v = 0$.

As a dynamical system, the full-domain micro-scale system (4.1.11) in vector notation, for the viscous shallow water PDEs (4.1.6) is

$$\frac{dx}{dt} = \mathbf{f}(\mathbf{x}), \quad (4.1.13)$$

where the state vector of the full-domain micro-scale system

$$\begin{aligned} \mathbf{x} = (& h_{0,0}, h_{0,2}, h_{0,4}, \dots, h_{2,0}, h_{2,2}, h_{2,4}, \dots, \\ & \dots, u_{1,0}, u_{1,2}, u_{1,4}, \dots, u_{3,0}, u_{3,2}, u_{3,4}, \dots, \\ & \dots, v_{0,1}, v_{0,3}, v_{0,5}, \dots, v_{2,1}, v_{2,3}, v_{2,5}, \dots), \end{aligned} \quad (4.1.14)$$

is the same as the state vector (2.2.3) of the full-domain system for generic wave-like system in §2.2.1

A full-domain micro-scale simulation is performed by numerical time-integration of the ODES (4.1.11) on the nodes of the micro-scale staggered grid (filled solid circles in Fig. 4.1.1), with the discrete macro-scale n -periodic boundary conditions in both i and j .

Fig. 4.1.2 shows two staggered patch grids with different number of layers of edge nodes. The patch grid in Fig. 4.1.2a (with two layer of edge nodes in normal direction to the edges and one layer of edge nodes in tangential direction to the edges), is sufficient for the general linear wave with viscous diffusion in Chapters 2 and 3. But, to use the finite difference equations (4.1.11) of the viscous shallow water flow as the micro-scale system within the patches, a staggered patch grid requires two layers of edge nodes in the normal direction to the edges, and one layer of edge nodes in the tangential direction to the edges, as in Fig. 4.1.2b.

1. A discussion in p. 43 of §3.1 shows that for computing the second spatial derivative of velocities (e.g., $\partial^2 u / \partial x^2$ in the viscous diffusion) within the patches requires a staggered patch grid with two layers of edge nodes in normal direction to the edges as in both Figs. 4.1.2a and 4.1.2b.
2. Computing the term (4.1.9) at the top-right interior u node (solid red filled circle) of the u -centred patch in Fig. 4.1.2b, requires the v edge value at the right-top patch corner, which does not exist in the Fig. 4.1.2a. Similarly, computing the term (4.1.10) at the top-right interior v node (solid blue filled circle) of the v -centred patch in Fig. 4.1.2b, requires the u edge value at the right-top patch corner, which does not exist in the Fig. 4.1.2a. Hence, a staggered patch scheme with the 2D viscous shallow water PDEs (4.1.11) as the underlying micro-scale system within the patches, requires a patch grid with one layer of edge nodes in tangential direction to the edges as in Fig. 4.1.2b.

Throughout this chapter, for the viscous shallow water flow, the staggered patch schemes use the patch grid in Fig. 4.1.2b, with two layers of edge nodes in the normal direction to the edges, and one layer of edge nodes in the tangential direction to the edges. For the staggered patch grid in Fig. 4.1.2b, the left and right edge values are $\circ h_{i,j}^{I,J}$, $\circ u_{i,j}^{I,J}$, $\circ v_{i,j}^{I,J}$, for $i \in \{-1, 0, n, n+1\}$ and $j \in \{0, 1, 2, \dots, n-1, n\}$. Similarly the bottom and top edge value indices are $i \in \{0, 1, 2, \dots, n-1, n\}$ and $j \in \{-1, 0, n, n+1\}$.

Using the full-domain micro-scale system (4.1.11) within the patches of a suitable staggered patch grid (e.g., Fig. 4.1.2b with $n = 6$), gives the *staggered patch scheme* (notationally same as the full-domain micro-scale system (4.1.11) with patch index I, J in the superscript)

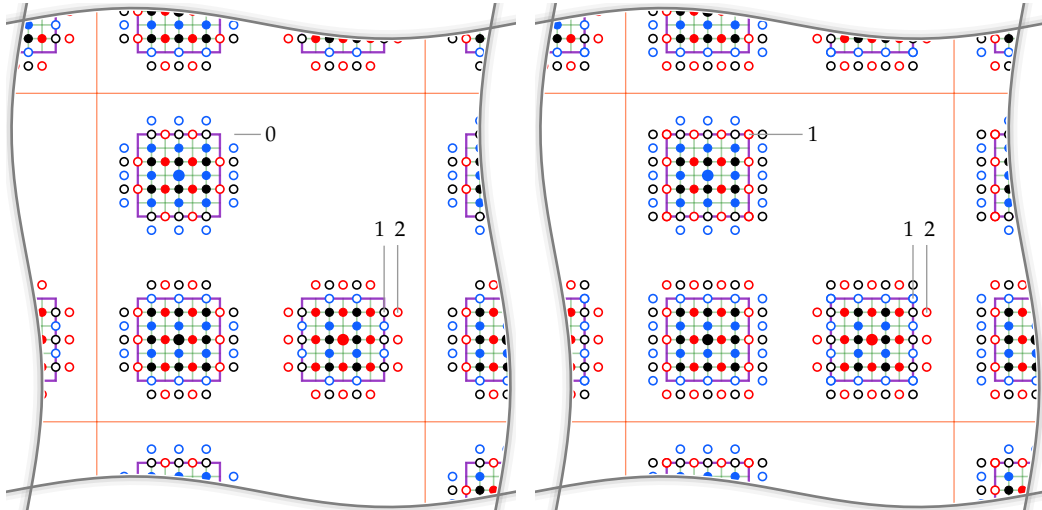
$$\begin{aligned}
 \bullet \frac{1}{h_M} \frac{dh_{i,j}^{I,J}}{dt} &= -\frac{(h_{i,j}^{I,J} + h_{i+2,j}^{I,J}) u_{i+1,j}^{I,J} - (h_{i-2,j}^{I,J} + h_{i,j}^{I,J}) u_{i-1,j}^{I,J}}{4\delta} \\
 &\quad - \frac{(h_{i,j}^{I,J} + h_{i,j+2}^{I,J}) v_{i,j+1}^{I,J} - (h_{i,j-2}^{I,J} + h_{i,j}^{I,J}) v_{i,j-1}^{I,J}}{4\delta}, \tag{4.1.15a} \\
 \bullet \frac{\text{Re}}{h_M^2} \frac{du_{i,j}^{I,J}}{dt} &= -\frac{\pi^2}{4} \frac{u_{i,j}^{I,J}}{[(h_{i-1,j}^{I,J} + h_{i+1,j}^{I,J}) / 2]^2} + \frac{\pi^2 \text{Re}}{12 h_M^2} \left[g_x + g_n \frac{h_{i+1,j}^{I,J} - h_{i-1,j}^{I,J}}{2\delta} \right] \\
 &\quad - \frac{\text{Re}}{h_M} \left[1.5041 u_{i,j}^{I,J} \frac{u_{i+2,j}^{I,J} - u_{i-2,j}^{I,J}}{4\delta} \right. \\
 &\quad \left. + 1.3464 \frac{(v_{i-1,j-1}^{I,J} + v_{i+1,j-1}^{I,J} + v_{i-1,j+1}^{I,J} + v_{i+1,j+1}^{I,J})}{4} \frac{u_{i,j+2}^{I,J} - u_{i,j-2}^{I,J}}{4\delta} \right]
 \end{aligned}$$

$$\begin{aligned}
& + 0.1577 u_{i,j}^{I,J} \frac{(v_{i-1,j+1}^{I,J} + v_{i+1,j+1}^{I,J})/2 - (v_{i-1,j-1}^{I,J} + v_{i+1,j-1}^{I,J})/2}{2\delta} \\
& + 4.093 \frac{u_{i-2,j}^{I,J} - 2u_{i,j}^{I,J} + u_{i+2,j}^{I,J}}{4\delta^2} + \frac{u_{i,j-2}^{I,J} - 2u_{i,j}^{I,J} + u_{i,j+2}^{I,J}}{4\delta^2} \\
& + 3.093 \frac{(v_{i+1,j+1}^{I,J} - v_{i+1,j-1}^{I,J})/(2\delta) - (v_{i-1,j+1}^{I,J} - v_{i-1,j-1}^{I,J})/(2\delta)}{2\delta}, \tag{4.1.15b}
\end{aligned}$$

- $\frac{\text{Re}}{h_M^2} \frac{dv_{i,j}^{I,J}}{dt} = -\frac{\pi^2}{4} \frac{v_{i,j}^{I,J}}{[(h_{i,j-1}^{I,J} + h_{i,j+1}^{I,J})/2]^2} + \frac{\pi^2 \text{Re}}{12 h_M^2} \left[g_y + g_n \frac{h_{i,j+1}^{I,J} - h_{i,j-1}^{I,J}}{2\delta} \right]$
 $- \frac{\text{Re}}{h_M} \left[1.5041 v_{i,j}^{I,J} \frac{v_{i,j+2}^{I,J} - v_{i,j-2}^{I,J}}{4\delta} \right.$
 $\left. + 1.3464 \frac{(u_{i-1,j-1}^{I,J} + u_{i+1,j-1}^{I,J} + u_{i-1,j+1}^{I,J} + u_{i+1,j+1}^{I,J})}{4} \frac{v_{i+2,j}^{I,J} - v_{i-2,j}^{I,J}}{4\delta} \right]$

Figure 4.1.2: For viscous shallow water flow micro-scale system (4.1.15), a staggered patch grid requires two layers of edge nodes in the normal direction to edges, and one layer of edge nodes in the tangential direction to edges, as in Fig. 4.1.2b.

- (a) Same as Fig. 2.2.5a for general linear wave. Two layers of edge nodes in normal direction to edges, no edge nodes in tangential direction to edges.
- (b) Two layers of edge nodes in normal direction to the edges, one layer of edge nodes in tangential direction to the edges.



$$\begin{aligned}
& + 0.1577 v_{i,j}^{I,J} \frac{(u_{i+1,j-1}^{I,J} + u_{i+1,j+1}^{I,J})/2 - (u_{i-1,j-1}^{I,J} + u_{i-1,j+1}^{I,J})/2}{2\delta} \Big] \\
& + 4.093 \frac{v_{i,j-2}^{I,J} - 2v_{i,j}^{I,J} + v_{i,j+2}^{I,J}}{4\delta^2} + \frac{v_{i-2,j}^{I,J} - 2v_{i,j}^{I,J} + v_{i+2,j}^{I,J}}{4\delta^2} \\
& + 3.093 \frac{(u_{i+1,j+1}^{I,J} - u_{i-1,j+1}^{I,J})/(2\delta) - (u_{i+1,j-1}^{I,J} - u_{i-1,j-1}^{I,J})/(2\delta)}{2\delta},
\end{aligned} \tag{4.1.15c}$$

and a patch coupling (e.g., Square-p4) to compute the edge values

$\circ h_{i,j}^{I,J}$, $\circ u_{i,j}^{I,J}$, $\circ v_{i,j}^{I,J}$ for

$i \in \{-1, 0, n, n+1\}$, $j \in \{0, 1, \dots, n\}$ for left and right edges and

$i \in \{0, 1, \dots, n\}$, $j \in \{-1, 0, n, n+1\}$ for bottom and top edges,

(4.1.15d)

for the same interior indices i, j and patch indices I, J in (2.2.5) of §2.2.1.

Analogous to the periodic boundary conditions for the full-domain micro-scale system (4.1.11), the three fields h, u, v in the patch scheme (4.1.15) are macro-scale N -periodic in both I and J , where $N = L/\Delta$. A specific patch coupling (e.g., Square-p4) computes patch edge values ($\circ h_{i,j}^{I,J}$, $\circ u_{i,j}^{I,J}$, $\circ v_{i,j}^{I,J}$ in Fig. 2.2.5a) from the centre values of neighbouring patches ($\bullet h_{i,j}^{I,J}$, $\bullet u_{i,j}^{I,J}$, $\bullet v_{i,j}^{I,J}$ with $i = j = n/2$ in Fig. 2.2.5a). The patch coupling provides a mechanism whereby patches influence each other, §2.3 discusses various details of different patch couplings.

Arranging the patch interior values of (4.1.15), (with the same index convention as in Fig. 2.2.4 of §2.2.2), into a vector gives the state vector x^I of the staggered patch scheme, which is a dynamic state variable evolving in time. As in §2.2.2, the superscript $(\cdot)^I$ is not an index or exponent, instead a qualifier denoting the patch interior nodes. For the viscous shallow water flow, the general form of a staggered patch scheme state vector x^I of size n_p^I containing all the interior values of all the patches is same as the state vector (2.2.6) of §2.2.2 for the general linear wave. That is, the number of patch interior nodes which is also the size of the state vector x^I is (same as expression (2.2.7) of §2.2.2),

$$n_p^I = (N^2/4)(9n^2/4 - 4n + 2), \tag{4.1.16}$$

where N is the number of macro-grid intervals and n is the number of sub-patch micro-grid intervals. For example, for $N = 6, 10, 14, 18, 22, 26$ macro-grid intervals with $n = 6$ sub-patch micro-grid intervals, $n_p^I = 531, 1475, 2891, 4779, 7139, 9971$ respectively.

For the staggered patch grid in Fig. 4.1.2b, the left and right edge values are $\circ h_{i,j}^{I,J}$, $\circ u_{i,j}^{I,J}$, $\circ v_{i,j}^{I,J}$, for $i \in \{-1, 0, n, n+1\}$ and $j \in \{0, 1, 2, \dots, n-1, n\}$. Similarly the bottom and top edge value indices are $i \in \{0, 1, 2, \dots, n-1, n\}$ and $j \in \{-1, 0, n, n+1\}$. Arranging these patch edge values of all the patches into a vector gives the edge vector \mathbf{x}^E of size n_p^E . The edge vector \mathbf{x}^E is computed by the patch coupling $\mathbf{x}^E(\mathbf{x}^I)$ of a particular patch scheme. For the staggered patch grid in Fig. 4.1.2b, the total number of patch edge nodes, that is the size of the edge vector \mathbf{x}^E ,

$$n_p^E = (N^2/4)(18n + 16), \quad (4.1.17)$$

where N is the number of macro-grid intervals and n is the number of sub-patch micro-grid intervals. Compared to the expression (2.2.8) (p. 18 of §2.2.2) for the general linear wave, the expression (4.1.17) for the viscous shallow water flow has 32 more edge nodes per macro-cell. For example, for the staggered patch grid in Fig. 4.1.2b with $N = 6, 10, 14, 18, 22, 26$ and $n = 6$, $n_p^E = 1116, 3100, 6076, 10044, 15004, 20956$ respectively.

As a dynamical system, the staggered patch scheme (4.1.15) in vector notation, corresponding to the full-domain micro-scale system (4.1.11) of viscous shallow water flow is

$$\frac{d\mathbf{x}^I}{dt} = \mathbf{F}(\mathbf{x}^I; \mathbf{x}^E(\mathbf{x}^I)). \quad (4.1.18)$$

with the same state vector \mathbf{x}^I (2.2.6) and a similar edge vector \mathbf{x}^E as those of the patch scheme for generic wave-like system in §2.2.2. The $\mathbf{F}(\mathbf{x}^I; \mathbf{x}^E(\mathbf{x}^I))$ in the staggered patch scheme dynamical system (4.1.18) corresponds to the $\mathbf{f}(\mathbf{x})$ in the full-domain micro-scale system (4.1.13). The functions \mathbf{F} and \mathbf{f} encode same the full-domain micro-scale system for the viscous shallow water PDEs (4.1.6); Section 2.2.2 explains this difference for the generic wave-like system.

Patch scheme simulation is performed by numerical time-integration of the ODEs (4.1.15) on the interior nodes of the staggered patch grid (filled solid circles in Fig. 4.1.2b), with the discrete macro-scale N -periodic boundary conditions in both I and J . As in §2.2.2, evaluating the time derivatives in the staggered patch scheme (4.1.15) is done in two steps: first, edge values $\mathbf{x}^E(\mathbf{x}^I)$ are computed via patch coupling; second, using both interior and edge values of each patch in the staggered patch grid, the time derivatives of \mathbf{x}^I are computed for the full-domain micro-scale system (4.1.11) of viscous shallow water flow.

Table 4.1.1: Dimensional parameter ranges relevant for the exploration of viscous shallow water PDEs. Height H is within the shallow water regime such that ($H/L \in [1/100, 1/20]$). Range of density ρ and dynamic viscosity μ are from Haynes, Lide, and Bruno (2016, p.6-7–6-8, p.6-247).

Parameter	Range of values
domain size L	0.5 to 100 cm
wavelength λ	0.5 to 100 cm
characteristic mean water height H	0.005 to 5 cm ($H/L \in [1/100, 1/20]$)
inviscid wave velocity $U = \sqrt{gH}$	10 to 70 cm/s
density ρ	992 to 1000 kg/m ³
dynamic viscosity μ	0.65 to 1.8 m Pa s
kinematic viscosity $\nu = \mu/\rho$	0.0066 to 0.018 cm ² /s
bed inclination angle θ	-10° to 10°

Table 4.1.2: Non-dimensional parameter ranges for viscous shallow water PDEs corresponding to the dimensional parameters in Table 4.1.1.

Parameter	Range of values
Mean height $h_M = 2\pi H/L$	0.025 to 0.4
Mean velocity $u_M = u/U$	0 to 1
Reynolds number Re	5 to 2000

4.1.3 Selection of relevant parameter regime for patch scheme exploration

Table 4.1.1 lists the dimensional parameter ranges we choose for viscous shallow water PDEs:

- Height H is within the shallow water regime such that $H/L \in [1/100, 1/20]$;
- Range of density ρ and dynamic viscosity μ are from Haynes, Lide, and Bruno (2016, p.6-7–6-8, p.6-247) for the temperature range from 0°C to 40°C at standard atmospheric pressure.

The non-dimensional parameter ranges within the dimensional parameters in Table 4.1.1 are listed in Table 4.1.2:

- Characteristic mean non-dimensional height $h_M = 2\pi H/L$ for the H and L values listed in Table 4.1.2;
- We heuristically choose $u_M = u/U$ around the mid point of the range of U in Table 4.1.2;

Table 4.1.3: Chosen parameters for patch scheme convergence study using viscous shallow water PDEs.

Parameter	Values
Linearisation points (Non-dimensional)	$\{(h_M, u_M, v_M)\}$ where $h_M \in \{0.025, 0.05, \dots, 0.035, 0.4\}$, $u_M \in \{0, 0.05, \dots, 0.95, 1\}$, $v_M = 0$
Reynolds number	$Re \in \{10, 50, 250, 1250\}$
Bed inclination angle	$\theta = 0$, i.e., $g_x = 0, g_y = 1$

- Reynolds number Re is limited to be within the regime of laminar flow.

Based on the eigenvalues of Spectral patch scheme ([TODO/xref]) for different combinations of the parameter values in Table 4.1.2, we select the sets of parameters listed in Table 4.1.3 for exploring the patch schemes for the simplified viscous shallow water flow. Following are the key reasons for this choice:

- Extent and spacing of the parameters are such that they cover significant variations in the structure of patch scheme eigenvalues.
- For $Re \lesssim 10$ there is no wave modes in the patch scheme eigenvalue spectrum.

4.2 Staggered patch schemes are accurate

This section shows that the developed five staggered patch schemes are accurate for the viscous shallow water flows. We establish the accuracy of the staggered patch schemes globally (as opposed one initial condition) by comparing the eigenvalues of the staggered patch schemes with the eigenvalues of fine- and coarse-grid full-domain micro-scale system, and for completeness also compare with the eigenvalues of the viscous shallow water PDEs (4.1.6). The objective of the staggered patch scheme is to perform reduced order multiscale simulation of the underlying micro-scale system. Hence, as p. 11 of §2.2.1 explains, the reference eigenvalues for us are the eigenvalues of the full domain micro-scale system, not that of the PDEs. The eigenvalue analysis for accuracy in this section is done for a representative subset of the system parameters (Reynolds number Re and mean flow h_M, u_M, v_M) and the grid parameters (macro-grid intervals N ,

sub-patch micro-grid intervals n , patch scale ratio r). [Section 4.5](#) on the consistency of the patch schemes establish the accuracy over a wider range of parameters. The following paragraphs introduce the approach of studying the accuracy of the staggered patch schemes and discuss the conventions adapted.

Time dependent solutions of linear/linearised ODEs are linear combinations of the spatial modes (i.e., eigenvectors) where the initial condition gives the amplitudes of the modes [TODO/cite]. Due to spatial homogeneity on the macro-scale dynamics in both the original system and the patch scheme, the macro-scale modes in both the systems are the same macro-scale Fourier modes. Hence, there is no error in the macro-scale spatial structures. The only error in the patch scheme is in the eigenvalues. Thus, when a patch scheme eigenvalues agree closely with the corresponding eigenvalues of the full-domain micro-scale system, the patch scheme simulation is accurate *globally for any initial condition*. The eigenvalues of the staggered patch schemes consist of the two scales.

1. *Macro-scale* eigenvalues correspond to the small wavenumber macro-scale modes over the domain.
2. *Micro-scale* eigenvalues correspond to large wavenumber micro-scale sub-patch modes.

We aim to design the multiscale staggered patch schemes to accurately simulate the large scale waves that are characterised by the macro-scale eigenvalues. So we define a staggered patch scheme to be accurate when the macro-scale eigenvalues of that patch scheme agree closely with the corresponding macro-scale eigenvalues of the full-domain micro-scale system. Thus, we aim to design the staggered patch schemes with the macro-scale eigenvalues as close as possible to the corresponding macro-scale eigenvalues of the full domain micro-scale system [\(4.1.11\)](#). Hence, in the eigenvalue analysis for accuracy in this section, we compare in the complex plane the eigenvalues of the staggered patch schemes with the eigenvalues of the full-domain micro-scale system.

[Sections 4.2.1 to 4.2.5](#) describe the methods of analytically deriving and numerically computing the eigenvalues for

1. the 2D viscous shallow water PDEs [\(4.1.6\)](#),
2. the full-domain micro-scale system [\(4.1.11\)](#), and
3. the staggered patch scheme [\(4.1.15\)](#).

Following a standard approach of substituting an arbitrary Fourier mode into the PDES/ODEs, §§4.2.1 and 4.2.2 derive the analytic eigenvalues of the viscous shallow water PDEs (4.1.6) and the corresponding discrete full-domain micro-scale system (4.1.11). Similarly §4.2.3 derives the analytic eigenvalues of a staggered patch scheme. To numerically compute the eigenvalues of the numerical staggered patch scheme, which includes any instabilities and inaccuracies due to the numerical roundoff errors, §§4.2.4 and 4.2.5 numerically differentiate the evolution functions $f(x)$ in the full-domain system (4.1.13), $\mathbf{F}(x^I; x^E(x^I))$ in the patch scheme (4.1.18) respectively.

Section 4.2.6 compares and contrasts various eigenvalues (e.g., analytic and numerical eigenvalues of the PDEs, full-domain micro-scale system, and patch schemes). We use the following notational convention to identify the various eigenvalues.

- Eigenvalue *subscripts* in $\lambda_p^{()}, \lambda_{m\delta}^{()}, \lambda_{m\Delta}^{()}, \lambda_{PDE}^{()}$ denote the system.
 - Eigenvalues $\lambda_p^{()}$ are for staggered patch schemes (e.g., λ_p^{NE1} of §4.2.3 and λ_p^N of §4.2.5).
 - Eigenvalues $\lambda_{m\delta}^{()}$ are for fine-grid full domain micro-scale system with same grid-spacing as sub-patch micro-grid interval δ (e.g., $\lambda_{m\delta}^A$ of §4.2.2 and $\lambda_{m\delta}^N$ of §4.2.4).
 - Eigenvalues $\lambda_{m\Delta}^{()}$ are for fine-grid full domain micro-scale system with same grid-spacing as the inter-patch distance Δ (e.g., $\lambda_{m\Delta}^A$ of §4.2.2 and $\lambda_{m\Delta}^N$ of §4.2.4).
 - Eigenvalues $\lambda_{PDE}^{()}$ are for the viscous shallow water PDE (e.g., λ_{PDE}^A of §4.2.1).
- Eigenvalue *superscripts* in $\lambda_{()}^N, \lambda_{()}^{NE1}, \lambda_{()}^A$ denote the method of computing numerical eigenvalues values.
 - Eigenvalues $\lambda_{()}^N$ are computed from the numerical Jacobian of the system (e.g., $\lambda_{m\delta}^N, \lambda_{m\Delta}^N$ of §4.2.4 and λ_p^N of §4.2.5).
 - Eigenvalues $\lambda_{()}^{NE1}$ are computed from numerically evaluated analytic one-cell Jacobian of the system (e.g., λ_p^{NE1} of §4.2.3).
 - Eigenvalues $\lambda_{()}^A$ are computed from the closed-form analytic expressions for the eigenvalues (e.g., λ_{PDE}^A of §4.2.1 and $\lambda_{m\delta}^A, \lambda_{m\Delta}^A$ of §4.2.2).

4.2.1 Eigenvalue analysis of the PDEs

This subsection discusses the method of computing the eigenvalues of the 2D viscous shallow water PDEs (4.1.6) compare for a sanity check with the eigenvalues of the full-domain micro-scale system (4.1.11) and the various staggered patch schemes.

We want to characterise the accuracy and stability of the patch schemes for the non-trivial nonlinear evolution of the viscous shallow water flow, apart from the mean flow and any constant drift with time in the solution h , u , v . Hence, in contrast to the arbitrary Fourier mode for the general *linear* wave in §3.2.1, we consider an arbitrary Fourier mode for the perturbation about h_M , $u_M + a_1 t$ and $v_M + a_2 t$ of the *nonlinear* viscous shallow water PDE (4.1.6), where h_M is the mean height, u_M , v_M are the mean velocities, and a_1 , a_2 are the constant mean accelerations. That is, for the viscous shallow water PDE (4.1.6), we consider an arbitrary Fourier mode of the perturbation about the mean accelerating flow, with real wavenumber (k_x, k_y) and complex growth rate λ ,

$$h(x, y, t) = h_M + H e^{i(k_x x + k_y y) + \lambda t}, \quad (4.2.1a)$$

$$u(x, y, t) = u_M + a_1 t + U e^{i(k_x x + k_y y) + \lambda t}, \quad (4.2.1b)$$

$$v(x, y, t) = v_M + a_2 t + V e^{i(k_x x + k_y y) + \lambda t}. \quad (4.2.1c)$$

With zero perturbation $U = V = 0$, taking time derivative of the Fourier mode (4.2.1b) and (4.2.1c) about the mean flow state $x_M = (h_M, u_M, v_M)$,

$$\left[\frac{\partial u}{\partial t} \right]_{x_M} = a_1; \quad \left[\frac{\partial v}{\partial t} \right]_{x_M} = a_2. \quad (4.2.2)$$

Substituting $h(x, y, t) = h_M$, $u(x, y, t) = u_M$, and $v(x, y, t) = v_M$, into the momentum equations (4.1.6b) and (4.1.6c) and comparing with the equation (4.2.2) gives the constant mean accelerations for the viscous shallow water PDE (4.1.6)

$$\left[\frac{\partial u}{\partial t} \right]_{x_M} = a_1 = \frac{\pi^2 g_x}{12} - \frac{\pi^2 u_M}{4 \operatorname{Re}}, \quad (4.2.3a)$$

$$\left[\frac{\partial v}{\partial t} \right]_{x_M} = a_2 = \frac{\pi^2 g_y}{12} - \frac{\pi^2 v_M}{4 \operatorname{Re}}. \quad (4.2.3b)$$

Substituting the Fourier mode (4.2.1) into the viscous shallow water PDE (4.1.6), neglecting the terms that are nonlinear in H , U , V , algebraic

simplifications, and arranging in matrix form give the eigensystem

$$\mathbf{J}(\mathbf{x}_M) \begin{bmatrix} H \\ U \\ V \end{bmatrix} = \lambda \begin{bmatrix} H \\ U \\ V \end{bmatrix}, \quad (4.2.4)$$

where the elements of the 3×3 Jacobian $\mathbf{J}(\mathbf{x}_M)$ are

$$\mathbf{J}_{1,1} = -i h_M u_M k_x - i h_M v_M k_y, \quad (4.2.5a)$$

$$\mathbf{J}_{1,2} = -i h_M^2 k_x, \quad (4.2.5b)$$

$$\mathbf{J}_{1,3} = -i h_M^2 k_y, \quad (4.2.5c)$$

$$\mathbf{J}_{2,1} = i \frac{\pi^2 g_n}{12} k_x + \frac{\pi^2 u_M}{2 \operatorname{Re} h_M}, \quad (4.2.5d)$$

$$\begin{aligned} \mathbf{J}_{2,2} = & -1.5041 i h_M u_M k_x - 1.3464 i h_M v_M k_y \\ & - \frac{4.093 h_M^2}{\operatorname{Re}} k_x^2 - \frac{h_M^2}{\operatorname{Re}} k_y^2 - \frac{\pi^2}{4 \operatorname{Re}}, \end{aligned} \quad (4.2.5e)$$

$$\mathbf{J}_{2,3} = -0.1577 i h_M u_M k_y - \frac{3.093 h_M^2}{\operatorname{Re}} k_x k_y, \quad (4.2.5f)$$

$$\mathbf{J}_{3,1} = i \frac{\pi^2 g_n}{12} k_y + \frac{\pi^2 v_M}{2 \operatorname{Re} h_M}, \quad (4.2.5g)$$

$$\mathbf{J}_{3,2} = -0.1577 i h_M v_M k_x - \frac{3.093 h_M^2}{\operatorname{Re}} k_x k_y, \quad (4.2.5h)$$

$$\mathbf{J}_{3,3} = -1.3464 i h_M u_M k_x - 1.5041 i h_M v_M k_y \quad (4.2.5i)$$

$$- \frac{h_M^2}{\operatorname{Re}} k_x^2 - \frac{4.093 h_M^2}{\operatorname{Re}} k_y^2 - \frac{\pi^2}{4 \operatorname{Re}}. \quad (4.2.5j)$$

The Jacobian in the eigensystem (3.2.2) for the general linear wave depends only on the system parameters c_D, c_V and the wavenumber (k_x, k_y) . But the Jacobian $\mathbf{J}(\mathbf{x}_M)$ for the nonlinear viscous shallow water flow depends on

1. the system parameters $\operatorname{Re}, g_n,$
2. the wavenumber $(k_x, k_y),$
3. and *also on the linearisation point $\mathbf{x}_M = (h_M, u_M, v_M)$, which is the mean flow state.*

Section 3.2.2 derives analytic expression (3.2.3) for the eigenvalues of the general linear wave. Similarly, using Sympy CAS, we derived the analytic expression for the eigenvalues of the Jacobian $\mathbf{J}(\mathbf{x}_M)$ in the eigen-system (3.2.2), for the viscous shallow water PDEs (4.1.6). The analytic

expression for the eigenvalues of the viscous shallow water is too long to be useful. Hence, we compute the eigenvalues $\lambda_{\text{PDE}}^{\text{NE1}}$ of the numerically evaluated Jacobian $\mathbf{J}(\mathbf{x}_M)$ in the eigensystem (3.2.2) for specific system parameters, wavenumber and the linearisation point \mathbf{x}_M .

For various macro-scale wavenumbers, we compute the eigenvalues $\lambda_{\text{PDE}}^{\text{NE1}}$ of the numerically evaluated Jacobian $\mathbf{J}(\mathbf{x}_M)$, and compare for a sanity check with the eigenvalues of the full domain micro-scale system and the patch schemes while assessing the accuracy of the patch schemes in §4.2.6.

4.2.2 Eigenvalue analysis of staggered grid full-domain micro-scale system

This subsection discusses the method of computing the eigenvalues of the staggered grid full-domain micro-scale system (4.1.11) for the 2D viscous shallow water PDEs (4.1.6). Comparing these eigenvalues of the full-domain system with the eigenvalues of the staggered patch schemes, §4.2.6 studies the accuracy of the patch schemes and §4.4 studies stability of the patch schemes.

We follow the same analytic approach in §4.2.1 for the 2D viscous shallow water PDEs in §4.2.1, but over a discrete infinite staggered grid (number of grid intervals $n \rightarrow \infty$ in Fig. 4.1.1). We consider an arbitrary Fourier mode for the perturbation about h_M , $u_M + a_1 t$ and $v_M + a_2 t$ of the full-domain micro-scale system (4.1.11) for the viscous shallow water flow, where h_M is the mean height, u_M , v_M are the mean velocities, and a_1 , a_2 are the constant mean accelerations. That is, for the full-domain micro-scale system (4.1.11), we consider an arbitrary Fourier mode of the perturbation about the mean accelerating flow, with real wavenumber (k_x, k_y) and complex growth rate λ ,

$$\bullet h_{i,j}(t) = h_M + H e^{i(k_x i \delta + k_y j \delta) + \lambda t}, \quad (4.2.6a)$$

$$\bullet u_{i,j}(t) = u_M + a_1 t + U e^{i(k_x i \delta + k_y j \delta) + \lambda t}, \quad (4.2.6b)$$

$$\bullet v_{i,j}(t) = v_M + a_2 t + V e^{i(k_x i \delta + k_y j \delta) + \lambda t}. \quad (4.2.6c)$$

Throughout this thesis, i denotes the micro-grid index in x -direction (for both full-domain and sub-patch micro-grids), whereas $i = \sqrt{-1}$ is the imaginary unit.

With zero perturbation $U = V = 0$, taking time derivative of the Fourier mode (4.2.13b) and (4.2.13c) about the mean flow state $\mathbf{x}_M = (h_M, u_M, v_M)$,

$$\left[\frac{du_{i,j}}{dt} \right]_{x_M} = a_1; \quad \left[\frac{dv_{i,j}}{dt} \right]_{x_M} = a_2. \quad (4.2.7)$$

Substituting $h_{i,j}(t) = h_M$, $u_{i,j}(t) = u_M$, and $v_{i,j}(t) = v_M$, into the momentum equations (4.1.11b) and (4.1.11c) and comparing with the equation (4.2.7) gives the constant mean accelerations for the full-domain micro-scale system (4.1.11)

$$\left[\frac{du_{i,j}}{dt} \right]_{x_M} = a_1 = \frac{\pi^2 g_x}{12} - \frac{\pi^2 u_M}{4 Re}, \quad (4.2.8a)$$

$$\left[\frac{dv_{i,j}}{dt} \right]_{x_M} = a_2 = \frac{\pi^2 g_y}{12} - \frac{\pi^2 v_M}{4 Re}, \quad (4.2.8b)$$

which are same as the constant mean accelerations (4.2.3) for the viscous shallow water PDE (4.1.6).

Substituting the Fourier mode (4.2.1) into the full-domain micro-scale system (4.1.11), neglecting the terms that are nonlinear in H , U , V , algebraic simplifications, and arranging in matrix form give the eigensystem

$$\mathbf{J}(x_M) \begin{bmatrix} H \\ U \\ V \end{bmatrix} = \lambda \begin{bmatrix} H \\ U \\ V \end{bmatrix}, \quad (4.2.9)$$

where the elements of the 3×3 Jacobian $\mathbf{J}(\mathbf{x}_M)$ are

$$\mathbf{J}_{1,1} = -i h_M u_M \frac{\sin(2\delta k_x)}{2\delta} - i h_M v_M \frac{\sin(2\delta k_y)}{2\delta}, \quad (4.2.10a)$$

$$\mathbf{J}_{1,2} = -i h_M^2 \frac{\sin(\delta k_x)}{\delta}, \quad (4.2.10b)$$

$$\mathbf{J}_{1,3} = -i h_M^2 \frac{\sin(\delta k_y)}{\delta}, \quad (4.2.10c)$$

$$\mathbf{J}_{2,1} = i \frac{\pi^2 g_n}{12} \frac{\sin(\delta k_x)}{\delta} + \frac{\pi^2 u_M}{2 \operatorname{Re} h_M} \cos(\delta k_x), \quad (4.2.10d)$$

$$\begin{aligned} \mathbf{J}_{2,2} = & -1.5041 i h_M u_M \frac{\sin(2\delta k_x)}{2\delta} - 1.3464 i h_M v_M \frac{\sin(2\delta k_y)}{2\delta} \\ & - \frac{4.0930 h_M^2}{\operatorname{Re}} \left[\frac{\sin(\delta k_x)}{\delta} \right]^2 - \frac{h_M^2}{\operatorname{Re}} \left[\frac{\sin(\delta k_y)}{\delta} \right]^2 - \frac{\pi^2}{4 \operatorname{Re}}, \end{aligned} \quad (4.2.10e)$$

$$\mathbf{J}_{2,3} = -0.1577 i h_M u_M \frac{\sin(\delta k_y)}{\delta} \cos(\delta k_x) - \frac{3.0930 h_M^2}{\operatorname{Re}} \frac{\sin(\delta k_x)}{\delta} \frac{\sin(\delta k_y)}{\delta}, \quad (4.2.10f)$$

$$\mathbf{J}_{3,1} = i \frac{\pi^2 g_n}{12} \frac{\sin(\delta k_y)}{\delta} + \frac{\pi^2 v_M}{2 \operatorname{Re} h_M} \cos(\delta k_y), \quad (4.2.10g)$$

$$\mathbf{J}_{3,2} = -0.1577 i h_M v_M \frac{\sin(\delta k_x)}{\delta} \cos(\delta k_y) - \frac{3.0930 h_M^2}{\operatorname{Re}} \frac{\sin(\delta k_x)}{\delta} \frac{\sin(\delta k_y)}{\delta}, \quad (4.2.10h)$$

$$\begin{aligned} \mathbf{J}_{3,3} = & -1.3464 i h_M u_M \frac{\sin(2\delta k_x)}{2\delta} - 1.5041 i h_M v_M \frac{\sin(2\delta k_y)}{2\delta} \\ & - \frac{h_M^2}{\operatorname{Re}} \left[\frac{\sin(\delta k_x)}{\delta} \right]^2 - \frac{4.0930 h_M^2}{\operatorname{Re}} \left[\frac{\sin(\delta k_y)}{\delta} \right]^2 - \frac{\pi^2}{4 \operatorname{Re}}. \end{aligned} \quad (4.2.10i)$$

As the grid interval $\delta \rightarrow 0$ and/or the wavenumber $(k_x, k_y) \rightarrow (0, 0)$, we get following limits for the terms in the Jacobian elements (4.2.10)

$$\begin{aligned} \frac{\sin(\delta k_x)}{\delta} & \rightarrow k_x & \frac{\sin(\delta k_y)}{\delta} & \rightarrow k_y, \\ \frac{\sin(2\delta k_x)}{2\delta} & \rightarrow k_x & \frac{\sin(2\delta k_y)}{2\delta} & \rightarrow k_y, \\ \cos(\delta k_x) & \rightarrow 1 & \cos(\delta k_y) & \rightarrow 1. \end{aligned} \quad (4.2.11)$$

The limits in 4.2.11 are evident from the limits of the power series, as $a \rightarrow 0$ and/or $x \rightarrow 0$,

$$\begin{aligned} \frac{\sin(ax)}{a} &= x - \frac{a^2 x^3}{3!} + \frac{a^4 x^5}{5!} - \frac{a^6 x^7}{7!} + \mathcal{O}(a^8 x^9) \rightarrow x \\ \cos(ax) &= 1 - \frac{a^2 x^2}{2!} + \frac{a^4 x^4}{4!} - \frac{a^6 x^6}{6!} + \mathcal{O}(a^8 x^8) \rightarrow 1 \end{aligned} \quad (4.2.12)$$

In the limits (4.2.11), the Jacobian elements (4.2.10) of the full-domain micro-scale system converge to the Jacobian elements (4.2.5) of the viscous shallow water PDEs. Hence, the eigenvalues of the full-domain micro-scale system (4.1.11) converge to the analytic eigenvalues of the PDEs (4.1.6) as we decrease the grid interval δ and/or wavenumber (k_x, k_y).

We compute the eigenvalues λ_m^{NE1} of the numerically evaluated Jacobian $\mathbf{J}(\mathbf{x}_M)$ in the eigensystem (4.2.9) for specific system parameters, wavenumber and the linearisation point \mathbf{x}_M . When we compute the eigenvalues λ_m^{NE1} of the full-domain micro-scale system,

- for the same grid-spacing δ as the sub-patch micro-grid interval (also called δ), we call the eigenvalues $\lambda_{m\delta}^{NE1}$,
- for the same grid-spacing Δ as the inter-patch distance Δ , we call the eigenvalues $\lambda_{m\Delta}^{NE1}$.

For various macro-scale wavenumbers, we compute the eigenvalues of the numerically evaluated Jacobian $\mathbf{J}(\mathbf{x}_M)$, and compare with the eigenvalues of the viscous shallow water PDEs and the patch schemes while assessing the accuracy (§4.2.6) and stability (§4.4) of the patch schemes.

4.2.3 Analytic eigenvalue analysis of staggered patch schemes

This subsection discusses a method of deriving analytic eigenvalues of a generic staggered patch scheme (4.1.15) over a staggered patch grid, for the 2D viscous shallow water PDEs (4.1.6). Section 4.3 uses the analytic patch scheme eigenvalues to assess the numerical roundoff errors in the patch schemes. Section 3.3 uses the analytic patch scheme eigenvalues to separate the micro- and macro-scale eigenvalues and in establishing wavenumber-wise association of eigenvalues with the full-domain system, the numerical eigenvalue error computations passively use analytic eigenvalues to establish this association. Hence, the analytic patch scheme eigenvalues are used to assess accuracy (§4.2.6), stability (§4.4), and consistency (§4.5) of the staggered patch schemes.

To derive the analytic one-cell Jacobian for the patch scheme (4.1.15), we follow the same approach in §3.2.3 for the general linear wave, except the following two differences.

1. For viscous shallow water flows, we use a patch grid in Fig. 4.1.2b with two layers of edge nodes in normal direction to the edges, one layer of edge nodes in tangential direction to the edges. Page 161 of

§4.1.2 discusses why the staggered patch grid in Fig. 4.1.2b with such edge node arrangement is required for the viscous shallow water flow.

2. We adapt the analytic approach in §4.2.1 for the staggered grid full-domain micro-scale system (4.1.11), to an infinite *staggered patch grid* (number of macro-scale grid intervals $N \rightarrow \infty$ in Fig. 4.1.2b). That is, we use an arbitrary Fourier mode for the perturbation about h_M , $u_M + a_1 t$ and $v_M + a_2 t$ of the patch scheme (4.1.15) for the viscous shallow water flow, where h_M is the mean height, u_M , v_M are the mean velocities, and a_1 , a_2 are the constant mean accelerations. Thus, for the patch scheme (4.1.15), we use an arbitrary Fourier mode of the perturbation about the mean accelerating flow, with real wavenumber (k_x , k_y) and complex growth rate λ ,

$$\bullet h_{i,j}^{I,J}(t) = h_M + h_{i,j}^{p,q}(t) e^{i[k_x I \Delta + k_y J \Delta]}, \quad (4.2.13a)$$

$$\bullet u_{i,j}^{I,J}(t) = u_M + a_1 t + u_{i,j}^{p,q}(t) e^{i[k_x I \Delta + k_y J \Delta]}, \quad (4.2.13b)$$

$$\bullet v_{i,j}^{I,J}(t) = v_M + a_2 t + v_{i,j}^{p,q}(t) e^{i[k_x I \Delta + k_y J \Delta]}, \quad (4.2.13c)$$

where the pair I, J is the global macro-scale patch index, $p, q \in \{0, 1\}$ is the local sub-macro-cell patch index with $p = I \bmod 2$ and $q = J \bmod 2$. The sub-patch micro-grid node index $i, j \in \{1, \dots, n - 1\}$ for all the patch interior nodes. Figure 2.2.4 of §2.2.2 illustrates these indices for the case of finite number of macro-grid intervals N where the global macro-scale patch index $I, J \in \{0, 1, \dots, N - 1\}$. But for our present case of $N \rightarrow \infty$ for analytic eigenvalue analysis, we use the global macro-scale patch index $I, J \in \{\dots, -1, 0, 1, \dots\}$.

In contrast to the Fourier mode (3.2.10) for the state variables of the general linear wave, the Fourier mode (4.2.13) are for perturbations of the state variables of the viscous shallow water flow. As explained in §3.2.3, in the patch scheme Fourier mode (4.2.13), the time-dependent micro-scale structure $h_{i,j}^{p,q}(t)$, $u_{i,j}^{p,q}(t)$, $v_{i,j}^{p,q}(t)$ is modulated over the macro-scale wave form $\exp(i[k_x I \Delta + k_y J \Delta])$. So, the micro-scale structure $h_{i,j}^{p,q}(t)$, $u_{i,j}^{p,q}(t)$, $v_{i,j}^{p,q}(t)$ depends only on the sub-macro-cell patch index p, q and the sub-patch micro-grid node index i, j , but not on the global patch index I, J due to the 2Δ -translational symmetry in space because of the Fourier shift.

As in §3.2.3, collecting the interior values of all three patches in the centre macro-cell into a vector gives the *state vector* x^i . For a given number of macro-grid interval N and sub-path micro-grid grid intervals n , the number of patch interior nodes n_p^i per macro-cell, that is the size of x^i , is

same for different number of layers of the edge nodes. Hence, the n_p^i is for the viscous shallow water flow is same as the expression (3.2.11) of §3.2.3 for the general linear wave. That is, the total number of patch interior nodes per macro-cell

$$n_p^i = 9n^2/4 - 4n + 2, \quad (4.2.14)$$

where n is the number of sub-patch grid intervals. For example, for $n = 6, 10, 14$ sub-patch micro-grid intervals, $n_p^i = 59, 187, 387$ respectively. The state vector for the staggered patch grid in Fig. 4.1.2b for the viscous shallow water flow, is same as the state vector (3.2.12) for the general linear wave.

Applying a specific patch coupling (Spectral, Square-p2, Square-p4, etc.) gives edge values of all the patches in centre macro-cell, in terms of the substituted Fourier mode. That is, patch coupling gives the edge values of each patch in the centre macro-cell from the centre-node values of patches in other macro-cells, which are Fourier shifted centre-node values (by multiples of 2Δ) of the centre macro-cell. Collecting the edge values of all three patches in the centre macro-cell into a vector gives the *edge vector* \mathbf{x}^e . The total number of patch edge nodes per macro-cell for the compatible staggered patch grid (Fig. 4.1.2b) for viscous shallow water flow, that is the size of \mathbf{x}^e ,

$$n_p^e = 18n + 8, \quad (4.2.15)$$

where n is the number of sub-patch grid intervals. For example, for the cases of $n = 6, 10, 14$ sub-patch micro-grid intervals, $n_p^e = 116, 188, 260$ respectively. The patch grid in Fig. 4.1.2b for the viscous shallow water flow, has larger number of edge nodes compared to the staggered patch grid in Fig. 4.1.2a for the general linear wave. Hence the $n_p^e = 18n + 8$ for the viscous shallow water flow, compared to the $n_p^e = 18n - 16$ as in the expression (3.2.13) of §3.2.3 for the general linear wave. Page 55 of §3.2.3 presents some example coupling expressions (3.2.14) for the edge nodes using the simplest staggered patch scheme Square-p2.

For one macro-cell, substituting into the staggered patch scheme (4.1.15), the Fourier mode (4.2.13) and the coupled patch edge values (e.g., expressions (3.2.14) in p. 55 of §3.2.3) computed by a specific patch coupling, and cancelling the exponential factors on both sides, gives the time evolution of a staggered patch scheme as a dynamical system

$$\frac{d\mathbf{x}^i}{dt} = \mathbf{F}(\mathbf{x}^i; \mathbf{x}^e(\mathbf{x}^i)), \quad (4.2.16)$$

only for the specific modes of macro-scale wavenumber (k_x, k_y). The dynamical system (4.2.16) is in the same form as the full-size staggered patch scheme dynamical system (4.1.18) of §4.1. The state vector \mathbf{x}^i of the full-size

staggered patch scheme dynamical system (4.1.18) contain interior values of all the patches in a staggered patch grid, but the state vector \mathbf{x}^i of the staggered patch scheme dynamical system (4.2.16) for one macro-scale wavenumber (k_x, k_y) contain interior values of only one macro-cell. Hence, similar to the general linear wave, we call the equation (4.2.16) as one-cell staggered patch scheme dynamical system for viscous shallow water flow. Unlike the full-size staggered patch scheme dynamical system (4.1.18), the one-cell staggered patch scheme dynamical system (4.2.16) is the evolution about the mean accelerating flow.

The one-cell staggered patch scheme dynamical system (4.2.16), written separately for h, u , and v is similar to the corresponding full-size staggered patch scheme (4.1.15) of §4.1.2 with the following two differences.

1. The state variables $h_{i,j}^{I,J}, u_{i,j}^{I,J}, v_{i,j}^{I,J}$ in \mathbf{x}^i of the full-size system (4.1.15) are from all the macro-cells expressed in the global patch index $I, J \in \{\dots, -1, 0, 1, \dots\}$. But the state variables $h_{i,j}^{p,q}, u_{i,j}^{p,q}, v_{i,j}^{p,q}$ in \mathbf{x}^i of the one-cell system (4.2.16) are node values only from one macro-cell, expressed in sub-macro-cell patch index $p, q \in \{0, 1\}$.
2. The state variables $h_{i,j}^{I,J}, u_{i,j}^{I,J}, v_{i,j}^{I,J}$ in \mathbf{x}^i of the full-size system (4.1.15) are the values of h, u , and v . But the state variables $h_{i,j}^{p,q}, u_{i,j}^{p,q}, v_{i,j}^{p,q}$ in \mathbf{x}^i of the one-cell system (4.2.16) are only perturbations about the mean accelerating flow.

From the one-cell patch system (4.2.16), we aim to derive an eigensystem, following an approach similar to deriving the eigensystem (4.2.9) of §4.2.2 for the full-domain system. The one-cell patch system (4.2.16) for the viscous shallow water flowr wave are nonlinear in the state variables $h_{i,j}^{p,q}, u_{i,j}^{p,q}, v_{i,j}^{p,q}$. Linearising the one-cell patch system (4.2.16) by neglecting the terms that are nonlinear in the state variables $h_{i,j}^{p,q}, u_{i,j}^{p,q}, v_{i,j}^{p,q}$ and algebraic simplifications give the eigensystem

$$\mathbf{J}(\mathbf{x}_M) \mathbf{x}^i = \lambda \mathbf{x}^i, \quad (4.2.17)$$

where $\mathbf{J}(\mathbf{x}_M) = [\partial \mathbf{F} / \partial \mathbf{x}^i]_{\mathbf{x}_M}$ is the $n_p^i \times n_p^i$ one-cell Jacobian of the staggered patch scheme. The number of state variables $n_p^i = 9n^2/4 - 4n + 2$ for the one-cell patch scheme system, as in the expression (4.2.14).

The Jacobian in the one-cell patch system (3.2.16) for the linear wave depends only on the system parameters c_D, c_V and the wavenumber (k_x, k_y) . But the Jacobian $\mathbf{J}(\mathbf{x}_M)$ in the eigensystem (4.2.17) for the one-cell patch system for the nonlinear viscous shallow water flow depends on

1. the system parameters $Re, g_x, g_n,$

2. the wavenumber (k_x, k_y) ,
3. and also on the linearisation point $\mathbf{x}_M = (h_M, u_M, v_M)$, which is the mean flow state.

For example, similar to the case of general linear wave, for $n = 6$ sub-patch grid intervals, the one-cell Jacobian $\mathbf{J}(\mathbf{x}_M)$ for the viscous shallow water flow, is a 59×59 sparse matrix generally with only 318 of the 3481 elements being nonzero irrespective of the particular patch coupling interpolation of the staggered patch schemes (i.e., same for both the Spectral patch scheme and all the polynomial patch schemes). For some particular combination of numerical values of the parameters the sparsity is higher. The 318 nonzero elements of the one-cell Jacobian of a staggered patch scheme (for $n = 6$) contain all the information about the underlying micro-scale system and the patch coupling, for the macro-scale waves of wavenumber (k_x, k_y) . A few elements of the one-cell Jacobian of the simplest staggered patch scheme Square-p2 are,

$$\begin{aligned}\mathbf{J}_{1,1} &= 0, \quad \mathbf{J}_{1,16} = -\frac{h_M^2}{2\delta}, \quad \mathbf{J}_{4,10} = \frac{h_M^2}{2\delta}, \quad \mathbf{J}_{12,11} = \frac{0.3366h_Mv_M}{\delta} + \frac{h_M^2}{4\operatorname{Re}\delta^2}, \\ \mathbf{J}_{16,16} &= -\frac{2.4674}{\operatorname{Re}} - \frac{2.5465h_M^2}{\operatorname{Re}\delta^2}, \\ \mathbf{J}_{18,36} &= \left(\frac{0.188h_Mv_M}{\delta} + \frac{0.5116h_M^2}{\operatorname{Re}\delta^2} + \frac{0.564h_Mv_M}{\Delta} + \frac{1.5349h_M^2}{\Delta\operatorname{Re}\delta} \right) e^{-2\Delta i k_y} \\ &\quad + \frac{0.188h_Mv_M}{\delta} + \frac{0.5116h_M^2}{\operatorname{Re}\delta^2} - \frac{0.564h_Mv_M}{\Delta} - \frac{1.5349h_M^2}{\Delta\operatorname{Re}\delta} \\ \mathbf{J}_{46,36} &= \left(-\frac{h_M^2}{8\delta} - \frac{h_M^2}{2\Delta} - \frac{3\delta h_M^2}{8\Delta^2} \right) e^{2\Delta i k_x} + \left(-\frac{h_M^2}{8\delta} + \frac{h_M^2}{2\Delta} - \frac{3\delta h_M^2}{8\Delta^2} \right) e^{-2\Delta i k_y} \\ &\quad + \left(-\frac{h_M^2}{8\delta} + \frac{h_M^2}{4\Delta} + \frac{3\delta h_M^2}{8\Delta^2} \right) e^{2\Delta i k_x - 2\Delta i k_y} - \frac{h_M^2}{8\delta} - \frac{h_M^2}{4\Delta} + \frac{3\delta h_M^2}{8\Delta^2} \\ \mathbf{J}_{50,51} &= \left(-\frac{0.3366h_Mv_M}{\Delta} - \frac{h_M^2}{4\Delta\operatorname{Re}\delta} + \frac{0.6732\delta h_Mv_M}{\Delta^2} + \frac{h_M^2}{2\Delta^2\operatorname{Re}} \right) e^{2\Delta i k_y} \\ &\quad + \left(\frac{0.3366h_Mv_M}{\Delta} + \frac{h_M^2}{4\Delta\operatorname{Re}\delta} + \frac{0.6732\delta h_Mv_M}{\Delta^2} + \frac{h_M^2}{2\Delta^2\operatorname{Re}} \right) e^{-2\Delta i k_y} \\ &\quad + \frac{h_M^2}{2\operatorname{Re}\delta^2} - \frac{1.3464\delta h_Mv_M}{\Delta^2} - \frac{h_M^2}{\Delta^2\operatorname{Re}}.\end{aligned}$$

The example expressions for $\mathbf{J}_{1,16}$, $\mathbf{J}_{4,10}$, $\mathbf{J}_{12,11}$ and $\mathbf{J}_{16,16}$ are independent of the macro-scale wavenumber (k_x, k_y) and macro-grid interval Δ and hence characterise the micro-scale flow physics:

- $\mathbf{J}_{1,16}, \mathbf{J}_{4,10}$ characterise the micro-scale flow physics;
- Re in $\mathbf{J}_{12,11}$ characterise the micro-scale viscous diffusion, for general linear wave $\mathbf{J}_{12,11} = c_V/(4\delta^2)$ in p. 57 of §3.2.3;
- Re in $\mathbf{J}_{16,16}$ characterise the micro-scale drag and viscous diffusion, for general linear wave $\mathbf{J}_{16,16} = -c_D - c_V/\delta^2$.

All the nonzero diagonal elements of the Jacobian elements are precisely the same for the viscous shallow water flow, similar to the Jacobian elements of the general linear wave (i.e., expression (3.2.17) in p. 57 of §3.2.3). That is, all the nonzero diagonal elements

$$\mathbf{J}_{i,i} = -\frac{2.4674}{Re} - \frac{2.5465h_M^2}{Re\delta^2} \quad (4.2.18)$$

for $i \in \{10, 11, \dots, 21, 28, 29, \dots, 40, 47, 48, \dots, 59\}$.

The drag term $-\left[\pi^2/(4Re)\right] u_{i,j}^{I,J} h_M^2 / [(h_{i-1,j}^{I,J} + h_{i+1,j}^{I,J})/2]^2$ and the drag term $-\left[\pi^2/(4Re)\right] v_{i,j}^{I,J} h_M^2 / [(h_{i-1,j}^{I,J} + h_{i+1,j}^{I,J})/2]^2$ in the staggered patch scheme equations (4.1.15b) and (4.1.15c), after linearisation become $-u_{i,j}^{I,J} \pi^2/(4Re)$ and $-v_{i,j}^{I,J} \pi^2/(4Re)$ respectively. These drag terms involving only the constant $\pi^2/(4Re) = 2.4674/Re$ and the respective velocities, contribute only to the diagonal elements of the Jacobian, without depending on macro-grid interval Δ , patch scale ratio r and the patch coupling.

The example expressions for $\mathbf{J}_{18,36}$, $\mathbf{J}_{46,36}$ and $\mathbf{J}_{50,51}$ depend on the macro-scale wavenumber (k_x, k_y) and macro-grid interval Δ and hence characterise the macro-scale flow physics:

- Expressions for $\mathbf{J}_{18,36}$ and $\mathbf{J}_{50,51}$ characterise macro-scale wave with only viscous diffusion;
- $\mathbf{J}_{46,36}$ characterises a macro-scale wave without any dissipation.

The 2Δ in the argument of the exponential factors in $\mathbf{J}_{18,36}$, $\mathbf{J}_{46,36}$, and $\mathbf{J}_{50,51}$ indicate the patch coupling influence by the patches in surrounding macro-cells which are 2Δ away from the centre macro-cell. Compared to the listed example Jacobian elements of the simple patch coupling Square-p2, more surrounding macro-cells influence the Jacobian elements for the cases of patch coupling with higher order interpolations (Square-p4, Square-p6, and Square-p8). Hence the expressions for the one-cell Jacobian elements are much longer than the listed example expressions.

Due to the large Jacobian size (e.g., 59×59 for $n = 6$) and the long expressions in their elements, all the CAS packages we tried (Sympy, Reduce and Maple) fail to compute the analytic eigenvalues of the one-cell

Jacobian, even for the simplest staggered patch scheme Square-p2 with $n = 6$ sub-patch micro-grid intervals. So we numerically evaluate the one-cell Jacobian for numerical values of $\Delta, \delta, Re, g_x, g_n, h_M, u_M, v_M, k_x, k_y$ and compute the eigenvalues λ_p^{NE1} . We compare with the eigenvalues λ_p^{NE1} of the numerically evaluated one-cell Jacobian of the patch schemes, with the eigenvalues of the full domain micro-scale system and the eigenvalues of the general linear wave PDEs, while assessing the accuracy ([§4.2.6](#)) and stability ([§4.4](#)) of the patch schemes.

4.2.4 Computing numerical Jacobian of the staggered grid full-domain micro-scale system

This subsection discusses a method to compute the numerical *full-size* Jacobian of the staggered grid full-domain micro-scale system ([\(4.1.15\)](#)) for the viscous shallow water flow, in contrast to the analytic 3×3 Jacobian in [§4.2.3](#). [Section 4.2.6](#) uses the eigenvalues of the numerical Jacobian of the full-domain micro-scale system, while comparing the eigenvalues of the staggered grid full-domain system with the eigenvalues of the patch scheme for the viscous shallow water flow.

[Section 3.2.4](#) for the general linear wave, discusses some key differences between the 3×3 analytic Jacobian and the corresponding full-size numerical Jacobian for the full-domain system. For example, a full-domain numerical scheme on a staggered grid (e.g., [Fig. 4.1.1](#)) with $n \times n$ grid intervals, has $n_m \times n_m$ Jacobian, with $n_m = 3n^2/4$. In practice, the full-domain micro-scale simulation is done using the full-size numerical scheme (not the 3×3 analytic system), which is subject to the practical issues like numerical roundoff errors. Hence we also compute the eigenvalues λ_m^N of the full-size numerical Jacobian of the full-domain micro-scale system as discussed in this subsection.

Consider the full-domain micro-scale system ([\(4.1.13\)](#)), $dx/dt = f(x)$, where x is the state vector ([\(4.1.14\)](#)), for the viscous shallow water flow, over a full-domain staggered grid (e.g., [Fig. 4.1.1](#)) with $n \times n$ grid intervals. We want to characterise the accuracy and stability of the staggered grid full-domain system for the non-trivial nonlinear evolution of the viscous shallow water flow, apart from the mean flow and any constant drift with time in the solution x . Hence, consider the solution $x(t)$ as a small perturbation $\epsilon(t)$ for small t , about the mean accelerating flow, that is,

$$x(t) = x_M + a_M t + \epsilon(t), \quad (4.2.19)$$

where the mean flow state $x_M = (h_M, u_M, v_M)$ and the mean acceleration $a_M = (0, a_1, a_2)$ with a_1 and a_2 being constants in terms of u_M and

v_M as in equations (4.2.8). Substituting the solution form (4.2.19) into the full-domain micro-scale system (4.1.13) (i.e., $dx/dt = f(x)$) gives

$$a_M + \frac{d\epsilon}{dt} = f(x_M + a_M t + \epsilon(t)). \quad (4.2.20)$$

The time derivative of the state vector dx/dt at the constant mean flow state $x_M = (h_M, u_M, v_M)$ is

$$\left[\frac{dx}{dt} \right]_{x_M} = a_M = f(x_M). \quad (4.2.21)$$

Expanding the RHS of the equation (4.2.20) as Taylor series about x_M gives

$$\begin{aligned} a_M + \frac{d\epsilon}{dt} &= f(x_M) + \left[\frac{\partial f}{\partial x} \right]_{x_M} \cdot (a_M t + \epsilon) + \mathcal{O}(\|a_M t + \epsilon\|^2), \quad \text{as } t, \|\epsilon\| \rightarrow 0 \\ &= a_M + J(x_M) \cdot (a_M t + \epsilon) + \mathcal{O}(\|a_M t + \epsilon\|^2), \quad \text{as } t, \|\epsilon\| \rightarrow 0 \\ \implies \frac{d\epsilon}{dt} &= J(x_M) \cdot (a_M t + \epsilon) + \mathcal{O}(\|a_M t + \epsilon\|^2), \quad \text{as } t, \|\epsilon\| \rightarrow 0. \end{aligned}$$

Thus, for sufficiently small time t , we get the eigensystem

$$\frac{d\epsilon}{dt} \approx J(x_M) \cdot \epsilon = \left[\frac{\partial f}{\partial x} \right]_{x_M} \cdot \epsilon, \quad (4.2.22)$$

in terms of the perturbation $\epsilon(t)$ about the mean accelerating flow. In the eigensystem (4.2.22), $J(x_M)$ is the numerical *full-size* Jacobian of the staggered grid full-domain micro-scale system (4.2.19), in contrast to the analytic 3×3 Jacobian in the eigensystem (4.2.9) of §4.2.2. We calculate the j th column of the Jacobian $J(x_M)$ by numerical differentiation to second order approximation (error $\sim \mathcal{O}(\varepsilon^2)$) as,

$$J_j(x_M) = \frac{f(x_M + \varepsilon e_i) - f(x_M - \varepsilon e_i)}{2\varepsilon}, \quad (4.2.23)$$

where e_i is the canonical Euclidean basis vector of size n_m whose i th element is one and all other elements are zero. We use $\varepsilon = 5 \cdot 10^{-6}$ to balance discretisation and roundoff errors in the calculation of numerical Jacobian. For example, with $\varepsilon = 5 \cdot 10^{-6}$, the discretisation error in Jacobian calculation is roughly about $\varepsilon^2 = 2.5 \cdot 10^{-11}$ and the numerical roundoff error is roughly about $10^{-16}/(2\varepsilon) = 10^{-11}$ for 64 bit floating point representation.

The full-size numerical Jacobian $J(x_M)$ of the staggered grid full-domain micro-scale system, depends only on the system parameters Re , g_x , g_n , and

discretisation parameters n , δ , and the mean state x_M , not on the wavenumber. That is the full-size numerical Jacobian $J(x_M)$ encodes the information for all the wavenumbers for the time evolution about the mean accelerating flow.

Section 4.2.6 uses the eigenvalues of the numerical Jacobian of the full-domain micro-scale system, while comparing the eigenvalues of the staggered grid full-domain system with the eigenvalues of the patch scheme for the viscous shallow water flow. For example, Figs. 3.2.1 and 3.2.2 [TODO/update these figrefs] of §3.2.6, plot the eigenvalues $\lambda_{m\delta}^N, \lambda_{m\Delta}^N$ of the numerical Jacobian of the full-domain micro-scale system, with grid interval equal to the sub-patch grid interval δ and the inter-patch distance Δ respectively, of a staggered patch grid.

4.2.5 Computing numerical Jacobian of the staggered patch schemes

The one-cell Jacobian of the staggered patch schemes in §4.2.3, is useful in giving insights about the staggered patch schemes and to compute eigenvalues corresponding to a small macro-scale wavenumber (k_x, k_y) for a patch grid any size N . But, in practice, the staggered patch scheme numerical time simulation is done using the *full-size* evolution equation (4.1.15), not using the one-cell evolution equations (4.2.16). To confirm that full-size staggered patch scheme (4.1.18) is accurate, stable and not too sensitive to numerical roundoff errors, this subsection discusses a method to compute the numerical eigenvalues λ_p^N of the staggered patch schemes for the full evolution equations (4.1.15).

The $F(x^I; x^E(x^I))$ in the staggered patch scheme dynamical system (4.1.18) corresponds to the $f(x)$ in the full-domain micro-scale system (4.1.13). The functions F and f encode same the full-domain micro-scale system for the viscous shallow water PDEs (4.1.6); Section 2.2.2 explains this difference for the generic wave-like system. Consider the full-size staggered patch scheme dynamical system (4.1.18), $dx^I/dt = F(x^I; x^E(x^I))$ for viscous shallow water flow, with the same state vector x^I (2.2.6) and a similar edge vector x^E as those of the patch scheme for generic wave-like system in §2.2.2. We want to characterise the accuracy and stability of the patch schemes for the non-trivial nonlinear evolution of the viscous shallow water flow, apart from the mean flow and any constant drift with time in the solution x^I . Hence, consider the solution $x^I(t)$ as a small perturbation $\epsilon(t)$ for small t , about the mean accelerating flow, that is,

$$x^I(t) = x_M + a_M t + \epsilon(t), \quad (4.2.24)$$

where the mean flow state $\mathbf{x}_M = (h_M, u_M, v_M)$ and the mean acceleration $\mathbf{a}_M = (0, a_1, a_2)$ with a_1 and a_2 being constants in terms of u_M and v_M as in equations (4.2.8). Substituting the solution form (4.2.24) into the staggered patch scheme dynamical system (4.1.18), $d\mathbf{x}^I/dt = \mathbf{F}(\mathbf{x}^I; \mathbf{x}^E(\mathbf{x}^I))$, and following the same steps described in §4.2.4, gives the eigensystem

$$\frac{d\boldsymbol{\epsilon}}{dt} \approx \mathbf{J}(\mathbf{x}_M) \cdot \boldsymbol{\epsilon} = \left[\frac{\partial \mathbf{f}}{\partial \mathbf{x}} \right]_{\mathbf{x}_M} \cdot \boldsymbol{\epsilon}, \quad (4.2.25)$$

in terms of the perturbation $\boldsymbol{\epsilon}(t)$ about the mean accelerating flow. In the eigensystem (4.2.25), $\mathbf{J}(\mathbf{x}_M)$ is the numerical *full-size* $n_p^I \times n_p^I$ Jacobian of the staggered patch scheme (4.1.15), in contrast to the analytic one-cell Jacobian in the eigensystem (4.2.17) of §4.2.3. The number of state variables $n_p^I = (N^2/4)(9n^2/4 - 4n + 2)$ for the full-size patch scheme system, as in the expression (2.2.7). We calculate the columns of the numerical full-size Jacobian $\mathbf{J}(\mathbf{x}_M)$ by numerical differentiation to second order approximation (error $\sim \mathcal{O}(\varepsilon^2)$) as described in §4.2.4,

The full-size numerical Jacobian $\mathbf{J}(\mathbf{x}_M)$ of the staggered patch scheme, depends only on the system parameters Re , g_x , g_n , and discretisation parameters N, n, r, δ, Δ , and the mean state \mathbf{x}_M , not on the wavenumber. That is the full-size numerical Jacobian $\mathbf{J}(\mathbf{x}_M)$ encodes the information for all the wavenumbers for the time evolution about the mean accelerating flow.

The eigenvalues λ_p^N of the numerical staggered patch scheme Jacobian $\mathbf{J}(\mathbf{x}_M)$ characterises the accuracy and stability of the numerical staggered patch schemes over a particular finite sized domain (i.e., N is finite as opposed to infinite staggered patch grid for the on-cell Jacobian). We compare with the eigenvalues λ_p^N of the staggered patch scheme numerical Jacobian, with the eigenvalues of the full domain micro-scale system and the eigenvalues of the viscous shallow water PDEs, while assessing the accuracy (§4.2.6) and stability (§4.4) of the patch schemes.

4.2.6 Staggered patch schemes are accurate for macro-scale waves

Similar to §3.2.6 for the general linear wave, this section explains the qualitative structure of the staggered patch scheme eigenvalues and eigenvectors, and qualitatively demonstrate the accuracy of the staggered patch schemes for the *viscous shallow water flow* for few representative cases. Section 4.5 on the consistency of the staggered patch schemes, quantitatively establish

the patch scheme accuracy in more detail, over a much broader range of parameters.

Similar to §3.2.6, this section demonstrates the accuracy of the developed five staggered patch schemes (Spectral, Square-p2, Square-p4, Square-p6, and Square-p8) by comparing the following eigenvalues in complex plane plots.

1. Eigenvalues λ_p^N of the numerical Jacobian of a staggered patch scheme on a finite domain (§4.2.5).
2. Eigenvalues λ_p^{NE1} of the numerically evaluated one-cell Jacobian in eigensystem (4.2.17) in §4.2.3, of a staggered patch scheme on an infinite domain.
3. Eigenvalues $\lambda_{m\delta}^{NE1}$ of the numerically evaluated analytic Jacobian in eigensystem (4.2.9) in §4.2.2, of fine-grid full-domain micro-scale system, with grid interval equal to the sub-patch grid interval δ . We use the same symbol δ for the grid interval for both the full-domain micro-grid and the sub-patch micro-grid.
4. Eigenvalues $\lambda_{m\Delta}^{NE1}$ of the numerically evaluated analytic Jacobian in eigensystem (4.2.9), of coarse grid version of the full-domain micro-scale system, with $\delta = \Delta$.
5. Eigenvalues λ_{PDE}^{NE1} of the numerically evaluated analytic Jacobian in eigensystem (4.2.4) in §4.2.1, of viscous shallow water PDEs (4.1.6). Comparison with the eigenvalues λ_{PDE}^{NE1} is only for completeness.

All the analytic eigenvalues ($\lambda_p^{NE1}, \lambda_{m\delta}^{NE1}, \lambda_{m\Delta}^{NE1}, \lambda_{PDE}^{NE1}$) are numerically evaluated for all *macro-scale wavenumbers* resolved on a corresponding finite staggered patch grid. To illustrate the complete structure of eigenvalues (i.e., for all wavenumbers) of the full-domain micro-scale system and to cross-verify analytic and numerical computation of the full-domain micro-scale system eigenvalues, we also compute the eigenvalues of the numerical Jacobian of the full-domain micro-scale system for few cases (e.g., Figs. 4.2.1 and 4.2.2).

The sets of eigenvalues (e.g., $\lambda_p^N, \lambda_p^{NE1}, \lambda_{m\delta}^N, \lambda_{m\Delta}^N, \lambda_{PDE}^{NE1}$), in all the complex plane plots, are numbered in the legend entries on the left. In all the complex plane plots, system parameters for each of these eigenvalues are listed in groups *below the legend entries* in a style similar to listing author affiliations. Page 62 of §3.2.6 explains with an example, the conventions of this parameter listing.

Figure 4.2.1: Spectral staggered patch scheme ($N = 6, n = 6$) eigenvalues ($\lambda_p^N, \lambda_p^{NE1}$) on complex plane (*linear scale*) for viscous shallow water flow. Due to large range of magnitudes of eigenvalues, details of eigenvalues for macro-scale modes (mid-right cluster 1) are not clear.

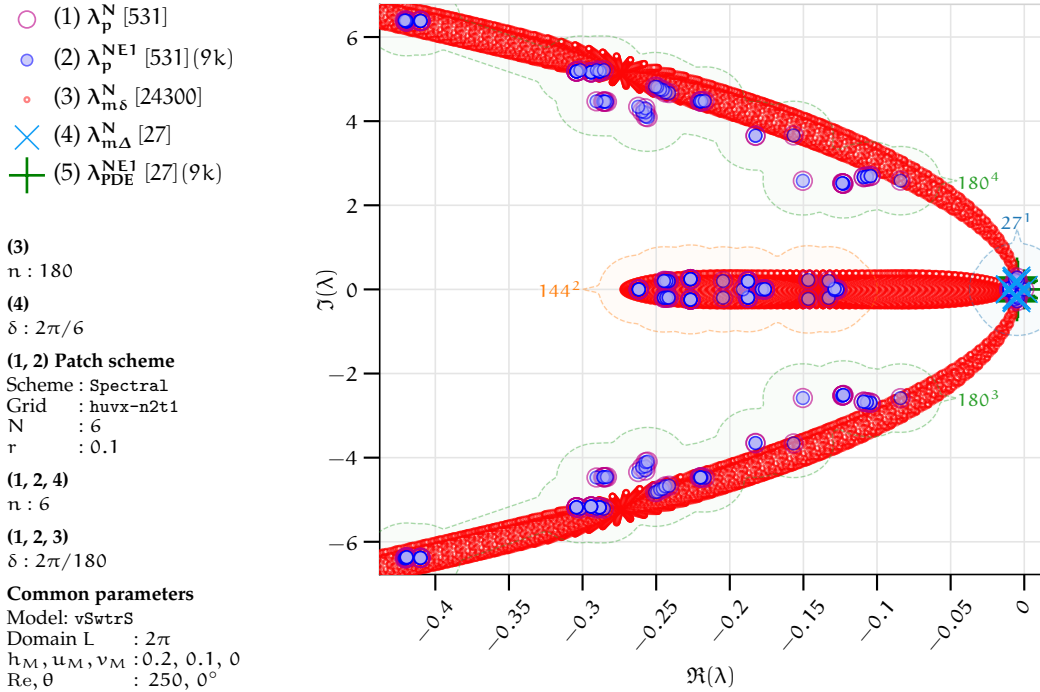
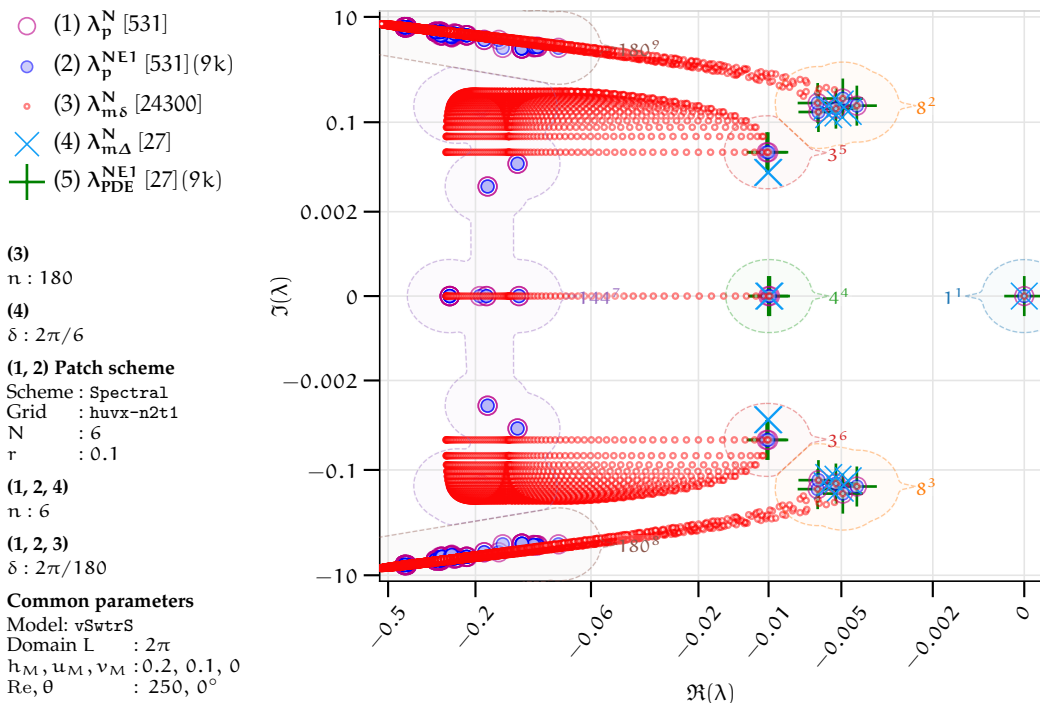


Figure 4.2.2: Spectral staggered patch scheme ($N = 6, n = 6$) eigenvalues ($\lambda_p^N, \lambda_p^{NE1}$) on complex plane (*arcsinh nonlinear scale*) for viscous shallow water flow. The arcsinh scaling zooms out the eigenvalues of macro-scale modes (mid-right cluster 1 in Fig. 4.2.1 to clusters 1–6 here).



Figures 4.2.1 and **4.2.2** plot the eigenvalues $(\lambda_p^N, \lambda_p^{NE1})$ of the Spectral patch scheme on a staggered patch grid with 6×6 macro-grid intervals ($N = 6$) and each patch containing 6×6 sub-patch micro-grid intervals ($n = 6$). Also plotted are the eigenvalues $\lambda_{m\delta}^N, \lambda_{m\Delta}^N$ of respectively the fine- and coarse-grid versions of the full-domain micro-scale system (4.1.11) and the eigenvalues λ_{PDE}^{NE1} of the PDE (4.1.6). Similar to Figs. 4.2.1 and 4.2.2, in all the complex plane eigenvalue plots, eigenvalues are grouped within clusters based on eigenvalues λ_p^{NE1} of the staggered patch scheme Jacobian. Each cluster is annotated with the number of eigenvalues λ_p^{NE1} in the cluster and the cluster number in the superscript.

Page 64 of §3.2.6 explains the rationale and utility of the arcsinh scaling. For example, the clusters of macro-scale eigenvalues on arcsinh scaling (i.e., clusters 1–6 in Fig. 4.2.2) reveal more details, compared to the clusters of macro-scale eigenvalues on linear scaling (i.e., cluster 1 in Fig. 4.2.1). Hence, *most complex plane eigenvalue plots in this thesis are on arcsinh scaling*. Specifically, the complex plane plots on arcsinh scaling, plot an eigenvalue λ as a point on a 2D space with coordinates $(\text{arcsinh}(S_h [\Re \lambda - O_h])/S_h + O_h, \text{arcsinh}(S_v \Im \lambda)/S_v)$, where S_h, S_v are the horizontal and vertical scale factors and $(O_h, 0)$ is the centre of zoom. In this chapter, most plots on arcsinh scaling use the scale factors $S_h = 500, S_v = 10^4$ and the centre of zoom $(O_h, 0) = (-0.001, 0)$ (different from those in §3.2.6 for general linear wave).

As Figs. 4.2.1 and 4.2.2 show, a patch scheme contains only the small wavenumber macro-scale modes on the right (clusters 1–6 in Fig. 4.2.2) and large wavenumber micro-scale modes on the left (clusters 7, 8, 9 in Fig. 4.2.2), not the modes of the intermediate scale. On the other hand, the eigenvalues $\lambda_{m\delta}^N$ of the full-domain micro-scale system, span the eigenvalue plot nearly uniformly from left to right, corresponding to all the wavenumbers resolved on the full-domain micro-scale staggered grid. Figures 4.2.1 and 4.2.2 show a good qualitative agreement of the structure of micro- and macro-scale patch scheme eigenvalues λ_p^N and the complete structure of the eigenvalues $\lambda_{m\delta}^N$ (i.e, for all wavenumbers) of the full-domain micro-scale system. For the accurate multiscale modelling of the macro-scale waves, the agreement between the macro-scale eigenvalues of the patch scheme and those of the full-domain system is the primary focus. Figure 4.2.2 shows that, within the clusters 1–6, the numerical macro-scale eigenvalues λ_p^N of the patch scheme (large magenta circles) and the numerical macro-scale eigenvalues $\lambda_{m\delta}^N$ (small red circles) visually agree.

As Fig. 4.2.2 shows, for both micro-scale and macro-scale modes, the patch scheme eigenvalues λ_p^{NE1} of the numerically evaluated one-cell analytic Jacobian (§4.2.3) and the patch scheme eigenvalues λ_p^N of the numerical

Jacobian ([§4.2.5](#)), agree (i.e., the large magenta and blue circles). Hence, *all other complex plane plots in this subsection §4.2.6 use eigenvalues λ_p^{NE1} of the numerically evaluated one-cell analytic Jacobian ([§4.2.3](#)), as opposed to the numerical eigenvalues λ_p^N .*

[Figures 4.2.1](#) and [4.2.2](#) show the complete structure of eigenvalues $\lambda_{m\delta}^N$ (i.e, for all wavenumbers) of the full-domain micro-scale system, for a full-domain staggered grid with the same grid interval δ as the sub-patch micro-grid interval of a patch grid with $N = 6$ and patch scale ratio $r = 0.1$. As [p. 64](#) of [§3.2.6](#) explains, for patch grids with $N > 6$ and/or $r < 0.1$, the corresponding full-size Jacobians of the fine-grid full-domain micro-scale system, rapidly increase in size, requiring substantially larger computational effort and memory. For the accurate multiscale modelling of the macro-scale waves, the agreement between the macro-scale eigenvalues of the patch scheme and those of the full-domain system is the primary focus, not the eigenvalues corresponding to all the wavenumbers. That is, to assess the patch scheme accuracy, as in [Fig. 4.2.4](#) it suffices to compare only the patch scheme macro-scale eigenvalues with the macro-scale eigenvalues $\lambda_{m\delta}^{NE1}$ of the full-domain micro-scale system (by numerically evaluating the analytic Jacobian ([§4.2.2](#)) only for macro-scale wavenumbers resolved on a staggered patch grid). Hence, to avoid large computational effort and as the primary focus is on the macro-scale eigenvalues, *all other complex plane plots in this subsection §4.2.6 use eigenvalues $\lambda_{m\delta}^{NE1}$ of the numerically evaluated analytic Jacobian ([§4.2.2](#)), as opposed to the numerical eigenvalues $\lambda_{m\delta}^N$.*

This paragraph explains the general qualitative structure of the patch scheme eigenvalues for the viscous shallow water flow. [Figures 4.2.3](#) to [4.2.10](#) plot the Spectral patch scheme eigenvalues, over a staggered patch grid with 10×10 macro-grid intervals ($N = 10$) and each patch containing 6×6 sub-patch micro-grid intervals ($n = 6$). [Figures 4.2.3](#) to [4.2.6](#) plot the eigenvalues for different linearisation point (h_M, u_M, v_M) , where h_M is the mean height and u_M, v_M are the mean horizontal velocities. [Figures 4.2.9](#) to [4.2.10](#) plot the eigenvalues for different Reynolds numbers Re . The following points are mainly based on the Spectral patch scheme eigenvalues in [Figs. 4.2.3](#) to [4.2.6](#) and the corresponding eigenvectors (the patch scheme modes) in [Figs. 3.2.13](#) to [3.2.18](#) and [Figs. 4.2.11](#) and [4.2.12](#). But *these points hold in general for the eigenvalues of, the PDE, full-domain micro-scale system, and all the patch schemes including the polynomial schemes, for the viscous shallow water flow*. The number just next to each cluster is the number of eigenvalues in that cluster. The cluster numbers referred to below are indicated on the plots by the *superscript* of the number just next to each cluster.

Figure 4.2.3: Spectral staggered patch scheme ($N = 10, n = 6$) eigenvalues for viscous shallow water flow for $(h_M, u_M, v_M) = (0.2, 0, 0)$. The macro-scale eigenvalues λ_p^{NE1} in clusters 1–4 agree with the macro-scale eigenvalues $\lambda_{m\delta}^{NE1}$ of the fine-grid full-domain micro-scale system.

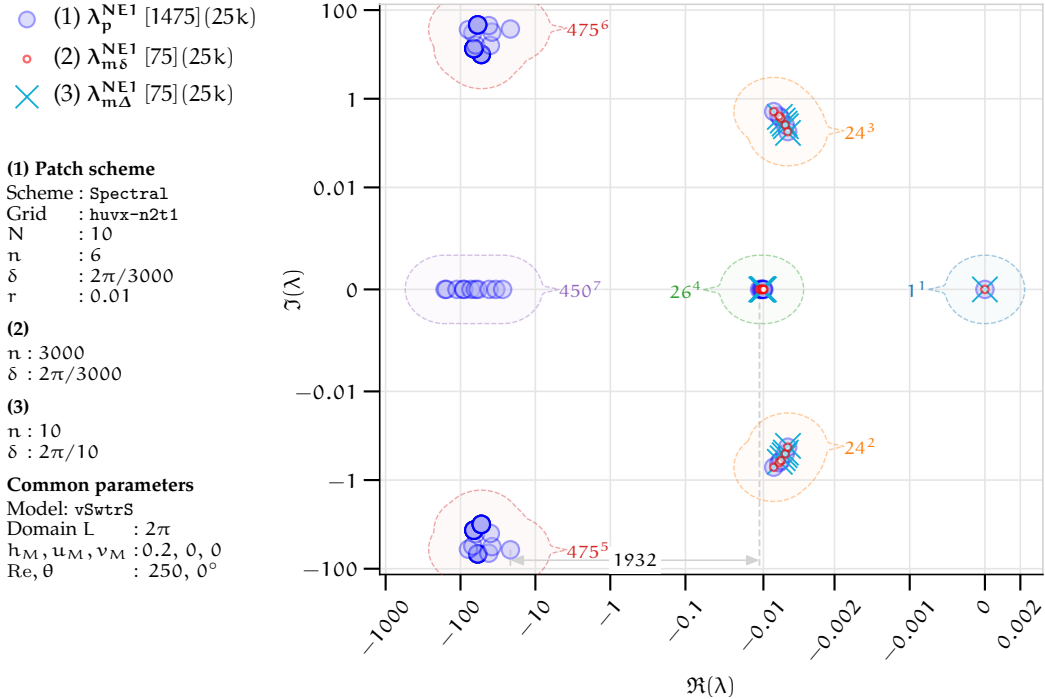


Figure 4.2.4: Spectral staggered patch scheme ($N = 10, n = 6$) eigenvalues for viscous shallow water flow for $(h_M, u_M, v_M) = (0.2, 0.1, 0)$. The macro-scale eigenvalues λ_p^{NE1} in clusters 1–6 agree with the macro-scale eigenvalues $\lambda_{m\delta}^{NE1}$ of the fine-grid full-domain micro-scale system.

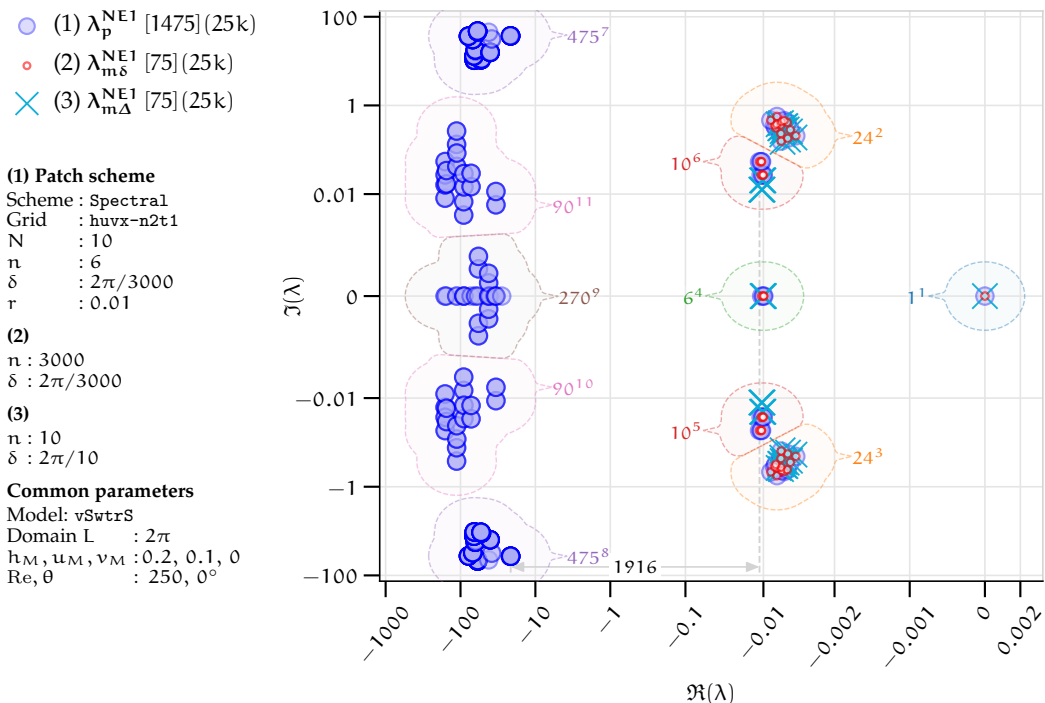


Figure 4.2.5: Spectral patch scheme ($N = 10, n = 6$) eigenvalues for viscous shallow water flow for $(h_M, u_M, v_M) = (0.2, 0.4, 0)$. Eigenvalues λ_p^{NE1} and $\lambda_{m\delta}^{NE1}$ agree for macro-scale modes in clusters 1–6. Minimum real parts $\min \Re \lambda_{p\mu}^{NE1} = -156$ (micro-scale), $\min \Re \lambda_{pM}^{NE1} = -0.011$ (macro-scale).

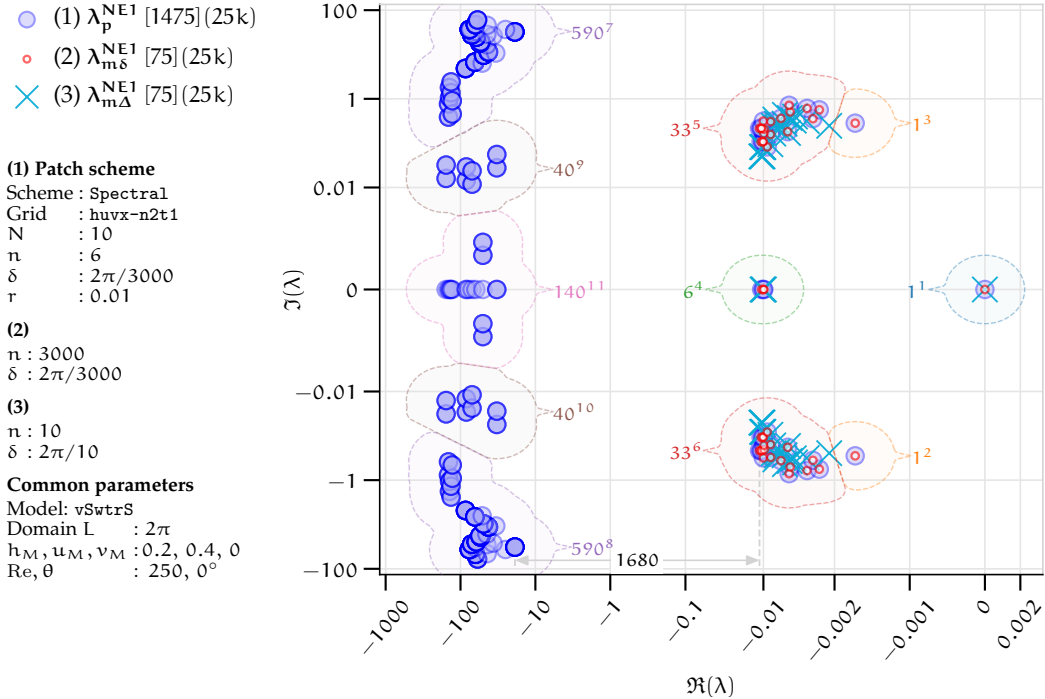
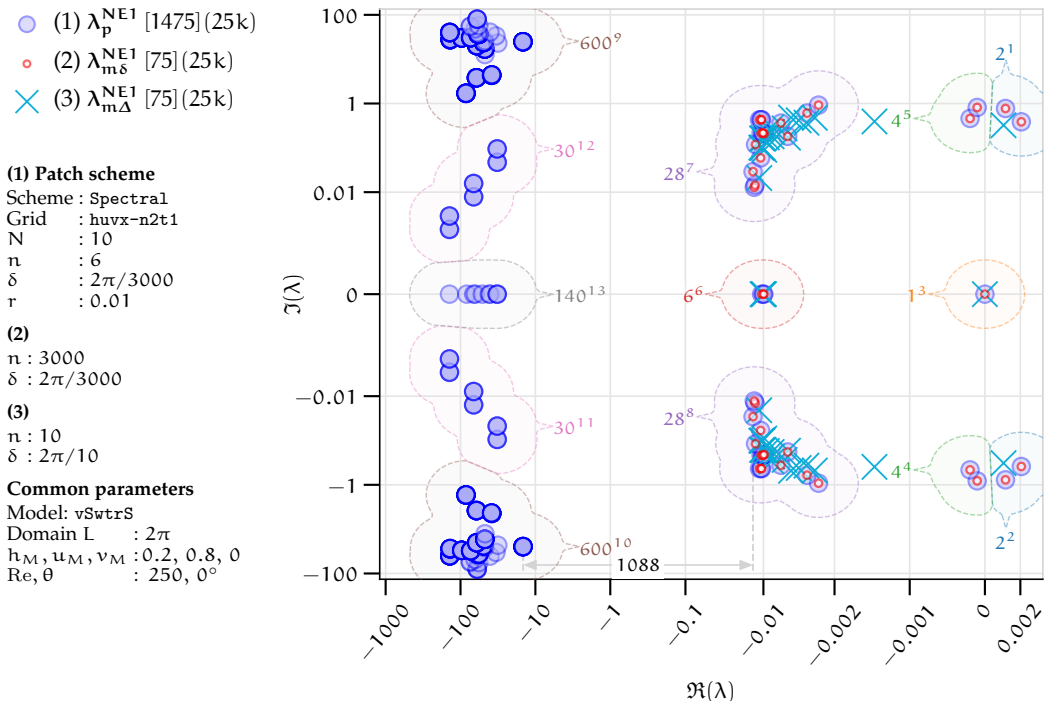


Figure 4.2.6: Spectral staggered patch scheme ($N = 10, n = 6$) eigenvalues for viscous shallow water flow for $(h_M, u_M, v_M) = (0.2, 0.8, 0)$. Eigenvalues λ_p^{NE1} and $\lambda_{m\delta}^{NE1}$ agree for macro-scale modes in clusters 1–8. Maximum real parts $\max \Re \lambda_{m\delta}^{NE1} = \max \Re \lambda_p^{NE1} = 0.0021$ indicate *physical instability*.



- The *macro-scale clusters* (containing macro-scale eigenvalues) are identified in the caption for each of Figs. 4.2.3 to 4.2.10. The eigenvalues within all *other* clusters correspond to sub-patch *micro-scale modes*. There are $3N^2/4$ macro-scale modes and $(N^2/4)(9n^2/4 - 4n - 1)$ micro-scale modes, same as those of the general linear wave in p. 71 of §3.2.6. All the following points in this listing are about the patch scheme macro-scale modes for the viscous shallow water flow.
- Increasing N computes more macro-scale modes for larger wavenumbers, for example the clusters 2–6 in Fig. 4.2.2 extend to the left along the eigenvalues of the full-domain system (small red circles).
- Some of the complex conjugate eigenvalues with small negative real parts, correspond to slowly decaying *macro-scale wave modes* with small wavenumber. These macro-scale wave modes are qualitatively same as the macro-scale wave modes of the general linear wave (e.g., the eigenvector in Fig. 3.2.15 of §3.2.6). Such eigenvalues of macro-scale wave modes are present in all of Figs. 4.2.3 to 4.2.10. For small mean velocity $u_M \lesssim 0.1$, these eigenvalues of macro-scale wave modes form clearly separated clusters. For example, all the 24 eigenvalues in each of the clusters 2, 3 in Figs. 4.2.3 and 4.2.4 are of macro-scale wave modes. There are $2(N^2/4 - 1)$ macro-scale wave modes, same as those of the general linear wave in p. 71 of §3.2.6.
- For nonzero mean velocities, $u_M > 0$ or $v_M > 0$, some of the complex conjugate eigenvalues with small negative real parts correspond to slowly decaying *macro-scale translatory wave modes* with small wavenumber. For example, all the eigenvalues in the clusters 5, 6 in Fig. 4.2.4 are of macro-scale translatory wave modes as Fig. 4.2.11 shows. In Fig. 4.2.11, only v is nonzero, indicating the translatory wave mode (static spatial v -profile) without any dynamic energy exchange with height (i.e., $h = 0$). That is, in contrast to the dynamical wave modes, the translatory waves modes are static (non-oscillatory) wavy spatial profiles advected by the mean velocity (e.g., $u_M = 0.1$ in Fig. 4.2.11), without any energy exchange between the potential (height h) and kinetic energy (velocity u, v). The translatory wave modes are *not* present in general linear wave.
- When $u_M > 0$ and/or $v_M > 0$, there are $N^2/4 - N/2$ macro-scale translatory wave modes. For small mean velocity $u_M \lesssim 0.1$, the eigenvalues of macro-scale translatory wave modes form clearly separated clusters as in Fig. 4.2.4. For larger mean velocity $u_M \gtrsim 0.1$,

the eigenvalue clusters of the macro-scale (dynamical/oscillatory) wave modes and those of the macro-scale translatory wave modes distort and overlap, as in Figs. 4.2.5 to 4.2.10. For zero mean velocity $u_M, v_M = 0$, there are $N^2/4 - 1$ vortex modes, same as those of the general linear wave in p. 71 of §3.2.6. For example, 24 eigenvalues within the cluster 4 of Fig. 4.2.3 ($N = 10$) are of the macro-scale vortex modes. For nonzero u_M and/or v_M , the $N^2/4 - 1$ macro-scale vortex modes split into $N/2 - 1$ macro-scale vortex modes with real negative eigenvalues and $N^2/4 - N/2$ macro-scale translatory wave modes with $N^2/8 - N/4$ pairs of complex conjugate eigenvalues. For example, in Fig. 4.2.4 for $N = 10$, the four eigenvalues in the cluster 4 are macro-scale vortex modes, the ten eigenvalues in each of the clusters 5, 6 are macro-scale translatory wave modes.

- Same as for the general linear wave, *two* of the small real negative eigenvalues correspond to the macro-scale mode of decelerating uniform mean flow irrespective of N, n . For example, two eigenvalues within the cluster 4 of Figs. 4.2.3 and 4.2.4 and are of the macro-scale modes of decelerating uniform mean flow. These modes of decelerating uniform mean flow are qualitatively same as the modes of the general linear wave (e.g., the eigenvector in Fig. 3.2.14 of §3.2.6).
- Some of the small real negative eigenvalues correspond to slowly decaying *macro-scale vortex modes* with small wavenumber. These macro-scale wave modes are qualitatively same as the macro-scale vortex modes of the general linear wave (e.g., the eigenvector in Fig. 3.2.16 of §3.2.6).
- For zero mean velocity $u_M, v_M = 0$, there is one zero eigenvalue as in the cluster 1 of Fig. 4.2.3, that corresponds to the *macro-scale mode of stagnant water* (zero eigenvalue, hence temporally constant) with uniform height and no flow (i.e., $u = v = 0$). This stagnant water mode is qualitatively same as the macro-scale mode of the general linear wave (e.g., eigenvector in Fig. 3.2.13). For nonzero u_M and/or v_M , the macro-scale stagnant water mode change into the macro-scale steady (zero eigenvalue, hence temporally constant) uniform flow (spatially constant height and velocity). For example, Fig. 4.2.12 shows the *macro-scale mode of steady uniform flow* corresponding to the cluster 1 of Fig. 4.2.4.

As Page 74 of §3.2.6 defines, a *staggered patch scheme is accurate* when the macro-scale eigenvalues (e.g., $\lambda_p^N, \lambda_p^{NE1}$) of the staggered patch schemes

are close to the macro-scale eigenvalues (e.g., $\lambda_{m\delta}^{NE1}$) of the corresponding fine-grid full-domain micro-scale system with the same grid interval as the sub-patch micro-grid interval. Comparing macro-scale eigenvalues λ_p^{NE1} , $\lambda_{m\delta}^{NE1}$ the following paragraphs show that the staggered patch schemes are accurate for macro-scale viscous shallow water flows for different linearisation point h_M , u_M , v_M and Reynolds number Re .

The *staggered patch schemes are accurate for macro-scale viscous shallow water flows for different mean velocity u_M, v_M* . In contrast to the eigenvalues of the general linear wave in §3.2.6, due to the nonlinearity, the *eigenvalues of the viscous shallow water flow depend on the mean height h_M and the mean velocity h_M, v_M* . That is, the eigenvalues of the viscous shallow water flow depends on the linearisation point (h_M, u_M, v_M) . Figures 4.2.3 to 4.2.6 plot the Spectral patch scheme ($N = 10, n = 6$) eigenvalues for different mean velocity $u_M = 0, 0.1, 0.4, 0.8$ respectively, keeping $h_M = 0.2$ and $v_M = 0$. The following points summarise the key dependence of the patch scheme eigenvalues on increasing mean velocity u_M . As §4.6 on frame invariance of staggered patch schemes establish, the patch schemes are invariant (within discretisation errors) with different flow angle α for macro-scale waves, where $q = \sqrt{u_M^2 + v_M^2}$, $u_M = q \cos(\alpha)$ and $v_M = q \sin(\alpha)$. Hence, whereas the following points are based on increasing u_M keeping $v_M = 0$, they hold in general for increasing u_M and/or v_M . All the characteristics in the following listing also hold for the polynomial patch schemes.

- Figures 4.2.3 to 4.2.6 show that for the different mean velocity of $u_M = 0, 0.1, 0.4, 0.8$, the macro-scale eigenvalues λ_p^{NE1} of the Spectral patch scheme (large blue circles within macro-scale clusters identified in figure caption), agree with the macro-scale eigenvalues $\lambda_{m\delta}^{NE1}$ (small red circles) of the fine-grid full-domain micro-scale system. This macro-scale agreement of eigenvalues $\lambda_p^{NE1}, \lambda_{m\delta}^{NE1}$ indicates that the *patch schemes are accurate for macro-scale viscous shallow water flows of different mean velocity*.
- While increasing u_M from zero to 0.8, as the previous paragraph explains, first the vortex modes (e.g., cluster 4 in Fig. 4.2.3) split into vortex modes and translatory wave modes (e.g., clusters 4, 5, 6 in Fig. 4.2.4), next the clusters of translatory wave modes distort and overlap with the clusters of the (dynamical/oscillatory) wave mode (e.g., clusters 5, 6 in Figs. 4.2.5 and 4.2.6).
- The *spectral gap* (between the micro-scale and macro-scale patch scheme eigenvalues) *decreases with increasing mean velocity u_M* . For

example, in Figs. 4.2.3 to 4.2.6 for $u_M = 0, 0.1, 0.4, 0.8$, the corresponding spectral gaps are 1932, 1916, 1680, 1088. This decreasing spectral gap with increasing u_M is the most prevalent trend among the various combinations of u_M , Reynolds number Re , mean height h_M , and patch scale ratio r . But, *in general increasing u_M increases or decreases spectral gap depending upon the combinations of the grid parameters (N, n, r) and system parameters (Re, h_M, u_M)*.

- For large mean velocity $u_M \gtrsim 0.5$, the viscous shallow water flow has inherent *physical instability*, that is, full-domain micro-scale system itself is unstable. Such physical instability is evident from the positive real part eigenvalues of the full-domain micro-scale system in Fig. 4.2.6 (clusters 1, 2). Section 4.4.1 shows the detailed trends of such physical instabilities as captured by the patch scheme for a wide range of parameters such as h_M, u_M, Re, N, r, n .

The *staggered patch schemes are accurate for macro-scale viscous shallow water flows for different mean height h_M* . Figures 4.2.7, 4.2.4 and 4.2.8 plot the Spectral patch scheme ($N = 10, n = 6$) eigenvalues for different mean heights $h_M = 0.1, 0.2, 0.3$ respectively, keeping $u_M = 0.1$ and $v_M = 0$. The following points summarise the key dependence of the patch scheme eigenvalues on increasing mean height h_M . All the characteristics in the following listing also hold for the polynomial patch schemes.

- Figures 4.2.7, 4.2.4 and 4.2.8 show that for the different mean heights of $h_M = 0.1, 0.2, 0.3$, the macro-scale eigenvalues λ_p^{NE1} of the Spectral patch scheme (large blue circles within macro-scale clusters identified in figure caption), agree with the macro-scale eigenvalues $\lambda_{m\delta}^{NE1}$ (small red circles) of the fine-grid full-domain micro-scale system. This macro-scale agreement of eigenvalues $\lambda_p^{NE1}, \lambda_{m\delta}^{NE1}$ indicates that the *patch schemes are accurate for macro-scale viscous shallow water flow for different mean heights*.
- While increasing h_M from 0.1 to 0.3, both the micro-scale and macro-scale eigenvalues move to the left, taking larger negative real parts. That is, increasing h_M increases both the micro-scale and macro-scale dissipation.
- Whereas both the micro-scale and macro-scale dissipation increases with increasing h_M , the micro-scale dissipation increases at larger rate. That is, increasing h_M decreases the real parts of micro-scale eigenvalues (e.g., on the left most clusters in Figs. 4.2.7, 4.2.4 and 4.2.8)

Figure 4.2.7: Spectral staggered patch scheme ($N = 10, n = 6$) eigenvalues for viscous shallow water flow for $(h_M, u_M, v_M) = (0.1, 0.4, 0)$. Eigenvalues λ_p^{NE1} and $\lambda_{m\delta}^{NE1}$ agree for macro-scale modes in clusters 1–6. Increasing mean height h_M increases spectral gap (Figs. 4.2.7, 4.2.4 and 4.2.8).

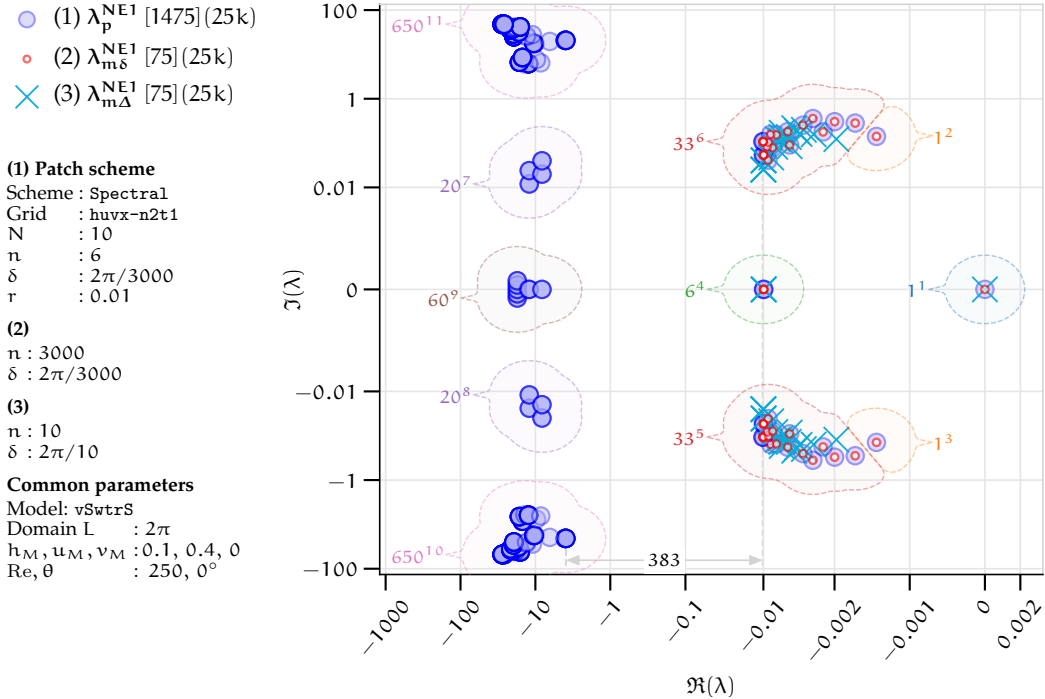
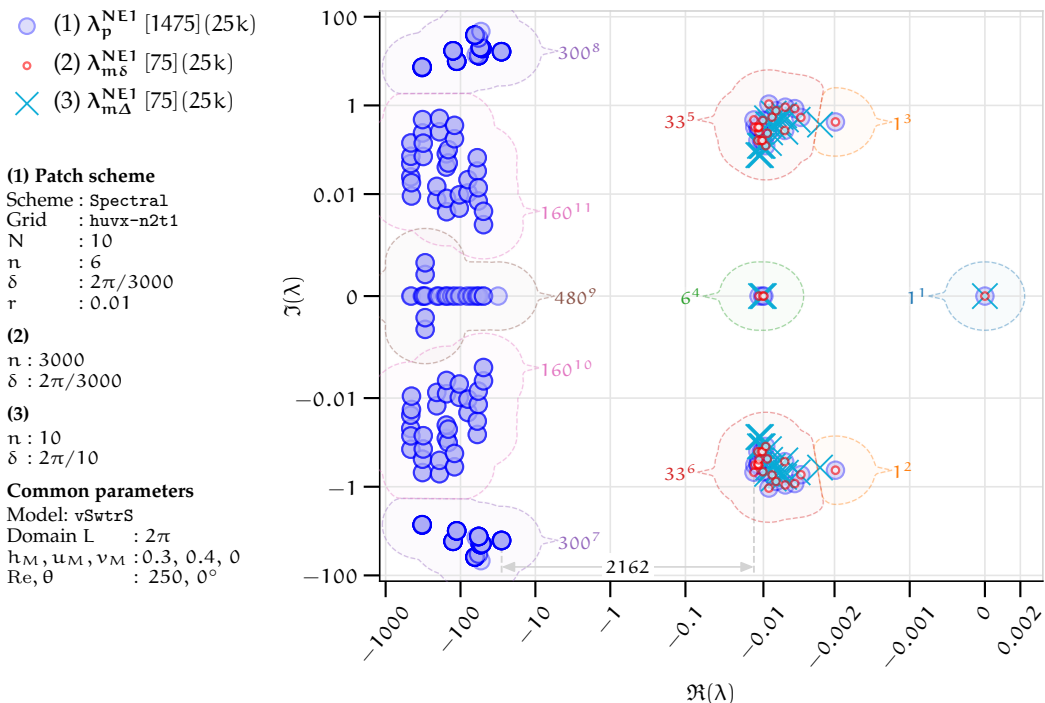


Figure 4.2.8: Spectral staggered patch scheme ($N = 10, n = 6$) eigenvalues for viscous shallow water flow for $(h_M, u_M, v_M) = (0.3, 0.4, 0)$. Eigenvalues λ_p^{NE1} and $\lambda_{m\delta}^{NE1}$ agree for macro-scale modes in clusters 1–6. Increasing mean height h_M increases spectral gap (Figs. 4.2.7, 4.2.4 and 4.2.8).



at larger rate than increasing the real parts of macro-scale eigenvalues, resulting in increasing spectral gap. Hence, the spectral gap increases with increasing mean height h_M . For example, in Figs. 4.2.7, 4.2.4 and 4.2.8 for mean heights $h_M = 0.1, 0.2, 0.3$, the corresponding spectral gaps are 383, 1916, 2162. But, for some combinations of the grid parameters (N, n, r) and system parameters (Re, h_M, u_M), increasing h_M also pushes some of the micro-scale eigenvalues to the right. Hence, the spectral gap decreases with increasing mean height h_M . *In general increasing h_M increases or decreases spectral gap depending upon the combinations of the grid parameters (N, n, r) and system parameters (Re, h_M, u_M).*

The staggered patch schemes are accurate for macro-scale viscous shallow water flows for different Reynolds number Re . Figures 4.2.9, 4.2.10 and 4.2.5 plot the Spectral patch scheme ($N = 10, n = 6$) eigenvalues for different Reynolds numbers $Re = 10, 50, 250, 1250$ respectively. The following points summarise the key dependence of the patch scheme eigenvalues on increasing Reynolds numbers Re . All the characteristics in the following listing also hold for the polynomial patch schemes.

- Figures 4.2.9, 4.2.10 and 4.2.5 show that for the different Reynolds numbers of $Re = 10, 50, 250$, the macro-scale eigenvalues λ_p^{NE1} of the Spectral patch scheme (large blue circles within macro-scale clusters identified in figure caption), agree with the macro-scale eigenvalues $\lambda_{m\delta}^{NE1}$ (small red circles) of the fine-grid full-domain micro-scale system. This macro-scale agreement of eigenvalues $\lambda_p^{NE1}, \lambda_{m\delta}^{NE1}$ indicates that the *patch schemes are accurate for macro-scale viscous shallow water flows of different Reynolds numbers*.
- Increasing Reynolds number Re decreases the dissipation for both macro-scale and sub-patch micro-scale modes of the patch schemes. Decreasing dissipation increases the real parts of the patch scheme macro-scale and micro-scale eigenvalues, moving to the right in the complex plane plots. For example, in Figs. 4.2.9, 4.2.10 and 4.2.5 for $Re = 10, 50, 250$, the minimum real parts of the patch scheme for micro-scale eigenvalues are $\min \Re \lambda_{p\mu}^{NE1} = -5785, -1147, -156$, and for macro-scale eigenvalues are $\min \Re \lambda_{pM}^{NE1} = -0.28, -0.056, -0.011$ respectively.
- The *spectral gap* (between the micro-scale and macro-scale patch scheme eigenvalues) *increases with increasing Reynolds number Re* . For example, in Figs. 4.2.9, 4.2.10 and 4.2.5 for $Re = 10, 50, 250$, the corresponding spectral gaps are 3.1, 65, and 1680. This increasing spectral

Figure 4.2.9: Spectral staggered patch scheme ($N = 10, n = 6$) eigenvalues for viscous shallow water flow for $Re = 10$. Eigenvalues λ_p^{NE1} and $\lambda_{m\delta}^{NE1}$ agree for macro-scale modes in clusters 1–4. Minimum real parts $\min \Re \lambda_{p\mu}^{NE1} = -5785$ (micro-scale), $\min \Re \lambda_{pM}^{NE1} = -0.28$ (macro-scale).

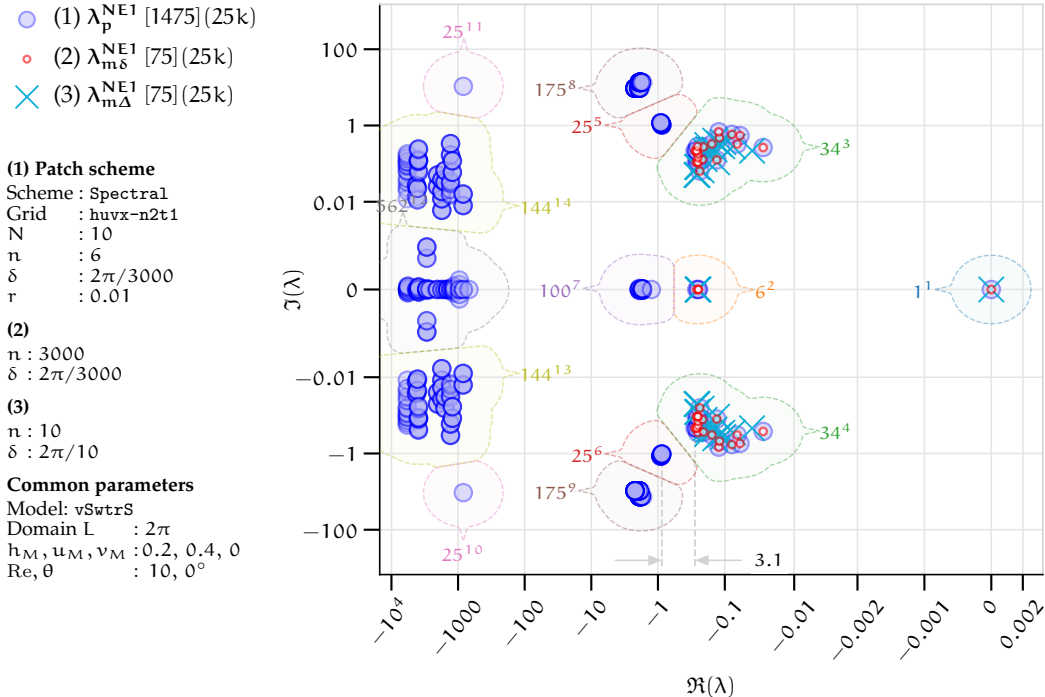
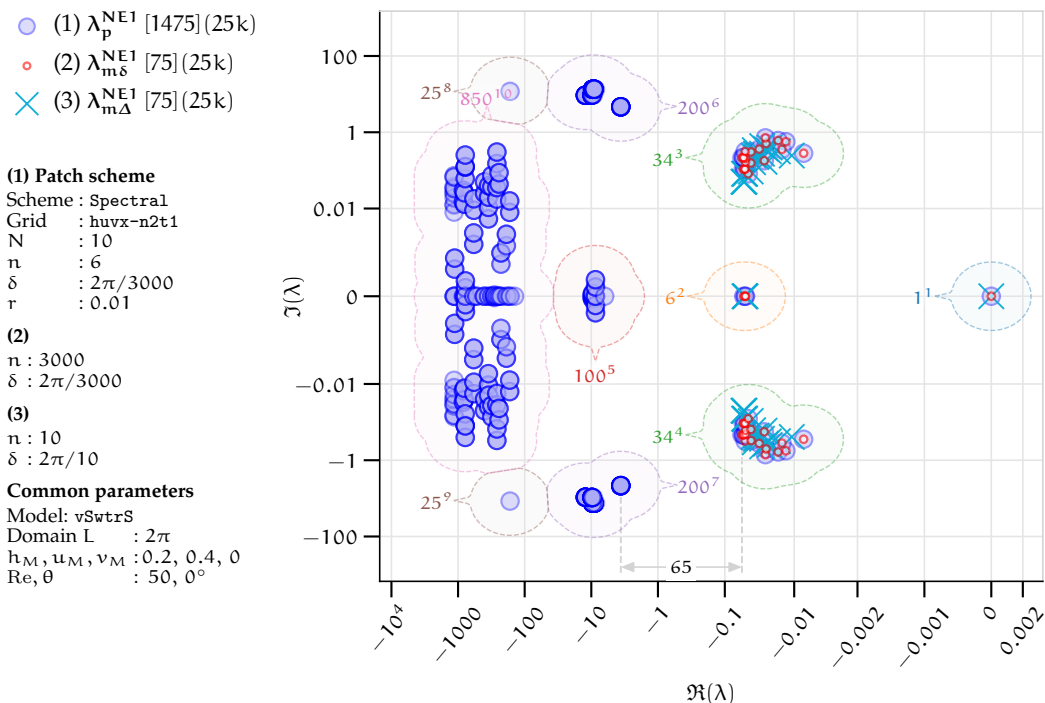


Figure 4.2.10: Spectral staggered patch scheme ($N = 10, n = 6$) eigenvalues for viscous shallow water flow for $Re = 50$. Eigenvalues λ_p^{NE1} and $\lambda_{m\delta}^{NE1}$ agree for macro-scale modes in clusters 1–4. Minimum real parts $\min \Re \lambda_{p\mu}^{NE1} = -1147$ (micro-scale), $\min \Re \lambda_{pM}^{NE1} = -0.056$ (macro-scale).



gap with increasing Re is the most prevalent trend among the various combinations of mean height h_M , mean velocity u_M , Reynolds number Re , and patch scale ratio r . Increasing Re also decreases the spectral gap for some combinations of the grid parameters (N, n, r) and system parameters (Re, h_M, u_M).

In Figs. 4.2.3 to 4.2.8 for different linearisation point h_M, u_M, v_M , and in Figs. 4.2.9, 4.2.10 and 4.2.5 for different Reynolds number Re , the macro-scale eigenvalues λ_p^{NE1} of the Spectral patch scheme (large blue circles within macro-scale clusters identified in figure caption), agree with the macro-scale eigenvalues $\lambda_{m\delta}^{NE1}$ (small red circles) of the fine-grid full-domain micro-scale system. This agreement of the Spectral patch scheme macro-scale eigenvalues with those of the fine-grid full-domain system, is exact (within numerical roundoff errors). The polynomial patch scheme macro-scale eigenvalues also agree with those of the fine-grid full-domain system. Unlike the exact accuracy of the Spectral patch scheme, the polynomial patch scheme accuracy increases with increasing polynomial interpolation order p and decreasing macro-grid interval Δ (§4.5 show such parametric dependence of the accuracy). Thus, the *staggered patch schemes are accurate for macro-scale viscous shallow water flow, about different linearisation points, and for different Reynolds number*. Section 4.5 on the consistency of the staggered patch schemes, quantitatively demonstrate the accuracy for wider range of parameters such as h_M, u_M, Re, N, r, n .

Figures 4.2.11 and 4.2.12 plot two patch scheme eigenvectors (modes) for the viscous shallow water flow, that are qualitatively different from the patch scheme modes of the general linear wave in Figs. 3.2.13 to 3.2.18. As p. 191 of this §4.2.6 explains, Fig. 4.2.11 plots the macro-scale translatory wave mode corresponding to an eigenvalue in cluster 6 of Fig. 4.2.4. As p. 192 of this §4.2.6 explains, Fig. 4.2.12 plots the steady uniform flow mode corresponding to the zero eigenvalues in cluster 1 of Fig. 4.2.4. These eigenvectors are computed for the numerical Jacobian (§3.2.5) of the Spectral staggered patch scheme. The qualitative shapes of the eigenvectors in Figs. 4.2.11 and 4.2.12 are the same for the Spectral (§2.3.1) and polynomial (§2.3.2) staggered patch schemes Square-p2, Square-p4, Square-p6, and Square-p8.

[qqq] =====

Figure 4.2.11: Eigenvector for eigenvalue $\lambda_p^N = 0.0100 + 0.0269 i$ (cluster 6 in Fig. 4.2.4), for Spectral staggered patch scheme with $N = 10$, $n = 6$, $r = 0.01$. Only v is nonzero, indicating *translatory wave mode* (static spatial v -profile) without any dynamic energy exchange with height (i.e., $h = 0$).

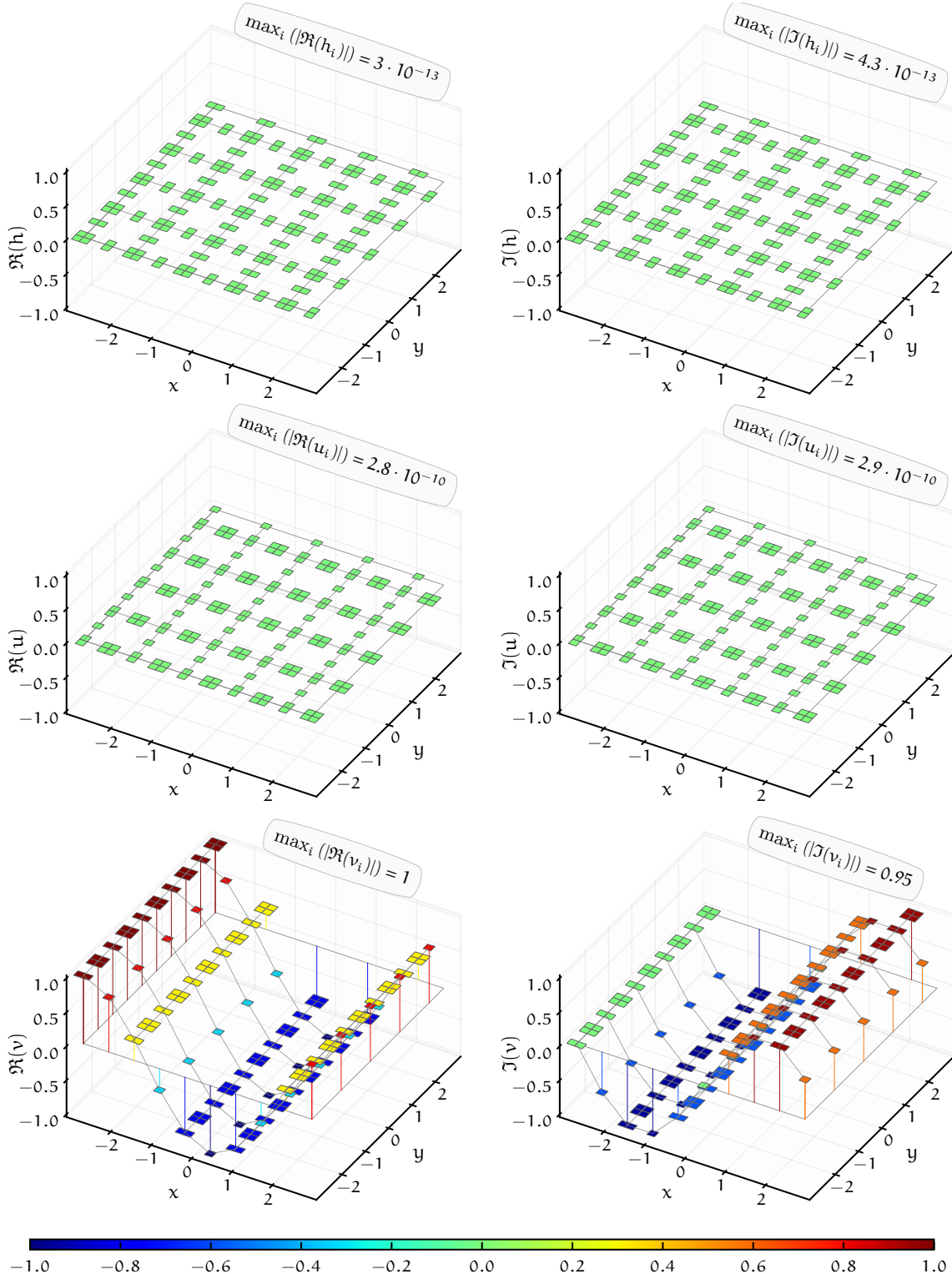


Figure 4.2.12: Eigenvector for eigenvalue $\lambda_p^N = 0 + 0i$ (cluster 1 in Fig. 4.2.4), for Spectral staggered patch scheme with $N = 10$, $n = 6$, $r = 0.01$. For $u_M = 0.1$, the macro-scale mode of steady (zero eigenvalue, hence temporally constant) uniform flow (spatially constant height h and velocity u).

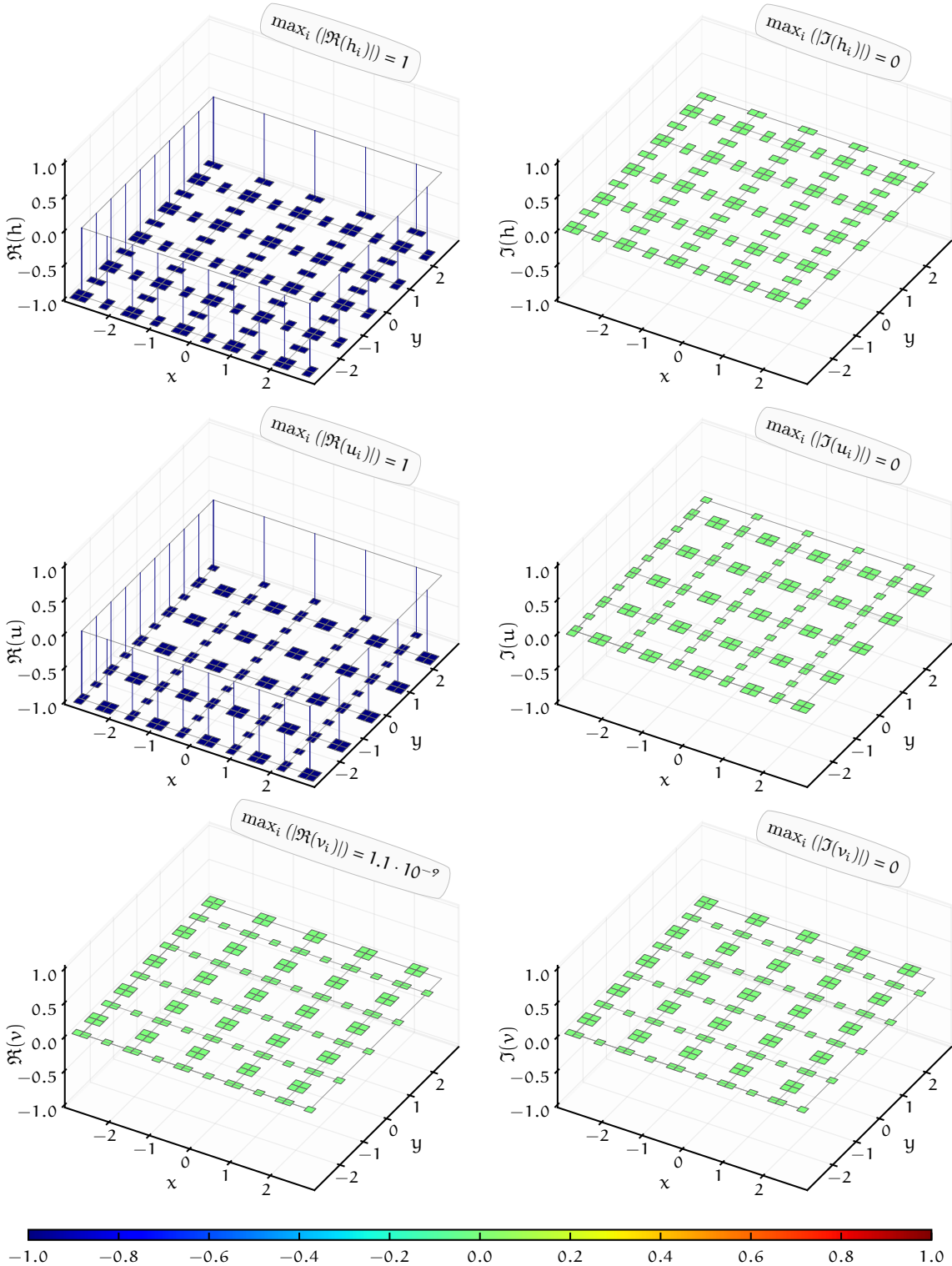


Figure 4.2.13: Spectral staggered patch scheme ($N = 10, n = 6, r = 0.1$) eigenvalues for viscous shallow water flow for $(h_M, u_M, v_M) = (0.1, 0.1, 0)$. Eigenvalues λ_p^{NE1} and $\lambda_{m\delta}^{NE1}$ agree for macro-scale modes in clusters 1–6. Decreasing r increases spectral gap (Figs. 4.2.13, 4.2.7 and 4.2.14).

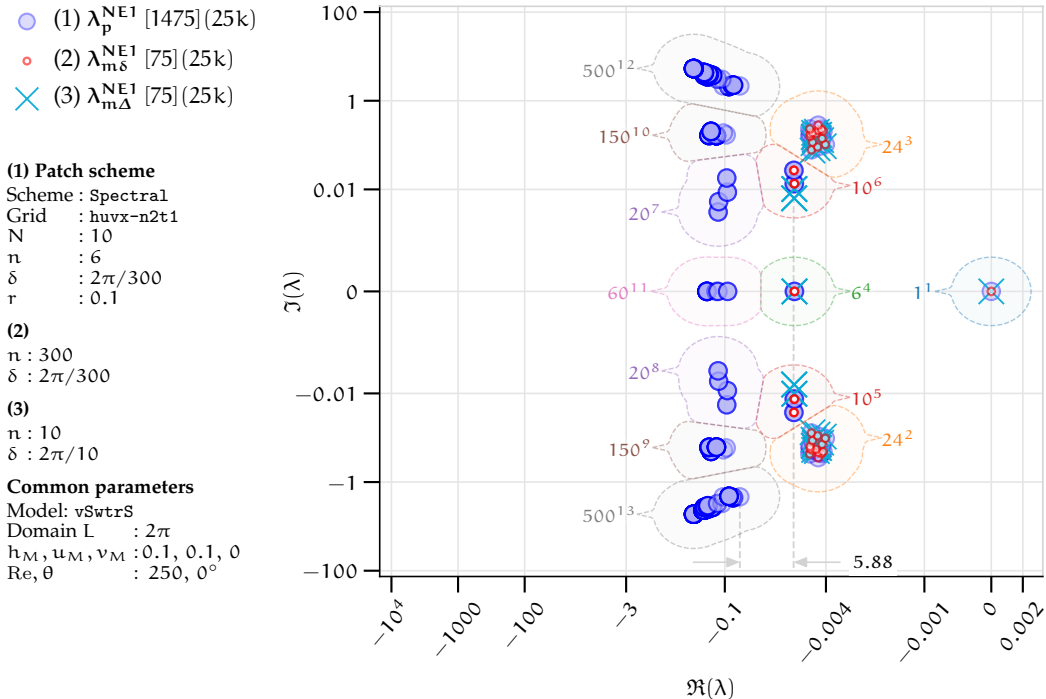
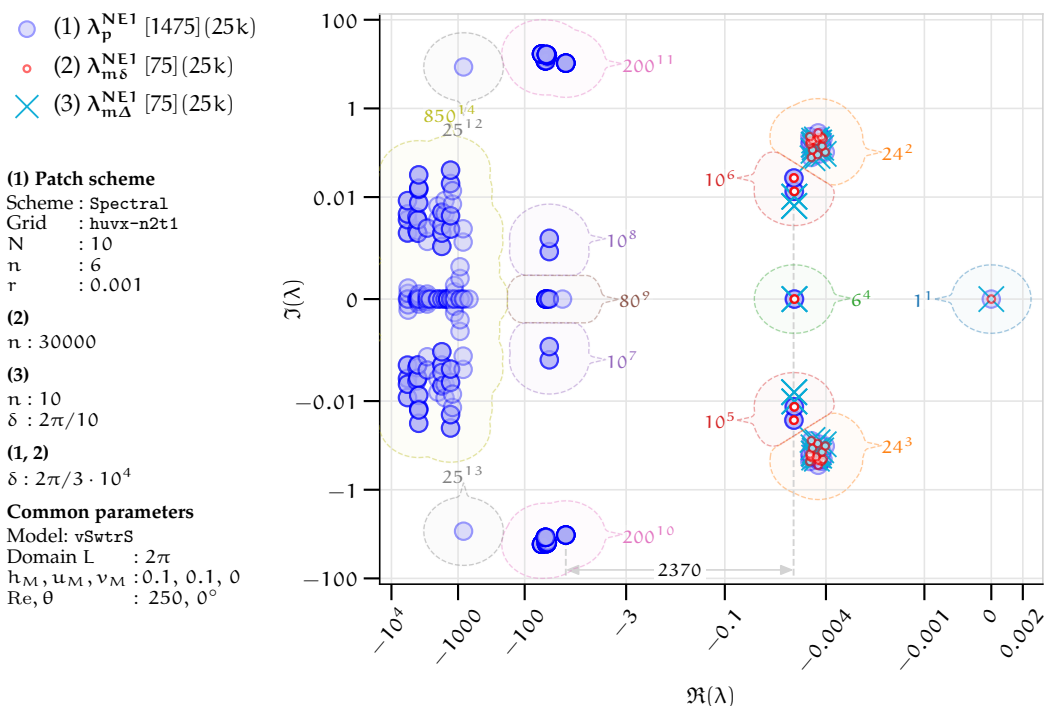


Figure 4.2.14: Spectral staggered patch scheme ($N = 10, n = 6, r = 0.001$) eigenvalues for viscous shallow water flow for $(h_M, u_M, v_M) = (0.1, 0.1, 0)$. Eigenvalues λ_p^{NE1} and $\lambda_{m\delta}^{NE1}$ agree for macro-scale modes in clusters 1–6. Decreasing r increases spectral gap (Figs. 4.2.13, 4.2.7 and 4.2.14).



4.3 Staggered patch schemes are not sensitive to numerical roundoff errors

Despite the attractive characteristics, if the staggered patch schemes are very sensitive to numerical roundoff errors, they will not be suitable for practical numerical simulations using finite precision floating point representations, for example the common 64 bit format of IEEE754 (Goldberg 1991). From both qualitative arguments and quantitative evidence, this section shows that staggered the patch schemes are not sensitive to numerical roundoff errors for the viscous shallow water flow.

The staggered patch scheme eigenvalues λ_p^{NE1} (for both the micro-scale and macro-scale mdoes) of the numerically evaluated one-cell Jacobian ([§4.2.3](#)) and the staggered patch scheme eigenvalues λ_p^N of the numerical Jacobian ([§4.2.5](#)), *visually* agree in the complex plane eigenvalue plots of [§4.2.6](#) (i.e., the large magenta and blue circles in [Fig. 4.2.2](#)). That the numerical and analytic eigenvalues $(\lambda_p^N, \lambda_p^{NE1})$ of a patch scheme visually agree indicates that the patch scheme is not sensitive to numerical roundoff errors. **[TODO/adapt] this finishing sentences from general linear wave** This subsection first *quantitatively* compares the numerical and analytic eigenvalues of the staggered patch schemes to show that the staggered patch schemes are not sensitive to numerical roundoff errors when sub-patch micro-grid interval is not too small (i.e., $\delta \gtrsim 10^{-5}$). The later part of this subsection argues that even when the sub-patch micro-grid interval δ is too small, the numerical roundoff errors were not due to the patch scheme computations.

As in [§3.4](#) for the general linear wave, this section for the viscous shallow water flow assess the sensitivity of the staggered patch scheme time simulations to numerical roundoff errors, globally for all the possible initial conditions by studying *how sensitive the patch scheme eigenvalues are to the numerical roundoff errors*. Hence we compare the eigenvalues λ_p^{NE1} of the analytically derived Jacobian ([§4.2.3](#)) with the eigenvalues λ_p^N of the numerically computed Jacobian ([§4.2.5](#)) for a total of 7776 patch scheme cases as [Table 4.3.1](#) lists.

This subsection uses the same definition [\(3.4.1\)](#) in p. 91 of [§3.4](#) for the *micro- and macro-scale numerical roundoff errors* of the staggered patch scheme eigenvalues. If the errors $\epsilon_\mu^{\text{Num}}$ and ϵ_M^{Num} in [\(3.4.1\)](#) are negligibly small, that is, if the numerical and analytic macro-scale eigenvalues $(\lambda_{pM}^N, \lambda_{pM}^{NE1})$ of a patch scheme agree very closely, the patch scheme is not sensitive to the numerical roundoff errors.

The eigenvalues in the numerical roundoff errors [\(3.4.1a\)](#) and [\(3.4.1b\)](#)

Table 4.3.1: [Section 4.3](#) studies the sensitivity of the patch scheme eigenvalues to numerical roundoff errors for all the 7776 combinations (cartesian product) of the listed parameters.

Patch schemes	Spectral, Square-p2, Square-p4, Square-p6, and Square-p8
Mean height	$h_M \in \{0.1, 0.2, 0.3\}$
Mean velocity	$u_M \in \{0, 0.4, 0.8\}$, $v_M = 0$ (§4.6 on frame invariance show the flow direction is immaterial)
Reynold number	$Re \in \{10, 50, 250, 1250\}$
Macro-grid intervals	$N \in \{6, 10, 14\}$ for Spectral scheme, $N \in \{6, 10, 14, 18, 22, 26\}$ for polynomial schemes.
Sub-patch micro-grid intervals	$n \in \{6, 10\}$
Patch scale ratio	$r \in \{0.0001, 0.001, 0.01, 0.1\}$

require separating the micro- and macro-scale patch scheme eigenvalues and the association between the analytic and numerical eigenvalues. In the method of wavenumber-wise scale separation in [§3.3](#), using the full-domain micro-scale eigenvalues $\lambda_{m\delta}^{NE1}$ in place of the eigenvalues $\lambda_{m\delta}^A$ gives the required eigenvalues as the following 3D arrays (analytic eigenvalues only for $N \leq 14$ for Spectral patch scheme)

1. An $N/2 \times N/2 \times 3$ array of macro-scale *analytic* patch scheme eigenvalues λ_{pM}^{NE1} .
2. An $N/2 \times N/2 \times 3$ array of macro-scale *numerical* patch scheme eigenvalues λ_{pM}^N .
3. An $N/2 \times N/2 \times (n_p^i - 3)$ array of micro-scale *analytic* patch scheme eigenvalues λ_{pM}^{NE1} .
4. An $N/2 \times N/2 \times (n_p^i - 3)$ array of micro-scale *numerical* patch scheme eigenvalues λ_{pM}^N .

The micro- and macro-scale numerical roundoff errors in [\(3.4.1\)](#) are defined for the eigenvalues of a patch scheme for one specific set of parameters. We define the *peak micro- and macro-scale numerical roundoff errors* as the maximum value of $\max_{h_M, u_M} \epsilon_\mu^{\text{Num}}$ and $\max_{h_M, u_M} \epsilon_M^{\text{Num}}$, over the nine combinations of the mean flows $h_M \in \{0.1, 0.2, 0.3\}$ and $u_M \in \{0, 0.4, 0.8\}$ as [Table 3.4.1](#) lists.

Table 4.3.2: Maximum numerical roundoff errors over all the combinations of the five patch schemes and h_M , u_M , Re and N in [Table 4.3.1](#) for different patch scale ratio r and n. Red colour highlights largest value in each column (based on full precision).

		Patch scale ratio r			
		0.0001	0.001	0.01	0.1
$\max \epsilon_{\mu}^{\text{Num}}$	n = 6	0.02	$9 \cdot 10^{-5}$	10^{-5}	$4 \cdot 10^{-9}$
	n = 10	0.07	0.0002	$2 \cdot 10^{-5}$	$7 \cdot 10^{-8}$
$\max \epsilon_M^{\text{Num}}$	n = 6	0.01	$2 \cdot 10^{-5}$	$2 \cdot 10^{-7}$	$2 \cdot 10^{-9}$
	n = 10	0.01	$2 \cdot 10^{-5}$	10^{-8}	$2 \cdot 10^{-10}$

*Non-negligible numerical roundoff errors arise only for very small sub-patch micro-grid intervals $\delta \lesssim 10^{-5}$ (i.e., small r and large N, n). For each Reynolds number $\text{Re} \in \{10, 50, 250, 1250\}$, 3D plots of peak numerical roundoff errors $\max_{h_M, u_M} \epsilon_{\mu}^{\text{Num}}$ and $\max_{h_M, u_M} \epsilon_M^{\text{Num}}$ versus (N, r), are qualitatively same as the figures [Figs. 3.4.1](#) and [3.4.2](#) for general linear wave. [Table 4.3.2](#) lists the maximum peak numerical roundoff errors for different patch scale ratios r (i.e peak value for each r-slice in 3D plots similar to [Figs. 3.4.1](#) and [3.4.2](#)). The largest micro- and macro-scale numerical roundoff errors among the 7776 cases are 0.07 and 0.01 respectively, both corresponding to the smallest patch scale ratio r = 0.0001. The trend in [Table 4.3.2](#) and the omitted 3D plots qualitatively agree with [Table 3.4.2](#) and [Figs. 3.4.1](#) and [3.4.2](#) of general linear wave in that *the combination of large N, large n and small r leads to large numerical roundoff errors*. For the viscous shallow water waves, the largest numerical roundoff error for the macro-scale eigenvalues are about 100 times larger than that of the general linear wave in [Table 3.4.2](#). The following are some key observations from [Table 3.4.2](#) and 3D plots of peak numerical roundoff errors versus (N, r) (omitted here as qualitatively same as [Figs. 3.4.1](#) and [3.4.2](#)).*

1. For a given set of patch grid parameters N, n, r, the peak macro-scale numerical roundoff errors $\max_{h_M, u_M} \epsilon_M^{\text{Num}}$ are about the same as the peak micro-scale numerical roundoff errors $\max_{h_M, u_M} \epsilon_{\mu}^{\text{Num}}$ (i.e., within the same order of magnitude). For general linear wave ([p. 93](#) of [§3.4](#)) in where peak numerical roundoff errors are about ten to thousand times smaller for macro-scale eigenvalues compared to the micro-scale eigenvalues. Thus, the macro-scale eigenvalue of the viscous shallow water flow are relatively more sensitive to numerical roundoff errors than that of the general linear wave. The subsequent

paragraphs in this subsection show [TODO/ensure] this is shown that the sensitivity to numerical roundoff error (in general both for micro- and macro-scale eigenvalues) is not due to the patch scheme, but comes from the underlying micro-scale model within the patches.

2. Both the micro-scale and macro-scale peak numerical roundoff errors $\max_{h_M, u_M} \epsilon_\mu^{\text{Num}}$, $\max_{h_M, u_M} \epsilon_M^{\text{Num}}$, monotonically increase with increasing number of macro-grid intervals N and decreasing patch scale ratio r . For a staggered patch grid, increasing N , decreasing r , and increasing n , all these lead to decreasing sub-patch micro-grid interval $\delta = 2Lr/(Nn)$. For example, for $r = 0.001$, $N = 26$, $n = 10$, sub-patch micro-grid interval $\delta \approx 5 \cdot 10^{-5}$. Thus, as for the general linear wave, also for the viscous shallow water flow, the *non-negligible numerical roundoff errors arise only for very small sub-patch micro-grid intervals $\delta \lesssim 10^{-5}$ (i.e., small r and large N, n)*.
3. In general, except $\epsilon_\mu^{\text{Num}}$ for $N \gtrsim 22$, $r = 0.0001$, the numerical roundoff errors of all the five patch schemes are roughly the same, similar to Figs. 3.4.1 and 3.4.2 for general linear wave. That is, the numerical roundoff errors do not have strong dependence on the specific patch scheme. If the numerical roundoff errors were due to the patch scheme, the numerical roundoff errors must also depend on the specific patch scheme, showing a clear trend. The lack of such trends, among the patch schemes with different amounts of numerical computations, indicates that the numerical roundoff errors are not due to the patch scheme computations.

The *numerical roundoff errors in the patch scheme eigenvalues decrease with increasing Reynolds number*. Table 4.3.3 lists the maximum numerical roundoff errors ($\max \epsilon_\mu^{\text{Num}}$, $\max \epsilon_M^{\text{Num}}$) for micro- and macro-scale eigenvalues over all the combinations of the five patch schemes and h_M , u_M , N and r in Table 4.3.1 for different Reynolds number Re and patch scale ratio r . In the columns of Table 4.3.3, the decreasing numerical roundoff errors from top to bottom shows that the numerical roundoff errors decreases with increasing small Reynolds number Re . The numerical roundoff errors decrease roughly as $\epsilon_\mu^{\text{Num}}, \epsilon_M^{\text{Num}} \propto 1/Re$. In the rows of Table 4.3.3, the decreasing numerical roundoff errors from left to right shows that the numerical roundoff errors decreases with increasing patch scale ratio r . The numerical roundoff errors decrease roughly as $\epsilon_\mu^{\text{Num}}, \epsilon_M^{\text{Num}} \propto 1/r^2$. That is, the numerical roundoff errors decrease more rapidly with increasing patch scale ratio, than with decreasing Reynolds number. As the Table 4.3.3 lists

Table 4.3.3: Maximum numerical roundoff errors over all the combinations of the five patch schemes and h_M , u_M , N and r in [Table 4.3.1](#) for different Reynolds number Re and n . Red colour highlights largest value in each column.

		Patch scale ratio r			
		0.0001	0.001	0.01	0.1
$\max \epsilon_{\mu}^{\text{Num}}$	Re = 10	0.07	0.0002	$2 \cdot 10^{-5}$	$7 \cdot 10^{-8}$
	Re = 50	0.01	$8 \cdot 10^{-5}$	$9 \cdot 10^{-6}$	$4 \cdot 10^{-9}$
	Re = 250	0.006	$3 \cdot 10^{-5}$	10^{-7}	$3 \cdot 10^{-10}$
$\max \epsilon_M^{\text{Num}}$	Re = 1250	0.001	$5 \cdot 10^{-6}$	$2 \cdot 10^{-7}$	$4 \cdot 10^{-10}$
	Re = 10	0.01	$2 \cdot 10^{-5}$	$2 \cdot 10^{-7}$	$2 \cdot 10^{-9}$
	Re = 50	0.0003	10^{-6}	$2 \cdot 10^{-8}$	$2 \cdot 10^{-10}$
$\max \epsilon_M^{\text{Num}}$	Re = 250	$9 \cdot 10^{-6}$	$5 \cdot 10^{-8}$	10^{-9}	$3 \cdot 10^{-11}$
	Re = 1250	$9 \cdot 10^{-6}$	$5 \cdot 10^{-8}$	10^{-9}	$3 \cdot 10^{-11}$

the maximum numerical roundoff errors for all the combinations of the parameters in [Table 4.3.3](#), even for large $N \sim 26$ and $n = 10$, *using appropriately large patch scale ratio removes the non-negligible numerical roundoff errors for small Reynolds number $Re \lesssim 10$.*

The patch scheme macro-scale eigenvalues, which are of primary interest are less sensitive to numerical roundoff errors than corresponding the micro-scale eigenvalues. Based on [Table 4.3.2](#), a preceding paragraph states that the peak macro-scale numerical roundoff errors $\max_{h_M, u_M} \epsilon_M^{\text{Num}}$ are about the same as the peak micro-scale numerical roundoff errors $\max_{h_M, u_M} \epsilon_{\mu}^{\text{Num}}$ (i.e., within the same order of magnitude). [Table 4.3.3](#) shows that the maximum numerical roundoff errors (over h_M, u_M, N) of micro- and macro-scale eigenvalues are about the same only for small Reynolds number $Re \lesssim 10$. Even for small Reynolds number the numerical roundoff errors for macro-scale eigenvalues are less than that of the micro-scale eigenvalues. [Table 4.3.3](#) also shows that for large Reynolds number $Re \gtrsim 250$, the numerical roundoff errors for macro-scale eigenvalues are ten to hundred times smaller than that of the micro-scale eigenvalues. Thus, the patch scheme macro-scale eigenvalues for viscous shallow water flow, despite being more sensitive compared to the general linear wave, are less sensitive to numerical roundoff errors than corresponding the micro-scale eigenvalues.

For shallow and/or slow viscous shallow water flows (mean height $h_M \lesssim 0.1$ and/or mean velocity $u_M \lesssim 0.4$), patch scheme eigenvalues of are least sensitive

Table 4.3.4: Maximum numerical roundoff errors $\max \epsilon_{\mu}^{\text{Num}}$ in micro-scale eigenvalues over the five patch schemes and all the combinations of N , n , r in [Table 3.4.1](#), for different mean flow (h_M, u_M) and Reynolds number Re . Red colour highlights the largest $\max \epsilon_{\mu}^{\text{Num}}$ in each column for each height h_M (based on full precision)

	Reynolds number Re			
	10	50	250	1250
$h_M = 0.1, u_M = 0$	0.0007	0.0001	$2 \cdot 10^{-5}$	$2 \cdot 10^{-5}$
$h_M = 0.1, u_M = 0.4$	0.003	0.0005	0.0003	$4 \cdot 10^{-5}$
$h_M = 0.1, u_M = 0.8$	0.01	0.003	0.0006	0.0001
$h_M = 0.2, u_M = 0$	0.01	0.0005	10^{-5}	$2 \cdot 10^{-5}$
$h_M = 0.2, u_M = 0.4$	0.02	0.006	0.0006	0.0001
$h_M = 0.2, u_M = 0.8$	0.02	0.005	0.002	0.0005
$h_M = 0.3, u_M = 0$	0.04	0.0008	0.0002	0.0002
$h_M = 0.3, u_M = 0.4$	0.07	0.01	0.001	0.0009
$h_M = 0.3, u_M = 0.8$	0.05	0.009	0.006	0.001

Table 4.3.5: Maximum numerical roundoff errors $\max \epsilon_M^{\text{Num}}$ in macro-scale eigenvalues over the five patch schemes and all the combinations of N , n , r in [Table 3.4.1](#), for different mean flow (h_M, u_M) and Reynolds number Re . Red colour highlights the largest $\max \epsilon_{\mu}^{\text{Num}}$ in each column for each height h_M (based on full precision)

	Reynolds number Re			
	10	50	250	1250
$h_M = 0.1, u_M = 0$	0.0003	$4 \cdot 10^{-6}$	$2 \cdot 10^{-7}$	10^{-8}
$h_M = 0.1, u_M = 0.4$	0.0001	$3 \cdot 10^{-6}$	$3 \cdot 10^{-7}$	$5 \cdot 10^{-8}$
$h_M = 0.1, u_M = 0.8$	0.0002	$2 \cdot 10^{-5}$	$5 \cdot 10^{-6}$	$9 \cdot 10^{-7}$
$h_M = 0.2, u_M = 0$	0.001	$4 \cdot 10^{-5}$	10^{-6}	$5 \cdot 10^{-8}$
$h_M = 0.2, u_M = 0.4$	0.0007	$5 \cdot 10^{-5}$	10^{-5}	10^{-6}
$h_M = 0.2, u_M = 0.8$	0.002	0.0001	$3 \cdot 10^{-5}$	$6 \cdot 10^{-6}$
$h_M = 0.3, u_M = 0$	0.01	$7 \cdot 10^{-5}$	$3 \cdot 10^{-6}$	10^{-7}
$h_M = 0.3, u_M = 0.4$	0.01	$7 \cdot 10^{-5}$	$9 \cdot 10^{-6}$	$2 \cdot 10^{-6}$
$h_M = 0.3, u_M = 0.8$	0.009	0.0003	$5 \cdot 10^{-5}$	$9 \cdot 10^{-6}$

to numerical roundoff errors, compared to the deep and fast waves. Tables 4.3.4 and 4.3.5 lists the maximum numerical roundoff errors ($\max \epsilon_{\mu}^{\text{Num}}$, $\max \epsilon_M^{\text{Num}}$) for micro- and macro-scale eigenvalues respectively over all the combinations of the five patch schemes and N , n , and r in Table 4.3.1 for different mean flow (h_M , u_M) and Reynolds number Re . Tables 4.3.4 and 4.3.5 show that the maximum numerical roundoff errors for both micro- and macro-scale eigenvalues are the smallest for smallest mean height h_M , for any Reynolds number Re and mean velocity u_M . Due to the dominance of nonlinearity, the shallow water flows are more challenging to simulate accurately. *Being least sensitive to numerical roundoff errors for shallow water flows, the staggered patch schemes enable accurate multiscale simulation of the viscous shallow waters.* Tables 4.3.4 and 4.3.5 show that, except the off trend of $\max \epsilon_M^{\text{Num}}$ for $h_M = 0.1$, $u_M = 0$, the maximum numerical roundoff errors are the smallest for the smallest mean velocity $u_M \sim 0$ (for all large Reynolds number $Re \in \{10, 50, 250, 1250\}$). Thus, for shallow and/or slow viscous shallow water flows (mean height $h_M \lesssim 0.1$ and/or mean velocity $u_M \lesssim 0.4$), patch schemes are least sensitive to numerical roundoff errors, compared to the deep and fast waves.

In summary, the preceding paragraphs establish the contribution of the following extreme parameters to the non-negligible numerical roundoff errors (e.g., $\epsilon_{\mu}^{\text{Num}}, \epsilon_M^{\text{Num}} > 10^{-5}$) in the patch scheme eigenvalues (in the order of roughly decreasing dominance):

1. very small sub-patch micro-grid intervals $\delta \lesssim 10^{-5}$, due to combination of small patch scale ratio $r \lesssim 0.0001$, many macro-scale intervals $N \gtrsim 26$, and many sub-patch micro-grid intervals $n \gtrsim 10$;
2. small Reynolds number $Re \lesssim 10$;
3. large mean height $h_M \gtrsim 0.2$;

As in §3.4 for the general linear wave, the numerical roundoff errors in the patch scheme eigenvalues have the following main sources.

1. The numerical roundoff errors due to the numerical computations in a patch scheme due to the patch coupling.
2. The numerical roundoff errors due to the numerical computations of the underlying micro-scale system (e.g., the finite difference computations).
3. The numerical roundoff errors in numerically computing the eigenvalues of the patch scheme numerical Jacobian.

We take the numerical roundoff errors in numerically computing the Jacobian ([§3.2.5](#)) of a patch scheme, to be small compared to the much higher number of numerical computations in the patch coupling, sub-patch micro-scale system and the eigenvalue computation.

Similar to [p. 94](#) of [§3.4](#) for the general linear wave, the dependence of the numerical roundoff errors on the system parameters (Reynolds number Re and mean flow h_M, u_M) and the lack of dependence of the specific patch schemes show that *the numerical roundoff errors are due to the underlying micro-scale system, not due to the staggered patch scheme*. [Page 94](#) of [§3.4](#) for general linear wave shows the strong dependence of numerical roundoff errors in the patch scheme eigenvalues on the viscous diffusion via the coefficient c_V . The preceding paragraph in [p. 205](#) using [Tables 4.3.3, 4.3.4](#) and [4.3.5](#) shows that the numerical roundoff errors strongly depend on the Reynolds number especially for $Re \lesssim 10$ where viscous diffusion is large. That is, similar to the general linear wave, *the numerical roundoff errors for the viscous shallow water strongly depends on the viscous diffusion*. The preceding paragraph in [p. 206](#) using [Tables 4.3.4](#) and [4.3.5](#) shows that the numerical roundoff errors depend on the linearisation point, that is the mean flow, especially for large mean height $h_M \gtrsim 0.2$ and large mean velocity $u_M \gtrsim 0.4$. In general, the staggered patch schemes are largely agnostic of the underlying micro-scale system. More specifically, for each Reynolds number $Re \in \{10, 50, 250, 1250\}$, 3D plots of peak numerical roundoff errors $\max_{h_M, u_M} \epsilon_\mu^{\text{Num}}$ and $\max_{h_M, u_M} \epsilon_M^{\text{Num}}$ versus (N, r) , (similar to [Figs. 3.4.1](#) and [3.4.2](#) for general linear wave) show that the numerical roundoff errors do not have strong dependence on the specific patch scheme. This lack of dependence on the specific patch schemes despite with different amounts of numerical computations, indicates that the numerical roundoff errors are not due to the patch scheme computations. Moreover, if the patch schemes were sensitive to numerical roundoff errors, the errors must have been large irrespective of the system parameters (Reynolds number Re and mean flow h_M, u_M). For example, in [Tables 4.3.3, 4.3.4](#) and [4.3.5](#), the numerical roundoff errors $\epsilon_\mu^{\text{Num}}$ and ϵ_M^{Num} must have been large also for large Reynolds number $Re \gtrsim 10$, small mean height $h_M \lesssim 0.2$ and small mean height $h_M \lesssim 0.2$, which is not the case. Thus, the dependence of the numerical roundoff errors on the system parameters (Reynolds number Re and mean flow h_M, u_M) and the lack of dependence of the specific patch schemes show that *the numerical roundoff errors are due to the underlying micro-scale system, not due to the staggered patch scheme*

Scaling arguments on the viscous shallow water flow confirm the inherent sensitivity of the micro-scale system to numerical roundoff errors. In the full-domain micro-scale system ([4.1.11b](#)) of [§4.1.2](#), let us compare how the terms

scale with the grid-interval δ . The equation (4.1.11b) after multiplying by h_M^2 / Re and expanding becomes

$$\begin{aligned} \frac{du_{i,j}}{dt} = & -\frac{\pi^2}{4} \frac{h_M^2}{Re} \frac{u_{i,j}}{[(h_{i-1,j} + h_{i+1,j})/2]^2} + \frac{\pi^2}{12} g_x + \frac{\pi^2}{12} g_n \frac{h_{i+1,j} - h_{i-1,j}}{2\delta} \\ & - 1.5041 h_M u_{i,j} \frac{u_{i+2,j} - u_{i-2,j}}{4\delta} \\ & - 1.3464 h_M \frac{(v_{i-1,j-1} + v_{i+1,j-1} + v_{i-1,j+1} + v_{i+1,j+1})}{4} \frac{u_{i,j+2} - u_{i,j-2}}{4\delta} \\ & - 0.1577 h_M u_{i,j} \frac{(v_{i-1,j+1} + v_{i+1,j+1})/2 - (v_{i-1,j-1} + v_{i+1,j-1})/2}{2\delta} \\ & + 4.093 \frac{h_M^2}{Re} \frac{u_{i-2,j} - 2u_{i,j} + u_{i+2,j}}{4\delta^2} + \frac{h_M^2}{Re} \frac{u_{i,j-2} - 2u_{i,j} + u_{i,j+2}}{4\delta^2} \\ & + 3.093 \frac{h_M^2}{Re} \frac{(v_{i+1,j+1} - v_{i+1,j-1})/(2\delta) - (v_{i-1,j+1} - v_{i-1,j-1})/(2\delta)}{2\delta}. \end{aligned}$$

Taking g_x, g_n, h, u are of the order of one, the nine terms in the time derivative of $u_{i,j}$ scale respectively as

$$\frac{du_{i,j}}{dt} \sim -\frac{h_M^2}{Re} + 1 + \frac{1}{\delta} - \frac{h_M}{\delta} - \frac{h_M}{\delta} - \frac{h_M}{\delta} + \frac{h_M^2}{Re \delta^2} + \frac{h_M^2}{Re \delta^2} + \frac{h_M^2}{Re \delta^2}.$$

That is, the time derivative of $u_{i,j}$ scales as

$$\frac{du_{i,j}}{dt} \sim -\frac{h_M^2}{Re} + 1 + \frac{1}{\delta} - \frac{h_M}{\delta} + \frac{h_M^2}{Re \delta^2}. \quad (4.3.1)$$

For example, for small grid interval $\delta = 10^{-5}$, the terms in the right hand side of the scaling relation (4.3.1) are about $-h_M^2 / Re$, 1, 10^5 , $-10^5 h_M$, $10^{10} h_M^2 / Re$ respectively. For large mean height $h_M \gtrsim 0.2$ and small Reynolds number $Re \lesssim 10$, the addition (subtraction) of these small and large values leads to the loss of floating point precision while lining up the decimal points in the finite precision arithmetic (Heister, Rebholz, and Xue 2019, p. 8; Goldberg 1991, pp. 16, 19). Hence, for large mean height $h_M \gtrsim 0.2$ and small Reynolds number $Re \lesssim 10$, both the full-domain micro-scale scheme and the sub-patch micro-scale system, are inherently sensitive to numerical roundoff errors, for small grid interval $\delta \lesssim 10^{-5}$. This inherent sensitivity of the micro-scale system to numerical roundoff errors is not severe for the time simulation [TODO xref to time sim subsection], but impacts the eigenvalue computation for both the full-domain micro-scale system and the patch scheme. Whereas this inherent sensitivity

impacts both the micro- and macro-scale eigenvalues, the macro-scale numerical roundoff errors ϵ_M^{Num} are in general ten to thousand times smaller than the peak micro-scale numerical roundoff errors $\epsilon_\mu^{\text{Num}}$. We expect that this relatively smaller ϵ_M^{Num} is due to the macro-scale interpolation in the patch coupling, which acts as averaging/smoothing the inherent numerical roundoff errors of the computations within the patches. Thus, for small grid interval $\delta \lesssim 10^{-5}$, large mean height $h_M \gtrsim 0.2$, and small Reynolds number $\text{Re} \lesssim 10$, the non-negligible *numerical roundoff errors in both micro- and macro-scale patch scheme eigenvalues are due to the inherent sensitivity of the micro-scale system to numerical roundoff errors*. As in the discussion for the general linear wave in §3.4 of §3.4, for viscous shallow water flows too a part of the numerical roundoff errors are due to numerical computation of near zero repeated eigenvalues. The numerical roundoff errors in the numerical computation of near zero repeated eigenvalues is amplified by the micro-scale model's sensitivity to numerical roundoff errors.

The following listing summarises the study of numerical sensitivity in this subsection.

1. For large patch scale ratios $r \gtrsim 0.001$ the patch scheme eigenvalue are not sensitive numerical roundoff errors (columns 2-4 in Table 4.3.3). Hence for large r the staggered the patch schemes are not sensitive to numerical roundoff errors.
2. For small patch scale ratios $r \lesssim 0.001$ the patch scheme eigenvalues are sensitive numerical roundoff errors (column 1 in Table 4.3.3). But this sensitivity to numerical roundoff errors for small sub-patch micro-grid interval $\delta \lesssim 10^{-5}$ is due to both the inherent sensitivity of the micro-scale system (due to viscous diffusion $\text{Re} \lesssim 10$) and the sensitivity of eigenvalue computation of near zero repeated eigenvalues. Hence, even for small patch scale ratios, *the computations of staggered the patch schemes are not sensitive numerical roundoff errors*.

4.4 Staggered patch schemes are not artificially unstable for appropriate patch grids

As the general linear wave and its staggered full-domain micro-scale system are inherently stable (i.e., maximum real part of the eigenvalues is nonpositive), §3.5 establishes the patch scheme stability by showing that the maximum real part of the patch scheme eigenvalues are nonpositive. In contrast to the general linear wave, the viscous shallow water flow has

physical instability, that is, full-domain micro-scale system itself is unstable depending upon the system parameters (Reynolds number Re , mean flow height h_M , u_M , v_M). Such physical instability is evident from the positive real part eigenvalues of the full-domain micro-scale system in Fig. 4.2.6 (clusters 1, 2) of §4.2.6. Thus, for viscous shallow water flow, a positive real part of the patch scheme eigenvalue does not necessarily mean that the patch scheme computations are erroneous or unphysical. That is, a good patch scheme must be stable as well as unstable in correspondence to the the physical system depending upon the system parameters (Re , h_M , u_M , v_M), but *without any additional/artificial instability*. Hence, we define *artificial instability* as a characteristic of a patch scheme to be *more unstable* than the corresponding full-domain micro-scale system. That is, *a patch scheme is artificially unstable when the maximum real part of the patch scheme eigenvalues is both positive and larger than the maximum real part of the corresponding full-domain micro-scale system*. To quantitatively study the patch scheme artificial instability, we define the *condition of no artificial instability* as

$$\max \Re(\lambda_p^N) > 0 \implies \max \Re(\lambda_p^N) \leq \max \Re \lambda_{m\delta}^{NE1}, \quad (4.4.1)$$

within a tolerance of 10^{-5} .

As p. 193 of §4.2.6 states, in contrast to the eigenvalues of the general linear wave in §3.2.6, due to the nonlinearity, the *eigenvalues of the viscous shallow water flow depend on the mean height h_M and the mean velocity h_M, v_M* . That is, the eigenvalues and hence the stability of the viscous shallow water flow depends on the linearisation point (h_M, u_M, v_M). So, §4.4.1 shows that for an appropriate patch grid the Spectral patch scheme is not artificially unstable, for *a wide range of system parameters* (Reynolds number Re , mean height h_M , and horizontal mean velocity (u_m, v_M)) for *a small representative set of patch grid parameters* (number of macro-grid intervals N , number of sub-patch micro-grid intervals n , patch scale ratio r).

Page 215 of §4.4.1 establish that the patch scheme artificial instability arises only for the sub-patch micro-scale modes. That is, the patch scheme macro-scale modes which is of primary interest, do not have artificial instability. Section 4.4.2 more specifically shows that the maximum artificial instability of patch schemes is due to sub-patch micro-scale modes modulated over the smallest resolved macro-scale waves moving along the resultant horizontal mean velocity (u_M, v_M).

Section 4.4.3 shows that the five staggered patch schemes are not artificially unstable, for *a wide range of patch grid parameters* (macro-grid intervals N , sub-patch micro-grid intervals n , and patch scale ratio r), for *a small representative set of system parameters* (Reynolds number Re , mean

height h_M , and horizontal mean velocity (u_m, v_M) indicated by nine black squares in Figs. 4.4.3 to 4.4.5 of §4.4.1). Section 4.4.3 also gives a general rule to get rid of artificial instability, when a patch scheme has artificial instability for some combinations of system and patch grid parameters.

4.4.1 Spectral staggered patch scheme is not artificially unstable for different system parameters

This subsection shows that for an appropriate patch grid the Spectral staggered patch scheme is not artificially unstable for *a wide range of system parameters* (Reynolds number Re , mean height h_M , horizontal mean velocity u_M) for *a small representative set of patch grid parameters* (number of macro-grid intervals $N \in \{10, 14\}$, number of sub-patch micro-grid intervals $n \in \{6, 10\}$, patch scale ratio $(r \in \{0.0001, 0.001\})$). That is, this subsection shows that for a wide range of system parameters and a small representative set of patch grid parameters, the maximum real part of the patch scheme eigenvalues (analytic λ_p^{NE1} , numerical λ_p^N) is *not* both positive and larger than the maximum real part of the eigenvalues $\lambda_{m\delta}^{NE1}$ of the corresponding full-domain micro-scale system, that is the condition of no artificial instability (4.4.1) holds (within a tolerance of 10^{-5}).

This subsection studies the artificial instability via the Spectral patch scheme eigenvalues for a total of 21 504 cases consisting of all the combinations (cartesian product) of the system parameters:

1. mean height $h_M \in \{0.025, 0.05, \dots, 0.035, 0.4\}$;
2. mean velocity $u_M \in \{0, 0.05, \dots, 0.95, 1\}$, $v_M = 0$ (§4.6 on frame invariance show the flow direction is immaterial);
3. Reynold number $Re \in \{10, 50, 250, 1250\}$;

and the patch grid parameters:

- Number of macro-scale intervals $N \in \{10, 14\}$;
- Number of sub-patch micro-grid intervals $n \in \{6, 10\}$;
- Patch scale ratio $r \in \{0.0001, 0.001, 0.01, 0.1\}$.

For some combinations of the system parameters (Reynolds number Re , mean height h_M , and horizontal mean velocity (u_m, v_M)) and the patch grid parameters (e.g., number of macro-grid intervals N , number of sub-patch micro-grid intervals n , patch scale ratio r), some patch scheme modes are

Figure 4.4.1: Spectral patch scheme ($N = 10$, $n = 6$, $r = 0.1$) has artificial instability for viscous shallow water flow for $(h_M, u_M, v_M) = (0.2, 0.3, 0)$, in contrast to Fig. 4.2.5 for same parameters except $r = 0.01$. Maximum real parts $\max \Re \lambda_{m,\delta}^{NE1} = 0$, $\max \Re \lambda_p^{NE1} = 0.062$.

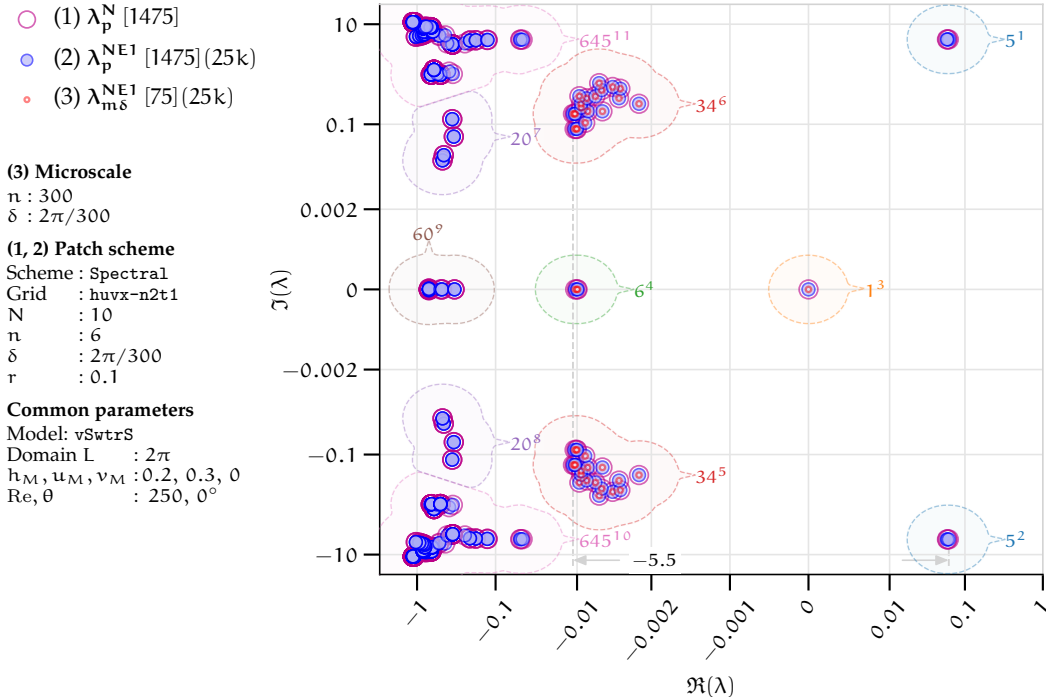
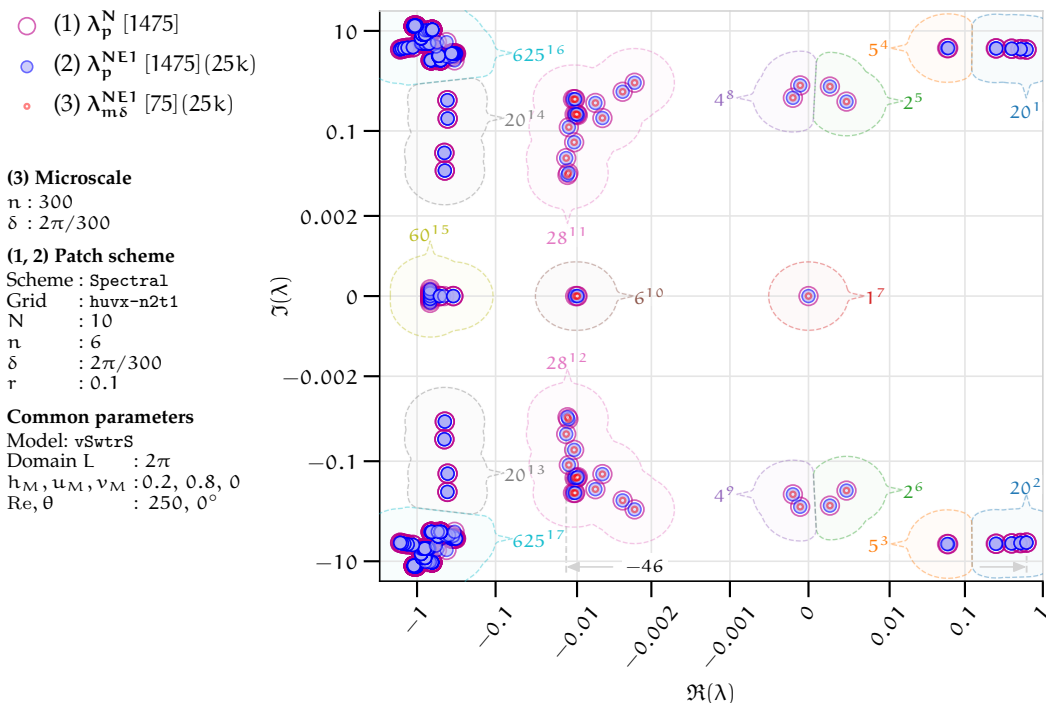


Figure 4.4.2: Spectral patch scheme ($N = 10, n = 6, r = 0.1$) has artificial instability for viscous shallow water flow for $(h_M, u_M, v_M) = (0.2, 0.8, 0)$, in contrast to Fig. 4.2.6 for same parameters except $r = 0.01$. Maximum real parts $\max \Re \lambda_{m,\delta}^{NE1} = 0.0021$, $\max \Re \lambda_p^{NE1} = 0.62$ (point d in Fig. 4.4.5c).



artificially unstable. That is, some patch scheme modes are unstable (positive real part eigenvalues) while the corresponding modes of the full-domain micro-scale system are stable (no positive real part eigenvalues). For example, in Figs. 4.4.1 and 4.4.2, the clusters 1, 2 and the clusters 1–4 (blue and magenta circles on the right) respectively, contain the eigenvalues of artificial instability as for these clusters $0 < \Re(\lambda_p^{NE1}) = \Re(\lambda_p^N) > \max \Re(\lambda_{m\delta}^{NE1}) = 0$; that is, the condition of no artificial instability (4.4.1) does not hold. *Decreasing the patch scale ratio r removes such artificial instability of the staggered patch schemes,* as evident from the nonpositive real part patch scheme eigenvalues in Fig. 4.2.6 of §4.2.6 for $r = 0.01$, compared to those in Fig. 4.4.2 for $r = 0.1$, keeping all other parameters the same. Despite the artificial instability in Figs. 4.4.1 and 4.4.2 for small patch scale ratio $r = 0.1$, the macro-scale patch scheme eigenvalues ($\lambda_p^N, \lambda_p^{NE1}$) of the Spectral patch scheme (large blue and magenta circles) in clusters 3–6 and clusters 5–12 respectively, agree with the macro-scale eigenvalues $\lambda_{m\delta}^{NE1}$ (small red circles) of the fine-grid full-domain micro-scale system. That is, despite the artificial instability for some parameter combinations for the viscous shallow water flow, the *staggered patch schemes are accurate for macro-scale wave modes.*

The artificial instability of the patch schemes arises only for the sub-patch micro-scale modes. That is, the patch scheme macro-scale modes which is of primary interest, do not have artificial instability. For example, consider the patch scheme eigenvalues in Figs. 4.4.1 and 4.4.2 with artificial instability. In Figs. 4.4.1 and 4.4.2, the clusters 1, 2 and the clusters 1–4 respectively, contain the eigenvalues of artificial instability as for these clusters $0 < \Re(\lambda_p^{NE1}) = \Re(\lambda_p^N) > \max \Re(\lambda_{m\delta}^{NE1}) = 0$, that is, the condition of no artificial instability (4.4.1) does not hold. In Figs. 4.4.1 and 4.4.2, each of the patch scheme eigenvalues λ_p^{NE1} in clusters 3–6 and clusters 5–12 respectively, agree with the corresponding eigenvalues $\lambda_{m\delta}^{NE1}$ of the full-domain system that are evaluated for all the $N^2/4 = 25$ macro-scale wavenumbers (k_x, k_y) where $k_x, k_y \in \{-2, -1, 0, 1, 2\}$ resolved by a patch grid. That is, in Figs. 4.4.1 and 4.4.2, the clusters 3–6 and clusters 5–12 respectively, contain the eigenvalues of all the $n_p^I = 75$ macro-scale modes ($n_p^I = 3N^2/4$ as in p. 188 of §4.2.6). Figure 4.4.1 shows that the macro-scale modes are not artificially unstable as for the eigenvalues in the clusters 3–6, $\max \Re(\lambda_p^{NE1}) = \max \Re(\lambda_{m\delta}^{NE1}) = 0$. Figure 4.4.2 shows that the macro-scale modes are not artificially unstable as for the eigenvalues in the clusters 5–12, $\max \Re(\lambda_p^{NE1}) = \max \Re(\lambda_{m\delta}^{NE1}) = 0.0021$. The large imaginary parts of the artificially unstable modes, in clusters 1, 2 and clusters 1–4 in Figs. 4.4.1 and 4.4.2 respectively, compared to the imaginary parts of the corresponding macro-scale eigenvalues in the clusters 3–6 and clusters 5–12 respectively, also indicate that artificially unstable modes must be micro-

scale modes. The eigenvector plots in Figs. 4.4.9 and 4.4.11 of §4.4.2 show the artificially unstable sub-patch micro-scale mode modulated over the macro-scale wave mode with wavenumbers $(k_x, k_y) = (1, 0), -(2, 0)$ respectively of the Spectral staggered patch scheme. In the eigenvector plot of Figs. 4.4.9 and 4.4.11, the grey curves connecting the patch centre values (patch mean) indicate the unmodulated macro-scale wave. The eigenvector plots in Figs. 4.4.9 and 4.4.11 of §4.4.2 corresponding to the eigenvalues of the artificially unstable modes in cluster 2 of Fig. 4.4.2 definitively confirm that *the patch scheme artificially unstable modes are micro-scale modes modulated over the macro-scale wave*. More specifically, §4.4.2 shows that the maximum artificial instability of patch schemes is due to sub-patch micro-scale modes modulated over the smallest resolved macro-scale waves moving along the resultant horizontal mean velocity (u_M, v_M) .

Each subplot in Figs. 4.4.3 to 4.4.5 plot the maximum real part of the following eigenvalues for viscous shallow water flow, linearising about 336 cases of mean flow (h_M, u_M, v_M) , for 16 mean heights $h_M \in \{0.025, 0.05, \dots, 0.035, 0.4\}$, and 21 mean velocities $u_M \in \{0, 0.05, \dots, 0.95, 1\}$ with $v_M = 0$ and bed inclination $\theta = 0^\circ$.

1. Eigenvalues λ_p^N of the Spectral patch scheme.
2. Eigenvalues $\lambda_{m\delta}^{NE1}$ of full-domain micro-scale system with same value of micro-scale grid interval $\delta_{m\delta}$ as the sub-patch micro-grid interval δ , that is, $\delta_{m\delta} \equiv L/n_{m\delta} = \delta \equiv l/n \equiv 2Lr/(Nn)$ as $r = l/(2\Delta)$ and $\Delta = L/N$, where $n_{m\delta}$ is the number of full-domain micro-scale grid intervals and n is the number of sub-patch micro-grid intervals. When the context is clear we drop the subscript $m\delta$ in $n_{m\delta}$ and $\delta_{m\delta}$ for the case of full-domain micro-scale system.
3. Eigenvalues λ_{PDE}^{NE1} of the viscous shallow water PDE.

The analytic eigenvalues $\lambda_{m\delta}^{NE1}$ and λ_{PDE}^{NE1} are numerically evaluated for all the $N^2/4$ *macro-scale wavenumbers* (k_x, k_y) resolved on a corresponding finite staggered patch grid with $N \times N$ macro-grid intervals. The following listing explains the various visual elements in Figs. 4.4.3 to 4.4.5.

- For each of the subplot, the blue plus shows the maximum value of $\max \Re(\lambda_p^N)$ and the red circle shows the maximum value of $\max \Re(\lambda_{m\delta}^{NE1})$.
- The nine black squares show the chosen subset of the mean flow $\{(h_M, u_M) : h_M \in \{0.1, 0.2, 0.3\}, u_M \in \{0.0, 0.4, 0.8\}\}$ for further study of stability (§4.4.1) and consistency (§4.5).

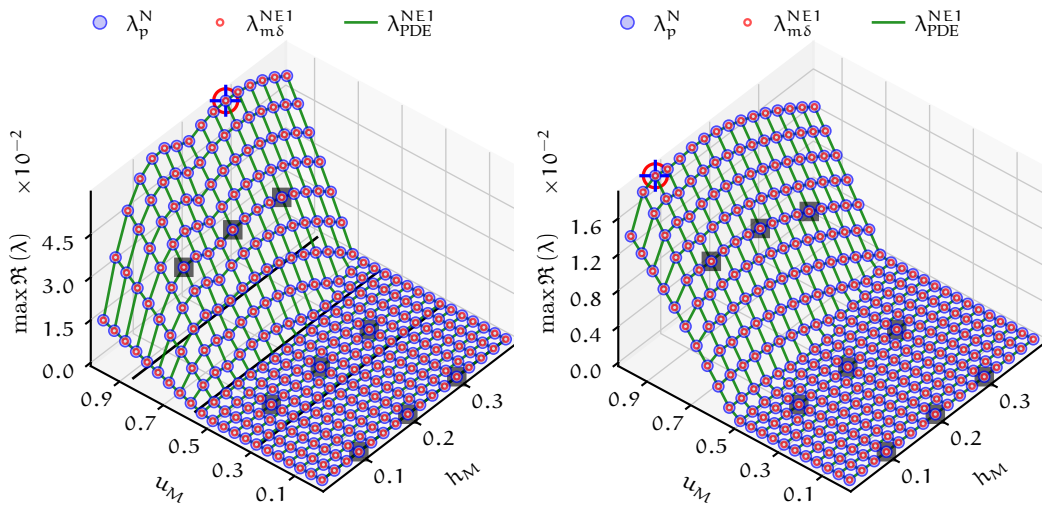
- The annotated points a–d in the subplots for $\text{Re} = 250$, correspond to increasing mean velocity $u_M = 0, 0.1, 0.4, 0.8$ keeping $h_M = 0.2$, $v_M = 0$. For patch scale ratio $r = 0.01$, the complex plane eigenvalue plots in Figs. 4.2.3 to 4.2.6 of §4.2.6 correspond to these four points a–d. The annotated points e, c, f in the subplots for $\text{Re} = 250$, correspond to increasing mean height $h_M = 0.1, 0.2, 0.3$ keeping $u_M = 0.1, v_M = 0$. For $r = 0.01$, the complex plane eigenvalue plots in Figs. 4.2.7, 4.2.4 and 4.2.8 of §4.2.6 correspond to these three points e, c, f.
- The four black lines at the bottom of the subplots for $\text{Re} = 10$, are the set of equilibrium points (h_M, u_M) of the viscous shallow water flow. For Reynolds number $\text{Re} = 10$ with $v = v_M = 0$ and the bed inclination angles $\theta = 0, 5, 10, 15$, the equilibrium solution (4.1.12) gives the equilibrium velocity $u = u_M = \text{Re } g_x/3 \equiv \text{Re } \sin(\theta)/3 = 0, 0.29, 0.58, 0.86$ respectively. The four lines in the subplots for $\text{Re} = 10$ corresponds to these four equilibrium velocities. In the subplots for Reynolds number $\text{Re} \in \{50, 250, 1250\}$ there are no black lines of equilibrium points (h_M, u_M) , because equilibrium velocities are larger than one and outside the plot limits $u_M \in [0, 1]$.

For small patch scale ratio $r \lesssim 0.001$, the staggered patch schemes do not have any artificial instability over a wide range of mean flow and Reynolds numbers. Figure 4.4.3 plot the maximum real part of the eigenvalues versus (h_M, u_M) , for the Spectral staggered patch scheme with a small patch scale ratio $r = 0.001$. The maximum real part of the eigenvalues in Fig. 4.4.3 correspond to a staggered patch grid with 10×10 macro-grid intervals ($N = 10$) and each patch patch containing 6×6 sub-patch micro-grid intervals ($n = 6$). Figure 4.4.3 shows that either $\max \Re(\lambda_p^N) = 0$ or $\max \Re(\lambda_p^N) = \max \Re(\lambda_{m\delta}^{NE1}) > 0$ (within a tolerance of 10^{-5}), over the chosen wide range of mean flows ($h_M \in [0.025, 0.4]$, $u_M \in [0, 1]$) and Reynolds numbers ($\text{Re} \in \{10, 50, 250, 1250\}$). That is, the condition of no artificial instability (4.4.1) holds. All the plots of the maximum real parts of the Spectral patch scheme eigenvalues versus (h_M, u_M) are identical to Figure 4.4.3 number of macro-grid intervals $N \in \{10, 14\}$, number of sub-patch micro-grid intervals $n \in \{6, 10\}$, patch scale ratio ($r \in \{0.0001, 0.001\}$). Thus, *for small patch scale ratio $r \lesssim 0.001$, the Spectral staggered patch scheme does not have any artificial instability over a wide range of mean flows and Reynolds numbers.* As §4.4.3 shows, this characteristic of no artificial instability for small patch scale ratio holds also for the polynomial patch schemes.

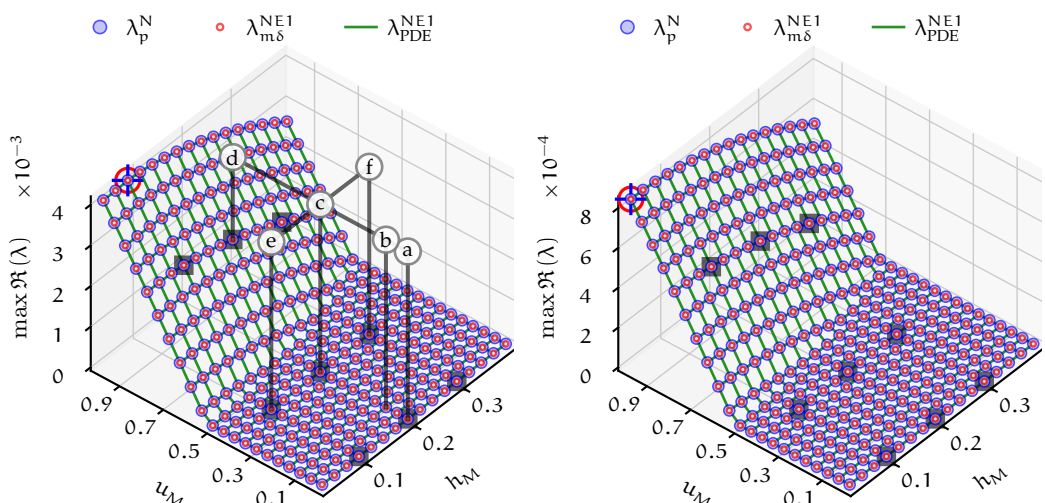
To quantify the physical and artificial instability, we define the following two terms over 336 cases of mean flow (h_M, u_M, v_M) , for 16 mean

Figure 4.4.3: Maximum real part of the eigenvalues for, λ_p^N of Spectral patch scheme ($N = 10$, $n = 6$, $r = 0.001$), $\lambda_{m\delta}^{NE1}$ of full-domain micro-scale system, and λ_{PDE}^{NE1} of the viscous shallow water PDE, about different mean flow (h_M, u_M) with $v_M = 0$ and bed inclination $\theta = 0^\circ$. Increasing Re decreases physical instability. No artificial instability for wide range of mean flow $\{(h_M, u_M) : h_M \in [0.025, 0.4], u_M \in [0, 1]\}$ and $Re \in \{10, 50, 250, 1250\}$.

(a) Reynolds number $Re = 10$. No artificial instability, as $\max \Re(\lambda_p^N) = 0$ or $\max \Re(\lambda_{m\delta}^{NE1}) > 0$. Peak values (blue plus and red circle) are $\max \Re(\lambda_p^N) = 0.059 = \max \Re(\lambda_{m\delta}^{NE1})$.



(c) Reynolds number $Re = 250$. No artificial instability. Peak values are $\max \Re(\lambda_p^N) = 0.0041 = \max \Re(\lambda_{m\delta}^{NE1})$. Points a-d $h_M = 0.2$, $u_M = 0, 0.1, 0.4, 0.8$. Points e-f $h_M = 0.1, 0.2, 0.3$, $u_M = 0.1$.



(d) Reynolds number $Re = 1250$. No artificial instability. Peak values are $\max \Re(\lambda_p^N) = 0.00084 = \max \Re(\lambda_{m\delta}^{NE1})$.

heights $h_M \in \{0.025, 0.05, \dots, 0.035, 0.4\}$, and 21 horizontal mean velocities $u_M \in \{0, 0.05, \dots, 0.95, 1\}$.

1. The *peak physical instability* is $\max_{h_M, u_M} [\max \Re(\lambda_{m\delta}^{NE1})]$, that is, the peak value of $\max \Re(\lambda_{m\delta}^{NE1})$ (red circle) for each of the subplots.
2. The *peak artificial instability* is $\max_{h_M, u_M} [\max \Re(\lambda_p^N) - \max \Re(\lambda_{m\delta}^{NE1})]$, that is, the difference between the peak value of $\max \Re(\lambda_p^N)$ (blue plus) and the peak value of $\max \Re(\lambda_{m\delta}^{NE1})$ (red circle) for each of the subplots.

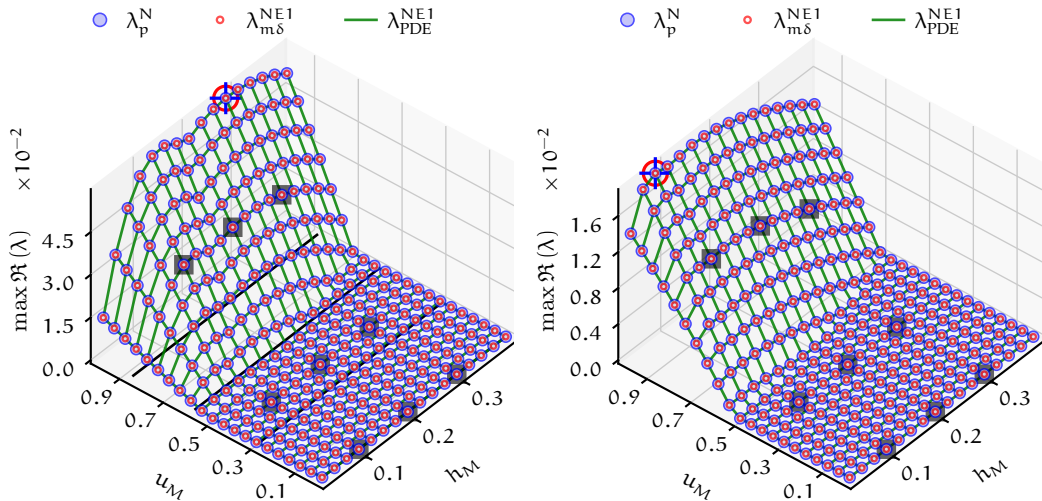
For large patch scale ratio $r \sim 0.1$, the staggered patch schemes are stable for small mean velocity $u_M \lesssim 0.3$ where the underlying full-domain micro-scale system is stable. Figures 4.4.4 and 4.4.5 plot the maximum real part of the eigenvalues versus (h_M, u_M) , for the Spectral staggered patch scheme ($N = 10, n = 6$) with large patch scale ratios $r = 0.01, 0.1$ respectively. Figures 4.4.4 and 4.4.5 show that the Spectral patch scheme is stable ($\max \Re(\lambda_p^{NE1}) > 0$) even for large patch scale ratio $r = 0.01, 0.1$, for small mean velocity $u_M \lesssim 0.3$ where the underlying full-domain micro-scale system is stable ($\max \Re(\lambda_{m\delta}^{NE1}) > 0$). Similarly, for small mean velocity $u_M \lesssim 0.3$, all the four polynomial staggered patch schemes are also stable for patch scale ratio $r \in \{0.0001, 0.001, 0.01, 0.1\}$ for $h_M \in [0.025, 4]$.

For large patch scale ratio $r \gtrsim 0.01$, the staggered patch schemes have artificial instability for some mean flows (h_M, u_M) for the combination of large mean velocity u_M and large Reynolds number Re . Figures 4.4.4 and 4.4.5 show that the Spectral patch scheme ($N = 10, n = 6, r = 0.01, 0.1$) has artificial instability $\max \Re(\lambda_p^{NE1}) > \max \Re(\lambda_{m\delta}^{NE1})$ (condition (4.4.1) does not hold) for the combination of large mean velocity $u_M \gtrsim 0.3$ and large Reynolds number $Re \gtrsim 10$. For example, Figs. 4.4.1 and 4.4.2 show the artificial instability in complex plane plots for $(h_m, u_M) = (0.2, 0.3)$ and $(h_m, u_M) = (0.2, 0.8)$ (the point d in Fig. 4.4.5c) respectively, with Reynolds number $Re = 250$ for the Spectral patch scheme ($N = 10, n = 6, r = 0.1$). The patch scheme artificial instability in Fig. 4.4.1 arises as $\max \Re(\lambda_p^N) = \max \Re(\lambda_p^{NE1}) = 0.062 > \max \Re(\lambda_{m\delta}^{NE1}) = 0$. Figure 4.4.2 for $r = 0.1$ shows patch scheme artificial instability, in contrast to Fig. 4.2.6 for the same parameters except $r = 0.01$. Compared to the $\max \Re(\lambda_p^{NE1}) = 0.0021$ (physical instability) in Fig. 4.2.6 for $r = 0.01$, Fig. 4.4.2 for $r = 0.1$ has $\max \Re(\lambda_p^{NE1}) = 0.62 > \max \Re(\lambda_{m\delta}^{NE1}) = 0.0021$ (artificial instability).

Figures 4.4.4 and 4.4.5 illustrate the following key trends about the patch scheme stability. All the trends in the following listing also hold for the polynomial patch schemes, we omit the corresponding figures for brevity.

Figure 4.4.4: Maximum real part of the eigenvalues for, λ_p^N of Spectral patch scheme ($N = 10$, $n = 6$, $r = 0.01$), $\lambda_{m\delta}^{NE1}$ and λ_{PDE}^{NE1} of the viscous shallow water flow, about different mean flow (h_M, u_M) with $v_M = 0$ and $\theta = 0^\circ$. No artificial instability for Reynolds number $Re \in \{10, 50\}$. Increasing Re increases the (h_M, u_M) -region of artificial instability for $Re \in \{250, 1250\}$.

- (a) Reynolds number $Re = 10$. Identical to Fig. 4.4.3a of $r = 0.001$ and Spectral patch scheme has *no artificial instability*. Peak values (blue plus and red circle) are $\max \Re(\lambda_p^N) = 0.059 = \max \Re(\lambda_{m\delta}^{NE1})$.
- (b) Reynolds number $Re = 50$. Identical to Fig. 4.4.3b of $r = 0.001$ and Spectral patch scheme has *no artificial instability*. Peak values (blue plus and red circle) are $\max \Re(\lambda_p^N) = 0.019 = \max \Re(\lambda_{m\delta}^{NE1})$.



- (c) $Re = 250$. *Artificial instability* (i.e., $\max \Re(\lambda_p^N) > \max \Re(\lambda_{m\delta}^{NE1}) \geq 0$) for very shallow mean flow $h_M \lesssim 0.05$ and large $u_M \gtrsim 0.3$; $\max \Re(\lambda_p^N) = 0.52$, $\max \Re(\lambda_{m\delta}^{NE1}) = 0.0041$.
- (d) $Re = 1250$. *Artificial instability* (i.e., $\max \Re(\lambda_p^N) > \max \Re(\lambda_{m\delta}^{NE1}) \geq 0$) for moderately shallow mean flow $h_M \lesssim 0.25$ and large $u_M \gtrsim 0.3$; $\max \Re(\lambda_p^N) = 2.66$, $\max \Re(\lambda_{m\delta}^{NE1}) = 0.00084$.

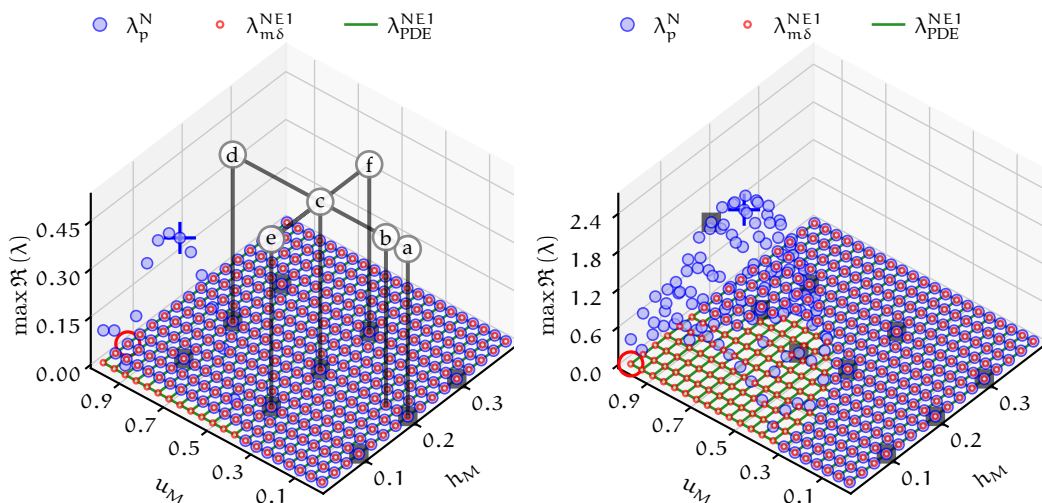
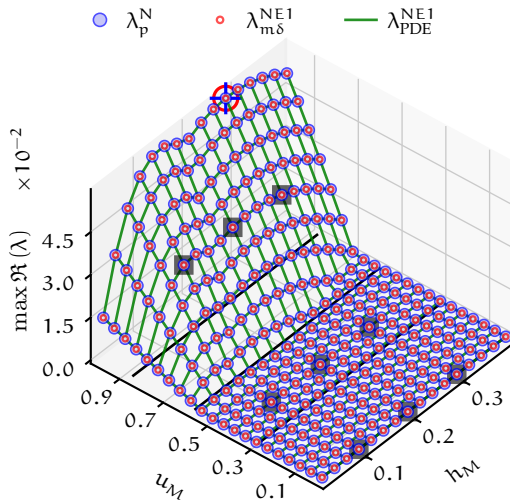
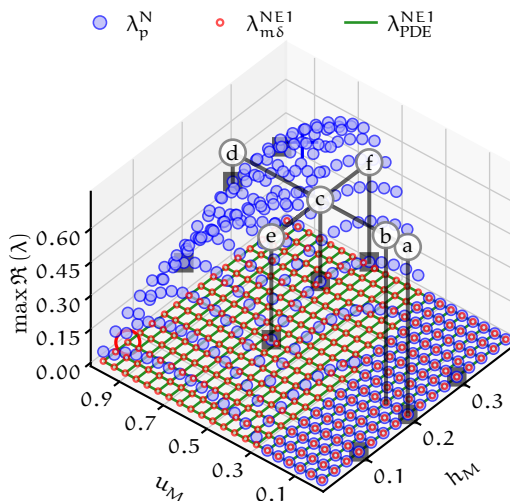


Figure 4.4.5: Maximum real part of the eigenvalues for, λ_p^N of Spectral patch scheme ($N = 10, n = 6, r = 0.1$), $\lambda_{m\delta}^{NE1}$ and λ_{PDE}^{NE1} of the viscous shallow water flow, about different mean flow (h_M, u_M) with $v_M = 0$ and $\theta = 0^\circ$. No artificial instability only for $Re = 10$. Artificial instability spreads to smaller Re with increasing r , Figs. 4.4.3 to 4.4.5 for $r = 0.001, 0.01, 0.1$.

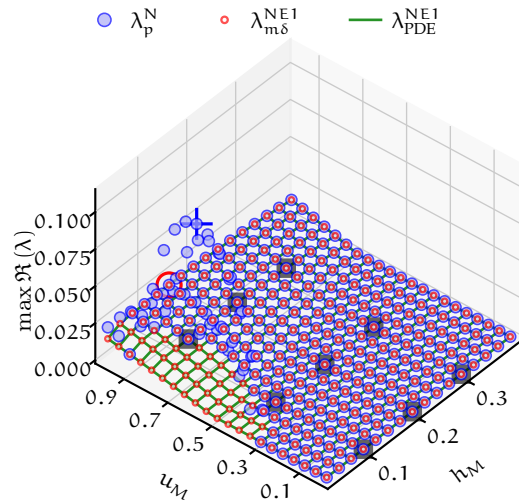
(a) Reynolds number $Re = 10$. Identical to Fig. 4.4.3a of $r = 0.001$ and Fig. 4.4.4a of $r = 0.01$; no artificial instability. Peak values (blue plus and red circle) are $\max \Re(\lambda_p^N) = 0.059 = \max \Re(\lambda_{m\delta}^{NE1})$.



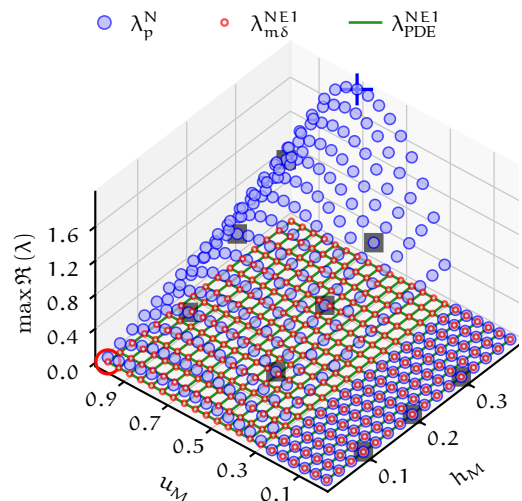
(c) $Re = 250$. Artificial instability (i.e., $\max \Re(\lambda_p^N) > \max \Re(\lambda_{m\delta}^{NE1}) \geq 0$) for nearly all mean height $h_M \in [0.025, 0.4]$ and large $u_M \gtrsim 0.3$; $\max \Re(\lambda_p^N) = 0.75$, $\max \Re(\lambda_{m\delta}^{NE1}) = 0.0041$.



(b) $Re = 50$. Artificial instability (i.e., $\max \Re(\lambda_p^N) > \max \Re(\lambda_{m\delta}^{NE1}) \geq 0$) for very shallow mean flow $h_M \lesssim 0.1$ and large $u_M \gtrsim 0.3$; $\max \Re(\lambda_p^N) = 0.11$, $\max \Re(\lambda_{m\delta}^{NE1}) = 0.019$.



(d) $Re = 1250$. Artificial instability (i.e., $\max \Re(\lambda_p^N) > \max \Re(\lambda_{m\delta}^{NE1}) \geq 0$) for all mean height $h_M \in [0.025, 0.4]$ and large $u_M \gtrsim 0.3$; $\max \Re(\lambda_p^N) = 2$, $\max \Re(\lambda_{m\delta}^{NE1}) = 0.00084$.

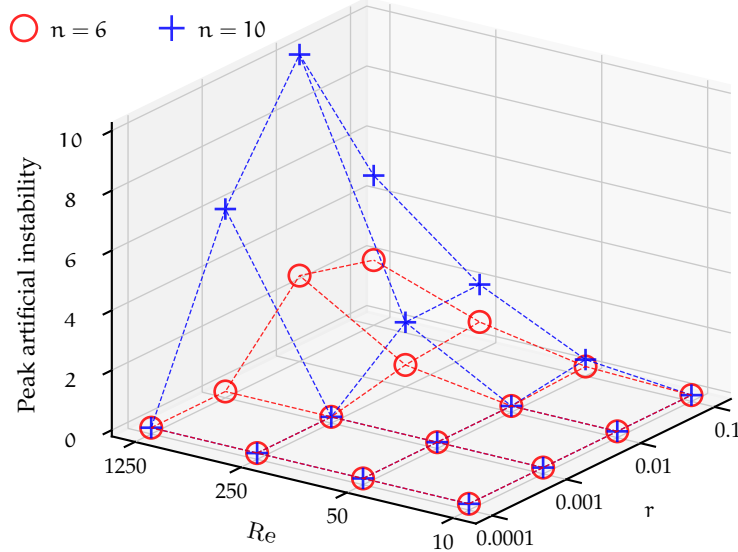


- For small Reynolds numbers $Re \sim 10$, the Spectral patch scheme does not have any artificial instability (condition (4.4.1) holds) for $h_M \in [0.025, 0.4]$, $u_M \in [0, 1]$, Reynolds number $Re \in \{10, 50, 250, 1250\}$, and patch scale ratio $r \in \{0.001, 0.01, 0.1\}$.
- Increasing Reynolds number Re increases the peak artificial instability. For example, Figs. 4.4.5a to 4.4.5d for patch scale ratio $r = 0.1$ show that for Reynolds number $Re = 10, 50, 250, 1250$ the peak artificial instability, $\max_{h_M, u_M} [\max \Re(\lambda_p^N) - \max \Re(\lambda_{m\delta}^{NE})] = 0, 0.11, 0.75, 2$ respectively.
- Increasing Re from $Re \gtrsim 10$ causes a small region of artificial instability to develop for the Spectral patch scheme for the very shallow flow (small h_M) with large mean velocity u_M (Figs. 4.4.4c and 4.4.5b). Increasing Re further from $Re \gtrsim 50$ causes the region of artificial instability to grow large towards larger values of mean height h_M and smaller values of mean velocity u_M (Figs. 4.4.4d and 4.4.5d).
- Increasing Re also causes the h_M for peak instability of the Spectral patch scheme $\max_{h_M} (\max \Re(\lambda_p^N))$ to move towards larger values of h_M ; but the u_M for peak instability $\max_{u_M} (\max \Re(\lambda_p^N))$ remains the same at $u_M \approx 0.7$ and unaffected by the Reynolds number.

The *patch scheme artificial instability for large Reynolds numbers is removed by appropriately decreasing the patch scale ratio r*. Figures 4.4.4 and 4.4.5 show that the Spectral patch scheme ($N = 10, n = 6, r = 0.01, 0.1$) has artificial instability. Figures 4.4.3 to 4.4.5 show how the variation of maximum real part of eigenvalues with h_M, u_M depend on Reynolds number $Re \in \{10, 50, 250, 1250\}$ and patch scale ratio $r \in \{0.001, 0.01, 0.1\}$, for the Spectral patch scheme ($N = 10, n = 6$). Figures 4.4.3 to 4.4.5 shows the following key trends about the stability of the Spectral patch scheme, all of which also hold for the polynomial patch schemes.

- For small mean velocity $u_M \in [0, 0.3]$ where the underlying full-domain micro-scale system is stable ($\max \Re(\lambda_{m\delta}^{NE}) \neq 0$), the Spectral patch scheme is also stable for $h_M \in [0.025, 0.4]$, Reynolds number $Re \in \{10, 50, 250, 1250\}$ and patch scale ratio $r \in \{0.001, 0.01, 0.1\}$.
- Similar to the trend with increasing Re , increasing patch scale ratio r increases the peak artificial instability. For example, Figs. 4.4.3c, 4.4.4c and 4.4.5c for Reynolds number $Re = 250$ show that for increasing patch scale ratio $r = 0.001, 0.01, 0.1$ the peak artificial instability, $\max_{h_M, u_M} [\max \Re(\lambda_p^N) - \max \Re(\lambda_{m\delta}^{NE})] = 0, 0.52, 0.75$ respectively.

Figure 4.4.6: Variation of Spectral patch scheme peak artificial instability $\max_{h_M, u_M} [\max \Re(\lambda_p^N) - \max \Re(\lambda_{m\delta}^{NE1})]$ (over $h_M \in [0.025, 0.4]$, $u_M \in [0, 1]$), with the Reynolds number Re and the patch scale ratio r . Artificial instability increases with increasing sub-patch micro-grid intervals n for large r and Re . Artificial instability decreases, with decreasing Reynolds number Re , and with decreasing patch scale ratio r .



- Similar to the trend with increasing Re , increasing r from $r \gtrsim 0.001$ causes a small region of artificial instability to develop for the Spectral patch scheme for the very shallow flow (small h_M) with large mean velocity u_M . Increasing r further from $r \gtrsim 0.01$ causes the region of artificial instability to grow large for the Spectral patch scheme towards larger values of mean height h_M and smaller values of mean velocity u_M .
- Similar to the trend with increasing Re , increasing r also causes the h_M for peak instability of the Spectral patch scheme $\max_{h_M} (\max \Re(\lambda_p^N))$ to move towards larger values of h_M ; but the u_M for peak instability $\max_{u_M} (\max \Re(\lambda_p^N))$ remains the same at $u_M \approx 0.7$ and unaffected by the Reynolds number.

In summary, both increasing Reynolds number Re and increasing patch scale ratio r cause the patch scheme artificial instability to develop and spread to larger regions of mean flow (h_M, u_M). In other words, increasing Re causes artificial instability to develop and grow, but decreasing r causes the artificial instability to shrink and disappear. [Figure 4.4.6](#) shows this trend plotting peak artificial instability $\max_{h_M, u_M} [\max \Re(\lambda_p^N) - \max \Re(\lambda_{m\delta}^{NE1})]$

(over $h_M \in [0.025, 0.4]$, $u_M \in [0, 1]$), with the Reynolds number $Re \in \{10, 50, 250, 1250\}$ and the patch scale ratio $r \in \{0.0001, 0.001, 0.01, 0.01, 0.1\}$. Thus, the *patch scheme artificial instability for large Reynolds numbers is removed by appropriately decreasing the patch scale ratio r*.

Increasing the number of sub-patch micro-grid intervals n increases the artificial instability of the Spectral patch scheme for large patch scale ratio. The preceding two paragraphs show that both increasing Reynolds number Re and increasing patch scale ratio r cause the patch scheme artificial instability to develop and spread to larger regions of mean flow (h_M, u_M) . [Figure 4.4.6](#) shows this trend plotting peak artificial instability $\max_{h_M, u_M} [\max \Re(\lambda_p^N) - \max \Re(\lambda_{m,\delta}^{N \times 1})]$ (over $h_M \in [0.025, 0.4]$, $u_M \in [0, 1]$), with the Reynolds number $Re \in \{10, 50, 250, 1250\}$ and the patch scale ratio $r \in \{0.0001, 0.001, 0.01, 0.01, 0.1\}$ for different number of sub-patch micro-grid intervals $n \in \{6, 10\}$. [Figure 4.4.6](#) shows that for large patch scale ratio $r \gtrsim 0.01$, increasing n increases the peak artificial instability of the Spectral patch scheme. This trend of increasing peak artificial instability with increasing n , is large for large Reynolds numbers $Re \gtrsim 250$. But [p. 236 of §4.4.3](#) shows that increasing the number of sub-patch micro-grid intervals to $n = 10$ removes the artificial instability of the polynomial patch schemes due to small patch scale ratio r and/or large number macro-grid intervals N .

Overall the following listing summarises the stability characteristics of the Spectral patch scheme for viscous shallow water flow. All the following characteristics also hold for all the four polynomial patch schemes.

1. For small mean velocity $u_M \in [0, 0.2]$ where the underlying full-domain micro-scale system is stable ($\max \Re(\lambda_{m,\delta}^{N \times 1}) \leq 0$), the Spectral patch scheme is stable for a wide range of patch scale ratio $r \in [0.001, 0.1]$ and Reynolds number $Re \in [10, 1250]$.
2. For large mean velocity $u_M \gtrsim 0.2$ and large Reynolds number $Re > 10$, the Spectral patch scheme with large patch scale ratio $r \gtrsim 0.01$ has artificial instability for both when the underlying full-domain micro-scale system is stable and physically unstable.
3. For large mean velocity $u_M \gtrsim 0.2$, the Spectral patch scheme with large patch scale ratio $r \gtrsim 0.01$ has artificial instability for when the underlying full-domain micro-scale system is both stable and physically unstable. Increasing the Reynolds number $Re \gtrsim 10$ causes artificial instability to develop and spread to larger regions of mean flow (h_M, u_M) . But decreasing patch scale ratio $r \lesssim 0.01$ causes the artificial instability to shrink and disappear.

4. The artificial instability of the patch schemes arises only for the sub-patch micro-scale modes.
5. Increasing the number of sub-patch micro-grid intervals n increases the patch scheme artificial instability for large patch scale ratio.

As §4.6 on frame invariance of staggered patch schemes establish, the patch schemes are invariant (within discretisation errors) with different flow angle α for macro-scale waves, where $q = \sqrt{u_M^2 + v_M^2}$, $u_M = q \cos(\alpha)$ and $v_M = q \sin(\alpha)$. Hence, whereas all the points in the preceding summary are based on the Spectral patch scheme over a wide range of mean height h_M and the mean velocity u_M keeping $v_m = 0$, they also hold for the resultant mean velocity $q = \sqrt{u_M^2 + v_M^2}$ (u_M, v_M) along any orientation. Thus, *for an appropriate patch grid the Spectral patch scheme is not artificially unstable, for a wide range of system parameters* (Reynolds number Re , mean height h_M , and horizontal mean velocity (u_m, v_M)).

4.4.2 Maximum artificial instability is due to micro-scale modes modulated over smallest macro-scale waves

Page 215 of §4.4.1 establish that the patch scheme artificial instability arises only for the sub-patch micro-scale modes. That is, the patch scheme macro-scale modes which is of primary interest, do not have artificial instability. More specifically, this subsection shows that the maximum artificial instability of patch schemes is due to sub-patch micro-scale modes modulated over the smallest resolved macro-scale waves moving along the resultant horizontal mean velocity (u_M, v_M) . The patch scheme Fourier mode (3.2.10) in p. 52 of 3.2.3 gives an analytic form of the modulation of micro-scale wave modes over macro-scale wave modes. For example, the eigenvector plots in Figs. 4.4.9 and 4.4.11 show the artificially unstable sub-patch micro-scale mode modulated over the macro-scale wave mode with wavenumbers $(k_x, k_y) = (1, 0), (2, 0)$ respectively of the Spectral staggered patch scheme. In the eigenvector plot of Figs. 4.4.9 and 4.4.11, the grey curves connecting the patch centre values (patch mean) indicate the unmodulated macro-scale wave.

The study in this section uses Spectral patch scheme over a patch grid with $N = 10$ macro-grid intervals, each patch containing $n = 6$ sub-patch micro-grid intervals, and a patch scale ratio $r = 0.1$. But all qualitative characteristics in this subsection also hold for other patch grid parameters (N, n, r) and for the polynomial patch schemes.

Figure 4.4.7: Spectral patch scheme ($N = 10, n = 6, r = 0.1$) has artificial instability for viscous shallow water flow for $(h_M, u_M, v_M) = (0.2, 0.3, 0)$. Same plot as Fig. 4.4.1, but analytic eigenvalues λ_p^{NE1} and $\lambda_{m\delta}^{NE1}$ are evaluated only for macro-scale wavenumber $(k_x, k_y) = (1, 0)$ over a $2\pi \times 2\pi$ domain.

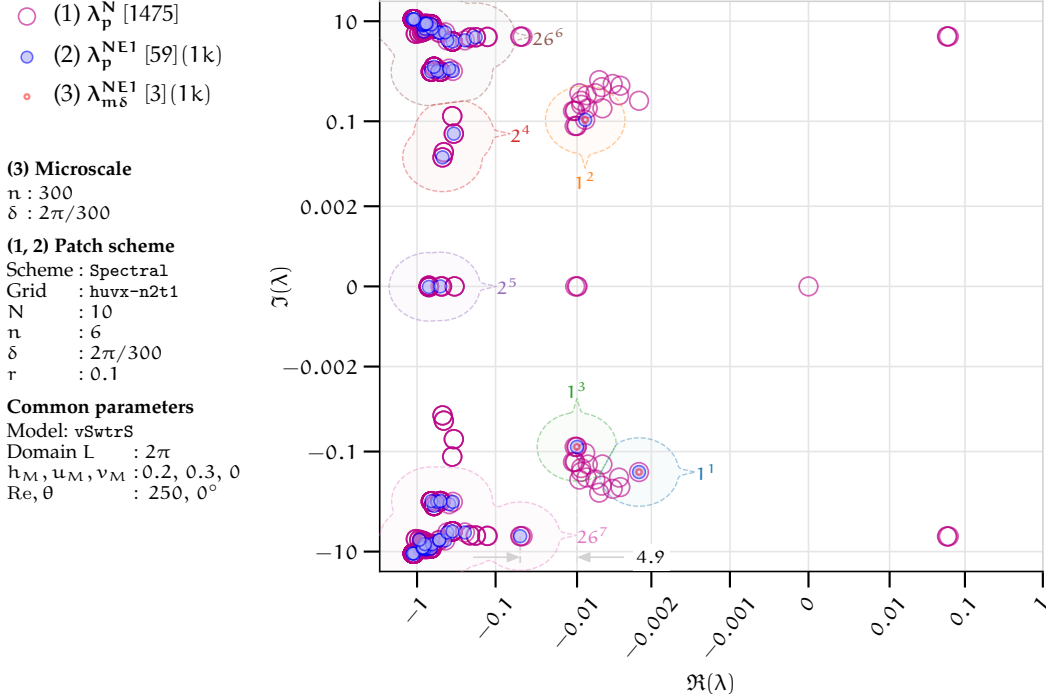


Figure 4.4.8: Spectral patch scheme ($N = 10, n = 6, r = 0.1$) has artificial instability for viscous shallow water flow for $(h_M, u_M, v_M) = (0.2, 0.8, 0)$. Same plot as Fig. 4.4.2, but analytic eigenvalues λ_p^{NE1} and $\lambda_{m\delta}^{NE1}$ are evaluated only for macro-scale wavenumber $(k_x, k_y) = (1, 0)$ over a $2\pi \times 2\pi$ domain.

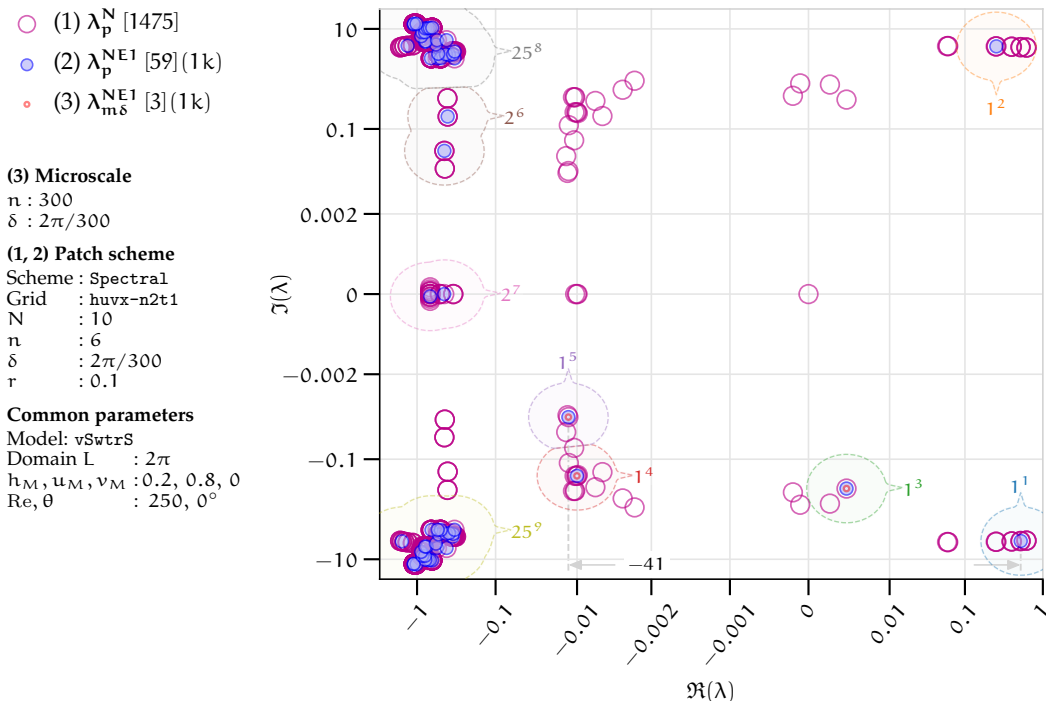
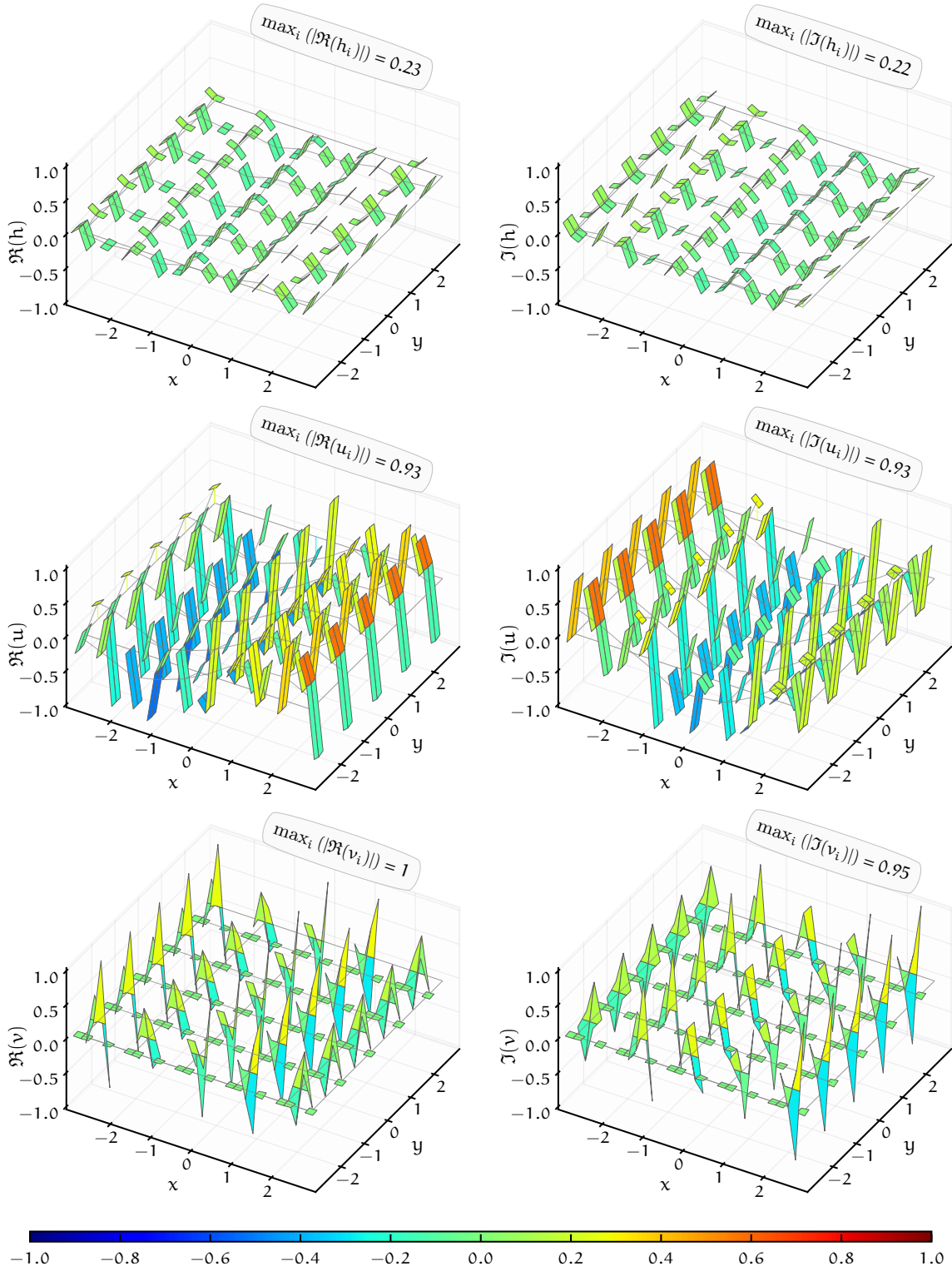


Figure 4.4.9: Eigenvector for eigenvalue $\lambda_p^{NE1} = \lambda_p^N = 0.52 - 4.3237i$ (cluster 1 in Fig. 4.4.8) corresponding to artificial instability of Spectral staggered patch scheme ($N = 10$, $n = 6$, $r = 0.1$) with $(k_x, k_y) = (1, 0)$ for viscous shallow water flow with $Re = 250$, $(h_M, u_M, v_M) = (0.2, 0.8, 0)$.



This paragraph explains the wavenumber-dependence of the artificially unstable sub-patch micro-scale modes. [Figure 4.4.1](#) of §4.4.1 shows that there are ten artificially unstable sub-patch micro-scale modes in clusters 1, 2, and [Fig. 4.4.2](#) of §4.4.1 shows that there are fifty artificially unstable micro-scale modes in clusters 1–4. [Figures 4.4.7 and 4.4.8](#) show the same complex plane plot as [Figs. 4.4.1 and 4.4.2](#) of §4.4.1 (artificial instability of Spectral patch scheme for $N = 10$, $n = 6$, $r = 0.1$ with $u_M = 0.3, 0.4$ respectively) except one difference:

- analytic eigenvalues λ_p^{NE1} and $\lambda_{m\delta}^{NE1}$ in [Figs. 4.4.1](#) and [4.4.2](#) of §4.4.1 are evaluated for all the $N^2/4 = 25$ macro-scale wavenumbers (k_x, k_y) where $k_x, k_y \in \{-2, -1, 0, 1, 2\}$ resolved by a patch grid;
- analytic eigenvalues λ_p^{NE1} and $\lambda_{m\delta}^{NE1}$ in [Figs. 4.4.7](#) and [4.4.8](#) are evaluated only for one macro-scale wavenumber $(k_x, k_y) = (1, 0)$.

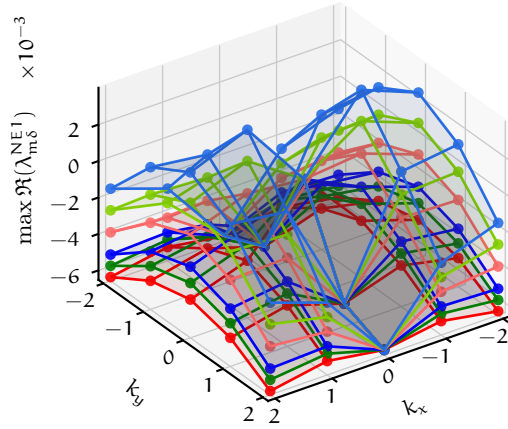
For $n = 6$ sub-patch micro-grid intervals, the expression (4.2.14) of §4.2.3 gives the total number of patch interior nodes per macro-cell as $n_p^i = 9n^2/4 - 4n + 2 = 59$. Hence, for one wavenumber (k_x, k_y) , there are $n_p^i = 59$ eigenvalues λ_p^{NE1} for the one-cell analytic patch scheme Jacobian ([§4.2.3](#)). Among the total $n_p^i = 59$ eigenvalues λ_p^{NE1} for one wavenumber, three are macro-scale eigenvalues corresponding to three patches in a macro-cell; the remaining 53 eigenvalues correspond to micro-scale modes. In [Figs. 4.4.7](#) and [4.4.8](#), for the macro-scale wavenumber $(k_x, k_y) = (1, 0)$, the three macro-scale eigenvalues λ_p^{NE1} are in clusters 1, 2, 3 and clusters 3, 4, 5 respectively. For $u_M = 0.3$ in [Fig. 4.4.7](#), for $(k_x, k_y) = (1, 0)$ there are no artificially unstable micro-scale modes as $\max \Re(\lambda_p^{NE1}) > \max \Re(\lambda_{m\delta}^{NE1})$. But for $u_M = 0.8$ in [Fig. 4.4.8](#), for $(k_x, k_y) = (1, 0)$ two of micro-scale modes in clusters 1, 2 are artificially unstable as $\max \Re(\lambda_p^{NE1}) = 0.52 > \max \Re(\lambda_{m\delta}^{NE1}) = 0.0021$. Thus, *the artificial instability of the sub-patch micro-scale modes depend on the specific macro-scale wavenumber (k_x, k_y) over which the micro-scale modes are modulated.* The eigenvector plot in [Fig. 4.4.9](#) show the artificially unstable sub-patch micro-scale mode modulated over the macro-scale wave mode with wavenumber $(k_x, k_y) = (1, 0), (2, 0)$ respectively, which correspond to the eigenvalue $\lambda_p^{NE1} = \lambda_p^N = 0.52 - 4.3237i$ in cluster 2 of [Fig. 4.4.8](#). In the eigenvector plot of [Fig. 4.4.9](#), the grey curves connecting the patch centre values (patch mean) indicate the unmodulated macro-scale wave.

Increasing the mean velocity u_M increases monotonically the physical instability of the viscous shallow water. [Figure 4.4.10a](#) plot wavenumber-wise contribution to the physical instability $\max \Re(\lambda_{m\delta}^{NE1})$ for the full-micro-scale domain system, for the macro-scale wavenumbers resolved by a patch scheme with $N = 10$ macro-grid intervals and each patch containing $n = 6$

Figure 4.4.10: Wavenumber-wise contribution to viscous shallow water flow instability for different mean velocity u_M ($h_M = 0.2$, $v_M = 0$, $Re = 250$): (a) and (b) plot physical instability and number of unstable modes of *full-domain system*; (c) and (d) plot artificial instability and number of unstable modes of *Spectral patch scheme* ($N = 10$, $n = 6$, $r = 0.1$).

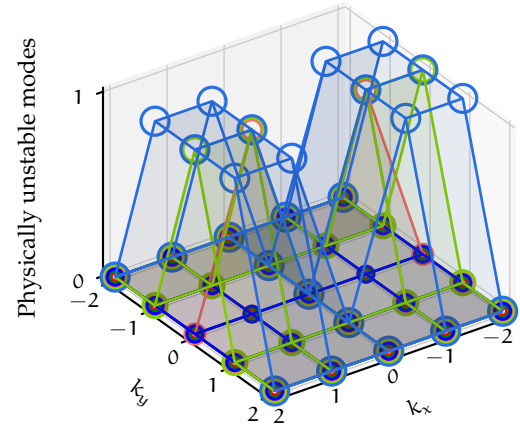
(a) Increasing u_M increases physical instability monotonically, with two peaks at $(k_x, k_y) = (-1, 0), (1, 0)$ to each side of a valley along k_x -axis. For $v_M \neq 0$, the valley is along line $k_y = (v_M/u_M)k_x$.

Legend:
● $u_M = 0.2$ ● $u_M = 0.3$ ● $u_M = 0.4$
● $u_M = 0.6$ ● $u_M = 0.8$ ● $u_M = 1$



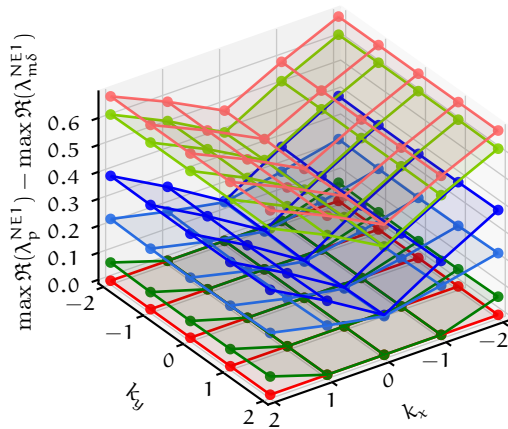
(b) Increasing u_M increases the number of physically unstable modes monotonically, symmetrically to each side of a valley along k_x -axis. For $v_M \neq 0$, the valley is along line $k_y = (v_M/u_M)k_x$.

Legend:
● $u_M = 0.2$ ● $u_M = 0.3$ ● $u_M = 0.4$
○ $u_M = 0.6$ ○ $u_M = 0.8$ ○ $u_M = 1$



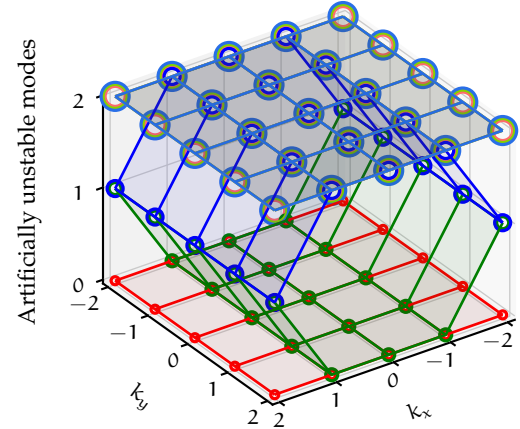
(c) Increasing u_M increases artificial instability for $u_M \lesssim 0.6$, then decreases. Artificial instability increase with $|k_x|$ for $|k_x| \lesssim 2$. Valley is along k_x -axis for $v_M = 0$, i.e., along $k_y = (v_M/u_M)k_x$.

Legend:
● $u_M = 0.2$ ● $u_M = 0.3$ ● $u_M = 0.4$
● $u_M = 0.6$ ● $u_M = 0.8$ ● $u_M = 1$



(d) Increasing $u_M \in [0, 1]$ increases number of artificially unstable micro-scale modes, symmetrically on both sides of the ridge/valley along k_x -axis, that is along $k_y = (v_M/u_M)k_x$.

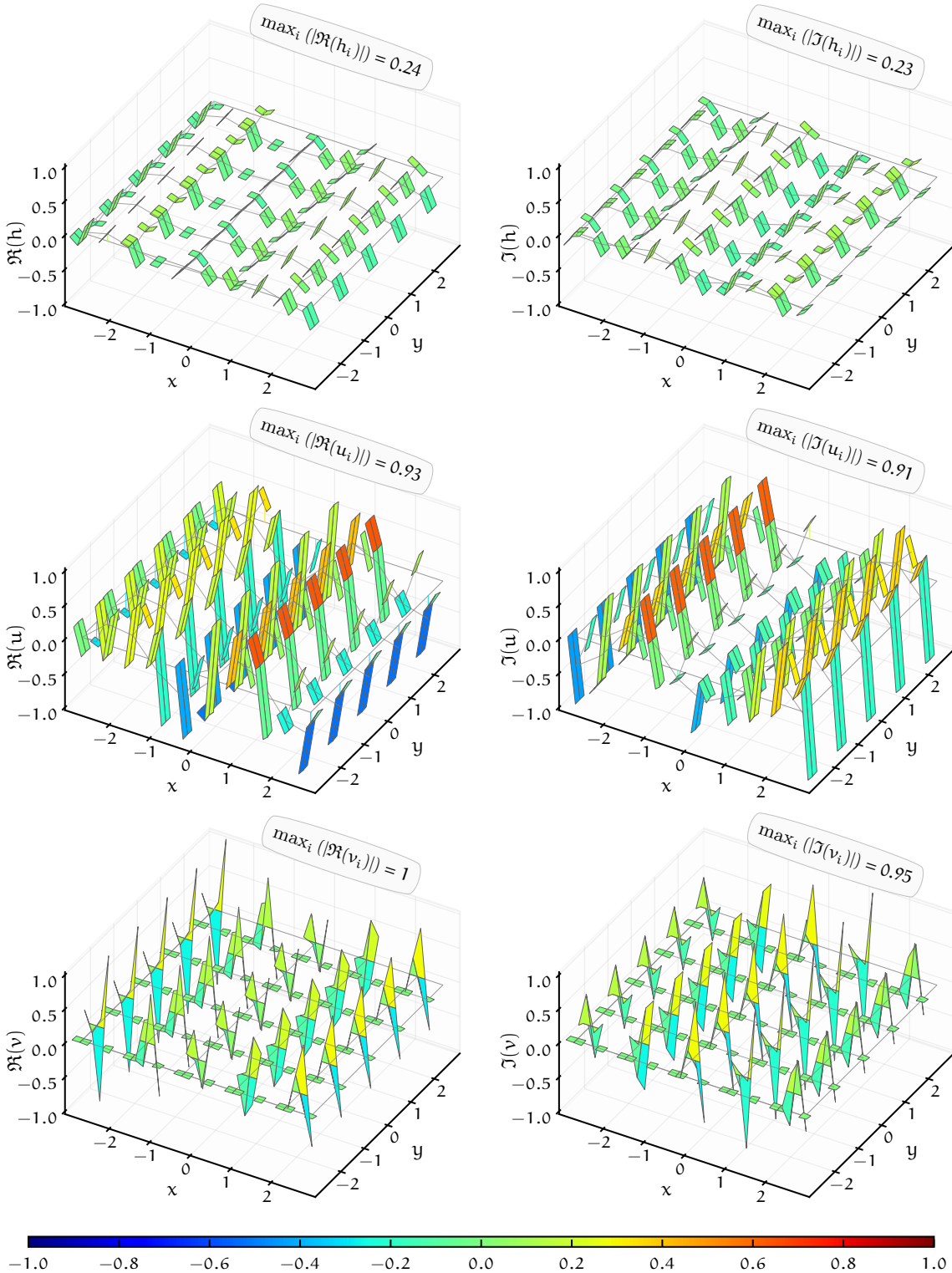
Legend:
● $u_M = 0.2$ ● $u_M = 0.3$ ● $u_M = 0.4$
○ $u_M = 0.6$ ○ $u_M = 0.8$ ○ $u_M = 1$



sub-patch intervals. [Figure 4.4.10a](#) shows that increasing mean velocity u_M increases physical instability monotonically, with two peaks at $(k_x, k_y) = (-1, 0), (1, 0)$ to each side of a valley along k_x -axis (for $v_M = 0$). This maximum physical instability for wavenumber $(k_x, k_y) = (1, 0)$ is also evident in [Fig. 4.4.8](#) as $(k_x, k_y) = (1, 0)$ gives the maximum real part value of $\max \Re(\lambda_{m\delta}^{NE1}) = 0.0021$ in cluster 3. For nonzero v_M , the valley is along the line $k_y = (v_M/u_M)k_x$. That is, the maximum physical instability is due to two largest macro-scale waves on the domain moving along the resultant horizontal mean velocity (u_M, v_M) , with smallest two macro-scale wavenumber (k_x, k_y) on each side of the valley in [Fig. 4.4.10a](#).

Similar to the physical instability, increasing the mean velocity u_M increases the artificial instability of the patch schemes for the viscous shallow water, but only for $u_M \lesssim 0.6$. [Figure 4.4.10c](#) plot wavenumber-wise contribution to the artificial instability ($\max \Re(\lambda_p^{NE1}) - \max \Re(\lambda_{m\delta}^{NE1}) > 0$) of the Spectral patch scheme with $N = 10$, $n = 6$, $r = 0.1$, for all the $N^2/4 = 25$ macro-scale wavenumbers (k_x, k_y) where $k_x, k_y \in \{-2, -1, 0, 1, 2\}$. [Figure 4.4.10c](#) shows that increasing mean velocity u_M increases the patch scheme artificial instability for up to $u_M \lesssim 0.6$ (light red small discs near top region) after which the artificial instability decreases (light green and light blue small discs). But the artificial instability does not disappear, instead further increase in mean velocity $u_M \gtrsim 2$ increases the artificial instability again. This increasing and then decreasing patch scheme artificial instability with increasing u_M , is also evident along the line a-d in [Fig. 4.4.5c](#). The artificial instability for any mean velocity u_M linearly increases with increasing $|k_x|$, symmetrically on each side of a valley along k_x -axis (for $v_M = 0$). For nonzero v_M , the valley is along the line $k_y = (v_M/u_M)k_x$. As opposed to the maximum physical instability for the smallest two macro-scale wavenumbers on each side of the valley in [Fig. 4.4.10a](#), the maximum artificial instability is due to sub-patch micro-scale modes modulated over the largest resolved macro-scale wavenumbers on each side of the valley. For $v_M = 0$ in [Fig. 4.4.10c](#), the maximum artificial instability is due to $k_x = -2, 2$ for all the resolved $k_y = -2, -1, 0, 1, 2$. That is, the maximum artificial instability of the patch schemes is due to sub-patch micro-scale modes modulated over the smallest resolved macro-scale waves moving along the resultant horizontal mean velocity (u_M, v_M) (with largest wavenumber (k_x, k_y) on each side of the valley). For example, in the complex plane plot of [Fig. 4.4.2](#) in [§4.4.1](#) for $u_M = 0.8$, the maximum artificial instability of $\max \Re \lambda_p^{NE1} = 0.62$ correspond to the light green discs with $k_x = -2, 2$ in [Fig. 4.4.10c](#). The eigenvector plot in [Fig. 4.4.11](#) show the unstable sub-patch micro-scale mode modulated over the macro-scale wave mode with wavenumber $(k_x, k_y) = (2, 0), = (2, 0)$ respectively, which correspond to the

Figure 4.4.11: Eigenvector for eigenvalue $\lambda_p^{N\text{E}1} = \lambda_p^N = 0.62 - 4.2439i$ (cluster 2 in Fig. 4.4.2) corresponding to maximum artificial instability of Spectral patch scheme ($N = 10$, $n = 6$, $r = 0.1$) with $(k_x, k_y) = (2, 0)$ for viscous shallow water flow with $\text{Re} = 250$, $(h_M, u_M, v_M) = (0.2, 0.8, 0)$.



maximum artificial instability of the eigenvalue $\lambda_p^{N\neq 1} = \lambda_p^N = 0.62 - 4.2439i$ (cluster 2 in Fig. 4.4.2 of §4.4.1). In the eigenvector plot of Fig. 4.4.11, the grey curves connecting the patch centre values (patch mean) indicate the unmodulated macro-scale wave. [TODO/correct] that the peak artificial instability around (2,0) and decreases for large wavenumbers

Increasing the mean velocity u_M increases monotonically the number of physically unstable modes of the viscous shallow water. Figure 4.4.10b plot wavenumber-wise contribution to the number of physically unstable modes respectively for the full-micro-scale domain system, for all the macro-scale wavenumbers resolved by a patch grid with $N = 10$ macro-grid intervals. Figure 4.4.10b shows that increasing mean velocity u_M increases the number of physically unstable modes for the full-domain micro-scale system, symmetrically to each side of a valley along k_x -axis (for $v_M = 0$). For nonzero v_M , the valley is along line $k_y = (v_M/u_M)k_x$. The small circles of dark red, dark green and dark blue colours at the bottom of Fig. 4.4.10b shows that for mean velocity up to $u_M = 0.4$, there are no unstable modes. Two light red inner circles in central region of Fig. 4.4.10b show that increasing the mean velocity to $u_M = 0.6$ leads to physical instability in two smallest wavenumber $(k_x, k_y) = (-1, 0), (1, 0)$ on each side of the valley. With further increase in $u_M = 0.8, 1$, the initially developed physical instability for two small wavenumbers spread to larger wavenumbers, and increase to four and twelve artificially unstable micro-scale modes respectively. For example, for $u_M = 0.8$, the top four light green inner circles in Fig. 4.4.10b show that the wavenumbers $(k_x, k_y) \in \{(-2, 0), (-1, 0), (1, 0), (2, 0)\}$ each has one artificially unstable mode, corresponding to the four physically unstable modes in clusters 5, 6 of Fig. 4.4.2.

Increasing the mean velocity u_M increases the number of artificially unstable micro-scale modes for the patch schemes. Figures 4.4.1 and 4.4.2 for $u_M = 0.3, 0.8$ with ten and fifty artificially unstable micro-scale modes, suggest that the number of artificially unstable micro-scale modes increases with mean velocity u_M . This increasing number of artificially unstable micro-scale modes is due to two sources:

1. increasing mean velocity u_M increases the number of wavenumbers for which a patch scheme is unstable;
2. increasing mean velocity u_M also increases the number of artificially unstable micro-scale modes per wavenumber;

Figure 4.4.10d plot wavenumber-wise contribution to the number of artificially unstable micro-scale modes of the Spectral patch scheme with

$N = 10$, $n = 6$, $r = 0.1$, for all the $N^2/4 = 25$ macro-scale wavenumbers (k_x, k_y) where $k_x, k_y \in \{-2, -1, 0, 1, 2\}$. [Figure 4.4.10d](#) shows that for increasing mean velocity $u_M = 0.2, 0.3, 0.4, 0.6, 0.8, 1$ (along the line a-d in [Fig. 4.4.5c](#)) the number of artificially unstable micro-scale modes increases, symmetrically to each side of a valley/ridge along k_x -axis (for $v_M = 0$). For nonzero v_M , the valley/ridge is along line $k_y = (v_M/u_M)k_x$. Increasing the mean velocity u_M increases the number of wavenumbers for which a patch scheme is unstable, for up to $u_M \lesssim 0.4$ after which a patch scheme is unstable for all the 25 wavenumbers. For example, for $u_M = 0.2, 0.3, 0.4$, [Figure 4.4.10d](#) (dark red, dark green and dark blue circles near the bottom) shows that the *number of wavenumbers* for which the Spectral patch scheme is unstable are 0, 10, 25 respectively. The corresponding total *number of artificially unstable micro-scale modes* for $u_M = 0.2, 0.3, 0.4, 0.6, 0.8, 1$ are 0, 10, 40, 50, 50, 50 respectively.

- The small dark red circles at the bottom of [Fig. 4.4.10d](#) show that for mean velocity $u_M = 0.2$, there are no artificially unstable micro-scale modes.
- The small dark green circles near the bottom of [Fig. 4.4.10d](#) show that increasing to $u_M = 0.3$ triggers the patch scheme artificial instability, but only for $k_x = -2, 2$. That is the sub-patch micro-scale modes are artificially unstable corresponding to the largest ten macro-scale wave modes moving along the resultant horizontal mean velocity (u_M, v_M) (five on each side of the green valley in [Fig. 4.4.10d](#)).
- The dark blue circles near the middle and top region of [Fig. 4.4.10d](#) show that increasing to $u_M = 0.4$ makes the patch scheme artificially unstable for all 25 wavenumbers. There is one unstable micro-scale mode for each of ten wavenumbers with $k_x = -2, 2$ (corresponding to ten largest macro-scale wave modes) and there are two unstable micro-scale modes for each of fifteen wavenumbers with $k_x = -1, 0, 1$ (corresponding to thirty macro-scale wave modes).
- All the large circles of light red, light green, and light blue circles at the of [Fig. 4.4.10d](#) show that for $u_M \gtrsim 0.6$ the patch scheme is artificially unstable for all 25 wavenumbers. There are two unstable micro-scale modes for each of 25 wavenumbers with $k_x = -1, 0, 1$ (corresponding to all fifty macro-scale wave modes). For example, [Fig. 4.4.2](#) for $u_M = 0.8$ shows the fifty artificially unstable micro-scale modes contained within the clusters 1–4.

From Fig. 4.4.2, the total number of maximum artificially unstable micro-scale modes remain the same as fifty for $u_M = 0.6, 0.8, 1$ (two unstable modes for each of 25 wavenumbers). But this total number of maximum artificially unstable micro-scale modes is an upper bound. With further increase in mean velocity $u_M > 1$, the total number of artificially unstable micro-scale modes increase larger than fifty.

Overall the following listing summarises the characteristics of physically unstable modes of the full-domain system and the artificially unstable modes of the Spectral patch scheme for viscous shallow water flow. Whereas all the following points are based on the Spectral patch scheme with $N = 10, n = 6, r = 0.1$, they also hold for other patch grid parameters (N, n, r) and for the polynomial patch schemes.

- Increasing the mean velocity u_M increases monotonically the physical instability and the number of physically unstable modes of the viscous shallow water
- The maximum physical instability is due to two largest macro-scale waves on the domain moving along the resultant horizontal mean velocity (u_M, v_M) , with smallest two macro-scale wavenumber (k_x, k_y) .
- The artificial instability of the sub-patch micro-scale modes depend on the specific macro-scale wavenumber (k_x, k_y) over which the micro-scale modes are modulated.
- Increasing number of artificially unstable micro-scale modes with increasing mean velocity u_M , is due to two sources:
 1. increasing mean velocity u_M increases the number of wavenumbers for which a patch scheme is unstable;
 2. increasing mean velocity u_M also increases the number of artificially unstable micro-scale modes per wavenumber;
- The artificial instability of the sub-patch micro-scale modes linearly increases with increasing magnitude of the macro-scale wavenumber of waves moving along the resultant horizontal mean velocity (u_M, v_M) .
- The maximum artificial instability of the patch schemes is due to sub-patch micro-scale modes modulated over the smallest resolved macro-scale waves moving along the resultant horizontal mean velocity (u_M, v_M)

4.4.3 The five staggered patch schemes are not artificially unstable for different grid parameters

[Section 4.4.1](#) shows that for an appropriate patch grid the Spectral patch scheme is not artificially unstable, for *a wide range of system parameters* (Reynolds number Re , mean height h_M , and horizontal mean velocity (u_m, v_M)) for *a small representative set of patch grid parameters* (number of macro-grid intervals N , number of sub-patch micro-grid intervals n , patch scale ratio r). This subsection shows that the five staggered patch schemes are not artificially unstable, for *a wide range of patch grid parameters* (macro-grid intervals N , sub-patch micro-grid intervals n , and patch scale ratio r), for *a small representative set of system parameters* (Reynolds number Re , mean height h_M , and horizontal mean velocity (u_m, v_M)) indicated by nine black squares in [Figs. 4.4.3 to 4.4.5 of §4.4.1](#)). That is, this subsection shows that for a wide range of patch grid parameters a small representative set of system parameters, the maximum real part of the patch scheme eigenvalues (analytic $\lambda_p^{N \times 1}$, numerical λ_p^N) is *not* both positive and larger than the maximum real part of the eigenvalues $\lambda_{m\delta}^{N \times 1}$ of the corresponding full-domain micro-scale system, that is the condition of no artificial instability [\(4.4.1\)](#) holds (within a tolerance of 10^{-5}). This subsection also gives *a general rule to get rid of artificial instability*, when a patch scheme has artificial instability for some combinations of system and patch grid parameters.

We expect the polynomial patch schemes to follow similar stability trend with different mean flow (h_M, u_M) as the Spectral patch scheme for which [§4.4.1](#) studies in detail for 336 combinations of the mean flow (h_M, u_M) . So, as opposed to the many combinations (336) of linearisation points $\{(h_M, u_M, v_M)\}$ in [§4.4.1](#), this subsection limits the study of artificial stability of path schemes to the nine linearisation points $\{(h_M, u_M, v_M)\}$ where $h_M \in \{0.1, 0.2, 0.3\}$, $u_M \in \{0, 0.4, 0.8\}$, $v_M = 0$ (the black squares in [Figs. 4.4.3 to 4.4.5 of §4.4.1](#)). Thus, this subsection studies the artificial instability via the patch scheme eigenvalues for a total of 7 776 cases consisting of all the combinations (cartesian product) of the Spectral and polynomial patch schemes (Square-p2, Square-p4, Square-p6, and Square-p8) for the patch grid parameters

- Number of macro-scale intervals $N \in \{6, 10, 14, 18, 22, 26\}$;
- Number of sub-patch micro-grid intervals $n \in \{6, 10\}$;
- Patch scale ratio $r \in \{0.0001, 0.001, 0.01, 0.1\}$,

and the system parameters:

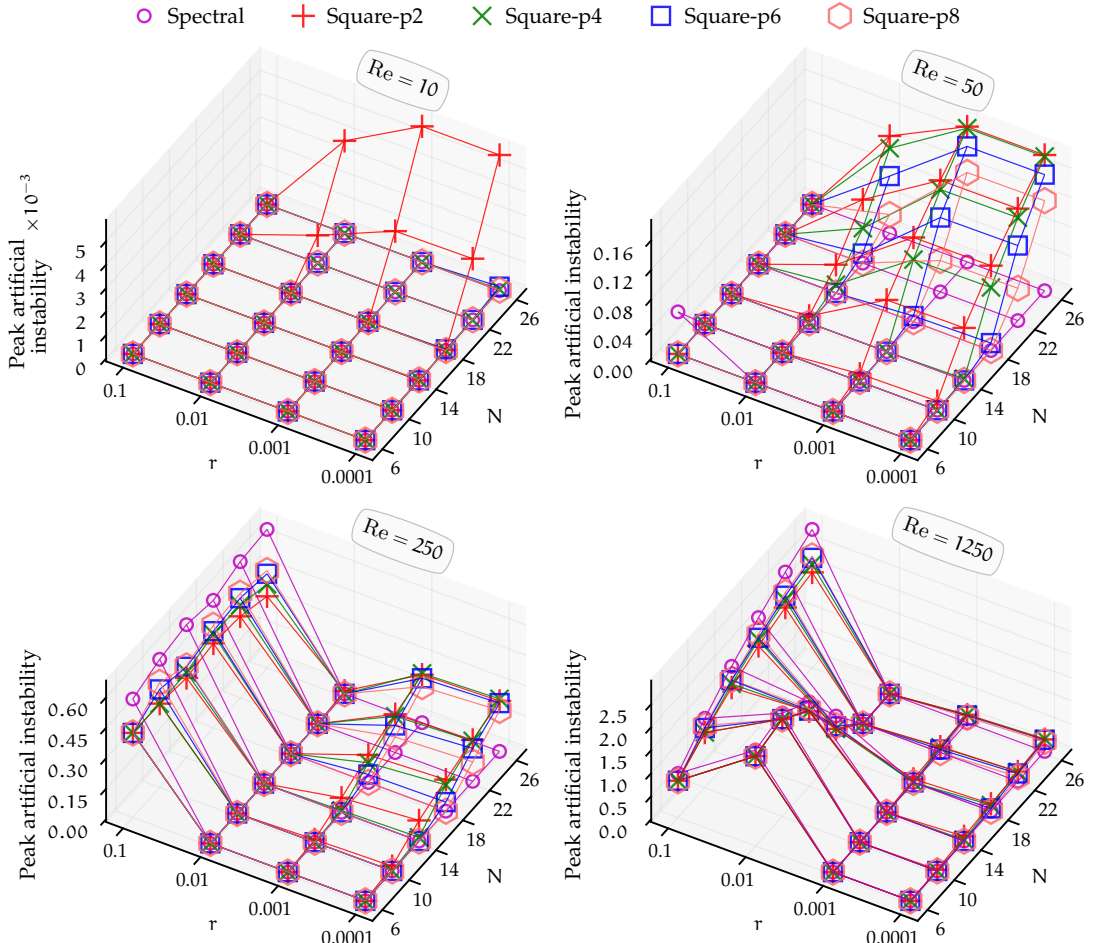
1. mean height $h_M \in \{0.1, 0.2, 0.3\}$;
2. mean velocity $u_M \in \{0, 0.4, 0.8\}$, $v_M = 0$ ([§4.6](#) on frame invariance show the flow direction is immaterial);
3. Reynold number $Re \in \{10, 50, 250, 1250\}$;

As opposed to the definition of peak artificial instability in [p. 217](#) of [§4.4.1](#) over 336 cases, the term *peak artificial instability* throughout this subsection refers to $\max_{h_M, u_M} [\max \Re(\lambda_p^N) - \max \Re(\lambda_{m\delta}^{NE1})]$ or using analytic eigenvalues $\max_{h_M, u_M} [\max \Re(\lambda_p^{NE1}) - \max \Re(\lambda_{m\delta}^{NE1})]$, over the nine cases of the mean height $h_M \in \{0.1, 0.2, 0.3\}$ and the mean velocity $u_M \in \{0.0, 0.4, 0.8\}$.

For small number of sub-patch micro-grid intervals $n = 6$, *accurate patch coupling interpolation removes the artificial instability for small patch scale ratio r*. For small number of sub-patch micro-grid intervals ([Fig. 4.4.12](#) for $n = 6$), the artificial instability increases with increasing N. For large patch scale ratio $r \gtrsim 0.1$, increasing patch coupling accuracy increases the artificial instability for large Reynolds number $Re \gtrsim 250$. For example, in the bottom two subplots of [Fig. 4.4.12](#) for Reynolds number $Re = 250, 1250$, for large patch scale ratio $r = 0.1$, going from Square-p2 to Spectral patch scheme the increasing patch coupling accuracy increases the peak artificial instability (red plus to magenta circle). *The only way to remove artificial instability due to large patch scale ratio is to reduce the patch scale ratio to $r \lesssim 0.01$* . But for small patch scale ratio $r \lesssim 0.01$, the trend is opposite, increasing patch coupling accuracy decreases the artificial instability. For example, in the subplots of [Fig. 4.4.12](#) for Reynolds number $Re = 50, 250, 1250$, for small patch scale ratio $r \lesssim 0.01$, going from Square-p2 to Spectral patch scheme the increasing patch coupling accuracy decreases the peak artificial instability (red plus to magenta circle). For the highly accurate Spectral staggered patch scheme there is no artificial instability for small patch scale ratio $r \lesssim 0.01$ in [Fig. 4.4.12](#) for all Reynolds numbers $Re \in \{10, 50, 250, 1250\}$. This effect of decreasing artificial instability with increasing patch coupling accuracy decreases with increasing Reynolds number Re.

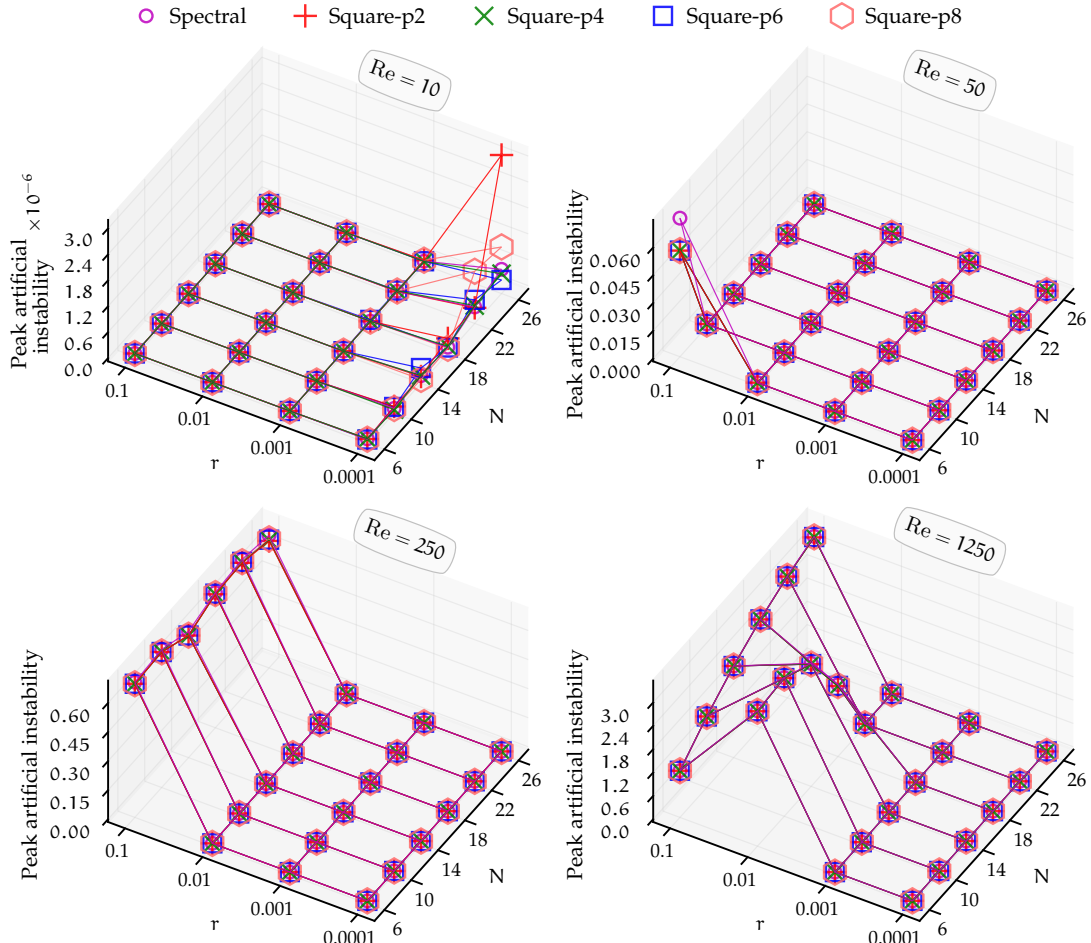
Sufficient number of sub-patch micro-grid intervals n remove the artificial instability of the polynomial patch schemes for small patch scale ratio r and/or large number macro-grid intervals N. For small number of sub-patch micro-grid intervals ([Fig. 4.4.12](#) for $n = 6$), all the polynomial staggered patch schemes have varying degree of artificial instability which increases with increasing N. Sufficient number of sub-patch micro-grid grid intervals, which is $n = 10$ for viscous shallow water flow, removes such artificial instabilities of the polynomial patch schemes. For example, comparing [Figs. 4.4.12](#) and [4.4.13](#) shows that the sufficient number of sub-patch

Figure 4.4.12: Variation of the patch scheme peak ($n = 6$) artificial instability $\max_{h_M, u_M} [\max \Re(\lambda_p^N) - \max \Re(\lambda_{m\delta}^{N+1})]$ (over $h_M \in \{0.1, 0.2, 0.3\}$, $u_M \in \{0.0, 0.4, 0.8\}$), with patch scale ratio r and macro-grid intervals N , for different Reynolds number $Re \in \{10, 50, 250, 1250\}$. Artificial instability increases with increasing N for $n = 6$. Large artificial instability decreases, with increasing accuracy of patch coupling interpolation, and decreasing r .



micro-grid intervals $n = 10$ remove the artificial instability for small patch scale ratio $r \lesssim 0.001$ for all the Reynolds numbers $Re \in \{10, 50, 250, 1250\}$ and macro-grid intervals $N \in \{6, 10, 14, 18, 22, 26\}$ for all the polynomial staggered patch schemes. The maximum peak artificial instabilities in Fig. 4.4.13 for $r \in \{0.0001, 0.001\}$ are $3.1 \cdot 10^{-6}, 3.9 \cdot 10^{-7}, 9.8 \cdot 10^{-8}, 1.5 \cdot 10^{-8}$ corresponding to the Reynolds numbers $Re \in \{10, 50, 250, 1250\}$ respectively, all of which satisfy the condition of no artificial instability (4.4.1) (within a tolerance of 10^{-5}). Thus, sufficient number of sub-patch micro-grid intervals n

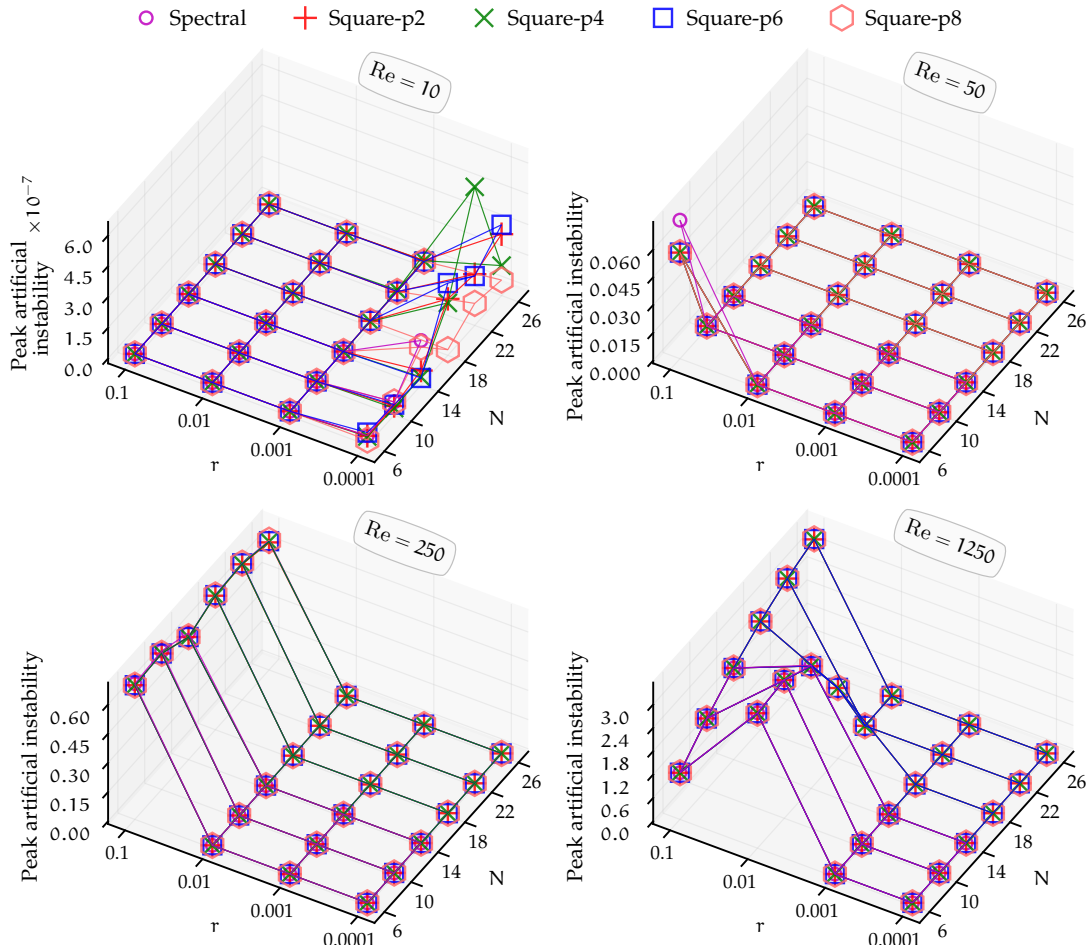
Figure 4.4.13: Variation of the patch scheme ($n = 10$) peak artificial instability $\max_{h_M, u_M} [\max \Re(\lambda_p^N) - \max \Re(\lambda_{m\delta}^{N+1})]$ (over $h_M \in \{0.1, 0.2, 0.3\}$, $u_M \in \{0.0, 0.4, 0.8\}$), with patch scale ratio r and macro-grid intervals N , for different Reynolds number Re . For $r \lesssim 0.01$, except roundoff errors (e.g., $Re = 10$) *artificial instability does not significantly increase with N compared to $n = 6$ in Fig. 4.4.12*. No artificial instability for $r \in \{0.001, 0.0001\}$.



remove the artificial instability of the polynomial patch schemes for small patch scale ratio $r \lesssim 0.001$ and/or large number macro-grid intervals $N \gtrsim 10$. On the other hand, p. 224 of §4.4.1 shows that increasing the number of sub-patch micro-grid intervals n increases the artificial instability of the Spectral patch scheme for large patch scale ratio.

The preceding paragraph shows that the increasing the number of sub-patch micro-grid intervals from $n = 6$ to $n = 10$ removes the artificial instability for small patch scale ratio $r \lesssim 0.001$ and/or large number macro-

Figure 4.4.14: Variation of the patch scheme ($n = 10$) peak artificial instability $\max_{h_M, u_M} [\max \Re(\lambda_p^{NE1}) - \max \Re(\lambda_{m\delta}^{NE1})]$, with patch scale ratio r and macro-grid intervals N , for the same parameters in Fig. 4.4.13 but using analytic eigenvalues λ_p^{NE1} of the patch schemes. Numerical roundoff errors cause the off-trend in artificial instability for small $Re \lesssim 10$ for the combination of small $r \lesssim 0.001$ and large number of macro-grid intervals $N \gtrsim 14$.



grid intervals $N \gtrsim 10$. But any further increase in the number of sub-patch micro-grid intervals $n > 10$ does not remove the remaining artificial instability for large patch scale ratio $r \gtrsim 0.01$ (e.g., the bottom-right subplot in Fig. 4.4.13 for $Re = 1250$). That is increasing $n > 10$ does not have significant influence on the artificial instability. On the other hand, p.XX ([TOSO/xref to page] of §4.7 shows that increasing the number of sub-patch micro-grid intervals n rapidly increases the patch scheme compute time.

In the left-top subplot of Fig. 4.4.13 for $\text{Re} = 10$, the seemingly large and off-trend artificial instability for small patch scale ratio $r \lesssim 0.001$ (i.e., increasing artificial instability with increasing N and increasing patch coupling accuracy) is due to floating point numerical roundoff errors. Figure 4.4.14 shows a plot of variation of the patch scheme ($n = 10$) peak artificial instability $\max_{h_M, u_M} [\max \Re(\lambda_p^{NE1}) - \max \Re(\lambda_{m\delta}^{NE1})]$, with patch scale ratio r and macro-grid intervals N , for the same parameters in Fig. 4.4.13 but using analytic eigenvalues λ_p^{NE1} of the patch schemes. For the Spectral patch scheme, Fig. 4.4.14 includes the analytic eigenvalues λ_p^{NE1} (magenta circles) only for macro-grid intervals $N \in \{6, 10, 14\}$ to avoid numerically evaluating very long analytic expressions. Figure 4.4.14 shows that for small Reynolds number $\text{Re} = 10$ (top-left subplot) the peak artificial instability of analytic eigenvalues λ_p^{NE1} are different from the corresponding artificial instability of numerical eigenvalues λ_p^N .

In many numerical simulations, divergence of a numerical scheme is a common issue for some combinations of the system parameters and discretisation/grid parameters. The patch scheme artificial instability leads to such diverging time solution during ODE integration for numerical simulation. Based on the discussions in the preceding paragraphs, when a patch scheme has artificial instability for some combinations of system and patch grid parameters, a general rule to get rid of artificial instability is to take the following steps (in the order of large to small impact)

1. Decrease patch scale ratio r .
2. Increase the sub-patch micro-grid intervals n to a sufficient value (e.g., $n = 10$). Further increase in n is not beneficial.
3. Increase patch coupling interpolation accuracy, for example choose a higher order polynomial patch scheme.
4. Increase the macro-grid intervals N .

As §4.6 on frame invariance of staggered patch schemes establish, the patch schemes are invariant (within discretisation errors) with different flow angle α for macro-scale waves, where $q = \sqrt{u_M^2 + v_M^2}$, $u_M = q \cos(\alpha)$ and $v_M = q \sin(\alpha)$. Hence, whereas all preceding discussions in this subsection §4.4.3 are based on the five patch schemes over a range of mean height h_M and the mean velocity u_M keeping $v_m = 0$, they also hold for the resultant mean velocity $q = \sqrt{u_M^2 + v_M^2}$ (u_M, v_M) along any orientation. Thus, the five staggered patch schemes are not artificially unstable, for a wide range of patch grid parameters (macro-grid intervals N , sub-patch micro-grid intervals n , and patch scale ratio r).

4.5 Staggered patch schemes are consistent

This section shows that the staggered patch schemes are consistent with the full-domain micro-scale system of viscous shallow water flows, via convergence of the patch scheme eigenvalues. Similar to §3.6 for the general linear wave, subsections of this section establish the consistency of the patch schemes for the viscous shallow water flow by comparing the macro-scale eigenvalues of the patch scheme with the corresponding eigenvalues of the full-domain micro-scale system for increasingly finer patch grids. Section 4.5.1 shows that the Spectral patch scheme is uniformly consistent without any strong dependence on the macro-grid interval Δ . Section 4.5.2 shows that the polynomial patch schemes are consistent to the order of the polynomial interpolation with decreasing macro-grid interval Δ .

The full-domain micro-scale system (4.1.11) is consistent, when the discretized equations (4.1.11) approach to the corresponding PDEs (4.1.6), as the grid interval $\delta \rightarrow 0$ (on the full-domain grid Fig. 4.1.1). Such standard definition of consistency (e.g., Ferziger, Peric, and Street 2020, p. 34) is useful for analysing the full-domain discrete systems whose goal is to accurately represent the corresponding PDEs. But the goal of our multiscale staggered patch scheme (4.1.15) is to accurately represent the *macro-scale* waves of the corresponding *discrete* full-domain micro-scale system (§4.2.2). As defined in §3.6, a staggered patch scheme is consistent, when the macro-scale characteristics of the patch scheme equations (e.g., (4.1.15)) approach to the corresponding macro-scale characteristics of the full-domain micro-scale system (e.g., (4.1.11)), when the macro-grid interval $\Delta \rightarrow 0$ (on the patch grid grid Fig. 2.2.3b).

As in §3.6 for the general linear wave, for the viscous shallow water we show the consistency of the staggered patch schemes by demonstrating that the macro-scale eigenvalues λ_{pM}^N of the patch schemes *converge* to the macro-scale eigenvalues of the corresponding full-domain micro-scale system as $\Delta \rightarrow 0$. The eigenvalue spectra in Figs. 4.2.2 to 4.2.10, show that the staggered patch scheme macro-scale eigenvalues λ_{pM}^{NE1} (e.g., clusters 1, 2, 3, 4, 5 in Fig. 4.2.6) are qualitatively similar, and visually close, to the corresponding macro-scale eigenvalues $\lambda_{m\delta}^A$ of the fine-grid full-domain micro-scale system (by varying degrees depending upon the specific staggered patch scheme, N , n , and r). To numerically quantify the discrepancy between the macro-scale eigenvalues λ_{pM}^N of staggered patch scheme and the corresponding macro-scale eigenvalues $\lambda_{m\delta}^A$ of fine grid full domain micro-scale system, we use the *eigenvalue error* defined in §3.6 for the *macro-*

Table 4.5.1: [Section 4.5](#) studies the consistency of the patch schemes using eigenvalues for all the 8 640 combinations (cartesian product) of the listed parameters.

Patch schemes	Spectral, Square-p2, Square-p4, Square-p6, and Square-p8
Mean height	$h_M \in \{0.1, 0.2, 0.3\}$
Mean velocity	$u_M \in \{0, 0.4, 0.8\}$, $v_M = 0$ (§4.6 on frame invariance show the flow direction is immaterial)
Reynold number	$Re \in \{10, 50, 250, 1250\}$
Macro-grid intervals	$N \in \{6, 10, 14, 18, 22, 26\}$
Sub-patch micro-grid intervals	$n \in \{6, 10\}$
Patch scale ratio	$r \in \{0.0001, 0.001, 0.01, 0.1\}$

scale wavenumber (k_x, k_y) which is

$$\epsilon^{k_x, k_y} = \|\underline{\lambda}_{pM}^N(k_x, k_y) - \underline{\lambda}_{m\delta}^A(k_x, k_y)\| / \|\underline{\lambda}_{m\delta}^A(k_x, k_y)\|, \quad (4.5.1)$$

where $\|\cdot\|$ is the Euclidean norm of the three element complex vectors of eigenvalues $\underline{\lambda}_{pM}^N$ and $\underline{\lambda}_{m\delta}^A$ (three macro-scale eigenvalues for each macro-scale wavenumber).

As in [§3.6](#) for the general linear wave, to assess the patch scheme consistency in this section (i.e., eigenvalue convergence) for the viscous shallow water flow, we compute the three eigenvalue errors $\epsilon^{1,0}$, $\epsilon^{1,1}$ and $\epsilon^{2,1}$, for the patch schemes on different staggered patch grids, corresponding to the three macro-scale (angular) wavenumbers $(k_x, k_y) \in \{(1, 0), (1, 1), (2, 1)\}$ over the $2\pi \times 2\pi$ domain. The smallest wavenumber $(1, 0)$ corresponds to the largest wavelength $(2\pi/L, 0)$ for an $L \times L$ domain. Specifically, to show the consistency of the staggered patch schemes, this section computes the three macro-scale eigenvalue errors $\epsilon^{1,0}$, $\epsilon^{1,1}$ and $\epsilon^{2,1}$ for the 8 640 combinations of the parameters listed in [Table 3.6.1](#).

Computing the three element vector of eigenvalues $\underline{\lambda}_{m\delta}^A(k_x, k_y)$ in the eigenvalue error (4.5.1), is straightforward, we evaluate the analytic expression (3.2.7) to get three eigenvalues for each macro-scale wavenumber $(k_x, k_y) \in \{(1, 0), (1, 1), (2, 1)\}$. Among the numerical eigenvalues λ_p^N , finding which three eigenvalues correspond to the three eigenvalues in $\underline{\lambda}_{m\delta}^A(k_x, k_y)$ (for the same macro-scale wavenumber), is not straightforward. A method we name as the *method of wavenumber-wise scale separation* in [§3.3](#), perform wavenumber-wise classification and separation of micro- and

macro-scale patch scheme eigenvalues. In the method of wavenumber-wise scale separation in §3.3, using the full-domain micro-scale eigenvalues $\lambda_{m\delta}^{NE1}$ in place of the eigenvalues $\lambda_{m\delta}^A$ gives the required eigenvalues as the following 3D arrays (analytic eigenvalues only for $N \leq 14$ for Spectral patch scheme)

1. An $N/2 \times N/2 \times 3$ array of *analytic* eigenvalues $\lambda_{m\delta}^{NE1}$ of the full-domain micro-scale system.
2. An $N/2 \times N/2 \times 3$ array of macro-scale *analytic* patch scheme eigenvalues λ_{pM}^{NE1} .
3. An $N/2 \times N/2 \times 3$ array of macro-scale *numerical* patch scheme eigenvalues λ_{pM}^N .

The third dimension of the arrays in the preceding listing will establish the wavenumber-wise correspondence among the three eigenvalues $\lambda_{m\delta}^{NE1}$, λ_{pM}^{NE1} and λ_{pM}^N . For any macro-scale wavenumber (k_x, k_y) resolved on a patch grid, each of the three elements along the third dimension of the eigenvalues $\lambda_{m\delta}^{NE1}$ and λ_{pM}^N gives required the three element vectors $\underline{\lambda}_{m\delta}^A$ and $\underline{\lambda}_{pM}^N$ in the patch scheme eigenvalue error (4.5.1).

A staggered patch grid with $N \times N$ macro-grid intervals, irrespective of which patch scheme, resolves $3N^2/4$ macro-scale modes (p. 191 of §4.2.6). That is, with increasing macro-grid intervals N , all the patch schemes resolve increasing number of macro-scale modes of increasing wavenumbers. A patch grid with $N = 6$ macro-grid intervals resolves nine macro-scale wavenumbers such that $k_x, k_y \in \{-1, 0, 1\}$. For $N = 6$, since there are no macro-scale eigenvalues with wavenumber $(k_x, k_y) = (2, 1)$, the eigenvalue error $\epsilon^{2,1}$ is computed only for $N > 6$.

4.5.1 Spectral patch scheme is uniformly consistent without any dependence on the macro-grid interval

With the highly accurate global spectral interpolation (§2.3.1), as in §3.6.1 for the general linear wave, we expect the Spectral patch scheme to resolve the macro-scale modes exactly (within numerical roundoff errors), irrespective of the number of macro-grid intervals N (e.g., the spectra in Figs. 4.2.5 and 4.2.6). That is, the Spectral patch scheme is uniformly consistent with the full-domain micro-scale model without any dependence on the macro-grid interval Δ . To confirm this uniform consistency of the Spectral patch scheme, this subsection shows that the accuracy of the macro-scale modes indeed do not deteriorate with decreasing macro-grid

interval Δ (increasing N). Specifically, this subsection studies the eigenvalue errors $\epsilon^{1,0}$, $\epsilon^{1,1}$ and $\epsilon^{2,1}$ of the Spectral patch scheme for all the 1728 combinations of the parameters h_M, u_M, Re, N, n, r listed in [Table 4.5.1](#).

For large Reynolds number $Re \gtrsim 250$, Spectral patch scheme is uniformly consistent without any dependence on the macro-grid interval Δ . [Figure 4.5.1](#) plots the eigenvalue errors $\epsilon^{1,0}$ versus macro-grid intervals Δ for the best case (with smallest errors) of large Reynolds number $Re = 1250$, and mean flow $(h_M, u_M) = (0.1, 0)$ for different patch scale ratio r . [Figure 4.5.1](#) shows that maximum eigenvalue error $\epsilon^{1,0} \approx 8 \cdot 10^{-9}$ for smallest patch scale ratio $r = 0.0001$ and smallest macro-grid interval $\Delta = 2\pi/26$. For larger patch scale ratio $r > 0.0001$, the eigenvalue errors are even smaller. That is, for large Reynolds number $Re \gtrsim 250$, Spectral patch scheme is uniformly consistent without any dependence on the macro-grid interval Δ .

For large Reynolds number $Re \gtrsim 250$, Spectral patch scheme is uniformly consistent over a wide range of the mean flow (h_m, u_M) . For a large Reynolds number $Re = 1250$, for various mean flow (h_M, u_M) , patch scale ratio r , and the number of sub-patch micro-grid intervals n , [Table 4.5.2](#) lists the maximum logarithmic eigenvalue errors $\min_N \log_{10}(\epsilon^{1,0})$ of the Spectral patch scheme over six different number of macro-grid intervals N in [Table 4.5.1](#). [Table 4.5.2](#) shows that for a large Reynolds number $Re = 1250$, the maximum eigenvalue error $\max_{N, h_M, u_M} \epsilon^{1,0} = 10^{-5}$ over the six different number of macro-grid intervals N and nine different mean flows (h_M, u_M) in [Table 4.5.1](#). This small maximum eigenvalue error $\max_{N, h_M, u_M} \epsilon^{1,0}$ shows that for large Reynolds number $Re \gtrsim 250$, Spectral patch scheme is uniformly consistent over a wide range of the mean flow (h_m, u_M) .

For small Reynolds number $Re \lesssim 250$ the seemingly large eigenvalue errors of the Spectral patch scheme is due to numerical roundoff error. [Page 211](#) of [§4.3](#) shows that for small grid interval $\delta \lesssim 10^{-5}$ (i.e., small r and/or small Δ), large mean height $h_M \gtrsim 0.2$ and small Reynolds number $Re \lesssim 10$, the numerically computed patch scheme eigenvalues have non-negligible numerical roundoff errors. Both from the parametric trends of the numerical roundoff errors and from using scaling arguments on the viscous shallow water flow, [§4.3](#) shows that the non-negligible numerical roundoff errors in the patch scheme eigenvalues is due to the inherent sensitivity of the underlying micro-scale model and the numerical computation of near zero repeated eigenvalues. As [§4.3](#) shows, the numerical roundoff errors in the patch scheme eigenvalues are non-negligible only for small Reynolds Re . Yet the onset of the effect of numerical roundoff errors is seen even for large Reynolds number $Re \sim 1250$. For example, in [Fig. 4.5.1](#), for small patch scale ratio $r = 0.0001$ the monotonically increasing eigenvalue error $\epsilon^{1,0}$ (magenta circles) with decreasing macro-grid intervals Δ is due to the numerical

Figure 4.5.1: Reynolds number $\text{Re} = 1250$, $(h_M, u_M) = (0.1, 0)$. Best case eigenvalue errors $\epsilon^{1,0}$ (log scale) of the Spectral staggered patch scheme for different macro-grid intervals Δ and patch scale ratio r (as in Table 4.5.2, for $r = 0.1$, $n = 6$, $\min(\max_N \epsilon^{1,0}) = 10^{-12.3} = 4.6 \cdot 10^{-13}$).

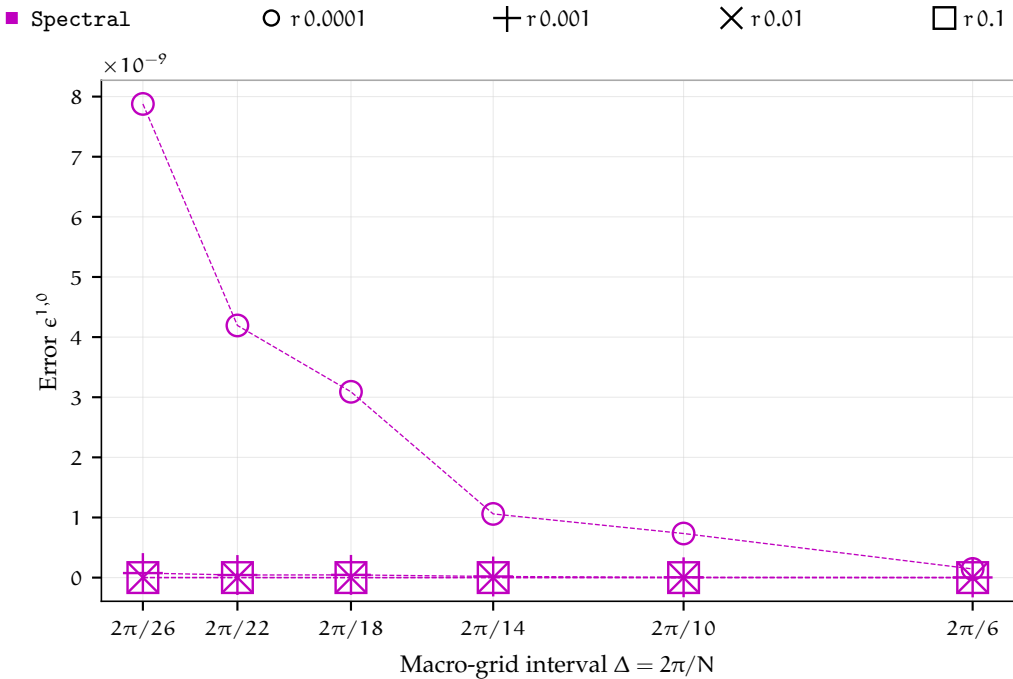


Table 4.5.2: Reynolds number $\text{Re} = 1250$. Maximum logarithmic eigenvalue error $\min_N \log_{10}(\epsilon^{1,0})$ of the Spectral staggered patch scheme over the number of macro-grid intervals N in Table 4.5.1. Grey box highlights smallest value (largest error) in each column. Eigenvalue errors $\epsilon^{1,0} \leq 10^{-5}$. Overall $\min(\max_N \epsilon^{1,0}) = 10^{-12.3}$ for $(h_M, u_M) = (0.1, 0)$, $r = 0.1$, $n = 6$.

h_M, u_M	Patch scale ratio r							
	0.0001		0.001		0.01		0.1	
h_M, u_M	$n = 6$	$n = 10$	$n = 6$	$n = 10$	$n = 6$	$n = 10$	$n = 6$	$n = 10$
0.1, 0	-8.1	-7.5	-10	-9.3	-12	-11	-12	-12
0.1, 0.4	-6.6	-8.3	-8.6	-8.9	-11	-10	-11	-11
0.1, 0.8	-5.5	-7.9	-7.5	-8.5	-9.4	-9.1	-11	-11
0.2, 0	-7.6	-6.9	-9.7	-8.9	-11	-11	-12	-12
0.2, 0.4	-5.7	-7.8	-7.6	-8.3	-9.6	-9.4	-11	-11
0.2, 0.8	-5	-7.8	-7	-8.4	-9	-8.9	-11	-11
0.3, 0	-7.3	-6.7	-9.4	-8.9	-11	-11	-12	-12
0.3, 0.4	-6.2	-7.1	-8.2	-9.2	-10	-10	-12	-12
0.3, 0.8	-5.1	-7.8	-7.2	-8.7	-9.2	-9.2	-11	-11

Figure 4.5.2: Reynolds number $\text{Re} = 10$, $(h_M, u_M) = (0.3, 0)$. Worst case eigenvalue errors $\epsilon^{1,0}$ (log scale) of the Spectral staggered patch scheme for different macro-grid intervals Δ and patch scale ratio r (as in Table 4.5.3, for $r = 0.0001$, $n = 10$, $\max(\max_N \epsilon^{1,0}) = 10^{-2.5} = 0.0034$). [TODO/amend] discrepancy is slightly large for $n=10$ compared to $n=6$, using small δ for small r and many numerical operations in spectral scheme, attribute large errors to roundoff errors.

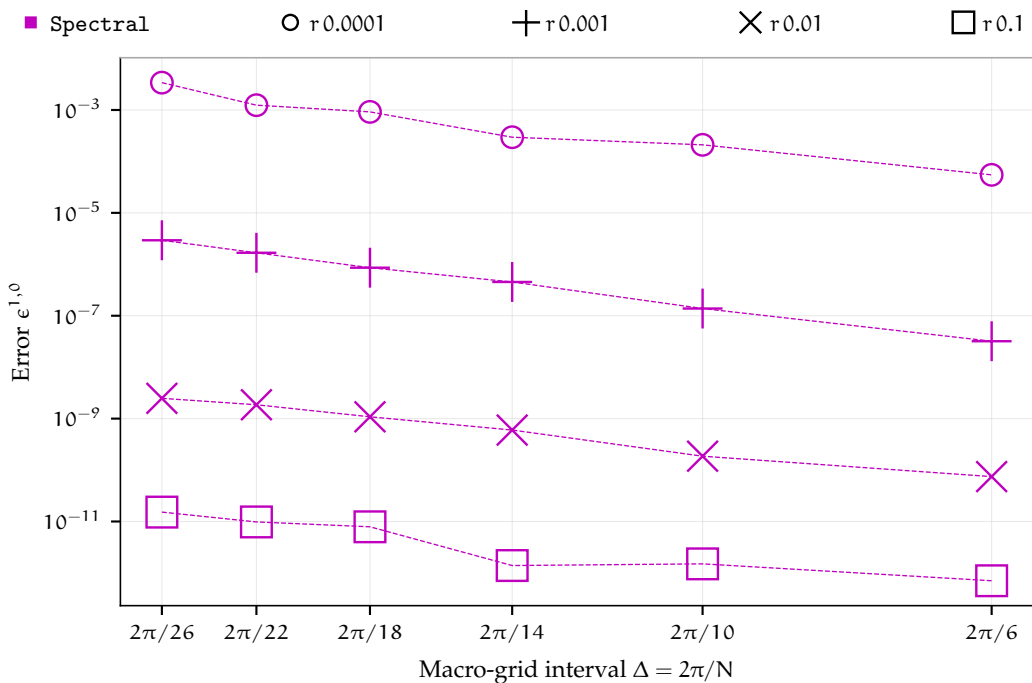


Table 4.5.3: Reynolds number $\text{Re} = 10$. Maximum logarithmic eigenvalue error $\min_N \log_{10}(\epsilon^{1,0})$ for Spectral patch scheme over six different number of macro-grid intervals N in Table 4.5.1. Grey box highlights smallest value (largest error) in each column, red colour highlights $\epsilon^{1,0} > 10^{-5}$. Overall $\max(\max_N \epsilon^{1,0}) = 10^{-2.5}$ for $(h_M, u_M) = (0.3, 0)$, $r = 0.0001$, $n = 10$.

h_M, u_M	Patch scale ratio r							
	0.0001		0.001		0.01		0.1	
	$n = 6$	$n = 10$	$n = 6$	$n = 10$	$n = 6$	$n = 10$	$n = 6$	$n = 10$
0.1, 0	-4.4	-3.6	-7.4	-6.7	-10	-9.6	-12	-11
0.1, 0.4	-4.7	-4.4	-7.1	-7.4	-9.1	-9.5	-9.5	-9.5
0.1, 0.8	-3.5	-4.7	-5.6	-7.8	-7.6	-9.3	-9.4	-9.4
0.2, 0	-3.5	-2.9	-6.6	-5.8	-9.5	-8.8	-11	-11
0.2, 0.4	-3.7	-4.1	-5.6	-6.9	-7.7	-9.7	-9.8	-10
0.2, 0.8	-2.9	-3.9	-4.8	-6.8	-6.9	-9.6	-8.9	-10
0.3, 0	-3	-2.5	-6.3	-5.5	-9.2	-8.6	-11	-11
0.3, 0.4	-3.8	-3.4	-6	-6	-8.3	-9.2	-10	-10
0.3, 0.8	-3	-3	-5	-6.5	-7	-9.4	-9	-10

roundoff errors. Except fluctuating small deviations, [Table 4.5.2](#) shows that in general the maximum eigenvalue error $\max_N \epsilon^{1,0}$ increases with decreasing patch scale ratio r and increasing mean height h_M , which is also due to numerical roundoff error. For small Reynolds number $Re \lesssim 250$ the patch scheme eigenvalues have large numerical roundoff errors. For example, for a small Reynolds number $Re = 10$, [Fig. 4.5.2](#) shows large eigenvalue error $\epsilon^{1,0} = 0.0034$. [Figure 4.5.2](#) and [Table 4.5.3](#) also show that the large eigenvalues errors $\max_N \epsilon^{1,0}$ correspond to small grid interval $\delta \lesssim 10^{-5}$ (i.e., small r and/or small Δ) and large mean height $h_M \gtrsim 0.2$, for which the numerically computed patch scheme eigenvalues have non-negligible numerical roundoff errors ([p. 211](#) of [§4.3](#)). That is, for small Reynolds $Re \lesssim 250$ the seemingly large eigenvalue error $\epsilon^{1,0}$ for the Spectral patch scheme is not reflecting the characteristic of the patch scheme, but an artifact due to numerical roundoff errors in numerically computing the patch scheme eigenvalues.

The preceding paragraph deductively shows along with evidence that the seemingly large Spectral patch scheme eigenvalue errors $\epsilon^{1,0}$ for small Reynolds number are due to numerical roundoff errors. The *arbitrary-precision floating point arithmetic definitively confirm that the seemingly large eigenvalue errors $\epsilon^{1,0}$ for small Reynolds number are indeed due to numerical roundoff errors* in numerical eigenvalue computation. Using the analytic patch scheme eigenvalues λ_{pM}^{NE1} of the numerically evaluated analytic one-cell Jacobian ([§4.2.3](#)) in place of the numerical eigenvalues λ_{pM}^N in the eigenvalue error ([4.5.1](#)), gives about five times smaller eigenvalue error $\epsilon^{1,0}$ compared to the eigenvalue error $\epsilon^{1,0}$ of the numerical patch scheme eigenvalues. For example, in [Fig. 4.5.2](#) for Reynolds number $Re = 10$, mean flow $(h_M, u_M) = (0.3, 0)$ on a patch grid with $N = 10$ macro-grid intervals, $n = 6$ sub-patch micro-grid intervals and patch scale ratio $r = 0.0001$, the error $\epsilon^{1,0} = 7.5 \cdot 10^{-5}$ for numerical eigenvalue λ_{pM}^N , but the error $\epsilon^{1,0} = 1.5 \cdot 10^{-5}$ for the analytic patch scheme eigenvalues λ_{pM}^{NE1} . The analytic eigenvalues λ_{pM}^{NE1} are still computed numerically after evaluating the one-cell Jacobian for specific numeric values of the wavenumber (k_x, k_y) and system parameters Re, h_M, u_M . So, the analytic eigenvalues λ_{pM}^{NE1} too have numerical roundoff errors due to the numerical eigenvalue computation. As a further step to confirm that the seemingly large eigenvalue errors of the Spectral patch scheme is indeed due to numerical roundoff error, we resort to `mpmath`, a Python library for arbitrary-precision floating point arithmetic ([Johansson et al. 2018](#)). Specifically, we evaluate the one-cell analytic Jacobian ([§4.2.3](#)) using the higher precision `mpmath` floating-point number format and compute the eigenvalues using `mpmath`'s arbitrary-precision eigenvalue function. For the case of $N = 10$, $r = 0.0001$

in Fig. 4.5.2 with $\text{Re} = 10$, $(h_M, u_M) = (0.3, 0)$, analytic eigenvalues $\lambda_p^{N \times 1}$ evaluated using mpmath with the precision of 80 decimal places gives the eigenvalue error $\epsilon^{1,0} = 6.8 \cdot 10^{-8}$, compared to the large $\epsilon^{1,0} = 7.5 \cdot 10^{-5}$ of the numerical eigenvalues $\lambda_p^{N \times 1}$ (four orders of magnitude less error). This small eigenvalue error $\epsilon^{1,0}$ of the arbitrary-precision floating point arithmetic definitively confirm that the seemingly large eigenvalue errors $\epsilon^{1,0}$ for small Reynolds number are indeed due to numerical roundoff errors in numerical eigenvalue computation. That is, the accuracy of the Spectral patch scheme eigenvalues do not deteriorate with decreasing macro-grid interval Δ (increasing N).

The preceding paragraphs explore the eigenvalue errors $\max_N \epsilon^{1,0}$ for small and large Reynolds numbers $\text{Re} \in \{10, 1250\}$ (i.e., the worst and best case errors). For various Reynolds number Re , patch scale ratio r , and number of sub-patch micro-grid intervals n , Table 4.5.4 lists the maximum logarithmic eigenvalue error $\min_{N, h_M, u_M} \log_{10}(\epsilon^{1,0})$ of the Spectral patch scheme over six different number of macro-grid intervals N and nine different mean flows (h_M, u_M) in Table 4.5.1. Table 4.5.4 shows the progressively decreasing maximum eigenvalue error $\min_{N, h_M, u_M} \epsilon^{1,0}$ with increasing Reynolds number Re for both $n = 6$ and $n = 10$. Similarly, Tables 4.5.5 and 4.5.6 show the progressively decreasing maximum eigenvalue errors $\min_{N, h_M, u_M} \epsilon^{1,1}$ and $\min_{N, h_M, u_M} \epsilon^{2,1}$ (for wavenumbers $(k_x, k_y) = (1, 1), (2, 1)$) with increasing Reynolds number Re for both $n = 6$ and $n = 10$. Both the magnitudes and the trends of the eigenvalue errors $\epsilon^{1,1}$ and $\epsilon^{2,1}$ are similar to that of the eigenvalues errors $\epsilon^{1,0}$ in Figs. 4.5.1 and 4.5.2 and Tables 4.5.2 and 4.5.3. As the previous paragraphs in this subsection

Table 4.5.4: Maximum logarithmic eigenvalue error $\min_{N, h_M, u_M} \log_{10}(\epsilon^{1,0})$ of the Spectral patch scheme over the number of macro-grid intervals N and mean flows (h_M, u_M) in Table 4.5.1. Grey box highlights smallest value (largest error) in each column, red colour highlights large $\epsilon^{1,0} > 10^{-5}$. Overall $\max \epsilon^{1,0} = 10^{-2.5}$ for $\text{Re} = 10$, $r = 0.0001$, $n = 10$.

	Patch scale ratio r							
	0.0001		0.001		0.01		0.1	
Re	$n = 6$	$n = 10$	$n = 6$	$n = 10$	$n = 6$	$n = 10$	$n = 6$	$n = 10$
10	-2.9	-2.5	-4.8	-5.5	-6.9	-8.6	-8.9	-9.4
50	-3.6	-4.1	-5.6	-7	-7.6	-9.5	-9.5	-9.6
250	-4.3	-5.4	-6.3	-8.4	-8.3	-9.1	-10	-10
1250	-5	-6.7	-7	-8.3	-9	-8.9	-11	-11

Table 4.5.5: Maximum logarithmic eigenvalue error $\min_{N, h_M, u_M} \log_{10}(\epsilon^{1,1})$ of the Spectral patch scheme over the number of macro-grid intervals N and mean flows (h_M, u_M) in [Table 4.5.1](#). Grey box highlights smallest value (largest error) in each column, red colour highlights large $\epsilon^{1,1} > 10^{-5}$. Overall max $\epsilon^{1,1} = 10^{-2.8}$ for $Re = 10, r = 0.0001, n = 10$.

		Patch scale ratio r							
		0.0001		0.001		0.01		0.1	
Re		$n = 6$	$n = 10$	$n = 6$	$n = 10$	$n = 6$	$n = 10$	$n = 6$	$n = 10$
10		-2.8	-2.8	-4.8	-5.7	-6.9	-8.5	-8.9	-9.4
50		-3.7	-4.1	-5.7	-7.2	-7.8	-9.4	-9.7	-9.7
250		-4.5	-5.5	-6.4	-8	-8.5	-9.3	-10	-10
1250		-5.2	-6.9	-7.1	-8.5	-9.2	-9	-11	-11

Table 4.5.6: Maximum logarithmic eigenvalue error $\min_{N, h_M, u_M} \log_{10}(\epsilon^{2,1})$ of the Spectral patch scheme over the number of macro-grid intervals N and mean flows (h_M, u_M) in [Table 4.5.1](#). Grey box highlights smallest value (largest error) in each column, red colour highlights large $\epsilon^{2,1} > 10^{-5}$. Overall max $\epsilon^{2,1} = 10^{-2.7}$ for $Re = 10, r = 0.0001, n = 10$.

		Patch scale ratio r							
		0.0001		0.001		0.01		0.1	
Re		$n = 6$	$n = 10$	$n = 6$	$n = 10$	$n = 6$	$n = 10$	$n = 6$	$n = 10$
10		-3.1	-2.7	-5	-5.7	-7.1	-8.7	-9.1	-9.4
50		-3.9	-4.2	-5.9	-7.1	-7.9	-9.8	-9.8	-9.9
250		-4.6	-5.5	-6.6	-8.4	-8.7	-9.5	-10	-10
1250		-5.3	-7	-7.3	-8.7	-9.4	-9.2	-11	-11

tion show, the seemingly large eigenvalue errors $\epsilon^{1,0}$, $\epsilon^{1,1}$, $\epsilon^{2,1}$ for small Reynolds number $Re \lesssim 250$ are due to numerical roundoff errors in numerical eigenvalue computation, not due to any inaccuracy/deficiency in the Spectral patch scheme. That is, for all the explored Reynolds numbers $Re \in \{10, 50, 250, 1250\}$, the accuracy of the Spectral patch scheme eigenvalues do not deteriorate with decreasing macro-grid interval Δ (increasing N). Hence, *the Spectral patch scheme itself is uniformly consistent with the full-domain micro-scale model without any dependence on the macro-grid interval.*

4.5.2 The four polynomial patch schemes are consistent to the order of the polynomial interpolation

Due to the highly accurate global spectral interpolation (§2.3.1), as §4.5.1 shows, the Spectral patch scheme is uniformly consistent with the full-domain micro-scale model without any dependence on the macro-grid interval. That is, the Spectral patch scheme resolves the macro-scale modes exactly (within numerical roundoff errors), irrespective of the number of macro-grid intervals N (e.g., the matching blue circles and red circles for the spectra in Figs. 4.2.5 and 4.2.6). But as §3.6.2 for the general linear wave shows, the accuracy of the polynomial patch schemes (Square-p2, Square-p4, Square-p6, Square-p8) increase with decreasing macro-grid interval Δ to the same order p as the patch coupling interpolation. This subsection shows that for the viscous shallow water flow the accuracy of the polynomial patch schemes increase with decreasing macro-grid interval Δ to the same order p as the patch coupling interpolation (in other words patch scheme macro-scale eigenvalues converge with decreasing Δ). That is, this subsection shows that for the viscous shallow water flow the polynomial patch schemes are consistent with the full-domain micro-scale model to the same order p as the patch coupling interpolation. Specifically, this subsection shows the consistency of the polynomial patch schemes through the eigenvalue errors $\epsilon^{1,0}$, $\epsilon^{1,1}$ and $\epsilon^{2,1}$ corresponding to macro-scale wavenumbers $(k_x, k_y) = (1, 0), (1, 1), (2, 1)$, for all the 6912 combinations of the parameters h_M, u_M, Re, N, n, r listed in Table 4.5.1.

To establish the consistency of the polynomial patch schemes, this subsection studies the convergence of patch scheme eigenvalue errors with decreasing macro-grid Δ , via convergence plots such as Figs. 4.5.4 and 4.5.3. All the convergence plots also contain a power law curve fit (grey solid lines) for the eigenvalue error of the form $\tilde{\epsilon}^{k_x, k_y} = a(b\Delta)^p$. Each convergence plot, contains an eigenvalue error (e.g., $\epsilon^{1,0}$ in Fig. 4.5.4) for a total

of 96 cases among the 6 912 cases listed in [Table 4.5.1](#): four polynomial patch schemes, one specific number of sub-patch micro-grid intervals n , six macro-grid intervals Δ , four patch scale ratios r , for one set of system parameters (e.g., Re, h_M, u_M). Hence for each eigenvalue error (e.g., $\epsilon^{1,0}$), the total of 6 912 cases listed in [Table 4.5.1](#) lead to 72 convergence plots such as [Fig. 4.5.4](#); the three eigenvalue errors $\epsilon^{1,0}, \epsilon^{1,1}, \epsilon^{2,1}$ lead to a total of 216 convergence plots.

For large Reynolds number $Re \gtrsim 250$ the macro-scale eigenvalues of all the polynomial patch schemes converge to the same order p as the interpolation for the patch coupling. For the eigenvalue error $\epsilon^{1,0}$ of the macro-scale wavenumber $(k_x, k_y) = (1, 0)$, many among the 72 convergence plots (each for different n, Re, h_M, u_M in [Table 4.5.1](#)) show good convergence, where the eigenvalue error $\epsilon^{1,0}$ closely follows the power law curve fit (grey solid lines). That is, the eigenvalue errors $\epsilon^{1,0} \approx a(b\Delta)^p$, where p is the interpolation order of the polynomial patch scheme (e.g., $p = 4$ for the patch scheme Square-p4). For example, for one of the best case convergence of the eigenvalue error $\epsilon^{1,0}$ for Reynolds number $Re = 1250$, mean flow $(h_M, u_M) = (0.2, 0)$ over a patch grid with $n = 6$ sub-patch micro-grid intervals, the convergence plot is visually identical to [Fig. 3.6.4](#) of [§3.6.2](#) for the general linear wave, but with different coefficients $a = 0.66$, $b = 0.66$ in the power law curve fit (i.e., $\epsilon^{1,0} \approx 0.66 \cdot (0.66 \cdot \Delta)^p$). As with the general linear wave, also for the viscous shallow water flow, the best case convergence plots of the eigenvalue error $\epsilon^{1,1}$ are identical to the best case convergence plots of the eigenvalue errors $\epsilon^{1,0}$ both visually and quantitatively. The best case convergence plots of the eigenvalue error $\epsilon^{2,1}$ for the viscous shallow water flow, are visually identical to [Fig. 3.6.8](#) of [§3.6.2](#) for the general linear wave, but with different coefficients in the power law curve fit. Hence, for brevity we omit such best case convergence plots throughout this subsection. For the general linear wave in [§3.6.2](#) the coefficients a, b in the power law curve fit are the same for different system parameters c_D, c_V . But for the nonlinear viscous shallow water flow, the coefficients a, b in the power law curve fit are different for different system parameters Re, h_M, v_M .

Except the numerical roundoff errors for small patch scale ratio, *also for small Reynolds number $Re \lesssim 250$ the macro-scale eigenvalues of all the polynomial patch schemes converge to the same order p as the interpolation for the patch coupling.* [Figure 4.5.3](#) shows the worst case convergence of the eigenvalue error $\epsilon^{1,0}$ among the 72 convergence plots (each for different n, Re, h_M, u_M in [Table 4.5.1](#)), for the small Reynolds number $Re = 10$, mean flow $(h_M, u_M) = (0.3, 0)$ over a patch grid with $n = 10$ sub-patch micro-grid intervals. In [Fig. 4.5.3](#), except the numerical roundoff errors for higher order patch schemes with $p \geq 4$ and small patch scale ratio $r \leq 0.01$ (green, blue

Figure 4.5.3: Reynolds number $Re = 10$, $(h_M, u_M) = (0.3, 0)$, $n = 10$. Worst case convergence of $\epsilon^{1,0}$ (log scale) with macro-grid interval Δ , for polynomial patch schemes with interpolation orders $p \in \{2, 4, 6, 8\}$ and different patch scale ratio r . Except numerical roundoff errors for $p \geq 4, r \leq 0.001$, $\epsilon^{1,0}$ converge with power law curve fit $\tilde{\epsilon}^{1,0} = 0.66 \cdot (0.66 \cdot \Delta)^p$ (grey solid lines). [TODO/amend] discrepancy is large for $n=10$ compared to $n=6$

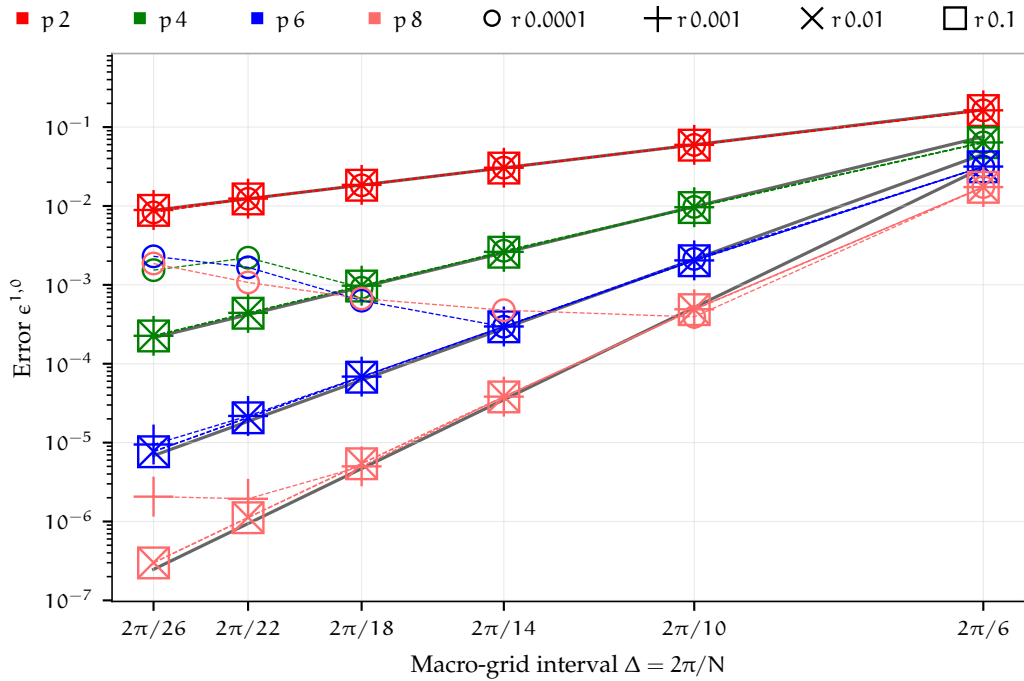
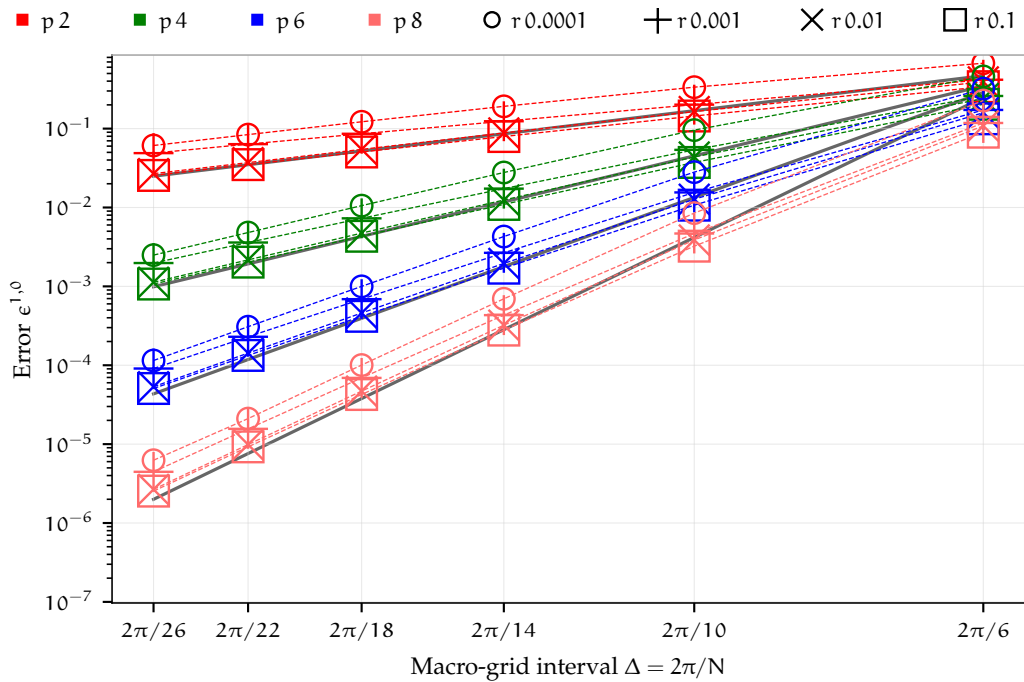


Figure 4.5.4: Reynolds number $Re = 1250$, $(h_M, u_M) = (0.2, 0.4)$, $n = 6$. For small $r \lesssim 0.001$, convergence of $\epsilon^{1,0}$ deteriorates for all macro-grid interval Δ due to numerical roundoff error [TODO/correct] wrong! discrepancy disappears for $n=10$, for all polynomial patch schemes with interpolation orders $p \in \{2, 4, 6, 8\}$. Convergence deterioration is only via coefficients in the power law $\epsilon^{1,0} \approx 0.83 \cdot (0.82 \cdot \Delta)^p$.



and light red circles), the eigenvalue error $\epsilon^{1,0}$ of all the polynomial patch schemes converge to the same order p as the patch coupling interpolation. That is, except for $p \geq 4, r \leq 0.01$, eigenvalues converge as $\epsilon^{1,0} \approx 0.66 \cdot (0.66 \cdot \Delta)^p$. As in §4.5.1 for the Spectral patch scheme, the seemingly large deterioration of the eigenvalue convergence in Fig. 4.5.3, for higher order patch schemes with $p \geq 4$ and small patch scale ratio $r \leq 0.01$ is due to numerical roundoff errors for the small Reynolds number $Re = 10$; §4.3 shows the detailed trends of the numerical roundoff errors in the patch scheme eigenvalues. Hence, as for large Reynolds numbers, also for small Reynolds number $Re \lesssim 250$ the macro-scale eigenvalues of all the polynomial patch schemes converge to the same order p as the patch coupling interpolation.

TODO/amend this discrepancy disappears for n=10, maybe not numerical roundoff error For large Reynolds number $Re \gtrsim 250$, the numerical roundoff errors for small patch scale ratio $r \lesssim 0.001$ do not affect the order of convergence. Figure 4.5.3 shows that for small Reynolds number $Re = 10$, for higher order patch schemes with $p \geq 4$ and small patch scale ratio $r \leq 0.01$, the eigenvalue convergence deteriorates only for small $\Delta \lesssim 2\pi/14$ due to numerical roundoff error. On the other hand, Fig. 4.5.4 shows that for large Reynolds number $Re = 1250$, and $u_M = 0.2$, for all the polynomial patch schemes with small patch scale ratio $r \leq 0.01$, the eigenvalue convergence deteriorates for all macro-grid interval Δ , which is also due to numerical roundoff error. But, unlike for the small Reynolds number $Re = 10$ in Fig. 4.5.3, Fig. 4.5.4 shows that for large Reynolds number $Re = 1250$ the eigenvalue convergence deterioration is only via the coefficients a, b in the power law $\epsilon^{1,0} \approx a(b)^p$. This trend of eigenvalue convergence deterioration via coefficients a, b in the power law due to numerical roundoff errors, also extend to other large Reynolds number $Re \gtrsim 250$. That is, for large Reynolds number $Re \gtrsim 250$, the numerical roundoff errors for small patch scale ratio $r \lesssim 0.01$ do not affect the order of convergence.

All the qualitative characteristics of the preceding paragraphs in this subsection about the convergence of eigenvalue error $\epsilon^{1,0}$ and the numerical roundoff errors, also hold for the eigenvalue errors $\epsilon^{1,1}$ and $\epsilon^{2,1}$. For example, Figs. 4.5.5 and 4.5.6 show the worst case convergence of the eigenvalue errors $\epsilon^{1,1}$ and $\epsilon^{2,1}$ respectively. A patch grid with 6×6 macro-grid intervals resolves only the nine macro-scale wavenumber $(k_x, k_y) : k_x, k_y = -1, 0, 1$, hence there are no data points of $\epsilon^{2,1}$ for $\Delta = 2\pi/6$ in Fig. 4.5.6. As in Fig. 4.5.3 for the eigenvalue error $\epsilon^{1,0}$, the seemingly large deterioration of the eigenvalue convergence of $\epsilon^{1,1}$ and $\epsilon^{2,1}$ in Figs. 4.5.5 and 4.5.6, for higher order patch schemes with $p \geq 4$ and small patch scale ratio $r \leq 0.01$ is due to numerical roundoff errors for the small Reynolds

Figure 4.5.5: Reynolds number $Re = 10$, $(h_M, u_M) = (0.3, 0)$, $n = 10$. Worst case convergence of $\epsilon^{1,1}$ (log scale) with macro-grid interval Δ , for polynomial patch schemes with interpolation orders $p \in \{2, 4, 6, 8\}$ and different patch scale ratio r . Except numerical roundoff errors for $p \geq 4, r \leq 0.001$, $\epsilon^{1,1}$ converge with power law curve fit $\tilde{\epsilon}^{1,1} = 0.65 \cdot (0.65 \cdot \Delta)^p$ (grey solid lines).

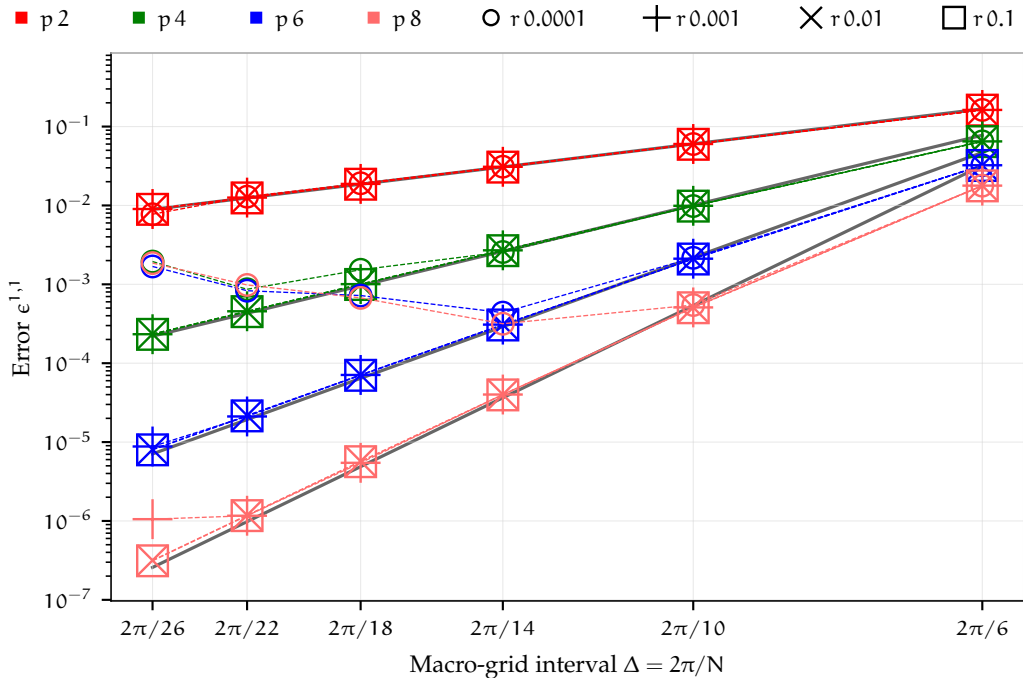
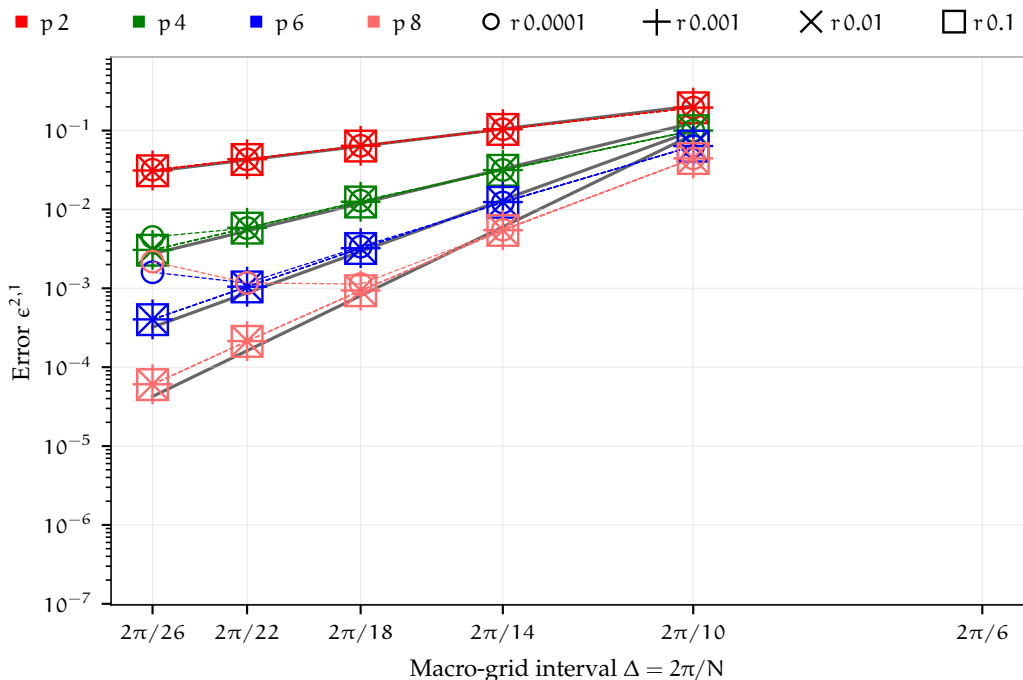


Figure 4.5.6: Reynolds number $Re = 10$, $(h_M, u_M) = (0.3, 0)$, $n = 10$. Worst case convergence of $\epsilon^{2,1}$ (log scale) with macro-grid interval Δ , for polynomial patch schemes with interpolation orders $p \in \{2, 4, 6, 8\}$ and different patch scale ratio r . Except numerical roundoff errors for $p \geq 4, r \leq 0.001$, $\epsilon^{2,1}$ converge with power law curve fit $\tilde{\epsilon}^{2,1} = 0.64 \cdot (1.2 \cdot \Delta)^p$ (grey solid lines).



number $\text{Re} = 10$; §4.3 shows the detailed trends of the numerical roundoff errors in the patch scheme eigenvalues. Hence, as the macro-scale eigenvalue of wavenumber $(k_x, k_y) = (1, 0)$, also the macro-scale eigenvalues of macro-scale wavenumbers $(k_x, k_y) = (1, 1), (2, 1)$ of all the polynomial patch schemes converge to the same order p as the patch coupling interpolation.

Except the numerical roundoff errors, the following listing gives two global trends about the dependence of the eigenvalue errors $\epsilon^{1,0}$, $\epsilon^{1,1}$ and $\epsilon^{2,1}$ on the mean height h_M and mean velocity u_M . The following points hold for all the macro-grid interval Δ , for all the patch scale ratio r and for the patch schemes of all interpolation order p .

1. For any fixed Reynolds number Re and any fixed mean height h_M , increasing the mean velocity u_M increases the eigenvalue errors monotonically. That is, all the points in a convergence plot move up retaining the same order of convergence and slight changes to the coefficients of the power law. These increasing errors are still within worst convergence shown in Figs. 4.5.3, 4.5.5 and 4.5.6 for the eigenvalue errors $\epsilon^{1,0}$, $\epsilon^{1,1}$ and $\epsilon^{2,1}$ respectively. This dependence of eigenvalue errors on mean velocity u_M remains the same for all mean height $h_M \in \{0.1, 0.2, 0.3\}$, and all Reynolds numbers $\text{Re} \in \{10, 50, 250, 1250\}$.
2. For a fixed small Reynolds number $\text{Re} \lesssim 250$ and any fixed mean velocity u_M , increasing the mean height h_M increases the eigenvalue errors up to about $h_M = 0.4$ and then decreases. That is, all the points in a convergence plot move up retaining the same order of convergence and slight changes to the coefficients of the power law. These increasing errors are still within worst convergence shown in Figs. 4.5.3, 4.5.5 and 4.5.6 for the eigenvalue errors $\epsilon^{1,0}$, $\epsilon^{1,1}$ and $\epsilon^{2,1}$ respectively. This dependence of eigenvalue errors on mean height h_M decreases with increasing mean velocity $u_M \in \{0, 0.4, 0.8\}$, and is negligible for large Reynolds number $\text{Re} \gtrsim 250$.

As the preceding listing explains, the change in the eigenvalue errors with increasing h_M , u_M retain the same order of convergence p with macro-grid interval Δ as the order p of the patch coupling interpolation. Thus, for the viscous shallow water flow all the *four polynomial patch schemes are consistent with the full-domain micro-scale model to the same order p as the patch coupling interpolation*, and with *the same order of convergence p for all the system parameters Re, h_M, v_M* .

4.6 Staggered patch schemes are frame invariant

Almost all the key studies in this chapter are performed for a range of parameters but keeping the horizontal mean velocity $v_M = 0$. That is, most results in this chapter correspond to flow angle $\alpha = \arctan(v_M/u_M) = 0$ for the resultant mean velocity $q = \sqrt{u_M^2 + v_M^2}$ of the macro-scale waves, where the velocities are $u_M = q \cos(\alpha)$ and $v_M = q \sin(\alpha)$. For example, the following portions in this chapter are based on the results for mean velocity $v_M = 0$, that is the horizontal flow angle $\alpha = \arctan(v_M/u_M) = 0$, with the assumption that the staggered patch schemes are frame invariant (i.e., the flow direction is immaterial).

- [Section 4.2.6](#) shows that the staggered patch schemes are accurate showing the results for $\alpha = 0$.
- [Section 4.3](#) shows that the patch schemes are not sensitive to numerical roundoff errors based on a study over a range of velocities, but all with $v_M = 0$, that is with $\alpha = 0$.
- [Section 4.4](#) establish that the staggered patch schemes are not artificially unstable showing the results over a range of velocities all with $\alpha = 0$.
- [Section 4.5](#) establish the consistency of the staggered patch scheme showing the results for different velocities all with $\alpha = 0$.

This section validates that assumption, by showing that the variation of the patch scheme eigenvalue errors are negligible with varying flow angles α , or equivalently for varying coordinate frame orientation.

To establish that the patch schemes are invariant (within discretisation errors) with flow angle $\alpha = \arctan(v_M/u_M)$ for the resultant mean velocity $q = \sqrt{u_M^2 + v_M^2}$ of the macro-scale waves, this subsection shows that the eigenvalue errors $\epsilon^{1,0}$, $\epsilon^{1,1}$, and $\epsilon^{2,1}$ are small for all the flow angles $\alpha \in \{0, 10, 20, \dots, 360\}$ in degree.

Patch scheme eigenvalue errors are small irrespective of the flow angles α and the magnitude of velocity q . For Spectral and Square-p8 patch schemes, [Figs. 4.6.1](#) and [4.6.2](#) plot the variation of the eigenvalue error $\epsilon^{1,0}$ with the flow angle α , for different magnitudes $q = \sqrt{u_M^2 + v_M^2}$ of mean velocity. In [Figs. 4.6.1](#) and [4.6.2](#), the patch schemes use $N = 22$ macro-grid intervals, $n = 6$ sub-patch micro-grid intervals, and the patch scale ratio $r = 0.001$, for Reynolds number $Re = 250$ and mean height $h_M = 0.2$. [Figures 4.6.1](#) and [4.6.2](#) show that the eigenvalue error $\epsilon^{1,0}$ are small irrespective of the flow angles $\alpha \in \{0, 10, 20, \dots, 360\}$ and the magnitude of horizontal

Figure 4.6.1: Variation of Spectral patch scheme eigenvalue error $\epsilon^{1,0}$ with flow angle α for different magnitudes $q = \sqrt{u_M^2 + v_M^2}$ of mean velocity. Grid parameters are $N = 22$ macro-grid intervals, $n = 6$ sub-patch micro-grid intervals, patch scale ratio $r = 0.001$. System parameters are Reynolds number $Re = 250$, mean height $h_M = 0.2$.

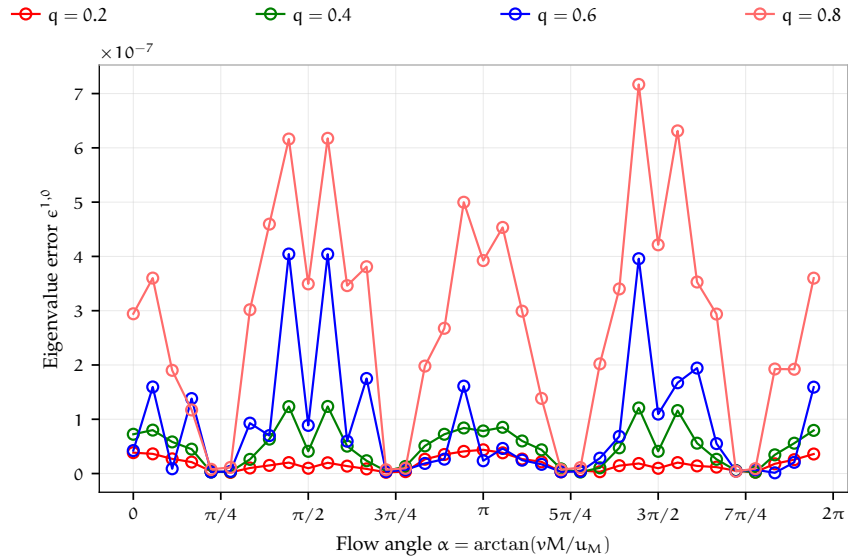
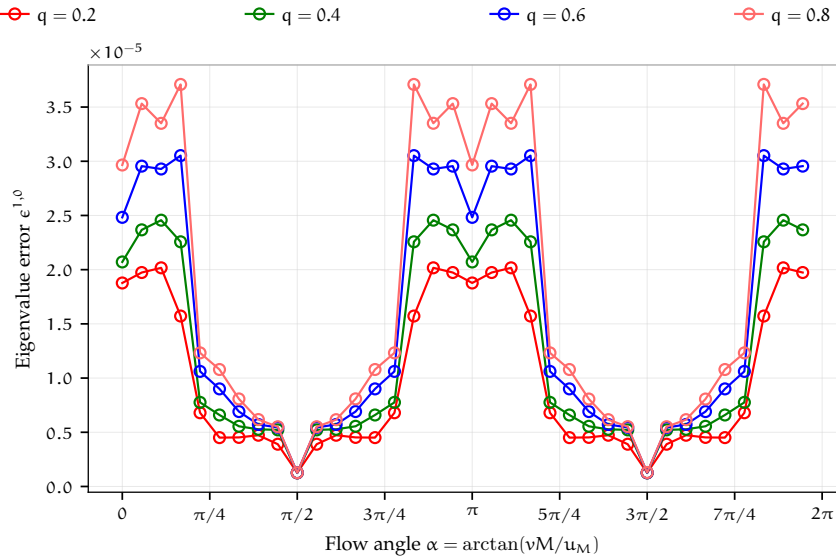


Figure 4.6.2: Variation of Square-p8 patch scheme eigenvalue error $\epsilon^{1,0}$ with flow angle α for different magnitudes $q = \sqrt{u_M^2 + v_M^2}$ of mean velocity for the same grid and system parameters in Fig. 4.6.1.



velocity $q = \sqrt{u_M^2 + v_M^2} \in \{0.2, 0.4, 0.6, 0.8\}$; specifically, $\epsilon^{1,0} < 8 \cdot 10^{-7}$ for the Spectral and $\epsilon^{1,0} < 4 \cdot 10^{-5}$ for the Square-p8 patch schemes.

Variation of the patch scheme eigenvalue errors with the flow angle α is negligibly small. As Figs. 4.6.1 and 4.6.2 show, the variation of the eigenvalue error $\epsilon^{1,0}$ is small; specifically the eigenvalue error $\epsilon^{1,0}$ is within the same order of magnitude. As the previous paragraph explains, the magnitude of the error itself is small, so this small variation of the eigenvalue errors with the flow angle is negligible. This trend of negligibly small variation of the patch scheme eigenvalue error also holds for the eigenvalue errors $\epsilon^{1,1}$ and $\epsilon^{2,1}$, and also for other patch grid parameters (N, n, r). In general, depending upon the specific patch scheme and the grid parameters, the patch scheme eigenvalue errors vary. Yet, this trend of negligible variation of the patch scheme eigenvalue errors hold for all the five staggered patch schemes (Spectral, Square-p2, Square-p4, Square-p6, Square-p8) irrespective of the patch grid parameters.

The small variation of the patch scheme eigenvalue errors with the flow angle α is due to discretisation error, not a deficiency of the patch schemes. Any discrete grid including that of the full-domain system and a patch scheme, introduces non-isotropy for any discrete numerical simulations, especially in cartesian coordinates. This non-isotropy due to discretisation error leads to small changes in the solution with a change in orientation of flow features (e.g., a wave in some direction), or equivalently the orientation of the coordinate frame. Thus, the small variation of the patch scheme eigenvalue errors with the flow angle α (e.g., in Figs. 4.6.1 and 4.6.2), is mainly due to the discretisation error, not a deficiency of the patch schemes.

The previous three paragraphs in this section establish the following three points respectively.

1. Patch scheme eigenvalue errors are small irrespective of the flow angles α and the magnitude of velocity q .
2. Variation of the patch scheme eigenvalue errors with the flow angle α is negligibly small.
3. The small variation of the patch scheme eigenvalue errors with the flow angle α is due to discretisation error, not a deficiency of the patch schemes.

These points together establish that any change in the patch scheme solution with a change in orientation of flow features (e.g., a wave in some direction), or equivalently the orientation of the coordinate frame, is not due to the patch scheme. Thus, *the staggered patch schemes are frame invariant*.

4.7 Large computational savings in patch scheme time simulation

Following very closely §3.7 for the general linear wave, this section quantifies and demonstrates the large computational savings of the staggered patch schemes for the viscous shallow water flow. Section 4.7.1 shows the computational savings of the 2D staggered patch schemes theoretically in terms of the ratio of the space over which the patch schemes and the full-domain system computes. Section 4.7.1 shows the computational savings of the patch schemes in terms of the ratio of the number of state variables for which the patch schemes and the full-domain system computes. Section 4.7.2 demonstrates the computational savings of the 2D staggered patch schemes by measuring the actual time taken to compute the time derivative of the state vector (one time iteration) using a specific implementation. Section 4.7.4 demonstrates the accuracy and the effectiveness of the staggered patch schemes by numerically simulating a localised nearly discontinuous macro-scale viscous roll waves (e.g., Balmforth and Mandre 2004) emerging from the initial condition of a simple progressive wave within the small sparsely located patches. Section 4.7.5 establishes the accuracy of the staggered patch scheme simulations more quantitatively and explain some subtle details of the practical issues in the patch scheme simulations.

4.7.1 Staggered patch schemes compute only for a small number of dynamical state variables over small space

As for the general linear wave, also for the viscous shallow water flow, *the staggered patch schemes compute only within a small fraction of the space in the full domain*. Section 3.7.1 for the general linear wave shows that for a small patch scale ratio $r = l/(2\Delta)$, the 2D staggered patch schemes compute only within a small fraction $3r^2$ of the area in the full domain. As all the discussions in §3.7.1 are based on only the area over which computations are performed (i.e., disregarding the specific number of discrete nodes), all the discussions in §3.7.1 also hold for the viscous shallow water flow. That is, the total area of the simulated space in a patch scheme is $3r^2L^2$ whereas the corresponding total area of the simulated space in a fine-grid full-domain micro-scale system is L^2 . For example, for $r = 0.1, 0.01, 0.001, 0.0001$, the staggered patch schemes compute over the fraction of area $0.03, 3 \cdot 10^{-4}, 3 \cdot 10^{-6}, 3 \cdot 10^{-8}$ respectively. Similar 3D staggered patch schemes compute only within a small fraction $3r^3$ of the volume in the full domain,

where the computational saving is much more. Thus, for the viscous shallow water flow, the staggered patch schemes compute only within a small fraction of the space in the full domain.

The *staggered patch schemes compute only for a small number of dynamical state variables* compared to the corresponding fine-grid full-domain micro-scale system with the same grid interval as the sub-patch micro-grid interval δ . The preceding paragraph shows that 2D staggered patch schemes compute only within a small fraction $3r^2$ of the space in the full domain, which is a rough indication of the computational savings of the staggered patch schemes. This paragraph discusses the computational savings of the staggered patch schemes, more concretely in terms of the number of the dynamical state variables of the 2D staggered patch schemes and that of the corresponding fine-grid full-domain micro-scale system. As in §4.1.2, for viscous shallow water flow micro-scale system (4.1.15), a staggered patch grid requires two layers of edge nodes in the normal direction to the edges, and one layer of edge nodes in the tangential direction to the edges, as in Fig. 4.1.2b. Yet the patch grid in Fig. 4.1.2a for the general linear wave and the patch grid in Fig. 4.1.2b for the viscous shallow water flow have the same number of patch interior nodes (the filled circles), $n_p^I = (N^2/4)(9n^2/4 - 4n + 2)$, which is same as the number of state variables (p. 18 of §2.2.2). Hence, all the discussions in §3.7.2 for the general linear wave also hold for the viscous shallow water flow. Specifically, the ratio of the number of state variables of the staggered patch scheme to that of the fine-grid full-domain micro-scale system (same as the expression (3.7.1) of §3.7.2),

$$n_p^I/n_{m\delta}^I = 3r^2 \left(1 - \frac{16}{9n} + \frac{8}{9n^2} \right). \quad (4.7.1)$$

With increasing n , the ratio $n_p^I/n_{m\delta}^I$ tends to $3r^2$, which is the same fraction of the space derived in §3.7.1 over which the patch schemes compute. For example, for $n = 6, 10, 14$ sub-patch micro-grid intervals with a fixed patch scale ratio $r = 0.1$, the ratio $n_p^I/n_{m\delta}^I = 0.022, 0.025, 0.026$ respectively. For $r = 0.1, 0.01, 0.001, 0.0001$ with a fixed $n = 6$, the ratio of number of nodes $n_p^I/n_{m\delta}^I = 0.022, 2.2 \cdot 10^{-4}, 2.2 \cdot 10^{-6}, 2.2 \cdot 10^{-8}$ respectively. Thus, the *staggered patch schemes compute only for a small number of dynamical state variables* compared to the corresponding fine-grid full-domain micro-scale system with the same grid interval as the sub-patch micro-grid interval δ .

4.7.2 Computational complexity of the staggered patch schemes

As §3.7.3 for the general linear wave, for viscous shallow water flow this subsection compares the compute times of the staggered patch schemes and that of the full-domain micro-scale system. As in §3.7.3, to simplify and keep the smaller uncertainties aside, for the patch schemes and the full-domain micro-scale system this subsection assumes a similar level of vectorisation, and a similar pattern of cache and memory access.

Let the average compute time for computing the time derivative of one state variable is T_M for the fine-grid full-domain micro-scale system. As in §3.7.3, we call T_M , the *model compute time* per interior node. There are $n_{m\delta}^I = 3N^2n^2/(16r^2)$ state variables in the fine-grid full-domain micro-scale system. Hence, the total compute time for computing the time derivative of the state vector (i.e., the compute time for one iteration in time simulation),

$$T_{m\delta} = n_{m\delta}^I T_M = 3N^2n^2 T_M/(16r^2), \quad (4.7.2)$$

which is same as the expression (3.7.2) of §3.7.3 for the general linear wave.

The compute time T_p for computing the time derivative of the state vector dx^I/dt in the patch system (4.1.18) has two components: time for computing the patch coupling; and time for computing the node values using the micro-scale system.

- Let the average compute time for computing one patch edge node from the patch coupling is T_C . As in §3.7.3, we call T_C , the *coupling compute time* per edge node. There are $n_p^E = (N^2/4)(18n + 16)$ edge nodes (expression (4.1.17) in p. 165 of §4.1.2) in the staggered patch grid of Fig. 4.1.2b for the viscous shallow water flow. Hence, the total compute time for computing the patch edge vector x^E in the patch system (4.1.18) (i.e., the patch coupling compute time for one iteration in time simulation) is $n_p^E T_C = (N^2/4)(18n + 16) T_C$ (different from that of the general linear wave in p. 130 of §3.7.3).
- Using the same micro-scale system within the patches as that of the full-domain micro-scale system costs the same average compute time T_M for computing the time derivative of one state variable of patch scheme. There are $n_p^I = (N^2/4)(9n^2/4 - 4n + 2)$ state variables in the staggered patch scheme (expression (4.1.16) in p. 164 of §4.1.2). Hence, using the known values of the patch edge nodes x^E and the patch interior nodes x^I , the compute time for computing the time derivative of the state vector dx^I/dt in the patch system (4.1.18) is

$$n_p^I T_M = (N^2/4)(9n^2/4 - 4n + 2) T_M \text{ (same as that of the general linear wave in p. 130 of §3.7.3).}$$

Thus, the total compute time for computing the time derivative of the state vector dx^I/dt in the patch system (4.1.18),

$$T_p = n_p^E T_C + n_p^I T_M = (N^2/4)(18n + 16) T_C + (N^2/4)(9n^2/4 - 4n + 2) T_M. \quad (4.7.3)$$

The ratio of the compute time for computing the time derivative of the state vector of a patch scheme (4.7.3) to that of the fine-grid ful-domain micro-scale system (4.7.2),

$$T_p/T_{m\delta} = (n_p^E T_C + n_p^I T_M)/(n_{m\delta}^I T_M) = (n_p^E/n_{m\delta}^I) (T_C/T_M) + n_p^I/n_{m\delta}^I. \quad (4.7.4)$$

From the expressions for the number of state variables in a fine-grid full-domain micro-scale system $n_{m\delta}^I = 3N^2n^2/(16r^2)$ and the number of patch edge nodes $n_p^E = (N^2/4)(18n + 16)$, the ratio

$$n_p^E/n_{m\delta}^I = 24r^2/n + 64r^2/(3n^2). \quad (4.7.5)$$

Due to the larger number of edge nodes in the patch grid for the viscous shallow water flow (Fig. 4.1.2b) compared to the general linear wave (Fig. 4.1.2a), the expression (4.7.5) has $+ 64r^2/(3n^2)$ as opposed to $- 64r^2/(3n^2)$ in the corresponding expression (3.7.5) of $n_p^E/n_{m\delta}^I$ for the general linear wave (p. 130 of §4.1.2). Using the expressions (4.7.1) and (4.7.5), the ratio of compute time for computing the time derivative of the state vector of a patch scheme to that of the fine-grid ful-domain micro-scale system (i.e., the compute time ratio for one iteration in time simulation) is

$$T_p/T_{m\delta} = (T_C/T_M) \left(\frac{24r^2}{n} + \frac{64r^2}{3n^2} \right) + 3r^2 \left(1 - \frac{16}{9n} + \frac{8}{9n^2} \right). \quad (4.7.6)$$

The expression (4.7.6) has $+ 64r^2/(3n^2)$ as opposed to $- 64r^2/(3n^2)$ in the corresponding expression (3.7.6) of $T_p/T_{m\delta}$ for the general linear wave (p. 130 of §4.1.2).

The compute time ratio (4.7.6) for one iteration in time simulation, describes the computational cost savings of the staggered patch schemes. The ratio T_C/T_M of coupling compute time to model compute time, in the compute time ratio (4.7.6), encapsulates the following:

1. the details of the specific patch scheme (Spectral or polynomial patch scheme, interpolation order p of the polynomial patch scheme, etc.);

- the details of the specific implementation (specific algorithmic choices, data structures, serial or parallel computations, etc.).

In general, for modelling any reasonably complex physical process (e.g., non-hydrostatic nonlinear waves, sediment transport, etc), the model compute time per interior node T_M is greater than the coupling compute time per edge node T_C , with $T_C/T_M \lesssim 1$. Hence, substituting $T_C/T_M = 1$ into the compute time ratio (4.7.6) gives a rough indication of the possible computational cost savings of the staggered patch schemes as

$$T_p/T_{m\delta} \lesssim 3r^2 + \frac{56r^2}{3n} + \frac{24r^2}{n^2}. \quad (4.7.7)$$

The expression (4.7.7) has $+ 24r^2/(n^2)$ as opposed to $- 36r^2/(3n^2)$ in the corresponding expression (3.7.7) for the general linear wave (p. 131 of §4.1.2).

4.7.3 Staggered patch schemes simulate macro-scale waves with small compute time

Section 4.7.1 shows the computational savings of the 2D staggered patch schemes theoretically in terms of the ratio of the space and the ratio of the number of state variables respectively. As in §3.7.4 for the general linear wave, this section shows the computational savings of the 2D staggered patch schemes by measuring the actual time taken to compute the time derivative of the state vector (one time iteration) using a specific implementation in Julia programming language.

As in §3.7.4, this subsection measures the compute time ratio $T_p/T_{m\delta}$ for a specific implementation and compares with the expression (4.7.6) by empirically estimating the model compute time per interior node T_M and the coupling compute time per edge node T_C . As in §3.7.4, the compute times in this subsection are measured on a custom assembled liquid-cooled workstation with Intel i7-6900k processor and 64GB DDR4 RAM. Both the full-domain micro-scale system and the patch schemes are implemented as serial programs.

Figure 4.7.1 plots the measured compute time $T_{m\delta}$ of the fine-grid full-domain micro-scale system (4.1.11) (p. 160 of §4.1.2), for computing the time derivative of the state vector (i.e., the compute time for one iteration in time simulation) for the initial condition (3.7.8) of the simple progressive wave (p. 141 of §3.7.5). Figure 4.7.1 plots the compute time $T_{m\delta}$ of the fine-grid full-domain system with the same grid-interval as the sub-patch micro-grid interval δ of a staggered patch grid with different number of

[6] TODO/update IC
ref to a chap4 sec

Figure 4.7.1: Measured compute times $T_{m\delta}$ of the fine-grid full-domain system (viscous shallow water flow) with the same grid-interval as the sub-patch micro-grid interval δ of a staggered patch grid with different N , n , and patch scale ratio r . Solid lines represent expression (4.7.2) with the estimated model compute time $T_M = 0.19 \mu\text{s}$.

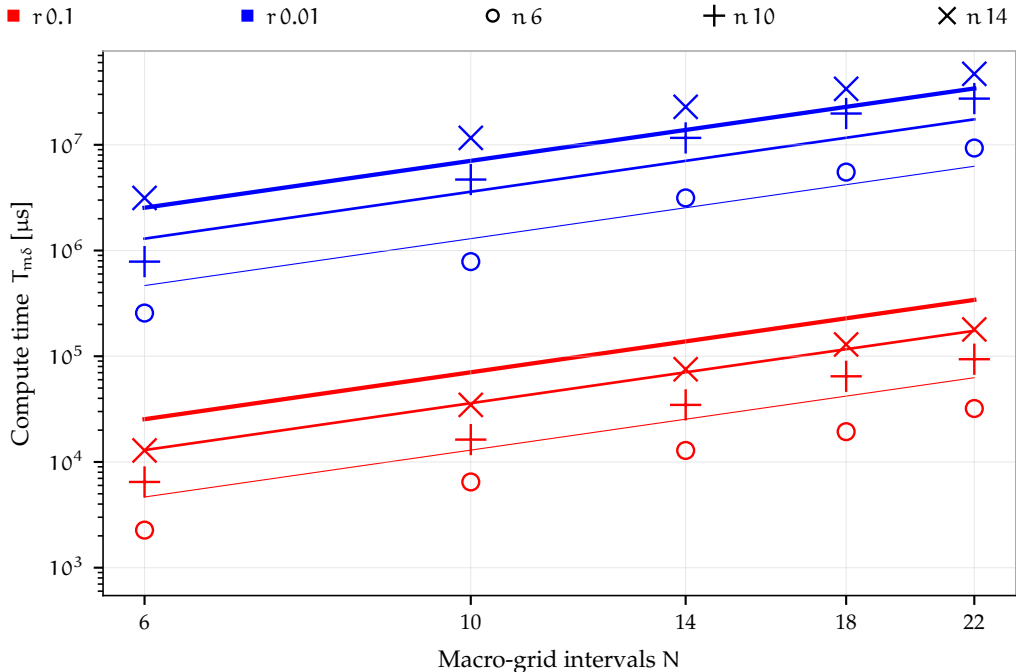
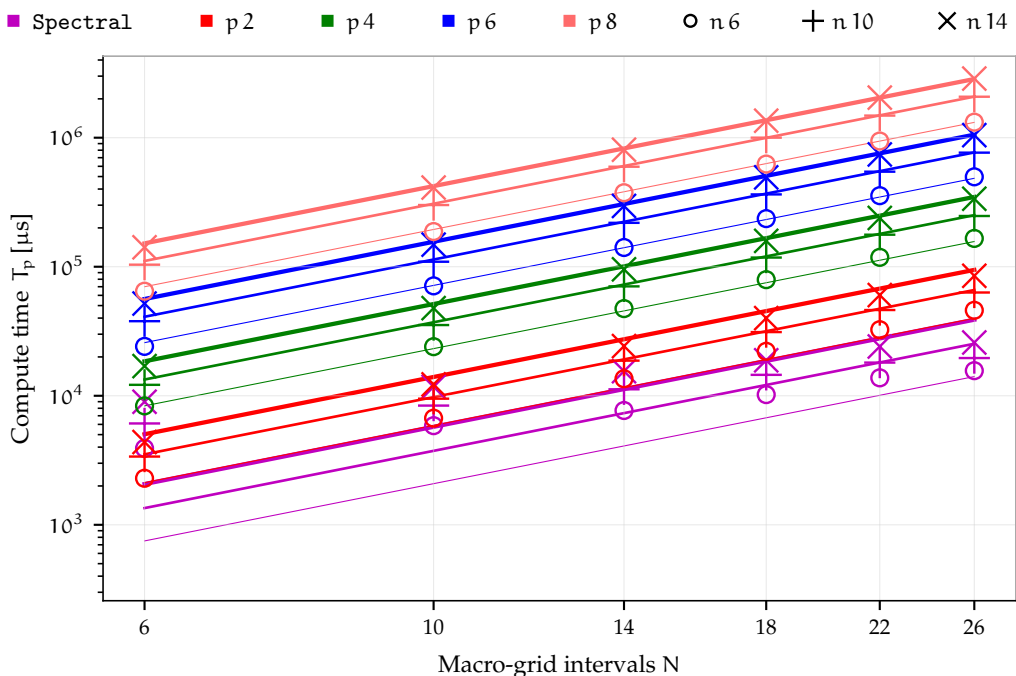


Figure 4.7.2: Measured compute times T_p of the five staggered patch schemes (viscous shallow water flow) with different N and n . Solid lines represent expression (4.7.3) using the estimated model compute time $T_M = 0.19 \mu\text{s}$ and the respective estimated coupling compute times T_C for the five patch schemes.



macro-grid intervals N , sub-patch micro-grid intervals n , and patch scale ratio r . We measured hundred samples of compute times $T_{m\delta}$ for each of the four Reynolds numbers $Re \in \{10, 50, 250, 1250\}$. Each point in Fig. 4.7.1 is the mean over the four Reynolds numbers Re . For the measured compute times $T_{m\delta}$, fitting one common power law curve (solid lines in Fig. 4.7.1) using the expression (4.7.2), we estimate the model compute time per interior node $T_M = 0.19 \mu s$ (same value for all n, r). The measured compute times $T_{m\delta}$ reasonably closely follow the trend of the expression (4.7.2) (solid lines). *For the viscous shallow water flow, the model compute time $T_M = 0.19 \mu s$ is about three times larger than the model compute time $T_M = 0.062 \mu s$ of the general linear wave (p. 133 of §3.7.4).* This larger model compute time T_M is due to the relatively larger complexity and computations of the micro-scale system (4.1.11) for the viscous shallow water flow (p. 160 of §4.1.2) compared to the micro-scale system (3.1.2) for the general linear wave (p. 43 of §3.1).

Figure 4.7.2 plots the measured compute time T_p of the five staggered patch schemes for computing the time derivative of the state vector (i.e., the compute time for one iteration in time simulation), for different macro-grid intervals N and sub-patch micro-grid intervals n . We measured hundred samples of compute times T_p for each of the four Reynolds numbers $Re \in \{10, 50, 250, 1250\}$. Each point in Fig. 4.7.2 is the mean over the four Reynolds numbers Re . For the measured compute times T_p , fitting a power law curve for each patch scheme (solid lines in Fig. 4.7.2) using the model compute time $T_M = 0.19 \mu s$ in the expression (4.7.3), we estimate the approximate coupling compute times per edge node $T_C = 0.58, 1.8, 7.4, 23, 63 \mu s$ for the five staggered patch schemes Spectral, Square-p2, Square-p4, Square-p6, and Square-p8 respectively. The measured compute times T_p of all the five staggered patch schemes reasonably closely follow the trend of the expression (4.7.3) (solid lines).

Except the Spectral patch scheme, the estimated coupling compute times $T_C = 0.58, 1.8, 7.4, 23, 63 \mu s$ for the viscous shallow water flow are about the same as the coupling compute times $T_C = 0.44, 1.8, 7.6, 24, 63 \mu s$ of the general linear wave (p. 133 of §3.7.4). There are additional layers of edge nodes in the staggered patch grid for the viscous shallow water flow (Fig. 4.1.2b) compared to the general linear wave (Fig. 4.1.2a). But as the coupling compute times T_C are average patch coupling compute time *per edge node*, the T_C of the viscous shallow water flow and that of the general linear wave are about the same. Yet, as the total patch coupling time $n_p^E T_C$ depends on the number of edge nodes, the total compute time for one iteration T_p in (4.7.3) is larger for the viscous shallow water flow compared to that of the general linear wave. For example, the compute

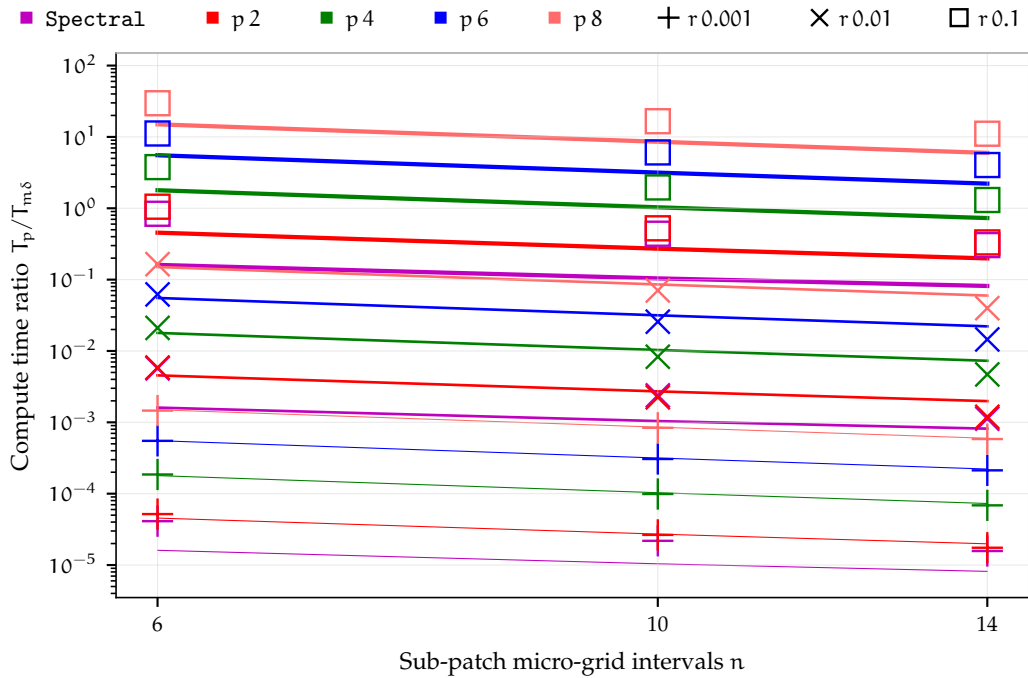
times for one iteration T_p in Fig. 4.7.2 for the viscous shallow water flow are about 15 to 40% larger (depending upon the patch scheme) compared to the T_p in Fig. 3.7.2 of §3.7.4 for the general linear wave.

As in §3.7.4 for the general linear wave, the smallest coupling compute time $T_C = 0.58 \mu\text{s}$ for the spectral patch scheme is because Algorithm 1 efficiently calculates the edge values for all the h/u/v-centred patches in one shot using the fast Fourier transform via the Fourier shift property. But for the polynomial patch schemes, Algorithm 2 calculates looping over each of the h/u/v-centred patches patches individually. As in §3.7.4, for the polynomial patch schemes, the coupling compute time per edge node T_C increases monotonically from $1.8 \mu\text{s}$ to $63 \mu\text{s}$ with increase in the order p of interpolation from two to eight. This increasing T_C with increasing p is expected as there are more computations involved in higher order interpolation.

The focus of the current patch scheme implementation is on the flexibility to explore a large number of possible designs of the patch grid and a large number of possible patch schemes. So, the current patch scheme implementation, being not computationally efficient, leads to large coupling compute times per edge node T_C from Fig. 4.7.2. Hence, the approximate ratios of the coupling compute times to the model compute times are $T_C/T_M = 3, 9, 39, 120, 326$, for the five staggered patch schemes Spectral, Square-p2, Square-p4, Square-p6, and Square-p8 respectively. Compared to the ratio $T_C/T_M = 7, 29, 123, 381, 1020$ in §3.7.4 for the general linear wave, *ratio T_C/T_M of the coupling compute times to the model compute times for the viscous shallow water flow is about three times lesser*. Compared to the general linear wave, the smaller ratio T_C/T_M for the viscous shallow water flow is because the coupling compute times T_C are about the same as general linear wave but the model compute time is about three times larger (due to relatively larger complexity and computations of the micro-scale system as in p. 265 of this §4.7.3).

Figure 4.7.3 plots the ratio $T_p/T_{m\delta}$ of the measured compute time of the fine-grid full-domain system to that of the staggered patch schemes, for different number of sub-patch micro-grid intervals n and patch scale ratio r . Solid lines represent expression (4.7.6) for $T_p/T_{m\delta}$ using the estimated model compute time $T_M = 0.19 \mu\text{s}$ and the respective estimated coupling compute times T_C for each patch scheme. A fine-grid for full-domain system (with the same grid interval δ as the sub-patch micro-grid interval), has very large number of interior nodes $n_{m\delta}^I = 3N^2n^2/(16r^2)$ corresponding to a small patch scale ratio, requiring memory larger than 64 GB. Hence, as in §4.7.3, for $r = 0.001$ we compute $T_p/T_{m\delta}$ (plusses in Fig. 4.7.3) using the measured T_p of the patch schemes and the estimated $T_{m\delta}$ of the full-domain system

Figure 4.7.3: Ratio $T_p/T_{m\delta}$ of the measured compute time of the staggered patch schemes (viscous shallow water flow) to that of the fine-grid full-domain system, for different n , r . Solid lines represent expression (4.7.6) for $T_p/T_{m\delta}$ using the estimated model compute time $T_M = 0.19 \mu s$ and the respective estimated coupling compute times T_C for each patch scheme.



using the expression (4.7.6). The measured compute time ratio $T_p/T_{m\delta}$ reasonably closely follow the trend of the expression (4.7.6) (solid lines) for the five staggered patch schemes (with the respective T_C).

In Fig. 4.7.3, the compute time ratio $T_p/T_{m\delta}$ for the viscous shallow water flow is about half of the compute time ratio $T_p/T_{m\delta}$ of the general linear wave in Fig. 3.7.3 of §3.7.4. The preceding paragraph reports that the ratio T_C/T_M of the coupling compute times to the model compute times for the viscous shallow water flow is about three times lesser than that of the general linear wave. Due to the additional layers of edge nodes in the staggered patch grid for the viscous shallow water flow (Fig. 4.1.2b) compared to the general linear wave (Fig. 4.1.2a), the expression (4.7.6) for $T_p/T_{m\delta}$ has $+64r^2/(3n^2)$ as opposed to $-64r^2/(3n^2)$ in the corresponding expression (3.7.6) of $T_p/T_{m\delta}$ for the general linear wave (p. 130 of §4.1.2). Overall, the combined effect of the three times lesser T_C/T_M and the more edge nodes for the viscous shallow water flow leads to lesser compute time ratio $T_p/T_{m\delta}$, which is about half of the compute time ratio $T_p/T_{m\delta}$ of the general linear wave.

Figure 4.7.3 show that despite the estimated large T_C/T_M (between

3 and 326 for the five patch schemes), for sufficiently small patch scale ratio $r = 0.01, 0.001$ the compute time ratios $T_p/T_{m\delta}$ are about $10^{-2}, 10^{-4}$. That is, despite the large T_C/T_M , for small patch scale ratios, *the compute times of the multi-scale patch schemes are about 100 to 10 000 times smaller than the corresponding fine-grid full-domain micro-scale system*. A reduction of 10 000 times is equivalent to reducing the computation time from one week to one minute. These patch scheme computational savings for the viscous shallow water flow are about twice as those for the general linear wave. With finer detail, the patch scheme computational saving for the viscous shallow water flow is twice as that of the general linear wave in §3.7.4.

As in §4.7.3 for the general linear wave, for patch scheme simulations with fixed grid geometry, the patch coupling coefficients can be precomputed as a sparse matrix, which gives the patch edge values when multiplied by the patch centre values at each instant in time. Such patch coupling via sparse matrix multiplication instead of direct patch coupling reduces the coupling compute time T_C , leading to smaller T_C/T_M in (4.7.6), and hence larger computational savings of the staggered patch schemes via smaller $T_p/T_{m\delta}$. Using the sparse matrix multiplication for the patch coupling of the five staggered patch schemes, Fig. 4.7.4 plots the measured compute time T_p for computing the time derivative of the state vector (i.e., the compute time for one iteration in time simulation), for different N and n . We measured 10 000 samples of compute times T_p for each of the four Reynolds numbers $Re \in \{10, 50, 250, 1250\}$. Each point in Fig. 4.7.4 is the mean over the four Reynolds numbers Re .

Similar to §3.7.4 for the measured compute times T_p in Fig. 3.7.4, fitting a power law curve (solid lines in Fig. 3.7.4) using the model compute time $T_M = 0.19 \mu s$ in the expression (3.7.3), we estimate the approximate coupling compute times per edge node $T_C = 0.62, 0.41, 0.4, 0.43, 0.47 \mu s$ for the five staggered patch schemes Spectral, Square-p2, Square-p4, Square-p6, and Square-p8 respectively. The patch coupling via sparse matrix multiplication reduces the coupling compute time T_C by as large as 170 times compared to the direct coupling compute times ($T_C = 0.58, 1.8, 7.4, 23, 63 \mu s$ computed from Fig. 3.7.2). Similar to §3.7.4 for the general linear wave, in contrast to the direct patch coupling, via sparse matrix multiplication the coupling compute time $T_C = 0.62 \mu s$ for the Spectral patch scheme is not the smallest among the five patch schemes. The large $T_C = 0.62 \mu s$ for the Spectral patch scheme, compared to $T_C = 0.41 \mu s$ for the Square-p2 patch scheme, comes from the smaller sparsity of the coupling matrix due to the global spectral interpolation, compared to the larger sparsity of the quadratic interpolation of Square-p2 patch scheme. Compared to the patch scheme compute times T_p in Fig. 4.7.2 via direct coupling, the patch scheme

Figure 4.7.4: Measured compute times T_p , with *patch coupling via sparse matrix multiplication*, for the five staggered patch schemes with different N and n . Solid lines represent expression (4.7.3) using the estimated model compute time $T_M = 0.19 \mu\text{s}$ and the respective estimated coupling compute times T_C for the five patch schemes.

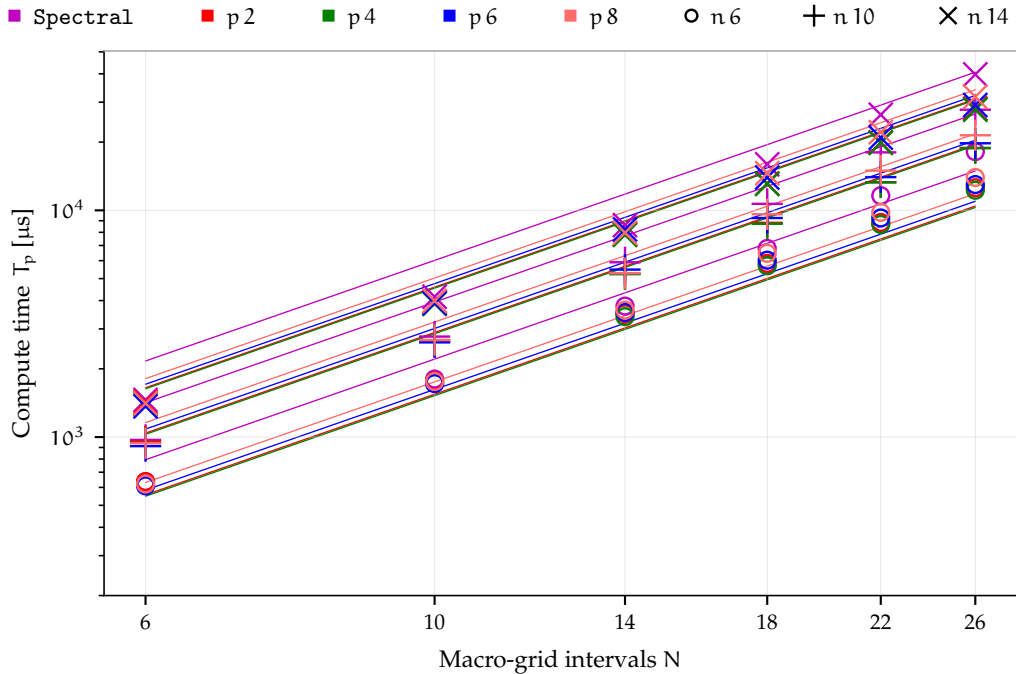
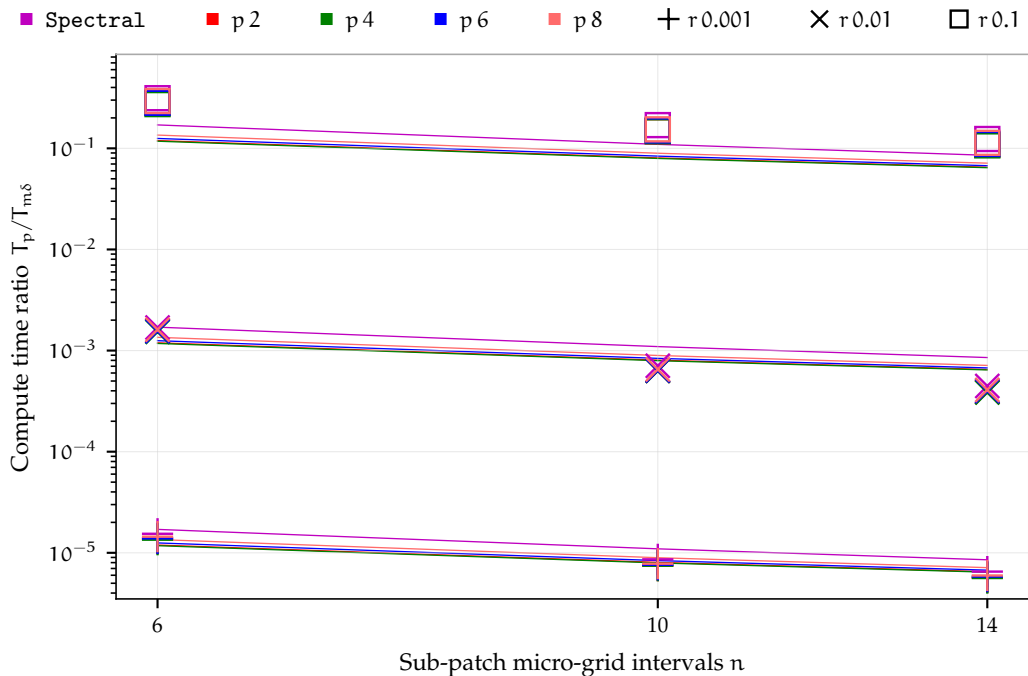


Figure 4.7.5: Ratio $T_p/T_{m\delta}$ of the measured compute time of the staggered patch schemes with *patch coupling via sparse matrix multiplication* to that of the fine-grid full-domain system, for different n , r . Solid lines represent expression (4.7.6) for $T_p/T_{m\delta}$ using the estimated $T_M = 0.19 \mu\text{s}$ and the respective estimated coupling compute times T_C for each patch scheme.



compute times T_p in Fig. 4.7.4 with patch coupling via sparse matrix multiplication, do not have strong dependence on the specific patch schemes nor the number of sub-patch intervals n .

Compared to the direct patch coupling, the smaller coupling compute time T_C for the patch coupling via sparse matrix multiplication leads to smaller ratio of the coupling compute time to the model compute time. Using $T_M = 0.19 \mu\text{s}$, the ratio $T_C/T_M = 3.2, 2.1, 2.1, 2.3, 2.5$ for the patch coupling via sparse matrix multiplication, is much smaller compared to the ratio $T_C/T_M = 7, 29, 123, 381, 1020$ of the direct coupling, for the five staggered patch schemes Spectral, Square-p2, Square-p4, Square-p6, and Square-p8 respectively. As per the expression (4.7.6), this smaller T_C/T_M also results in smaller ratio $T_p/T_{m\delta}$ of the measured compute time of the staggered patch schemes to that of the fine-grid full-domain system. Compared to the ratio $T_C/T_M = 8.1, 4.3, 4.7, 5.2, 5.9$ for the general linear wave (§3.7.4) via sparse matrix multiplication, ratio T_C/T_M of the coupling compute times to the model compute times for the viscous shallow water flow is about half as that of the general linear wave. Compared to the general linear wave, the smaller ratio T_C/T_M for the viscous shallow water flow is because the coupling compute times T_C are larger only by about 20–50% compared to the general linear wave but the model compute time is about three times larger (due to relatively larger complexity and computations of the micro-scale system as explained in p. 265 of this §4.7.3).

Figure 4.7.5 plots the ratio $T_p/T_{m\delta}$ of the measured compute time of the staggered patch schemes with *patch coupling via sparse matrix multiplication* to that of the fine-grid full-domain system, for different number of sub-patch micro-grid intervals n and patch scale ratio r . Solid lines represent expression (4.7.6) for $T_p/T_{m\delta}$ using the estimated $T_M = 0.19 \mu\text{s}$ and the respective estimated coupling compute times T_C for each patch scheme. As discussed in the paragraph before (for direct coupling), the computation for fine-grid full-domain system corresponding to a patch grid with small patch scale ratio, requires large memory. Hence, for $r = 0.001$ we compute $T_p/T_{m\delta}$ (plusses in Fig. 4.7.5) using the measured T_p of the patch schemes and the estimated $T_{m\delta}$ of the full-domain system using the expression (4.7.6). The measured compute time ratio $T_p/T_{m\delta}$ reasonably closely follow the trend of the expression (4.7.6) (solid lines) for the five staggered patch schemes (through the respective T_C). As in §3.7.4 for the general linear wave, compared to the compute time ratios $T_p/T_{m\delta}$ in Fig. 4.7.3 via direct coupling, the compute time ratios $T_p/T_{m\delta}$ in Fig. 4.7.5 with patch coupling via sparse matrix multiplication, do not have strong dependence on the specific patch schemes nor the patch scale ratio r . Compared to the compute time ratios $T_p/T_{m\delta}$ in Fig. 4.7.3 via direct coupling, the patch

coupling via sparse matrix multiplication (for fixed grid) reduces the compute time ratios $T_p/T_{m\delta}$ by about ten times as in Fig. 4.7.5, especially for higher order patch schemes.

As for the direct coupling (p. 267 of this §4.7.3), in Fig. 4.7.5 *the compute time ratio $T_p/T_{m\delta}$ for the viscous shallow water flow with patch coupling via sparse matrix multiplication is about half as that of the general linear wave in Fig. 3.7.5 of §3.7.4*. As for the direct coupling (p. 267 of this §4.7.3), the combined effect of the lesser T_C/T_M and the more edge nodes for the viscous shallow water flow leads to lesser compute time ratio $T_p/T_{m\delta}$, which is about half of the compute time ratio $T_p/T_{m\delta}$ of the general linear wave.

As in the previous paragraph, due to the overall combined effect of larger complexity of the micro-scale system and the more edge nodes for the viscous shallow water flow, the ratio T_C/T_M (of coupling compute time to model compute time) for the viscous shallow water flow is about half as that of the general linear wave. Yet, even for the viscous shallow water flow, the ratio $T_C/T_M > 1$ (between two and three). Figure 4.7.5 shows that despite $T_C/T_M > 1$, for sufficiently small patch scale ratio $r = 0.01, 0.001$ the compute time ratios $T_p/T_{m\delta}$ are about $10^{-3}, 10^{-5}$. That is, for small patch scale ratios, *the compute times of the multi-scale patch schemes are about 1000 to 10^5 times smaller than the corresponding fine-grid full-domain micro-scale system*. A reduction of 10^5 times is equivalent to reducing the computation time from one week to six seconds. With finer detail, the patch scheme computational saving for the viscous shallow water flow is twice as that of the general linear wave in §3.7.4.

The demonstrated large computational savings of the patch schemes via compute time ratio $T_p/T_{m\delta}$ in Figs. 4.7.3 and 4.7.5 are for the case of ratio of coupling compute time to model compute time $T_C/T_M > 1$. As explained in §3.7.4 for the general linear wave, even larger computational savings of the patch schemes are possible with smaller ratio T_C/T_M in (4.7.6) in the following cases.

1. Compared to the current viscous shallow water, modelling more complex physical process (non-hydrostatic nonlinear waves, sediment transport, etc) with a larger model compute time T_M , leads to smaller T_C/T_M in (4.7.6), and hence smaller $T_p/T_{m\delta}$, that is larger computational savings of the staggered patch schemes.
2. Compared to the current computationally not efficient implementation (with a focus on exploratory studies), a more efficient implementation (via code specialisation, code optimisation, parallelisation, etc) with a smaller coupling compute time T_C , leads to smaller T_C/T_M in (4.7.6), and larger computational savings of the staggered patch

schemes. As discussed in the article by Bunder et al. (2020, p. 962), in a parallel implementation, patch schemes require lesser communication across the compute nodes compared to the fine-grid grid full-domain system, due shorter messages across the patches in different compute nodes. This lesser communication across the compute nodes, leads to additional computational savings of the parallel implementation of the staggered patch schemes compared to the current serial implementation.

4.7.4 Staggered patch scheme time simulations of viscous shallow water flows

This subsection demonstrates the accuracy and the effectiveness of the staggered patch schemes by numerically simulating a viscous roll waves (e.g., Balmforth and Mandre 2004). The patch schemes accurately simulate the localised nearly discontinuous macro-scale viscous roll waves emerging from the initial condition of a simple progressive wave within the small sparsely located patches.

Page 141 of §3.7.5 for the general linear wave, selects the BS3 ODE integrator of the Julia package DifferentialEquations.jl for the time simulations, considering the simulation error, compute time and the memory usage of various ODE integrators. As in §3.7.5 for the general linear wave, also for the viscous shallow water flow *this subsection uses the BS3 ODE integrator for all the time simulations* with the relative and absolute error tolerances of 10^{-3} and 10^{-6} respectively. The BS3 is a lower oder Bogacki–Shampine 3/2 method (Bogacki and L. Shampine 1989; L. F. Shampine and Reichelt 1997), similar to the ode23 of MATLAB (DifferentialEquations.jl 2021).

Figures 4.7.6 to 4.7.8 show the time evolution of a viscous roll wave (height h and velocities u, v) for Reynolds number $Re = 10$ over a bed inclined 10° downwards along downstream, emerging from the initial condition of a simple progressive wave

$$h_0(x, y) = 0.2 + 0.05 \sin(x) \cdot \exp[-y^2/(2 \cdot 2)^2], \quad (4.7.8a)$$

$$u_0(x, y) = 0.6 + (0.05/\sqrt{2}) \sin(x) \cdot \exp[-y^2/(2 \cdot 2)^2], \quad (4.7.8b)$$

$$v_0(x, y) = 0. \quad (4.7.8c)$$

Figures 4.7.6 to 4.7.8 show that the time evolution using the Square-p4 patch scheme (colour-coded ribbons, with $N = 14$, $n = 6$, and $r = 0.01$) agrees reasonably with that of the 4200×4200 fine-grid full-domain system (grey mesh) with the same full-domain grid interval as the sub-patch

Figure 4.7.6: Time evolution of a roll wave (height h) for $t = 0$ to 10π , emerging from the initial condition of simple progressive wave (4.7.8), using Square-p4 patch scheme (colour-coded ribbons, with $N = 14$, $n = 6$, and $r = 0.01$) agrees reasonably with that of the fine-grid full-domain system (grey mesh). Black circles on h -centred patches show the discrepancy.

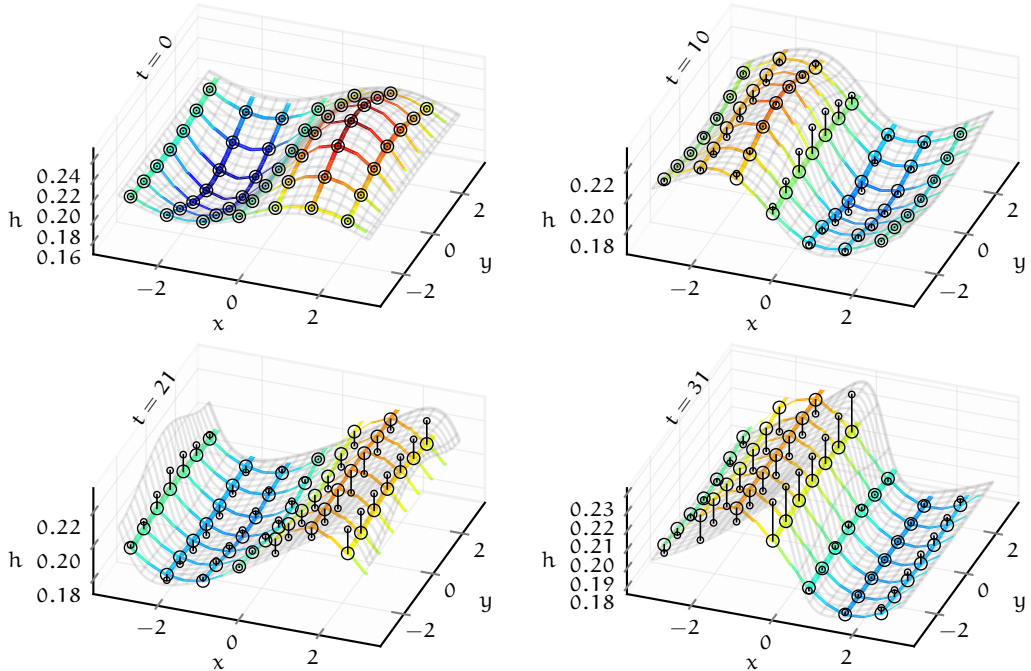


Figure 4.7.7: Time evolution of a roll wave (velocity u) for $t = 0$ to 10π , emerging from the initial condition of simple progressive wave (4.7.8), using Square-p4 patch scheme (colour-coded ribbons, with $N = 14$, $n = 6$, and $r = 0.01$) agrees reasonably with that of the fine-grid full-domain system (grey mesh). Black circles on u -centred patches show the discrepancy.

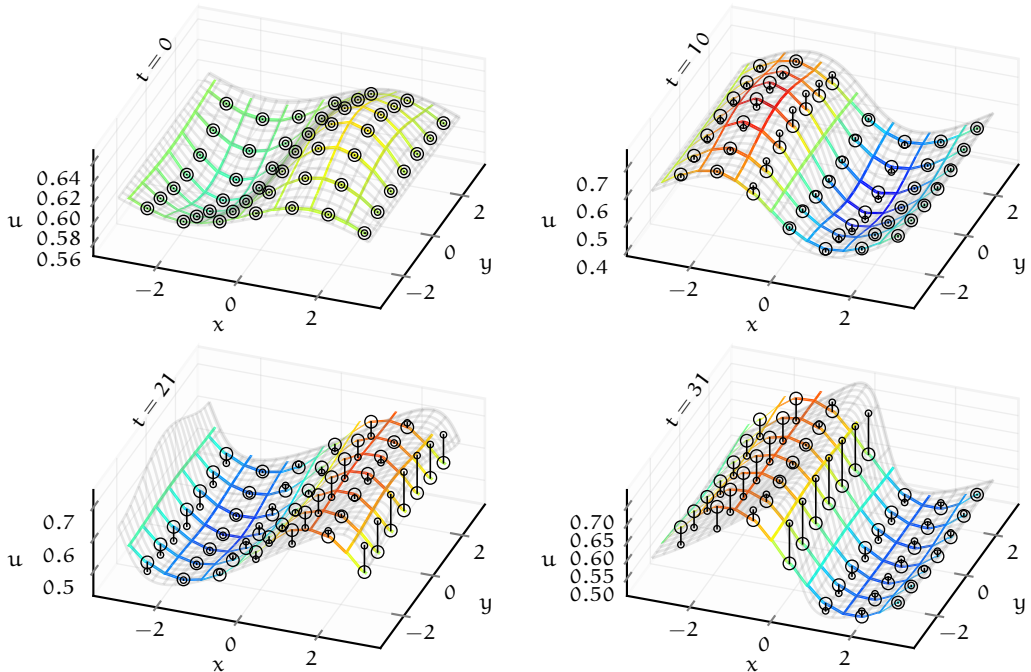
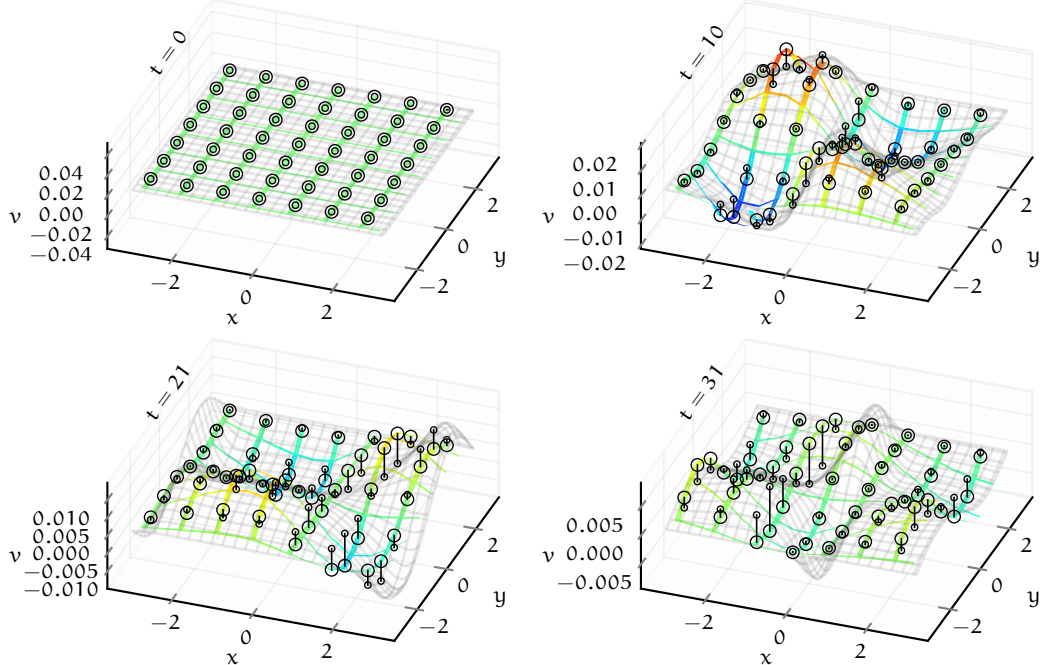


Figure 4.7.8: Time evolution of a roll wave (height v) for $t = 0$ to 10π , emerging from the initial condition of simple progressive wave (4.7.8), using Square-p4 patch scheme (colour-coded ribbons, with $N = 14$, $n = 6$, and $r = 0.01$) agrees reasonably with that of the fine-grid full-domain system (grey mesh). Black circles on h -centred patches show the discrepancy.

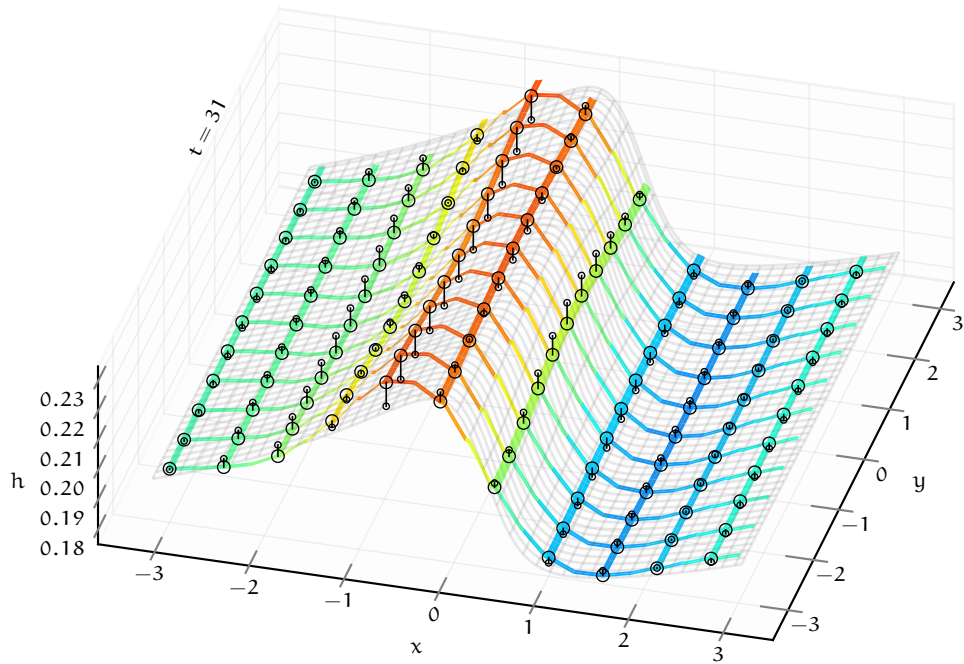


micro-grid interval $\delta = 2Lr/(Nn) = 2\pi/4200$. Despite the small number of macro-grid intervals ($N = 14$) and a low order patch coupling (fourth order polynomial interpolation), the Square-p4 patch scheme captures the localised nearly discontinuous macro-scale roll wave. Figures 4.7.6 and 4.7.7 show that the lateral (i.e., along y axis) local initial disturbance (4.7.8) to the mean flow spreads side-ways while emerging as a roll wave.

In Figs. 4.7.6 to 4.7.8 for the viscous roll wave simulation, the fine-grid full-domain micro-scale system (4.7.2) (grey mesh) uses same grid interval as the sub-patch micro-grid interval $\delta = 2Lr/(Nn)$. But the grey mesh of full-domain system plots only 24 of the 4201 grid lines, skipping many lines for visual clarity. The colour-coded ribbons of the patch scheme in Fig. 4.7.6 consist of all the lines (along the coordinate axes x and y) passing through all the h nodes within all the patches; similarly Figs. 4.7.7 and 4.7.8 for u , v nodes within all the patches respectively. Whereas the true patch scale ratio is $r = 0.01$, the patches are enlarged for visual clarity so that the ribbons appear wider. In Figs. 4.7.6 to 4.7.8, the solutions $h/u/v$ of fine-grid full-domain micro-scale system are linearly interpolated using nearest four

Figure 4.7.9: Snapshot of the emergent viscous roll wave (height h at $t = 31$), from the initial condition of simple progressive wave (4.7.8), using Square-p6 patch scheme (colour-coded ribbons, with $N = 22$, $n = 6$, and $r = 0.1$) agrees very closely with that of the fine-grid full-domain system (grey mesh). Black circles on h -centred patches show the discrepancy.

[8] TODO. Move this to the Chapter 1 to arouse some early interest for the reader.



values to the centres of the respective $h/u/v$ -centred patches, illustrated by small black circles. The large circles are the patch scheme solution $h/u/v$.

For sufficient number of macro-grid intervals and accurate patch coupling, patch schemes accurately simulate the viscous shallow water flows. Figures 4.7.6 to 4.7.8 show that for small number of macro-grid intervals ($N = 14$) and a low order patch coupling (fourth order polynomial interpolation), the Square-p4 patch scheme reasonably accurately simulates the localised nearly discontinuous macro-scale roll wave. Figure 4.7.9 compares the Square-p4 patch scheme patch scheme solution for larger $N = 22$ ($n = 6$, $r = 0.1$), with the full-domain solution for the same grid interval as the sub-patch micro-grid interval $\delta = 2Lr/(Nn) = 2\pi/660$. Increasing the number of macro-grid intervals sufficient enough to resolve the localised roll wave, leads to more accurate multiscale patch scheme simulation. Increasing the order p of the patch coupling interpolation also increase the accuracy of the patch scheme simulations. For example, compared to Fig. 4.7.6 of Square-p4 patch scheme with $N = 14$, Fig. 4.7.9 of Square-p6 patch scheme with $N = 22$ simulates the macro-scale viscous roll wave more accurately.

(other than p and N all other parameters are same for Figs. 4.7.6 and 4.7.9). Figure 4.7.9 visually show that the discrepancy between the patch scheme and fine-grid full-domain system is small, non concentric black circles are offset only slightly. This small discrepancy at $t = 31$ (distance between centres of non concentric black circles) also includes the accumulation of the ODE integrator error due to several time iterations before $t = 31$. Thus, for sufficient number of macro-grid intervals and accurate patch coupling, *patch schemes accurately simulate the viscous shallow water flows.*

4.7.5 Some practical issues in staggered patch scheme simulations of viscous shallow water flows

Section 4.7.4 (e.g., Fig. 4.7.9) qualitatively shows that for sufficient number of macro-grid intervals and accurate patch coupling, patch schemes accurately simulate the viscous shallow water flows. This subsection establishes the accuracy of the staggered patch scheme simulations more quantitatively and explain some subtle details of the practical issues in the patch scheme simulations.

As in §3.7.5 for the general linear wave, to numerically quantify the discrepancy, we compute the solutions $h_{m\delta}^c, u_{m\delta}^c, v_{m\delta}^c$ of the fine-grid full-domain micro-scale system, at the positions of the respective $h/u/v$ -centred patches, by a bilinear interpolation using the four nearest full-domain node values. For example, Figs. 4.7.6 to 4.7.8 of §4.7.4 indicate the full-domain solutions at the respective patch centres as small black circles.

Figure 4.7.10 plots the *solution convergence* of the staggered patch schemes with decreasing macro-grid interval Δ , for the relatively complex nearly discontinuous roll wave simulation visualised in §4.7.4. Figure 4.7.10 shows the convergence via the relative *simulation error* (3.7.9a) (of §3.7.5) for height h . In Fig. 4.7.10, except for the range of macro-grid intervals N and patch scale ratio r , all other parameters are the same as in Figs. 4.7.6 to 4.7.9 of §4.7.4. Figure 4.7.10 shows that, in general, the simulation error $\epsilon_{2\pi}^h$ decreases with decreasing macro-grid intervals $\Delta = 2\pi/N$ (over the domain size $L = 2\pi$). Smaller patch scale ratio ($r \lesssim 0.01$) leads to small degradation in accuracy (about 10–50%) compared to $r = 0.1$, yet the solution errors decrease with decreasing number of macro-grid intervals N , roughly with the same order p as the polynomial interpolation for patch coupling. This decreasing simulation error with decreasing macro-grid intervals, that is the solution convergence similar to the eigenvalue convergence in §4.5, quantitatively establish the accuracy of the staggered patch scheme time simulations.

Figure 4.7.10: Convergence of patch scheme time solution h using BS3 *non-stiff* ODE integrator, in terms of simulation error $\epsilon_{2\pi}^h$ of (3.7.9a) for the roll wave (e.g., in Fig. 4.7.6) at $t = 2\pi$. For sufficient number of macro-grid intervals N and accurate patch coupling, *patch schemes accurately simulate the viscous shallow water flows*.

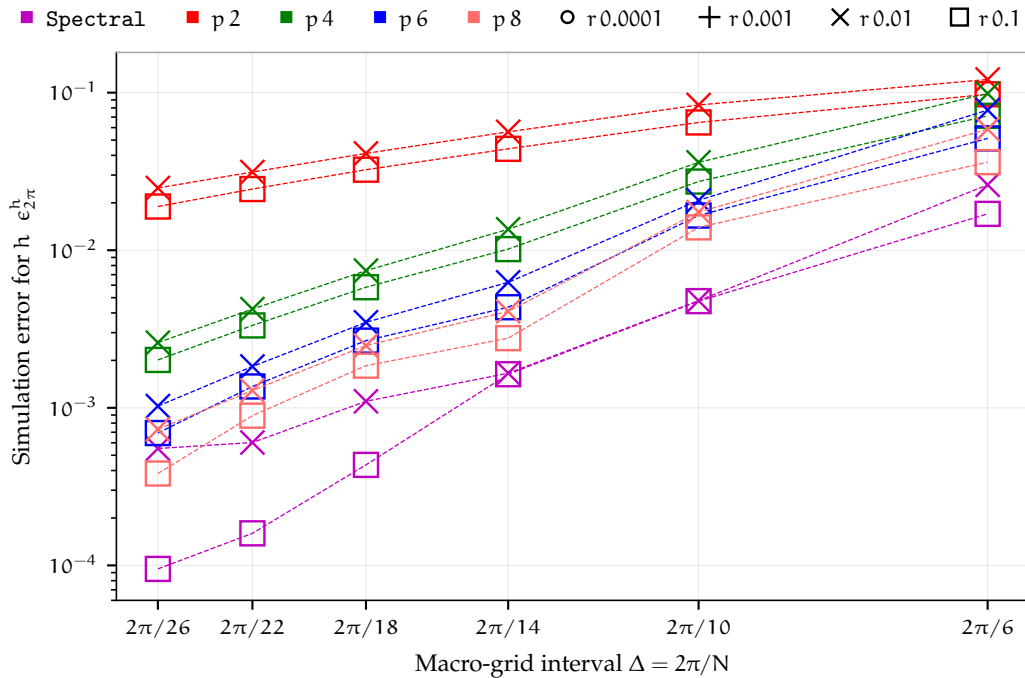
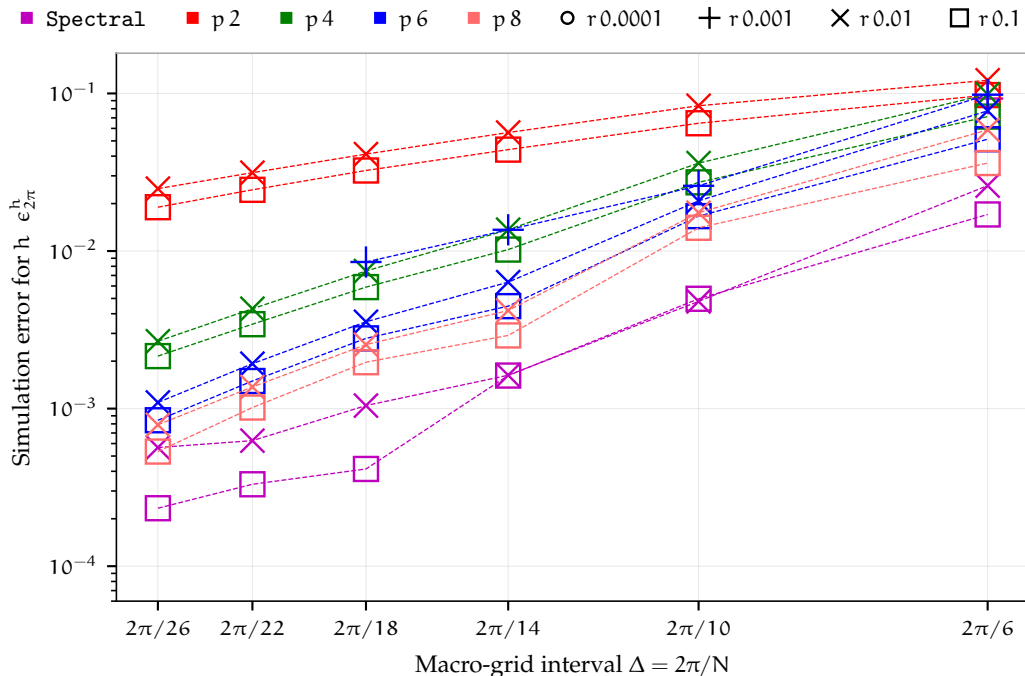


Figure 4.7.11: Patch scheme simulations using QNDF *stiff* ODE integrator gives with almost the same accuracy as the BS3 *non-stiff* ODE integrator (Fig. 4.7.10). For small patch scale ratio $r \lesssim 0.01$, the QNDF *stiff* integrator takes about ten to hundred times less compute time compared to the *non-stiff* BS3 (Fig. 4.7.12) due to fewer function evaluations (Fig. 4.7.13).



The accuracy of the Spectral patch scheme does not deteriorate for large macro-grid interval Δ for the viscous shallow water flow. Figures 3.7.12 to 3.7.14 (of §3.7.5) for the general linear wave show that the simulation errors of the Spectral patch scheme are small (about 10^{-3}), without any dependence on the macro-grid interval Δ . In contrast to the general linear wave, the convergence of the Spectral patch scheme solution for the viscous roll wave in Figure 4.7.10 shows a strong dependence on the macro-grid intervals. That is, just as the polynomial patch schemes, the simulation error of the Spectral patch scheme decrease with decreasing macro-grid interval Δ . This dependence of Spectral patch scheme accuracy on macro-grid interval Δ is because the increasing number of macro-grid intervals N (decreasing macro-grid interval Δ) resolves increasingly larger wavenumbers which captures the localised roll wave with increasing geometric detail. In other words, the Spectral patch scheme with a large macro-grid interval Δ (small number of macro-grid intervals Δ) is as accurate as with a small macro-grid interval Δ for all the wavenumbers the small patch grid resolves (i.e., the small wavenumbers). Thus, the accuracy of the Spectral patch scheme does not deteriorate for large macro-grid interval Δ .

Compute times of the ODE integrators for the patch scheme simulations increase with decreasing patch scale ratio r . The solution convergence plot in Fig. 4.7.10 does not have data points for patch scale ratio $r \lesssim 0.001$ (no plusses or circles). That is because the patch scheme simulation for small patch scale ratio using *non-stiff* ODE integrators (e.g., BS3 in Fig. 4.7.10) requires a large compute time. As in §3.7.5 for the general linear wave, all the compute times in this subsection are measured on a custom assembled liquid-cooled workstation with Intel i7-6900k processor and 64GB DDR4 RAM. For $N = 10, n = 6$, keeping all other parameters the same as in Fig. 4.7.10, using BS3 non-stiff ODE integrator, the roll wave patch scheme simulation with patch scale ratios $r = 0.1, 0.01$, complete in about 0.1 minute and 14 minutes respectively. That is about 140 fold increase in compute time going from $r = 0.1$ to $r = 0.01$. The same roll wave patch scheme simulation with a patch scale ratio $r = 0.001$ ($N = 10, n = 6$) using BS3 non-stiff ODE integrator does not complete even after five days. On the other hand, the same roll wave patch scheme simulation (i.e., $r = 0.001, N = 10, n = 6$) using QNDF *stiff* ODE integrator completes in 1.2 minutes. The QNDF stiff integrator of the Julia package DifferentialEquations.jl (2021) is a quasi-constant time step variable-order NDF (numerical differentiation) method, roughly equivalent to the common variable-step, variable-order (VSVO) ode15 integrator (L. F. Shampine and Reichelt 1997, p. 4) of MATLAB (with the default option to use NDF).

For the patch scheme simulations with small patch scale ratio $r \lesssim 0.001$,

Figure 4.7.12: Compute times of three ODE integrators (*non-stiff* BS3, *stiff* CVODE_BDF, and *stiff* QNDF) for Square-p6 patch scheme simulation in Fig. 4.7.6 for different system dimension n_p^I and patch scale ratio r . For $r \lesssim 0.01$, compute times of *stiff* integrators are about ten to hundred times lesser than *non-stiff* BS3 due to fewer function evaluations (Fig. 4.7.13).

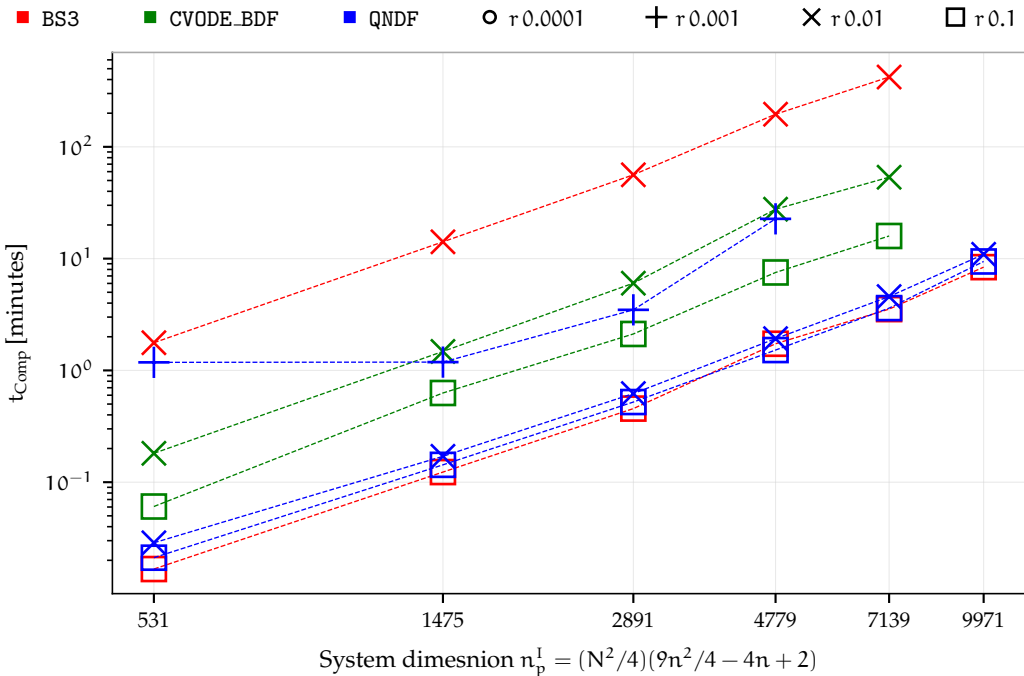
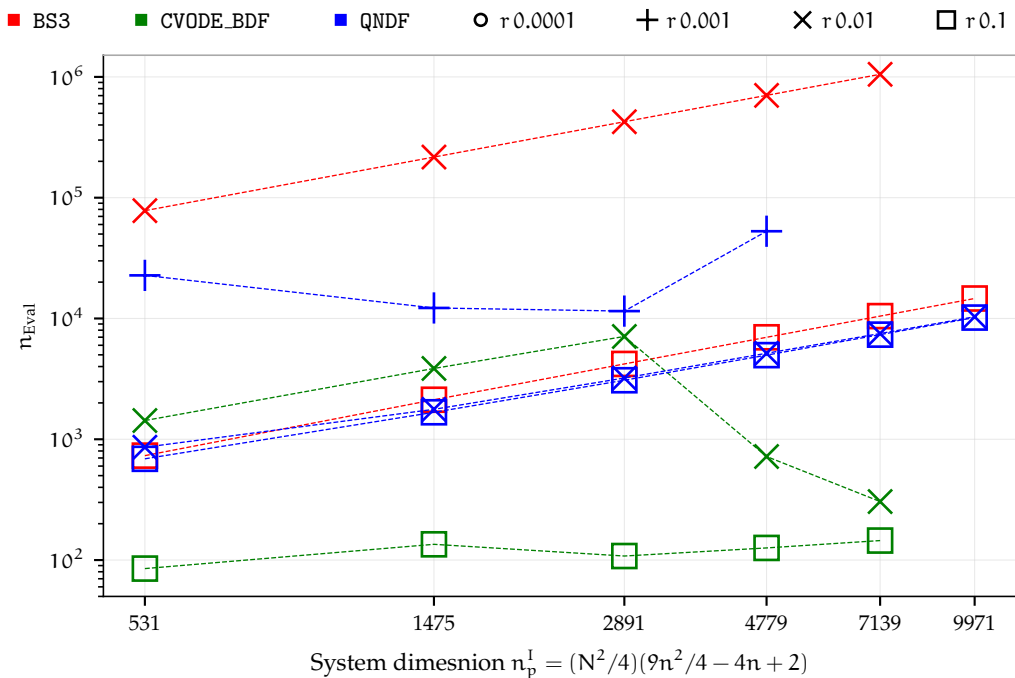


Figure 4.7.13: Number of function evaluations of three ODE integrators (*non-stiff* BS3, *stiff* CVODE_BDF, and *stiff* QNDF) for Square-p6 patch scheme simulation in Fig. 4.7.6 for different system dimension n_p^I and patch scale ratio r . For small patch scale ratio $r \lesssim 0.01$, *stiff* integrators perform about ten to hundred times less function evaluations than *non-stiff* BS3.



stiff ODE integrators are much faster yet as accurate as the non-stiff ODE integrators. Figure 4.7.12 plots the compute times of three ODE integrators (non-stiff BS3, stiff CVODE_BDF, and stiff QNDF) for Square-p6 patch scheme simulation in Fig. 4.7.6 for different system dimension n_p^I (size of state vector) and patch scale ratio r . A plot of compute times versus system dimension n_p^I for all the other four staggered patch schemes have identical trend and approximately same magnitudes as in Fig. 4.7.12. Figure 4.7.12 shows that for both the stiff (BS3) and the non-stiff (CVODE_BDF, and stiff QNDF) ODE integrators, the compute times increase with decreasing patch scale ratio r , for all system dimensions $n_p^I = (N^2/4)(9n^2/4 - 4n + 2)$ corresponding to the macro-grid intervals $N \in \{6, 10, 14, 18, 22, 26\}$. Specifically, comparing the red crosses with the green and blue crosses in Fig. 4.7.12 shows that for small patch scale ratio $r \lesssim 0.01$, the compute times of stiff integrators are about ten to hundred times lesser than non-stiff BS3. Figure 4.7.11 plots the *solution convergence* using the QNDF stiff ODE integrator for the same relative and absolute error tolerances (10^{-3} and 10^{-6}) and other parameters as used by BS3 non-stiff ODE in Fig. 4.7.10. Comparing Figs. 4.7.10 and 4.7.11 shows that both the stiff and non-stiff ODE integrators, give same accuracy, except a small deviation for the Spectral patch scheme for small macro-grid interval $\Delta \lesssim 2\pi/22$. With a smaller relative and absolute error tolerances of 10^{-7} and 10^{-6} respectively, a convergence plot using the QNDF stiff ODE integrator is identical to Fig. 4.7.10, also for the Spectral patch scheme for small macro-grid interval $\Delta \lesssim 2\pi/22$. That is, despite the large differences in the compute times among the stiff and non-stiff ODE integrators, both gives reasonably the same accuracy. Especially, for the patch scheme simulations with small patch scale ratio $r \lesssim 0.001$, stiff ODE integrators are must faster (ten to hundred times) yet as accurate as the non-stiff ODE integrators.

Patch scheme simulations for small patch scale ratio $r \lesssim 0.001$ require ODE integrator that can handle stiff systems. Figure 3.7.7 of §3.7.5 for the general linear wave shows that the compute times of the stiff ODE integrators (sp.BDF, sp.Radau) are ten to hundred times larger compared the non-stiff ode integrators (BS3, DP5, Tsit5, Vern7). Similarly, for an even simpler linear system $du/dt = Au + b$, Maclean, Bunder, and Roberts (2021, p. 1742, Fig.4) comment that “The stiff integrator is fast and reasonably accurate at low system dimension, but performs poorly at dimension 60 and above.” In contrast, the preceding paragraph shows, for the patch scheme simulations with small patch scale ratio $r \lesssim 0.001$, stiff ODE integrators are much faster yet as accurate as the non-stiff ODE integrators. From Figs. 4.7.10 and 4.7.11 and Fig. 4.7.12, it is evident that this trend of stiff ODE integrators being much faster yet as accurate as the non-stiff ODE integrators, also holds for

different system dimensions as small as about five hundred to as large as ten thousand for viscous shallow water flow. Based on study for a simple linear system $\mathbf{du}/dt = \mathbf{Au} + \mathbf{b}$, Maclean, Bunder, and Roberts (2021, §3.1.4) find that that projective ODE integrator (Gear and Kevrekidis 2003) which specifically utilises the spectral gap in a system outperforms the stiff ODE integrator both in accuracy and compute times. A detailed comparative study of different ODE integrators including the projective ODE integrator, for a complex viscous shallow water flow is left as a future work. The current work shows that for nonlinear micro-scale models (e.g., viscous shallow water flow) patch scheme simulations for small patch scale ratio $r \lesssim 0.01$ require a ODE integrator that can handle stiff systems efficiently.

The following paragraphs investigate why the compute times (ODE integration times) of the patch scheme simulations increase with decreasing patch scale ratio r , and hence necessitating a ODE integrator that can handle stiff systems efficiently.

For the patch scheme simulations, the *increasing compute times with decreasing patch scale ratio is not due to patch scheme computations, but due to increasing function evaluations of the ODE integrators*. Figure 4.7.13 plots the number of function evaluations to compute the time derivative of a patch system corresponding to the compute times in Fig. 4.7.12, for different system dimension n_p^1 and patch scale ratio r . Figure 4.7.13 shows that, except some deviations, in general the number of function evaluation increases with decreasing patch scale ratio r . On the other hand, as §4.7.3 (e.g., Fig. 4.7.5) shows, the compute time to compute the time derivative of a patch scheme system (one iteration of simulation) is much smaller by several orders of magnitude compared to the corresponding full-domain micro-scale system. That is, the increasing total compute times of the patch scheme simulations are not due to the patch scheme computations per iteration, but due to the ODE integrators calling the function to compute the time derivative of a patch scheme many times.

A patch scheme becomes an increasingly stiff system of ODES with decreasing patch scale ratio r . Moler (2004, p. 203, §7.9) discusses the classical example of a stiff ODE $dy/dt = y^2 - y^3$, $y(0) = \delta$, $0 \leq t \leq 2/\delta$ that models the flame propagation of a lighted match stick. This model of flame propagation becomes increasingly stiff with decreasing the parameter δ . In a somewhat similar manner, the patch schemes become increasingly stiff with decreasing patch scale ratio r . For a patch grid with fixed number of macro-grid intervals N and sub-patch micro-grid intervals n , decreasing the patch scale ratio r leads to large wavenumber structures within the patches for the same smooth macro-scale structure in the solution. For example, consider the patch scheme eigenvalue spectrum in Figs. 4.2.13

and 4.2.14 for patch scale ratio $r = 0.1, 0.001$ respectively, keeping all other parameters the same. Figures 4.2.13 and 4.2.14 show that with decreasing patch scale ratio r , the micro-scale eigenvalues (blue circles on the left) both moves to the left (taking larger negative real part values) and spreads up and down (taking large magnitudes of imaginary parts) without any change to the macro-scale eigenvalues on the right. That is, decreasing the patch scale ratio r leads to increasing wavenumber for the sub-patch micro-scale modes. This *intrinsic tendency of a patch scheme* (for both the usual collocated and the present staggered patch scheme) *makes the system of ODEs increasingly stiff with decreasing patch scale ratio*, necessitating a ODE integrator that can handle stiff systems efficiently.

Chapter 5

Patch schemes accurately simulate turbulent shallow water flows over large space

5.1 Introduction

This chapter shows that the staggered patch schemes accurately simulate the macro-scale dynamics of the Smagorinski-based turbulent shallow water flow, using the PDEs derived by Cao and Roberts (2016) as the micro-scale system within the patches.

aim is to empower better predictions of floods, tsunamis, ...

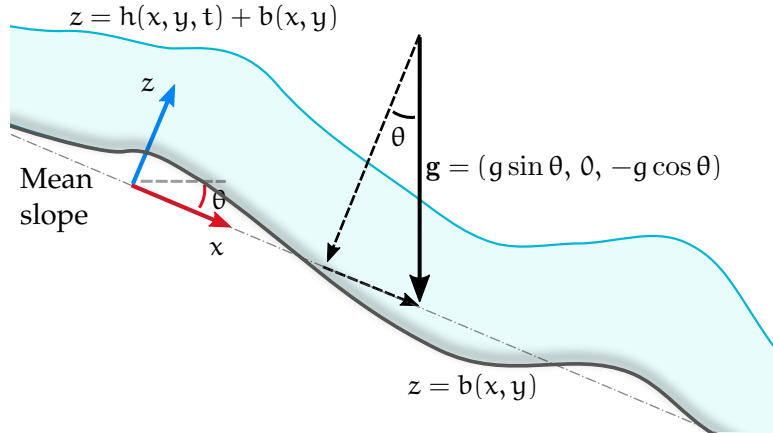
The article by Cao and Roberts (2016) derives Smagorinski-based turbulent 2D shallow water PDEs, in terms of the depth-averaged variables, but without depth averaging the PDEs. Instead, from the 3D Reynolds averaged Navier–Stokes (RANS) equation and the Smagorinski turbulence model, they derive the 2D shallow water flow using the centre manifold theory, in terms of the depth-averaged variables.

create a plot of just the full-domain microscale solution of Fig.5.5.1, placed next page, and discussed briefly here-about as an example of the turbulent flows to be addressed.

Section 5.1.1 non-dimensionalises the turbulent shallow water PDEs and the boundary conditions derived by Cao and Roberts (2016) using a reference length in terms of domain size as opposed to the characteristic height used by Cao and Roberts (2016). Section 5.1.2 derives a full-domain micro-scale finite difference system for the turbulent shallow water PDEs of §5.1.1. Section 5.1.3 chooses a set of values for the non-dimensional parameters towards exploration of patch schemes for turbulent shallow water PDEs.

Section 5.2 shows that the developed five staggered patch schemes are accurate for the turbulent shallow water flows by comparing the eigenvalues of the staggered patch schemes with the eigenvalues of fine-grid

Figure 5.1.1: Shallow turbulent flow over an inclined smooth non-flat bed. The non-dimensional gravity vector $\mathbf{g}' = \mathbf{g}/(g \cos \theta)$, that is, $\mathbf{g}' = (\tan \theta, 0, -1)$ where \mathbf{g} is gravitational acceleration and θ is the mean bed inclination angle.



full-domain micro-scale system. The eigenvalue analysis for accuracy in §5.2 is done for a representative subset of the system parameters and the grid parameters. Section 5.4 on the consistency of the patch schemes establish the accuracy over a wider range of parameters. Using the maximum real parts of the patch scheme eigenvalues, §5.3 shows that for appropriate grid parameters the staggered patch schemes are not artificially unstable. §5.5 demonstrates the accuracy and the effectiveness of the staggered patch schemes by numerically simulating a turbulent roll wave.

5.1.1 Non-dimensionalise turbulent shallow water PDEs to keep same domain size

Consider the non-dimensional *comprehensive Smagorinski-based* turbulent shallow water PDEs (27a)–(27c) in the article by Cao and Roberts (2016) for the flow schematic in Figure 5.1.1. With the magnitude of horizontal velocity $q = \sqrt{u^2 + v^2}$, the same PDEs, after dropping the over bar for depth-averaged dependent variables, omitting the sediment concentra-

tion $c(x, y, t)$, and setting bed height $b(x, y) = 0$, are

$$\frac{\partial h}{\partial t} \approx -\frac{\partial hu}{\partial x} - \frac{\partial hv}{\partial y}, \quad (5.1.1a)$$

$$\begin{aligned} \frac{\partial u}{\partial t} &\approx -0.003 \frac{uq}{h} + 0.993 \left[\tan \theta - \frac{\partial h}{\partial x} \right] - 1.030u \frac{\partial u}{\partial x} - 1.020v \frac{\partial u}{\partial y} \\ &\quad - 0.008 \left(\frac{u^2}{h} \frac{\partial h}{\partial x} - \frac{uv}{h} \frac{\partial h}{\partial y} \right) + 0.094 \frac{q}{h} \left[\frac{\partial}{\partial x} \left(h^2 \frac{\partial u}{\partial x} \right) + \frac{\partial}{\partial y} \left(h^2 \frac{\partial u}{\partial y} \right) \right] \\ &\quad + 0.084 \frac{u^2 - v^2}{hq} \left[\frac{\partial}{\partial x} \left(h^2 \frac{\partial u}{\partial x} \right) - \frac{\partial}{\partial y} \left(h^2 \frac{\partial u}{\partial y} \right) \right], \end{aligned} \quad (5.1.1b)$$

$$\begin{aligned} \frac{\partial v}{\partial t} &\approx -0.003 \frac{vq}{h} - 0.993 \frac{\partial h}{\partial y} - 1.030v \frac{\partial v}{\partial y} - 1.020u \frac{\partial v}{\partial x} \\ &\quad - 0.008 \left(\frac{uv}{h} \frac{\partial h}{\partial x} - \frac{v^2}{h} \frac{\partial h}{\partial y} \right) + 0.094 \frac{q}{h} \left[\frac{\partial}{\partial x} \left(h^2 \frac{\partial v}{\partial x} \right) + \frac{\partial}{\partial y} \left(h^2 \frac{\partial v}{\partial y} \right) \right] \\ &\quad + 0.084 \frac{u^2 - v^2}{hq} \left[\frac{\partial}{\partial x} \left(h^2 \frac{\partial v}{\partial x} \right) - \frac{\partial}{\partial y} \left(h^2 \frac{\partial v}{\partial y} \right) \right]. \end{aligned} \quad (5.1.1c)$$

have been

The PDES (5.1.1) are non-dimensionalised using the characteristic height H and the long wave speed $\sqrt{g_z H}$, which leads to different non-dimensional domain sizes for different characteristic water heights. We want to explore patch schemes for the same dimensional domain size with different characteristic water height H , and in doing so we also want to keep the non-dimensional domain size the same, to reuse some of the patch scheme computations. Hence, as in §4.1.1 for the viscous shallow water flows, non-dimensionalising the 2D space by a reference length $L/(2\pi)$ gives our non-dimensional comprehensive Smagorinski-based turbulent shallow water

be more precise. write something like "following exactly the same non-dimensionalisation rescaling ..."

PDES

$$\frac{1}{h_M} \frac{\partial h}{\partial t} \approx -\frac{\partial hu}{\partial x} - \frac{\partial hv}{\partial y}, \quad (5.1.2a)$$

$$\begin{aligned} \frac{1}{h_M} \frac{\partial u}{\partial t} &\approx -0.003 \frac{uq}{h} + \frac{0.993}{h_M} \left[\tan \theta - \frac{\partial h}{\partial x} \right] - \left[1.030u \frac{\partial u}{\partial x} + 1.020v \frac{\partial u}{\partial y} \right] \\ &\quad - 0.008 \left[\frac{u^2}{h} \frac{\partial h}{\partial x} - \frac{uv}{h} \frac{\partial h}{\partial y} \right] + 0.094 \frac{q}{h} \left[\frac{\partial}{\partial x} \left(h^2 \frac{\partial u}{\partial x} \right) + \frac{\partial}{\partial y} \left(h^2 \frac{\partial u}{\partial y} \right) \right] \\ &\quad + 0.084 \frac{u^2 - v^2}{hq} \left[\frac{\partial}{\partial x} \left(h^2 \frac{\partial u}{\partial x} \right) - \frac{\partial}{\partial y} \left(h^2 \frac{\partial u}{\partial y} \right) \right], \end{aligned} \quad (5.1.2b)$$

$$\begin{aligned} \frac{1}{h_M} \frac{\partial v}{\partial t} &\approx -0.003 \frac{vq}{h} - \frac{0.993}{h_M} \frac{\partial h}{\partial y} - \left[-1.030v \frac{\partial v}{\partial y} - 1.020u \frac{\partial v}{\partial x} \right] \\ &\quad - 0.008 \left[\frac{uv}{h} \frac{\partial h}{\partial x} - \frac{v^2}{h} \frac{\partial h}{\partial y} \right] + 0.094 \frac{q}{h} \left[\frac{\partial}{\partial x} \left(h^2 \frac{\partial v}{\partial x} \right) + \frac{\partial}{\partial y} \left(h^2 \frac{\partial v}{\partial y} \right) \right] \\ &\quad + 0.084 \frac{u^2 - v^2}{hq} \left[\frac{\partial}{\partial x} \left(h^2 \frac{\partial v}{\partial x} \right) - \frac{\partial}{\partial y} \left(h^2 \frac{\partial v}{\partial y} \right) \right]. \end{aligned} \quad (5.1.2c)$$

As in §4.1.1 for the viscous shallow water flows, also for the turbulent shallow water PDEs (5.1.3), the dimensional domain $[0, L] \times [0, L]$ correspond to the non-dimensional domain $[0, 2\pi] \times [0, 2\pi]$ irrespective of the characteristic height H . a

Neglecting few small terms in the comprehensive turbulent shallow water PDEs (5.1.2), using “=” instead of “ \approx ”, and simplifying, we get the following *simplified Smagorinski-based turbulent shallow water PDEs* (with magnitude of horizontal velocity $q = \sqrt{u^2 + v^2}$),

$$\frac{1}{h_M} \frac{\partial h}{\partial t} = -\frac{\partial hu}{\partial x} - \frac{\partial hv}{\partial y}, \quad (5.1.3a)$$

$$\frac{1}{h_M} \frac{\partial u}{\partial t} = -0.003 \frac{uq}{h} + \frac{0.993}{h_M} \left[\tan \theta - \frac{\partial h}{\partial x} \right] - 1.030u \frac{\partial u}{\partial x} - 1.020v \frac{\partial u}{\partial y} + 0.094qh \nabla^2 u, \quad (5.1.3b)$$

$$\frac{1}{h_M} \frac{\partial v}{\partial t} = -0.003 \frac{vq}{h} - \frac{0.993}{h_M} \frac{\partial h}{\partial y} - 1.030v \frac{\partial v}{\partial y} - 1.020u \frac{\partial v}{\partial x} + 0.094qh \nabla^2 v. \quad (5.1.3c)$$

The PDE (5.1.3a) represents the mass conservation, and the PDEs (5.1.3b) and (5.1.3c) represent the momentum equations in the x and y directions respectively. Simplified Smagorinski-based turbulent shallow water

The pdes represent the key physical mechanisms of quasi-hydrostatic acceleration, of advection, and of nonlinear bed drag and eddy diffusion.

PDES (5.1.3) are equations (11a)–(11c) of Bunder et al. (2020), but non-dimensionalised using $L/(2\pi)$ as reference length scale instead of their reference length H .

We use the simplified Smagorinski-based turbulent shallow water PDEs (5.1.3) as the micro-scale system within the patches in our study of the staggered patch schemes. In all our further use “turbulent shallow water PDEs” means these *simplified* Smagorinski-based turbulent shallow water PDEs (5.1.3). For the turbulent shallow water PDEs (5.1.3), throughout this chapter, we consider the boundary conditions that the three fields h , u and v are L -periodic in both x and y . 2\pi

rephrase to avoid overfull hbox

5.1.2 Full-domain micro-scale system and staggered patch schemes for turbulent shallow water PDEs

This subsection derives a full-domain micro-scale finite difference system for the turbulent shallow water PDEs (5.1.3) of §5.1.1.

x-ref the new earlier fig.

Approximating the spatial derivatives in the turbulent shallow water PDEs (5.1.3) by central finite differences on the nodes of the full-domain staggered grid (filled solid circles in ??), gives the *full-domain micro-scale system*

$$\bullet \frac{1}{h_M} \frac{dh_{i,j}}{dt} = -\frac{(h_{i,j} + h_{i+2,j}) u_{i+1,j} - (h_{i-2,j} + h_{i,j}) u_{i-1,j}}{4\delta} - \frac{(h_{i,j} + h_{i,j+2}) v_{i,j+1} - (h_{i,j-2} + h_{i,j}) v_{i,j-1}}{4\delta} \quad (5.1.4a)$$

for $i \in \{0, 2, 4, \dots, n-2\}$, $j \in \{0, 2, 4, \dots, n-2\}$;

$$\bullet \frac{1}{h_M} \frac{du_{i,j}}{dt} = -0.003 u_{i,j} \frac{\sqrt{u_{i,j}^2 + [(v_{i-1,j-1} + v_{i+1,j-1} + v_{i-1,j+1} + v_{i+1,j+1})/4]^2}}{(h_{i+1,j} + h_{i-1,j})/2} + \frac{0.993}{h_M} \left[\tan \theta - \frac{h_{i+1,j} - h_{i-1,j}}{2\delta} \right] - 1.03 u_{i,j} \frac{u_{i+2,j} - u_{i-2,j}}{4\delta} - 1.02 [(v_{i-1,j-1} + v_{i+1,j-1} + v_{i-1,j+1} + v_{i+1,j+1})/4] \frac{(u_{i,j+2} - u_{i,j-2})}{4\delta} + 0.094 \sqrt{u_{i,j}^2 + [(v_{i-1,j-1} + v_{i+1,j-1} + v_{i-1,j+1} + v_{i+1,j+1})/4]^2} \frac{h_{i-1,j} + h_{i+1,j}}{2} \left(\frac{u_{i-2,j} - 2u_{i,j} + u_{i+2,j}}{4\delta^2} + \frac{+u_{i,j-2} - 2u_{i,j} + u_{i,j+2}}{4\delta^2} \right) \quad (5.1.4b)$$

for $i \in \{1, 3, 5, \dots, n - 1\}$, $j \in \{0, 2, 4, \dots, n - 2\}$;

$$\bullet \frac{1}{h_M} \frac{dv_{i,j}}{dt} = -0.003 v_{i,j} \sqrt{\frac{v_{i,j}^2 + [(u_{i-1,j-1} + u_{i+1,j-1} + u_{i-1,j+1} u_{i+1,j+1}) / 4]^2}{(h_{i,j+1} + h_{i,j-1}) / 2}} \\ - \frac{0.993}{h_M} \frac{(h_{i,j+1} - h_{i,j-1})}{2\delta} - 1.03 v_{i,j} \frac{(v_{i,j+2} - v_{i,j-2})}{4\delta} \\ - 1.02 [(u_{i-1,j-1} + u_{i+1,j-1} + u_{i-1,j+1} u_{i+1,j+1}) / 4] \frac{(v_{i+2,j} - v_{i-2,j})}{4\delta} \\ + 0.094 \sqrt{[(u_{i-1,j-1} + u_{i+1,j-1} + u_{i-1,j+1} u_{i+1,j+1}) / 4]^2 + v_{i,j}^2} \\ \frac{h_{i,j-1} + h_{i,j+1}}{2} \left(\frac{v_{i-2,j} - 2v_{i,j} + v_{i+2,j}}{4\delta^2} + \frac{v_{i,j-2} - 2v_{i,j} + v_{i,j+2}}{4\delta^2} \right) \quad (5.1.4c)$$

for $i \in \{0, 2, 4, \dots, n - 2\}$, $j \in \{1, 3, 5, \dots, n - 1\}$.

Analogous to the periodic boundary conditions of the PDEs (5.1.3), the three fields h, u, v are n -periodic in both i and j , where $n = L/\delta$. Section 4.1.2 explains the discretisation involving averaging on the staggered grids for some of the similar terms for the viscous shallow water flow.

Substituting the solution of a steady uniform flow $h = h_M, u = u_M, v = v_M$ with mean height h_M and horizontal mean velocity u_M, v_M into the full-domain micro-scale system (5.1.4) and setting the time derivatives to zero gives the fixed points or the *equilibrium solution*

$$h = h_M, u = \sqrt{(0.993 \tan \theta) / 0.003}, v = 0, \quad (5.1.5)$$

for the full-domain micro-scale system (5.1.4) for the turbulent shallow water flow. The equilibrium solution (5.1.5) is also the equilibrium solution for the turbulent shallow water PDEs (5.1.3). The velocity $v = 0$ in the fixed point (5.1.5) is due to that the bed is sloping down only along x direction (e.g., Fig. 5.1.1). For a bed with a positive slope (downward inclination along x), the turbulent shallow water flow reaches the equilibrium velocity of the fixed point (5.1.5) when the bed drag and gravitational force are in balance. That is, larger the inclination, larger the equilibrium velocity is; for a horizontal bed, the only fixed point is stagnant water with $u = 0, v = 0$.

A full-domain micro-scale simulation is performed by numerical time-integration of the ODEs (5.1.4) on the nodes of the micro-scale staggered

if not using, use three separate math environments, one for each eqn. Also it is $h_{i,j}$ etc on the LHSs.

remember to separate equations on a displayed line by \quad space

x-ref earlier fig.

grid (filled solid circles in Fig. 4.1.1 of §4.1.2), with the discrete macro-scale n -periodic boundary conditions in both i and j .

Similar to the full-domain micro-scale system (4.1.11) of the viscous shallow water flow, the full-domain micro-scale system (5.1.4) of the turbulent shallow water flow also has terms involving average of the neighbouring values on the staggered grid. Based on the terms in the full-domain micro-scale system, p. 161 of §4.1.2 discusses the requirement of the number of layers of the edge nodes for a staggered patch grid, for the viscous shallow water flow. A similar study shows that, to use the finite difference equations (5.1.4) of the turbulent shallow water flow as the micro-scale system within the patches, a staggered patch grid requires two layers of edge nodes in the normal direction to the edges, and one layer of edge nodes in the tangential direction to the edges, as in Fig. 4.1.2b (same patch grid required for the viscous shallow water flow). Throughout this chapter, *for the turbulent shallow water flow, the staggered patch schemes use the patch grid in Fig. 4.1.2b.*

Using the full-domain micro-scale system (5.1.4) within the patches of a suitable staggered patch grid (e.g., patch grid of Fig. 4.1.2b with $n = 6$), gives the *staggered patch scheme* on the patch interior nodes, whose equations are same as (5.1.3) with patch index I, J as the superscript in each of the terms. Analogous to the periodic boundary conditions for the full-domain micro-scale system (5.1.4), the three fields h, u, v in the patch scheme are macro-scale N -periodic in both I and J , where $N = L/\Delta$. For the staggered patch grid in Fig. 4.1.2b, the left and right edge values are $\circ h_{i,j}^{I,J}$, $\circ u_{i,j}^{I,J}$, $\circ v_{i,j}^{I,J}$, for $i \in \{-1, 0, n, n+1\}$ and $j \in \{0, 1, 2, \dots, n-1, n\}$. Similarly the bottom and top edge value indices are $i \in \{0, 1, 2, \dots, n-1, n\}$ and $j \in \{-1, 0, n, n+1\}$. A specific patch coupling (e.g., Square-p4) computes patch edge values ($\circ h_{i,j}^{I,J}, \circ u_{i,j}^{I,J}, \circ v_{i,j}^{I,J}$ in Fig. 4.1.2a) from the centre values of neighbouring patches ($\bullet h_{i,j}^{I,J}, \bullet u_{i,j}^{I,J}, \bullet v_{i,j}^{I,J}$ with $i = j = n/2$ in Fig. 4.1.2a). The patch coupling provides a mechanism whereby patches influence each other, §2.3 discusses various details of different patch couplings.

Patch scheme simulation is performed by numerical time-integration of the ODEs ?? on the interior nodes of the staggered patch grid (filled solid circles in Fig. 4.1.2b), with the discrete macro-scale N -periodic boundary conditions in both I and J . As in §2.2.2, evaluating the time derivatives in the staggered patch scheme is done in two steps: first, edge values $x^E(x^I)$ are computed via patch coupling; second, using both interior and edge values of each patch in the staggered patch grid, the time derivatives of x^I are computed for the full-domain micro-scale system (5.1.4) of turbulent shallow water flow.

(5.1.4)

$\circ h_{i,j}^{I,J}$ on each

Table 5.1.1: Approximate dimensional parameter ranges relevant for the turbulent shallow water equations for simulating floods and tsunamis. The domain size L is constrained to be within the shallow water regime ($H/L \in [1/100, 1/20]$).

Parameter	Range of values
characteristic mean water height H	1 to 10 m
characteristic flow velocity U	0.1 to 5 m/s
domain size L, depending on H (i.e., $H/L \in [1/100, 1/20]$)	20 m to 1000 m

5.1.3 Selection of relevant parameter regime for patch scheme exploration

We propose that

Large-scale turbulent waves of floods and tsunamis are among the main application areas of the patch schemes. The characteristic parameter values (such as the mean water height H, flow velocity U and the bed inclination angle θ) of the floods are within the range of the parameters of tsunamis; for example Cohen et al. (2019) gives a typical range of flood water heights. Hence we choose the range of parameters primarily based on the relevant parameters of tsunamis.

important

- Ghobarah, Saatcioglu, and Nistor (2006) reports various field investigations of the 26 December 2004 tsunami in Thailand and Indonesia. In page 314, they list various wave run-up heights approximately ranging 1 m to 49 m. Röbke and Vött (2017, p.298) and IOC (2014, p.4) present the various depths (characteristic mean height H) and instantaneous velocities relevant for the Tsunami wave shoaling from deep sea to the shore. With our focus on the tsunami waves near the shore, and based on the range of the heights in these articles (Ghobarah, Saatcioglu, and Nistor 2006, p.314; Röbke and Vött 2017, p.298; IOC 2014, p.4), we choose the range of characteristic mean heights H from 1 m to 10 m.
- Based on the typical instantaneous velocity of the Tsunami wave near the shore from Röbke and Vött (2017, p.298) and IOC (2014, p.4), our focus is on the range of instantaneous velocities from 1 m/s to 10 m/s. Hence we choose the range of characteristic mean velocities U from 0.1 m/s to 5 m/s to cover both floods and tsunamis.

to explore

Table 5.1.1 lists the dimensional parameter ranges we choose for the turbulent shallow water equations. The non-dimensional parameter ranges we

Table 5.1.2: Approximate non-dimensional parameter ranges for general study of the patch schemes for turbulent shallow water equations corresponding to the dimensional parameter ranges in [Table 5.1.1](#).

Parameter	Range of values
characteristic mean non-dimensional height $h_M = 2\pi H/L$	$0.05 \approx 2\pi/100$ to $0.3 \approx 2\pi/20$
characteristic mean non-dimensional velocity $u_M = U/\sqrt{g_z H}$	0.03 to 0.5
bed inclination angle θ	-10° to 10°

choose roughly corresponding to the dimensional parameters in [Table 5.1.1](#) are listed in [Table 5.1.2](#):

- Characteristic non-dimensional mean height $h_M = 2\pi H/L$ is so as to be within the shallow water regime ($H/L \in [1/100, 1/20]$).
- Characteristic non-dimensional velocity $u_M = U/\sqrt{g_z H}$ is computed by non-dimensionalising using the long wave speed $\sqrt{g_z H}$ (Cao and Roberts 2016, p.190) for the respective dimensional mean water heights H .
- We choose the range of bed inclination angle θ (positive downwards) to be from -10° to 10° , mainly for exploring the patch scheme simulations in time domain. But, as θ enters into the turbulent shallow water equation via a constant term, the Jacobian of the linearised the turbulent shallow water equation are independent of the bed inclination angle θ . Hence, for our study of eigenvalues for stability and consistency of the patch schemes, we use the simple case of horizontal bed with $\theta = 0$.

5.2 Staggered patch schemes are accurate

Following [§4.2](#) for the viscous shallow water flow, this [§5.2](#) shows that the developed five staggered patch schemes are accurate for the turbulent shallow water flows. As in [§4.2](#), we establish the accuracy of the staggered patch schemes globally (as opposed one initial condition) by comparing the eigenvalues of the staggered patch schemes with the eigenvalues of fine- and coarse-grid full-domain micro-scale system, and for completeness also compare with the eigenvalues of the turbulent shallow water PDEs [\(5.1.3\)](#). The eigenvalue analysis for accuracy in this section is done for

there is no Reynolds number for Smag model.

a representative subset of the system parameters (**Reynolds number Re** and mean flow h_M, u_M, v_M) and the grid parameters (macro-grid intervals N , sub-patch micro-grid intervals n , patch scale ratio r). [Section 5.4](#) on the consistency of the patch schemes establish the accuracy over a wider range of parameters.

The approach of studying the accuracy of the staggered patch schemes and the conventions are same as discussed in [§4.2](#) for the viscous shallow water flows. The eigenvalues of the staggered patch schemes consist of the two scales.

1. The *macro-scale* eigenvalues are those that correspond to the small wavenumber macro-scale modes over the domain.
2. The *micro-scale* eigenvalues are those that correspond to large wavenumber micro-scale sub-patch modes.

As defined in [§4.2](#), the staggered patch schemes are accurate when the macro-scale eigenvalues of that patch scheme agree closely with the corresponding macro-scale eigenvalues of the full-domain micro-scale system. Hence, in the eigenvalue analysis for accuracy in this section, we compare in the complex plane the eigenvalues of the staggered patch schemes with the eigenvalues of the full-domain micro-scale system.

As in [§4.2](#), we follow the method of substituting an arbitrary Fourier mode into the governing partial/ordinary differential equations to derive the eigenvalues in [§§5.2.1](#) to [5.2.3](#). [Sections 5.2.1](#) to [5.2.3](#) derive the eigenvalues for

1. the 2D turbulent shallow water PDEs [\(5.1.3\)](#),
2. the full-domain micro-scale system [\(5.1.4\)](#), and
3. the staggered patch scheme.

To numerically compute the eigenvalues of the numerical staggered patch scheme, which includes any instabilities and inaccuracies due to the numerical roundoff errors, we numerically differentiate the evolution function as discussed in [§§4.2.4](#) and [4.2.5](#) for the viscous shallow water flows.

[Section 5.??](#)

[Section 4.2.6](#) compares and contrasts various eigenvalues (e.g., analytic and numerical eigenvalues of the PDEs, full-domain micro-scale system, and patch schemes) to demonstrate the accuracy of the patch schemes. We use the same notational convention as in [§4.2](#) to identify the various eigenvalues.

5.2.1 Eigenvalue analysis of the PDEs

Following the same approach of §4.2.1 for the viscous shallow water flows, substituting the Fourier mode (4.2.1) into the turbulent shallow water PDEs (5.1.3), followed by linearisation and algebraic simplifications give an eigensystem with the Jacobian $\mathbf{J}(\mathbf{x}_M)$ about the linearisation point of mean flow $\mathbf{x}_M = (h_M, u_M, v_M)$. The elements of the 3×3 Jacobian $\mathbf{J}(\mathbf{x}_M)$ of the 2D turbulent shallow water PDEs (5.1.3) are

$$\mathbf{J}_{1,1} = -i h_M u_M k_x - i h_M v_M k_y, \quad (5.2.1a)$$

$$\mathbf{J}_{1,2} = -i h_M^2 k_x, \quad (5.2.1b)$$

$$\mathbf{J}_{1,3} = -i h_M^2 k_y, \quad (5.2.1c)$$

$$\mathbf{J}_{2,1} = -0.993 i k_x + \frac{0.003 u_M q_M}{h_M}, \quad (5.2.1d)$$

$$\mathbf{J}_{2,2} = -0.094 h_M^2 q_M k_x^2 - 0.094 h_M^2 q_M k_y^2$$

$$- 1.030 i h_M u_M k_x - 1.020 i h_M v_M k_y \\ - 0.003 q_M - \frac{0.003 u_M^2}{q_M}, \quad (5.2.1e)$$

$$\mathbf{J}_{2,3} = -\frac{0.003 u_M v_M}{q_M}, \quad (5.2.1f)$$

$$\mathbf{J}_{3,1} = -0.993 i k_y + \frac{0.003 v_M q_M}{h_M}, \quad (5.2.1g)$$

$$\mathbf{J}_{3,2} = -\frac{0.003 u_M v_M}{q_M}, \quad (5.2.1h)$$

$$\mathbf{J}_{3,3} = -0.094 h_M^2 q_M k_x^2 - 0.094 h_M^2 q_M k_y^2$$

$$- 1.020 i h_M u_M k_x - 1.030 i h_M v_M k_y \\ - 0.003 q_M - \frac{0.003 v_M^2}{q_M}. \quad (5.2.1i)$$

Similar to the Jacobian in the eigensystem (4.2.4) for the viscous shallow water flow, the Jacobian $\mathbf{J}(\mathbf{x}_M)$ for the nonlinear turbulent shallow water flow depends on the wavenumber (k_x, k_y) and the linearisation point $\mathbf{x}_M = (h_M, u_M, v_M)$, which is the mean flow state.

For various macro-scale wavenumbers, we compute the eigenvalues of the numerically evaluated Jacobian $\mathbf{J}(\mathbf{x}_M)$, and compare for a sanity check with the eigenvalues of the full domain micro-scale system and the patch schemes while assessing the accuracy of the patch schemes in §5.2.4.

say "proportional to
 $\exp[i(k_{xx}+k_{yy})]$ "

5.2.2 Eigenvalue analysis of staggered grid full-domain micro-scale system

Following the same approach of §4.2.2 for the full-domain micro-scale system of the viscous shallow water flows, substituting the discrete Fourier mode (4.2.6) into the full-domain micro-scale system (5.1.4) of turbulent shallow water flows, followed by linearisation and algebraic simplifications give an eigensystem with the Jacobian $\mathbf{J}(\mathbf{x}_M)$ about the linearisation point of mean flow $\mathbf{x}_M = (h_M, u_M, v_M)$. The elements of the 3×3 Jacobian $\mathbf{J}(\mathbf{x}_M)$ of the full-domain micro-scale system (5.1.4) are

$$\mathbf{J}_{1,1} = -i h_M u_M \frac{\sin(2\delta k_x)}{2\delta} - i h_M v_M \frac{\sin(2\delta k_y)}{2\delta}, \quad (5.2.2a)$$

$$\mathbf{J}_{1,2} = -i h_M^2 \frac{\sin(\delta k_x)}{\delta}, \quad (5.2.2b)$$

$$\mathbf{J}_{1,3} = -i h_M^2 \frac{\sin(\delta k_y)}{\delta}, \quad (5.2.2c)$$

$$\mathbf{J}_{2,1} = -0.993i \frac{\sin(\delta k_x)}{\delta} + \frac{0.003u_M q_M}{h_M} \cos(\delta k_x), \quad (5.2.2d)$$

$$\begin{aligned} \mathbf{J}_{2,2} = & -0.094h_M^2 q_M \left[\frac{\sin(\delta k_x)}{\delta} \right]^2 - 0.094h_M^2 q_M \left[\frac{\sin(\delta k_y)}{\delta} \right]^2 \\ & - 1.030i h_M u_M \frac{\sin(2\delta k_x)}{2\delta} - 1.020i h_M v_M \frac{\sin(2\delta k_y)}{2\delta} \\ & - 0.003q_M - \frac{0.003u_M^2}{q_M}, \end{aligned} \quad (5.2.2e)$$

$$\mathbf{J}_{2,3} = -\frac{0.003u_M v_M}{q_M} \cos(\delta k_x) \cos(\delta k_y), \quad (5.2.2f)$$

$$\mathbf{J}_{3,1} = -0.993i \frac{\sin(\delta k_y)}{\delta} + \frac{0.003v_M q_M}{h_M} \cos(\delta k_y), \quad (5.2.2g)$$

$$\mathbf{J}_{3,2} = -\frac{0.003u_M v_M}{q_M} \cos(\delta k_x) \cos(\delta k_y), \quad (5.2.2h)$$

$$\begin{aligned} \mathbf{J}_{3,3} = & -0.094h_M^2 q_M \left[\frac{\sin(\delta k_x)}{\delta} \right]^2 - 0.094h_M^2 q_M \left[\frac{\sin(\delta k_y)}{\delta} \right]^2 \\ & - 1.020i h_M u_M \frac{\sin(2\delta k_x)}{2\delta} - 1.030i h_M v_M \frac{\sin(2\delta k_y)}{2\delta} \\ & - 0.003q_M - \frac{0.003v_M^2}{q_M}, \end{aligned} \quad (5.2.2i)$$

$$(5.2.2j)$$

say "proportional to
 $\exp[i\delta(k_x + k_y)]"$

As in §4.2.2, as the grid interval $\delta \rightarrow 0$ and/or the wavenumber $(k_x, k_y) \rightarrow$

$(0, 0)$, the Jacobian elements (5.2.2) of the full-domain micro-scale system converge to the Jacobian elements (5.2.1) of the turbulent shallow water PDEs. Hence, the eigenvalues of the full-domain micro-scale system (5.1.4) converge to the analytic eigenvalues of the PDEs (5.1.3) as we decrease the grid interval δ and/or wavenumber (k_x, k_y) .

We compute the eigenvalues λ_m^{NE1} of the numerically evaluated Jacobian $\mathbf{J}(\mathbf{x}_M)$ for specific wavenumber and the linearisation point \mathbf{x}_M . As in §4.2.2, when we compute the eigenvalues λ_m^{NE1} of the full-domain micro-scale system,

- for the same grid-spacing δ as the sub-patch micro-grid interval (also called δ), we call the eigenvalues $\lambda_{m\delta}^{NE1}$,
- for the same grid-spacing Δ as the inter-patch distance Δ , we call the eigenvalues $\lambda_{m\Delta}^{NE1}$.

For various macro-scale wavenumbers, we compute the eigenvalues of the numerically evaluated Jacobian $\mathbf{J}(\mathbf{x}_M)$, and compare with the eigenvalues of the turbulent shallow water PDEs and the patch schemes while assessing the accuracy (§5.2.4) and stability (§5.3) of the patch schemes.

5.2.3 Analytic eigenvalue analysis of staggered patch schemes

This subsection derives analytic eigenvalues of a generic staggered patch scheme over a staggered patch grid, for the 2D turbulent shallow water PDEs (5.1.3). We use the patch scheme eigenvalues to assess accuracy (§5.2.4), stability (§5.3), and consistency (§5.4) of the staggered patch schemes.

The staggered patch schemes for turbulent shallow water flow uses the same patch grid as viscous shallow water flow, as in Fig. 4.1.2b, with two layers of edge nodes in normal direction to the edges, one layer of edge nodes in tangential direction to the edges. Page 161 of §4.1.2 discusses why the staggered patch grid with such edge node arrangement is required for the viscous shallow water flow, the same arguments apply for the turbulent shallow water flow.

Following the same approach of §4.2.3 for the viscous shallow water flow, substituting the patch scheme Fourier mode (4.2.13) into the patch scheme equations (equations (5.1.4) with the patch index I, J in superscript) for the turbulent shallow water flow, followed by linearisation and algebraic simplifications give an eigensystem (e.g., eigensystem (4.2.17)) with the one-cell analytic Jacobian $\mathbf{J}(\mathbf{x}_M)$ for the patch scheme about the linearisation

point of mean flow $\mathbf{x}_M = (h_M, u_M, v_M)$. The only system parameter in the patch scheme for turbulent shallow water flow is the bed inclination angle θ . The system parameter θ occurs only as a constant term $0.993 \tan \theta$ (without being multiplied by a state value) in the equations **?????** Hence, none of the Jacobian elements depend on the system parameter θ .

For example, similar to the case of general linear wave and viscous shallow water flow, for $n = 6$ sub-patch grid intervals, the one-cell Jacobian $\mathbf{J}(\mathbf{x}_M)$ for the turbulent shallow water flow, is a 59×59 sparse matrix generally with only 318 of the 3481 elements being nonzero irrespective of the particular patch coupling interpolation of the staggered patch schemes (i.e., same for both the spectral patch scheme and all the polynomial patch schemes). For some particular combination of numerical values of the parameters the sparsity is higher. The 318 nonzero elements of the one-cell Jacobian of a staggered patch scheme (for $n = 6$) contain all the information about the underlying micro-scale system and the patch coupling, for the macro-scale wave of wavenumber (k_x, k_y) . A few elements of the one-cell Jacobian of the simplest staggered patch scheme Square-p2 are,

You could easily omit all this and next pages. It is of minor interest, and closely parallels what you have previously reported. Just say the Jacobians "are like Ch.4 ... but with differences due to the different nonlinearities. The increasing complexity with order of interpolation is also the same."

$$\begin{aligned}\mathbf{J}_{1,1} &= 0, \quad \mathbf{J}_{1,16} = -\frac{h_M^2}{2\delta}, \quad \mathbf{J}_{4,10} = \frac{h_M^2}{2\delta}, \quad \mathbf{J}_{12,11} = \frac{0.255h_Mv_M}{\delta} + \frac{0.0235h_M^2q_M}{\delta^2} \\ \mathbf{J}_{16,16} &= -\frac{0.003u_M^2}{q_M} - 0.003q_M - \frac{0.094h_M^2q_M}{\delta^2}, \\ \mathbf{J}_{18,36} &= \left(\frac{0.1288h_Mv_M}{\delta} + \frac{0.0118h_M^2q_M}{\delta^2} + \frac{0.3862h_Mv_M}{\Delta} + \frac{0.0352h_M^2q_M}{\Delta\delta} \right) e^{-2\Delta i k_y} \\ &\quad + \frac{0.1288h_Mv_M}{\delta} + \frac{0.0118h_M^2q_M}{\delta^2} - \frac{0.3862h_Mv_M}{\Delta} - \frac{0.0352h_M^2q_M}{\Delta\delta} \\ \mathbf{J}_{46,36} &= \left(-\frac{h_M^2}{8\delta} - \frac{h_M^2}{2\Delta} - \frac{3\delta h_M^2}{8\Delta^2} \right) e^{2\Delta i k_x} + \left(-\frac{h_M^2}{8\delta} + \frac{h_M^2}{2\Delta} - \frac{3\delta h_M^2}{8\Delta^2} \right) e^{-2\Delta i k_y} \\ &\quad + \left(-\frac{h_M^2}{8\delta} + \frac{h_M^2}{4\Delta} + \frac{3\delta h_M^2}{8\Delta^2} \right) e^{2\Delta i k_x - 2\Delta i k_y} - \frac{h_M^2}{8\delta} - \frac{h_M^2}{4\Delta} + \frac{3\delta h_M^2}{8\Delta^2} \\ \mathbf{J}_{50,51} &= \left(-\frac{0.255h_Mv_M}{\Delta} - \frac{0.0235h_M^2q_M}{\Delta\delta} + \frac{0.51\delta h_Mv_M}{\Delta^2} + \frac{0.047h_M^2q_M}{\Delta^2} \right) e^{2\Delta i k_y} \\ &\quad + \left(\frac{0.255h_Mv_M}{\Delta} + \frac{0.0235h_M^2q_M}{\Delta\delta} + \frac{0.51\delta h_Mv_M}{\Delta^2} + \frac{0.047h_M^2q_M}{\Delta^2} \right) e^{-2\Delta i k_y} \\ &\quad + \frac{0.047h_M^2q_M}{\delta^2} - \frac{1.02\delta h_Mv_M}{\Delta^2} - \frac{0.094h_M^2q_M}{\Delta^2}.\end{aligned}$$

The example expressions for $\mathbf{J}_{1,16}$, $\mathbf{J}_{4,10}$, $\mathbf{J}_{12,11}$ and $\mathbf{J}_{16,16}$ are independent of the macro-scale wavenumber (k_x, k_y) and macro-grid interval Δ and

hence characterise the micro-scale flow physics:

- $\mathbf{J}_{1,16}, \mathbf{J}_{4,10}$ characterise the micro-scale flow physics;
- $h_M^2 q_M / \delta^2$ in $\mathbf{J}_{12,11}$ characterise the micro-scale viscous diffusion, for general linear wave $\mathbf{J}_{12,11} = c_V / (4\delta^2)$ in p. 57 of §3.2.3;
- $\mathbf{J}_{16,16}$ characterise the micro-scale drag ($-0.003u_M^2/q_M - 0.003q_M$) and viscous diffusion ($h_M^2 q_M / \delta^2$), for general linear wave the element $\mathbf{J}_{16,16} = -c_D - c_V / \delta^2$.

All the nonzero diagonal elements of the Jacobian elements are precisely the same for the turbulent shallow water flow, similar to the Jacobian elements of the general linear wave (i.e., expression (3.2.17) in p. 57 of §3.2.3) and the viscous shallow water flow (i.e., expression (4.2.18) in p. 180 of §4.2.3). That is, all the nonzero diagonal elements

$$\mathbf{J}_{i,i} = -\frac{0.003u_M^2}{q_M} - 0.003q_M - \frac{0.094h_M^2 q_M}{\delta^2} \quad (5.2.3)$$

for $i \in \{10, 11, \dots, 21, 28, 29, \dots, 40, 47, 48, \dots, 59\}$.

The first terms in the RHS of the micro-scale system (5.1.4b) and (5.1.4c) (also patch scheme) with a coefficient -0.003 are drag terms. After linearisation, these drag terms become $-0.003 u_{i,j}^{1,1} u_M^2 / q_M - 0.003 q_M$ and $-0.003 v_{i,j}^{1,1} v_M^2 / q_M - 0.003 q_M$ respectively. These drag terms involving only the constant and the respective velocities, contribute only to the diagonal elements of the Jacobian, without depending on macro-grid interval Δ , patch scale ratio r and the patch coupling.

The example expressions for $\mathbf{J}_{18,36}$, $\mathbf{J}_{46,36}$ and $\mathbf{J}_{50,51}$ depend on the macro-scale wavenumber (k_x, k_y) and macro-grid interval Δ and hence characterise the macro-scale flow physics:

- Expressions for $\mathbf{J}_{18,36}$ and $\mathbf{J}_{50,51}$ characterise macro-scale wave with only viscous diffusion;
- $\mathbf{J}_{46,36}$ characterises a macro-scale wave without any dissipation.

The 2Δ in the argument of the exponential factors in $\mathbf{J}_{18,36}$, $\mathbf{J}_{46,36}$, and $\mathbf{J}_{50,51}$ indicate the patch coupling influence by the patches in surrounding macro-cells which are 2Δ away from the centre macro-cell. Compared to the listed example Jacobian elements of the simple patch coupling Square-p2, more surrounding macro-cells influence the Jacobian elements for the cases of patch coupling with higher order interpolations (Square-p4, Square-p6,

and Square-p8). Hence the expressions for the one-cell Jacobian elements are much longer than the listed example expressions.

Due to the large Jacobian size (e.g., 59×59 for $n = 6$) and the long expressions in their elements, all the CAS packages we tried (Sympy, Reduce and Maple) fail to compute the analytic eigenvalues of the one-cell Jacobian, even for the simplest staggered patch scheme Square-p2 with $n = 6$ sub-patch micro-grid intervals. So we numerically evaluate the one-cell Jacobian for numerical values of $\Delta, \delta, h_M, u_M, v_M, k_x, k_y$ and compute the eigenvalues λ_p^{NE1} . We compare with the eigenvalues λ_p^{NE1} of the numerically evaluated one-cell Jacobian of the patch schemes, with the eigenvalues of the full domain micro-scale system and the eigenvalues of the general linear wave PDEs, while assessing the accuracy ([§5.2.4](#)) and stability ([§5.3](#)) of the patch schemes.

5.2.4 Staggered patch schemes are accurate for macro-scale waves

Similar to [§§3.2.6](#) and [4.2.6](#) for the general linear wave and viscous shallow water flow, this section explains the qualitative structure of the staggered patch scheme eigenvalues and eigenvectors, and qualitatively demonstrate the accuracy of the staggered patch schemes for the *turbulent shallow water flow* for few representative cases. [Section 5.4](#) on the consistency of the staggered patch schemes, quantitatively establish the patch scheme accuracy in more detail, over a much broader range of parameters.

Similar to [§§3.2.6](#) and [4.2.6](#), this section demonstrates the accuracy of the developed five staggered patch schemes (Spectral, Square-p2, Square-p4, Square-p6, and Square-p8) by comparing the following eigenvalues in complex plane plots.

1. Eigenvalues λ_p^N of the numerical Jacobian of a staggered patch scheme on a finite domain (e.g., [§4.2.5](#)).
2. Eigenvalues λ_p^{NE1} of the numerically evaluated one-cell Jacobian in [§5.2.3](#), of a staggered patch scheme on an infinite domain.
3. Eigenvalues $\lambda_{m\delta}^{NE1}$ of the numerically evaluated analytic Jacobian in [§5.2.2](#), of fine-grid full-domain micro-scale system, with grid interval equal to the sub-patch grid interval δ . ~~We use the same symbol δ for the grid interval for both the full-domain micro-grid and the sub-patch micro-grid.~~

4. Eigenvalues $\lambda_{m\Delta}^{NE1}$ of the numerically evaluated analytic Jacobian in §5.2.2, of coarse grid version of the full-domain micro-scale system, with $\delta = \Delta$.
5. Eigenvalues λ_{PDE}^{NE1} of the numerically evaluated analytic Jacobian in §5.2.1, of turbulent shallow water PDEs (5.1.3). Comparison with the eigenvalues λ_{PDE}^{NE1} is only for completeness.

All the analytic eigenvalues ($\lambda_p^N, \lambda_p^{NE1}, \lambda_{m\delta}^N, \lambda_{m\Delta}^N, \lambda_{PDE}^{NE1}$) are numerically evaluated for all the $N^2/4$ *macro-scale wavenumbers* (k_x, k_y) resolved on a corresponding finite staggered patch grid with $N \times N$ macro-grid intervals. To illustrate the complete structure of eigenvalues (i.e., for all wavenumbers) of the full-domain micro-scale system and to cross-verify analytic and numerical computation of the full-domain micro-scale system eigenvalues, we also compute the eigenvalues of the numerical Jacobian of the full-domain micro-scale system for few cases (e.g., Figs. 5.2.1 and 5.2.2).

The sets of eigenvalues (e.g., $\lambda_p^N, \lambda_p^{NE1}, \lambda_{m\delta}^N, \lambda_{m\Delta}^N, \lambda_{PDE}^{NE1}$), in all the complex plane plots, are numbered in the legend entries on the left. In all the complex plane plots, system parameters for each of these eigenvalues are listed in groups *below the legend entries* in a style similar to listing author affiliations. Page 62 of §3.2.6 explains with an example, the conventions of this parameter listing.

Figures 5.2.1 and 5.2.2 plot the eigenvalues ($\lambda_p^N, \lambda_p^{NE1}$) of the Spectral patch scheme on a staggered patch grid with 6×6 macro-grid intervals ($N = 6$) and each patch containing 6×6 sub-patch micro-grid intervals ($n = 6$). Also plotted are the eigenvalues $\lambda_{m\delta}^N, \lambda_{m\Delta}^N$ of respectively the fine- and coarse-grid versions of the full-domain micro-scale system (5.1.4) and the eigenvalues λ_{PDE}^{NE1} of the PDE (5.1.3). Similar to Figs. 5.2.1 and 5.2.2, in all the complex plane eigenvalue plots, eigenvalues are grouped within clusters based on eigenvalues λ_p^{NE1} of the staggered patch scheme Jacobian. Each cluster is annotated with the number of eigenvalues λ_p^{NE1} in the cluster and the cluster number in the superscript.

Page 64 of §3.2.6 explains the rationale and utility of the arcsinh scaling. For example, the clusters of macro-scale eigenvalues on arcsinh scaling (i.e., clusters 1–7 in Fig. 5.2.2) reveal more details, compared to the clusters of macro-scale eigenvalues on linear scaling (i.e., cluster 1 in Fig. 5.2.1). Hence, *most complex plane eigenvalue plots in this thesis are on arcsinh scaling*. Specifically, the complex plane plots on arcsinh scaling, plot an eigenvalue λ as a point on a 2D space with coordinates $(\text{arcsinh}(S_h [\Re \lambda - O_h]) / S_h + O_h, \text{arcsinh}(S_v \Im \lambda) / S_v)$, where S_h, S_v are the horizontal and vertical scale factors and $(O_h, 0)$ is the the centre of zoom. In this chapter, most plots on arcsinh scaling use the scale factors $S_h = 10^4, S_v = 2000$ and the centre of

I still do not like this
O_h. I recommend
you omit.

used in Figure 5.2.2

Figure 5.2.1: Spectral staggered patch scheme ($N = 6, n = 6$) eigenvalues ($\lambda_p^N, \lambda_p^{N+1}$) on complex plane (*linear scale*) for turbulent shallow water flow. Due to large range of magnitudes of eigenvalues, details of eigenvalues for macro-scale modes (mid-right cluster 1) are not clear.

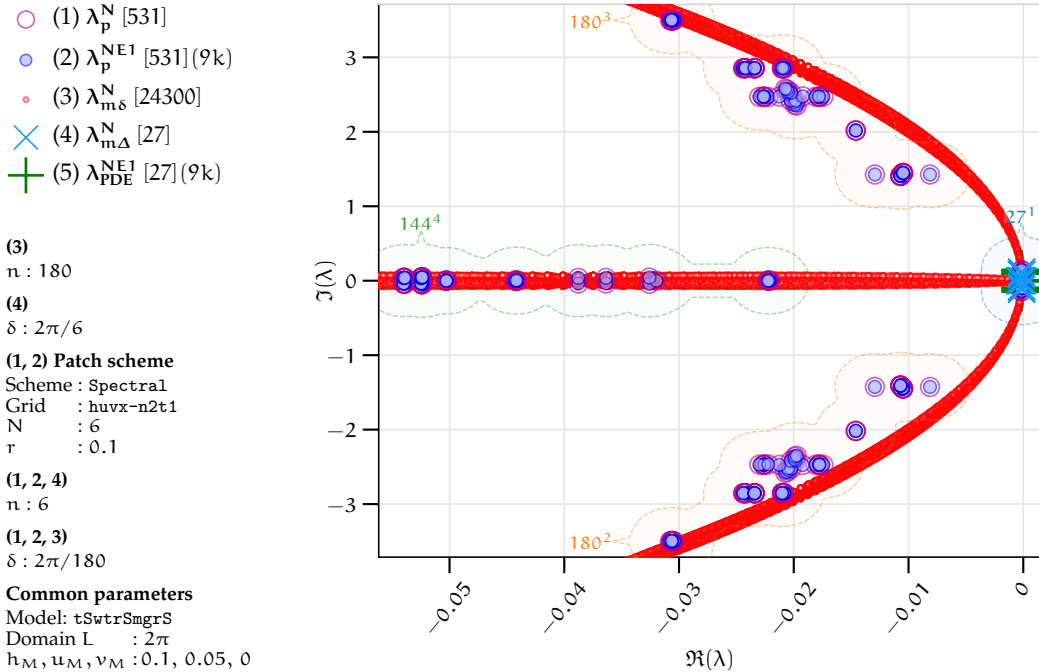
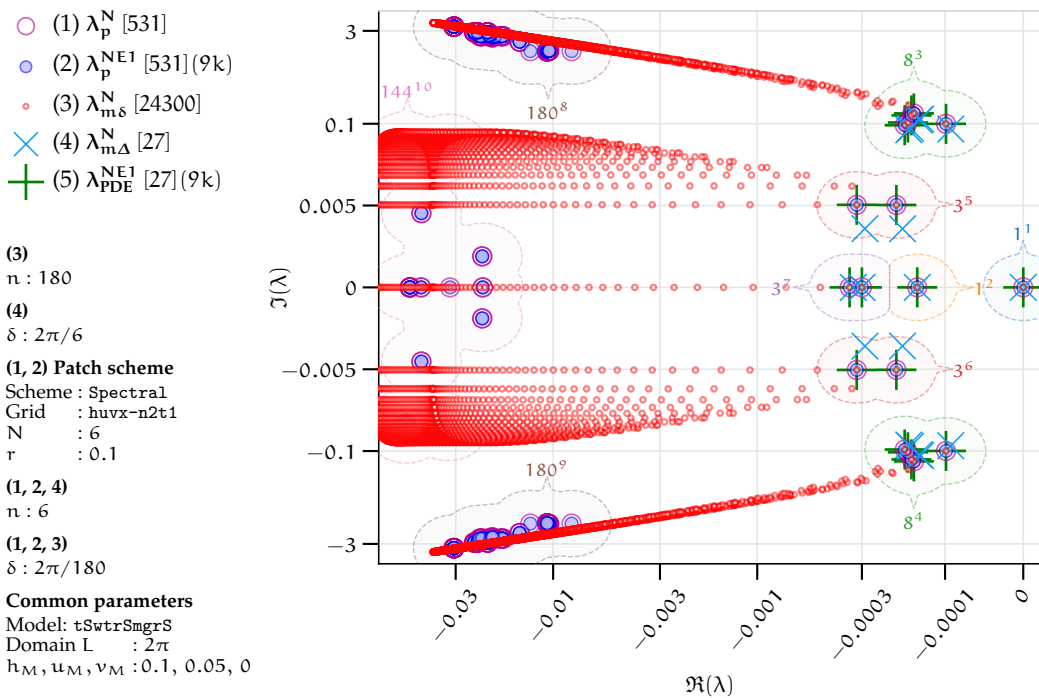


Figure 5.2.2: Spectral staggered patch scheme ($N = 6, n = 6$) eigenvalues ($\lambda_p^N, \lambda_p^{N+1}$) on complex plane (arcsinh *nonlinear scale*) for turbulent shallow water flow. The arcsinh scaling zooms out the eigenvalues of macro-scale modes (mid-right cluster 1 in Fig. 5.2.1 to clusters 1–7 here).



~~zoom~~ $(O_h, 0) = (0, 0)$ (different from those in §3.2.6 for general linear wave and §4.2.6 for viscous shallow water flow).

As Page 74 of §3.2.6 defines, a staggered patch scheme is accurate when the macro-scale eigenvalues (e.g., $\lambda_p^N, \lambda_{p\delta}^{NE1}$) of the staggered patch schemes are close to the macro-scale eigenvalues (e.g., $\lambda_{m\delta}^{NE1}$) of the corresponding fine-grid full-domain micro-scale system with the same grid interval as the sub-patch micro-grid interval. Figure 5.2.2 shows that, within the clusters 1–7 on the right, the numerical macro-scale eigenvalues λ_p^N of the patch scheme (large magenta circles) and the numerical macro-scale eigenvalues $\lambda_{m\delta}^N$ (small red circles) visually agree. That is the Spectral patch scheme accurately resolves the macro-scale waves.

As Fig. 5.2.2 shows, for both micro-scale and macro-scale modes, the patch scheme eigenvalues λ_p^{NE1} of the numerically evaluated one-cell analytic Jacobian (§5.2.3) and the patch scheme eigenvalues λ_p^N of the numerical Jacobian (e.g., §4.2.5), agree (i.e., the large magenta and blue circles). Hence, to avoid large computational effort and as the primary focus is on the macro-scale eigenvalues, all other complex plane plots in this subsection §5.2.4 use eigenvalues $\lambda_{m\delta}^{NE1}$ of the numerically evaluated analytic Jacobian (§5.2.2), as opposed to the numerical eigenvalues $\lambda_{m\delta}^N$.

~~Except the quantitative parameter dependence, the qualitative structure of the eigenvalues (e.g., in Fig. 5.2.2) of the turbulent shallow water flows are same as those of the viscous shallow water flows explained in p. 188 of §4.2.6.~~ The patch scheme eigenvectors of the turbulent shallow water flows are also qualitatively same as the eigenvectors in Figs. 3.2.13 to 3.2.18 (general linear wave) and Figs. 4.2.11 and 4.2.12 (viscous shallow water flow).

Sections 4.4 and 5.3 on patch scheme stability define *artificial instability* as a characteristic of a patch scheme to be *more unstable* than the corresponding full-domain micro-scale system. That is, a patch scheme is artificially unstable when the maximum real part of the patch scheme eigenvalues is positive and larger than the maximum real part of the the corresponding full-domain micro-scale system is stable. Unlike the general linear wave and the viscous shallow water flow, for $n = 6$ sub-patch micro-grid intervals, the staggered patch schemes for the turbulent shallow water flow have artificial instability for many combinations of the mean height h_M and horizontal mean velocities u_M, v_M . Figure 5.3.4 in p. 310 of §5.3 shows that $n = 10$ avoids such artificial instability. Hence, all the following complex plane plots in this subsection use $n = 10$ sub-patch micro-grid intervals.

Comparing macro-scale eigenvalues λ_p^{NE1} and $\lambda_{m\delta}^{NE1}$ the following two paragraphs show that the patch schemes are accurate for macro-scale turbulent shallow water flows for different linearisation points (h_M, u_M, v_M) , assuming $v_M = 0$ without loss of generality (§4.6 on frame invariance show

omit?

the flow direction is immaterial).

The staggered patch schemes are accurate for macro-scale turbulent shallow water flows of different mean velocity u_M . Except the quantitative parameter dependence, all the following points about the qualitative dependence of the turbulent shallow water flow on the mean velocity, are the same as those of the viscous shallow water flow in p. 193 of §4.2.6. Figures 5.2.3 to 5.2.6 plot the Spectral patch scheme ($N = 10, n = 10$) eigenvalues for different mean velocity $u_M = 10^{-5}, 0.05, 3, 5$ respectively, keeping $h_M = 0.1$ and $v_M = 0$. Whereas the following points are based on the Spectral patch scheme eigenvalues, they also hold for the polynomial patch schemes.

- Figures 5.2.3 to 5.2.6 show that for the different mean velocity of $u_M = 10^{-5}, 0.05, 3, 5$, the macro-scale eigenvalues λ_p^{NE1} of the Spectral patch scheme (large blue circles within macro-scale clusters identified in figure caption), agree with the macro-scale eigenvalues $\lambda_{m\delta}^{NE1}$ (small red circles) of the fine-grid full-domain micro-scale system. This macro-scale agreement of eigenvalues $\lambda_p^{NE1}, \lambda_{m\delta}^{NE1}$ indicates that the patch schemes are accurate for macro-scale turbulent shallow water flows for different mean velocity.

I do not think that you can call them "vortex" as they contain both vortex and wave modes. It is just that they are not discernably different in the plot. Maybe "combined vortex/wave modes"

- While increasing u_M from 10^{-5} to 5, as the previous paragraph explains, first the vortex modes (e.g., cluster 3 in Fig. 5.2.3) split into vortex modes and translatory wave modes (e.g., clusters 4, 5, 6 in Fig. 5.2.4), next the clusters of translatory wave modes distort and overlap with the clusters of the (dynamical/oscillatory) wave mode (e.g., clusters 5, 6 in Figs. 5.2.5 and 5.2.6).

I do not see this?? and I do not see that "translatory" has any meaning? Unless a wave is "standing", a wave is always translatory. Omit.

And even if "standing", a standing wave is just two ordinary waves travelling in opposite directions, combined. So do invoke "standing" either.

- The spectral gap (between the micro-scale and macro-scale patch scheme eigenvalues) decreases with increasing mean velocity u_M . For example, in Figs. 5.2.3 to 5.2.6 for mean velocities $u_M = 10^{-5}, 0.05, 3, 5$, the corresponding spectral gaps are 4841, 4661, 35, 11. This decreasing spectral gap with increasing u_M is the most prevalent trend among the various combinations of u_M , mean height h_M and patch scale ratio r . But, in general increasing u_M increases or decreases spectral gap depending upon the combinations of the grid parameters (N, n, r) and system parameters (h_M, u_M).

- Compared to the viscous shallow water flow in p. 193 of §4.2.6, increasing u_M decreases the spectral gap more rapidly. This rapid decrease in spectral gap is due to increasing real parts of the eigenvalues for some of the non-dissipating micro-scale modes such as clusters 7, 8, 9 in Figs. 5.2.5 and 5.2.6

These modes have real-part \approx -1 so they are dissipating. Revise.

I do not understand this physically. Increasing u_M , increases the bed drag faster than the effective viscosity increases and hence closes the gap. Where is any contrary evidence that the gap increases with u_M ??

Figure 5.2.3: Spectral staggered patch scheme ($N = 10, n = 10$) eigenvalues λ_p^{NE1} for turbulent shallow water flow for $(h_M, u_M, v_M) = (0.1, 10^{-5}, 0)$. Eigenvalues λ_p^{NE1} and $\lambda_{m\delta}^{NE1}$ of the fine-grid full-domain micro-scale system agree for macro-scale wavenumbers in clusters 1, 2, 3.

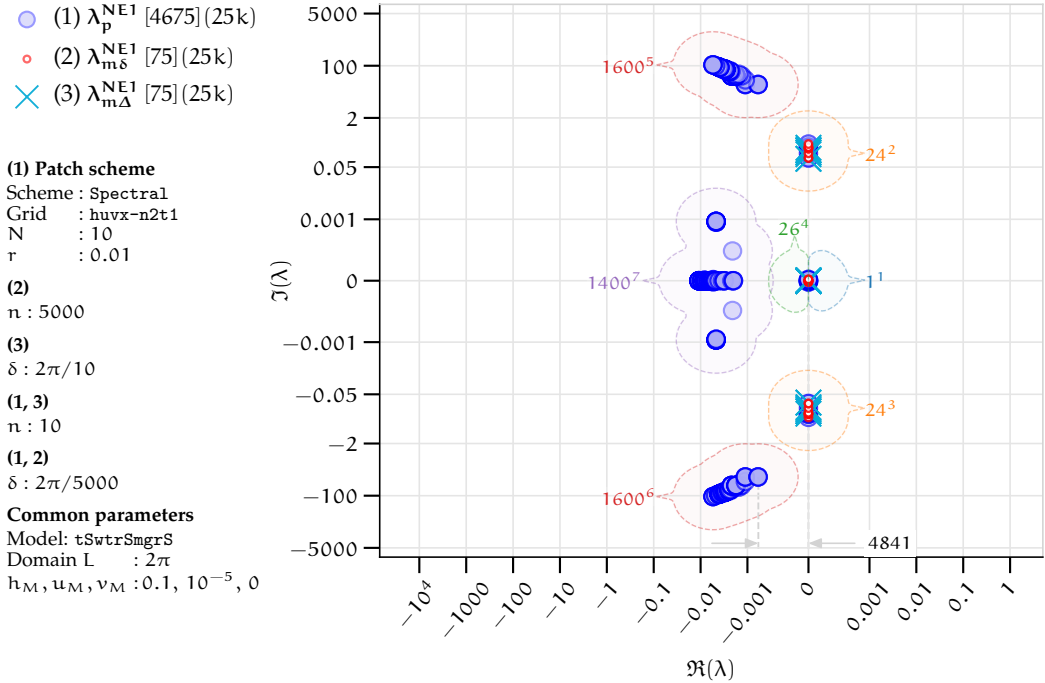


Figure 5.2.4: Spectral staggered patch scheme ($N = 10, n = 10$) eigenvalues λ_p^{NE1} for turbulent shallow water flow for $(h_M, u_M, v_M) = (0.1, 0.05, 0)$. Eigenvalues λ_p^{NE1} and $\lambda_{m\delta}^{NE1}$ of the fine-grid full-domain micro-scale system agree for macro-scale modes in clusters 1–6.

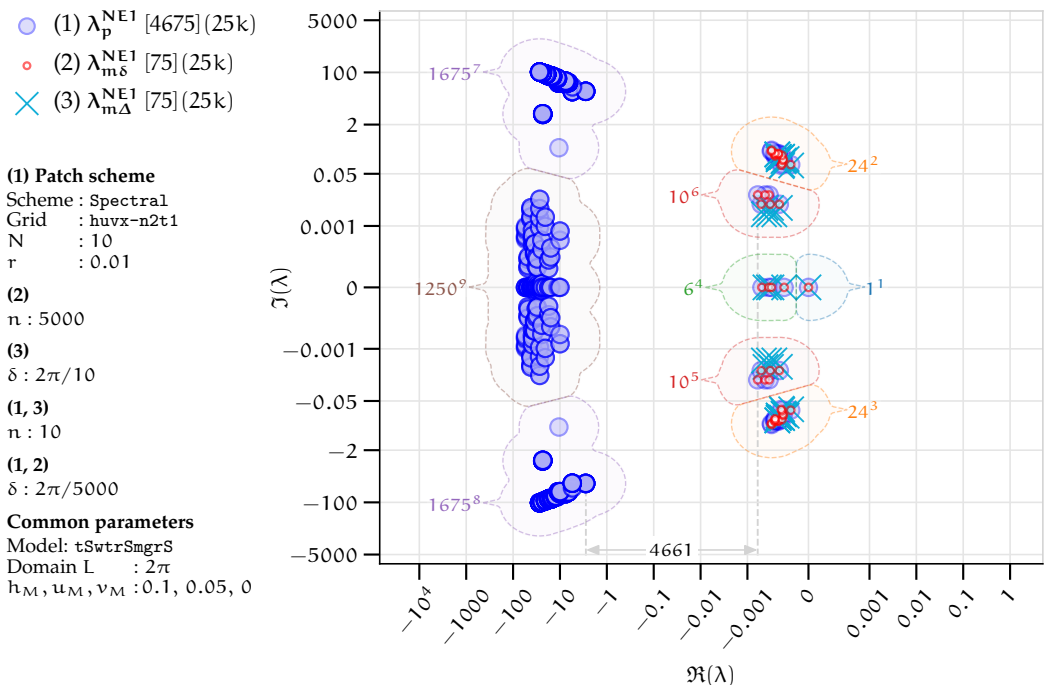


Figure 5.2.5: Spectral staggered patch scheme ($N = 10, n = 10$) eigenvalues λ_p^{NE1} for turbulent shallow water flow for $(h_M, u_M, v_M) = (0.1, 3, 0)$. Eigenvalues λ_p^{NE1} and $\lambda_{m\delta}^{NE1}$ agree for macro-scale modes in clusters 1–6. Physically unstable macro-scale wave modes in clusters 1, 2.

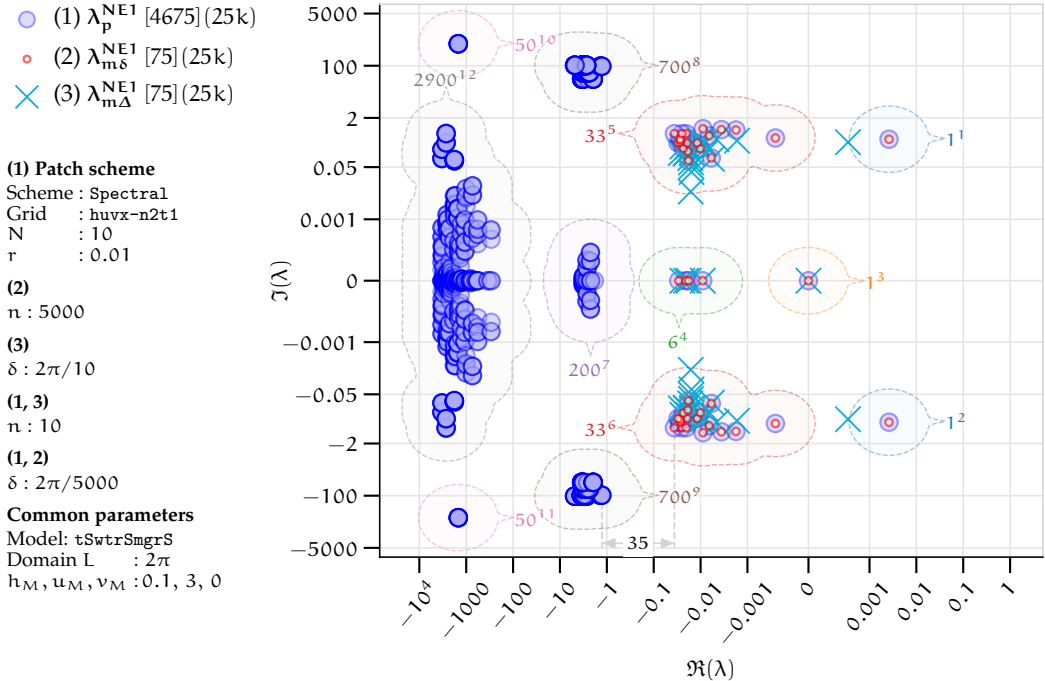
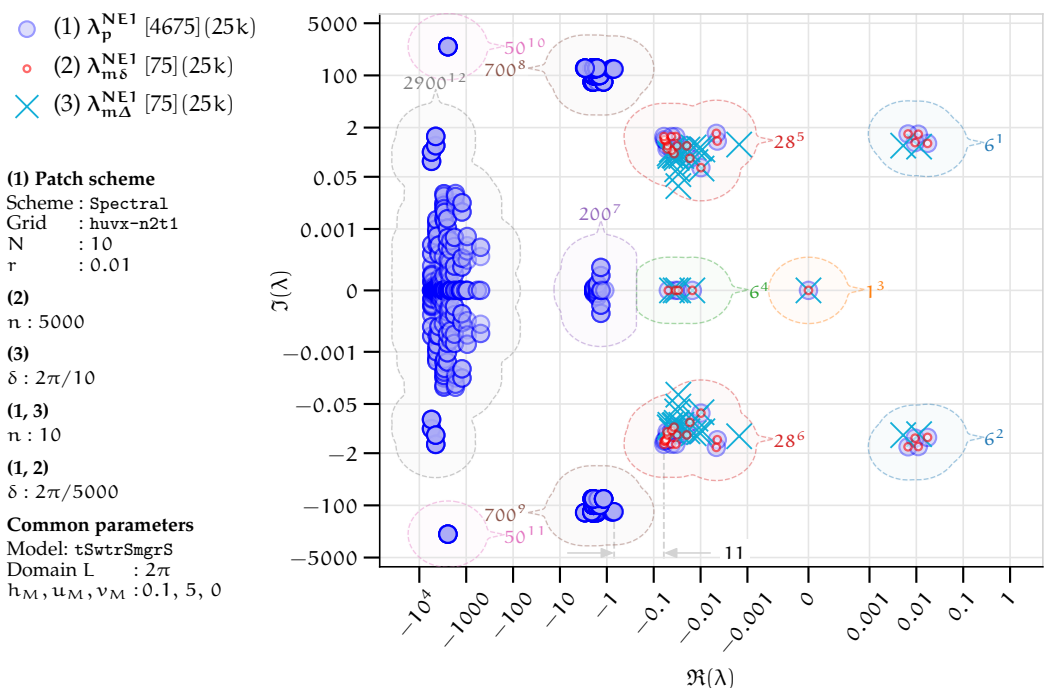


Figure 5.2.6: Spectral staggered patch scheme ($N = 10, n = 10$) eigenvalues λ_p^{NE1} for turbulent shallow water flow for $(h_M, u_M, v_M) = (0.1, 5, 0)$. Eigenvalues λ_p^{NE1} and $\lambda_{m\delta}^{NE1}$ agree for macro-scale modes in clusters 1–6. Physically unstable macro-scale wave modes in clusters 1, 2.



- For large mean velocity $u_M \gtrsim 2$, the turbulent shallow water flow has inherent physical instability, that is, full-domain micro-scale system itself is unstable. Such physical instability is evident from the positive real part eigenvalues of the full-domain micro-scale system in **Figs. 5.2.5 and 5.2.6** (clusters 1,2). **Section 4.4.1** shows the detailed trends of such physical instabilities as captured by the patch scheme for a wide range of parameters such as h_M, u_M, N, r, n .

Put this first in the sentence: "Figs... show the ..."

Clarify the qualitative trends are the same for Smag model, or

The staggered patch schemes are accurate for macro-scale viscous shallow water flows for different mean height h_M . **Figs. 5.2.5, 5.2.7** and **5.2.8** plot the Spectral patch scheme ($N = 10, n = 10$) eigenvalues for different mean heights $h_M = 0.1, 0.2, 0.3$ respectively, keeping $u_M = 3$ and $v_M = 0$. The following points summarise the key dependence of the patch scheme eigenvalues on increasing mean height h_M . All the characteristics in the following listing also hold for the polynomial patch schemes.

- Figures 5.2.5, 5.2.7 and 5.2.8** show that for the different mean heights of $h_M = 0.1, 0.2, 0.3$, the macro-scale eigenvalues λ_p^{NE1} of the Spectral patch scheme (large blue circles within macro-scale clusters identified in figure caption), agree with the macro-scale eigenvalues $\lambda_{m\delta}^{NE1}$ (small red circles) of the fine-grid full-domain micro-scale system. This macro-scale agreement of eigenvalues $\lambda_p^{NE1}, \lambda_{m\delta}^{NE1}$ indicates that the patch schemes are accurate for macro-scale turbulent shallow water flow for different mean heights.

Give physical explanation, that the turbulent bed drag is essential constant in h_M , but that the effective viscosity is quadratic with depth (maybe due to increased turbulent mixing because the bed is not so constraining??)

- As with the viscous shallow water flow, while increasing h_M from 0.1 to 0.3, both the micro-scale and macro-scale eigenvalues move to the left, taking larger negative real parts. That is, increasing h_M increases both the micro-scale and macro-scale dissipation.
- In contrast to the viscous shallow water flow, the spectral gap decreases with increasing mean height h_M . Whereas both the micro-scale and macro-scale dissipation increases with increasing h_M , the micro-scale dissipation increases at larger rate, same as in viscous shallow water flow. But, increasing h_M also pushes some of the micro-scale eigenvalues (non-dissipating micro-scale modes) to the right (e.g., clusters 5, 6, 7 in **Figs. 5.2.7** and **5.2.8**). Hence, the spectral gap decreases with increasing mean height h_M . For example, in **Figs. 5.2.5, 5.2.7** and **5.2.8** for mean heights $h_M = 0.1, 0.2, 0.3$, the corresponding spectral gaps are 35, 12, 5.6. Unlike the increasing spectral gap with increasing h_M for the viscous shallow water flow in p. 194 of §4.2.6 for some combinations of parameters, this increasing spectral gap

Better to give a physical explanation than to repeat that it is "unlike viscous..."

Figure 5.2.7: Spectral staggered patch scheme ($N = 10, n = 10$) eigenvalues for turbulent shallow water flow for $(h_M, u_M, v_M) = (0.2, 1, 0)$. The macro-scale eigenvalues λ_p^{NE1} clusters 1–6 agree with macro-scale eigenvalues $\lambda_{m\delta}^{NE1}$. Increasing h_M decreases spectral gap (Figs. 5.2.5, 5.2.7 and 5.2.8).

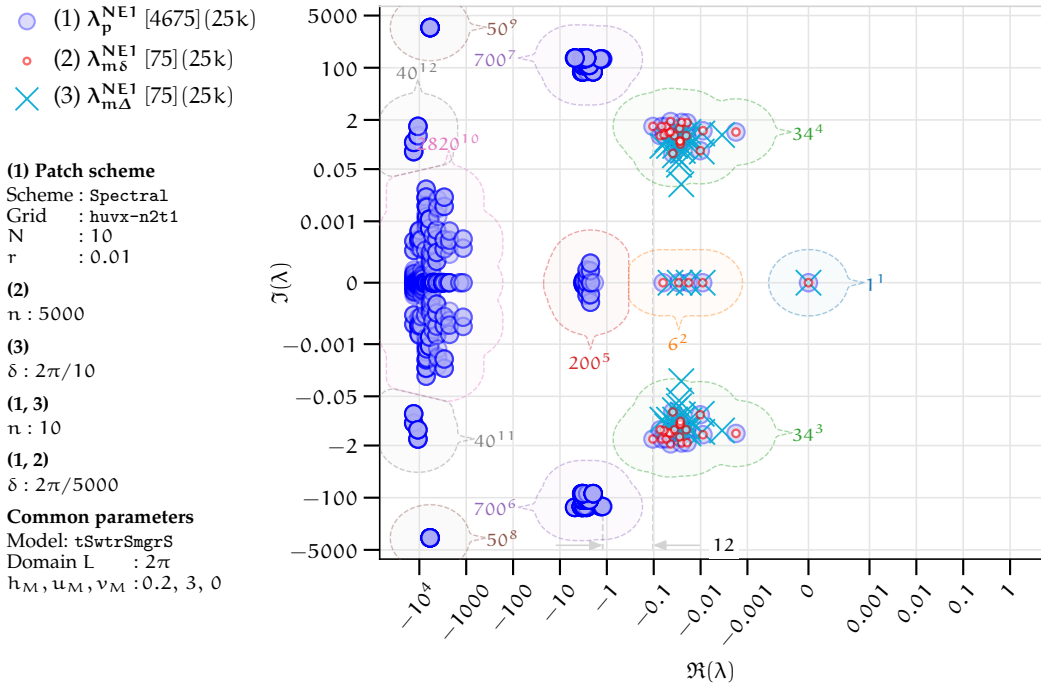
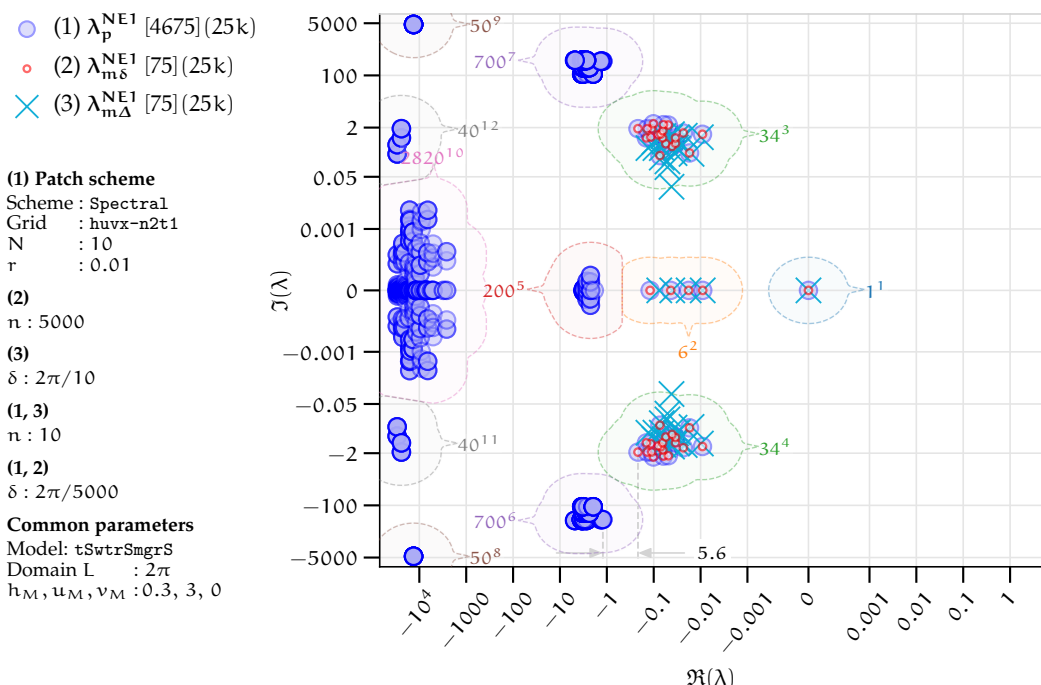


Figure 5.2.8: Spectral staggered patch scheme ($N = 10, n = 10$) eigenvalues for turbulent shallow water flow for $(h_M, u_M, v_M) = (0.3, 1, 0)$. The macro-scale eigenvalues λ_p^{NE1} in clusters 1–6 agree with macro-scale eigenvalues $\lambda_{m\delta}^{NE1}$. Increasing h_M decreases spectral gap (Figs. 5.2.5, 5.2.7 and 5.2.8).



~~with increasing h_M is the most prevalent trend among the various combinations of mean velocity h_M , u_M and patch scale ratio r . In general increasing h_M increases or decreases spectral gap depending upon the combinations of the grid parameters (N , n , r) and system parameters (Re , h_M , u_M).~~

The last two paragraphs demonstrate that for different linearisation points (h_M, u_M, v_M) , the macro-scale eigenvalues λ_p^{NE1} of the Spectral patch scheme agree with the macro-scale eigenvalues $\lambda_{m\delta}^{NE1}$ of the fine-grid full-domain micro-scale system. This agreement of the Spectral patch scheme macro-scale eigenvalues with those of the fine-grid full-domain system, is exact (within numerical roundoff errors). The polynomial patch scheme macro-scale eigenvalues also agree with those of the fine-grid full-domain system, but to a varying degree of accuracy ([§5.4](#) on consistency gives more details). Thus, the *staggered patch schemes are accurate for macro-scale turbulent shallow water flow, about different linearisation points*. [Section 5.4](#) on the consistency of the staggered patch schemes, establish the accuracy for wider range of parameters such as h_M , u_M , N , r , n .

5.3 Staggered patch schemes are not artificially unstable for appropriate patch grids

Similar to [§4.4](#) for viscous shallow water flows, a detailed study of the patch scheme eigenvalues shows that the staggered patch schemes are not artificially unstable for appropriate grid parameters. This section explains some notable trends.

For sufficiently large number of sub-patch micro-grid intervals $n \geq 10$, and sufficiently small patch scale ratio $r \lesssim 0.01$, the patch schemes do not have any artificial instability.

- [Figures 5.3.1](#) and [5.3.2](#) show the patch scheme eigenvalues for patch scale ratio $r = 0.01, 0.1$ respectively keeping all other parameters the same. [Figures 5.3.1](#) and [5.3.2](#) illustrate that using appropriately small patch scale ratio removes artificial instability. With few exceptions, the trend of decreasing artificial instability with decreasing patch scale ratio r hold in general also for other grid and system parameters such as N , n , h_M , u_M , v_M .
- Unlike for the viscous shallow water flows in [§4.4](#), for $n = 6$ sub-patch micro-grid intervals, decreasing patch scale ratio $r \in [0.0001, 0.1]$ does not remove the artificial instability of staggered patch schemes. That

Figure 5.3.1: Spectral staggered patch scheme ($N = 10, n = 10, r = 0.01$) eigenvalues λ_p^{NE1} for turbulent shallow water flow for $(h_M, u_M, v_M) = (0.1, 0.5, 0)$. Eigenvalues λ_p^{NE1} and $\lambda_{m\delta}^{NE1}$ agree for macro-scale modes in clusters 1–8. No artificial instability as in Fig. 5.3.2 for $r = 0.1$.

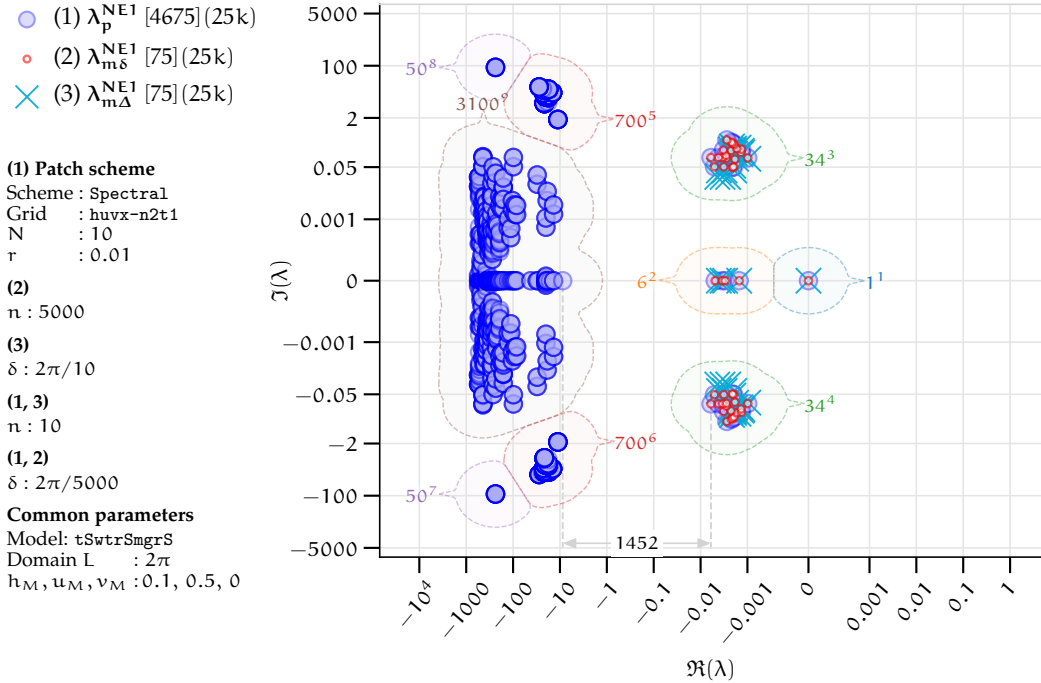


Figure 5.3.2: Spectral staggered patch scheme ($N = 10, n = 10, r = 0.1$) eigenvalues λ_p^{NE1} for turbulent shallow water flow for $(h_M, u_M, v_M) = (0.1, 0.5, 0)$. Artificially unstable sub-patch micro-scale wave modes in the clusters 1, 2.

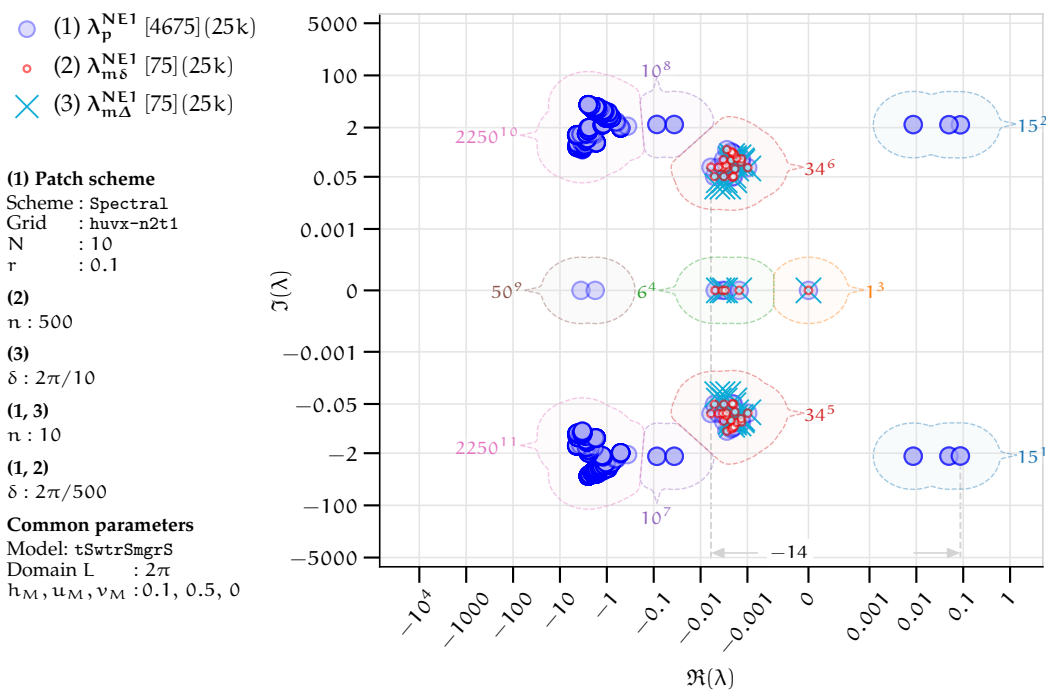
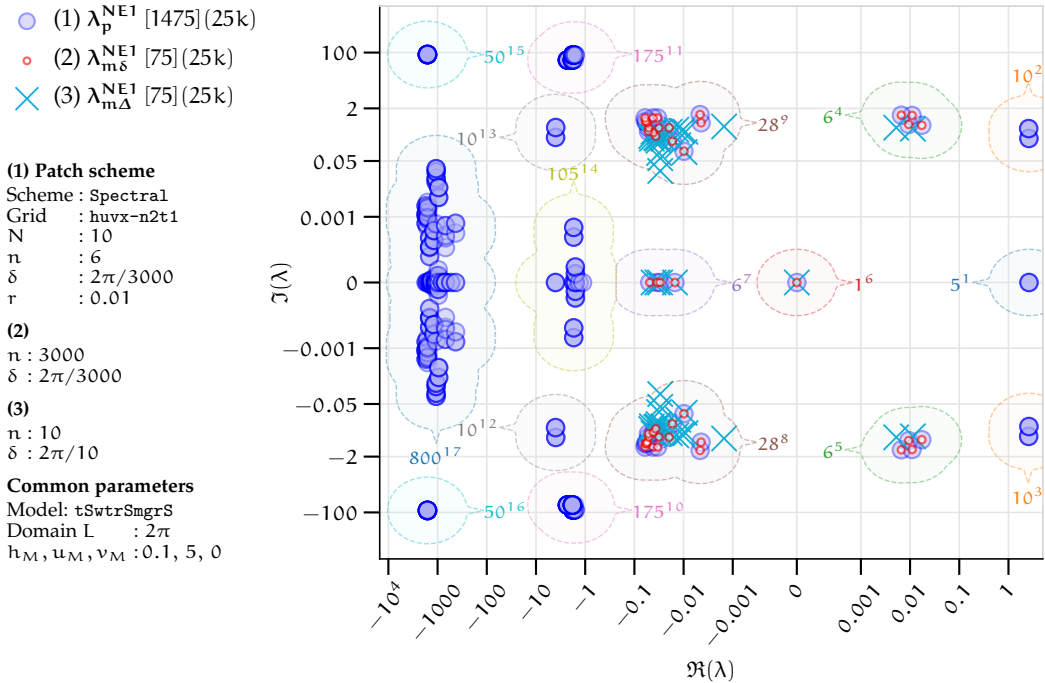


Figure 5.3.3: Spectral staggered patch scheme ($N = 10, n = 6, r = 0.01$) eigenvalues λ_p^{NE1} for turbulent shallow water flow for $(h_M, u_M, v_M) = (0.1, 5, 0)$. Artificially unstable sub-patch micro-scale wave modes in clusters 1–3; there is no such artificially unstable modes in Fig. 5.2.6 for $n = 10$.

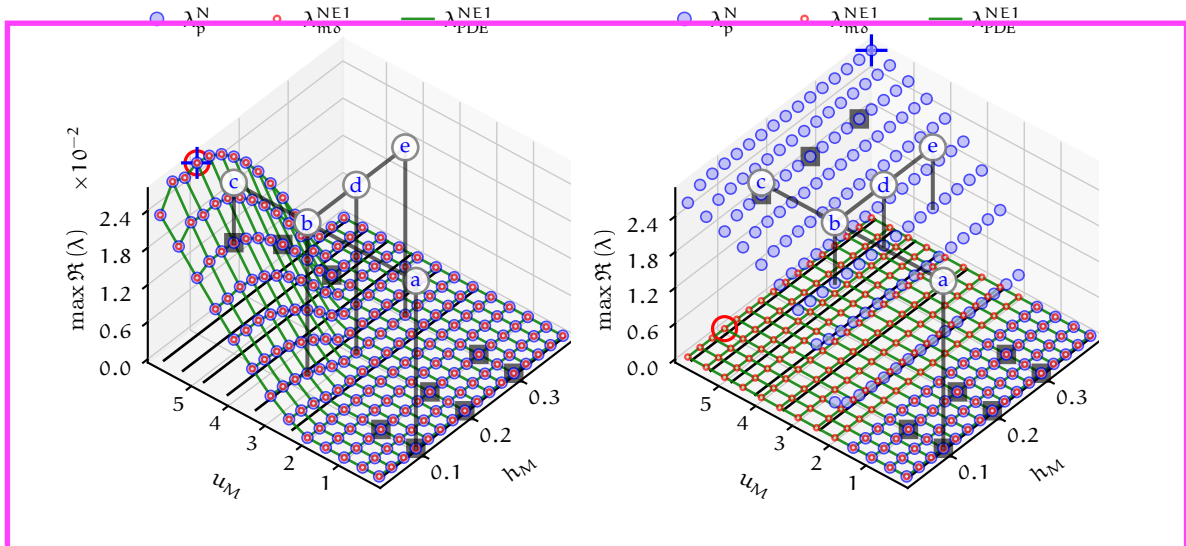


is, for the turbulent shallow water flows, the staggered patch schemes require at least $n = 6$ sub-patch micro-grid intervals. For example, Fig. 5.3.3 for $n = 6$ shows the eigenvalues of the artificially unstable modes in clusters 1–3; there is no such artificially unstable modes in Fig. 5.2.6 (of §5.2.4) for $n = 10$, keeping all other parameters the same.

The previous paragraph shows two examples for the stability trends of the patch schemes for the turbulent shallow water flows via two specific mean flows (linearisation points). Figure 5.3.4 plots the maximum real parts of the Spectral patch scheme for $n = 10$ (left) and $n = 6$ (right) for different mean flow (h_M, u_M) where $h_M \in \{0.025, 0.05, \dots, 0.4\}$ and $u_M \in \{0.05, 0.5, \dots, 6\}$. Figure 5.3.4 shows that the Spectral patch scheme is artificially unstable for $n = 6$, that is, $\max \Re(\lambda_p^N) > \max \Re(\lambda_{m\delta}^{NE1}) \geq 0$ for $u_M \gtrsim 1.5$; but there is no such artificial instability for $n = 10$. This trend of being artificially unstable for $n = 6$, but not for $n = 10$, holds for different patch scale ratio $r \in \{0.0001, 0.001, 0.01\}$ and also for the polynomial patch schemes. That is, for $n \geq 10$ and sufficiently small patch scale ratio $r \lesssim 0.01$, the staggered patch schemes do not have any artificial instability.

Figure 5.3.4: Maximum real part of the eigenvalues for, λ_p^N of Spectral patch scheme ($N = 10, r = 0.01$), $\lambda_{m\delta}^{NE1}$ of full-domain micro-scale system, and λ_{PDE}^{NE1} of the turbulent shallow water PDEs, about different mean flow (h_M, u_M) with $v_M = 0$ and bed inclination $\theta = 0^\circ$. For $n = 6$ (right), patch scheme has artificial instability for $u_M \gtrsim 1.5$. The seven black lines along h_M indicate equilibrium solution (5.1.5) for $\theta = 0, 1, \dots, 7$. Section 5.4 establish the consistency of the patch schemes for the linearisation points indicated by black squares. Points a-e correspond to the complex plane plots of eigenvalues in Figs. 5.2.4 to 5.2.8.

(a) *No artificial instability* for $n = 10$; (b) *Artificial instability* for $n = 6$; that is, that is, $\max \Re(\lambda_p^N) \approx \max \Re(\lambda_{m\delta}^{NE1}) \geq 0$. $\max \Re(\lambda_p^N) > \max \Re(\lambda_{m\delta}^{NE1}) \geq 0$. Peak values (blue plus and red circle) are $\max \Re(\lambda_p^N) = 2.81$ (blue plus) and $\max \Re(\lambda_{m\delta}^{NE1}) = 0.027 = \max \Re(\lambda_{PDE}^{NE1})$.



Better if these used
the same vertical axis.
What about log-axis?
Cut-off at say 1e-3.

5.4 Staggered patch schemes are consistent

This section shows that the staggered patch schemes are consistent with the full-domain micro-scale system of turbulent shallow water flows, via convergence of the patch scheme eigenvalues. Similar to §4.5 for viscous shallow water flows, we performed a detailed study of the eigenvalue convergence with decreasing macro-grid interval Δ using the eigenvalues for the 2 160 combinations of the parameters listed in Table 5.4.1. Based on such the detailed study, omitting the eigenvalues convergence plots such as Fig. 4.5.3 in §4.5, the following two paragraphs summarise the key overall characteristics.

The last two paragraphs in §5.2.4 show that for turbulent shallow water flows about different linearisation points (h_M, u_M, v_M) , the macro-scale eigenvalues λ_p^{NE1} of the Spectral patch scheme agree with the macro-scale eigenvalues $\lambda_{m\delta}^{NE1}$ of the fine-grid full-domain micro-scale system. Except for two edge cases of very small patch scale ratio $r \lesssim 0.0001$ and nearly stagnant water with very small velocity $u_M \lesssim 0.05$, this agreement of eigenvalues between λ_p^{NE1} and $\lambda_{m\delta}^{NE1}$ is exact (within numerical roundoff errors), without any dependence on macro-grid interval Δ . That is, as in §4.5.1 for viscous shallow water flows, also for the turbulent shallow water flows, in general, *the Spectral patch scheme is uniformly consistent with the full-domain system, without any strong dependence on the macro-grid interval Δ .*

Similar to the Spectral patch scheme, the four polynomial patch schemes' macro-scale eigenvalues also agree with those of the fine-grid full-domain system to a varying degree. That is, except for two edge cases of very small patch scale ratio $r \lesssim 0.0001$ and nearly stagnant water with very small velocity $u_M \lesssim 0.05$, the eigenvalues of the polynomial patch schemes are increasingly accurate, that is converge, with decreasing macro-grid interval Δ . Specifically, as in §4.5.2 for viscous shallow water flows, also for the turbulent shallow water flows, in general, *the polynomial patch schemes are consistent with the full-domain system, for decreasing macro-grid interval Δ , with the same order p as that of the polynomial interpolation.*

Thus, the staggered patch schemes are consistent with the full-domain micro-scale system for macro-scale turbulent shallow water flow, about different linearisation points.

The previous sentence says this.

clarify as what varies,
\Delta decreasing I
presume

Clarify what has the
same order? Is it
with "errors =
 $O(\Delta^p)$ " ??

"converge" to what?

Table 5.4.1: Section 5.4 establishes the consistency of the patch schemes using eigenvalues for all the 2160 combinations (cartesian product) of the listed parameters.

Patch schemes	Spectral, Square-p2, Square-p4, Square-p6, and Square-p8
Mean height	$h_M \in \{0.1, 0.2, 0.3\}$
Mean velocity	$u_M \in \{0.05, 1, 5\}$, $v_M = 0$ (S4.6 on frame invariance show the flow direction is immaterial) does it?
Macro-grid intervals	$N \in \{6, 10, 14, 18, 22, 26\}$
Sub-patch micro-grid intervals	$n \in \{6, 10\}$
Patch scale ratio	$r \in \{0.0001, 0.001, 0.01, 0.1\}$

5.5 Staggered patch scheme time simulations of turbulent shallow water flows

This subsection demonstrates the accuracy and the effectiveness of the staggered patch schemes by numerically simulating a turbulent roll wave. The patch schemes accurately simulate the localised nearly discontinuous macro-scale turbulent roll wave emerging from the initial condition of a moving Gaussian hump.

As in §§3.7.5 and 4.7.4 for the general linear wave and viscous shallow water flows, also for the turbulent shallow water flow *this subsection uses the BS3 ODE integrator for the time simulation* with the relative and absolute error tolerances of 10^{-3} and 10^{-6} respectively. The BS3 is a lower oder Bogacki–Shampine 3/2 method (Bogacki and L. Shampine 1989; L. F. Shampine and Reichelt 1997), similar to the ode23 of MATLAB (DifferentialEquations.jl 2021).

Figures 5.5.1 to 5.5.3 show the time evolution of a turbulent roll wave (height h and velocities u, v) over a bed inclined 1° downwards along downstream, emerging from the initial condition of a moving Gaussian hump

Should be $(x+1)^2$ and y^2 omit "4" $h_0(x, y) = 0.1 + 0.05 \exp \left[-(x + 1)/(2 \cdot 0.5)^2 - y/(2 \cdot 2)^2 \right]$, (5.5.1a)

$u_0(x, y) = 2.4 + 0.5 \exp \left[-(x + 1)/(2 \cdot 0.5)^2 - y/(2 \cdot 2)^2 \right]$, (5.5.1b)

$v_0(x, y) = 0$. (5.5.1c)

Is $h_M=0.1$, $u_M=2.4$ and equilibrium flow? Clarify.

Figures 5.5.1 to 5.5.3 show that the time evolution using the Spectral patch scheme (colour-coded ribbons, with $N = 26$, $n = 10$, and $r = 0.1$) agrees rea-

Clarify that in each figure time advances through $t=0, 18, \dots$ from top-left sub-plot to bottom-right.

clarify/remind that in the patch scheme, the computations are only done in the small squares of the intersections of the ribbons, the ribbons are only to enhance clarity.

what happens if u_0 is constant (say 2.4) ? and/or y-structure a bit thinner say $y^{2/3^2}$ or $y^{2/2^2}$?

Figure 5.5.1: Time evolution of a turbulent roll wave (height h), emerging from the initial condition of a moving Gaussian hump (5.5.1), using Spectral patch scheme (colour-coded ribbons, with $N = 26$, $n = 10$, and $r = 0.1$) agrees reasonably with that of the fine-grid full-domain system (grey mesh).

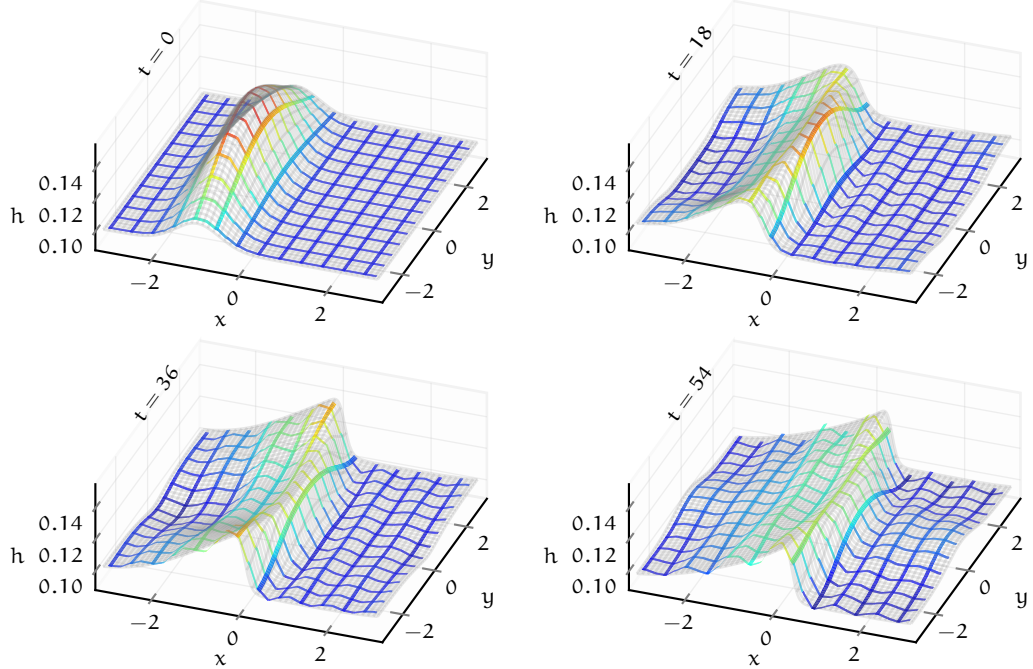


Figure 5.5.2: Time evolution of a turbulent roll wave (height u), emerging from the initial condition of a moving Gaussian hump (5.5.1), using Spectral patch scheme (colour-coded ribbons, with $N = 26$, $n = 10$, and $r = 0.1$) agrees reasonably with that of the fine-grid full-domain system (grey mesh).

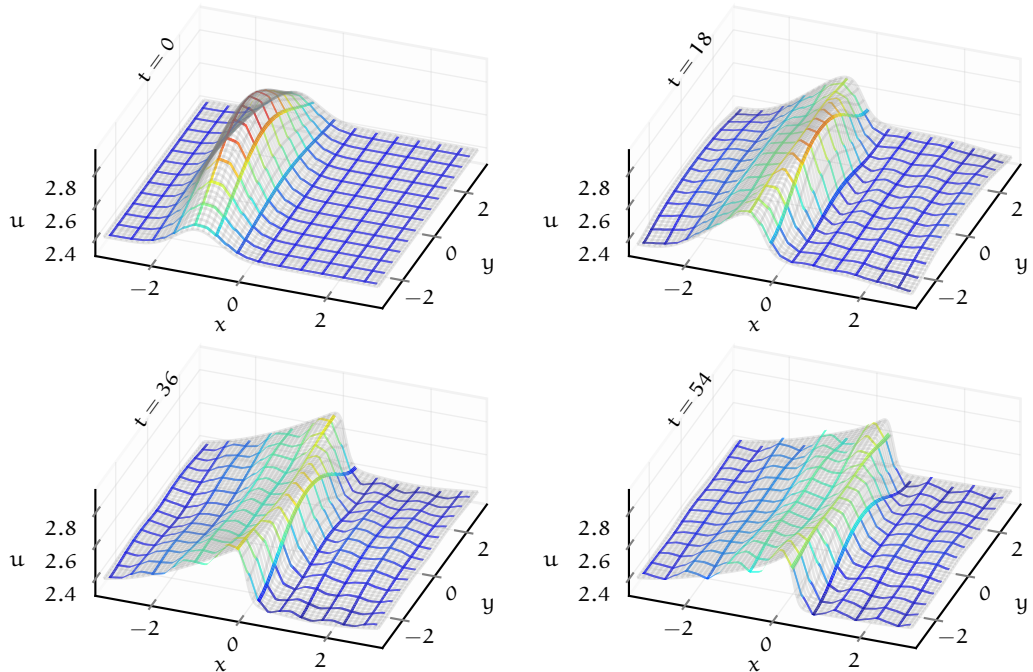
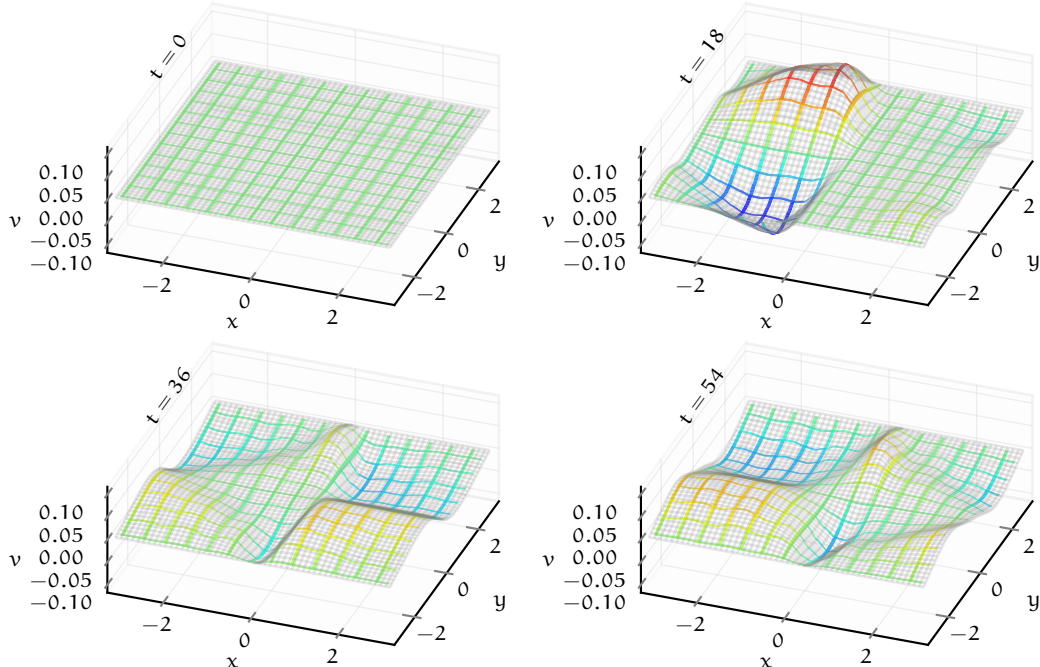


Figure 5.5.3: Time evolution of a turbulent roll wave (height v), emerging from the initial condition of a moving Gaussian hump (5.5.1), using Spectral patch scheme (colour-coded ribbons, with $N = 26$, $n = 10$, and $r = 0.1$) agrees reasonably with that of the fine-grid full-domain system (grey mesh).

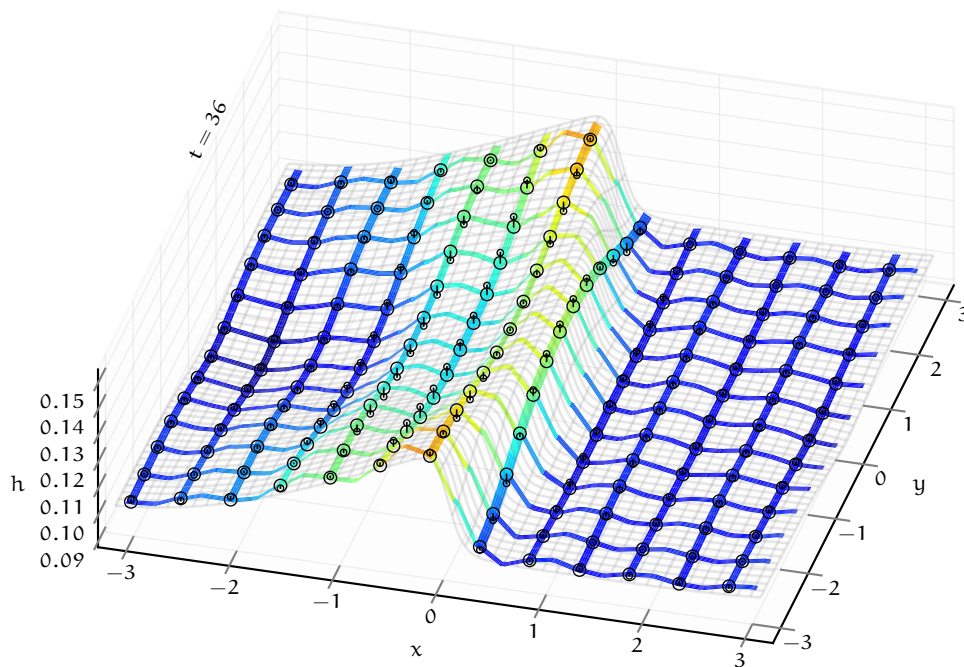


sonably with that of the 500×500 fine-grid full-domain system (grey mesh). The grey mesh of full-domain system plots fewer grid lines, skipping many lines for visual clarity. The colour-coded ribbons of the patch scheme in Fig. 5.5.1 consist of all the lines (along the coordinate axes x and y) passing through all the h nodes within all the patches; similarly Figs. 5.5.2 and 5.5.3 for u , v nodes within all the patches respectively. Although the true patch scale ratio is $r = 0.1$, the patches are enlarged for visual clarity so that the ribbons appear wider.

specify how many precisely.

Figure 5.5.4 shows an enlarged snapshot of the same roll wave as in left-bottom of Fig. 5.5.1 at $t = 36$, with more visual detail and clarity. In Fig. 5.5.4, the solution h of the fine-grid full-domain micro-scale system are linearly interpolated using nearest four values to the centres of the respective $h/u/v$ -centred patches, illustrated by small black circles. The large circles are the patch scheme solution $h/u/v$. That the non concentric large and small black circles are offset only slightly, shows that the discrepancy between the solutions of the patch scheme and the fine-grid full-domain system is small. The undulations in the patch scheme solution, away from the

Figure 5.5.4: Snapshot of the emergent viscous roll wave (height h at $t = 31$), from the initial condition of simple progressive wave (5.5.1), using Square-p6 patch scheme (colour-coded ribbons, with $N = 22$, $n = 6$, and $r = 0.1$) agrees very closely with that of the fine-grid full-domain system (grey mesh). Black circles on h -centred patches show the discrepancy.



[10] TODO. Move this to the Chapter 1 to arouse some early interest for the reader.

For Ch.1, better to plot a simpler version of this. Just have the micro-scale grid solution, and the square patches. No ribbons. No circles. No dots.

steep rise of the roll wave are due to the nearly discontinuous jump in the height. These undulations decrease with increasing number of patches (macro-grid intervals). The small discrepancy at $t = 36$ (distance between centres of non concentric black circles) also includes the accumulation of the ODE integrator error ~~due to several time iterations before $t = 36$~~ . Thus, for sufficient number of macro-grid intervals and accurate patch coupling, *patch schemes accurately simulate the turbulent shallow water flows*.

Patch scheme simulations of turbulent shallow water flows require larger number of sub-patch micro-grid intervals n , compared to the viscous shallow water flows. As opposed to $n = 6$ sub-patch micro-grid intervals in the time simulations of §§4.7.4 and 4.7.5 for the viscous shallow water flows, the time simulation in the previous paragraphs of this subsection use $n = 10$ sub-patch micro-grid intervals. This larger $n = 10$ is a necessity for the turbulent shallow water flows for mean velocity $u_M \gtrsim 1.5$ to avoid ~~any~~ artificial instability of the staggered patch schemes. *Figure 5.3.4* in p. 310 of §5.3 shows the artificial instability of the patch scheme for $n = 6$, via the maximum real parts of the patch scheme eigenvalues.

The practical issues of patch scheme simulation explained in §4.4.1 for the viscous shallow water flows also applies for the turbulent shallow water flows, perhaps ~~relatively~~ ^{restrictively?} more strongly. For example, the patch schemes for the turbulent shallow water flows are stiffer compared to the viscous shallow water flows. For example, the impacts of the stiffness and the artificial instability of the patch schemes for the turbulent shallow water flows, are relatively more severe than the viscous shallow water flows, especially for small patch scale ratio $r \lesssim 0.1$. Yet, with appropriate patch grids and the ODE integrators such as projective integrator (Gear and Kevrekidis 2003), the staggered patch schemes simulate the macro-scale turbulent shallow water flows accurately and efficiently.

You do not have any evidence for the efficacy of projective integration in this sort of context, so omit comment.

Maybe finish with something like “for a broad range of parameters this chapter shows that the patch scheme can effectively simulate and predict Smagorinsky-turbulence shallow water waves.

Leave “projective integration” to a comment in the conclusion.

Chapter 6

Conclusion

TODO

Bibliography

- Balmforth, N. J. and S. Mandre (2004). "Dynamics of roll waves". In: *Journal of Fluid Mechanics* 514, pp. 1–33. DOI: [10.1017/S0022112004009930](https://doi.org/10.1017/S0022112004009930) (cit. on pp. 153, 259, 272).
- Bezanson, Jeff, Alan Edelman, Stefan Karpinski, and Viral B. Shah (2017). "Julia: A Fresh Approach to Numerical Computing". In: *SIAM Review* 59.1, pp. 65–98. DOI: [10.1137/141000671](https://doi.org/10.1137/141000671) (cit. on p. 12).
- Bogacki, P. and L.F. Shampine (1989). "A 3(2) pair of Runge - Kutta formulas". In: *Applied Mathematics Letters* 2.4, pp. 321–325. ISSN: 0893-9659. DOI: [https://doi.org/10.1016/0893-9659\(89\)90079-7](https://doi.org/10.1016/0893-9659(89)90079-7) (cit. on pp. 141, 272, 312).
- Bunder, J. E., J. Divahar, I. G. Kevrekidis, Trent W. Mattner, and A.J. Roberts (2020). "Large-scale simulation of shallow water waves via computation only on small staggered patches". In: *International Journal for Numerical Methods in Fluids*. DOI: [10.1002/fld.4915](https://doi.org/10.1002/fld.4915) (cit. on pp. 23, 138, 272, 287).
- Cao, Meng and A. J. Roberts (June 2016). "Modelling suspended sediment in environmental turbulent fluids". In: *Journal of Engineering Mathematics* 98.1, pp. 187–204. ISSN: 1573-2703. DOI: [10.1007/s10665-015-9817-7](https://doi.org/10.1007/s10665-015-9817-7) (cit. on pp. 283, 284, 291).
- Chicone, Carmen (2006). *Ordinary differential equations with applications*. 2ed. Texts in Applied Mathematics. Springer. ISBN: 0387307699, 9780387307695. DOI: [10.1007/0-387-35794-7](https://doi.org/10.1007/0-387-35794-7) (cit. on p. 99).
- Cohen, S., A. Raney, D. Munasinghe, J. D. Loftis, A. Molthan, J. Bell, L. Rogers, J. Galantowicz, G. R. Brakenridge, A. J. Kettner, Y.-F. Huang, and Y.-P. Tsang (2019). "The Floodwater Depth Estimation Tool (FwDET v2.0) for improved remote sensing analysis of coastal flooding". In: *Natural Hazards and Earth System Sciences* 19.9, pp. 2053–2065. DOI: [10.5194/nhess-19-2053-2019](https://doi.org/10.5194/nhess-19-2053-2019) (cit. on p. 290).

- Dean, Robert G and Robert A Dalrymple (1991). *Water Wave Mechanics for Engineers and Scientists*. World Scientific. DOI: [10.1142/1232](https://doi.org/10.1142/1232) (cit. on p. 42).
- DifferentialEquations.jl (Aug. 27, 2021). *Solver Algorithms: ODE Solvers*. Version 6.19. URL: https://diffeq.sciml.ai/v6.19/solvers/ode_solve/ (cit. on pp. 12, 140, 141, 272, 278, 312).
- Emereuwa, Chigoziem A. (2020). "Mathematical homogenization and stochastic modeling of energy storage systems". In: *Current Opinion in Electrochemistry*. ISSN: 2451-9103. DOI: [10.1016/j.coelec.2020.01.009](https://doi.org/10.1016/j.coelec.2020.01.009) (cit. on p. 7).
- Ferziger, Joel H., Milovan Peric, and Robert L. Street (2020). *Computational Methods for Fluid Dynamics*. Cham, Switzerland: Springer International Publishing, p. 596. ISBN: 9783319996912. DOI: [10.1007/9783319996936](https://doi.org/10.1007/9783319996936) (cit. on pp. 114, 241).
- Franci, Alessandro, Massimiliano Cremonesi, Umberto Perego, and Eugenio Oñate (2020). "A Lagrangian nodal integration method for free-surface fluid flows". In: *Computer Methods in Applied Mechanics and Engineering* 361, p. 112816. ISSN: 0045-7825. DOI: [10.1016/j.cma.2019.112816](https://doi.org/10.1016/j.cma.2019.112816) (cit. on p. 9).
- Gear, C. W. and I. G. Kevrekidis (2003). "Projective Methods for Stiff Differential Equations: Problems with Gaps in Their Eigenvalue Spectrum". In: *SIAM Journal on Scientific Computing* 24.4, pp. 1091–1106. DOI: [10.1137/S1064827501388157](https://doi.org/10.1137/S1064827501388157) (cit. on pp. 281, 316).
- Ghobarah, Ahmed, Murat Saatcioglu, and Ioan Nistor (2006). "The impact of the 26 December 2004 earthquake and tsunami on structures and infrastructure". In: *Engineering Structures* 28.2, pp. 312–326. ISSN: 0141-0296. DOI: [10.1016/j.engstruct.2005.09.028](https://doi.org/10.1016/j.engstruct.2005.09.028) (cit. on p. 290).
- Goldberg, David (1991). "What every computer scientist should know about floating-point arithmetic". In: *ACM Computing Surveys (CSUR)* 23.1, pp. 5–48 (cit. on pp. 89, 96, 202, 210).
- Griffiths, Graham W. and William E. Schiesser (2011). *Traveling Wave Analysis of Partial Differential Equations: Numerical and Analytical Methods with Matlab and Maple*. 1st ed. Academic Press. ISBN: 9780123846525. DOI: [10.1016/C2009-0-64536-0](https://doi.org/10.1016/C2009-0-64536-0) (cit. on pp. 47, 49).

- Grooms, Ian and Keith Julien (Nov. 2018). "Multiscale models in geo-physical fluid dynamics". In: *Earth and Space Science*. DOI: [10.1029/2018EA000439](https://doi.org/10.1029/2018EA000439) (cit. on p. 7).
- Hairer, Ernst, Gerhard Wanner, and Syvert P. Nørsett (1993). *Solving Ordinary Differential Equations I*. Berlin, Germany: Springer. ISBN: 9783540788621. DOI: [10.1007/978-3-540-78862-1](https://doi.org/10.1007/978-3-540-78862-1) (cit. on p. 99).
- Haynes, W.M., David R. Lide, and Thomas J. Bruno (2016). *CRC Handbook of Chemistry and Physics*. Ed. by W.M. Haynes, David R. Lide, and Thomas J. Bruno. 97th. ISBN: 9781498754293 (cit. on p. 166).
- Heister, Timo, Leo G. Rebholz, and Fei Xue (2019). *Numerical Analysis*. De Gruyter. DOI: [doi:10.1515/9783110573329](https://doi.org/10.1515/9783110573329) (cit. on pp. 96, 210).
- Hinch, E. J. (Apr. 2020). *Think Before You Compute. A Prelude to Computational Fluid Dynamics*. Cambridge, England, UK: Cambridge University Press. ISBN: 978-1-10847954-7. DOI: [10.1017/9781108855297](https://doi.org/10.1017/9781108855297) (cit. on pp. 47, 49).
- Hyman, J. M. (May 2005). "Patch dynamics for multiscale problems". In: *Computing in Science Engineering* 7.3, pp. 47–53. ISSN: 1521-9615. DOI: [10.1109/MCSE.2005.57](https://doi.org/10.1109/MCSE.2005.57) (cit. on p. 8).
- Intergovernmental Oceanographic Commission, International Tsunami Information Centre (2014). *Tsunami, The Great Waves, Revised Edition*. URL: http://itic.ioc-unesco.org/images/stories/awareness_and_education/great_waves/great_waves_en_low_v14.pdf (cit. on p. 290).
- Kevrekidis, I. G., C. W. Gear, and G. Hummer (2004). "Equation-free: The computer-aided analysis of complex multiscale systems". In: *AIChE Journal* 50.7, pp. 1346–1355. DOI: [10.1002/aic.10106](https://doi.org/10.1002/aic.10106) (cit. on p. 8).
- Kevrekidis, I. G., C. W. Gear, J. M. Hyman, P. G. Kevrekidis, O. Runborg, and C. Theodoropoulos (2003). "Equation-free, coarse-grained multiscale computation: enabling microscopic simulators to perform system-level analysis". In: *Commun. Math. Sci.* 1.4, pp. 715–762 (cit. on p. 9).
- Kevrekidis, I. G. and Giovanni Samaey (2009). "Equation-Free Multiscale Computation: Algorithms and Applications". In: *Annual Review of Physical Chemistry* 60.1. PMID: 19335220, pp. 321–344. DOI: [10.1146/annurev.physchem.59.032607.093610](https://doi.org/10.1146/annurev.physchem.59.032607.093610) (cit. on p. 8).
- Maclean, John, J. E. Bunder, and A. J. Roberts (Aug. 2021). "A toolbox of equation-free functions in Matlab/Octave for efficient system level

- simulation". In: *Numerical Algorithms* 87.4, pp. 1729–1748. ISSN: 1572-9265. DOI: [10.1007/s11075-020-01027-z](https://doi.org/10.1007/s11075-020-01027-z) (cit. on pp. 280, 281).
- Mehaute, Bernard Le (1976). *An Introduction to Hydrodynamics and Water Waves*. 1st ed. Springer Study Edition. Springer Berlin Heidelberg. ISBN: 9783642855696. DOI: [10.1007/9783642855672](https://doi.org/10.1007/9783642855672) (cit. on p. 42).
- Moler, Cleve B. (2004). *Numerical Computing with Matlab*. Society for Industrial and Applied Mathematics. DOI: [10.1137/1.9780898717952](https://doi.org/10.1137/1.9780898717952) (cit. on p. 281).
- Johansson, Fredrik et al. (Dec. 2018). *mpmath: a Python library for arbitrary-precision floating-point arithmetic (version 1.2.1)*. URL: <http://mpmath.org/> (cit. on p. 247).
- Rackauckas, Christopher and Qing Nie (2017). "DifferentialEquations.jl—a performant and feature-rich ecosystem for solving differential equations in julia". In: *Journal of Open Research Software* 5.1. DOI: [10.5334/jors.151](https://doi.org/10.5334/jors.151) (cit. on pp. 12, 13, 140).
- Roberts, A. J. and I. G. Kevrekidis (2005). "Higher order accuracy in the gap-tooth scheme for large-scale dynamics using microscopic simulators". In: *ANZIAM Journal* 46.0, pp. 637–657. ISSN: 1446-8735. URL: <https://journal.austms.org.au/ojs/index.php/ANZIAMJ/article/view/981> (cit. on p. 8).
- (2007). "General Tooth Boundary Conditions for Equation Free Modeling". In: *SIAM Journal on Scientific Computing* 29.4, pp. 1495–1510. DOI: [10.1137/060654554](https://doi.org/10.1137/060654554) (cit. on p. 8).
- Roberts, A. J. and Zhenquan Li (2006). "An accurate and comprehensive model of thin fluid flows with inertia on curved substrates". In: *Journal of Fluid Mechanics* 553, pp. 33–73. DOI: [10.1017/S0022112006008640](https://doi.org/10.1017/S0022112006008640) (cit. on pp. 151, 153–155).
- Röbke, B.R. and A. Vött (2017). "The tsunami phenomenon". In: *Progress in Oceanography* 159, pp. 296–322. ISSN: 0079-6611. DOI: [10.1016/j.pocean.2017.09.003](https://doi.org/10.1016/j.pocean.2017.09.003) (cit. on p. 290).
- Shampine, Lawrence F. and Mark W. Reichelt (1997). "The MATLAB ODE Suite". In: *SIAM Journal on Scientific Computing* 18.1, pp. 1–22. DOI: [10.1137/S1064827594276424](https://doi.org/10.1137/S1064827594276424) (cit. on pp. 12, 141, 272, 278, 312).
- Welsh, Zachary, Matthew J. Simpson, Md Imran H. Khan, and M. A. Karim (2018). "Multiscale Modeling for Food Drying: State of the Art". In:

Comprehensive Reviews in Food Science and Food Safety 0.0. DOI: [10.1111/1541-4337.12380](https://doi.org/10.1111/1541-4337.12380) (cit. on p. 7).